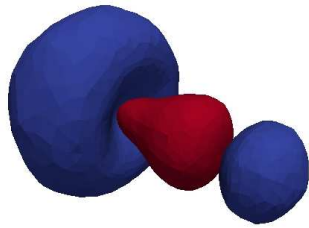


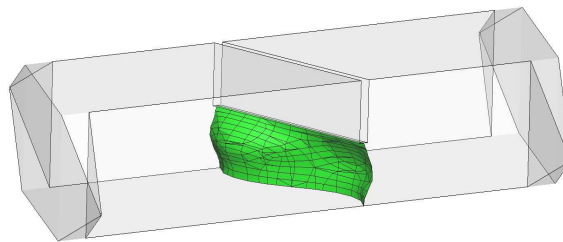
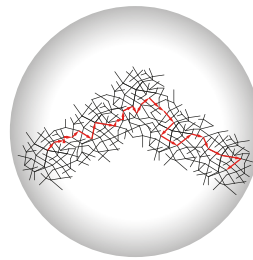
On the Computational Modeling of Micromechanical Phenomena in Solid Materials

Christian Linder

$$\left[-\frac{1}{2}\Delta + V_{\text{eff}}\right] \psi_i = \varepsilon_i \psi_i$$



$$\langle \boldsymbol{\lambda} \otimes \boldsymbol{\lambda}_0 \rangle = \frac{1}{3} \mathbf{F}$$



$$\mathbf{e}_{\boldsymbol{\lambda}}^{(10)} = (\boldsymbol{\lambda} \otimes \mathbf{s}) \mathcal{H}_{\Gamma_e^h} - \sum_{A \in \mathcal{B}_e^h} \bar{\mathbf{B}}_u^A(\boldsymbol{\lambda} \otimes \mathbf{s}) \bar{\mathbf{x}}_A$$

Bericht Nr.: I-26 (2013)
 Institut für Mechanik (Bauwesen), Lehrstuhl I
 Professor Dr.-Ing. C. Miehe
 Stuttgart 2013

On the Computational Modeling of Micromechanical Phenomena in Solid Materials

Von der Fakultät Bau- und Umweltingenieurwissenschaften
und dem “Stuttgart Research Center for Simulation Technology”
der Universität Stuttgart genehmigte Habilitationsschrift

von

Christian Linder

Hauptberichter: Prof. Dr.-Ing. habil. Christian Miehe
Mitberichter : Prof. Dr.-Ing. habil. Paul Steinmann

Tag der Einreichung: 17. Oktober 2012
Tag der mündlichen Prüfung: 29. November 2012

Institut für Mechanik (Bauwesen) der Universität Stuttgart
2013

Herausgeber:

Prof. Dr.-Ing. habil. C. Miehe

Organisation und Verwaltung:

Institut für Mechanik (Bauwesen)

Lehrstuhl I

Universität Stuttgart

Pfaffenwaldring 7

70550 Stuttgart

Tel.: +49.711.685.66378

Fax: +49.711.685.66347

© Christian Linder
Department of Civil
and Environmental Engineering
Stanford University
473 Via Ortega, Room 287
Stanford, CA 94305
Tel.: +1.650.723.2918
Fax: +1.650.723.7514

Alle Rechte, insbesondere das der Übersetzung in fremde Sprachen, vorbehalten. Ohne Genehmigung des Autors ist es nicht gestattet, dieses Heft ganz oder teilweise auf fotomechanischem Wege (Fotokopie, Mikrokopie) zu vervielfältigen.

ISBN 3-937859-14-4 (D 93 Stuttgart)

Abstract

This work aims to contribute to the research on the constitutive modeling of solid materials, by investigating three particular micromechanical phenomena on three different length scales. The first microscopic phenomenon to be considered on the macroscopic scale is the process of failure in solid materials. Its characteristic non-smoothness in the displacement field results in the need for sophisticated numerical techniques in case one aims to capture those failure zones in a discrete way. One of the few finite element based methods successfully applied to such challenging problems is the so called strong discontinuity approach, for which failure can be described within the individual finite elements. To avoid stress locking, a higher order approximation of the resulting strong discontinuities is developed in the first part of this work for both, purely mechanical as well as electromechanical coupled materials. A sophisticated crack propagation concept relying on a combination of the widely used global tracking algorithm and the computer graphics based marching cubes algorithm is employed to obtain realistic crack paths in three dimensional simulations. Secondly, materials with an inherent network microstructures such as elastomers, hydrogels, non-woven fabrics or biological tissues are considered. The development of advanced homogenization principles accounting for such microstructures is the main focus in the second part of this work to better understand the mechanical and time-dependent effects displayed by such soft materials. Finally, the incorporation of wave functions into finite element based electronic structure calculations at the microscopic scale aims to account for the fact that the properties of condensed matter as for example electric conductivity, magnetism as well as the mechanical response upon external excitations are determined by the electronic structure of a material.

Zusammenfassung

Diese Arbeit beschäftigt sich mit der konstitutiven Modellierung von Festkörpern, indem drei spezifische mikromechanische Phänomene auf drei unterschiedlichen Längenskalen analysiert werden. Der erste Teil der Arbeit befasst sich mit dem durch makroskopische Risse charakterisierten Phänomen des Materialversagens. Die dadurch resultierenden Unstetigkeiten im Verschiebungsfeld stellen eine immense Herausforderung an numerische Berechnungsverfahren dar. Eine der wenigen numerischen Methoden, die in der Lage ist diesen Anforderungen gerecht zu werden, ist die sogenannte Finite Element Methode mit eingebetteten starken Diskontinuitäten. Zur Vermeidung von Locking Phänomenen werden in dieser Arbeit neue finite Elemente mit einer höheren kinematischen Approximation der starken Diskontinuitäten für rein mechanische als auch elektromechanisch gekoppelte Materialien entwickelt. Realistische Rissfortschreitungen durch dreidimensionale Materialien werden mittels einer Kopplung von globalen Tracking Algorithmen und dem Marching Cubes Algorithmus erreicht. Im zweiten Teil dieser Arbeit werden Materialien mit netzwerkartiger Mikrostruktur, wie Elastomere, wässrige Lösungen, nicht-gewebte Textilien oder biologischen Materialien untersucht. Deren charakteristische Mikrostruktur findet Eingang in die entwickelten Homogenisierungsmethoden auf dieser mesoskopischen Skala, welche zum besseren Verständnis der mechanischen Eigenschaften solch weicher Materie führt. Schlussendlich befasst sich die Arbeit noch mit Finite Elemente basierten Elektronenstrukturberechnungen auf der mikroskopischen Skala, um deren Einfluss auf die Eigenschaft kondensierter Materien, wie jene der elektrischen Leitfähigkeit, der Magnetisierung oder auch der mechanischen Eigenschaften, zu bewerten.

Acknowledgments

The work presented in this Habilitation Thesis was carried out between 2008 and 2012, during which I was appointed as Juniorprofessor for “Micromechanics of Materials” at the Institute of Applied Mechanics in the Department of Civil and Environmental Engineering as well as at the “Stuttgart Research Center for Simulation Technology (SimTech)” at the University of Stuttgart.

I wish to express my sincere gratitude to Professor Christian Miehe. Pursuing research with him and seeing his dedication to science and education, his insight into physical phenomena of materials, and his deep knowledge of computational methods and mathematical frameworks has been a truly humbling experience. I also want to take the opportunity to thank Professor Wolfgang Ehlers for all his support. In his role as executive director of SimTech he was ensuring a perfect working environment for all the Juniorprofessors within our Excellence Cluster. I would also like to thank Professor Paul Steinmann for accepting to serve as co-referee of this thesis and for his interest in the work.

Furthermore, I want to thank Arun Raina, Volker Schauer, Mykola Tkachuk, and Xiaoxuan Zhang for being part of my “Micromechanics of Materials Research Group” at the University of Stuttgart. I have been privileged to work with each one of you. My discussions with Mykola and Volker on physical modeling and those with Arun and Xiaoxuan on computational method development have undoubtedly enriched the material presented in this work. Seeing you all excel in your academic career has been an amazing experience for me.

It has been a pleasure to know and interact with all colleagues at the Institute of Applied Mechanics. In particular, I want to thank Oliver Röhrle for his close friendship and the many stimulating discussions on science and beyond.

And finally, I want to thank my wife Sandra and my two wonderful children Lucas and Emily for enriching every second of my life. To them I owe a heartfelt gratitude for their sacrifice, encouragement, and love.

Stanford, February 2013

Christian Linder

Contents

1. Introduction	1
1.1. Modeling solids undergoing failure at the macroscopic scale	3
1.1.1. Numerical modeling of solids at failure	4
1.1.2. Numerical modeling of dynamic fracture problems	5
1.1.3. Numerical modeling of failure in electromechanical coupled materials	6
1.2. Modeling materials with network microstructures at the mesoscopic scale	7
1.2.1. Static network theories	8
1.2.2. Transient network theories	9
1.2.3. Semiflexible biopolymer network theories	10
1.2.4. Discrete network theories	12
1.2.5. Homogenized network models	13
1.3. Modeling the electronic structure of solids at the microscopic scale	14
1.4. Outline of the work	16
I Modeling solids undergoing failure at the macroscopic scale	19
2. The strong discontinuity approach for purely mechanical solids	21
2.1. Introduction	21
2.2. The purely mechanical strong discontinuity framework	23
2.2.1. Continuum modeling of failure in purely mechanical solids	23
2.2.2. Finite element modeling of failure in purely mechanical solids	25
2.3. Finite element design	29
2.3.1. Constant separation modes	29
2.3.2. Linear separation modes	31
2.4. Numerical aspects	33
2.4.1. Strong discontinuity initiation	33
2.4.2. Strong discontinuity propagation	34
2.4.3. The marching cubes algorithm	36
2.4.4. Treatment of non-planar failure surfaces	38
2.4.5. Numerical implementation	41
2.5. Numerical simulations	42
2.5.1. Single element tests	43
2.5.2. Three-point bending test	46
2.5.3. L-shape concrete specimen test	49
2.5.4. Brokenshire torsion test	52
2.5.5. Tensile test with two notches and holes	55
2.5.6. Four-point bending test with two notches	56

3. The strong discontinuity approach for electromechanical problems . . .	61
3.1. Introduction	61
3.2. The electromechanical coupled strong discontinuity framework	62
3.2.1. Continuum modeling of failure in electromechanical coupled solids .	63
3.2.2. Finite element modeling of failure in electromechanical coupled solids	72
3.3. Finite element design	75
3.3.1. Constant separation mode	76
3.3.2. Linear separation modes	77
3.4. Numerical aspects	79
3.4.1. Strong discontinuity initiation	79
3.4.2. Strong discontinuity propagation	80
3.4.3. Numerical implementation	80
3.5. Effect of electric displacement saturation	82
3.5.1. The exponential electric displacement saturation model	83
3.5.2. Effect of electric displacement saturation on the complex variable solution of a crack in an infinite medium	85
3.5.3. The exponential electric displacement saturation model for ferro- electric ceramics	92
3.6. Representative numerical simulations	94
3.6.1. Electric displacement saturation for ferroelectric ceramics	95
3.6.2. Fracture in piezoelectric ceramics - Single element tests	97
3.6.3. Fracture in piezoelectric ceramics - Compact tension test	100
3.6.4. Fracture in piezoelectric ceramics - Three point bending test	106
3.6.5. Fracture in piezoelectric ceramics - 3D simulations	113
II Modeling materials with network microstructures at the mesoscopic scale	115
4. The maximal advance path constraint	117
4.1. Introduction	117
4.2. Statistical description of random networks	119
4.3. The maximal advance path constraint	121
4.4. Network relaxation and homogenized response at equilibrium	126
4.5. Predicted non-affine microdeformation of flexible and stiff networks	129
4.5.1. MAPC predicted non-affine deformation in networks of flexible chains	130
4.5.2. MAPC predicted non-affine deformation in networks of stiff filaments	135
5. A diffusion-based transient network model for finite rubber viscoelas- ticity	143
5.1. Introduction	143
5.2. Basic network mechanisms of finite rubber viscoelasticity	146
5.3. Microscopic formulation of the diffusion-based transient network model . .	149
5.3.1. Gaussian statistics of a single polymer chain	150

5.3.2.	Brownian motion of non-interacting point particles	151
5.3.3.	Brownian motion of flexible polymer chains	153
5.4.	Macroscopic formulation of the diffusion-based transient network model . .	156
5.4.1.	Tensorial representation of the probability function evolution	157
5.4.2.	Isochoric viscous free energy and viscous overstress expressions . . .	159
5.4.3.	Algorithmic representation and implementation	161
5.5.	Representative numerical simulations	162
5.5.1.	Parameter fitting procedure	163
5.5.2.	Model verification through uniaxial cyclic tests	167
5.5.3.	Model verification through non-homogeneous 3D shear tests	169

III Modeling the electronic structure of solids at the microscopic scale

173

6.	A finite element based Kohn-Sham density functional theory	175
6.1.	Introduction	175
6.2.	Theoretical background based on density functional theory	176
6.3.	Discretization with finite elements and its numerical implementation	180
6.3.1.	Weak formulation and discretization in the finite element basis . . .	180
6.3.2.	Numerical implementation	184
6.4.	Numerical analysis of the implementation	185
6.4.1.	Treatment of the core singularity in all-electron calculations	186
6.4.2.	Analysis of the numerical approximations	190
6.4.3.	Analysis of simulation parameters	194
6.5.	Representative numerical results	197
6.5.1.	All-electron calculations on noble gases	197
6.5.2.	Calculation on small molecules	199
6.5.3.	External electric field	200
7.	Conclusion and outlook	203
7.1.	Modeling solids undergoing failure at the macroscopic scale	203
7.2.	Modeling materials with network microstructures at the mesoscopic scale .	205
7.3.	Modeling the electronic structure of solids at the microscopic scale	207

1 Introduction

The goal of this work is to summarize the effort spent by the “Micromechanics of materials group” headed by the author of this work on the development of new physical motivated models at microscopic scales together with the development of new numerical frameworks to allow for their incorporation into efficient simulation tools. In doing so, the group could contribute to the Vision I entitled “From empirical material description towards computational material design” of the Excellence Cluster Simulation Technology at the University of Stuttgart. The final goal of this vision is to develop new advanced materials, which are essential for the evolution of our society. To do so, properties of *soft matter* such as liquids, colloids, polymers, foams, gels, granular materials, and biological materials are combined with those of *hard matter* such as metallic alloys, ceramics, or glasses as illustrated in Figure 1.1. The simulation of such materials plays a central role within simulation technology. Besides applications in the classical disciplines of civil, environmental, mechanical, automotive, and aerospace engineering, the miniaturization of everyday-objects leads to the demand for highly sophisticated and new materials also within the disciplines of computer science or chemical and bio-engineering. Such simulations involve multi-field problems, such as electromechanical coupling effects, and span a multi-scale cascade of length and time scales. Focusing on civil engineering applications, Figure 1.2 illustrates possible new ways in designing our future built environment.

Whereas the final goal of SimTech’s Vision I aims for the highly challenging task of coupling those cascades of all the different scales together based on newly developed scale bridging techniques, this work is restricted to a coupling of at most two neighboring length scales. It will though be shown that depending on, at which scale the target application resides, different micromechanical phenomena can be incorporated. Clearly, a micromechanical phenomenon to be incorporated at the macroscopic scale, like a crack to model a failing solid, is very different from a micromechanical phenomenon to be incorporated at the mesoscopic scale, like the evolution of stretch and re-orientation of fibers in a soft matter material such as an elastomer or a biopolymer gel, and differs even more from the modeling of wave functions when computing the electronic structure of single atoms or molecules. In this work it will be shown, how by a physical based modeling exactly those three micromechanical phenomena can be incorporated theoretically and numerically into the next larger scale partially through newly developed homogenization principles. The modeling of those three phenomena will be distinguished based on the length- and time-scale into which they will be incorporated as it is illustrated in Figure 1.3, with the detailed explanation of those results postponed to the individual parts of this work.

In particular, it will be shown in Part I of this work, entitled “Modeling solids undergoing failure at the macroscopic scale”, how a crack can be incorporated into the numerical framework of the finite element method to model solids at failure. Part II, entitled “Modeling materials with network microstructures at the mesoscopic scale”, targets the modeling of elastic and time dependent effects in soft materials characterized by a random network microstructure. The final Part III is entitled “Modeling the electronic structure of solids at the microscopic scale” and will outline a finite element based framework of the density functional theory to compute the electronic structure of solid materials. Clearly, on each scale there exist many more physical phenomena, which could be modeled, and surely, coupling those phenomena over several length scales is intended to be the major

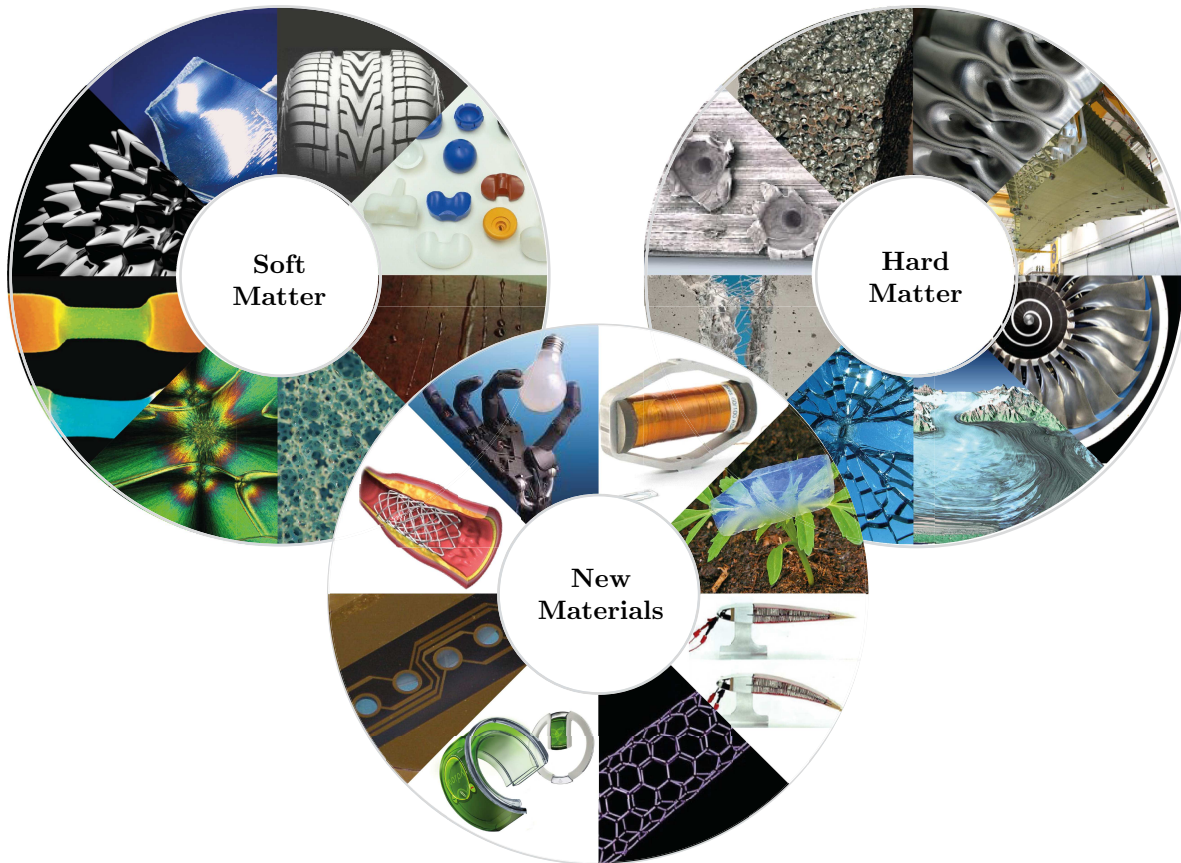


Figure 1.1: In Vision I of SimTech, properties of soft matter such as liquids, colloids, polymers, foams, gels, granular materials, and biological materials are combined with those of hard matter such as metallic alloys, ceramics, or glasses to develop new advanced engineering based materials.

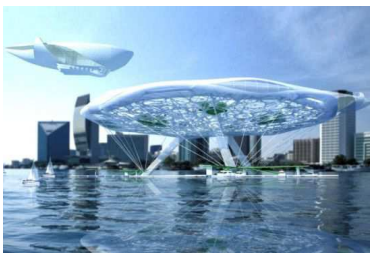


Figure 1.2: Illustration of a future built environment made possible by the developed new materials arising from concepts developed in simulation technology.

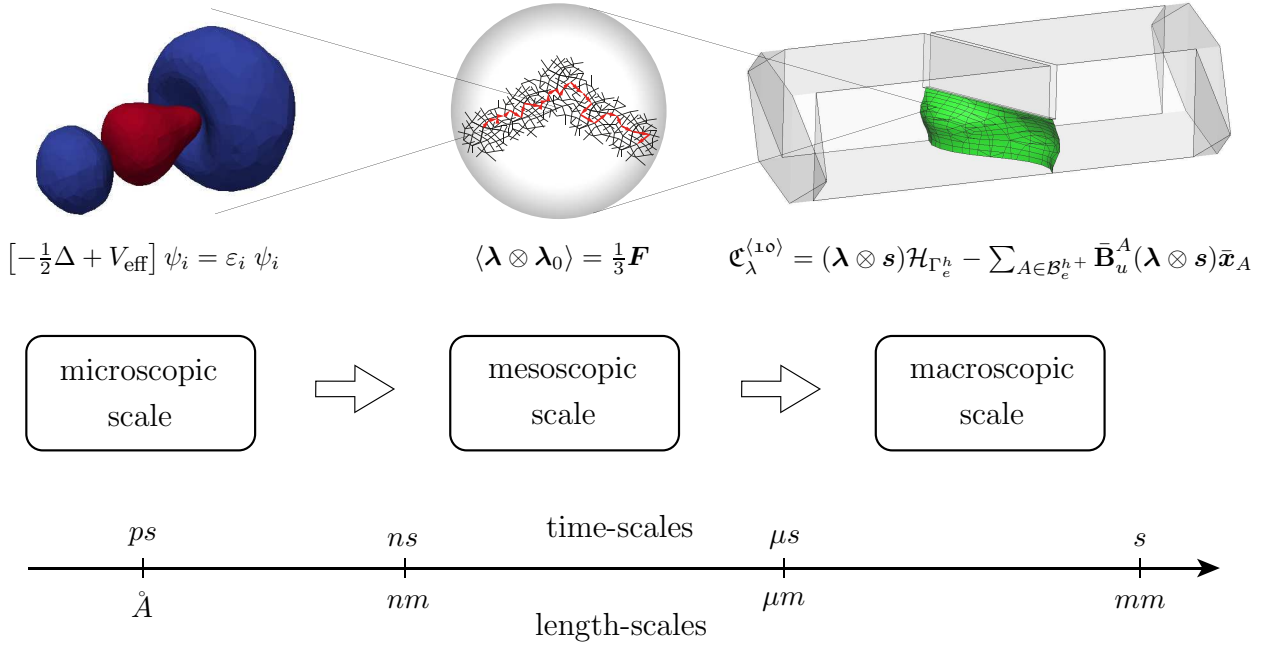


Figure 1.3: Illustration of the length- and time-scales of interest in this work with one of the numerical results shown on each scale and explained in detail in the corresponding Parts I, II, and III.

goal of future research.

In the following Sections 1.1, 1.2, and 1.3, a short introduction to the above mentioned three phenomena to be modeled in this work on the macro-, the meso-, and the micro-scale is provided. The chapter closes with Section 1.4, which provides a more detailed overview of the content of this work.

1.1 Modeling solids undergoing failure at the macroscopic scale

The modeling of solids at failure has attracted theoretical as well as computational experts from fields like engineering, physics and chemistry, or mathematics ever since. This research field combines various multiphysical challenges at multiple length- and time scales. Over the past decades a huge amount of information has been gathered to increase our understanding of why and how solids fail but there is still a long way to go until we fully understand the various phenomena of fracture. The appearance of defects as a certain deviation from a state otherwise being considered as perfect is characteristic for the engineering based design of structures and materials. Especially when it comes to the development of new materials the influence of possible defects must be accounted for, to better predict their properties like durability or strength. It is the goal of Part I of this work to contribute to the development of numerical methods capable of accounting for defects at the macroscopic level in a class of materials such as those illustrated in Figure 1.4.

A framework widely and successfully applied to model solids is the framework of *continuum mechanics* [360, 361]. To incorporate microstructural information into the framework, extended continuum theories have been developed [89, 90, 250] and later applied to investigate shear banding in DE BORST [70], STEINMANN [335], or EHLERS & VOLK



Figure 1.4: Illustration of materials at failure. Left: Bridge collapsing under an earthquake excitation. Center: Crack branching observed in brittle materials at dynamic loading. Right: Fracture in advanced electromechanical coupled materials.

[83, 84], among others, with detailed overviews provided in ERINGEN [87, 88] or FOREST & SIEVERT [110]. The incorporation of failure mechanisms into continuum theories can alternatively be established through the framework of *fracture mechanics*. The foundation of continuum fracture mechanics can be dated back to the two seminal papers by GRIF-FITH [128, 129], where he showed that scratches drastically increase the stress level. With extension of IRWIN [161] and OROWAN [272] to metals, these concepts serve as the foundation of classical *linear elastic fracture mechanics*. This elegant and powerful description of phenomena describing the failing solid, such as cracks or shear bands on a macroscopic length scale, ceases to be valid when significant plastic deformation precedes failure. This is overcome based on the developments in DUGDALE [78] or BARENBLATT [20], among others. Based on the contributions by ESHELBY [92, 93] and RICE [306] the J -integral, a line integral evaluated along an arbitrary contour around a crack, has been developed being a major component of the study of *configurational mechanics* [133, 176, 201, 228, 337, among others].

1.1.1 Numerical modeling of solids at failure

With the development of the finite element method [4, 63, 69, among others], a promising numerical tool was created for the investigation of solids at failure. Immediately, difficulties arose in the attempts to model cracks or shear bands through jumps in the displacement field, so called *strong discontinuities*, since in the finite element community the standard displacement field generally is represented by smooth polynomials. To overcome these problems, *damage models* were used allowing for an incorporation of the materials damage through a constitutive model for which the stresses tend to zero when subjected to sufficient large strain fields. Improvements were made in the *smearred crack model* [297] or the *band smearred crack model* [28], where a proper account of the dissipated energy is made. Alternative approaches to circumvent problems during strain softening through the incorporation of a characteristic length are *non-local continuum models* [27], *higher gradient models* [65], or *Cosserat continua* [71]. Due to the difficulties of representing displacement jumps within the individual finite elements, the *cohesive finite element method* [258] restricts the singularities to appear along the element boundaries through the incorporation of so called cohesive finite elements, employing cohesive traction-separation laws along those elements. SIMO ET AL. [331] were among the first ones to incorporate a strong discontinuity directly within the individual finite elements. The straightforward

implementation into standard finite element codes, available extensions to two- and three dimensional problems [265, 379] also within the geometrically nonlinear setting [12] of this methodology, often referred to as the *strong discontinuity approach* or the *embedded finite element method*, makes it appealing to a large number of scientists.

It is extended to three dimensions [96, 253, 269], to porous media [59, 336], or to beams and plates [10, 86]. In LINDER & ARMERO [205], ARMERO & LINDER [14, 15], and LINDER [203] the formulation is extended to account for a higher order kinematic resolution of the failure zone in the 2D continuum, in ARMERO & KIM [13] to account for an improved kinematic relation in 3D, in ARMERO [9] for antiplane/torsional problems, in LINDER & RAINA [208] and RAINA & LINDER [294] onto multiple levels, and combined with the margining cubes algorithm to improve the 3D crack propagation in LINDER & ZHANG [209] and ZHANG & LINDER [399].

Another method, receiving much attention lately, is the *extended finite element method* proposed in BELYTSCHKO & BLACK [31] and MOËS ET AL. [251] or the related method based on HANSBO & HANSBO [136], see also [235, 236]. Also in this approach the strong discontinuities are allowed to propagate through the individual finite elements. The improved kinematical description of the singularities comes along with the addition of global degrees of freedom making the method no longer that easily incorporable into standard finite element packages [32, 380, 381, among others]. Employing ideas coming from configurational mechanics, MIEHE & GÜRSES [240], MIEHE ET AL. [245], and GÜRSES & MIEHE [132] suggest a finite element implementation of brittle fracture based on a variational principle and energy minimization. Contrary to such discrete account for cracks or shear bands, in *phase field models* [51, 111, 246, 247] the strong discontinuity is smeared over a finite width with the advantage of allowing for a straightforward application to complicated cracking patterns without the need of complicated crack tracking algorithms, which especially in 3D become a tedious task. On the other hand, those methods though require heavily refined finite element discretizations in the region where failure occurs.

1.1.2 Numerical modeling of dynamic fracture problems

Modeling of fracture becomes an even more challenging problem when dynamic instabilities of the crack tip play a crucial role resulting in notable discrepancies between experimental and theoretical results. Once the flux of energy to a crack tip passes a critical value, the crack becomes unstable and propagates in increasingly complicated ways. As a result, the crack cannot travel as quickly as theory predicts, fracture surfaces become rough, microcracks that propagate away from the main crack begin to form and finally crack branching occurs so that the energy cost for crack motion increases considerably.

Early experimental literature about dynamic fracture can be found in experiments [178, 179, 295], and RAMULU ET AL. [296] on thin sheets of a brittle material Homalite-100 who attributed the phenomena of crack branching to the critical stress intensity factor at the crack-tip. Further experiments [299, 300, 301] of dynamic fracture also found similar relations of crack branching with the critical stress intensity factor. More recent experiments [98, 99, 321] as well as SHARON & FINEBERG [320] performed on the brittle material PMMA shed more light on the instabilities associated with the fast moving crack in dynamic fracture where micro-branching phenomena were observed before the main branching, which tend to take place at a critical main crack-tip velocity as suggested by

YOFFE [395]. A huge amount of literature is available with regard to numerical simulations of dynamic fracture using cohesive finite elements [389], the embedded finite element method [154], and the extended finite element method [32], to mention just a few among many.

The application of the finite elements with embedded strong discontinuities to the dynamic range is rare. In HUESPE ET AL. [154], solutions are presented with triangular elements with a constant approximation of the displacement jumps. This is extended in ARMERO & LINDER [16] and LINDER & ARMERO [206] to quadrilateral finite elements in the fully transient setting to simulate problems in dynamic fracture like crack branching or failure mode transitions with a higher order approximation of the displacement jumps. In particular, in the latter reference, the modeling of crack branching was accomplished by the design of new finite elements capable of modeling such phenomenon in a single finite element, a so called finite element with embedded branching. Additional contributions of the author in modeling dynamic fracture using the multilevel strong discontinuity approach are given in [292, 293].

1.1.3 Numerical modeling of failure in electromechanical coupled materials

The constitutive models mostly employed so far within the strong discontinuity approach are purely mechanical based models with strong discontinuities appearing in the resulting displacement field of the solid undergoing failure. Extensions to account for fluid-saturated porous media are developed in STEINMANN [336] and the incorporation of poroplastic effects is performed in CALLARI & ARMERO [59] where additional discontinuities in the fluid flow must be accounted for. It is therefore the goal to suggest a possible account for such coupled materials within the strong discontinuity approach where in addition to the jumps in the displacement field jumps in the electric potential must be accounted for in order to represent the failing electromechanical coupled material. This is achieved in Part I of this work by following the recently publications of LINDER ET AL. [210], LINDER & MIEHE [207], and LINDER [204], in which the original strong discontinuity approach is extended to account for electromechanical coupled effects present in piezo- and ferroelectric ceramics.

Experimental results of the fracture behavior of piezoelectric ceramics can be found in PARK & SUN [280] where in addition a finite element based investigation of possible fracture criteria is performed. In this latter work it is shown that the ultimate load of a piezoelectric ceramics depends on the sign of the applied electric field. In particular, a negative electric field impedes crack growth and therefore raises the ultimate load, whereas a positive electric field enhances crack growth and therefore lowers the ultimate load. It is noted though that the physics of failure in electromechanical coupled solids remains controversial which becomes apparent when looking at the experimental results reported in WANG & SINGH [375] or FU & ZHANG [113] showing an independence of the crack propagation on the sign of the electric field.

General frameworks describing electromechanical coupled materials are provided in TRUESDELL & TOUPIN [361] or LANDAU & LIFSHITZ [193], among many others. Applications in smart systems in the form of actuators and sensors led to a drastic increase of the demand of such smart materials over the previous decades. One particular class of such materials are *piezoelectric materials* which are widely used in various fields of engineer-

ing. An early reference within the linear theory is given by NOWACKI [262]. A survey of numerical studies for geometrically linear piezoelectric systems is given in BENJEDDOU [33] with a recent emphasis to develop invariant formulations in SCHRÖDER & GROSS [317]. Review articles concerning microscopically motivated and phenomenological models for piezoceramics can be found in KAMLAH [173], LANDIS [196], or HUBER [152]. Such materials can be classified as highly brittle due to their high ultimate strength and extremely low fracture energy and therefore are prone to defects like cracks. Theoretical investigations of fracture in piezoelectric ceramics are provided in PARTON [281], SUO ET AL. [342], MCMEEKING [229], or ZHANG ET AL. [396] among many others. Further references can be found in the recent review articles in KUNA [191, 192] outlining open problems and possible future research areas.

One particular area of controversy exists when it comes to the choice of appropriate boundary conditions along existing and propagating crack faces [74, 138, 195, 230, among others]. The choice of crack boundary condition becomes relevant when modeling the failure in such materials through the discrete account of the strong discontinuities. Constitutive models allowing for discontinuities in the displacement field as well as in the electric potential along the finite element boundaries are developed in ARIAS ET AL. [5] and VERHOUSEL & GUTIÉRREZ [368]. Simulations of cohesive fatigue effects in grain boundaries of a piezoelectric mesostructure are performed in UTZINGER ET AL. [364]. An application of nodally enriched techniques where the discontinuities are allowed to propagate through the individual finite elements of piezoelectric materials is achieved in BÉCHET ET AL. [29] by the incorporation of electric enrichment functions accounting for the appearing singularities of the electric fields within the assumptions of linear elastic fracture mechanics. Phase field models of fracture in electromechanical coupled materials are recently developed in VERHOUSEL ET AL. [369], MIEHE ET AL. [248], or ABDOLLAHI & ARIAS [1].

The scale of interest in most of the above mentioned techniques and the results shown in Part I of this work is the macroscale with length scales in the order of mm to m . Mesoscopic simulation methods operate on a smaller spatial scale when compared to the above mentioned macroscale approaches. Rather than putting a focus towards the incorporation of failure phenomena at the mesoscopic scale, in Part II of this work, the physical phenomena to be captured are those which can be related to the random network microstructures of soft matter materials.

1.2 Modeling materials with network microstructures at the mesoscopic scale

Network microstructures are commonly encountered in materials of artificial as well as natural origin. Elastomers [354], hydrogels and soft biological tissues [44, 85, 150, 174, 216], non-woven fabrics [142, 287], cellular foams [122], and muscles [48, 310, 311] are all on the microscopic level composed of elongated one-dimensional elements one can generally address as fibers, with some of them illustrated in Figure 1.5. When these soft materials are subject to a macroscopic strain or start to grow [3, 148, 184, 187, 234, 298, 371, 400], the underlying microstructure undergoes a peculiar deformation. The forces produced by the deformed filaments and their interaction within the irregular three-dimensional network constitute the macroscopic stress response of the material. The knowledge about

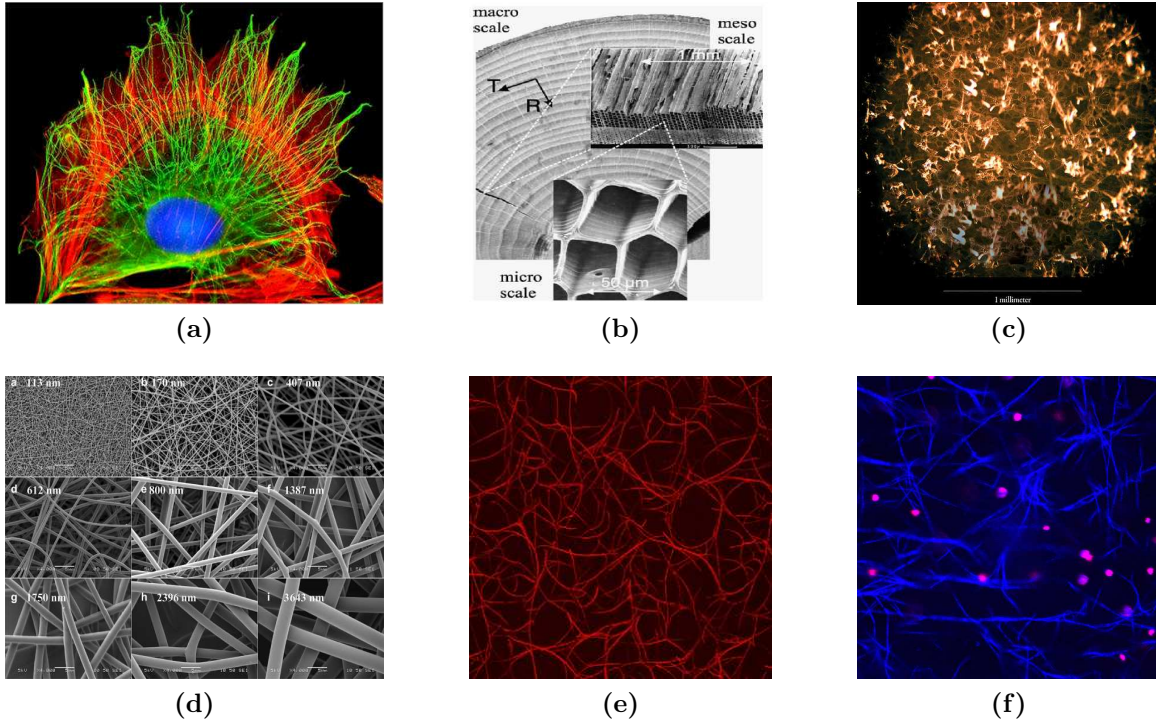


Figure 1.5: Illustration of (a) a cytoskeleton, (b) a piece of wood, (c) a shape memory polymer foam, (d) a nonwoven material, (e) an actin network, and (f) a collagen gel as examples of materials with network microstructures.

the micromechanics of random networks is therefore crucial for the understanding of mechanical properties like elasticity or time dependent effects displayed by the above mentioned soft materials. This is achieved in Part II of this work by following our recent work in LINDER ET AL. [211] and TKACHUK & LINDER [350].

1.2.1 Static network theories

From a molecular point of view, polymeric materials are characterized by a chain-like conformation of covalently linked atoms [104]. The countless non-regular conformations such chain may inhabit based on possible rotations of atoms around their covalent bonds results in the necessity of describing their properties within the framework of statistical mechanics. The probable most idealized approximation is the one denoted as the *freely jointed chain (FJC)* for which no constraints with regard to the orientation of the individual monomers, all assumed to be identical, in reference to their neighbors is made. This approximation results in typically coil-like random conformations of the chain together with a Gaussian distribution of the chain's end-to-end vector. Through the Boltzmann relation, this results in expressions through which the entropy and the free energy of the resulting Gaussian chain can be computed [134, 188, 189]. For highly stretched chains, this approximation loses its validity and must be replaced by a non-Gaussian relation [190], for which the maximal attainable chain length can not be surpassed. Those approximations build the foundation of frameworks capable to describe the behavior of long macromolecules in rubber-like polymers. An excellent monograph on the modeling of rubber-like polymers is given in REESE [302] with further noteworthy contributions in BÖL & REESE [46, 47].

Ultimately, rather than being interested in the behavior of individual chains, in this work a focus is laid towards improving our understanding of the role of the individual chains when being part of a network. Depending on the assumptions laid onto the individual chains, different network models emerge. A network comprised of Gaussian chains is called a *Gaussian network model* [102, 103, 166, 356, 357, 372], whereas one in which the chains comply with the maximal chain length constraint through a modified density functional distribution based on the inverse Langevin function is called *non-Gaussian network model*. Into the latter category fall the *three-chain model* of JAMES & GUTH [166] and WANG & GUTH [376], the *four-chain model* of TRELOAR [358] developed based on the model of FLORY & REHNER JR. [102], or the often used *eight-chain model* of ARRUDA & BOYCE [17]. There, the microstretch of non-Gaussian chains in directions depending on the principal stretches are related to the macroscopic applied deformation and results in the material response through averaging techniques. Those models can be interpreted as approximations of the *affine network model* [355, 388]. In the latter model, non-Gaussian chains with an identical initial length and an isotropic and homogeneous orientation are deformed in an affine way. The free energy then follows from an integration of the chain distribution vectors over a microsphere rather than based on a standard summation. Still, in particular the eight-chain model results in a more accurate agreement with experimental data due to its capability of allowing for possible re-orientation processes for the stretches of highly elongated chains. Such deformation at the microscale being different from the macroscopic applied deformation is commonly denoted as *non-affine* deformation. Even though good parameter fits can be achieved by many of those models, the overall complexity of a real polymeric network being comprised of randomly oriented polymer chains cannot be adequately described with those models, therefore supporting the content of Part II in which, following our recent work in TKACHUK & LINDER [350], a new micromechanical motivated network model is developed.

Even though the underlying mechanisms of the individual chain segments in these theories account for their finite extensibility, the possible chain conformations in between two junction points is not influenced by the surrounding polymer chain segments. This is on the contrary done within *constrained junction theories* [91, 105, 108, 109, 312] and within *constrained segment theories* [73, 82, 143, 144, 145, 171]. In MIEHE ET AL. [244] a micromechanically motivated network model, including a micro-tube constraint based on EDWARDS [81] to account for the surrounding polymer chains, together with a non-affine micro-to-macro transition based on a homogenization procedure defined on a micro-sphere of space orientations is developed. The resulting framework, called the *non-affine micro-sphere model*, yields an excellent performance in homogeneous and non-homogeneous tests. Further references on the elastic behavior of rubber-like materials can be found in TRELOAR [354] and the review articles by BOYCE & ARRUDA [53] or MARCKMANN & VERRON [224].

1.2.2 Transient network theories

Besides the elastic ground response of rubber-like materials, captured by the above outlined static network theories, their behavior is characterized by a finite viscoelastic overstress which governs rate-dependent effects such as relaxation and creep phenomena as well as frequency dependent hysteresis curves in cyclic loading processes. Experimental observations of such effects are reported in COTTEN & BOONSTRA [68], FERRY [97],

SULLIVAN [341], LION [213], MIEHE & KECK [241], or MIEHE & GÖKTEPE [239], among others.

When it comes to the numerical modeling of such phenomena, one again may distinguish purely phenomenological models with a strong focus on the numerical implementation developed within the mechanics and engineering community and approaches originating from physical chemistry and material science where the focus lies on molecular models of these phenomena and their experimental justification by microscopic studies. Within the phenomenological approaches, one can find models based on stress-type variables in the form of convolution integrals in the works of HOLZAPFEL & SIMO [151], LION [213], or KALISKE & ROTHERT [172]. Alternatively, the multiplicative split of the deformation gradient, originally suggested by LEE [197] in the context of elastoplasticity and by SIDOROFF [323] in non-linear viscoelasticity, into elastic and inelastic parts is used in LUBLINER [220], SIMO [332], BOYCE ET AL. [54], REESE & GOVINDJEE [303], GOVINDJEE & REESE [126], or BERGSTRÖM & BOYCE [34]. The description of the time dependent viscous effects based on the evolution of viscous metric tensors is chosen in MIEHE & KECK [241]. An extension of the above mentioned micro-sphere model of rubber elasticity to account for viscous effects is achieved in MIEHE & GÖKTEPE [239] and GÖKTEPE & MIEHE [125], whereas our recent contribution in LINDER ET AL. [211] is arising from the concept of a polymer chain undergoing a Brownian motion.

An alternative to these continuum approaches are the molecular-based theories. These have been developed recently to describe the viscous behavior of molten polymers and amorphous rubber-like materials. The *bead-spring model* [37], the *reptation-type tube models* [72, 75], and the *transient network models* [127, 348] are mentioned as examples in this area. Recently, an increasing activity in combining these two approaches can be observed, resulting in so called micromechanically motivated approaches [18, 34, 55, 211].

1.2.3 Semiflexible biopolymer network theories

In addition to networks made of freely jointed chains, the second part of this work also deals with networks made of semiflexible macromolecules, which differ from the flexible chains by the presence of a strong backbone, which results in much straighter chains and also is responsible for the appearance of distinct directions in biological materials. Again, a statistical mechanics based framework is exploited for the determination of the individual chain properties [349, 350, 351]. At zero temperature and without external loading such description results in the prediction of a totally straight chain without any appearance of bending and therefore minimal energy. Increasing the temperature changes this behavior and results in curved chain conformations with a probability density distribution given based on the Boltzmann relation. The higher is the temperature T , the higher is the probability of finding curved chain conformations, leading to a decrease of the end-to-end vector's length. In addition to the contour length, also the persistence length ℓ_p , which serves as an indicator for the stiffness of the polymer chain and is related to the bending stiffness κ of the chain by $\ell_p \propto \kappa/(k_B T)$ with k_B as the Boltzmann constant, plays a dominant role in the prediction of the semiflexible chain properties.

The quantitative description of semiflexible polymer chains, the derivation of the statistical distribution of its end-to-end vector, the computation of its free energy, as well as the derivation of its elongation versus force behavior relies on the computation of proper

partition functions, whose derivation strongly depends on the assumptions made. Many of the currently used models of polymeric materials with stiff chemical bonds between the monomers can be traced back to the work of POROD [289] and KRATKY & POROD [182]. There is assumed that each chain conformation can be related to a spatial curve with the curvature at each point being of stochastic nature [107]. This results in extended worm-like conformations so that often those chains are denoted as *worm like chains (WLC)*. Simplifying assumptions of the relation between persistence length ℓ_p and overall chain length L eventually lead to closed form solutions of the partition function for semiflexible polymer chains. In the limit $\ell_p \ll L$ the Gaussian solution with twice the persistence length as the Kuhn length is recovered. This assumption is used in the work of MARKO & SIGGIA [225] when investigating the stretch behavior of DNA. The opposite limiting case $\ell_p \gg L$ is characterized by short (L is small) or stiff (κ and therefore ℓ_p are large) semiflexible chains and investigated in WINKLER [387]. The assumption of small transversal movements of the semiflexible chains out of their main orientation in MACKINTOSH ET AL. [223] results in a further simplification of the mathematical complexity and though leading to a linear force-extension relation is capable of capturing the correct inverse scaling of the longitudinal stiffness of straight chain segments with their length. More sophisticated models of semiflexible polymer chains are e.g. given in BLUNDELL & THERENTJEV [40, 42], which on the one hand boil down to the results obtained in MARKO & SIGGIA [225] in the Gaussian limit, but on the other hand also results in an accurate description of the force-extension relation for different stiffnesses and stretches. A particular difference is given by an introduced non-entropic term not vanishing at zero temperature in BLUNDELL & THERENTJEV [42] mimicking the potential energy of an elastic spring undergoing bending. A good comparison between the properties of FJC models and WLC models is provided e.g. in KUHLE ET AL. [185].

Also for semiflexible chains, the ultimate goal lies in obtaining an improved understanding of their role when being part of a network as it appears in dilute solutions, melts, nematic crystals, amorphous or semi-crystalline plastics or rubber-like polymers and in that way drastically influencing their elastic properties. Depending on the nature of how the individual chains are connected, one distinguishes between permanent links, like in the case of elastomers or gels, and temporal links, as they appear e.g. in solutions, melts, natural rubber, or non-crosslinked gels. Whereas the elastic properties of a macroscopically stretched network consisting of FJC is simply governed by the change in entropy due to a reduction of the possible conformations of the thermal fluctuating chain, the elastic behavior of biopolymer networks made of WLC is much more complicated. It can be characterized by the following three mechanisms:

- (i) Axial stretching of semiflexible filaments as a result of the macroscopic deformation and the corresponding increase of junction-to-junction distances. This response may be *entropic and soft* when the chain is elongated below its contour length and can take curved conformations through thermal fluctuations at an energetic cost comparable to $k_B T$. Conversely, the filaments may display a stiffer *athermal* behavior for high extensions and bending stiffnesses corresponding to a *mechanical* deformation of interatomic bonds in the polymer backbone.
- (ii) Fibers that extend continuously over the junctions can also undergo *instant bending*. Initially straight or slightly undulated filaments may become essentially curved due to the out-of-line displacements of the junctions. The potential of this alternative

kinematic mechanism in complying with the macroscopic deformations of the polymer network depends on its geometry and connectivity, whereas the magnitude of the stress component associated with the bending forces is defined by the properties of the filaments themselves.

- (iii) In addition, the semiflexible molecules *interact with the solvent*, which has a great impact on the rheology of semiflexible biopolymer networks. This affects the behavior of single filaments favoring either their elongated straight conformations with a high exposure to the solvent, or alternatively, the compact folded states if such contact is avoided. The fluid enclosed in the polymer network largely defines the volumetric response of the network.

Which of those three mechanisms is activated strongly depends on the network geometry and the chain properties. Whereas in networks made of flexible polymer chains the average distance ℓ_c between the cross links is the sole relevant quantity characterizing the network geometry, a number of parameters are used to do so for networks made of WLC. Those are the concentration c of chains, defined as their overall length in a unit volume of the network, which scales inversely with ℓ_c , the averaged length L of the polydisperse single filaments, as well as the persistence length ℓ_p . It is to be noted that the identity of a semiflexible chain over the spacing distance ℓ_c of its cross links remains due to its continuous orientation over those connection points. The interplay of all these parameters drastically influences the overall behavior of the biopolymer network [140, 141]. For small concentrations as well as for short chain lengths, the material behaves like a solution or a loose gel with vanishing shear modulus. An increased concentration, leading to the appearance of a large enough number of cross links of a single chain affecting in this way the overall network, as well as an elongation of the chain so that L is in the order of ℓ_c , increases the network stiffness. When surpassing the percolation threshold, a highly non-affine behavior is obtained, which is characterized by bending of the semiflexible chain over the cross links due to a macroscopic applied deformation, rather than by the, in this case, energetic disadvantageous chain stretch. A further increase of the concentration or in the case of a network with even longer chains results in an affine network behavior caused majorly by stretching of the chains. Whether this stretch is of entropic or of mechanical origin depends on the persistence length ℓ_p . In case ℓ_p is smaller or in the order of ℓ_c this results in thermal transversal- and bending fluctuations and therefore in an entropic behavior. For chains with a large persistence length, bending of the short semiflexible chains between the cross links requires a larger energy than $k_B T$ so that thermal fluctuations are suppressed and the stretch has a mechanical origin.

It is the aim of Part II of this work to describe those challenging physical properties of materials with random network microstructures with newly developed computational models. This can be achieved either by discrete network models briefly discussed in the subsequent Section 1.2.4, or alternatively by a new class of homogenized network models briefly introduced in Section 1.2.5 and discussed in more detail in Part II of this work.

1.2.4 Discrete network theories

In the former approach, the structural elements of the network in the form of chains and cross links are discretely approximated. Various models exist in the literature, based

on which such networks can be generated. *Mikado type models* [140] place filaments in a 2D simulation box in such a way, that both, location of their centers of mass and their orientation, are chosen arbitrarily. Their crossing points are identified as cross links and loose ends, having no effect on the mechanical response, are removed. Such networks are primarily useful for networks made of stiff chains and are restricted to a coordination number of four. Such model is used in HEAD ET AL. [140] at small strains for the determination of the percolation limit. Under the assumption that the filaments in the network react purely mechanical when axially or transversally stretched, a critical behavior of L/ℓ_c when going from a solution to a shear resisting material, is observed. The obtained shear modulus scales with the ratio of bending and axial filament stiffness and identifies the transition from the non-affine, bending dominated soft behavior to the affine, stretching dominated behavior. Contrary to this work, where the chain rotations at the cross links are not restricted, additional rotational constraints are introduced in WILHELM & FREY [384]. The typical worm-like conformation of chains in semiflexible biopolymer networks is incorporated into the generation of networks stretched up to 25% in ONCK ET AL. [271]. In that way, the transition from the bending dominated regime at small stretches to the stretching dominated regime at large deformations and the accompanied non-affinity caused by chain re-orientation could be modeled. It is shown how undulations postpone the onset of the transition from the soft to the stiff regime but that the affine stretch of filaments is not majorly influenced. An extension to three dimensional networks was performed in HUISMAN ET AL. [157].

An alternative way to generate arbitrary networks is based on the idea to introduce disorder into an initially regular network. Starting from regular triangular, rectangular, or hexagonal networks, networks with functionality of 3, 4, and 6 are generated in PLAZA [288]. The disadvantage of such networks is the fact that the identity of long biopolymer chains beyond the individual cross links is lost. As a result, bending deformations can only be modeled by rigid cross links. Such networks are often used to model bone materials rather than real biopolymer networks and allow to qualitatively capture the dependency of the network on the orientation and deformation energy of its filaments. It was shown that networks with high connectivity and filaments with large bending stiffness deform in an affine manner resulting in highly stretched filaments in the direction of the applied macroscopic stretch. On the other hand, networks with low connectivity and moderately curved filaments deform in a non-affine way, resulting in high bending of the filaments transversal to its loading direction.

1.2.5 Homogenized network models

Rather than focusing on discrete network models, Part II of this work will put an emphasis towards the development of new homogenization approaches to computationally capture the response of materials made of random network microstructures.

Doing so, polymer networks are described based on characteristic parameters, like the distribution of the average chain length between crossing points. Those undergo changes when the overall network deforms. In case the network reacts to such deformation solely by stretches with no mechanical bending deformation, the network deformation is mostly approximated in an affine manner. As a result, the chain segments change their length as if the cross links are pinned onto the macroscopic solid material. The free energy of

the overall network follows then from averaging the energy of the individual chains in the deformed configuration. Such procedure is chosen in STORM ET AL. [338] with the distribution of chain lengths taken from WILHELM & FREY [383]. The obtained results indicated a missing isotropic compression to assure a stress free initial configuration. In BLUNDELL & THERENTJEV [41], the distribution calculated in HA & THIRUMALAI [135] is used for the undeformed network, which allowed them to compute the transition from the entropically caused stretching regime to the mechanically driven stretching regime. For networks with filaments deformed based on bending over the cross links, the affine assumption is not applicable. In HEUSSINGER ET AL. [147], such deformation modes are made possible by the kinematics of so called “floppy modes”, which would appear in polymer networks made of flexible chains. The statistics of those bending modes then allows for the computation of averaged stresses in the network.

The, through the homogenization approach, obtained averaged characteristic quantities of the network serve now convenient for the continuum based computation of the material response based on numerical methods like the finite element method. Networks of semiflexible polymer chains are important structural elements in artificial as well as in biological materials. Their elastic properties and peculiar stiffening behavior is responsible for the needed protection of tissues and organs. The achievement of an improved understanding of the stress-strain behavior of such materials with inherent network microstructures through large-scale continuum based calculations is therefore of utmost importance. Traditionally, semiflexible polymer models are employed to describe DNA as in MARKO & SIGGIA [225]. In BISCHOFF ET AL. [38, 39] and GARIKIPATI ET AL. [118], WLC models are used to describe the collagen triple-helix. An extension of the eight-chain model for the application of biopolymer networks is made possible in OGDEN ET AL. [263] or KUHL ET AL. [185] through the incorporation of the WLC statistics and an extension to account for the inherent anisotropy in such materials in the latter work, with a careful convexity analysis in KUHL ET AL. [186]. An extension of the “micro-sphere models” [244] to include anisotropic initial chain orientations and account for the WLC statistics rather than the FJC properties is achieved in MENZEL & WAFFENSCHMIDT [233] and applied to model biological tissues. The actin cytoskeleton is modeled based on a modified eight-chain model in PALMER & BOYCE [277] and continuum based models for blood vessels can be found in DRIESSEN ET AL. [76], GASSER ET AL. [120] or ALASTRUÉ ET AL. [2].

To summarize, materials with random network microstructures composed of semiflexible biopolymers are characterized through a complex non-linear behavior. A number of mechanisms, all strongly employed in biological materials to prevent failure, allow for various ways on how the applied loading is altering the individual chains of the network. Contributing to the research on transferring such mechanisms to engineering based materials is the major motivation for the research summarized in Part II of this work.

1.3 Modeling the electronic structure of solids at the microscopic scale

The properties of condensed matter as for example electric conductivity, magnetism as well as the mechanical response upon external excitations are determined by the electronic structure of a material. The governing Schrödinger equation represents a coupled, quantum mechanical many body problem, consisting of the positively charged atomic cores

and the negatively charged, fermionic electrons. The determination of its exact solution is only possible in trivial cases like that of an ionized atom with a single electron [64]. A variety of methods for gaining approximations for its solution were created [344].

One of the most successful approaches for electronic structure calculations is the density functional theory, founded by the Hohenberg-Kohn theorem in [149], which replaces the many body problem for the ground state calculation with an effective single electron problem. In principle it represents an exact theory, however it requires exchange correlation functionals, which can only be approximations, often adapted to model special kind of material properties, like for example the van der Waals forces. This also makes it difficult to improve calculations systematically as in the Hartree Fock case, where enlarging the ansatz is possible [344]. Nevertheless many successful applications have been found over the last decades and made the density functional theory a valuable tool in getting insight into the electronic structure of materials, which can also be attributed to the rise of available computational resources. In recent years however, a qualitative change in the increase of the computational resources has taken place, where because of technological obstacles like the rising power dissipation with increasing clock rate, the computational power available now only rises due to the higher amount of processors in the so called multicore-architecture. This development also effects the software side, where programs are more and more forced to take advantage of the new facilities. Algorithms, which were preferred on a single process might now lose their superior performance, due to their bad scaling properties when transferred to a multiprocessor environment so that many accepted standard solutions must be rethought.

This also affects algorithms for the numerical solution of density functional theory, where also another new aspect is gaining importance for the numerical implementation, the so called order-N methods, which intend the computational cost of a simulation to scale linearly with the system size. Classical solution procedures of the Kohn-Sham equations imply the orthogonalization of a set of wave functions, which only scales cubic with the amount of those wave functions. The so called nearsightedness suggests that many properties of the electronic structure, like for example the chemical bond, are only influenced by its close neighborhood. Even in the metallic case the locality concept still remains valid under certain circumstances. This observation leads to the development of new linear scaling electronic structure methods, which have as a common feature the requirement of a local basis set [52, 117, 124]. For the numerical minimization of the Kohn-Sham energy functional, different basis sets have been applied. One quite successful basis consists of plane wave functions, which are globally defined in the domain and the Fast Fourier Transformation can be successfully applied. However due to these globally defined basis functions, this approach is less efficient to parallelize. It is restricted to periodic boundary conditions on simple domain shapes, and as mentioned above, does not fall into the category of linear scaling algorithms [117, 333], which require localized basis sets. Solution procedures, which do not make use of the Fourier transformation are called *real space* in the context of density functional theory. In chemistry, usually in the spirit of the linear combination of atomic orbitals (LCAO) method, basis functions with the form of atomic orbitals are used. Examples are the Gaussian and the Slater type orbitals [180], which are centered at the atomic positions. Due to their orbital-like shape, often relatively small basis sets are sufficient to adequately describe the electronic wave functions properly. However they do not form a complete basis in space and there are situations where the introduction of additional linear-independent basis functions becomes difficult.

Following our recent work in SCHAUER & LINDER [316], in Part III of this work the finite element basis set is employed for minimizing the density functional. It represents a complete basis, which is due to its flexibility already widely spread in engineering disciplines. Its basis functions consist of low order local polynomials, whose position is related to a geometrical entity on a mesh of the physical domain, also called the grid. It has simple interpolation properties and additional basis functions can be added locally and adaptively through a refinement of the underlying grid. The locality of the basis functions results in sparse matrices, which are suitable for the application of fast iterative Krylow space methods for solving linear equations. Additionally the locality enables the parallelization via domain decomposition. Early implementations of the finite element method in the context of electronic structure theory date back to the 1980s [146, 219, 382]. In the latter of these references orthogonalized finite element basis functions have been constructed in order to reduce the involved generalized eigenvalue problem to a standard one. Some of the early works make use of the symmetry in simple radial- or axi-symmetric configurations like single atoms or diatomic systems and therefore only lower-dimensional finite elements were applied. The application to Kohn-Sham density functional theory was first accomplished by TSUCHIDA & TSUKADA [362], which also exploited successfully the adaptivity of the finite element basis in [363] together with a transformation to curvilinear coordinates for simplifying the solution process. The application to pseudopotentials has been done in PASK & STERNE [282] together with the usage of periodic boundary conditions. The Γ -convergence of the finite element discretization was proven in SURYANARAYANA ET AL. [343]. In the recent works [200, 254], the authors investigate in detail the performance of all-electron calculations with the finite element basis and it is here, where this work intends to contribute [314, 315, 316].

1.4 Outline of the work

In line with the titles of the previous three sections, this work is divided into three parts, briefly summarized below.

Part I is concerned with the modeling of solids undergoing failure at the macroscopic scale. Its first Chapter 2 describes in detail the strong discontinuity approach as the multiscale framework to be employed for the incorporation of strong discontinuities into the individual finite elements. It, in particular, emphasizes on a recent extension of this approach applicable for a higher kinematic approximation of the failure surface in three dimensions and employs a combination of a global tracking algorithm and the marching cubes algorithm as a sophisticated crack propagation framework. Chapter 3 then focuses on the extension of the mostly purely mechanical constitutive relations used within the strong discontinuity approach to model failure in electromechanical coupled materials in the plane and the three dimensional setting. The concept of electric displacement saturation is investigated for the hysteretic behavior of ferroelectric ceramics and the initiation and propagation of cracks in piezoelectric ceramics.

Part II is concerned with a smaller length scale and aims to contribute to the vast research area of the computational modeling of materials with network microstructures at the mesoscopic scale. In Chapter 4 an advanced homogenization approach applicable to materials with random network microstructures such as elastomers, hydrogels, soft biological tissues, non-woven fabrics, or cellular foams is developed. In that way, the effect of

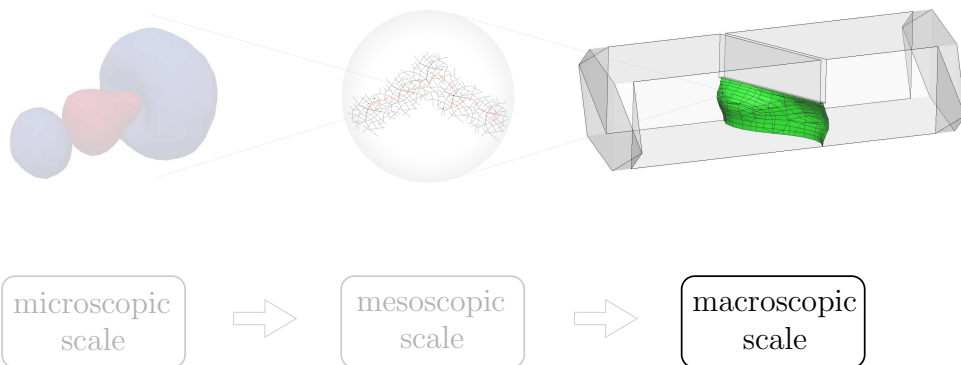
microscopic quantities relevant for the characterization of such networks, like their functionality, their molecular weight, or the stretch and force in the fibers comprising those networks can be incorporated into constitutive relations at the continuum scale. A successful scale bridging then permits the computational study of the performance of such advanced materials when used as sustainable building materials in large scale civil and environmental engineering applications. Chapter 5 presents a newly developed micromechanical constitutive model to predict the viscous behavior of rubber-like polymers. The model originates from diffusion processes of the highly mobile polymer chains described within the formalism of Brownian motion. Its combination with the non-affine microsphere model to represent the elastic response of the polymer yields to an overall good agreement of the computational results with those reported in experiments.

Finally, Part III is concerned with the quantum mechanical problem of modeling the electronic structure of solids. Here, the focus is laid on all-electron calculations of the Kohn-Sham density functional theory making use of the hierarchy of finite element bases. Chapter 6 presents a careful numerical analysis pointing out the numerical intricacies originating from the singularity of the nuclei and the necessity numerical approximations. The performance and reached chemical accuracy is reported for computations on noble gases and calculations of the bond-length and the dipole moment of the carbon monoxide molecule, finishing with the impact of an external electric field onto a single neon atom.

The work closes with some concluding remarks and possible future research directions in this field in Chapter 7.

Part I

Modeling solids undergoing failure at the macroscopic scale



2 The strong discontinuity approach for purely mechanical solids

In this chapter a particular methodology to model solids at failure is introduced. In the literature this approach is often called *strong discontinuity approach (SDA)* or *embedded finite element method (EFEM)*. The framework allows for the incorporation of strong discontinuities, representing cracks or shear bands as the physical phenomena appearing at the macroscale in solids at failure, into the finite element framework, and in particular for its treatment within the individual finite elements. This method will present the basis for the remaining chapters of Part I, which focuses on the computational modeling of micromechanical phenomena in solids at the macroscopic scale. This current Chapter 2 will provide a brief review of this methodology for the application of purely mechanical solid materials in three dimensional boundary value problems. The discussion in this chapter is based on the recent work of LINDER & ZHANG [209], where a marching cubes based failure surface propagation concept for 3D finite elements with non-planar embedded strong discontinuities of higher order kinematics is proposed. The subsequent Chapter 3 will show an extension of the strong discontinuity approach to account for failure in electromechanical coupled solids in two- and three dimensions.

2.1 Introduction

Failure in solids is characterized by the appearance of localized zones along which the fracture process takes place. When considering the macroscale as the scale of interest in this Part I of the work, such zones may represent cracks or shear bands along which strong discontinuities in the form of jumps of the primary variables like the displacement field in a purely mechanical based material appear. It is of particular importance to realize the challenge one faces when it comes to the constitutive modeling and the account of such zones within numerical methodologies like the finite element method as the formulation to be employed in this work. One distinguishes two basic approaches depending on the resolution of these localized zones which can either be accounted for in a *smearred* way or by a *discrete* modeling. The former approach accounts for the failure through a gradual growth of microcracks and microvoids resulting through homogenization techniques in constitutive damage type material models which are capable of representing softening mechanisms characteristic for solids at failure like the local damage models in ROTS ET AL. [313]. To describe size effects on the continuum level, nonlocal or gradient-type damage models need to be applied [71, 218]. Phase field models of fracture like the thermodynamic consistent variational formulation in MIEHE ET AL. [246, 247] also treat the localized zones in a smeared way. If such zone is discretely resolved one distinguishes between formulations where cohesive zones are added along the element boundaries and formulations where the localized zones are allowed to propagate through the individual finite elements. References associated with the former formulation include NEEDLEMAN [258], where traction separation laws are developed to describe the constitutive response along the strong discontinuity. Three dimensional simulations are performed in ORTIZ & PANDOLFI [274] including configurational-force driven propagation criteria in MIEHE & GÜRSES [240] or GÜRSES & MIEHE [132]. When the strong discontinuities are allowed to propagate through the individual finite elements, one distinguishes two further types

of methods based on the storage of the additional degrees of freedom needed for the description of the strong discontinuity being either locally on the element level [80, 265, 331] or globally at the finite element nodes [31, 136, 251].

The strong discontinuity approach, for which the localized zones of interest for the description of the failure process are allowed to go through the individual finite elements with a storage locally at the element level, is the method to be considered in Part I of this work. Originated in SIMO ET AL. [331] in a one dimensional context it was extended to a two dimensions setting in SIMO & OLIVER [328] through the introduction of a regularization parameter which became redundant in ARMERO & GARIKIPATI [11] where the formulation was embedded within the context of enhanced strain methods [329]. Extensions to the finite deformation theory are performed in ARMERO & GARIKIPATI [12] and the account for the propagation of the localized zones through three dimensional finite elements is accomplished in WELLS [378] or MOSLER & MESCHKE [253], among others. In ARMERO [7] the formulation is characterized as a multiscale approach where the localized zones are treated as the small scales appearing within the large scales representing the overall problem to be solved. This separation of the problem at hand serves convenient when extending the approach to beams in EHRLICH & ARMERO [86] and plates in ARMERO & EHRLICH [10]. Improvements with regard to the kinematic representation of the strong discontinuities for plane continuum problems are made in LINDER & ARMERO [205] within the infinitesimal theory and in ARMERO & LINDER [15] within the finite deformation context with the goal to avoid locking phenomena through the incorporation of mechanical separation modes directly into the formulation otherwise appearing within standard quadrilateral finite elements. Due to the challenges arising for the modeling of dynamic fracture, extensions from the quasi-static to the fully transient setting are only recently reported in HUESPE ET AL. [153] within a regularized approach and in ARMERO & LINDER [16] without the need for an additional regularization parameter. In LINDER & ARMERO [206] an investigation of dynamic fracture in the form of crack branching simulations in polymethylmethacrylate (PMMA) is performed.

In the following it is shown, how a discrete account of the arising strong discontinuities, appearing as jumps in the displacement field for the purely mechanical solids, can be achieved. It will be shown how their propagation through the individual finite elements without the need of remeshing or refinement strategies will be made possible. The decomposition of that methodology into a global problem, representing here the mechanical boundary value problem, and a local problem through which the strong discontinuities are introduced, is shown in Section 2.2. This serves convenient when developing the corresponding finite elements based on the requirement to avoid stress locking phenomena in Section 2.3. Numerical aspects are discussed in Section 2.4 including possibilities to initiate and propagate failure surfaces through an arbitrary three dimensional finite element mesh. For the latter, a marching cubes based propagation concept is combined with the global tracking algorithm [267, 269] and the strong discontinuity approach. After resolving scenarios of predicted non-planar failure surfaces by the marching cubes algorithm, the numerical implementation is outlined in detail in Section 2.4. Finally, the performance of the developed finite elements is illustrated in Section 2.5 based on several representative numerical simulations and compared with experimental results available in the literature.

2.2 The purely mechanical strong discontinuity framework

Following the developments in ARMERO [7, 8], in this section it will be briefly reviewed, how failure can be modeled for purely mechanical solids based on a sharp resolution of the failure zone by discontinuities in the displacement field. This will be done separately for the continuum framework in Section 2.2.1 and the finite element framework in Section 2.2.2.

2.2.1 Continuum modeling of failure in purely mechanical solids

The section starts with a brief summary of the mechanical boundary value problem at the infinitesimal range in Section 2.2.1.1 and continues in Section 2.2.1.2 by incorporating the required discontinuities into the formulation to model failure.

2.2.1.1 The mechanical boundary value problem. Let the purely mechanical solid \mathcal{B} occupy a configuration $\mathcal{B} \subset \mathbb{R}^{n_{\text{dim}}}$ for $1 \leq n_{\text{dim}} \leq 3$ characterized by the mechanical displacement field $\mathbf{u} : \mathcal{B} \rightarrow \mathbb{R}^{n_{\text{dim}}}$ as the primary unknown within the infinitesimal range of interest here. Associated with the solids material points labeled by their position $\mathbf{x} \in \mathcal{B}$ is the infinitesimal strain tensor $\boldsymbol{\varepsilon} : \mathcal{B} \rightarrow \mathbb{R}_{\text{sym}}^{n_{\text{dim}} \times n_{\text{dim}}}$, with $\mathbb{R}_{\text{sym}}^{n_{\text{dim}} \times n_{\text{dim}}}$ representing the space of symmetric tensors, defined by

$$\boldsymbol{\varepsilon}(\mathbf{u}) = \text{sym}[\nabla \mathbf{u}] = \frac{1}{2} [\nabla \mathbf{u} + (\nabla \mathbf{u})^T] \quad (2.1)$$

in terms of the standard gradient operator ∇ with respect to the coordinate \mathbf{x} . In addition, the stress tensor $\boldsymbol{\sigma} : \mathcal{B} \rightarrow \mathbb{R}_{\text{sym}}^{n_{\text{dim}} \times n_{\text{dim}}}$ is introduced as

$$\boldsymbol{\sigma} = \mathbb{C} \boldsymbol{\varepsilon} \quad \text{with} \quad \mathbb{C} = \lambda \mathbf{1} \otimes \mathbf{1} + 2\mu \mathbb{I} \quad (2.2)$$

in terms of the usual Lamé constants λ and μ as well as the second- and fourth order identity tensors $(\mathbf{1})_{ij} = \delta_{ij}$ and $(\mathbb{I})_{ijkl} = \frac{1}{2}(\delta_{ik}\delta_{jl} + \delta_{il}\delta_{jk})$. Together with the external volumetric loading $\rho \mathbf{b}$, the governing field equation follows as

$$\text{div} [\boldsymbol{\sigma}] + \rho \mathbf{b} = \mathbf{0} \quad (2.3)$$

in \mathcal{B} for the quasi-static case considered here. Within the purely mechanical setting, the boundary $\partial \mathcal{B}$ is separated into the parts $\partial \mathcal{B} = \overline{\partial_u \mathcal{B}} \cup \overline{\partial_t \mathcal{B}}$, where $\partial_u \mathcal{B}$ represents the part of the boundary with imposed displacement field $\mathbf{u} = \bar{\mathbf{u}}$ and $\partial_t \mathcal{B}$ represents the part of the boundary with imposed traction $\boldsymbol{\sigma} \mathbf{n} = \bar{\mathbf{t}}$ as it is illustrated in Figure 2.1. The usual argument of the form $\partial_u \mathcal{B} \cap \partial_t \mathcal{B} = \emptyset$ applies to ensure a well-posed problem.

The weak equations corresponding to the above field equation (2.3) now follows from standard arguments as

$$\int_{\mathcal{B}} \rho \mathbf{b} \cdot \delta \mathbf{u} \, dV + \int_{\partial_t \mathcal{B}} \bar{\mathbf{t}} \cdot \delta \mathbf{u} \, dA - \int_{\mathcal{B}} \boldsymbol{\sigma} : \text{sym}[\nabla \delta \mathbf{u}] \, dV = 0 \quad (2.4)$$

for all admissible variations $\delta \mathbf{u}$ with $\delta \mathbf{u} = \mathbf{0}$ on $\partial_u \mathcal{B} \subset \partial \mathcal{B}$. This equation (2.4) represents the starting point for a standard finite element approximation of a purely mechanical problem at hand without the appearance of strong discontinuities in the mechanical primary unknown. Such discontinuities are though required for the modeling of the characteristics of solids at failure and are therefore introduced in the subsequent Section 2.2.1.2.

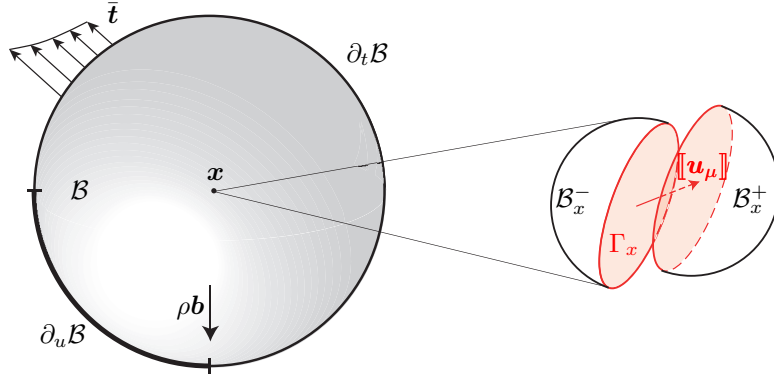


Figure 2.1: Incorporation of strong discontinuities into the continuum setting of a purely mechanical solid material. The global solution \mathbf{u} at a material point \mathbf{x} is equipped with the possibility of forming a strong discontinuity Γ_x in the local mechanical problem characterized by jumps $[[\mathbf{u}_\mu]]$ in the displacement field.

2.2.1.2 The continuous incorporation of strong discontinuities in the displacements. The main purpose of this Chapter 2 is to computationally model purely mechanical solids at failure where in addition to the global response of the solid in terms of the displacement field \mathbf{u} of the previous section, localized zones of failure $\Gamma_x \subset \mathbb{R}^{n_{\text{dim}}-1}$ are present in the form of cracks or shear bands. Such zones can locally be modeled by a strong discontinuity in the displacement field, meaning that the opening or sliding of such zone is represented by jumps $[[\circ]] = \circ^+ - \circ^-$ in the displacement field. Use is made of the convention to denote the side towards which the normal of the discontinuity surface points as the + side and the opposite side as the - side.

To capture both, the global as well as the local response, the following decomposition of the displacement field in the form of

$$\mathbf{u}_\mu = \mathbf{u} + \tilde{\mathbf{u}}([[\mathbf{u}_\mu]]) \quad (2.5)$$

is proposed for a material point $\mathbf{x} \in \mathcal{B}_x$ of a local neighborhood $\mathcal{B}_x \subset \mathcal{B}$. In (2.5), the arising local displacement field \mathbf{u}_μ is decomposed into contributions from the global displacement field \mathbf{u} and a discontinuous contribution $\tilde{\mathbf{u}}$ depending on the jumps $[[\mathbf{u}_\mu]]$ along the localized zone represented by the strong discontinuity Γ_x . The fact that each material point $\mathbf{x} \in \mathcal{B}_x$ is now equipped with the possibility of forming such strong discontinuities in the displacement field is illustrated in Figure 2.1.

This decomposition of the local displacement field can be extended to the definition of the local strain field defined as

$$\boldsymbol{\varepsilon}_\mu = \boldsymbol{\varepsilon}(\mathbf{u}) + \tilde{\boldsymbol{\varepsilon}}([[\mathbf{u}_\mu]]) \quad (2.6)$$

valid only in $\mathcal{B}_x \setminus \Gamma_x$, neglecting the resulting singular Dirac delta measures on Γ_x . Again, (2.6) consists of contributions from the global strain field $\boldsymbol{\varepsilon}$ defined in (2.1) and a contribution $\tilde{\boldsymbol{\varepsilon}}$ depending on the introduced displacement jumps $[[\mathbf{u}_\mu]]$ along the arising strong discontinuity. For a material point where now failure takes place, the constitutive relation (2.2) is replaced by

$$\boldsymbol{\sigma} = \mathbb{C} \boldsymbol{\varepsilon}_\mu \quad \text{in } \mathcal{B}_x \setminus \Gamma_x \quad (2.7)$$

now given in terms of the local strain field $\boldsymbol{\varepsilon}_\mu$. The introduction of the new unknown in the form of the jump in the displacement field $[[\mathbf{u}_\mu]]$ does require an additional equations for

its determination, which is provided by the enforcement of equilibrium along the strong discontinuity Γ_x . It is required that the traction $\mathbf{t} = \boldsymbol{\sigma}\mathbf{n}$ coming from the bulk of the material is in equilibrium with the traction \mathbf{t}_Γ resulting from a constitutive relation along the discontinuity Γ_x such as

$$\mathbf{t}_\Gamma = \mathbf{t}_\Gamma([\mathbf{u}_\mu]) \quad (2.8)$$

capable of describing an expected damage response of the traction vector with an increased opening of the strong discontinuity. Following ARMERO [7, 8], this requirement can be written in an integral sense as

$$\int_{\Gamma_x} \delta[\mathbf{u}_\mu] \cdot (\boldsymbol{\sigma}\mathbf{n} - \mathbf{t}_\Gamma) dA = 0 \quad (2.9)$$

for all test functions $\delta[\mathbf{u}_\mu] : \Gamma_x \rightarrow \mathbb{R}^{n_{\text{dim}}}$. It has to be kept in mind that the equations in (2.9) are local in nature and only have to be satisfied in the presence of a strong discontinuity Γ_x . This is emphasized in ARMERO [8], where it is shown that the existence of solutions of (2.9) is obtained in the limit

$$h_x = \frac{\text{measure}(\mathcal{B}_x)}{\text{measure}(\Gamma_x)} \longrightarrow 0. \quad (2.10)$$

2.2.2 Finite element modeling of failure in purely mechanical solids

Following the developments in ARMERO [7, 8], in an analogous way as in the previous section, the problem at hand is divided into a global problem consisting now of the discrete form of the mechanical boundary value problem, which will be discussed in Section 2.2.2.1 and a local problem representing the incorporation of strong discontinuities into the formulation to numerically model failure discussed in Section 2.2.2.2.

2.2.2.1 The discrete mechanical boundary value problem. The spatial discretization of the body \mathcal{B} is performed by in total n_{elem} isoparametric finite elements \mathcal{B}_e^h approximating the configuration $\mathcal{B} \approx \mathcal{B}^h = \bigcup_{e=1}^{n_{\text{elem}}} \mathcal{B}_e^h$ as it is illustrated in Figure 2.2 with the proper characterization of the boundary region $\partial\mathcal{B}^h = \overline{\partial_u\mathcal{B}^h} \cup \partial_t\mathcal{B}^h$. The primary unknowns in the form of the displacement field \mathbf{u}^h at a point $\mathbf{x}^h \in \mathcal{B}^h$ is approximated by

$$\mathbf{u}^h(\mathbf{x}^h) = \sum_{A=1}^{n_{\text{node}}} N_u^A(\mathbf{x}^h) \mathbf{d}_A = \mathbf{N}_u \mathbf{d} \quad (2.11)$$

in terms of standard shape functions N_u^A and the corresponding values of the displacement field \mathbf{d}_A of node A with in total n_{node} nodes. The approximation of the strain field $\boldsymbol{\varepsilon}^h$ is then given as

$$\nabla^s \mathbf{u}^h(\mathbf{x}^h) = \boldsymbol{\varepsilon}^h(\mathbf{x}^h) = \sum_{A=1}^{n_{\text{node}}} \bar{\mathbf{B}}_u^A(\mathbf{x}^h) \mathbf{d}_A = \bar{\mathbf{B}}_u \mathbf{d} \quad (2.12)$$

in terms of the generic ‘‘B-bar’’ matrices $\bar{\mathbf{B}}_u^A$, outlining the generality of the proposed formulation with regard to mixed, assumed, or enhanced methodologies [329].

Assuming a Bubnov Galerkin formulation [155], the corresponding variations of the displacement field and its gradient are approximated in terms of the same shape functions

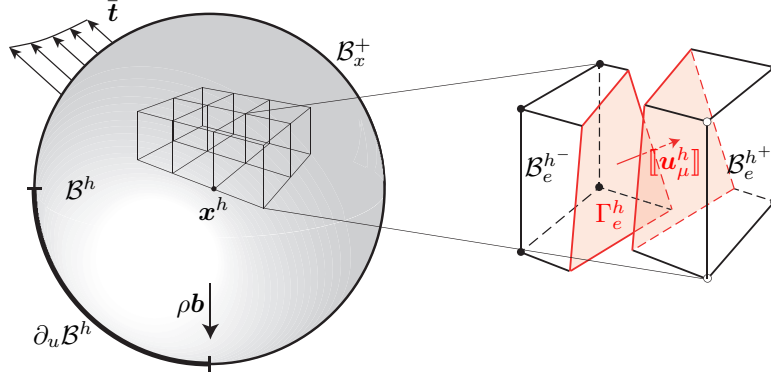


Figure 2.2: Incorporation of strong discontinuities into the finite element setting of purely mechanical solids. Each finite element \mathcal{B}_e^h of the global problem is equipped with the possibility of forming a strong discontinuity Γ_e^h in the local problem characterized by jumps $[[\mathbf{u}_\mu^h]]$ in the displacement field.

and “B-bar” matrices. Insertion into the continuum representation (2.4) then results in the discrete form of the global mechanical problem at hand as

$$\mathbf{R}_u = \mathbf{f}_u^{\text{ext}} - \mathbf{A} \int_{\mathcal{B}_e^h} \bar{\mathbf{B}}_u^T \boldsymbol{\sigma} dV \quad \text{with} \quad \mathbf{f}_u^{\text{ext}} = \mathbf{A} \left(\int_{\mathcal{B}_e^h} \rho \bar{\mathbf{N}}_u^T \mathbf{b} dV + \int_{\partial_t \mathcal{B}_e^h} \bar{\mathbf{N}}_u^T \bar{\mathbf{t}} dA \right) \quad (2.13)$$

in terms of the assembly of the internal response of the body based on standard integration techniques over the individual finite elements and the assembled external force vector $\mathbf{f}_u^{\text{ext}}$. The solution of the global problem proceeds by bringing to zero the residual equations in (2.13) based on an iterative solution procedure like Newton’s method, requiring in addition the linearization of that residual equation as it will be outlined in Section 2.4.5.

To make the discrete formulation capable of representing failure in purely mechanical solids, strong discontinuities, which have not been accounted for in the global problem considered in this section, need to be incorporated. This is done in the discrete local problem defined in the subsequent Section 2.2.2.2.

2.2.2.2 The discrete incorporation of strong discontinuities in the displacements. In this section the discrete counterpart to Section 2.2.1.2 is presented with the goal of incorporating the required strong discontinuities locally into the individual finite elements to model the fracture process within the purely mechanical solid.

To do so, consider a single finite element $\mathcal{B}_e^h \subset \mathcal{B}^h$ in which based on some criterion failure is detected along a localized zone Γ_e^h , as illustrated in Figure 2.2. The primary result of such detection is the appearance of a strong discontinuity $[[\mathbf{u}_\mu^h]]$ in the displacement field, modeling the mechanical response of the material with regard to failure. Within the discrete setting considered in this section, an approximation of this field is made in an analogous way as it is done for the global quantities in Section 2.2.2.1. Since valid along the localized zone Γ_e^h , it can be interpolated along that zone as

$$[[\mathbf{u}_\mu^h]](s, t) = \mathfrak{J}_u(s, t) \boldsymbol{\xi}_u \quad (2.14)$$

in terms of the associated jump interpolation function $\mathfrak{J}_u(s, t)$ depending on local coordinates s and t in the artificial plane computed in Section 2.4.4 as an approximation to the

possible non-planar actual failure surface Γ_e^h illustrated in Figure 2.2 and newly introduced degrees of freedom $\boldsymbol{\xi}_u$ containing the geometric information of the strong discontinuity within a certain element.

Motivated by the decomposition of the local displacement and strain field in (2.5) and (2.6), their discrete forms are given as

$$\boldsymbol{\varepsilon}_\mu^h = \boldsymbol{\varepsilon}^h(\mathbf{d}) + \tilde{\boldsymbol{\varepsilon}}^h(\boldsymbol{\xi}_u) \quad (2.15)$$

where the global term $\boldsymbol{\varepsilon}^h(\mathbf{d})$ is given in (2.12) based on the linear operator $\bar{\mathbf{B}}_u$ acting on the nodal displacements \mathbf{d} . A similar dependence is chosen for the local term $\tilde{\boldsymbol{\varepsilon}}^h(\boldsymbol{\xi}_u)$ in terms of newly introduced operator \mathfrak{C}_u resulting in

$$\boldsymbol{\varepsilon}_\mu^h = \bar{\mathbf{B}}_u \mathbf{d} + \mathfrak{C}_u \boldsymbol{\xi}_u \quad (2.16)$$

acting on the in (2.14) introduced internal degrees of freedom $\boldsymbol{\xi}_u$. The operator \mathfrak{C}_u is denoted as ‘‘compatibility operator’’ due to its appearance within the kinematic relation in (2.16). It will be outlined in detail in Section 2.3 how these operators can be determined.

One additional equation is introduced in Section 2.2.1.2 with the aim to yield additional information for the determination of the newly introduced jumps in the displacement field in that section. It remains to be shown in this section, how this additional equation in (2.9) can be approximated in a discrete setting. To do so, the approach proposed in LINDER & ARMERO [205] for the plane setting extended in ARMERO & KIM [13] is followed, which yields

$$\mathbf{r}_u^e = - \int_{\mathcal{B}_e^h} \mathfrak{C}_u^T \boldsymbol{\sigma} dV - \int_{\Gamma_e^h} \mathfrak{J}_u^T \mathbf{t}_\Gamma dA \quad (2.17)$$

in terms of the ‘‘equilibrium operator’’ \mathfrak{C}_u enforcing equilibrium along the discontinuity Γ_e^h . This operator represents a projection of the stresses $\boldsymbol{\sigma}$ from the integration points onto Γ_e^h . In particular, for an approximation of the variations of the displacement jumps in (2.14) as polynomials of order q of the local coordinates s and t in the form

$$\delta[\mathbf{u}_\mu^h] = \sum_{\substack{i,j=0 \\ i+j \leq q}}^q s^i t^j \delta \boldsymbol{\xi}_u^{(ij)} \quad (2.18)$$

the equilibrium operator is given as

$$\mathfrak{C}_u = [\boldsymbol{\varepsilon}_u^{(00)}, \boldsymbol{\varepsilon}_u^{(10)}, \boldsymbol{\varepsilon}_u^{(01)}, \boldsymbol{\varepsilon}_u^{(20)}, \boldsymbol{\varepsilon}_u^{(11)}, \boldsymbol{\varepsilon}_u^{(02)}, \dots] \quad \text{where} \quad \boldsymbol{\varepsilon}_u^{(ij)} \delta \boldsymbol{\xi}_u^{(ij)} = -\frac{1}{h_e} \boldsymbol{\varepsilon}^{(ij)} (\mathbf{n} \otimes \delta \boldsymbol{\xi}_u^{(ij)})^s \quad (2.19)$$

in terms of the element size $h_e = V_{\mathcal{B}_e^h} / A_{\Gamma_e^h}$ and polynomial functions $\boldsymbol{\varepsilon}^{(ij)}(x, y, z)$. These are approximations of the integrand $\boldsymbol{\sigma} \mathbf{n}$ in (2.9) of order up to p within a local Cartesian frame $\{x, y, z\}$ of an element \mathcal{B}_e^h , given as

$$\boldsymbol{\varepsilon}^{(ij)}(x, y, z) = \sum_{\substack{i,j,k=0 \\ i+j+k \leq p}}^p a_{(i,j,k)}^{(ij)} x^i y^j z^k \quad \text{with} \quad [a_{(i,j,k)}^{(ij)}] = [V_{(i,j,k),(m,n,o)}]^{-1} [A_{(m,n,o)}^{(ij)}] \quad (2.20)$$

where

$$[V_{(i,j,k),(m,n,o)}] = \frac{1}{V_{\mathcal{B}_e^h}} \int_{\mathcal{B}_e^h} x^{i+m} y^{j+n} z^{k+o} dV \quad \text{and} \quad [A_{(m,n,o)}^{(ij)}] = \frac{1}{A_{\Gamma_e^h}} \int_{\Gamma_e^h} s^i t^j x^m y^n z^o dA \quad (2.21)$$

for all $m, n, o = 0, 1, \dots, p$ with $m + n + o \leq p$ with the property of satisfying

$$\frac{1}{V_{\mathcal{B}_e^h}} \int_{\mathcal{B}_e^h} \mathbf{e}^{(ij)}(x, y, z) x^m y^n z^o dV = \frac{1}{A_{\Gamma_e^h}} \int_{\Gamma_e^h} s^i t^j x^m y^n z^o dA \quad (2.22)$$

needed for the conversion of the discontinuity to the bulk integral.

Writing the variations of the introduced local parameters in (2.18) in the local basis $\{\mathbf{n}, \mathbf{s}, \mathbf{t}\}$ in terms of the orthonormal unit normal and tangent vectors \mathbf{n} , \mathbf{s} , and \mathbf{t} as

$$\boldsymbol{\xi}_u^{(ij)} = \boldsymbol{\xi}_u^{(ijn)} \mathbf{n} + \boldsymbol{\xi}_u^{(ijs)} \mathbf{s} + \boldsymbol{\xi}_u^{(ijt)} \mathbf{t} \quad (2.23)$$

results in the following expression for the equilibrium operator

$$\boldsymbol{\mathfrak{E}}_u = \left[\underbrace{\{\boldsymbol{\mathfrak{E}}_u^{(oon)}, \boldsymbol{\mathfrak{E}}_u^{(oos)}, \boldsymbol{\mathfrak{E}}_u^{(oot)}\}}_{\boldsymbol{\mathfrak{E}}_u^{(oo)}}, \underbrace{\{\boldsymbol{\mathfrak{E}}_u^{(1on)}, \boldsymbol{\mathfrak{E}}_u^{(1os)}, \boldsymbol{\mathfrak{E}}_u^{(1ot)}\}}_{\boldsymbol{\mathfrak{E}}_u^{(1o)}}, \underbrace{\{\boldsymbol{\mathfrak{E}}_u^{(o1n)}, \boldsymbol{\mathfrak{E}}_u^{(o1s)}, \boldsymbol{\mathfrak{E}}_u^{(o1t)}\}}_{\boldsymbol{\mathfrak{E}}_u^{(o1)}}, \dots \right] \quad (2.24)$$

when working in that local basis with the components

$$\boldsymbol{\mathfrak{E}}_u^{(ijn)} = -\frac{1}{h_e} \mathbf{e}^{(ij)}(\mathbf{n} \otimes \mathbf{n}), \quad \boldsymbol{\mathfrak{E}}_u^{(ijs)} = -\frac{1}{h_e} \mathbf{e}^{(ij)}(\mathbf{n} \otimes \mathbf{s})^s, \quad \text{and} \quad \boldsymbol{\mathfrak{E}}_u^{(ijt)} = -\frac{1}{h_e} \mathbf{e}^{(ij)}(\mathbf{n} \otimes \mathbf{t})^s. \quad (2.25)$$

Remark 2.1. *In the two dimensional setting it is shown in LINDER & ARMERO [205], that an approximation of the variation of the displacement jumps*

$$\delta[\mathbf{u}_\mu^h] = \sum_{\mathfrak{k}=0}^q s^{\mathfrak{k}} \delta \boldsymbol{\xi}_u^{(\mathfrak{k})} \quad (2.26)$$

in terms of one coordinate $s \in [-l_{\Gamma_e^h}/2, l_{\Gamma_e^h}/2]$ along the one dimensional failure surface results in the expression for the equilibrium operator as

$$\boldsymbol{\mathfrak{E}}_u = [\boldsymbol{\mathfrak{E}}_u^{(o)}, \boldsymbol{\mathfrak{E}}_u^{(1)}, \dots, \boldsymbol{\mathfrak{E}}_u^{(q)}] \quad \text{where} \quad \boldsymbol{\mathfrak{E}}_u^{(\mathfrak{k})} \delta \boldsymbol{\xi}_u^{(\mathfrak{k})} = -\frac{1}{h_e} \mathbf{e}^{(\mathfrak{k})}(\mathbf{n} \otimes \delta \boldsymbol{\xi}_u^{(\mathfrak{k})})^s \quad (2.27)$$

in terms of the element size $h_e = A_{\mathcal{B}_e^h}/l_{\Gamma_e^h}$ and polynomial functions $\mathbf{e}^{(\mathfrak{k})}(x, y)$. In the plane setting, these are approximations of the integrand $\boldsymbol{\sigma} \mathbf{n}$ in (2.9) of order up to p within a local Cartesian frame $\{x, y\}$ of an element \mathcal{B}_e^h , given as

$$\mathbf{e}^{(\mathfrak{k})}(x, y) = \sum_{\substack{i, j=0 \\ i+j \leq p}}^p a_{(i, j)}^{(\mathfrak{k})} x^i y^j \quad \text{with} \quad [a_{(i, j)}^{(\mathfrak{k})}] = [A_{(i, j), (m, n)}]^{-1} [\ell_{(m, n)}^{(\mathfrak{k})}] \quad (2.28)$$

where

$$[A_{(i, j), (m, n)}] = \frac{1}{A_{\mathcal{B}_e^h}} \int_{\mathcal{B}_e^h} x^{i+m} y^{j+n} dV \quad \text{and} \quad [\ell_{(m, n)}^{(\mathfrak{k})}] = \frac{1}{l_{\Gamma_e^h}} \int_{\Gamma_e^h} s^{\mathfrak{k}} x^m y^n dA \quad (2.29)$$

for all $m, n = 0, 1, \dots, p$ with $m + n \leq p$ with the property of satisfying

$$\frac{1}{A_{\mathcal{B}_e^h}} \int_{\mathcal{B}_e^h} \mathbf{e}^{(\mathfrak{k})}(x, y) x^m y^n dV = \frac{1}{l_{\Gamma_e^h}} \int_{\Gamma_e^h} s^{\mathfrak{k}} x^m y^n dA. \quad (2.30)$$

2.3 Finite element design

This section follows the approaches suggested in LINDER & ARMERO [205] for the computation of the compatibility operator \mathfrak{C}_u in the plane setting and the one in ARMERO & KIM [13] in the three dimensional theory and outlines the development of three dimensional finite elements capable of modeling solids at failure. The strategy for the determination of the missing quantities based on a certain separation mode is as follows: Consider a single finite element in the 3D setting and assume that a discontinuity surface fully separates the element into two parts by a fully softened strong discontinuity. The nodal displacement field of this mode represents the global degrees of freedom, which are chosen for the separation mode in such a way that a jump of the corresponding quantity exists along the failure surface. A decomposition of the strain field as in (2.15) is assumed also for the separation mode under consideration. The separation mode should be chosen in a physical meaningful way since it is directly incorporated into the finite element formulation avoiding the existence of stress locking phenomena otherwise possibly appearing for such mode. Furthermore, the separation mode should be chosen in a way, such that the exact solution of the total part of the quantities stored at the integration points can be computed. With all this at hand, it is then possible to extract the missing information of the jump interpolation function \mathfrak{J}_u as well as the compatibility operator \mathfrak{C}_u , leading to the development of new finite elements. This is done in ARMERO & EHRLICH [10], EHRLICH & ARMERO [86] for beams and plates, in ARMERO & LINDER [15], LINDER & ARMERO [205] for the 2D continuum and recently in ARMERO & KIM [13] for the 3D continuum. In this latter reference, in total nine separation modes are identified to be of major importance for the 3D modeling of solids at failure. Those are three constant translation modes, three rotation modes, two stretch modes, and one in-plane shear mode. In this work, the rotation mode around the normal of the failure surface used in ARMERO & KIM [13] is replaced by an additional in-plane shear mode resulting in a slight difference in the closed form expressions of the operator.

2.3.1 Constant separation modes

Consider a single finite element \mathcal{B}_e^h and assume that a discontinuity Γ_e^h fully separates the element into two parts \mathcal{B}_e^{h+} and \mathcal{B}_e^{h-} . For the constant separation mode illustrated in Figure 2.3, the displacement field is chosen as

$$\mathbf{d}_A^{(\text{oo})} = \begin{cases} \mathbf{j}_u^{(\text{oo})} = \xi_u^{(\text{oon})} \mathbf{n} + \xi_u^{(\text{oos})} \mathbf{s} + \xi_u^{(\text{oot})} \mathbf{t} & \text{for node } A \in \mathcal{B}_e^{h+} \\ \mathbf{0} & \text{otherwise} \end{cases} \quad (2.31)$$

in terms of the unit normal vector \mathbf{n} and the unit tangent vectors \mathbf{s} and \mathbf{t} of the discontinuity plane and in terms of the n_{dim} local degrees of freedom $\boldsymbol{\xi}_u^{(\text{oo})} = [\xi_u^{(\text{oon})}, \xi_u^{(\text{oos})}, \xi_u^{(\text{oot})}]$ where $\xi_u^{(\text{oon})}$ represents the constant normal and $\xi_u^{(\text{oos})}$ and $\xi_u^{(\text{oot})}$ represent the tangential separation of the two parts of the single finite element, as illustrated in Figure 2.3. The jump interpolation matrix then follows from the computation of the actual displacement jump along the strong discontinuity for the separation mode given in (2.31) as

$$\llbracket \mathbf{u}_\mu^h \rrbracket_{(\text{oo})} = \mathbf{j}_u^{(\text{oo})} \Big|_{\Gamma_e^h} = \xi_u^{(\text{oon})} \mathbf{n} + \xi_u^{(\text{oos})} \mathbf{s} + \xi_u^{(\text{oot})} \mathbf{t}. \quad (2.32)$$

Since based on the first equation in (2.14) the displacement jumps can be written also as $\llbracket \mathbf{u}_\mu^h \rrbracket_{(\text{oo})} = \mathfrak{J}_u^{(\text{oo})} \boldsymbol{\xi}_u^{(\text{oo})}$, one can directly read off the jump interpolation matrix for the

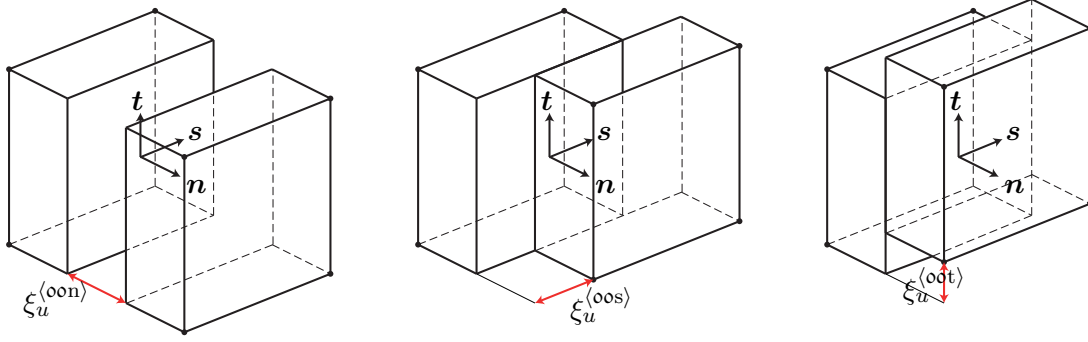


Figure 2.3: Illustration of the constant separation modes in terms of one constant normal opening $\xi_u^{(oon)}$ in \mathbf{n} direction and two constant tangential openings $\xi_u^{(oos)}$ and $\xi_u^{(oot)}$ in \mathbf{s} and \mathbf{t} direction, respectively.

constant separation mode as

$$\mathfrak{J}_u^{(oo)} = [\mathbf{n}, \mathbf{s}, \mathbf{t}] \quad (2.33)$$

an interpolation matrix depending on the unit normal and tangent vectors \mathbf{n} , \mathbf{s} , and \mathbf{t} only.

Next, the compatibility operator $\mathfrak{C}_u^{(oo)}$ corresponding to the constant separation mode is derived based on the decomposition of the strain field as in (2.15). For the constant separation mode in (2.31), one can write

$$\boldsymbol{\varepsilon}_{\mu, \langle oo \rangle}^h = \boldsymbol{\varepsilon}_{\langle oo \rangle}^h + \mathfrak{C}_u^{(oo)} \boldsymbol{\xi}_u^{(oo)} \quad (2.34)$$

where the global contribution can be easily computed and the final resulting strain is known corresponding to the fact that there are no strains appearing in both parts of the separated single finite element based on this separation mode, i.e.

$$\boldsymbol{\varepsilon}_{\langle oo \rangle}^h = \sum_{A \in \mathcal{B}_e^{h+}} \bar{\mathbf{B}}_u^A \mathbf{j}_u^{(oo)} \quad \text{and} \quad \boldsymbol{\varepsilon}_{\mu, \langle oo \rangle}^h = \mathbf{0}. \quad (2.35)$$

Therefore, an equation, based on which the operator $\mathfrak{C}_u^{(oo)}$ can be computed, is obtained. The final result can be written as $\mathfrak{C}_u^{(oo)} = [\mathfrak{C}_u^{(oon)}, \mathfrak{C}_u^{(oos)}, \mathfrak{C}_u^{(oot)}]$ where

$$\mathfrak{C}_u^{(oon)} = - \sum_{A \in \mathcal{B}_e^{h+}} \bar{\mathbf{B}}_u^A \mathbf{n}, \quad \mathfrak{C}_u^{(oos)} = - \sum_{A \in \mathcal{B}_e^{h+}} \bar{\mathbf{B}}_u^A \mathbf{s}, \quad \text{and} \quad \mathfrak{C}_u^{(oot)} = - \sum_{A \in \mathcal{B}_e^{h+}} \bar{\mathbf{B}}_u^A \mathbf{t} \quad (2.36)$$

are given as summations of the linearized strain operator matrix $\bar{\mathbf{B}}_u$ over the nodes on one side of the discontinuity multiplying the normal and tangent vectors \mathbf{n} , \mathbf{s} , and \mathbf{t} , respectively.

Remark 2.2. The results obtained in LINDER & ARMERO [205] for the plane setting in the local basis $\{\mathbf{n}, \mathbf{m}\}$ for the jump interpolation matrix and the components of the compatibility operator $\mathfrak{C}_u^{(o)} = [\mathfrak{C}_u^{(on)}, \mathfrak{C}_u^{(om)}]$ for the constant separation mode boil down to

$$\mathfrak{J}_u^{(o)} = [\mathbf{n}, \mathbf{m}] \quad \text{and} \quad \mathfrak{C}_u^{(on)} = - \sum_{A \in \mathcal{B}_e^{h+}} \bar{\mathbf{B}}_u^A \mathbf{n}, \quad \mathfrak{C}_u^{(om)} = - \sum_{A \in \mathcal{B}_e^{h+}} \bar{\mathbf{B}}_u^A \mathbf{m}. \quad (2.37)$$

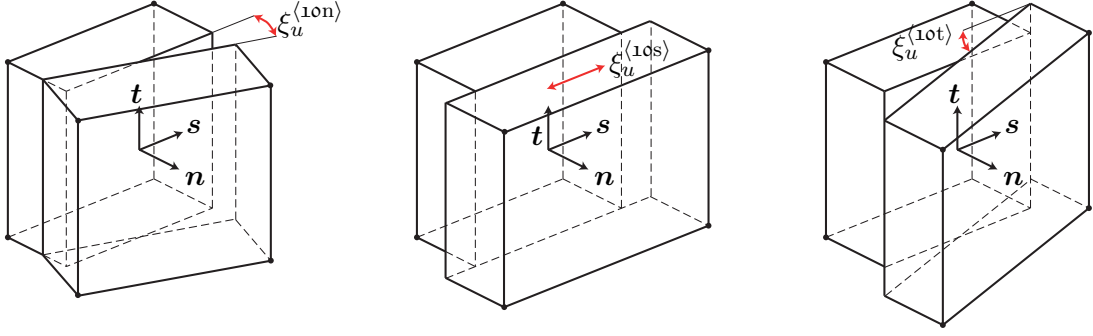


Figure 2.4: Illustration of the linear separation modes along the s -direction in terms of one rotational mode $\xi_u^{(10n)}$ around the t -direction, one stretch mode $\xi_u^{(10s)}$ in s -direction, and one shear mode $\xi_u^{(10t)}$, respectively.

2.3.2 Linear separation modes

To improve the kinematics of the strong discontinuity, in ARMERO & KIM [13] six linear separation modes are identified in addition to the usually used three constant separation modes. All those are directly incorporated into the finite element framework with embedded strong discontinuities so that their exact representation can be assured. As a slight difference, rather than choosing three rotation modes, two stretch modes, and one in-plane shear mode as in ARMERO & KIM [13], in this work the rotational mode around the normal direction is replaced by an additional in-plane shear mode resulting in slight differences of the closed form solutions for the compatibility operator, which is the key kinematic quantity in the framework of the finite elements with embedded strong discontinuities.

To do so, consider again a single finite element \mathcal{B}_e^h and assume that a discontinuity Γ_e^h fully separates the element into two parts \mathcal{B}_e^{h+} and \mathcal{B}_e^{h-} . First, the linear separation modes along the s -direction illustrated in Figure 2.4 are considered for which the displacement field is chosen as

$$\mathbf{d}_A^{(10)} = \begin{cases} \mathbf{j}_A^{(10)} = \mathbf{L}^{(10)} \bar{\mathbf{x}}^A & \text{for node } A \in \mathcal{B}_e^{h+} \\ \mathbf{0} & \text{otherwise} \end{cases} \quad (2.38)$$

with

$$\mathbf{L}^{(10)} = \xi_u^{(10n)} (\mathbf{n} \otimes \mathbf{s})^a + \xi_u^{(10s)} (\mathbf{s} \otimes \mathbf{s}) + \xi_u^{(10t)} (\mathbf{t} \otimes \mathbf{s})^a \quad \text{and} \quad \bar{\mathbf{x}}^A = \mathbf{x}^A - \mathbf{x}_\Gamma \quad (2.39)$$

where $(\bullet \otimes \circ)^a = (\bullet \otimes \circ) - (\circ \otimes \bullet)$. Use is made of the n_{dim} local degrees of freedom $\boldsymbol{\xi}_u^{(10)} = [\xi_u^{(10n)}, \xi_u^{(10s)}, \xi_u^{(10t)}]$ where $\xi_u^{(10n)}$ represents the linear normal and $\xi_u^{(10s)}$ and $\xi_u^{(10t)}$ represent the linear tangential separation of the two parts of the single finite element, as illustrated in Figure 2.4. The jump interpolation matrix then follows from the computation of the actual displacement jump along the strong discontinuity for the separation mode given in (2.38) as

$$\llbracket \mathbf{u}_\mu^h \rrbracket_{(10)} = \mathbf{j}_A^{(10)} \Big|_{\Gamma_e^h} = s \xi_u^{(10n)} \mathbf{n} + s \xi_u^{(10s)} \mathbf{s} + s \xi_u^{(10t)} \mathbf{t}. \quad (2.40)$$

Since based on the first equation in (2.14) the displacement jumps can be written also as $\llbracket \mathbf{u}_\mu^h \rrbracket_{(10)} = \tilde{\mathfrak{J}}_u^{(10)} \boldsymbol{\xi}_u^{(10)}$, one can directly read off the jump interpolation matrix for the linear separation mode along the s -direction as

$$\tilde{\mathfrak{J}}_u^{(10)} = [\mathbf{sn}, \mathbf{ss}, \mathbf{st}] \quad (2.41)$$

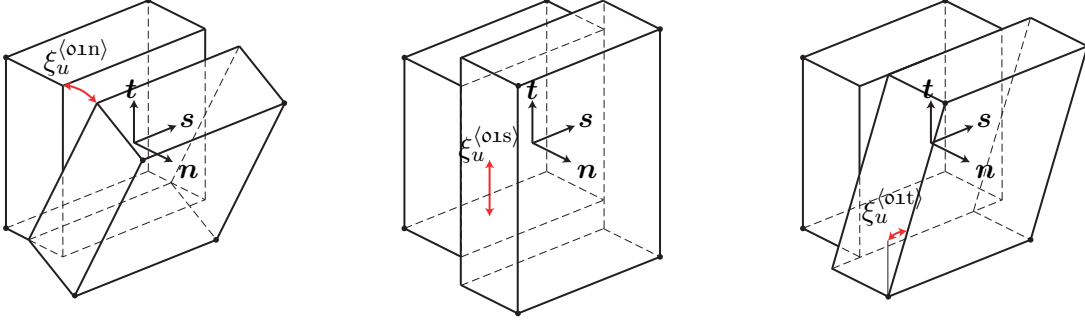


Figure 2.5: Illustration of the linear separation modes along the t -direction in terms of one rotational mode $\xi_u^{(o1n)}$ around the s -direction, one stretch mode $\xi_u^{(o1s)}$ in t -direction, and one shear mode $\xi_u^{(o1t)}$, respectively.

an interpolation matrix depending on the unit normal and tangent vectors \mathbf{n} , \mathbf{s} , and \mathbf{t} only and the coordinate s along the tangential direction \mathbf{s} .

Next, the compatibility operator $\mathfrak{C}_u^{(1o)}$ corresponding to this linear separation mode is derived based on the decomposition of the strain field as in (2.15). For the linear separation mode in (2.38), one can write

$$\boldsymbol{\varepsilon}_{\mu, \langle 1o \rangle}^h = \boldsymbol{\varepsilon}_{\langle 1o \rangle}^h + \mathfrak{C}_u^{(1o)} \boldsymbol{\xi}_u^{(1o)} \quad (2.42)$$

where the global contribution can be easily computed and the final resulting strain is known corresponding to the fact that there are no strains appearing due to the appearance of $\xi_u^{(1on)}$ but that a strain is expected due to the appearance of $\xi_u^{(1os)}$ and $\xi_u^{(1ot)}$, i.e.

$$\boldsymbol{\varepsilon}_{\langle 1o \rangle}^h = \sum_{A \in \mathcal{B}_e^{h+}} \bar{\mathbf{B}}_u^A \mathbf{j}_u^{(1o)} \quad \text{and} \quad \boldsymbol{\varepsilon}_{\mu, \langle 1o \rangle}^h = [\xi_u^{(1os)}(\mathbf{s} \otimes \mathbf{s}) + \xi_u^{(1ot)}(\mathbf{t} \otimes \mathbf{s})] \mathcal{H}_{\Gamma_e^h} \quad (2.43)$$

where the Heaviside function $\mathcal{H}_{\Gamma_e^h}$ is introduced, which takes the value 1 in \mathcal{B}_e^{h+} and 0 in \mathcal{B}_e^{h-} . Insertion of (2.43) into (2.42) results in an equation based on which the operator $\mathfrak{C}_u^{(1o)}$ can be computed. The final result can be written as $\mathfrak{C}_u^{(1o)} = [\mathfrak{C}_u^{(1on)}, \mathfrak{C}_u^{(1os)}, \mathfrak{C}_u^{(1ot)}]$ where

$$\mathfrak{C}_u^{(1on)} = - \sum_{A \in \mathcal{B}_e^{h+}} \bar{\mathbf{B}}_u^A (\mathbf{n} \otimes \mathbf{s})^a \bar{\mathbf{x}}_A \quad (2.44)$$

as well as

$$\mathfrak{C}_u^{(1os)} = (\mathbf{s} \otimes \mathbf{s}) \mathcal{H}_{\Gamma_e^h} - \sum_{A \in \mathcal{B}_e^{h+}} \bar{\mathbf{B}}_u^A (\mathbf{s} \otimes \mathbf{s}) \bar{\mathbf{x}}_A \quad \text{and} \quad \mathfrak{C}_u^{(1ot)} = (\mathbf{t} \otimes \mathbf{s}) \mathcal{H}_{\Gamma_e^h} - \sum_{A \in \mathcal{B}_e^{h+}} \bar{\mathbf{B}}_u^A (\mathbf{t} \otimes \mathbf{s})^a \bar{\mathbf{x}}_A. \quad (2.45)$$

Secondly, when considering the linear separation modes along the t -direction illustrated in Figure 2.5 analogous expressions are obtained as above. Those are summarized as

$$\begin{aligned} \mathfrak{J}_u^{(o1)} &= [\mathbf{tn}, \mathbf{ts}, \mathbf{tt}], \quad \mathfrak{C}_u^{(o1n)} = - \sum_{A \in \mathcal{B}_e^{h+}} \bar{\mathbf{B}}_u^A (\mathbf{n} \otimes \mathbf{t})^a \bar{\mathbf{x}}_A \\ \mathfrak{C}_u^{(o1s)} &= (\mathbf{s} \otimes \mathbf{t}) \mathcal{H}_{\Gamma_e^h} - \sum_{A \in \mathcal{B}_e^{h+}} \bar{\mathbf{B}}_u^A (\mathbf{s} \otimes \mathbf{t})^a \bar{\mathbf{x}}_A, \quad \text{and} \quad \mathfrak{C}_u^{(o1t)} = (\mathbf{t} \otimes \mathbf{t}) \mathcal{H}_{\Gamma_e^h} - \sum_{A \in \mathcal{B}_e^{h+}} \bar{\mathbf{B}}_u^A (\mathbf{t} \otimes \mathbf{t}) \bar{\mathbf{x}}_A. \end{aligned} \quad (2.46)$$

In general, the linear separation mode is considered in addition to the constant separation mode so that the final jump interpolation matrix and the final compatibility operator have the form

$$\mathfrak{J}_u = [\mathfrak{J}_u^{(00)}, \mathfrak{J}_u^{(10)}, \mathfrak{J}_u^{(01)}] \quad \text{and} \quad \mathfrak{C}_u = [\mathfrak{C}_u^{(00)}, \mathfrak{C}_u^{(10)}, \mathfrak{C}_u^{(01)}] \quad (2.47)$$

with the individual contributions given in (2.33), (2.36), (2.41), and (2.44)-(2.46), respectively.

Remark 2.3. *The results obtained in LINDER & ARMERO [205] for the plane setting in the local basis $\{\mathbf{n}, \mathbf{m}\}$ and a linear separation mode boil down to*

$$\mathfrak{J}_u^{(1)} = [s\mathbf{n}, s\mathbf{m}] \quad (2.48)$$

for the jump interpolation matrix and to $\mathfrak{C}_u^{(1)} = [\mathfrak{C}_u^{(1n)}, \mathfrak{C}_u^{(1m)}]$ for the compatibility operator with its components as

$$\mathfrak{C}_u^{(1n)} = - \sum_{A \in \mathcal{B}_e^{h+}} \bar{\mathbf{B}}_u^A (\mathbf{n} \otimes \mathbf{m})^a \bar{\mathbf{x}}_A \quad \text{and} \quad \mathfrak{C}_u^{(1m)} = (\mathbf{m} \otimes \mathbf{m}) \mathcal{H}_{\Gamma_e^h} - \sum_{A \in \mathcal{B}_e^{h+}} \bar{\mathbf{B}}_u^A (\mathbf{m} \otimes \mathbf{m}) \bar{\mathbf{x}}_A. \quad (2.49)$$

2.4 Numerical aspects

In this section, the focus is directed towards numerical aspects. Section 2.4.1 will summarize a criterion commonly used to identify crack initiation, whereas in Section 2.4.2 the actual failure surface propagation will be discussed based on an adoption of the well established global tracking algorithm. Section 2.4.3 includes an adaption of the marching cubes algorithm to be used in conjunction with the global tracking algorithm and the finite elements with embedded strong discontinuities whereas Section 2.4.4 outlines a remedy of the arising non-planar failure surfaces arising based on the marching cubes algorithm. Finally, Section 2.4.5 illustrates in detail aspects of the numerical implementation of the proposed framework.

2.4.1 Strong discontinuity initiation

A criterion is needed to decide when and in which direction the discontinuity is propagating through the specimen. A common criterion is based on the loss of ellipticity condition of the underlying problem in the bulk characterized by the singularity of the associated acoustic tensor of the problem at hand. An application of this criterion for purely mechanical models is presented in SIMO ET AL. [331] within the infinitesimal theory and extended in ARMERO & GARIKIPATI [11] or OLIVER ET AL. [268] to finite deformations. Extensions to the fully transient case resulting in a criterion based on the loss of hyperbolicity are applied in dynamic fracture problems in BELYTSCHKO ET AL. [32], among others.

Within the infinitesimal theory one seeks a solution to (2.3) for the particular constitutive relations outlined in (2.3) of the form

$$\mathbf{u}(\mathbf{x}, t) = \mathbf{a} e^{i(\mathbf{k} \cdot \mathbf{x} - \omega t)} \quad (2.50)$$

where \mathbf{a} is a constant quantity characterizing the amplitude of the harmonic wave, $\mathbf{k} = k\mathbf{n}$ with $\mathbf{n} \cdot \mathbf{n} = 1$ is the constant wave vector where k represents the wave number with \mathbf{n} as the propagation direction, and ω is the constant frequency of the wave. Insertion of (2.50) into (2.3) yields

$$A_{lm}a_m = 0 \quad \text{where} \quad A_{lm} = \mathbb{C}_{klmn}k_n k_k \quad (2.51)$$

is the so called acoustic tensor. Under the assumptions that the elasticity moduli is positive definite, i.e. $U_{kl}\mathbb{C}_{klmn}U_{mn} > 0$ for all U_{mn} with at least one non-zero element, it follows from (2.51) that

$$a_l A_{lm} a_m > 0 \quad (2.52)$$

for all non-zero vectors \mathbf{a} . This relation is the condition for ellipticity of the underlying equations of equilibrium in (2.3) which can also be viewed as a condition for the material stability since when (2.52) is satisfied it can be viewed as a stable response of an infinite medium in a uniform state of stress subjected to perturbations in the form (2.50).

For Rankine type models representing the mechanical response based on a yield criterion of the form

$$\phi = \max_{\|\mathbf{n}\|=1} \{\mathbf{n} \cdot \boldsymbol{\sigma} \mathbf{n}\} - \{f_{t_n} - \beta(\alpha)\} \leq 0 \quad (2.53)$$

where f_{t_n} is the tensile strength of the material against normal separation and β is the thermodynamic force conjugate to the rate of the internal variable α characterizing the softening response, the elastic moduli \mathbb{C} in (2.51) given in (2.2) needs to be replaced by the elastic-plastic counterpart defined for the case of no hardening as

$$\mathbb{C}^{ep} = \mathbb{C} - \frac{1}{\lambda + 2\mu} [\mathbb{C}(\mathbf{n} \otimes \mathbf{n}) \otimes \mathbb{C}(\mathbf{n} \otimes \mathbf{n})] \quad (2.54)$$

in terms of the maximum principal stress direction \mathbf{n} . Then the condition (2.52) results in

$$n_k a_l \mathbb{C}_{klmn}^{ep} a_m n_n = \mu [1 - (\mathbf{n} \cdot \mathbf{a})^2] \quad (2.55)$$

which can be interpreted in the way that when $\mathbf{a} = \mathbf{n}$, where \mathbf{n} is the maximum principal stress direction the fracture criterion is met with the propagation direction \mathbf{n} resulting in a Mode I fracture. It is to be noted, that the proposed propagation concept does not rely on the particular constitutive response in 2.53 and is applicable as long as failure can be detected locally at the individual material points.

2.4.2 Strong discontinuity propagation

This obtained criterion in (2.55) based on the loss of ellipticity for the detection of the crack initiation and the crack propagation direction is successfully applied in many works focusing on the two-dimensional setting [12, 205, 268]. Starting with an already existing crack tip or alternatively a point of crack initiation at the boundary of the two dimensional solid, the crack initiation criterion is checked in the corresponding finite element. When failure is detected, the failure line with the normal computed by the fracture criterion (2.55) is propagated through that finite element. After determination of the point at which this surface again emerges out of that finite element, the corresponding neighboring element is found and the procedure starts again with no limitation of the number of elements developing a strong discontinuity in a single time step.

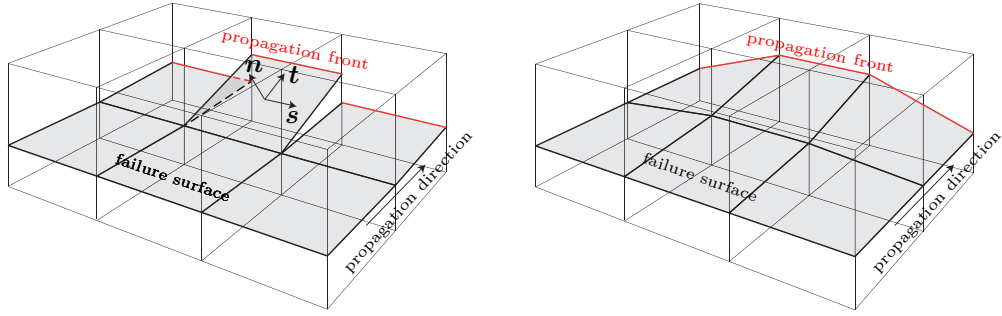


Figure 2.6: Illustration of a possible failure surface and propagation front using a simplified local algorithm to determine the crack propagation direction solely on the principal directions $\{\mathbf{n}, \mathbf{s}, \mathbf{t}\}$ of a single finite element (left) and a more advanced global tracking algorithm (right).

Extending such local propagation criterion to three dimensional simulations is easily possible but in general may lead to problems for complicated fracture surfaces. Even for a single propagating failure surface one may encounter scenarios like the one depicted in Figure 2.6 for which the crack path continuity in the overall domain may be lost. As a remedy, a global tracking algorithm is proposed in OLIVER ET AL. [267, 269], which even is applicable for scenarios where multiple strong discontinuities are present with possible interaction scenarios like coalescence, crossing or branching, which though lie out of the scope of this work.

The global tracking algorithm makes use of a globally obtained scalar level set function $\theta(\mathbf{x})$, which satisfies the conditions

$$\mathbf{s} \cdot \nabla \theta = 0 \quad \text{and} \quad \mathbf{t} \cdot \nabla \theta = 0 \quad (2.56)$$

where \mathbf{s} and \mathbf{t} are the two principal directions, which, in a three dimensional setting, span the failure surface orthogonal to the major principal direction \mathbf{n} obtained by the criterion outlined in (2.55). It is proposed in OLIVER ET AL. [267, 269], that the level set $\theta(\mathbf{x})$ can be obtained by the solution of a simplified heat-conduction-like problem by making to zero the divergence of a heat flux-like quantity

$$\nabla \cdot \mathbf{q} = 0 \quad \text{in } \mathcal{B} \quad \text{with} \quad \mathbf{q} = -\boldsymbol{\kappa}_\theta \cdot \nabla \theta \quad (2.57)$$

in terms of the anisotropic conductivity-like tensor given as

$$\boldsymbol{\kappa}_\theta = \mathbf{s} \otimes \mathbf{s} + \mathbf{t} \otimes \mathbf{t} + \epsilon \mathbf{1} \quad (2.58)$$

where $\epsilon > 0$ is a small perturbation parameter needed to overcome singularity problems [267, 269]. In the numerical simulations presented in Section 2.5, $\epsilon = 10^{-4}$ is chosen. For the numerical implementation, one may choose approximations of the form

$$\theta^h(\mathbf{x}^h) = \sum_{A=1}^{n_{\text{node}}} N_\theta^A(\mathbf{x}^h) \theta_A = \mathbf{N}_\theta \boldsymbol{\theta} \quad (2.59)$$

for all $\mathbf{x}^h \in \mathcal{B}^h$ in terms of temperature like nodal values θ^A and the shape functions N_θ^A , which are equivalent to those used for the approximation of the displacement field in (2.11). The nodal level set values $\boldsymbol{\theta}$ are finally obtained by solving the global system

$$\mathbf{K}_\theta \boldsymbol{\theta} = \mathbf{0} \quad \text{where} \quad \mathbf{K}_\theta = \sum_{e=1}^{n_{\text{elem}}} \int_{\mathcal{B}_e^h} \nabla \mathbf{N}_\theta^T \boldsymbol{\kappa}_\theta \nabla \mathbf{N}_\theta \, dV \quad (2.60)$$

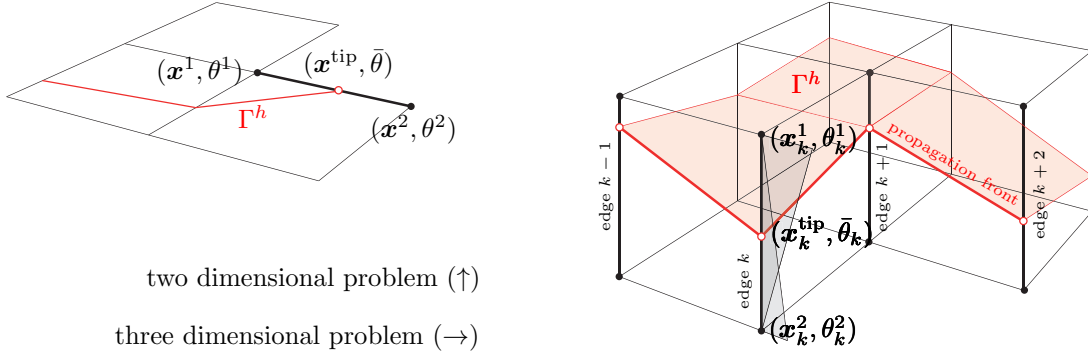


Figure 2.7: Illustration of the determination of $\bar{\theta}$ for two- and three-dimensional problems based on (2.61).

which is solved on the same finite element discretization as used for the computation of the mechanical boundary value problem with the boundary decomposed into $\partial\mathcal{B}^h = \partial\mathcal{B}_q^h \cup \partial\mathcal{B}_\theta^h$. The boundary conditions are such that $q_\nu = \mathbf{q} \cdot \boldsymbol{\nu} = \mathbf{0}$ for the outward normal $\boldsymbol{\nu}$ on $\partial\mathcal{B}_q^h$ of the solids boundary and that the temperature is prescribed as $\theta = \bar{\theta}$ in $\partial\mathcal{B}_\theta^h$, which consists of at least two points of the overall boundary to provide a unique solution other than the trivial result of a constant level set value [267, 269]. An alternative approach is presented in ARMERO & KIM [13], where rather than solving (2.60) globally, it is solved locally only for those finite elements ahead of a pre-existing failure surface but still assuring a globally smooth failure surface.

Once the global level set is obtained by solving (2.60), the two dimensional case proceeds by the computation of the level set $\bar{\theta}$ in the element ahead of the crack tip by a linear interpolation of the global values θ^1 and θ^2 along the edge of the element with the crack tip. Instead of a single crack tip, in three dimensional simulations a one dimensional propagation front is present as illustrated in Figure 2.7, which may span over various finite elements. To obtain the value for $\bar{\theta}$, an average of the values $k = 1, \dots, n_{\text{edge}}^{\text{front}}$ values $\bar{\theta}_k$ for all the $n_{\text{edge}}^{\text{front}}$ edges of elements intersecting the propagation front is computed as

$$\bar{\theta} = \frac{1}{n_{\text{edge}}^{\text{front}}} \sum_{k=1}^{n_{\text{edge}}^{\text{front}}} \bar{\theta}_k \quad \text{where} \quad \bar{\theta}_k = \eta_k \theta_k^1 + (1 - \eta_k) \theta_k^2 \quad (2.61)$$

with $\eta_k = |\mathbf{x}_k^{\text{tip}} - \mathbf{x}_k^1| / |\mathbf{x}_k^1 - \mathbf{x}_k^2| \in [0, 1]$ as illustrated in Figure 2.7. Note that (2.61) simplifies for the two dimensional setting since then $n_{\text{edge}}^{\text{front}} = 1$. Having identified the level set value of the crack front, the isosurface corresponding to this value are used as the potential propagating failure surface. It is to be noted, that the actual value of the level set can be artificially steered based on its applied value on $\partial\mathcal{B}_\theta^h$ and does not necessarily have to be zero.

2.4.3 The marching cubes algorithm

The main goal is now to determine how the failure surface continues to propagate through an element ahead of the propagation front in case the fracture criterion (2.55) is met. Depending on the nodal values of θ_A of all nodes in the element under consideration and the level set value $\bar{\theta}$ obtained by (2.61), various scenarios might arise on how the

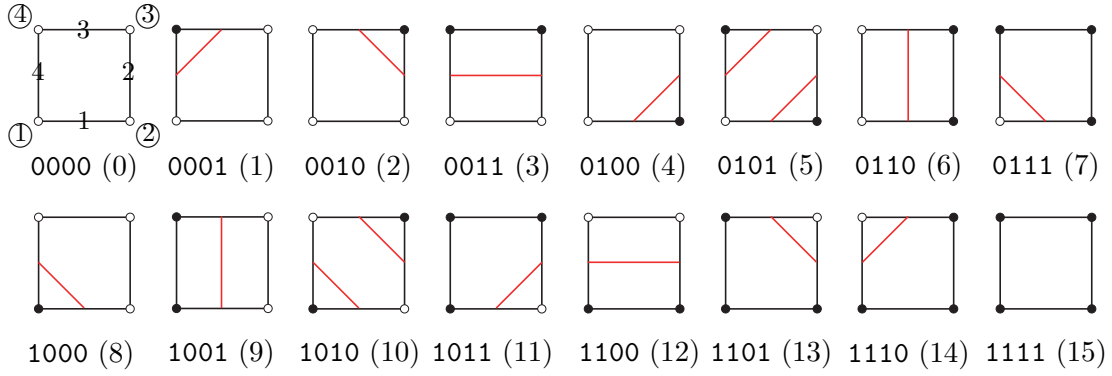


Figure 2.8: Classification of all 2^4 configurations of the marching square algorithm including the ambiguous cases 0101 and 1010 and characterization based on the 4-bit integer and decimal number. Filled nodes \bullet have values greater than $\bar{\theta}$ whereas empty nodes \circ have values smaller than $\bar{\theta}$.

failure surface may propagate through that element. To investigate all possibilities and to ensure a globally smooth failure surface, the marching squares algorithm is exploited for two dimensional simulations and the marching cubes algorithm proposed in LORENSEN & CLINE [217] in the field of computer graphics is exploited for three dimensional fracture simulations and combined with the global tracking algorithm and the finite elements with embedded strong discontinuities in this work. The marching cubes concept is a computer graphics algorithm for extracting a polygonal mesh of an isosurface from a 3D scalar field, called voxels. In REMPLER [305], those voxels are replaced by an eight node hexahedral finite element and the isosurface is replaced by the failure surface predicted from the global tracking algorithm. Doing so, use can be made of the table given in LORENSEN & CLINE [217] identifying the 15 unique possibilities out of all the $2^8 = 256$ cases of how a constant isosurface can intersect a voxel. One particular property of those unique cases is the fact that they are chosen in such a way that a smooth failure surface without the appearance of artifacts or holes is guaranteed. Neglecting some of those cases should therefore be avoided. Extensions of the original marching cubes algorithm are suggested in the literature [62, 259, 260], which though are not accounted for in this work.

The discussion starts by an explanation of the concept for the two dimensional case, where the square in the marching squares algorithm is represented by a plane quadrilateral finite element. Even though the advantages of the concept are not that apparent in the plane setting, it allows to explain the concept in detail. Thereafter the concept is extended to three dimensions, where rather than using a tetrahedral finite element, for which the advantages are again not that apparent, this work will focus on the exploitation of the marching cubes algorithm for the prediction of the failure surface in a hexahedron finite element.

Considering first a plane quadrilateral finite element, there are $2^4 = 16$ possible configurations of whether the nodal values of θ_A for $A = 1, \dots, 4$ are larger or smaller than $\bar{\theta}$. The particular configuration number is determined by the construction of a binary number (4-bits). As illustrated in Figure 2.8, surrounding the cell represented by the plane element in an anti-clockwise manner, a *zero* is obtained for $\theta_A < \bar{\theta}$ (represented by an empty node \circ in Figure 2.8) whereas a *one* is obtained for $\theta_A > \bar{\theta}$ (represented by a filled node \bullet in Figure 2.8). Within all the cases the qualitative location of the isoline with constant value $\bar{\theta}$ is depicted. It is this isoline, which can then be used to predict the propagation of

the strong discontinuity through that element under consideration. A particular emphasis is given to the cases 0101 and 1010 for which first of all two isolines appear within the finite element which in addition are not unique. This ambiguity is resolved in NIELSON & HAMANN [260] by taking into account the data value at the center of the cell. For both cases 0101 and 1010, if the center value is below $\bar{\theta}$, then the opposite case is considered. For the determination of which configuration to choose, one now has to take into account the location of the crack tip. If we consider e.g. that it is located on the fourth edge, and if we assume that $\theta_1 < \bar{\theta}$ and $\theta_4 > \bar{\theta}$, the necessary cases to be considered are the cases 0001, 0011, 0111, and 0101 including the above mentioned resolution of ambiguity for the latter. It then also becomes clear, that even though two constant isosurfaces appear in case 0101, that only the one intersecting edge 4 is of interest in this example.

As mentioned above, the full potential of this procedure is observed for three dimensional applications when using eight node hexahedron finite elements, this being also the major reason for using those elements in the simulations provided in Section 2.5. In such case, the marching cubes algorithm results in $2^8 = 256$ possible configurations of whether the nodal values of θ_A for $A = 1, \dots, 8$ are larger or smaller than $\bar{\theta}$. Based on the exploitation of rotational and reflective symmetries as well as sign changes, LORENSEN & CLINE [217] developed a table of 15 unique possibilities of how the isosurfaces with constant value $\bar{\theta}$ can be depicted. Those are illustrated in Figure 2.9 and can now be characterized by an 8-bit binary number constructed in the same way as above for the plane setting. These cases now serve as possible failure zone cases through the element under consideration. After identification of the proper case to be considered based on the nodal values θ_A and the computed value of the isoline $\bar{\theta}$ in (2.61) and after taking into account the actual position of the crack tip, the propagation of the strong discontinuity through that element is determined. It is to be noted, that the 15 configurations are chosen in such a way that a smooth failure surface without the appearance of wholes is guaranteed. As an example, a rotation of the cell in case 10100000 allows to conceptually put this cell onto the one of case 10010110. To avoid ambiguous cases as illustrated in Figure 2.8 for the plane quadrilaterals also in three dimensional simulations, extensions of the original marching cubes algorithm are suggested in NIELSON & HAMANN [260], CHERNYAEV [62], or NIELSON [259], which though are not accounted for in this work. A summary box showcasing the incorporation of the marching cubes algorithm into the global tracking algorithm and the strong discontinuity framework is given in Table 2.1. There the two arrays named “predicted crack front list” and “actual crack front list” are not to be confused. The former is a list of elements, within which the isosurface with constant value $\bar{\theta}$ is present, whereas the latter is a list of elements sharing a surface with an already existing crack front.

2.4.4 Treatment of non-planar failure surfaces

As expected in a complex three dimensional failure propagation through the solid, the marching cubes algorithm in Section 2.4.3 includes cases of failure surfaces in Figure 2.9, which are non-planar. This is in contradiction with the assumption of the introduced local degrees of freedom ξ_u in (2.14) and the identified local frame $\{\mathbf{n}, \mathbf{s}, \mathbf{t}\}$ used in Section 2.3 for the determination of the compatibility- and the equilibrium operators. Those constant quantities within the element, carrying e.g. the kinematic information of the amount of normal opening in direction \mathbf{n} or slip in the tangential directions \mathbf{s} and \mathbf{t} are

- A. *After convergence of the mechanical BVP, determine principal directions \mathbf{n} , \mathbf{s} , and \mathbf{t} :*
1. Compute the stresses $\boldsymbol{\sigma}$ at each integration point based on the solution of the mechanical boundary value problem by bringing to zero the residual (2.13).
 2. Compute the principal directions \mathbf{n} , \mathbf{s} , and \mathbf{t} at each integration point based on the stresses obtained in step (A1).
- B. *Compute the level set value $\bar{\theta}$ based on the solution of (2.60) with the principal directions \mathbf{n} , \mathbf{s} , and \mathbf{t} from step (A2) as input parameters.*
- C. *Predict the possible crack surfaces using the marching cubes algorithm:*
1. Loop over all the finite elements in the “predicted crack front list” and perform the steps (C2)-(C7).
 2. Number the 8 nodes and 12 edges of each hexahedral element as shown in Figure 2.9.
 3. Compare the value θ_A at each node A with $\bar{\theta}$ obtained in step (B) to get an 8-bit binary integer index. A *zero* is obtained for $\theta_A < \bar{\theta}$ whereas a *one* is obtained for $\theta_A > \bar{\theta}$.
 4. For the given 8-bit integer, obtain a list of edge numbers from the marching cubes table to determine the individual triangles spanning the non-planar isosurface (e.g. 1, 9, 4 and 2, 11, 3 for the depicted configuration 10100000 in Figure 2.9).
 5. Compute the local interpolation parameter η used in (2.61) on each edge intersected by the isosurface made up by the detected triangles identified in step (C4).
 6. For a configuration with multiple constant isosurfaces through the element (cases 3,6,7,10-13 in Figure 2.9), choose the one, which assures global continuity.
 7. Having identified the proper isosurface within the element under consideration, the new neighboring elements are added to the “predicted crack front list”.
- D. *Perform the crack propagation:*
1. Loop over all the elements in the “actual crack front list”.
 2. Check if the failure criterion (2.55) is met in those elements.
 3. If yes:
 - (a) Propagate the failure surface along the isosurface determined in step (C).
 - (b) Compute the artificial plane crack surface based on the discussion in Section 2.4.4.
 - (c) Update the “actual crack front list”.
 4. If no: Proceed to the next element in the “actual crack front list”.

Table 2.1: Summary box of the incorporation of the marching cubes algorithm into the global tracking algorithm and the strong discontinuity framework for a single loading step.

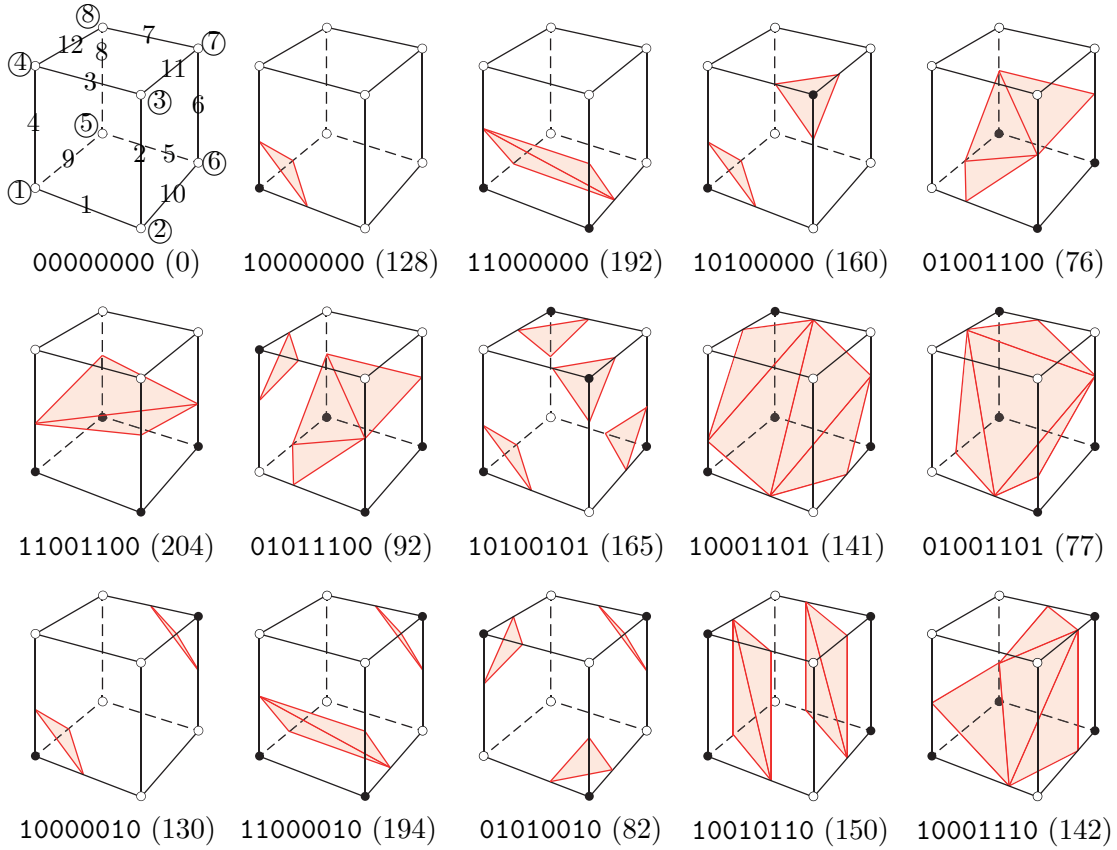


Figure 2.9: Classification of the 15 unique configurations of the marching cubes algorithm and characterization based on the 8-bit integer and decimal number. Filled nodes \bullet have values greater than $\bar{\theta}$ whereas empty nodes \circ have values smaller than $\bar{\theta}$.

interpretable as such only for a planar failure surface on which also their role in specific traction separation laws is valid. Therefore in such scenario, in this work an artificial plane failure surface is constructed with the minimal distance to the actual non-planar failure surface as illustrated in Figure 2.10. On this artificial failure surface, the interpretation of the local degrees of freedom ξ_u in (2.14) is valid and the integrations in (2.17) or (2.21) can be performed in a more straightforward way.

To do so, the normal vector \mathbf{n} of the artificial plane needs to ensure the condition

$$I(\mathbf{n}, d) = \frac{1}{n_{\text{nodes}}^{\Gamma}} \sum_{i=1}^{n_{\text{nodes}}^{\Gamma}} [\mathbf{n} \cdot \mathbf{x}_i - d]^2 \rightarrow \min \quad \text{with} \quad \mathbf{n} \cdot \mathbf{n} = 1 \quad (2.62)$$

where $n_{\text{nodes}}^{\Gamma}$ represents the number of nodes on the original surface, being between 3 and 6 for a hexahedral finite element as can be seen in Figure 2.9, \mathbf{x}_i are the coordinates of those nodes and the constant scalar value d is given as $d = \mathbf{n} \cdot \mathbf{x}_i^*$ with \mathbf{x}_i^* as the point located on the artificial plane corresponding to \mathbf{x}_i where the vector from \mathbf{x}_i to \mathbf{x}_i^* is parallel to \mathbf{n} . To solve the constrained minimization problem in (2.62), one makes stationary the Lagrangian

$$L(\mathbf{n}, d, \lambda) = \frac{1}{n_{\text{nodes}}^{\Gamma}} \sum_{i=1}^{n_{\text{nodes}}^{\Gamma}} [\mathbf{n} \cdot \mathbf{x}_i - d]^2 - \lambda(\mathbf{n} \cdot \mathbf{n} - 1) \rightarrow \text{stationary} \quad (2.63)$$

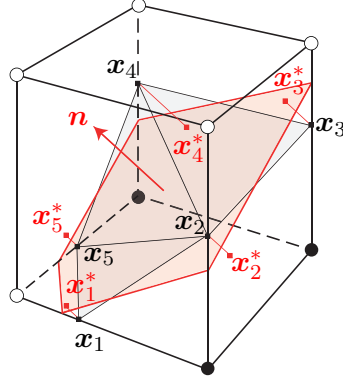


Figure 2.10: Illustration of the actual non-planar failure surface with $n_{\text{nodes}}^{\Gamma} = 5$ nodes and the constructed planar artificial failure surface defined by the normal vector \mathbf{n} .

by setting to zero its derivative with respect to d to get

$$\frac{\partial L}{\partial d} = \frac{1}{n_{\text{nodes}}^{\Gamma}} \sum_{i=1}^{n_{\text{nodes}}^{\Gamma}} 2[\mathbf{n} \cdot \mathbf{x}_i - d] = 0 \quad \longrightarrow \quad d = \mathbf{n} \cdot \tilde{\mathbf{x}} \quad \text{where} \quad \tilde{\mathbf{x}} = \frac{1}{n_{\text{nodes}}^{\Gamma}} \sum_{i=1}^{n_{\text{nodes}}^{\Gamma}} \mathbf{x}_i. \quad (2.64)$$

Substitution of the result for d in (2.63) into (2.63) yields after taking a derivative with respect to \mathbf{n}

$$\frac{\partial L}{\partial \mathbf{n}} = \frac{1}{n_{\text{nodes}}^{\Gamma}} \sum_{i=1}^{n_{\text{nodes}}^{\Gamma}} 2\mathbf{n} \cdot (\mathbf{x}_i - \tilde{\mathbf{x}}) (\mathbf{x}_i - \tilde{\mathbf{x}}) - 2\lambda \mathbf{n} = \mathbf{0} \quad (2.65)$$

which can be rewritten as a standard eigenvalue problem of the form

$$\frac{\partial L}{\partial \mathbf{n}} = \mathbf{M} \mathbf{n} = \mathbf{0} \quad \text{with} \quad \mathbf{M} = \frac{1}{n_{\text{nodes}}^{\Gamma}} \sum_{i=1}^{n_{\text{nodes}}^{\Gamma}} (\mathbf{x}_i - \tilde{\mathbf{x}}) \otimes (\mathbf{x}_i - \tilde{\mathbf{x}}) - \lambda \mathbb{I} \quad (2.66)$$

in terms of the fourth order identity \mathbb{I} . The eigenvector corresponding to the minimal eigenvalue of (2.66) will finally yield the solution for the normal \mathbf{n} , which together with $\tilde{\mathbf{x}}$ in (2.64) identifies the artificial failure surface.

2.4.5 Numerical implementation

Following ARMERO [7, 8], LINDER & ARMERO [205], or ARMERO & KIM [13], the numerical aspects of implementing this framework are summarized. The global residual equation given in (2.13) and the local residual equation given in (2.17) are collected here as

$$\mathbf{R}_u(\mathbf{d}, \boldsymbol{\xi}_u) = \mathbf{f}^{\text{ext}} - \sum_{e=1}^{n_{\text{elem}}} \int_{B_e^h} \bar{\mathbf{B}}^T \boldsymbol{\sigma} dV \quad \text{and} \quad \mathbf{r}^e(\mathbf{d}, \boldsymbol{\xi}_u) = - \int_{B_e^h} \boldsymbol{\mathfrak{E}}_u^T \boldsymbol{\sigma} dV - \int_{\Gamma_e^h} \mathfrak{J}_u^T \mathbf{t}_{\Gamma} dA. \quad (2.67)$$

Those have to be brought to zero through a Newton iterative procedure, which requires their linearization given as

$$\sum_{e=1}^{n_{\text{elem}}} \left[\mathbf{K}_{dd}^{e,k} \Delta \mathbf{d}_e^{k+1} + \mathbf{K}_{d\xi}^{e,k} \Delta \boldsymbol{\xi}_e^{k+1} \right] = \sum_{e=1}^{n_{\text{elem}}} \mathbf{R}_u^{e,k} \quad \text{and} \quad \mathbf{K}_{\xi d}^{e,k} \Delta \mathbf{d}_e^{k+1} + \mathbf{K}_{\xi\xi}^{e,k} \Delta \boldsymbol{\xi}_e^{k+1} = \mathbf{r}_u^{e,k} \quad (2.68)$$

with the second set of equations in (2.67) and (2.68) only present for those element with a strong discontinuity. The global and local quantities are then updated based on

$$\mathbf{d}^{k+1} = \mathbf{d}^k + \Delta \mathbf{d}^{k+1} \quad \text{and} \quad \boldsymbol{\xi}^{k+1} = \boldsymbol{\xi}^k + \Delta \boldsymbol{\xi}^{k+1} \quad (2.69)$$

in terms of the iteration index k . The individual contributions in (2.68) are given as

$$\begin{aligned} \mathbf{K}_{dd}^e &= \int_{\mathcal{B}_e^h} \bar{\mathbf{B}}_u^T \mathbb{C} \bar{\mathbf{B}}_u dV, & \mathbf{K}_{d\xi}^e &= \int_{\mathcal{B}_e^h} \bar{\mathbf{B}}_u^T \mathbb{C} \boldsymbol{\xi}_u dV, \\ \mathbf{K}_{\xi d}^e &= \int_{\mathcal{B}_e^h} \boldsymbol{\xi}_u^T \mathbb{C} \bar{\mathbf{B}}_u dV, & \text{and} \quad \mathbf{K}_{\xi\xi}^e &= \int_{\mathcal{B}_e^h} \boldsymbol{\xi}_u^T \mathbb{C} \boldsymbol{\xi}_u dV + \int_{\Gamma_e^h} \tilde{\mathfrak{J}}_u^T \mathbb{C}_\Gamma \tilde{\mathfrak{J}}_u dA \end{aligned} \quad (2.70)$$

for the stiffness matrices, respectively. The tangent \mathbb{C} in the bulk \mathcal{B}_e^h as well as its counterpart along the strong discontinuity \mathbb{C}_Γ in (2.70) are defined based on

$$\Delta \boldsymbol{\sigma} = \mathbb{C} \Delta \boldsymbol{\varepsilon}_\mu^h \quad \text{and} \quad \Delta \mathbf{t}_\Gamma = \mathbb{C}_\Gamma \Delta [\mathbf{u}_\mu^h] \quad (2.71)$$

with $\Delta [\mathbf{u}_\mu^h] = \tilde{\mathfrak{J}}_u \Delta \boldsymbol{\xi}_u$.

One major advantage of the considered formulation is the computational efficiency which comes with the fact that the internal degrees of freedom for the description of the strong discontinuity can be statically condensed out at the element level. From the second equation in (2.68) the increments of the enhanced parameters can be computed as

$$\Delta \boldsymbol{\xi}_e^{k+1} = (\mathbf{K}_{\xi\xi}^{e,k})^{-1} [\mathbf{r}_u^{e,k} - \mathbf{K}_{\xi d}^{e,k} \Delta \mathbf{d}_e^{k+1}] \quad (2.72)$$

locally for the elements with a strong discontinuity. Insertion of (2.72) into the first equation in (2.68) yields the statically condensed system

$$\mathbf{K}_*^k \Delta \mathbf{d}_e^{k+1} = \mathbf{R}_*^k \quad (2.73)$$

in terms of the effective residual $\mathbf{R}_*^k = \mathbf{A}_{e=1}^{n_{\text{elem}}} \mathbf{R}_*^{e,k}$ and the effective stiffness matrix $\mathbf{K}_*^k = \mathbf{A}_{e=1}^{n_{\text{elem}}} \mathbf{K}_*^{e,k}$ given as

$$\mathbf{R}_*^{e,k} = \mathbf{R}_u^{e,k} - \mathbf{K}_{d\xi}^{e,k} (\mathbf{K}_{\xi\xi}^{e,k})^{-1} \mathbf{r}_u^{e,k} \quad \text{and} \quad \mathbf{K}_*^{e,k} = \mathbf{K}_{dd}^{e,k} - \mathbf{K}_{d\xi}^{e,k} (\mathbf{K}_{\xi\xi}^{e,k})^{-1} \mathbf{K}_{\xi d}^{e,k} \quad (2.74)$$

in terms of the iteration index k . It is emphasized that the structure of the numerical implementation reported in LINDER & ARMERO [205] for the plane setting does not change when extending it to the three dimensional setting in ARMERO & KIM [13], which is also apparent here in this section.

2.5 Numerical simulations

This section presents the results obtained in a series of numerical tests designed to evaluate and illustrate the performance of the three dimensional finite elements with the incorporated linear separation modes as well as the performance of the proposed coupling of the marching cubes algorithm with the global tracking algorithm and the strong discontinuity framework. As in LINDER & ARMERO [205] for the plane setting and in ARMERO & KIM [13] for the three dimensional setting, we start in Section 2.5.1 with a number of single

element tests to outline the improved behavior originating from the incorporation of the higher order kinematics along the failure surface.

Next, a series of representative numerical simulations are presented to demonstrate the performance of the failure surface propagation concept proposed in this work. It is emphasized that rather than prescribing the failure surface propagation path, all the presented simulations in this section determine the crack path based on the proposed combination of the global tracking algorithm, the marching cubes algorithm, and the strong discontinuity framework. All the simulations are carried out with eight node hexahedral finite elements (bricks) through which the propagation of the failure surface is possible based on the 2^8 cases of the marching cubes algorithm categorized into the 15 unique configurations given in Figure 2.9. In Section 2.5.2, the classical concrete benchmark problem of a three-point bending test is investigated. The complexity of the almost planar failure surface in that test is increased in Section 2.5.3, where an L-shape concrete specimen is numerically investigated. Next, the Brokenshire torsion test is simulated in Section 2.5.4 resulting in a highly complicated curved failure surface justifying the advanced propagation concept proposed in this work. Finally, Sections 2.5.5 and 2.5.6 outline the applicability of that concept to cases where multiple failure surfaces appear within the solid based on a tensile test with two notches and two holes as well as based on a double notched four-point bending test, respectively.

2.5.1 Single element tests

In line with LINDER & ARMERO [205] in the plane setting and ARMERO & KIM [13] for the three dimensional formulation, single element tests are considered to outline the obtained improved behavior of the higher order kinematic approximation of the failure zone. In the following a partial bending test, a partial tension test, a partial shear, and a partial rotation test are considered. All tests are discretized by a single finite element of dimension $200 \times 200 \times 200 \text{ mm}^3$. To emphasize the general applicability of the strong discontinuity approach, in addition to the standard trilinear displacement based Q1 element, the 3D mixed element Q1/P0 [155], and the enhanced strain elements Q1/E9 and Q1/E12 [330] are used based on a proper modification of the $\bar{\mathbf{B}}_u$ matrix in (2.12). The bulk is modeled as linear elastic with a Young's modulus of $E = 30 \text{ GPa}$ and a Poisson ratio of $\nu = 0.0$. Whereas no initial strong discontinuity is present in the partial bending test, all other tests assume that the block is separated from the onset by a fully softened discontinuity through its center in two parts.

The constitutive model used along the strong discontinuity for the *partial bending test* is a traction-separation law with linear softening given as

$$t_{\Gamma_n} = \max\{0, f_{t_n} + \mathcal{S}[[u_{\mu_n}^h]]\} \quad \text{and} \quad t_{\Gamma_{s,t}} = k_{s,t}[[u_{\mu_{s,t}}^h]] \quad (2.75)$$

in terms of the tensile strength $f_{t_n} = 3 \text{ MPa}$ and the softening modulus $\mathcal{S} = -45 \text{ MPa/mm}$, which corresponds to a fracture energy of $G_f = f_{t_n}^2/(2|\mathcal{S}|) = 0.1 \text{ N/mm}$ as well as the small value $k_{s,t} = 3 \cdot 10^{-4} \text{ GPa/mm}$ in tangential direction to avoid possible singularities in the fully softened regime even though no tangential jumps are expected in this example. The boundary conditions are shown in Figure 2.11. Up to a displacement $\delta = 0.1 \text{ mm}$, at which the strong discontinuity is formed based on the failure criterion (2.55), the bottom and top corners are equally pulled apart in horizontal direction. Thereafter, the bottom

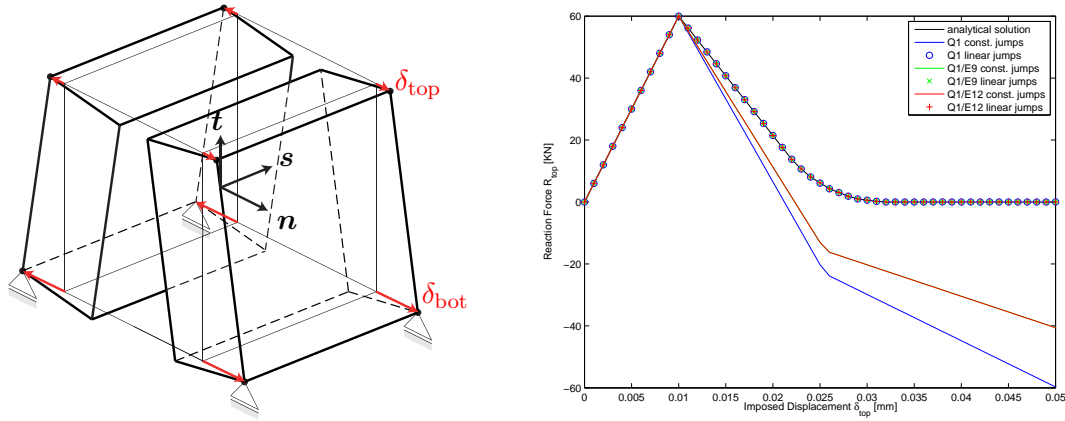


Figure 2.11: Single element tests. Illustration of geometry, boundary conditions, loading, and numerical results for the partial bending test.

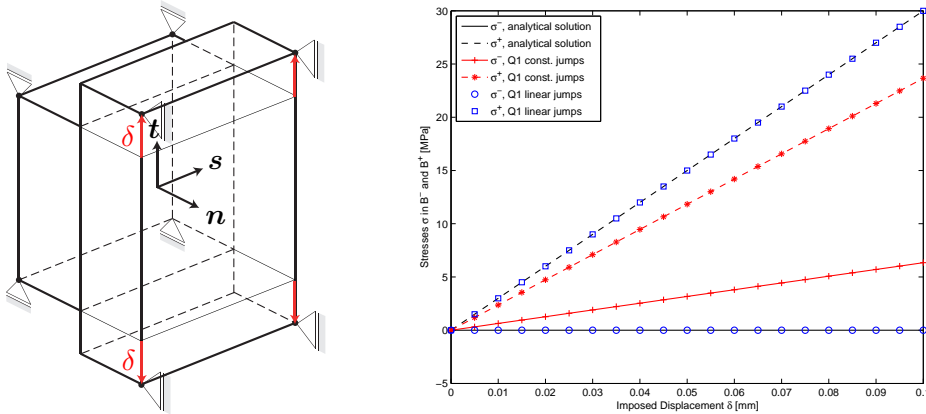


Figure 2.12: Single element tests. Illustration of geometry, boundary conditions, loading, and numerical results for the partial tension test.

displacement δ_{bot} increases twice as fast as the top displacement δ_{top} . The numerical results are compared with the analytical solution derived in LINDER & ARMERO [205]. This comparison outlines the drastic improvement obtained by the higher order kinematic resolution of the strong discontinuity when compared to the constant jump approximation, which, as in the plane setting, clearly leads to stress locking in the sense that the reaction cannot be relaxed completely for a fully opened discontinuity, neither with the standard displacement based element nor with the enhanced finite elements as illustrated in Figure 2.11.

For the remaining single element tests a pre-existing fully softened ($t_{\Gamma_{n,s,t}} = 0$) strong discontinuity is assumed to be present through the center of the element comprising the block of the same dimension and material parameters as in the previous partial bending test. The loading is such that for the *partial tension test* the four nodes on one side \mathcal{B}_e^{h+} are equally pulled apart by δ in \mathbf{t} direction so that in that part of the element the stress component $\sigma = E\delta/a$, with a as half the side length of the cube, is present as the only non-zero stress component. The results of the numerical simulation illustrated in Figure 2.12 reveal that no stresses are transferred over the fully softened strong discontinuity and that the only non-zero displacement jump present is $\xi_u^{(01s)}$ when considering the higher order kinematic approximation of the displacement jumps, whereas the interpolations

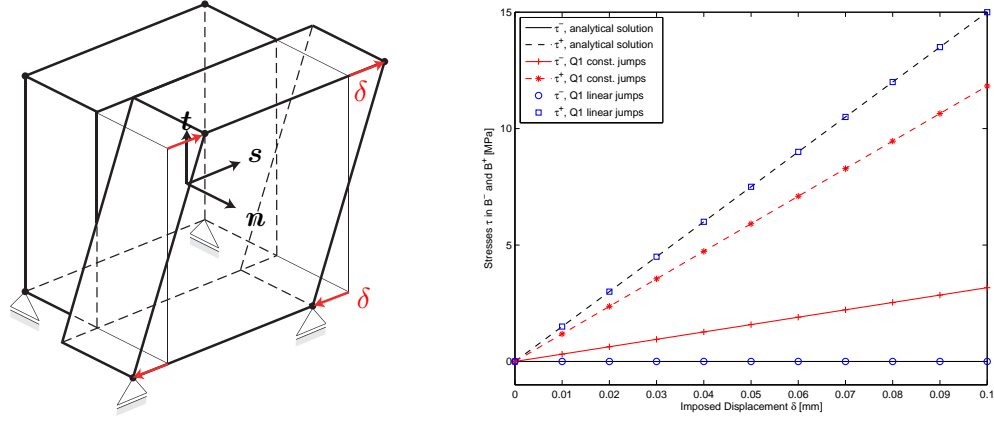


Figure 2.13: Single element tests. Illustration of geometry, boundary conditions, loading, and numerical results for the partial shear test.

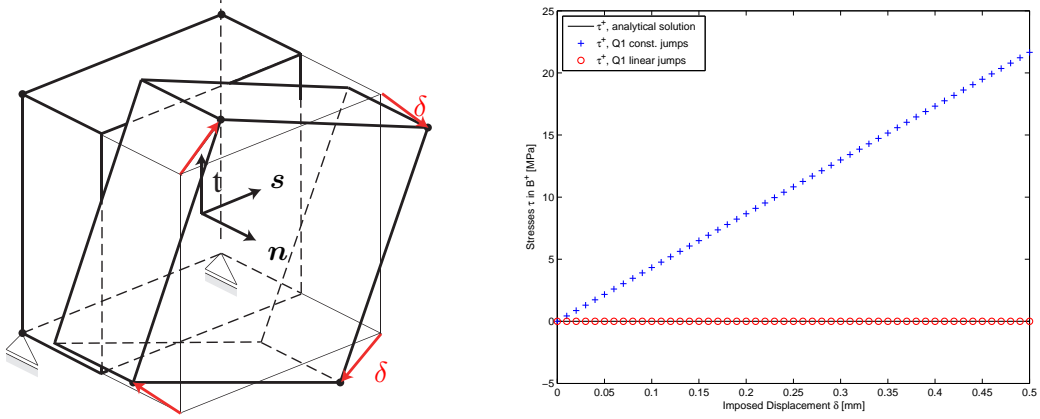


Figure 2.14: Single element tests. Illustration of geometry, boundary conditions, loading, and numerical results for the partial rotation test.

with constant jumps exhibit a transfer of the stress components and leads to the wrong results since that particular linear separation mode is not exactly captured.

In the *partial shear test* illustrated in Figure 2.13 the upper nodes in \mathcal{B}_e^{h+} are displaced by δ in \mathbf{s} direction, whereas the bottom nodes in \mathcal{B}_e^{h+} are displaced by δ in the negative \mathbf{s} direction. The finite elements with linear displacement jumps are capable to predict the expected shear stress $\tau = E\delta/a$ in \mathcal{B}_e^{h+} based on developing the only non-zero displacement jumps $\xi_u^{(oit)}$, whereas the finite elements with constant displacement jumps again lead to a transfer of stress into the whole block.

Finally, the *partial rotation test* is considered, where the nodes in \mathcal{B}_e^{h+} are displaced such that this part undergoes an infinitesimal rotation around \mathbf{n} . Clearly, no stress is expected in any of the two parts of the block due to the fully softened strong discontinuity present from the onset. The rotation is captured nicely for the finite elements with a higher order kinematic representation of the failure zone by a combination of nonzero $\xi_u^{(oit)}$ and $\xi_u^{(iot)}$ displacement jumps. Those are not present for the elements with constant displacement jumps so that for those the wrong result is predicted with a transfer of stress components into the whole block as shown in Figure 2.14.

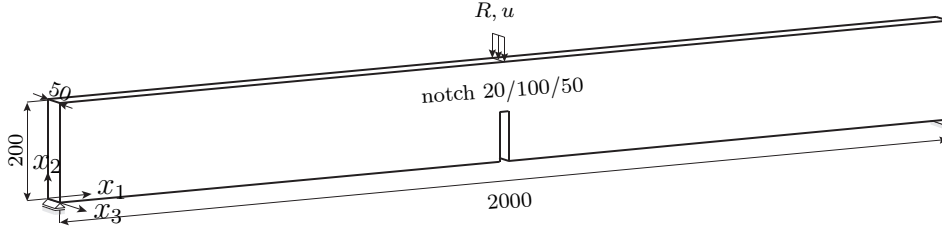
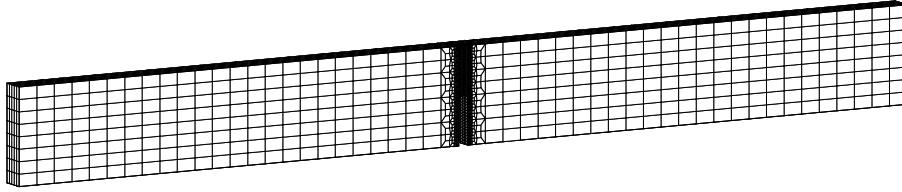
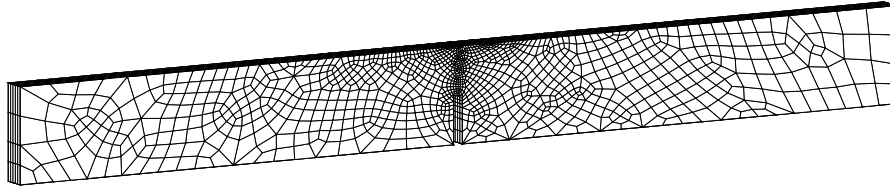


Figure 2.15: Three-point bending test: illustration of geometry (length units in mm), loading, and support of the notched concrete beam.



(a) structured mesh with 6000 brick elements



(b) unstructured mesh with 5525 brick elements

Figure 2.16: Three-point bending test: illustration of the finite element discretization using a structured- and an unstructured mesh.

2.5.2 Three-point bending test

In this first example the classical benchmark failure problem in the form of the three-point bending test is investigated. It consists of a notched concrete beam, which is supported on the two bottom edges and loaded at the center of the top surface as illustrated in Figure 2.15. The material response of the concrete beam is modeled as linear elastic with a Young's modulus of $E = 30$ GPa and a Poisson ratio of $\nu = 0.2$ in the bulk. Failure is detected based on the criterion outlined in Section 2.4.1 as soon as the tensile strength of $f_{tn} = 3.33$ MPa is surpassed. To model the material response within the propagating failure surface, the cohesive law considered in ARMERO & KIM [13], LINDER & ARMERO [205] is used for the response of the discontinuity in the normal direction as

$$t_{\Gamma_n} = \begin{cases} f_{tn} \left(1 - \left(\frac{\delta_a}{\delta_0} \right)^k \frac{[[u_{\mu_n}^h]]}{\delta_a} \right) & \text{for } [[u_{\mu_n}^h]] < \delta_a \\ \frac{f_{tn}}{1 - \left(\frac{\delta_a}{\delta_0} \right)^k} \left(1 - \left(\frac{[[u_{\mu_n}^h]]}{\delta_a} \right)^k \right)^2 & \text{for } [[u_{\mu_n}^h]] \geq \delta_a \end{cases} \quad (2.76)$$

in terms of the parameters $k = 0.5$, $\delta_a = 0.015$, and $\delta_0 = 0.16$, which corresponds to a fracture energy $G_f = 0.124$ N/mm. The linear relations $t_{\Gamma_s} = k_s [[u_{\mu_s}^h]]$ and $t_{\Gamma_t} = k_t [[u_{\mu_t}^h]]$ with the reduced shear stiffness of k_s and k_t equal to $3 \cdot 10^{-2}$ GPa/mm are considered for the response of the discontinuity in the two tangential directions \mathbf{s} and \mathbf{t} of the artificial planar failure surface constructed based on the discussion of Section 2.4.4.

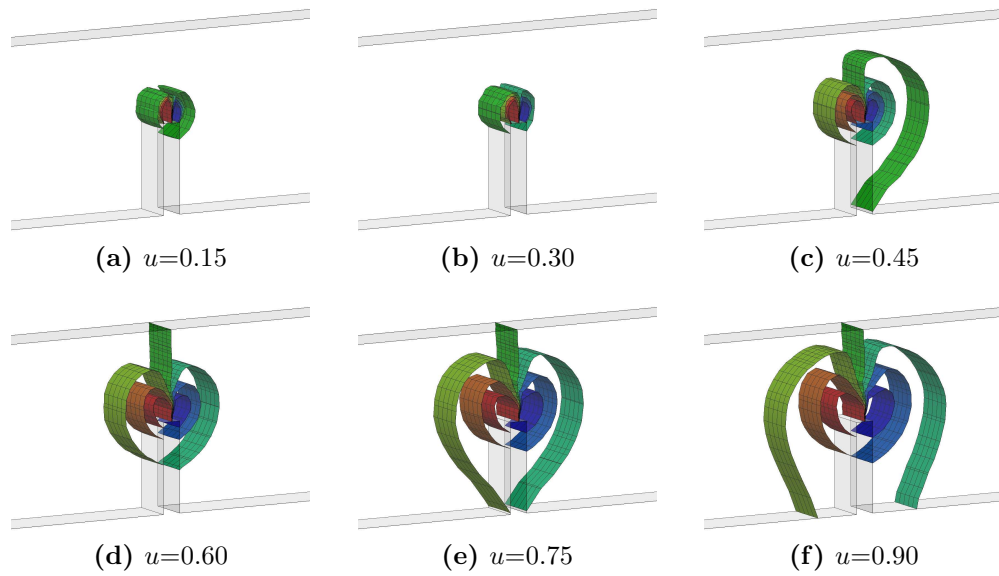


Figure 2.17: Three-point bending test: illustration of the evolution of different possible failure surfaces for different displacements u in mm predicted by the global tracking algorithm in conjunction with the marching cubes algorithm.

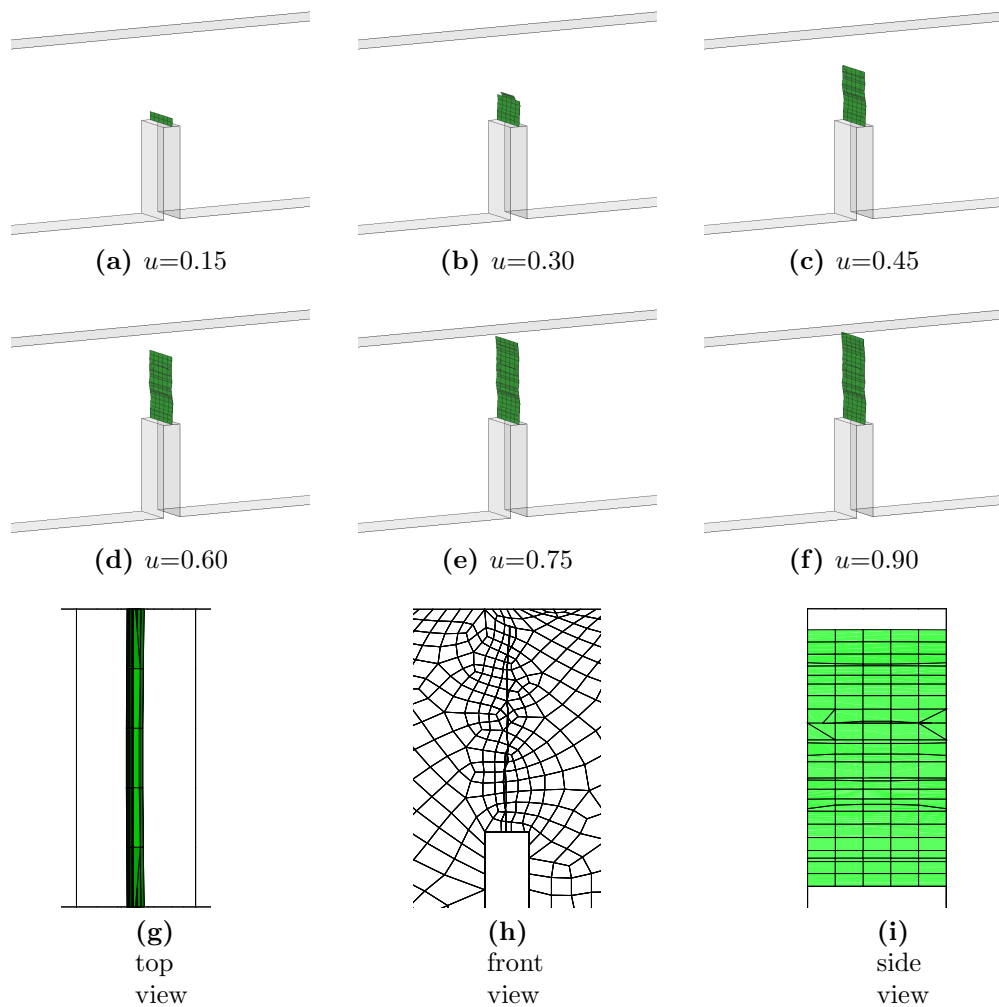


Figure 2.18: Three-point bending test: illustration of the actual failure surface for different applied loading stages u in mm (a-f) and a closer look at the final failure surface (g-i) from different perspectives.

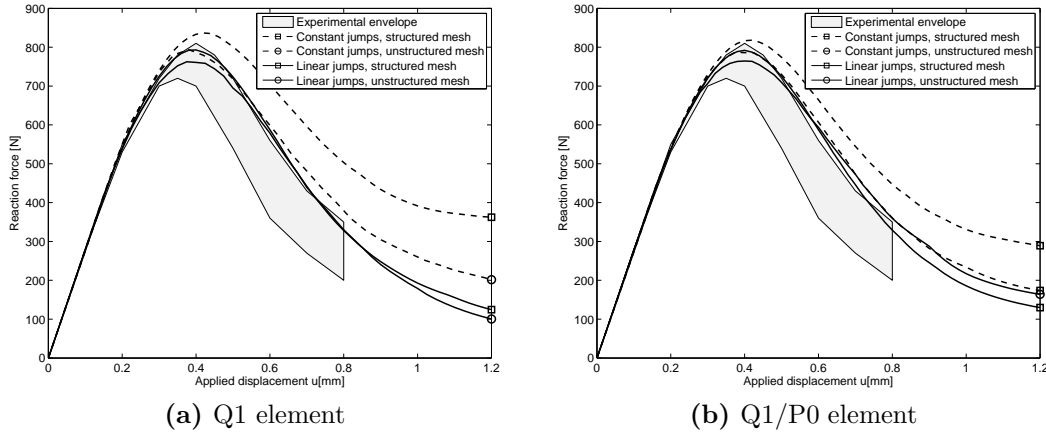


Figure 2.19: Three-point bending test: reaction force versus applied displacement relation for displacement based Q1 and mixed Q1/P0 elements with constant and linear jumps for structured and unstructured meshes.

The finite element discretization considers a structured mesh made of 6000 eight node hexahedral finite elements and an unstructured mesh consisting of 5525 bricks, both meshes with five element layers in thickness direction as shown in Figure 2.16. Displacement based Q1 elements as well as mixed Q1/P0 elements are used together with the constant as well as the linear separation modes initially developed in ARMERO & KIM [13] and illustrated with a slight modification in Figures 2.3-2.5. Figure 2.17 shows the resulting constant level set surfaces within the individual bricks of the unstructured mesh. Those surfaces are obtained based on the global tracking algorithm, where an initial value of $\theta = \pm 1$ at the left and right layer of nodes of the elements at which the failure surface is assumed to start is chosen, and the marching cubes algorithm allowing for the representation of those surfaces within the individual bricks. It is apparent in Figure 2.17 that those surfaces corresponding to a certain constant level set value do evolve for a changing applied load. As illustrated in Figure 2.18(a-f) for the different loading stages, the level set value obtained by the averaging procedure (2.61) determines the iso-surface to be used for the subsequent failure surface propagation in the elements for which the failure criterion (2.55) is satisfied. A closer investigation of the final failure surface illustrated in Figure 2.18(g-i) from the top, the front, and the side reveals in addition to the apparent non-symmetry in x_1 direction due to the non-symmetric unstructured finite element mesh in this direction also its slight non-symmetry in x_3 direction arising from the non-symmetric partition of the failure surfaces into triangles when performing integrations over the strong discontinuity.

Finally, the reaction force R versus applied displacement u relation is plotted in Figure 2.19 for both, the unstructured and the structured meshes illustrated in Figure 2.16 consisting of displacement based Q1 elements as well as mixed Q1/P0 elements and distinguished for the case when constant and when linear separation modes are allowed within the eight node hexahedral finite elements. In line with the results obtained in ARMERO & KIM [13], using the elements with a higher order approximation of the failure surface improves on the numerical results agreeing better with the experimental envelope presented in PETERSSON [286], ROTS ET AL. [313].

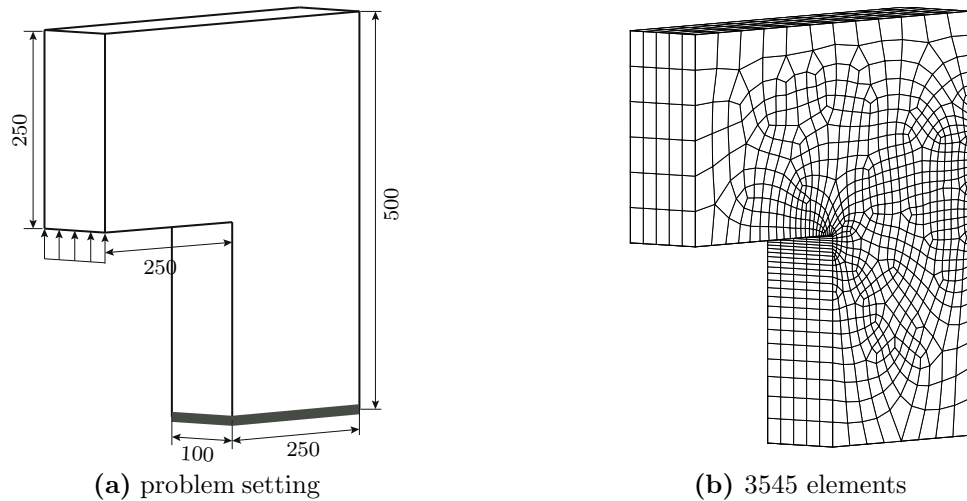


Figure 2.20: L-shape concrete specimen test: illustration of geometry (length units in mm), loading, and support of the L-shape concrete specimen on the left and illustration of the finite element discretization using an unstructured mesh on the right.

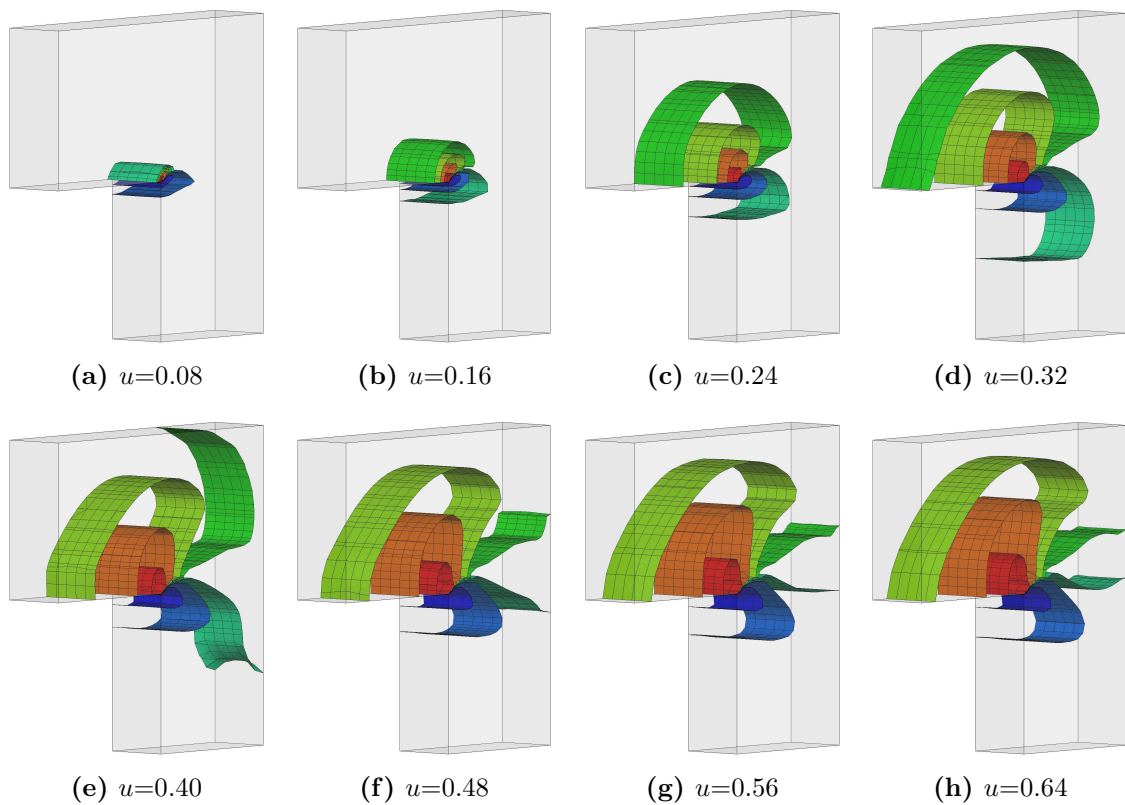


Figure 2.21: L-shape concrete specimen test: illustration of the evolution (u in mm) of different possible failure surfaces predicted by the global tracking algorithm in conjunction with the marching cubes algorithm.

2.5.3 L-shape concrete specimen test

In a similar manner, next the L-shape concrete specimen, whose geometry, loading (upwards displacement applied at the front edge), and boundary conditions (fully restrained

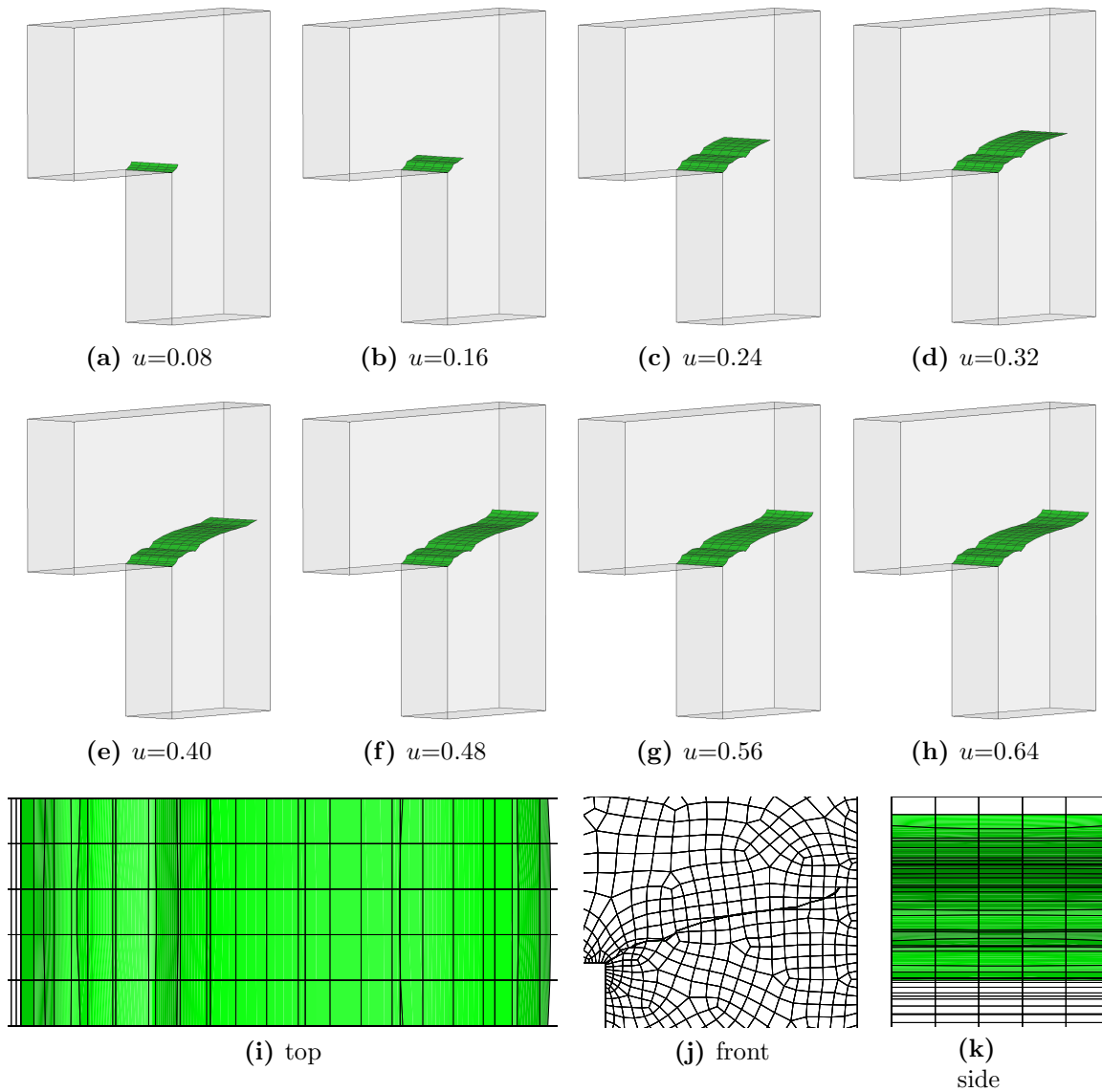


Figure 2.22: L-shape concrete specimen test: illustration of the actual failure surface for different applied loading stages (u in mm) (a-h) and a closer look at the final failure surface (i-k) from different perspectives.

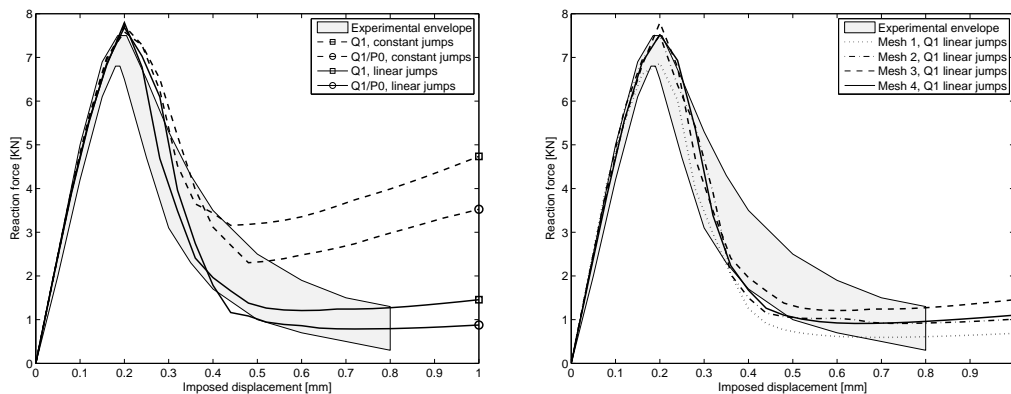


Figure 2.23: L-shape concrete specimen test: Left: reaction force versus applied displacement relation for displacement based Q1 and mixed Q1/P0 elements with constant and linear jumps. Right: reaction force versus applied displacement relation for the different meshes illustrated in the top row (a-d) of Figure 2.24.

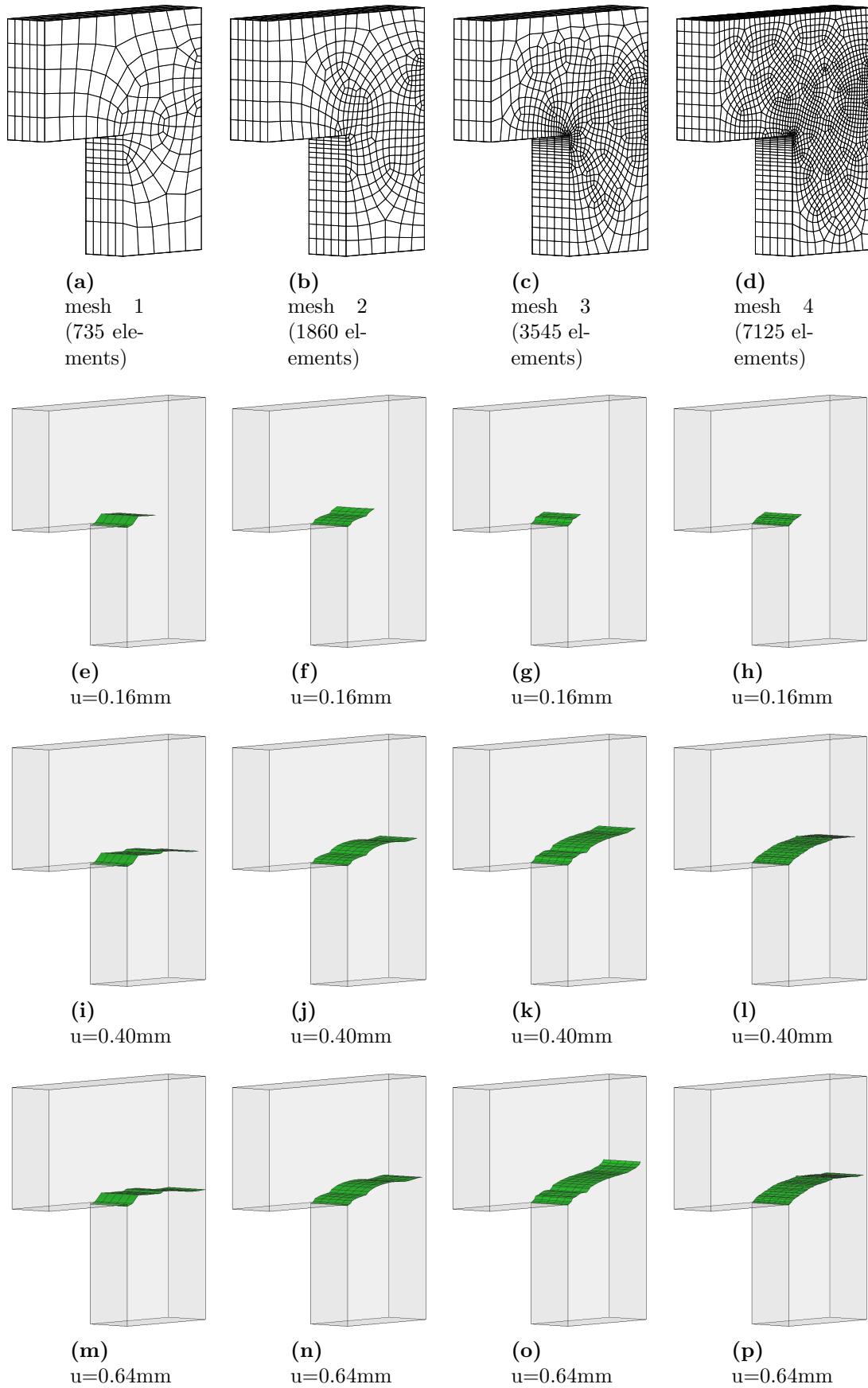


Figure 2.24: L-shape concrete specimen test: illustration of the actual failure surface (e-p) for different applied loading stages and different finite element discretizations (a-d) using displacement based Q1 elements with linear approximations of the displacement jumps.

at the bottom surface) are depicted in Figure 2.20(a), is investigated and compared with experimental results presented in WINKLER ET AL. [385], WINKLER [386] and alternative numerical results presented e.g. in DUMSTORFF & MESCHKE [79], HUND & RAMM [159], JÄGER ET AL. [163], based on which a more complicated failure surface is expected. Whereas the material response of the concrete bulk is modeled similar as in the previous problem in Section 2.5.2 but now with a Young's modulus $E = 25.85$ GPa and a Poisson ratio of $\nu = 0.18$, the constitutive model along the propagating failure surface makes use of an exponential softening law given as

$$t_{\Gamma_n} = \max\{0, f_{t_n} \cdot \exp(-a \llbracket u_{\mu_n}^h \rrbracket)\} \quad (2.77)$$

in normal direction of the artificial planar failure surface. A softening exponent of $a = 41.54 \text{ mm}^{-1}$ and a tensile strength of $f_{t_n} = 2.65$ MPa is chosen. Along the two tangential directions, a reduced stiffness of $k_s = k_t = 0.3$ MPa/mm is used.

The discretization of the specimen is performed with the in Figure 2.20(b) illustrated 3545 displacement based eight node brick elements with five layers of elements in the thickness direction. Again, the discussion starts with an illustration of the resulting constant level set surfaces in Figure 2.21, which are obtained using the global tracking algorithm with initial values of $\theta = \pm 1$ at the top and bottom layer of nodes of the elements at which the failure surface is assumed to start. Again it is apparent that those surfaces evolve with an increased loading. The iso-surface finally chosen based on the averaged value of the level set at the crack front based on (2.61) as the actual failure surface is illustrated in Figure 2.22. Whereas Figure 2.22(a-h) shows how this surface evolves for an increasing applied displacement, Figure 2.22(i-k) illustrate the final failure zone from different perspectives, which turns out to be in close agreement with experimental results reported in WINKLER [386]. The potentially possible non-symmetry in thickness direction seems to vanish in this test when having a closer look at the illustrations in Figure 2.22(i,k).

Next, the reaction force R versus applied displacement u relation is plotted on the left of Figure 2.23 for both, displacement based Q1 elements as well as mixed Q1/P0 elements and distinguished for the case when constant and when linear separation modes are allowed within the eight node hexahedral finite elements. Again, using the elements with a higher order approximation of the failure surface improves on the numerical results agreeing better with the experimental envelope presented in [386]. Finally, on the right of Figure 2.23 is shown the reaction force versus displacement relation for a varying density in the finite element discretization using displacement based Q1 elements with linear separation modes. The resulting influence of the different finite element meshes on the obtained failure surface is illustrated in Figure 2.24.

2.5.4 Brokenshire torsion test

As the third example, the Brokenshire torsion test is investigated and compared with experimental results performed in BROKENSHIRE [58] and alternative numerical simulation found e.g. in JEFFERSON ET AL. [169], GÜRSES & MIEHE [132], GASSER & HOLZAPFEL [119], or FRIES & BAYDOUN [112]. The problem setting is given in Figure 2.25 showing a prismatic concrete beam with a notch, inclined by 45° , through the center of the top surface. The beam is supported by two rigid anchors at both ends and loaded in torsion based on a downward displacement at one corner of one of the anchors. The material

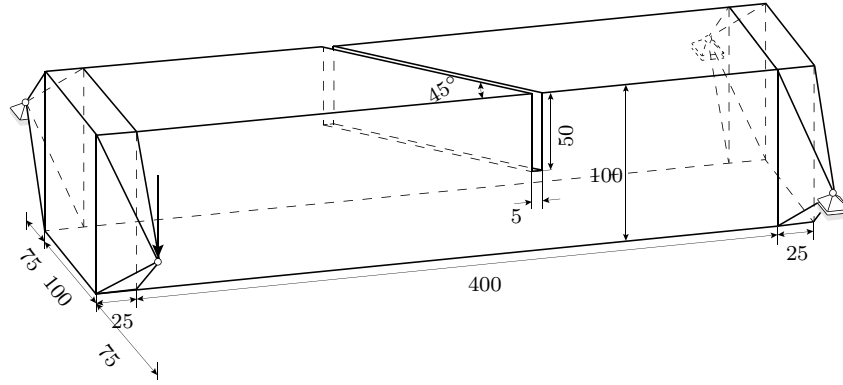


Figure 2.25: Brokenshire torsion test: illustration of geometry (length units in mm), loading, and support of the notched prismatic beam fixed by two rigid anchors on the left and right side.

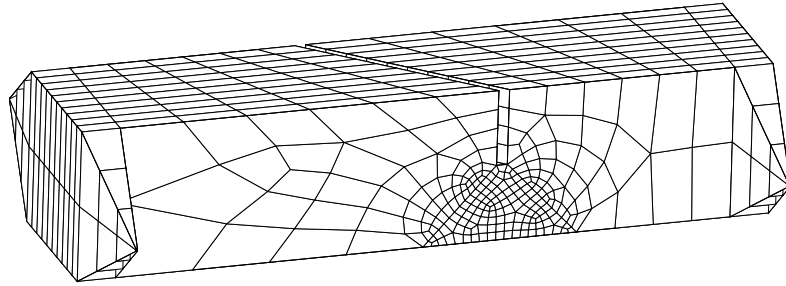


Figure 2.26: Brokenshire torsion test: illustration of the finite element discretization using an unstructured mesh with 2314 brick elements.

response of the concrete beam is modeled again as linear elastic with a Young's modulus of $E = 34.9$ GPa and a Poisson ratio of $\nu = 0.2$ in the bulk. After surpassing the tensile strength of $f_{tn} = 2.3$ MPa a failure surface is supposed to initiate at the tip of the pre-existing notch and supposed to propagate downwards until reaching the bottom surface. The same exponential softening law as in (2.77) is used with the same softening exponent in normal direction and the same reduced stiffness is used in the linear laws in tangential direction.

The finite element discretization consists of 2314 brick elements as illustrated in Figure 2.26. No repeated layers of elements are possible for this test due to the inclined pre-existing notch resulting in a fully unstructured mesh in all three directions, therefore serving as an excellent example for the proposed crack propagation concept in this work. The discussion again starts with an illustration of the resulting constant level set surfaces in Figure 2.27. Those are obtained by choosing $\theta = \pm 1$ for the nodes of elements on either side of the center of the pre-existing notch front in the global tracking algorithm. Figure 2.27 clearly shows the evolution of the very complex isosurfaces with increased loading. The iso-surface finally chosen based on the averaged value of the level set at the crack front based on (2.61) as the actual failure surface is illustrated in Figure 2.28. Whereas Figure 2.28(a-d) shows how this surface evolves for an increasing applied displacement, Figure 2.28(e-h) illustrate the final failure zone from different perspectives. A highly complex, double curved but very smooth failure surface is obtained based on the proposed crack propagation concept agreeing well with other numerical results reported in GASSER & HOLZAPFEL [119], GÜRSES & MIEHE [132], or FRIES & BAYDOUN [112].

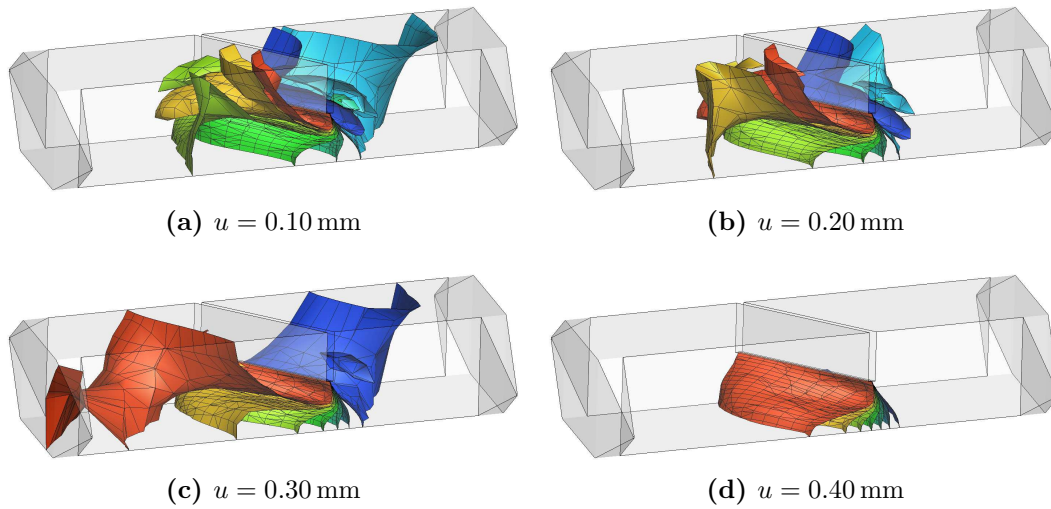


Figure 2.27: Brokenshire torsion test: illustration of the evolution of different possible failure surfaces predicted by the global tracking algorithm in conjunction with the marching cubes algorithm.

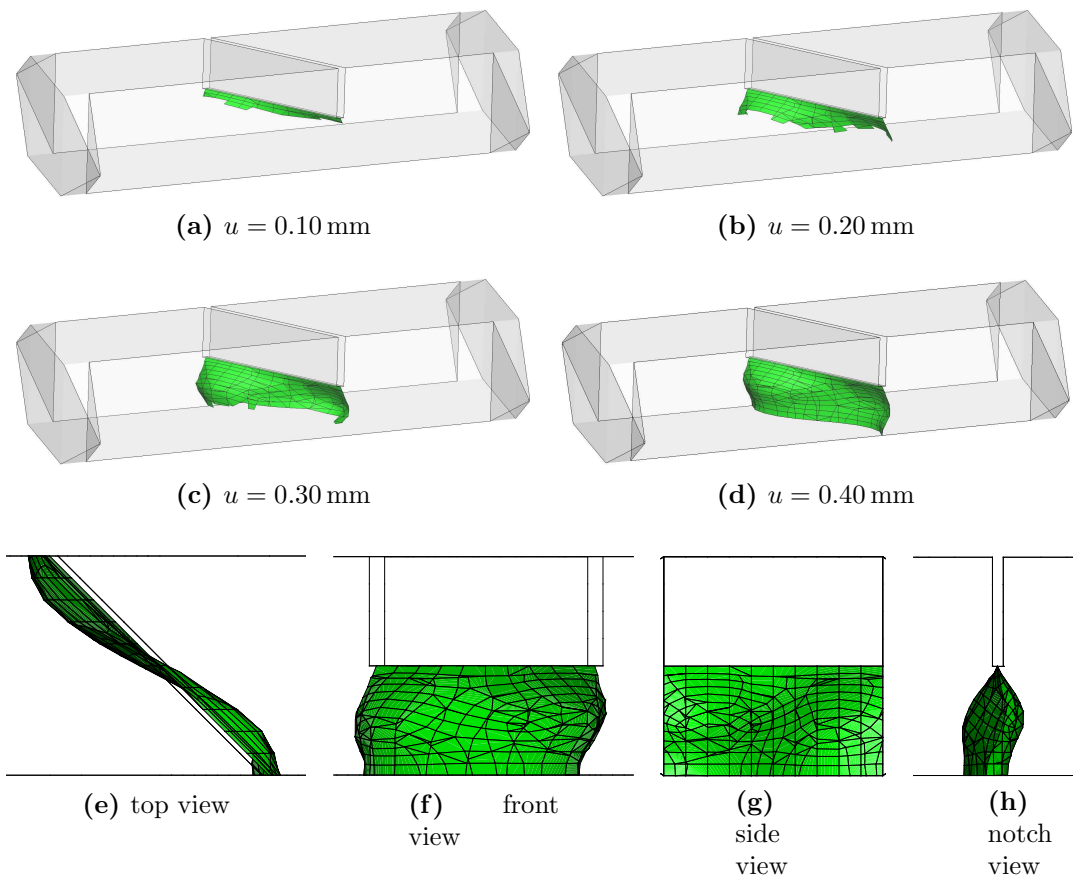


Figure 2.28: Brokenshire torsion test: illustration of the actual failure surface for different applied loading stages (a-d) and a closer look at the final failure surface (e-h) from different perspectives.

The complexity of the obtained constant level set isosurfaces serving as prediction for the actual failure surface becomes apparent when counting the number of elements being

load (mm)		unique configurations in the marching cubes algorithm														
		0	1	2	3*	4	5	6*	7*	8	9	10*	11*	12*	13*	14
0.10	I		59	64	2	51	34			4						1
	II		79	68		52	38			12	2					2
	III		100	111	1	75	57			15	4	3	1			1
	IV		66	136		48	33			9	1					1
	V		107	150	1	80	37	2		13	2	1	1			3
	VI		73	91		54	45			9	1					1
	VII		51	72	2	45	42			5						1
0.20	I		83	119	1	53	36			14	2		1			
	II		68	119		62	40			5						
	III		73	95		48	28			14						
	IV		56	113		45	23			7						
	V		79	113		69	33			8						1
	VI		87	102		67	49			10			2			2
	VII		65	82		56	43			4	1					1
0.30	I		71	124		59	38			6	1					
	II		77	104		56	38			13						
	III		56	121		44	14			7						
	IV		65	92		51	24			8						1
	V		83	100		69	20			9						
	VI		75	107		62	29			8						
	VII		80	83	2	62	37			8	2	2				
0.40	I		68	110		51	28			10						
	II		57	104		43	21			9						
	III		55	111		48	15			4						
	IV		67	104		47	23			12	1					
	V		77	100		65	33			6	2					
	VI		72	108	1	57	31			8		1				
	VII		82	76	1	24	34			10	1	1				

Table 2.2: Brokenshire torsion test: number of elements categorized into the 15 unique configurations of the marching cubes algorithm illustrated in Figure 2.9 for the different loading stages shown in Figure 2.27 and different level set values distinguished by color (I–red, II–yellow, III–light green, IV–dark green, V–turquoise, VI–cyan, and VII–blue). The 7 configurations with multiple isosurfaces in Figure 2.9 are marked by the superscript *.

categorized into the individual 15 unique configurations of the marching cubes algorithm illustrated in Figure 2.9. An overview is provided in Table 2.2 for the four loading stages with the isosurfaces illustrated in Figure 2.27. It becomes apparent, that even the cases with multiple discontinuities illustrated in Figure 2.9 are present, for which eventually the one continuous to the existing crack front is chosen. This confirms the assumption, that none of the 15 unique cases in Figure 2.9 can be neglected.

2.5.5 Tensile test with two notches and holes

Next, the tensile test with two pre-existing notches and two holes is investigated and compared with alternative numerical results given e.g. in BOUCHARD ET AL. [49, 50], MIEHE & GÜRSES [240] to demonstrate the versatility of the proposed crack propagation

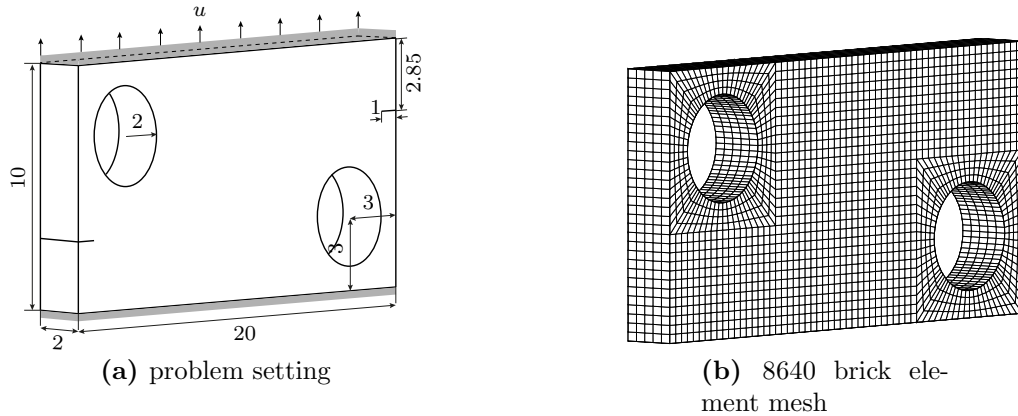


Figure 2.29: Tensile test: illustration of geometry (length units in mm), loading, and support of the concrete specimen on the left and illustration of the finite element discretization on the right.

concept to be used for multiple failure surfaces. The problem setting is illustrated in Figure 2.29(a) including the boundary condition being fixed at the bottom surface and the loading being applied in vertical direction along the top surface. The material is modeled as linear elastic in the bulk with a Young's modulus of $E = 25.85$ GPa and a Poisson ratio of $\nu = 0.18$. Two failure surfaces are supposed to initiate from the pre-existing notches after the tensile strength of $f_{tn} = 2.7$ MPa is surpassed. The same constitutive response along the failure surface is chosen as in the previous two examples of Sections 2.5.3 and 2.5.4.

The simulation is performed with the finite element mesh depicted in Figure 2.29(b) consisting of 8640 eight node brick elements. The pre-existing notch is modeled with finite elements having a fully softened strong discontinuity. The global tracking algorithm is run with initial values of $\theta = \pm 1$ at the bottom and top nodes of those elements in the initial crack front. In conjunction with the marching cubes algorithm, the constant isosurfaces shown in Figure 2.30 are obtained for different loading stages. The actual failure surface is illustrated in Figure 2.31, again at the different loading stages. It is seen, that the crack propagation concept indeed is capable of representing multiple failure surfaces as long as scenarios of multiple failure surfaces within a single finite element is circumvented.

2.5.6 Four-point bending test with two notches

Finally, the double notched four-point bending test is considered to further outline the applicability of the propagation concept for cases of multiple propagating failure surfaces. The problem setting is illustrated in Figure 2.32(a) including the boundary conditions and loading scenario. The concrete beam with dimension $900 \times 200 \times 100$ mm³ with the two center notches of dimension $5 \times 40 \times 100$ mm³ is supported at two steel caps at the lower surface over the whole thickness. The load is not applied as in the previous examples directly through an imposed displacement but rather through eccentric loads $5/6 P$ and $1/6 P$ at two steel caps on the upper surface. The load varies through an arc-length solution procedure that increases linearly in terms of the crack mouth opening displacement (cmo) u as the horizontal relative separation of the bottom edge of the notch. The material in the bulk is modeled as in the previous sections as linear elastic with

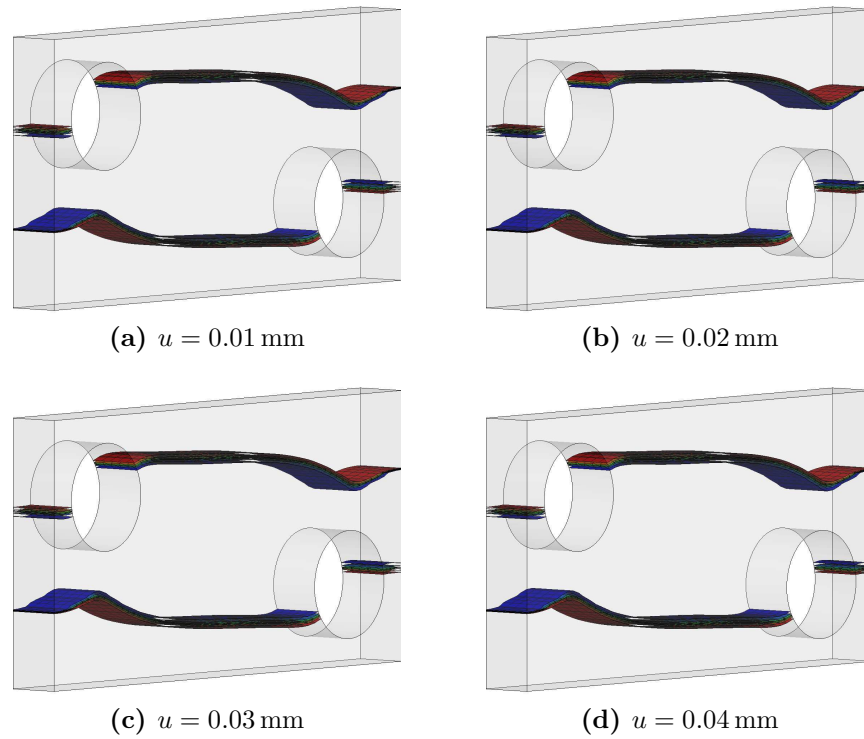


Figure 2.30: Tensile test: illustration of the evolution of different possible failure surfaces predicted by the global tracking algorithm in conjunction with the marching cubes algorithm.

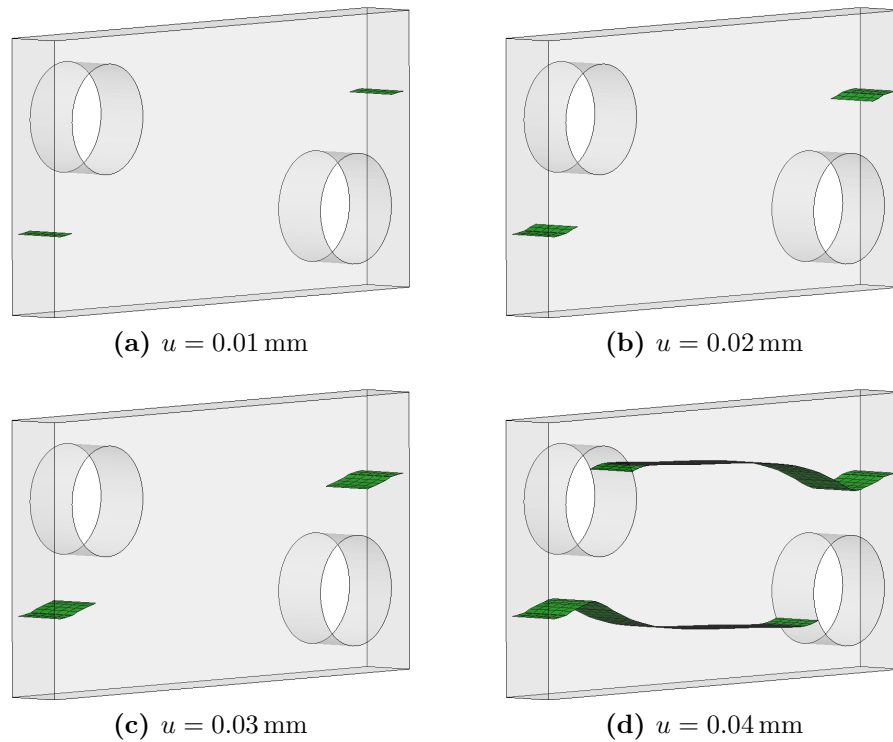
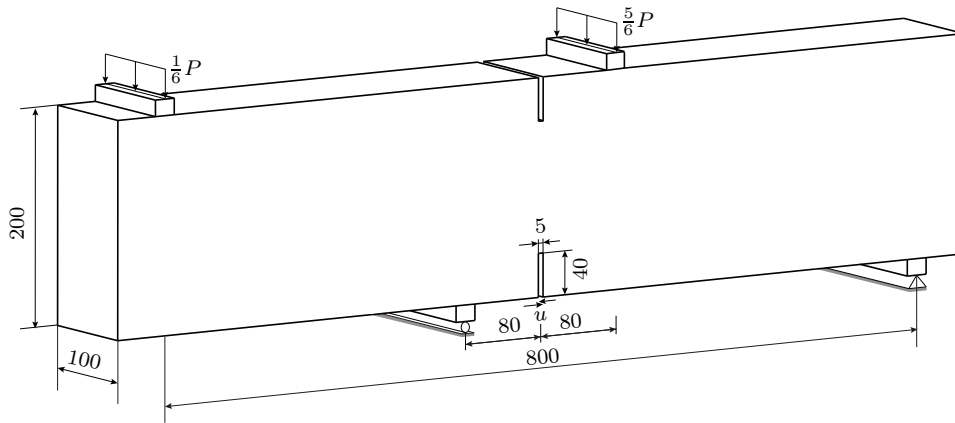
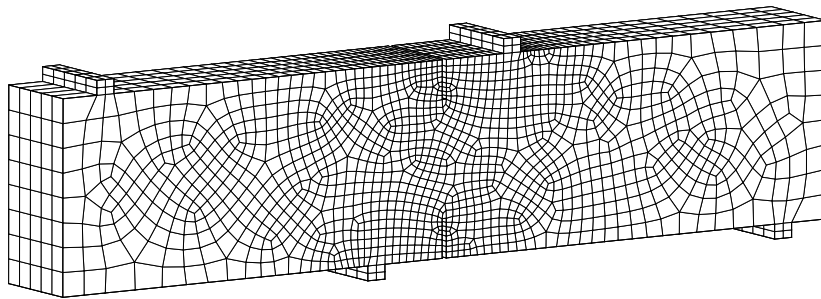


Figure 2.31: Tensile test: illustration of the actual failure surface for different applied loading stages.



(a) problem setting



(b) 6395 brick element mesh

Figure 2.32: Four-point bending test: illustration of geometry (length units in mm), loading, and support of the concrete specimen in the upper row and illustration of the finite element discretization using an unstructured mesh in the lower row.

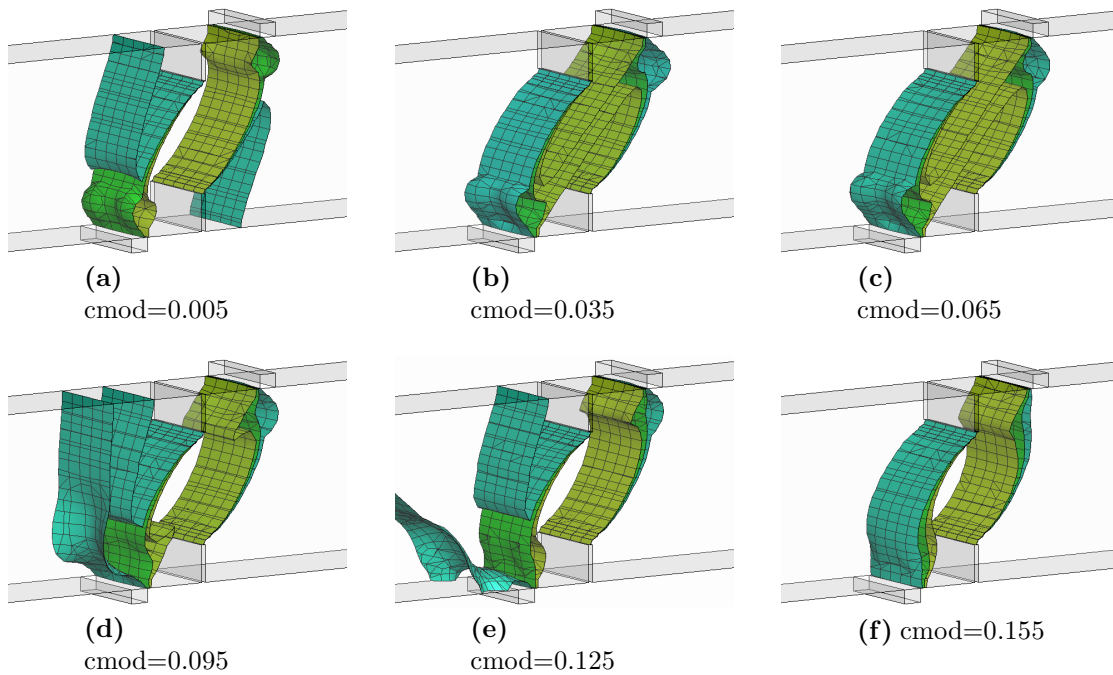


Figure 2.33: Four-point bending test: illustration of the evolution of different possible failure surfaces (cmod in mm) predicted by the global tracking algorithm in conjunction with the marching cubes algorithm.

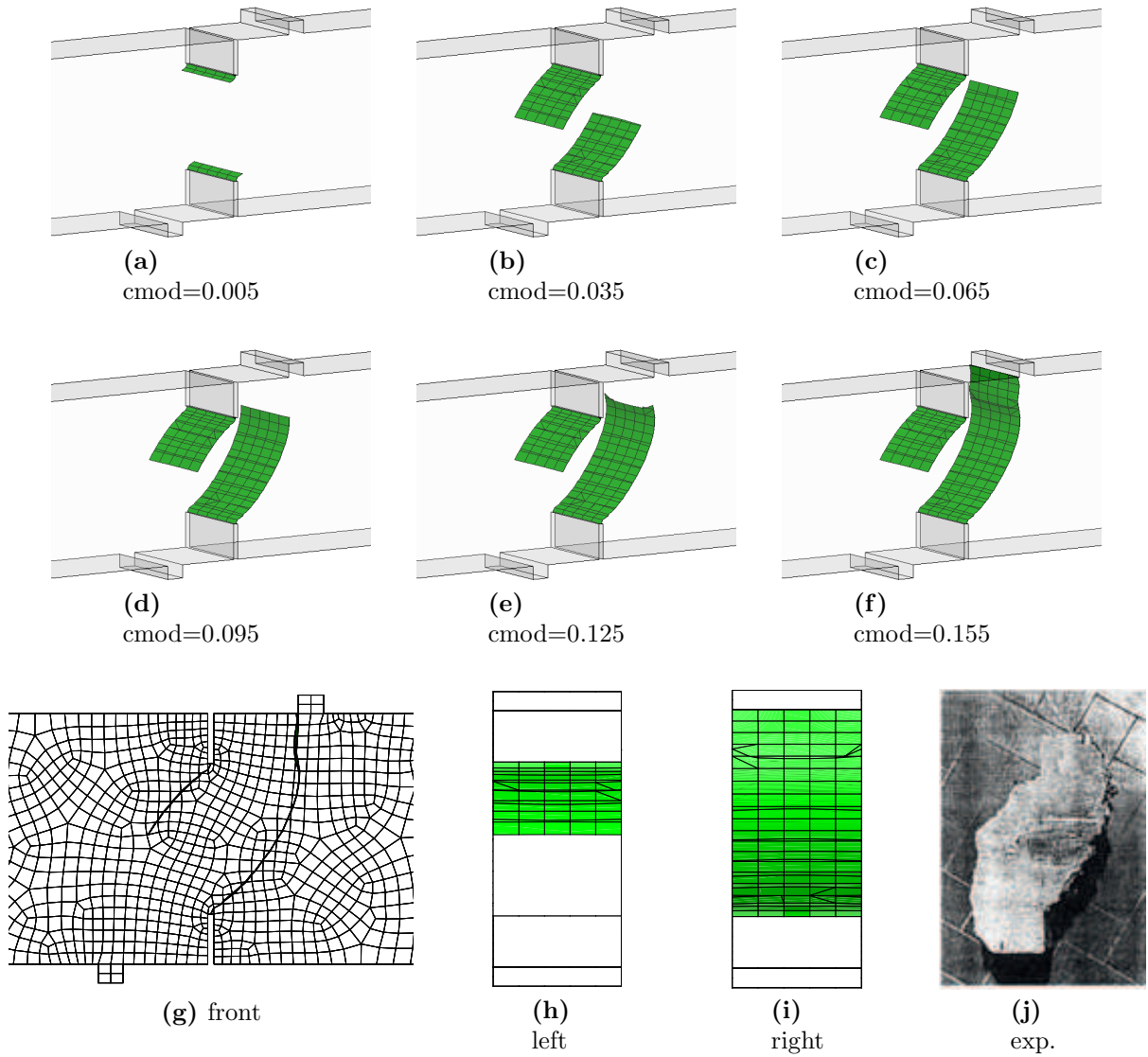


Figure 2.34: Four-point bending test: illustration of the actual failure surface for different c_{mod} (in mm) stages (a-f) and a closer look at the final failure surface (g-i) compared with the experimental result (j).

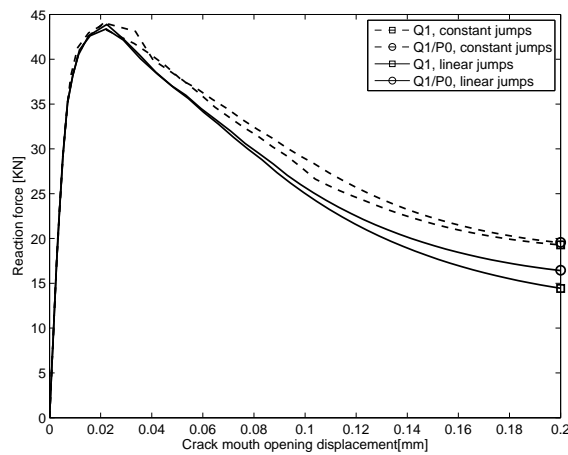


Figure 2.35: Four-point bending test: reaction force versus crack mouth opening displacement relation for displacement based Q1 and mixed Q1/P0 elements with constant and linear jumps.

a Young's modulus of $E = 27$ GPa and a Poisson ratio of $\nu = 0.18$. Experimental results in BOCCA ET AL. [45] and alternative numerical results for two- and three dimensional simulations [266, 269, 270, 291, 347, 393] indicate the appearance of two complicated failure surfaces originating from the pre-existing notches. To model the material behavior within an arising strong discontinuity, the same constitutive response (2.77) is used as in the previous examples but with a tensile strength of $f_{t_n} = 2$ MPa and a softening exponent of $a = 20 \text{ mm}^{-1}$.

The finite element discretization consists of 6395 eight node hexahedral finite elements as illustrated in Figure 2.32(b). Also in this simulation, the discussion starts with an illustration of the resulting constant level set surfaces in Figure 2.33. Those are obtained by choosing $\theta = \pm 1$ at the nodes along the edges of the two pre-existing notches. Again, the evolution of those isosurfaces with an increasing load controlled by the crack mouth opening displacement is observed. The two isosurfaces finally chosen based on the averaged value of the level set at the two crack fronts based on (2.61) as the actual failure surfaces are illustrated in Figure 2.34. Whereas Figure 2.34(a-f) shows how this surface evolves for an increasing applied load, Figure 2.34(g-i) illustrates the final failure zone from different perspectives and compares the obtained numerical solution with the experimental result in Figure 2.34(j), which outlines the good performance of the proposed crack propagation concept obtained as a combination of the global tracking algorithm and the marching cubes algorithm. Similar as for the three-point bending test in Section 2.5.2, a closer look at Figure 2.34(h,i) reveals a slight non-symmetry in the thickness direction again being the result of a possible non-symmetric partition of the failure surface into triangles when performing integrations over the strong discontinuity.

Finally, the reaction force versus crack mouth opening displacement relation is plotted in Figure 2.35. The result obtained in this work is close to the numerical results reported in OLIVER ET AL. [270] since only a slight deviation of the results with a constant and a linear approximation of the displacement jumps is observed for both, displacement based Q1 and mixed Q1/P0 elements.

3 The strong discontinuity approach for electromechanical problems

This chapter extends the strong discontinuity approach introduced in the previous Chapter 2 for purely mechanical solids to electromechanical coupled materials like piezo- and ferroelectric ceramics and closely investigates the physical phenomenon of electric displacement saturation on the influence of crack initiation and failure surface propagation. The recent publications of LINDER ET AL. [210], LINDER & MIEHE [207], and LINDER [204] serve as the basis for the content of this chapter.

3.1 Introduction

Making use of the decomposition of the strong discontinuity approach into a global problem, representing here the standard electromechanical boundary value problem, the strong discontinuities in the form of jumps in the displacement fields as well as jumps in the electric potential are subsequently incorporated through the local problem representing the localized zones of failure. This decomposition is further beneficiary when it comes to the development of constitutive relations along the strong discontinuities where now the mechanical displacement and the electric potential need to be related to the mechanical traction and the surface charge density, respectively. This can be achieved by the development of a localized electromechanical damage model along the strong discontinuity resulting from an anisotropic continuum based damage model developed in SIMO & JU [327] for a purely mechanical based material in the same line as the resulting mechanical damage model along the discontinuity is developed in ARMERO [6]. Localized constitutive relations in elastoplastic solids are developed in MIEHE & SCHRÖDER [243]. The decomposition of the method into global and local part can also be exploited within the resulting discrete finite element setting. Whereas the global problem is discretized with standard displacement based, mixed, or enhanced finite elements, the localized zones can be represented by finite elements equipped with the possibility of forming strong discontinuities in the displacement field as well as in the electric potential again based on underlying finite elements being either of displacement based, mixed, or enhanced type. To avoid locking phenomena, electric separation modes are introduced along the same line as the mechanical separation modes in the plane mechanical continuum problem are proposed in LINDER & ARMERO [205] resulting in the development of new finite elements which are capable of representing the electromechanical coupled failure. It is emphasized that the computational efficient property of the strong discontinuity approach can be kept due to the possibility to statically condense out all the information needed to describe the discontinuities in the mechanical and the electrical fields at the finite element level.

This chapter presents further a computational investigation of a proposed simplified account for electric displacement saturation on the hysteretic behavior of initially unpoled ferroelectric ceramics as well as on the initiation and propagation of cracks in poled ferroelectric ceramics within the linear regime of piezoelectricity. For the latter case, experimental observations suggest an odd dependency of the onset of crack initiation in these brittle materials on the orientation of the applied electric field with respect to their poling direction which contradicts theoretical results which propose an even dependency of the energy release rate on the applied electric field within the framework of anisotropic

linear piezoelectricity. Electric non-linearities arising at regions of inhomogeneities such as inclusions or at the crack tip are proposed in the literature to avoid this discrepancy. Electric displacement saturation is one such non-linear effect which is investigated in this work. A simplified account of this effect is proposed based on an exponential saturation model of the identified material parameters which can be related to this non-linearity. Its advantage over the superposition of a complex function onto the singular solution of a crack within the framework of linear piezoelectricity lies in the straightforward extension of the proposed approach to problems where no analytical solutions exist. This is outlined based on its incorporation into a rate-dependent ferroelectric model accounting for polarization switching as well as based on its incorporation into a finite element framework capable of simulating the initiation and propagation of cracks in piezoelectric ceramics through strong discontinuities in the displacement field and the electric potential. It is shown that besides the determination of the crack initiation onset also the crack propagation direction is influenced by the appearance of saturation zones arising at the crack tip normal to the polarization direction. The numerically obtained crack paths are found to be close to the experimentally reported results.

The chapter is organized as follows. Following the developments in Chapter 2 for purely mechanical based materials, strong discontinuities are incorporated into the coupled electromechanical problem in Section 3.2. This is done first within the continuum framework in Section 3.2.1. Additionally, the required constitutive relations in the bulk and along the strong discontinuity are introduced where a restriction to piezoelectric materials in the bulk is made even though the proposed formulation allows for more general ferroelectric dissipative material responses. The employed decomposition into global and local problem then allows for the incorporation of the strong discontinuities in both, the mechanical and the electric fields, within the discrete finite element setting in Section 3.2.2. Section 3.3 develops new finite elements based on the introduction of certain electric separation modes with the purpose of avoiding locking phenomena of the electromechanical coupled problem. Numerical aspects like failure initiation in electromechanical coupled materials or failure propagation through those as well as the development of a compact notation for its implementation is discussed in Section 3.4. The simplified account for the electric displacement saturation is discussed in Section 3.5, including its derivation for piezoelectric ceramics in Section 3.5.1, a complex variable solution in Section 3.5.1, and an extension to ferroelectric ceramics in Section 3.5.3. Finally, Section 3.6 outlines the performance of the new finite elements based on two simple academic single element tests and two realistic numerical simulations in the form of a compact tension test and a three point bending test for piezoelectric ceramics. Comparisons of the two latter simulations with experimental results in PARK & SUN [280] are made and the influence of electric displacement saturation is investigated in detail.

3.2 The electromechanical coupled strong discontinuity framework

Following the developments in Chapter 2, in this section it will be outlined how failure can be modeled within electromechanical coupled solids based on a sharp resolution of the failure zone by discontinuities in the mechanical as well as the electrical primary unknowns. This will be done separately for the continuum framework in Section 3.2.1

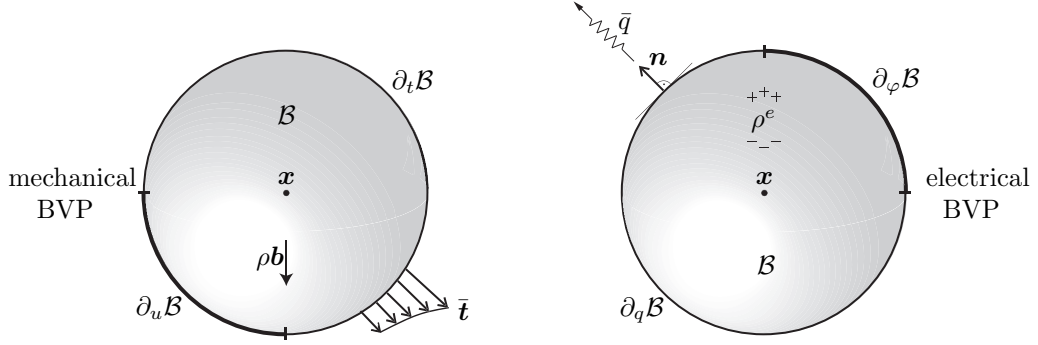


Figure 3.1: The electromechanical boundary value problem (BVP) of piezoelectric ceramics. The mechanical loading $\rho\mathbf{b}$, $\bar{\mathbf{t}}$ and corresponding decomposition of the mechanical boundary $\partial\mathcal{B} = \bar{\partial}_u\mathcal{B} \cup \partial_t\mathcal{B}$ is shown on the left whereas the electrical loading ρ^e , \bar{q} and corresponding decomposition of the boundary $\partial\mathcal{B} = \bar{\partial}_\varphi\mathcal{B} \cup \partial_q\mathcal{B}$ is illustrated on the right.

and the finite element framework in Section 3.2.2.

3.2.1 Continuum modeling of failure in electromechanical coupled solids

The section starts with a brief summary of the electromechanical boundary value problem at the infinitesimal range in Section 3.2.1.1 and continues in Section 3.2.1.2 by incorporating the required discontinuities into the formulation to model failure.

3.2.1.1 The electromechanical coupled boundary value problem. Let the electromechanical coupled solid \mathcal{B} occupy a configuration $\mathcal{B} \subset \mathbb{R}^{n_{\text{dim}}}$ for $1 \leq n_{\text{dim}} \leq 3$ characterized by the mechanical displacement field $\mathbf{u} : \mathcal{B} \rightarrow \mathbb{R}^{n_{\text{dim}}}$ as well as the electric potential $\varphi : \mathcal{B} \rightarrow \mathbb{R}^1$ as the primary unknowns within the infinitesimal range of interest here. Associated with the solids material points labeled by their position $\mathbf{x} \in \mathcal{B}$ is again the infinitesimal strain tensor $\boldsymbol{\varepsilon}$ defined in (2.1) but now in addition also the electric field $\mathbf{e} : \mathcal{B} \rightarrow \mathbb{R}^{n_{\text{dim}}}$ defined by

$$\mathbf{e}(\varphi) = -\nabla\varphi \quad (3.1)$$

in terms of the standard gradient operator ∇ with respect to the coordinate \mathbf{x} . In addition, the stresses $\boldsymbol{\sigma}$ introduced in (2.2) as well as the electric displacement field $\mathbf{d} : \mathcal{B} \rightarrow \mathbb{R}^{n_{\text{dim}}}$ are introduced, which together with the external volumetric loading $\rho\mathbf{b}$ and the density of free charge carriers ρ^e form the governing field equations (2.3) and now in addition

$$\text{div}[\mathbf{d}] = \rho^e \quad (3.2)$$

in \mathcal{B} for the quasi-static case considered here. Within the electromechanical coupled problem, the boundary $\partial\mathcal{B}$ is separated into mechanical and electrical parts $\partial\mathcal{B} = \bar{\partial}_u\mathcal{B} \cup \partial_t\mathcal{B}$ and $\partial\mathcal{B} = \bar{\partial}_\varphi\mathcal{B} \cup \partial_q\mathcal{B}$, respectively. $\bar{\partial}_u\mathcal{B}$ and $\bar{\partial}_\varphi\mathcal{B}$ represent the parts of the boundary with imposed displacement field $\mathbf{u} = \bar{\mathbf{u}}$ and imposed electric potential $\varphi = \bar{\varphi}$, whereas $\partial_t\mathcal{B}$ and $\partial_q\mathcal{B}$ represent the parts of the boundary with imposed traction $\boldsymbol{\sigma}\mathbf{n} = \bar{\mathbf{t}}$ and imposed surface charge density $\mathbf{d} \cdot \mathbf{n} = -\bar{q}$ as it is illustrated in Figure 3.1. The usual arguments of the form $\bar{\partial}_u\mathcal{B} \cap \partial_t\mathcal{B} = \emptyset$ and $\bar{\partial}_\varphi\mathcal{B} \cap \partial_q\mathcal{B} = \emptyset$ apply to ensure a well-posed problem.

The weak equations corresponding to (2.3) is given in (2.4) whereas the one corresponding

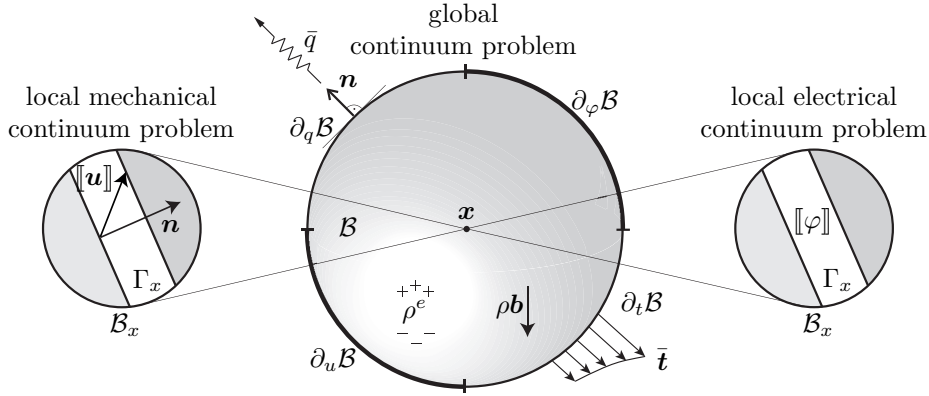


Figure 3.2: Incorporation of strong discontinuities into the continuum setting of piezoelectric ceramics. The global solution $\{\mathbf{u}, \varphi\}$ at a material point \mathbf{x} is equipped with the possibility of forming a strong discontinuity Γ_x in the local mechanical and electrical problems characterized by jumps $\{\llbracket \mathbf{u} \rrbracket, \llbracket \varphi \rrbracket\}$ in the displacement field and the electric potential.

to (3.2) follows from standard arguments as

$$\int_{\mathcal{B}} \rho^e \cdot \delta\varphi \, dV + \int_{\partial_q \mathcal{B}} \bar{q} \cdot \delta\varphi \, dA + \int_{\mathcal{B}} \mathbf{d} \cdot \nabla \delta\varphi \, dV = 0 \quad (3.3)$$

for all admissible variations $\delta\varphi$ with $\delta\varphi = 0$ on $\partial_\varphi \mathcal{B} \subset \partial \mathcal{B}$.

The equations in (2.4) and (3.3) represent the starting point for a standard finite element approximation of the electromechanical coupled problem at hand without the appearance of strong discontinuities in the mechanical as well as the electrical components. These are required though for the modeling of the characteristics of solids at failure and are therefore introduced in the subsequent Section 3.2.1.2.

3.2.1.2 The continuous incorporation of strong discontinuities in the electric potential. The main purpose of this section is to model electromechanical coupled solids at failure where in addition to the global response of the solid in terms of the displacement field \mathbf{u} and the electric potential φ of the previous section, localized zones of failure $\Gamma_x \subset \mathbb{R}^{n_{\text{dim}}-1}$ are present in the form of cracks or shear bands. In addition to strong discontinuities in the displacement field introduced in Section 2.2.1.2, now also the electric potential as the second primary electric unknown in the problem at hand, will experience a discontinuity which can be modeled by a jump in the value of the electric potential on either side of the discontinuity.

To capture both, the global as well as the local response, the decomposition of the displacement field given in (2.5) is appended by the decomposition of the electric potential in the form

$$\varphi_\mu = \varphi + \tilde{\varphi}(\llbracket \varphi_\mu \rrbracket) \quad (3.4)$$

for a material point $\mathbf{x} \in \mathcal{B}_x$ of a local neighborhood $\mathcal{B}_x \subset \mathcal{B}$. In (2.5) and (3.4), the local primary unknowns $\{\mathbf{u}_\mu, \varphi_\mu\}$ are decomposed into the global unknowns $\{\mathbf{u}, \varphi\}$ of the global electromechanical boundary value problem and the discontinuous contributions $\{\tilde{\mathbf{u}}, \tilde{\varphi}\}$ depending on the jumps $\{\llbracket \mathbf{u}_\mu \rrbracket, \llbracket \varphi_\mu \rrbracket\}$ along the localized zone represented by the strong discontinuity Γ_x . The fact that each material point $\mathbf{x} \in \mathcal{B}_x$ is now equipped with the possibility of forming such strong discontinuities in the displacement field as well as the electric potential is illustrated in Figure 3.2.

This decomposition of the local fields into global and discontinuous counterpart is extended to the strain field in (2.6) and can analogously be extended to the electric field defined in (3.1) as

$$\mathbf{e}_\mu = \mathbf{e}(\varphi) + \tilde{\mathbf{e}}(\llbracket \varphi_\mu \rrbracket) \quad (3.5)$$

valid only in $\mathcal{B}_x \setminus \Gamma_x$, neglecting the resulting singular Dirac delta measures on Γ_x .

The introduction of the new unknowns in the form of the jumps in the displacement field $\llbracket \mathbf{u}_\mu \rrbracket$ and the electric potential $\llbracket \varphi_\mu \rrbracket$ do require additional equations for their determination, which is provided by the enforcement of equilibrium along the strong discontinuity Γ_x . It is required that the traction $\mathbf{t} = \boldsymbol{\sigma} \mathbf{n}$ coming from the bulk of the material is in equilibrium with the traction \mathbf{t}_Γ resulting from a constitutive relation along the discontinuity, which is assured in a weak sense by (2.9). In addition, now the equilibrium between the surface charge density $q = -\mathbf{d} \cdot \mathbf{n}$ and the counterpart q_Γ is satisfied by

$$\int_{\Gamma_x} \delta \llbracket \varphi_\mu \rrbracket (\mathbf{d} \cdot \mathbf{n} + q_\Gamma) dA = 0 \quad (3.6)$$

in an integral sense along the strong discontinuity. It has to be kept in mind that the equations in (2.9) and (3.6) are local in nature and only have to be satisfied in the presence of a strong discontinuity Γ_x .

3.2.1.3 The constitutive model problem. Based on the above decomposition of the total problem into a global and a local problem, where the latter is responsible for the incorporation of the strong discontinuities, constitutive models for both problems are required. In particular, the models should be able to reflect the electromechanical coupled behavior of the material considered in this work as well as a required damage behavior for the modeling of failure along the strong discontinuity.

In the subsequent derivation of the constitutive model, a compact notation is used, where corresponding mechanical and electrical quantities are combined as

$$\mathcal{E} = \begin{bmatrix} \boldsymbol{\varepsilon}_\mu \\ \mathbf{e}_\mu \end{bmatrix}, \quad \mathfrak{S} = \begin{bmatrix} \boldsymbol{\sigma} \\ -\mathbf{d} \end{bmatrix}, \quad \mathfrak{j} = \begin{bmatrix} \llbracket \mathbf{u}_\mu \rrbracket \\ \llbracket \varphi_\mu \rrbracket \end{bmatrix}, \quad \mathfrak{t} = \begin{bmatrix} \mathbf{t}_\Gamma \\ q_\Gamma \end{bmatrix}. \quad (3.7)$$

This allows to write the dependence of the electric enthalpy H commonly used for the constitutive modeling of electromechanical coupled materials [262] on the strain field $\boldsymbol{\varepsilon}_\mu$ and electric field \mathbf{e}_μ as

$$H = H(\mathcal{E}; \mathcal{I}) \quad (3.8)$$

where the dependence on a set of internal variables \mathcal{I} is added to capture the damage response along the strong discontinuity. The energy dissipation in a neighborhood \mathcal{B}_x of a part of the body in the local problem is then given as

$$\mathcal{D} = \int_{\mathcal{B}_x} [\mathfrak{S} : \dot{\mathcal{E}} - \dot{H}] dV \quad (3.9)$$

in terms of the electric enthalpy in (3.8). It turns out that a complementary form of the constitutive model is beneficiary when it comes to the modeling of the damage response along the strong discontinuity since in such case use can be made of stress-like based damage criteria to represent the failing material. A stress based continuum damage model

is developed in SIMO & JU [327]. In ARMERO [6] a stress based damage model along a discontinuity is developed for a purely mechanical response of the material. Following this strategy an extension for electromechanical materials is considered in this section yielding a localized anisotropic electromechanical damage model along the strong discontinuity. To do so, a Legendre transformation is performed to obtain the complementary electric enthalpy as

$$\chi(\mathfrak{S}; \mathcal{I}) = \max_{\mathcal{E}} \{ \mathfrak{S} : \mathcal{E} - H(\mathcal{E}; \mathcal{I}) \} \quad (3.10)$$

with a dependence now on the stresses $\boldsymbol{\sigma}$ and the negative electric displacement field $-\mathbf{d}$, which are combined in the vector \mathfrak{S} as outlined in (3.7). The energy dissipation (3.9) then becomes

$$\mathcal{D} = \int_{\mathcal{B}_x} [\dot{\chi} - \dot{\mathfrak{S}} : \mathcal{E}] dV \quad (3.11)$$

in terms of the complementary electric enthalpy defined in (3.10). Following ARMERO [6] a decoupling of the material response into a part reflecting the constitutive response in the bulk and into a part reflecting the response along the strong discontinuity can be achieved by the decomposition of the energy dissipation as

$$\mathcal{D} = \underbrace{\int_{\mathcal{B}_x \setminus \Gamma_x} [\dot{\chi}_{\mathcal{B}} - \dot{\mathfrak{S}} : \mathcal{E}] dV}_{\mathcal{D}_{\mathcal{B}}} + \underbrace{\int_{\Gamma_x} [\dot{\chi}_{\Gamma} - \dot{\mathbf{t}}_{\Gamma} \cdot \mathbf{j}] dA}_{\mathcal{D}_{\Gamma}}, \quad (3.12)$$

where use is made of a chosen decomposition of the complementary electric enthalpy χ into a part characteristic for the response in the bulk $\chi_{\mathcal{B}}$ and a part valid along the strong discontinuity χ_{Γ} with the dependence on the product of the rate of \mathbf{t}_{Γ} and \mathbf{j} , both introduced in (3.7). Motivated by the approach outlined in ORTIZ [273] and SIMO & JU [327] for a purely mechanical continuum model, the response in the bulk $\chi_{\mathcal{B}}$ is chosen to depend on the compliance tensor of the material $\mathbb{D}_{\mathcal{B}}$ as well as a scalar variable $\alpha_{\mathcal{B}}$ characterizing the softening response in the bulk as the internal variables in addition to the primary dependence on \mathfrak{S} . Assuming an analogous dependence of χ_{Γ} on the corresponding quantities along the strong discontinuity results in the decoupled representation of the complementary electric enthalpy in the form

$$\chi = \underbrace{\frac{1}{2} \mathfrak{S} : \mathbb{D}_{\mathcal{B}} \mathfrak{S} - \mathcal{H}(\alpha_{\mathcal{B}})}_{\chi_{\mathcal{B}}} + \underbrace{\frac{1}{2} \mathbf{t}_{\Gamma} \cdot \mathbb{D}_{\Gamma} \mathbf{t}_{\Gamma} - \mathcal{H}(\alpha_{\Gamma})}_{\chi_{\Gamma}} \quad (3.13)$$

with the corresponding fourth and second order compliance tensors $\mathbb{D}_{\mathcal{B}}$ and \mathbb{D}_{Γ} relating the strain and stress like quantities in the bulk as well as along the strong discontinuity in the form $\mathcal{E} = \mathbb{D}_{\mathcal{B}} \mathfrak{S}$ and $\mathbf{j} = \mathbb{D}_{\Gamma} \mathbf{t}_{\Gamma}$, respectively. This fully decoupled representation in (3.12) and (3.13) allows now for the choice of constitutive models in the bulk based on $\mathcal{D}_{\mathcal{B}}$ and $\chi_{\mathcal{B}}$ totally independent from the choice of the constitutive models along the strong discontinuity based on \mathcal{D}_{Γ} and χ_{Γ} . Both responses are briefly discussed in the subsequent paragraphs.

A linear piezoelectric material model in the bulk. The constitutive model in the bulk of the material is based on the part $\mathcal{D}_{\mathcal{B}}$ of the energy dissipation in (3.12). As in ARMERO [6] it is assumed that the damage mechanisms are associated only with the discontinuity Γ_x so that $\mathbb{D}_{\mathcal{B}} = \text{constant}$ and $\alpha_{\mathcal{B}} = 0$ in (3.13). This yields to a

complementary electric enthalpy $\chi_{\mathcal{B}} = \chi_{\mathcal{B}}(\mathfrak{S})$ without a dependence on any internal variable related to the damage of the material. It is noted though that an additional dependence on internal variables in the form of e.g. the remanent polarization describing more general ferroelectric effects as considered in Section 3.5.3 can still be incorporated. To ease the notation, such a dependence is left aside in this section.

Since no damage of the bulk material is expected, it is convenient to again make use of the electric enthalpy $H_{\mathcal{B}}(\mathcal{E})$ of the bulk instead of its complementary representation $\chi_{\mathcal{B}}(\mathfrak{S})$. Doing so, the energy dissipation locally at a material point is given as

$$\mathcal{D}_{\mathcal{B}} = \mathfrak{S} : \dot{\mathcal{E}} - \dot{H}_{\mathcal{B}}(\mathcal{E}) \geq 0 \quad (3.14)$$

with a resulting zero dissipation $\mathcal{D}_{\mathcal{B}} = 0$ for stress like variables given as

$$\mathfrak{S} = \partial_{\mathcal{E}} H_{\mathcal{B}}(\mathcal{E}) \quad (3.15)$$

in terms of the partial derivative of $H_{\mathcal{B}}(\mathcal{E})$ with respect to the strain-like variables \mathcal{E} .

Remarks 3.1. (a) In linear piezoelectricity the electric enthalpy $H_{\mathcal{B}}(\mathcal{E})$ is given as

$$H_{\mathcal{B}}(\mathcal{E}) = \frac{1}{2} \boldsymbol{\epsilon}_{\mu} : \mathbb{C} \boldsymbol{\epsilon}_{\mu} - \mathbf{e}_{\mu} \cdot \mathbb{h} \boldsymbol{\epsilon}_{\mu} - \frac{1}{2} \mathbf{e}_{\mu} \cdot \mathbb{b} \mathbf{e}_{\mu} \quad (3.16)$$

in terms of the fourth order tensor \mathbb{C} as the elasticity moduli, the third order tensor \mathbb{h} of piezoelectric moduli, and the second order tensor \mathbb{b} known as the dielectric moduli, which take the form [173, 317, among others] given in index notation

$$\begin{aligned} \mathbb{C}_{ijkl} &= \lambda \delta_{ij} \delta_{kl} + \mu (\delta_{ik} \delta_{jl} + \delta_{il} \delta_{jk}) \\ \mathbb{h}_{ikl} &= -\beta_1 a_i \delta_{kl} - \beta_2 a_i a_k a_l - \frac{1}{2} \beta_3 (\delta_{il} a_k + \delta_{ik} a_l) \\ \mathbb{b}_{ik} &= \epsilon \delta_{ik} \end{aligned} \quad (3.17)$$

in terms of the Lamé constants λ and μ , the piezoelectric material parameters β_1 , β_2 , β_3 , the dielectric material parameter ϵ as the electric permittivity, and δ_{ij} as the standard Kronecker delta. The vector \mathbf{a} represents the constant polarization director $\mathbf{a} = \mathbf{p}/p$ with $p = |\mathbf{p}| = \sqrt{\overline{\mathbf{p}} \cdot \overline{\mathbf{p}}}$ in terms of the polarization vector \mathbf{p} describing the separation of the barycenters of negative and positive charges associated with a typical piezoelectric volume element. Based on (3.15), the stresses $\boldsymbol{\sigma}$ and the electric displacement \mathbf{d} follow then as

$$\boldsymbol{\sigma} = \mathbb{C} \boldsymbol{\epsilon}_{\mu} - \mathbb{h}^T \mathbf{e}_{\mu} \quad \text{and} \quad \mathbf{d} = \mathbb{h} \boldsymbol{\epsilon}_{\mu} + \mathbb{b} \mathbf{e}_{\mu}. \quad (3.18)$$

The relations $\mathfrak{S} = \mathbb{C}_{\mathcal{B}} \mathcal{E}$ and $\mathcal{E} = \mathbb{D}_{\mathcal{B}} \mathfrak{S}$ yield then the explicit forms of the material tangent $\mathbb{C}_{\mathcal{B}}$ and the bulk compliance tensor $\mathbb{D}_{\mathcal{B}} = \mathbb{C}^{-1}$ used in (3.13) as

$$\mathbb{C}_{\mathcal{B}} = \begin{bmatrix} \mathbb{C} & -\mathbb{h}^T \\ -\mathbb{h} & -\mathbb{b} \end{bmatrix} \quad \text{and} \quad \mathbb{D}_{\mathcal{B}} = \begin{bmatrix} \mathbb{C}^* & -\mathbb{h}^{*T} \\ -\mathbb{h}^* & -\mathbb{b}^* \end{bmatrix} \quad (3.19)$$

where $\mathbb{C}^* = \mathbb{C}^{-1}$, $\mathbb{h}^* = \mathbb{b}^{-1} \mathbb{h} \mathbb{C}^{-1}$, and $\mathbb{b}^* = \mathbb{b}^{-1}$ when accounting for the fact that $\mathcal{O}(\mathbb{b}^{-1} \mathbb{h} \mathbb{C}^{-1} \mathbb{h}) = \mathcal{O}(\mathbb{C}^{-1} \mathbb{h}^T \mathbb{b}^{-1} \mathbb{h}) = (\max \beta_i)^2 / (E\epsilon) \ll 1$ with ϵ and β_i introduced in (3.17) for $i = 1, 2, 3$. Note that when there is no discontinuity present at the material point for which the constitutive relation is embarked, the global expressions $\{\boldsymbol{\epsilon}, \mathbf{e}\}$ should be used in the relation (3.18) instead of the local fields $\{\boldsymbol{\epsilon}_{\mu}, \mathbf{e}_{\mu}\}$.

(b) Following the invariant formulation proposed in SCHRÖDER & GROSS [317], for which $\hat{H}(\boldsymbol{\varepsilon}, \mathbf{e}, \mathbf{a}) = \hat{H}(\mathbf{Q}\boldsymbol{\varepsilon}\mathbf{Q}^T, \mathbf{Q}\mathbf{e}, \mathbf{Q}\mathbf{a}) \forall \mathbf{Q} \in \mathcal{G}$ where $\mathcal{G} = \{\mathbf{Q} \in \mathcal{O}(3) | \mathbf{Q}\mathbf{a} = \mathbf{a}\}$ has to hold, the electric enthalpy is given as

$$H_{\mathcal{B}} = H_{\mathcal{B}}(I_i |_{i=1}^7) = H_{\mathcal{B}_1}(I_1, I_2, I_3, I_4) + H_{\mathcal{B}_2}(I_5, I_6) + H_{\mathcal{B}_3}(I_1, I_3, I_5, I_6, I_7) \quad (3.20)$$

where the purely mechanical contribution $H_{\mathcal{B}_1}$, the purely electrical contribution $H_{\mathcal{B}_2}$, and the electromechanical coupled part $H_{\mathcal{B}_3}$ are given as

$$H_{\mathcal{B}_1} = \frac{1}{2}\lambda I_1^2 + \mu I_2 + \alpha_1 I_4 + \alpha_2 I_3^2 + \alpha_3 I_1 I_3, \quad H_{\mathcal{B}_2} = \gamma_1 I_5 + \gamma_2 I_6^2, \quad H_{\mathcal{B}_3} = \beta_1 I_1 I_6 + \beta_2 I_3 I_5 + \beta_3 I_7 \quad (3.21)$$

in terms of the invariants $I_1 = \varepsilon_{ii}$, $I_2 = \varepsilon_{ij}\varepsilon_{ji}$, $I_3 = a_i\varepsilon_{ij}a_j$, $I_4 = a_i\varepsilon_{ik}\varepsilon_{kj}a_j$, $I_5 = e_i e_i$, $I_6 = e_i a_i$, $I_7 = a_i \varepsilon_{ij} e_j$ and the material parameters λ , μ , α_1 , α_2 , α_3 , β_1 , β_2 , β_3 , γ_1 , and γ_2 . Insertion of (3.20)-(3.21) into (3.15) results in the expressions for the stresses and the electric displacement given in index notation as

$$\sigma_{ij} = \sum_{n=1}^7 \frac{\partial \hat{H}}{\partial I_n} \frac{\partial I_n}{\partial \varepsilon_{ij}} = (\lambda I_1 + \alpha_3 I_3) \delta_{ij} + 2\mu \varepsilon_{ij} + \alpha_1 [\varepsilon_{ik} a_k a_j + a_i a_k \varepsilon_{kj}] + (2\alpha_2 I_3 + \alpha_3 I_1) a_i a_j + \beta_1 I_6 \delta_{ij} + \beta_2 I_6 a_i a_j + \frac{1}{2} \beta_3 [e_i a_j + a_i e_j] \quad (3.22)$$

$$d_i = \sum_{n=1}^7 \frac{\partial \hat{H}}{\partial I_n} \frac{\partial I_n}{\partial e_i} = -2\gamma_1 e_i - 2\gamma_2 I_6 a_i - [(\beta_1 I_1 + \beta_2 I_3) a_i + \beta_3 \varepsilon_{ik} a_k] \quad (3.23)$$

where δ_{ij} is the standard Kronecker delta. The sensitivities of the stresses and the electric displacement with respect to the strains and the electric field are given in terms of the fourth-order elasticity tensor \mathbb{C}_{ijkl} , the third-order tensor of piezoelectric moduli \mathbb{h}_{ikl} , and the second-order tensor of dielectric moduli \mathbb{b}_{ik} as

$$\mathbb{C}_{ijkl} = \frac{\partial \sigma_{ij}}{\partial \varepsilon_{kl}} = \lambda \delta_{ij} \delta_{kl} + \mu (\delta_{ik} \delta_{jl} + \delta_{il} \delta_{jk}) + \alpha_3 (\delta_{ij} a_k a_l + a_i a_j \delta_{kl}) + 2\alpha_2 a_i a_j a_k a_l + \alpha_1 \frac{1}{2} (\delta_{ik} a_j a_l + \delta_{il} a_j a_k + a_i \delta_{jl} a_k + a_i \delta_{jk} a_l) \quad (3.24)$$

$$\mathbb{h}_{ikl} = \frac{\partial d_i}{\partial \varepsilon_{kl}} = -\beta_1 a_i \delta_{kl} - \beta_2 a_i a_k a_l - \beta_3 \frac{1}{2} (\delta_{il} a_k + \delta_{ik} a_l) \quad (3.25)$$

$$\mathbb{b}_{ik} = \frac{\partial d_i}{\partial e_k} = -2\gamma_1 \delta_{ik} - 2\gamma_2 a_i a_k \quad (3.26)$$

replacing the expressions in (3.17) for the isotropic model when used in (3.18). A matrix representation of (3.17) in the case of transverse isotropy with x_3 as the preferred direction \mathbf{a} is obtained by insertion of $\mathbf{a} = [0 \ 0 \ 1]$ into (3.24)-(3.26) as

$$\begin{bmatrix} \sigma_{11} \\ \sigma_{22} \\ \sigma_{33} \\ \sigma_{12} \\ \sigma_{23} \\ \sigma_{13} \end{bmatrix} = \begin{bmatrix} c_{11} & c_{12} & c_{13} & 0 & 0 & 0 \\ c_{12} & c_{11} & c_{13} & 0 & 0 & 0 \\ c_{13} & c_{13} & c_{33} & 0 & 0 & 0 \\ 0 & 0 & 0 & \frac{1}{2}(c_{11} - c_{12}) & 0 & 0 \\ 0 & 0 & 0 & 0 & c_{44} & 0 \\ 0 & 0 & 0 & 0 & 0 & c_{44} \end{bmatrix} \begin{bmatrix} \varepsilon_{11} \\ \varepsilon_{22} \\ \varepsilon_{33} \\ 2\varepsilon_{12} \\ 2\varepsilon_{23} \\ 2\varepsilon_{13} \end{bmatrix} - \begin{bmatrix} 0 & 0 & e_{31} \\ 0 & 0 & e_{31} \\ 0 & 0 & e_{33} \\ 0 & 0 & 0 \\ 0 & e_{15} & 0 \\ e_{15} & 0 & 0 \end{bmatrix} \begin{bmatrix} e_1 \\ e_2 \\ e_3 \end{bmatrix} \quad (3.27)$$

$$\begin{bmatrix} d_1 \\ d_2 \\ d_3 \end{bmatrix} = \begin{bmatrix} 0 & 0 & 0 & 0 & 0 & e_{15} \\ 0 & 0 & 0 & 0 & e_{15} & 0 \\ e_{31} & e_{31} & e_{31} & 0 & 0 & 0 \end{bmatrix} \begin{bmatrix} \varepsilon_{11} \\ \varepsilon_{22} \\ \varepsilon_{33} \\ 2\varepsilon_{12} \\ 2\varepsilon_{23} \\ 2\varepsilon_{13} \end{bmatrix} + \begin{bmatrix} \epsilon_{11} & 0 & 0 \\ 0 & \epsilon_{11} & 0 \\ 0 & 0 & \epsilon_{33} \end{bmatrix} \begin{bmatrix} e_1 \\ e_2 \\ e_3 \end{bmatrix} \quad (3.28)$$

with the relation between the material parameters used in (3.21)-(3.26) and those used in (3.27)-(3.28) given as $\lambda = c_{12}$, $\mu = (c_{11} - c_{12})/2$, $\alpha_1 = 2c_{44} + c_{12} - c_{11}$, $\alpha_2 = (c_{11} + c_{33})/2 - 2c_{44} - c_{13}$, $\alpha_3 = c_{13} - c_{12}$, $\beta_1 = -e_{31}$, $\beta_2 = -e_{33} + 2e_{15} + e_{31}$, $\beta_3 = -2e_{15}$, $\gamma_1 = -\epsilon_{11}/2$, and $\gamma_2 = (\epsilon_{11} - \epsilon_{33})/2$.

A localized electromechanical damage model along the strong discontinuity.

The constitutive model along the strong discontinuity is based on the part \mathcal{D}_Γ of the energy dissipation in (3.12). Insertion of the dependence of χ_Γ in (3.13) into \mathcal{D}_Γ in (3.12) then results in the energy dissipation locally at a material point along the strong discontinuity as

$$\mathcal{D}_\Gamma(\mathbf{t}_\Gamma; \mathbb{D}_\Gamma, \alpha_\Gamma) = \frac{1}{2} (\mathbf{t}_\Gamma \otimes \mathbf{t}_\Gamma) : \dot{\mathbb{D}}_\Gamma + \beta \cdot \dot{\alpha}_\Gamma \geq 0 \quad (3.29)$$

identifying $\frac{1}{2} (\mathbf{t}_\Gamma \otimes \mathbf{t}_\Gamma)$ as the thermodynamic force conjugate to the rate of the internal variable $\dot{\mathbb{D}}_\Gamma$ and $\beta = -d\mathcal{H}/d\alpha_\Gamma$ as the one conjugate to $\dot{\alpha}_\Gamma$. Note that \mathbb{D}_Γ as the counterpart along the strong discontinuity of the compliance $\mathbb{D}_\mathcal{B}$ in the bulk given in (3.19) as well as its inverse $\mathbb{C}_\Gamma = \mathbb{D}_\Gamma^{-1}$ now take the form

$$\mathbb{C}_\Gamma = \begin{bmatrix} \mathbb{C}_\Gamma & -\mathbb{h}_\Gamma^T \\ -\mathbb{h}_\Gamma & -\mathbb{b}_\Gamma \end{bmatrix} \quad \text{and} \quad \mathbb{D}_\Gamma = \begin{bmatrix} \mathbb{C}_\Gamma^* & -\mathbb{h}_\Gamma^{*T} \\ -\mathbb{h}_\Gamma^* & -\mathbb{b}_\Gamma^* \end{bmatrix} \quad (3.30)$$

when written in terms of the counterparts \mathbb{C}_Γ , \mathbb{h}_Γ , \mathbb{b}_Γ , \mathbb{C}_Γ^* , \mathbb{h}_Γ^* , and \mathbb{b}_Γ^* along the strong discontinuity of the piezoelectric quantities in (3.19), respectively.

Following ARMERO [6], the softening response of the localized constitutive model is characterized by n_{surf} damage surfaces $\phi_j(\mathbf{t}_\Gamma \otimes \mathbf{t}_\Gamma, \beta)$ for $j = 1, \dots, n_{\text{surf}}$ so that the damage evolution equations are obtained based on the principle of *maximum damage dissipation* [327] in the form

$$\mathcal{L}_\Gamma = -\mathcal{D}_\Gamma + \sum_{j=1}^{n_{\text{surf}}} \gamma_j \phi_j(\mathbf{t}_\Gamma \otimes \mathbf{t}_\Gamma, \beta) \quad (3.31)$$

in terms of the negative dissipation $-\mathcal{D}_\Gamma$ with \mathcal{D}_Γ given in (3.29) under the n_{surf} constraints with regard to the damage surfaces of the form

$$\phi_j(\mathbf{t}_\Gamma \otimes \mathbf{t}_\Gamma, \beta) \leq 0 \quad (3.32)$$

enforced by the introduction of the consistency parameters γ_j introducing the Kuhn-Tucker complementary conditions for $j = 1, \dots, n_{\text{surf}}$ in the form

$$\gamma_j \geq 0, \quad \phi_j \leq 0, \quad \text{and} \quad \gamma_j \phi_j = 0. \quad (3.33)$$

Minimization of \mathcal{L}_Γ then results in

$$\dot{\mathbb{D}}_\Gamma = \sum_{j=1}^{n_{\text{surf}}} 2\gamma_j \frac{\partial \phi_j}{\partial (\mathbf{t}_\Gamma \otimes \mathbf{t}_\Gamma)} \quad \text{and} \quad \dot{\alpha}_\Gamma = \sum_{j=1}^{n_{\text{surf}}} \gamma_j \frac{\partial \phi_j}{\partial \beta} \quad (3.34)$$

which together with the consistency condition $\gamma_j \dot{\phi}_j = 0$ for $\phi_j = 0$ finalize the damage evolution equations. It is noted that the extension to electromechanical materials can be easily performed based on the developments in ARMERO [6] for purely mechanical based materials when using the compact notation introduced in the beginning of this section, resulting in the complete same structure of the equations as for the mechanical materials.

Remarks 3.2. (a) In ARMERO [6] a purely mechanical Mode I damage model in normal direction of the strong discontinuity is chosen, which is characterized by a damage surface and a softening response of the form

$$\phi_n = t_{\Gamma_n} + \beta(\alpha_\Gamma) - f_{t_n} \leq 0 \quad \text{with} \quad \beta(\alpha_\Gamma) = f_{t_n} \left(1 - \exp\left(\frac{\mathcal{S}_n}{f_{t_n}} \alpha_\Gamma\right)\right) \quad (3.35)$$

in terms of the traction t_{Γ_n} in normal direction and the tensile strength f_{t_n} of the material against normal separation as well as the softening modulus $\mathcal{S}_n < 0$ in normal direction to the strong discontinuity. For the $n_{surf} = 1$ damage surfaces considered in this case, the evolution equations in (3.34) simplify to

$$\dot{\mathbb{D}}_{\Gamma_{nn}} = 2\gamma_n \frac{\partial \phi_n}{\partial (t_{\Gamma_n}^2)} = \frac{\gamma_n}{t_{\Gamma_n}} \quad \text{and} \quad \dot{\alpha}_\Gamma = \gamma_n \frac{\partial \phi_n}{\partial \beta} = \gamma_n. \quad (3.36)$$

It is noted that all other components of $\dot{\mathbb{D}}_\Gamma$ do vanish in this specific case. This is also not changed when choosing a response parallel to the strong discontinuity based on a constant degraded compliance $\mathbb{D}_{\Gamma_{mm}} = k_m > 0$ [6].

Note that as a consequence of $\gamma_n \geq 0$ based on (3.33) and $t_{\Gamma_n} \geq 0$ (since no self penetration is allowed), $\dot{\mathbb{D}}_{\Gamma_{nn}} \geq 0$ shows the increase of degradation within the material for increasing damage. Combining both equations in (3.36) results in the relation $\dot{\mathbb{D}}_{\Gamma_{nn}} = \dot{\alpha}_\Gamma / t_{\Gamma_n}$. Inserting the resulting expression of t_{Γ_n} at $\phi_n = 0$ from (3.35) into this relation results in

$$\dot{\mathbb{D}}_{\Gamma_{nn}} = \frac{1}{f_{t_n}} \exp\left(-\frac{\mathcal{S}_n}{f_{t_n}} \alpha_\Gamma\right) \dot{\alpha}_\Gamma, \quad (3.37)$$

which yields after integration

$$\mathbb{D}_{\Gamma_{nn}} = \frac{1}{\mathcal{S}_n} \left[1 - \exp\left(-\frac{\mathcal{S}_n}{f_{t_n}} \alpha_\Gamma\right)\right] = \frac{1}{\mathcal{S}_n} \left(1 - \frac{f_{t_n}}{t_{\Gamma_n}}\right). \quad (3.38)$$

Since $\llbracket u_{\mu_n} \rrbracket = \mathbb{D}_{\Gamma_{nn}} t_{\Gamma_n}$, the final result of the purely mechanical Mode I damage model yields a relation between the normal jumps $\llbracket u_{\mu_n} \rrbracket$ and the corresponding traction in normal direction t_{Γ_n} of the form

$$t_{\Gamma_n} = \max \{0, f_{t_n} + \mathcal{S}_n \llbracket u_{\mu_n} \rrbracket\} \quad (3.39)$$

which is also used in Chapter 2 in (2.75). Positiveness of the dissipation defined in (3.29) can be assured by the fact that $t_{\Gamma_n} \leq f_{t_n}$ always holds as one may observe based on the left illustration of Figure 3.3 which in turn satisfies the resulting dissipation requirement at $\phi_n = 0$.

(b) In a similar way as in part (a) above, a purely electrical damage model and softening response along the strong discontinuity can be characterized by

$$\phi_\varphi = -|q_\Gamma| + \beta(\alpha_\Gamma) - f_\varphi \leq 0 \quad \text{with} \quad \beta(\alpha_\Gamma) = f_\varphi \left(1 - \exp\left(\frac{\mathcal{S}_\varphi}{f_\varphi} \alpha_\Gamma\right)\right) \quad (3.40)$$

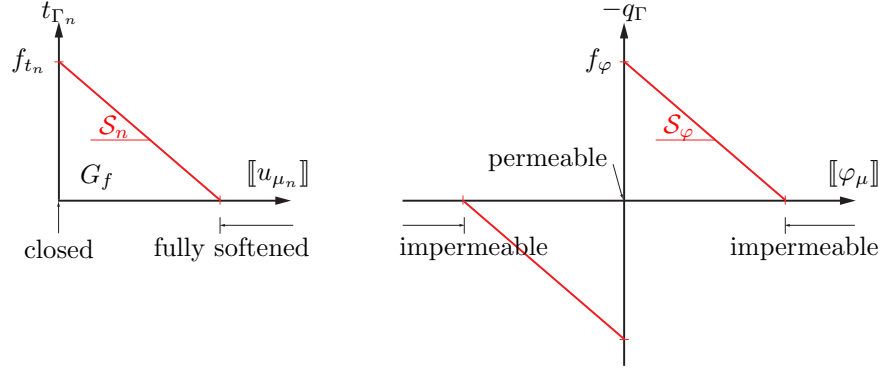


Figure 3.3: Mechanical (left) and electrical (right) constitutive damage relations along the strong discontinuity representing the results obtained in (3.39) and (3.42) based on the proposed localized electromechanical damage model along the strong discontinuity.

in terms of the surface charge density q_{Γ} and a quantity f_{φ} representing the normal component of the electric displacement present when the discontinuity is initiated as well as the softening modulus $\mathcal{S}_{\varphi} < 0$ of the electric fields. Analogous to part (a), the evolution equations can now be derived as

$$\dot{\mathbb{D}}_{\Gamma_{\varphi\varphi}} = -\frac{\gamma_{\varphi}}{|q_{\Gamma}|} \quad \text{and} \quad \dot{\alpha}_{\Gamma} = \gamma_{\varphi} \quad (3.41)$$

with vanishing other components of $\dot{\mathbb{D}}_{\Gamma}$. Note again that as a consequence of $\gamma_{\varphi} \geq 0$ based on (3.33) $\dot{\mathbb{D}}_{\Gamma_{\varphi\varphi}} \leq 0$ holds. Since $\mathbb{D}_{\Gamma_{\varphi\varphi}} = -\mathbb{b}_{\Gamma}^*$ based on (3.30), $\dot{\mathbb{b}}_{\Gamma}^* \geq 0$ holds and ensures that $\mathbb{b}_{\Gamma} \leq 0$ along the strong discontinuity. This is in agreement with the fact that the permittivity of the through the discontinuity created free space is much less than the permittivity of the original dielectric medium before the appearance of the strong discontinuity. Following the remaining steps of part (a) above, the final form of the relation between the jumps $[[\varphi_{\mu}]]$ in the electric potential and the corresponding surface charge density q_{Γ} is obtained in the form

$$-q_{\Gamma} = \frac{[[\varphi_{\mu}]]}{|[[\varphi_{\mu}]]|} \max \{0, f_{\varphi} + \mathcal{S}_{\varphi} |[[\varphi_{\mu}]]|\}. \quad (3.42)$$

Positiveness of the dissipation defined in (3.29) can again be assured by the fact that $|q_{\Gamma}| \leq f_{\varphi}$ always holds as one may observe based on the right illustration of Figure 3.3 which in turn satisfies the resulting dissipation requirement at $\phi_{\varphi} = 0$.

(c) Employing both, the mechanical damage model in normal direction of the strong discontinuity of part (a) and the electrical damage model of part (b) yields a decoupled electromechanical damage model along the strong discontinuity. Electromechanical coupled damage models can be obtained and incorporated by a modification of the damage surfaces used in (3.35) for the purely mechanical case and in (3.40) for the purely electrical case.

(d) Whereas the crack boundary conditions with regard to the mechanical quantities like the relation between the traction and the corresponding displacement jumps have a clear physical interpretation, the correct choice of the electric crack boundary condition is not that straightforward. In the mechanical case, illustrated on the left of Figure 3.3, the crack is initially “closed”. After surpassing a critical strength in the form of a limiting traction component f_{t_n} in normal direction to the crack, the normal traction component

decreases with increasing crack face separation $\llbracket u_{\mu_n} \rrbracket$ based on e.g. the linear softening relation (3.39) in terms of the linear softening modulus \mathcal{S}_n until the point where a zero traction is obtained. From that point on, the crack is considered mechanically “fully softened”. Since the area below the softening curve represents the fracture energy G_f a clear physical interpretation is given. A similar interpretation can be obtained for the electric crack boundary conditions outlined on the right of Figure 3.3 where the two limiting cases are now denoted as the “permeable” and the “impermeable” case, respectively. To the authors knowledge though, no physical interpretation of the area below the resulting normal component of the electric displacement versus jump in the electric potential curve is given in the literature. When considering one of the two extreme cases, a general consensus arises though, that the impermeable case is physically more realistic. It is for this reason, that this limiting case is considered throughout the numerical simulations presented in Section 3.6.

The correct choice of the electric boundary condition is receiving a large amount of attention in the literature [202]. The permeable boundary condition proposed in PARTON [281] results in a model where the electric field will experience a distribution as if the crack does not exist. On the other hand, the impermeable crack boundary condition proposed in DEEG [74] assumes that the permittivity of the crack gap can be approximated as zero resulting in a zero normal component of the electric displacement field. Exact or semi-impermeable boundary conditions are proposed in HAO & SHEN [138] which assume that the crack gap behaves like a linear dielectric material. Closer investigations of that model by MCMEEKING [230] revealed though a discrepancy between the total energy release rate and the crack tip energy release rate of that model. To resolve that problem, LANDIS [195] proposed the so called energetically consistent boundary conditions by adding additional closing traction on the crack faces.

3.2.2 Finite element modeling of failure in electromechanical coupled solids

In an analogous way as in the previous Section 3.2.1 for the continuum setting, now the discrete problem is divided into a global problem consisting now of the discrete form of the electromechanical boundary value problem, which will be discussed in Section 3.2.2.1, and a local problem outlined in Section 3.2.2.1, to representing the incorporation of strong discontinuities in the electric potential into the formulation to numerically model failure, analogous as done in Section 2.2.2 for the incorporation of discrete jumps in the displacement field of the mechanical boundary value problem.

3.2.2.1 The discrete electromechanical boundary value problem. Again, the spatial discretization of the body \mathcal{B} is performed by in total n_{elem} isoparametric finite elements \mathcal{B}_e^h approximating the configuration $\mathcal{B} \approx \mathcal{B}^h = \bigcup_{e=1}^{n_{\text{elem}}} \mathcal{B}_e^h$ as it is illustrated in Figure 3.4 with the proper characterization of the boundary regions $\partial\mathcal{B}^h = \overline{\partial_u\mathcal{B}^h} \cup \partial_t\mathcal{B}^h$ and $\partial\mathcal{B}^h = \overline{\partial_\varphi\mathcal{B}^h} \cup \partial_q\mathcal{B}^h$ for the mechanical and electrical components, respectively. The primary unknowns in the form of the displacement field \mathbf{u}^h is approximated as in (2.11) and the additional primary unknown in the form of the electric potential φ^h at a point $\mathbf{x}^h \in \mathcal{B}^h$ is approximated by

$$\varphi^h(\mathbf{x}^h) = \sum_{A=1}^{n_{\text{node}}} N_\varphi^A(\mathbf{x}^h)\phi_A = \mathbf{N}_\varphi\boldsymbol{\phi} \quad (3.43)$$

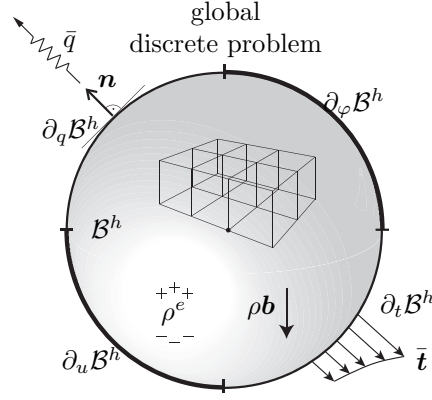


Figure 3.4: The discrete electromechanical boundary value problem. Decomposition of the body \mathcal{B}^h into n_{elem} finite elements \mathcal{B}_e^h with mechanical loading $\bar{\mathbf{t}}$ and electrical loading \bar{q} . The mechanical problem with the proper decomposition of the boundary in $\partial\mathcal{B}^h = \overline{\partial_u\mathcal{B}^h} \cup \partial_t\mathcal{B}^h$ and the electrical problem with the boundary regions $\partial\mathcal{B}^h = \partial_\varphi\mathcal{B}^h \cup \partial_q\mathcal{B}^h$ are illustrated.

in terms of standard shape functions N_φ^A and the corresponding values of the electric potential ϕ_A of node A with in total n_{node} nodes. The approximation of the strain field $\boldsymbol{\varepsilon}^h$ is given in (2.11) and the electric field \mathbf{e}^h is approximated as

$$\nabla\varphi^h = -\mathbf{e}^h(\mathbf{x}^h) = \sum_{A=1}^{n_{\text{node}}} \bar{\mathbf{B}}_\varphi^A(\mathbf{x}^h)\phi_A = \bar{\mathbf{B}}_\varphi\boldsymbol{\phi} \quad (3.44)$$

in terms of the generic “B-bar” matrices $\bar{\mathbf{B}}_\varphi^A$ for the electric fields, outlining again the generality of the proposed formulation with regard to mixed, assumed, or enhanced methodologies in the mechanical as well as the electrical contribution [326, 329, 345].

Assuming again a Bubnov Galerkin formulation [155], the corresponding variations of the displacement field, the electric potential as well as their gradients are approximated in terms of the same shape functions and “B-bar” matrices. Insertion into the continuum representation (2.4) and (3.3) then results in the discrete form of the global mechanical problem given in (2.13) and the global electrical problem given as

$$\mathbf{R}_\varphi = \mathbf{f}_\varphi^{\text{ext}} + \mathbf{A} \int_{\mathcal{B}_e^h} \bar{\mathbf{B}}_\varphi^T \mathbf{d} dV \quad \text{with} \quad \mathbf{f}_\varphi^{\text{ext}} = \mathbf{A} \left(\int_{\mathcal{B}_e^h} \bar{\mathbf{N}}_\varphi^T \rho^e dV + \int_{\partial_q\mathcal{B}_e^h} \bar{\mathbf{N}}_\varphi^T \bar{q} dA \right) \quad (3.45)$$

in terms of the assembly of the internal response of the body based on standard integration techniques over the individual finite elements. The solution of the global problem proceeds by bringing to zero the residual equations in (2.13) and (3.45) based on an iterative solution procedure like Newton’s method, requiring in addition the linearization of that residual equation as it will be outlined in Section 3.4.3.

To make the discrete formulation capable of representing failure in electromechanical coupled solids, strong discontinuities, which have not been accounted for in the discrete global problem considered in this section, need to be incorporated. This is done in the discrete local problem defined in the subsequent Section 3.2.2.2.

3.2.2.2 The discrete incorporation of strong discontinuities in the electric potential. In this section the discrete counterpart to Section 2.2.2.2 is presented with the goal of incorporating the required strong discontinuities in the electric potential locally

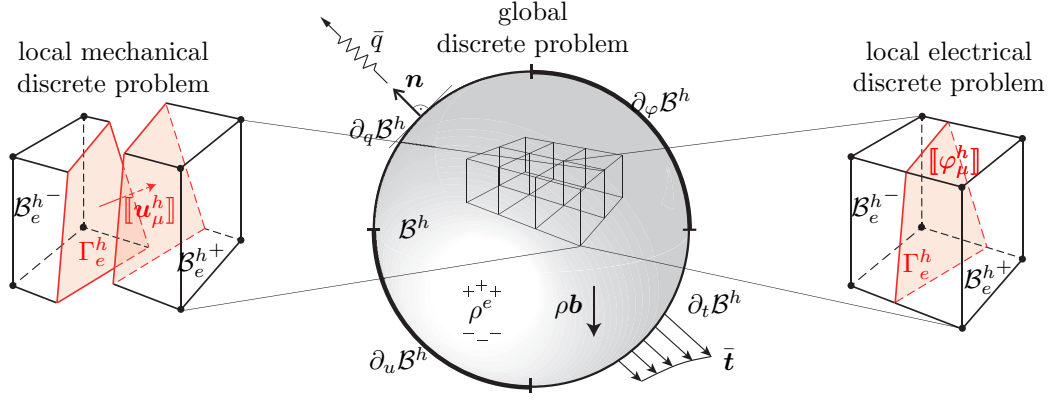


Figure 3.5: Incorporation of strong discontinuities into the finite element setting of piezoelectric ceramics. Each finite element \mathcal{B}_e^h of the global problem is equipped with the possibility of forming a strong discontinuity Γ_e^h in the local mechanical and electrical problems characterized by jumps $\{[[\mathbf{u}_\mu^h]], [[\varphi_\mu^h]]\}$ in the displacement field and the electric potential.

into the individual finite elements to model the fracture process within the electromechanical solid.

To do so, consider a single finite element $\mathcal{B}_e^h \subset \mathcal{B}^h$ in which, based on the criterion to be discussed in Section 3.4.1, failure is detected along a localized zone Γ_e^h , as illustrated in Figure 3.5. The primary result of such detection is the appearance of a strong discontinuity $[[\mathbf{u}_\mu^h]]$ in the displacement field, modeling the mechanical response of the material with regard to failure as outlined in detail in Section 2.2.2.2. Due to such mechanical discontinuity, the distribution of the electric fields is altered in a way such that as a consequence also strong discontinuities $[[\varphi_\mu^h]]$ in the electric potential arise.

Within the discrete setting considered in this section, approximations of electric potential are made in an analogous way as it is done for the global quantities in Section 3.2.2.1. Since valid along the localized zone Γ_e^h , it can be interpolated along that zone as

$$[[\varphi_\mu^h]](s, t) = \mathfrak{J}_\varphi(s, t) \boldsymbol{\xi}_\varphi \quad (3.46)$$

in terms of the associated jump interpolation functions $\mathfrak{J}_\varphi(s, t)$ depending on local coordinates s and t in the artificial plane computed in Section 2.4.4 as an approximation to the possible non-planar actual failure surface Γ_e^h also illustrated in Figure 3.5 and newly introduced degrees of freedom $\boldsymbol{\xi}_\varphi$ containing the electric information of the strong discontinuity within a certain element.

Motivated by the decomposition of the total electric potential and the electric field into local and discontinuous counterparts in (3.4) and (3.5), the discrete forms of the total electric field is given as

$$\mathbf{e}_\mu^h = \mathbf{e}^h(\phi) + \tilde{\mathbf{e}}^h(\boldsymbol{\xi}_\varphi) \quad (3.47)$$

where the global term $\mathbf{e}^h(\phi)$ is given in (3.44) based on the linear operator $\bar{\mathbf{B}}_\varphi$ acting on the nodal electric potential ϕ . A similar dependence is chosen for the discontinuous term $\tilde{\mathbf{e}}^h(\boldsymbol{\xi}_\varphi)$ in terms of the newly introduced operator \mathfrak{C}_φ resulting in the discrete local electric field approximation

$$\mathbf{e}_\mu^h = -\bar{\mathbf{B}}_\varphi \phi - \mathfrak{C}_\varphi \boldsymbol{\xi}_\varphi \quad (3.48)$$

acting on the in (3.46) introduced internal degrees of freedom $\boldsymbol{\xi}_\varphi$. This represents an extension of the analogous introduction of the ‘‘compatibility operator’’ in (2.16) to elec-

tromechanical coupled materials by introducing the electric counterpart \mathfrak{E}_φ in (3.48). It will be outlined in detail in Section 3.3 how this operator can be determined.

One additional equation is introduced in Section 3.2.1.2 with the aim to yield additional information for the determination of the newly introduced jumps in the electric potential in that section. It remains to be shown in this section, how this additional equation (3.6) can be approximated in a discrete setting. Analogous to the purely mechanical case one gets

$$\mathbf{r}_\varphi^e = \int_{\mathcal{B}_e^h} \mathfrak{E}_\varphi^T \mathbf{d} dV - \int_{\Gamma_e^h} \mathfrak{J}_\varphi^T q_\Gamma dA \quad (3.49)$$

in terms of the electric counterpart \mathfrak{E}_φ of the “equilibrium operator” \mathfrak{E}_u enforcing equilibrium along the discontinuity Γ_e^h for the electric components. This operator represents a projection of the normal component of the electric displacement field \mathbf{d} from the integration points onto Γ_e^h . In particular, for an approximation of the variations of the electric potential jumps in (3.46) as polynomials of order q of the local coordinates s and t in the form

$$\delta[\varphi_\mu^h] = \sum_{\substack{i,j=0 \\ i+j \leq q}}^q s^i t^j \delta \xi_\varphi^{(ij)} \quad (3.50)$$

the electric counterpart of the equilibrium operator is given as

$$\mathfrak{E}_\varphi = [\mathfrak{E}_\varphi^{(00)}, \mathfrak{E}_\varphi^{(10)}, \mathfrak{E}_\varphi^{(01)}, \mathfrak{E}_\varphi^{(20)}, \mathfrak{E}_\varphi^{(11)}, \mathfrak{E}_\varphi^{(02)}, \dots] \quad \text{where} \quad \mathfrak{E}_\varphi^{(ij)} = -\frac{1}{h_e} \mathbf{e}^{(ij)} \mathbf{n} \quad (3.51)$$

in terms of the element size h_e and polynomial functions $\mathbf{e}^{(ij)}$ already introduced in Section 2.2.2.2. These are now approximations of the integrand $\mathbf{d} \cdot \mathbf{n}$ in (3.6) of order up to p within a local Cartesian frame $\{x, y, z\}$ of an element \mathcal{B}_e^h .

Remark 3.1. *In the two dimensional setting it is shown in LINDER ET AL. [210], that an approximation of the variation of the electric potential jumps*

$$\delta[\varphi_\mu^h] = \sum_{t=0}^q s^t \delta \xi_\varphi^{(t)} \quad (3.52)$$

in terms of one coordinate $s \in [-l_{\Gamma_e^h}/2, l_{\Gamma_e^h}/2]$ along the one dimensional failure surface results in the expression for the electric counterpart of the equilibrium operator as

$$\mathfrak{E}_\varphi = [\mathfrak{E}_\varphi^{(0)}, \mathfrak{E}_\varphi^{(1)}, \dots, \mathfrak{E}_\varphi^{(q)}] \quad \text{where} \quad \mathfrak{E}_\varphi^{(t)} = -\frac{1}{h_e} \mathbf{e}^{(t)} \mathbf{n} \quad (3.53)$$

in terms of the element size $h_e = A_{\mathcal{B}_e^h}/l_{\Gamma_e^h}$ and polynomial functions $\mathbf{e}^{(t)}(x, y)$. In the plane setting, these are now approximations of the integrand $\mathbf{d} \cdot \mathbf{n}$ in (3.6) of order up to p within a local Cartesian frame $\{x, y\}$ of an element \mathcal{B}_e^h , given in (2.28).

3.3 Finite element design

This section follows the approach suggested in LINDER ET AL. [210] for the computation of the electric counterpart \mathfrak{E}_φ of the compatibility operator in the plane setting put extends it to the fully three dimensional framework. The same strategy of incorporating certain, now electrical, separation modes directly into the strong discontinuity framework is followed as in Section 2.3 for the mechanical separation modes.

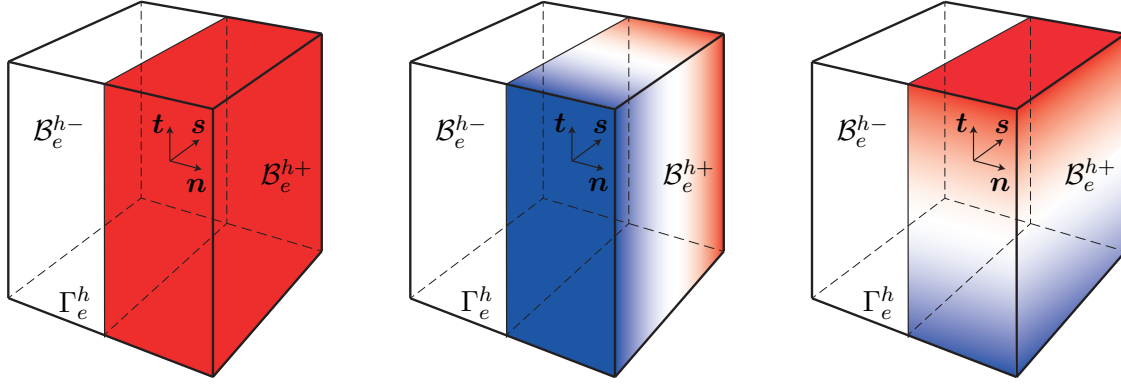


Figure 3.6: Electrical separation modes. The constant electrical separation mode is shown on the left in terms of the constant jump $\xi_\varphi^{(oo)}$ in the electric potential characterized by the difference in color, whereas the linear separation mode along the s -direction is given in the center in terms of $\xi_\varphi^{(1o)}$, and the linear separation model along the t -direction is shown on the right in terms of $\xi_\varphi^{(o1)}$. The two latter are characterized by a linear jump distribution of the electric potential in the tangential directions s and t of the strong discontinuity surface.

3.3.1 Constant separation mode

The electrical counterpart of the displacement field in terms of which the mechanical separation modes are given in (2.31) and (2.38) is the electric potential, a scalar degree of freedom at each node of the finite element under consideration. It is therefore reasonable to propose an electrical separation mode in terms of a distribution of the electric potential with a jump along the strong discontinuity.

Starting with one, which has a constant jump along the strong discontinuity Γ_e^h as it is illustrated on the left of Figure 3.6, the constant electrical separation mode representing the electrical counterpart of (2.31) is given as

$$\phi_A^{(oo)} = \begin{cases} j_\varphi^{(oo)} = \xi_\varphi^{(oo)} & \text{for node } A \in \mathcal{B}_e^{h+} \\ 0 & \text{otherwise} \end{cases} \quad (3.54)$$

based on which the constant electric jump interpolation function can be directly obtained as

$$\llbracket \varphi_\mu^h \rrbracket_{(oo)} = j_\varphi^{(oo)} \Big|_{\Gamma_e^h} = \xi_\varphi^{(oo)}. \quad (3.55)$$

Since based on (3.46) the electric potential jumps can be written also as $\llbracket \varphi_\mu^h \rrbracket_{(oo)} = \mathfrak{J}_\varphi^{(oo)} \xi_\varphi^{(oo)}$, one can directly read off the jump interpolation function for the constant electric separation mode as

$$\mathfrak{J}_\varphi^{(oo)} = 1. \quad (3.56)$$

When incorporating a mechanical separation mode, the mode is chosen in a way such that the solution of the local strain field of both parts of the separated element can be determined exactly. In this section, when making a proper choice of an electric separation mode like the one given in (3.54), the mode has to be chosen in a way such that the local electric field \mathbf{e}_μ which can be computed based on (3.1) as the negative gradient of the electric potential can be determined exactly in both parts of the separated element. Then, based on the decomposition of the local electric field in (3.47) for the particular mode (3.54) yields

$$\mathbf{e}_{\mu, \langle o \rangle}^h = \mathbf{e}_{\langle o \rangle}^h - \mathfrak{C}_{\varphi}^{\langle o \rangle} \xi_\varphi^{(o)} \quad (3.57)$$

i.e. an equation is obtained based on which the operator $\mathfrak{C}_\varphi^{(oo)}$ can be derived. For the constant electric separation mode in (3.54) the local and the global electric fields are given as

$$\mathbf{e}_{\mu, \langle oo \rangle}^h = \mathbf{0} \quad \text{and} \quad \mathbf{e}_{\langle oo \rangle}^h = - \sum_{A \in \mathcal{B}_e^{h+}} \bar{\mathbf{B}}_\varphi^A \xi_\varphi^{(oo)}, \quad (3.58)$$

which yields after insertion into (3.57) the electric counterpart of the constant mechanical compatibility operator $\mathfrak{C}_u^{(oo)}$ in (2.36) as

$$\mathfrak{C}_\varphi^{(oo)} = - \sum_{A \in \mathcal{B}_e^{h+}} \bar{\mathbf{B}}_\varphi^A \quad (3.59)$$

again as a summation of the now electric part of the “B-bar” matrix over the nodes residing on the + side of the element under consideration.

3.3.2 Linear separation modes

In this section the constant electrical separation mode is improved by allowing in addition for a linear separation in the electric potential along the discontinuity Γ_e^h of the element under consideration. To do so, the electric potential is first chosen as illustrated in the center of Figure 3.6 in terms of the linear separation mode along the s -direction given as

$$\phi_A^{(1)} = \begin{cases} j_\varphi^{(10)} = \xi_\varphi^{(10)} \mathbf{s} \cdot \bar{\mathbf{x}}_A & \text{for node } A \in \mathcal{B}_e^{h+} \\ 0 & \text{otherwise} \end{cases} \quad (3.60)$$

where $\mathbf{s} \cdot \bar{\mathbf{x}}_A = s^A$ can be expressed in terms of the local coordinate s of node A in one of the tangential directions of the failure surface. The linear electric jump interpolation function follows from the evaluation of the jump along Γ_e^h based on

$$\llbracket \varphi_\mu^h \rrbracket_{\langle 10 \rangle} = j_\varphi^{(10)} \Big|_{\Gamma_e^h} = s \xi_\varphi^{(10)}. \quad (3.61)$$

Since based on (3.46) the electric potential jumps can be written also as $\llbracket \varphi_\mu^h \rrbracket_{\langle 10 \rangle} = \mathfrak{J}_\varphi^{(10)} \xi_\varphi^{(10)}$, one can directly read off the jump interpolation function for the linear electric separation mode as

$$\mathfrak{J}_\varphi^{(10)} = s. \quad (3.62)$$

The operator $\mathfrak{C}_\varphi^{(10)}$ corresponding to the linear separation mode (3.60) can then be computed again based on the decomposition of the local electric field as

$$\mathbf{e}_{\mu, \langle 10 \rangle}^h = \mathbf{e}_{\langle 10 \rangle}^h - \mathfrak{C}_\varphi^{(10)} \xi_\varphi^{(10)} \quad (3.63)$$

into global and discontinuous contribution. For the linear electric separation mode, the local and the global parts are given as

$$\mathbf{e}_{\mu, \langle 10 \rangle}^h = -\xi_\varphi^{(10)} \mathbf{s} \mathcal{H}_{\Gamma_e^h} \quad \text{and} \quad \mathbf{e}_{\langle 10 \rangle}^h = - \sum_{A \in \mathcal{B}_e^{h+}} s^A \bar{\mathbf{B}}_\varphi^A \xi_\varphi^{(10)}, \quad (3.64)$$

which yields after insertion into (3.63) the electric counterpart of the linear mechanical compatibility operator $\mathfrak{C}_u^{(10)}$ in (2.44) and (2.45) as

$$\mathfrak{C}_\varphi^{(10)} = \mathbf{s} \mathcal{H}_{\Gamma_e^h} - \sum_{A \in \mathcal{B}_e^{h+}} s^A \bar{\mathbf{B}}_\varphi^A \quad (3.65)$$

again as a summation of the electric part of the “B-bar” matrix over the nodes residing on the + side of the element under consideration and an additional contribution written in terms of the Heaviside function $\mathcal{H}_{\Gamma_e^h}$ accounting for the nonzero total electric field of the linear electrical separation mode at hand.

Secondly, when considering the linear electrical separation mode along the t -direction illustrated on the right of Figure 3.6, analogous expressions are obtained as above. Those are summarized as

$$\mathfrak{J}_\varphi^{(01)} = t \quad \text{and} \quad \mathfrak{C}_\varphi^{(01)} = t\mathcal{H}_{\Gamma_e^h} - \sum_{A \in \mathcal{B}_e^{h+}} t^A \bar{\mathbf{B}}_\varphi^A. \quad (3.66)$$

Remarks 3.3. (a) Comparing the results obtained in this Section 3.3 for the three dimensional framework with those in LINDER ET AL. [210] for the plane setting reveals that the only additional contribution is the one given in (3.66) since the planar failure surface is now given in terms of the two unit tangent vectors \mathbf{s} and \mathbf{t} .

(b) It is outlined in detail in LINDER & ARMERO [205] that the choice of one side or the other for the definition of \mathcal{B}_e^{h+} does not affect the elements considered in Chapter 2 for the purely mechanical part. This independence can be extended also for the electrical counterpart by showing the invariance under change of sides \mathcal{B}_e^{h+} and \mathcal{B}_e^{h-} of the enhanced electric operators in (3.59), (3.65), and (3.66). One can immediately deduce the required conclusion from the requirement of the electric patch test to correctly represent constant electric field modes.

Starting with the constant electric operator $\mathfrak{C}_\varphi^{(00)}$ given in (3.59) and assuming a constant distribution of the electric potential ϕ_A^c for all nodes A of the element one gets

$$\mathbf{0} = \sum_{A=1}^{n_{\text{node}}} \bar{\mathbf{B}}_\varphi^A \phi_A^c \rightarrow \mathbf{0} = \sum_{A=1}^{n_{\text{node}}} \bar{\mathbf{B}}_\varphi^A \rightarrow \sum_{A \in \mathcal{B}_e^{h+}} \bar{\mathbf{B}}_\varphi^A = - \sum_{A \in \mathcal{B}_e^{h-}} \bar{\mathbf{B}}_\varphi^A \quad (3.67)$$

showing that the constant electric mode can equally be represented by $-\xi_\varphi^{(00)}$ with the reversal of the local coordinate system $\{\mathbf{n}, \mathbf{s}, \mathbf{t}\}$ leading to a summation over \mathcal{B}_e^{h-} instead of \mathcal{B}_e^{h+} in (3.59).

To deduce a similar conclusion for the linear electrical separation modes in (3.65) and (3.66) one can start with a constant electric field distribution over the whole element in tangential direction to the discontinuity based on a linear distribution of the electric potential $\phi_A^\ell = \boldsymbol{\lambda} \cdot \bar{\mathbf{x}}_\Gamma = \lambda^A$ in terms of the local coordinate λ^A for all nodes A of the element. Thus, the relation

$$-\boldsymbol{\lambda} = -\bar{\mathbf{B}}_\varphi \phi^\ell = - \sum_{A=1}^{n_{\text{node}}} \lambda^A \bar{\mathbf{B}}_\varphi^A \rightarrow \sum_{A \in \mathcal{B}_e^{h+}} \lambda^A \bar{\mathbf{B}}_\varphi^A = \boldsymbol{\lambda} - \sum_{A \in \mathcal{B}_e^{h-}} \lambda^A \bar{\mathbf{B}}_\varphi^A \quad (3.68)$$

holds, which after insertion into (3.65) and (3.66) for $\boldsymbol{\lambda} = \{\mathbf{s}, \mathbf{t}\}$ respectively, results in the equality

$$\boldsymbol{\lambda} \mathcal{H}_{\Gamma_e^h} - \sum_{A \in \mathcal{B}_e^{h+}} \lambda^A \bar{\mathbf{B}}_\varphi^A = -\boldsymbol{\lambda} (1 - \mathcal{H}_{\Gamma_e^h}) + \sum_{A \in \mathcal{B}_e^{h-}} \lambda^A \bar{\mathbf{B}}_\varphi^A \quad (3.69)$$

showing that the linear electric modes can equally be represented by $-\xi_\varphi^{(10)}$ or $-\xi_\varphi^{(01)}$ with the reversal of the local coordinate system $\{\mathbf{n}, \mathbf{s}, \mathbf{t}\}$ leading to a summation over \mathcal{B}_e^{h-}

instead of \mathcal{B}_e^{h+} in (3.65) and (3.66) as well as a reversal in the term containing the Heaviside function $\mathcal{H}_{\Gamma_e^h}$.

(c) It is outlined in detail in LINDER & ARMERO [205] in the plane setting and in ARMERO & KIM [13] in the three dimensional setting, that the linear independence of the columns of the operator \mathfrak{C}_u in (2.47) is required to perform the inversion of the matrix $\mathbf{K}_{\xi\xi}^{e_k}$ needed in (2.72). For the mechanical contribution a linear dependence can be observed between the constant and linear mechanical modes for the special case of a single node being separated by the discontinuity. Investigation of this special situation for the electrical separation modes which yield the columns $\mathfrak{C}_\varphi^{(00)}$, $\mathfrak{C}_\varphi^{(10)}$, and $\mathfrak{C}_\varphi^{(01)}$ in (3.59), (3.65), and (3.66) for that special case where only a single node I is in \mathcal{B}_e^{h+} results in

$$\mathfrak{C}_\varphi^{(0\lambda)} = \lambda \mathcal{H}_{\Gamma_e^h} - \lambda^I \bar{\mathbf{B}}_\varphi^I = \lambda \mathcal{H}_{\Gamma_e^h} + \lambda^I \mathfrak{C}_\varphi^{(00)} \quad (3.70)$$

so that due to the Heaviside function a direct dependence of the two columns is avoided.

3.4 Numerical aspects

Analogous to Section 2.4 of the mechanical boundary value problem, in this section numerical aspects of modeling failure within an electromechanical coupled solid are discussed. In particular, Section 3.4.1 is concerned with the detection of failure, whereas Section 3.4.2 discusses aspects of the failure surface propagation. Finally, Section 3.4.3 outlines the numerical implementation using the compact notation introduced in Section 3.2.1.3.

3.4.1 Strong discontinuity initiation

A criterion is needed to decide when and in which direction the discontinuity is propagating through the electromechanical coupled specimen. In Section 2.4.1 the commonly used criterion based on the loss of ellipticity condition of the underlying problem in the bulk characterized by the singularity of the associated acoustic tensor of the problem at hand is illustrated for the mechanical boundary value problem. In the following the loss of ellipticity condition is employed for finding also a propagation criterion for piezoelectric materials considered in this Chapter 3. Following standard arguments in wave propagation calculations in piezoelectric materials [19, 325] one seeks solutions to (2.3) and (3.2) for the particular constitutive relations outlined in (3.18) of the form

$$\mathbf{u}(\mathbf{x}, t) = \mathbf{a} e^{i(\mathbf{k} \cdot \mathbf{x} - \omega t)} \quad \text{and} \quad \varphi(\mathbf{x}, t) = a e^{i(\mathbf{k} \cdot \mathbf{x} - \omega t)} \quad (3.71)$$

where \mathbf{a} and a are constant quantities characterizing the amplitude of the harmonic wave, $\mathbf{k} = k\mathbf{n}$ with $\mathbf{n} \cdot \mathbf{n} = 1$ is the constant wave vector where k represents the wave number with \mathbf{n} as the propagation direction, and ω is the constant frequency of the wave. Insertion of (3.71) into (2.3) and (3.2) yields

$$\Gamma_{lm} a_m + \Gamma_l a = 0 \quad \text{and} \quad -\Gamma_m a_m + \Gamma a = 0, \quad (3.72)$$

where the newly introduced quantities are given as

$$\Gamma_{lm} = \mathbb{C}_{klmn} k_n k_k, \quad \Gamma_l = \mathbb{h}_{mkl} k_m k_k, \quad \text{and} \quad \Gamma = \mathbb{b}_{kl} k_k k_l \quad (3.73)$$

in terms of the elasticity moduli \mathbb{C} , the piezoelectric moduli \mathbb{h} , and the dielectric moduli \mathbb{b} given in (3.17) in closed form for an isotropic linear piezoelectric material response. The second equation in (3.73) allows for the computation of a which can then be inserted into the first equation in (3.73) to yield

$$A_{lm}a_m = 0, \quad \text{where} \quad A_{lm} = \Gamma_{lm} + \frac{\Gamma_l \Gamma_m}{\Gamma} \quad (3.74)$$

is called the electro-acoustic tensor. Under the assumptions that the elasticity moduli and the dielectric moduli are positive definite, i.e. $U_{kl}\mathbb{C}_{klmn}U_{mn} > 0$ and $u_k\mathbb{b}_{kl}u_l > 0$ for all U_{mn} and u_k with at least one non-zero element, it follows that based on (3.73) $a_l\Gamma_{lm}a_m > 0$ and $\Gamma > 0$ so that from (3.74) one gets

$$a_l A_{lm} a_m = a_l \Gamma_{lm} a_m + \frac{1}{\Gamma} (a_l \Gamma_l)^2 > 0 \quad (3.75)$$

for all non-zero vectors \mathbf{a} . This relation is the condition for ellipticity of the underlying equations of equilibrium in (2.3) and (3.2), which can also be viewed as a condition for the material stability since when (3.75) is satisfied it can be viewed as a stable response of an infinite medium in a uniform state of stress and electric displacement distribution subjected to perturbations in the form (3.71). The obtained result can also be viewed as an extension of the discontinuous material bifurcation outlined in OLIVER & HUESPE [266] within the strong discontinuity approach to electromechanical coupled materials.

A simplification of the fracture criterion (3.75) proposed in LINDER ET AL. [210] for piezoelectric materials is to separately enforce conditions with regard to the mechanical and the electrical part as

$$a_l \Gamma_{lm} a_m > 0 \quad \text{and} \quad \Gamma > 0 \quad (3.76)$$

where the second part is always satisfied for materials with a dielectric moduli of the form (3.17)₃ when $\epsilon > 0$. Therefore, the fracture criterion for piezoelectric materials boils down to the fracture criterion for purely mechanical materials by checking the first condition in (3.76).

3.4.2 Strong discontinuity propagation

After detecting the onset of failure based on (3.76), the strong discontinuity must be propagated through the finite element mesh. For the two dimensional simulations shown in Section 3.6.3 and 3.6.4, a commonly used local propagation concept is used, whereas in Section 3.6.5 an extension to three dimensional simulations of the global tracking algorithm and its combination with the marching cubes algorithm as illustrated in Sections 2.4.2 and 2.4.3 is used.

3.4.3 Numerical implementation

Using the compact notation introduced in (3.7), the global residual equations stated in (2.13) and (3.45) can be compactly written as

$$\mathbf{R} = \mathbf{f}^{\text{ext}} - \sum_{e=1}^{n_{\text{elem}}} \int_{\mathcal{B}_e^h} \bar{\mathbf{B}}^T \mathfrak{S} dV \quad \text{with} \quad \mathbf{f}^{\text{ext}} = \int_{\mathcal{B}^h} \mathbf{N}^T \mathbf{b} dV + \int_{\partial_t \mathcal{B}^h} \mathbf{N}^T \bar{\mathbf{t}} dA \quad (3.77)$$

whereas the local residual equation stated in (2.17) and (3.49) can be written in compact form as

$$\mathbf{r}^e = - \int_{\mathcal{B}_e^h} \boldsymbol{\mathfrak{E}}^T \boldsymbol{\mathfrak{S}} dV - \int_{\Gamma_e^h} \tilde{\mathfrak{J}}^T \mathbf{t}_\Gamma dA \quad (3.78)$$

in terms of the additionally introduced combined arrays

$$\begin{aligned} \mathbf{R} &= \begin{bmatrix} \mathbf{R}_u \\ \mathbf{R}_\varphi \end{bmatrix}, \quad \mathbf{r}^e = \begin{bmatrix} \mathbf{r}_u^e \\ \mathbf{r}_\varphi^e \end{bmatrix}, \quad \mathbf{N} = \begin{bmatrix} \mathbf{N}_u & \mathbf{0} \\ \mathbf{0} & \mathbf{N}_\varphi \end{bmatrix}, \quad \bar{\mathbf{B}} = \begin{bmatrix} \bar{\mathbf{B}}_u & \mathbf{0} \\ \mathbf{0} & \bar{\mathbf{B}}_\varphi \end{bmatrix}, \\ \mathbf{b} &= \begin{bmatrix} \rho \mathbf{b} \\ \rho^e \end{bmatrix}, \quad \boldsymbol{\mathfrak{C}} = \begin{bmatrix} \boldsymbol{\mathfrak{C}}_u & \mathbf{0} \\ \mathbf{0} & \boldsymbol{\mathfrak{C}}_\varphi \end{bmatrix}, \quad \boldsymbol{\mathfrak{E}} = \begin{bmatrix} \boldsymbol{\mathfrak{E}}_u & \mathbf{0} \\ \mathbf{0} & \boldsymbol{\mathfrak{E}}_\varphi \end{bmatrix}, \quad \tilde{\mathfrak{J}} = \begin{bmatrix} \tilde{\mathfrak{J}}_u & \mathbf{0} \\ \mathbf{0} & \tilde{\mathfrak{J}}_\varphi \end{bmatrix}. \end{aligned} \quad (3.79)$$

The form of the residual equations as they appear in (3.77) and (3.78) is furthermore beneficiary when it comes to their linearization as

$$\begin{aligned} \mathbf{A}_{e=1}^{n_{\text{elem}}} \left[\mathbf{K}_{\mathfrak{d}\mathfrak{d}}^{e^k} \Delta \mathfrak{d}_e^{k+1} + \mathbf{K}_{\mathfrak{d}\boldsymbol{\xi}}^{e^k} \Delta \boldsymbol{\xi}_e^{k+1} \right] &= \mathbf{A}_{e=1}^{n_{\text{elem}}} \mathbf{R}^{e^k} \\ \mathbf{K}_{\boldsymbol{\xi}\mathfrak{d}}^{e^k} \Delta \mathfrak{d}_e^{k+1} + \mathbf{K}_{\boldsymbol{\xi}\boldsymbol{\xi}}^{e^k} \Delta \boldsymbol{\xi}_e^{k+1} &= \mathbf{r}^{e^k} \end{aligned} \quad (3.80)$$

where use of the compact notation $\mathfrak{d} = [\mathbf{d} \ \boldsymbol{\phi}]^T$ and $\boldsymbol{\xi} = [\boldsymbol{\xi}_u \ \boldsymbol{\xi}_\varphi]^T$ is made. Note further that the second equation is valid for finite elements with a strong discontinuity Γ_e^h only. The global and local quantities are then updated based on

$$\mathfrak{d}^{k+1} = \mathfrak{d}^k + \Delta \mathfrak{d}^{k+1} \quad \text{and} \quad \boldsymbol{\xi}^{k+1} = \boldsymbol{\xi}^k + \Delta \boldsymbol{\xi}^{k+1} \quad (3.81)$$

in terms of the iteration index k . The compact notation used here allows for the following individual contributions in (3.80) as

$$\begin{aligned} \mathbf{K}_{\mathfrak{d}\mathfrak{d}}^e &= \int_{\mathcal{B}_e^h} \bar{\mathbf{B}}^T \mathbf{C}_\mathcal{B} \bar{\mathbf{B}} dV, & \mathbf{K}_{\mathfrak{d}\boldsymbol{\xi}}^e &= \int_{\mathcal{B}_e^h} \bar{\mathbf{B}}^T \mathbf{C}_\mathcal{B} \boldsymbol{\mathfrak{C}} dV, \\ \mathbf{K}_{\boldsymbol{\xi}\mathfrak{d}}^e &= \int_{\mathcal{B}_e^h} \boldsymbol{\mathfrak{E}}^T \mathbf{C}_\mathcal{B} \bar{\mathbf{B}} dV, & \text{and} & \\ \mathbf{K}_{\boldsymbol{\xi}\boldsymbol{\xi}}^e &= \int_{\mathcal{B}_e^h} \boldsymbol{\mathfrak{E}}^T \mathbf{C}_\mathcal{B} \boldsymbol{\mathfrak{E}} dV + \int_{\Gamma_e^h} \tilde{\mathfrak{J}}^T \mathbf{C}_\Gamma \tilde{\mathfrak{J}} dA \end{aligned} \quad (3.82)$$

for the stiffness matrices, respectively. The tangent $\mathbf{C}_\mathcal{B}$ in the bulk \mathcal{B}_e^h as well as its counterpart along the strong discontinuity \mathbf{C}_Γ in (3.82) are given in (3.19) and (3.30), respectively.

One major advantage of the considered formulation is the computational efficiency which comes with the fact that the internal degrees of freedom for the description of the strong discontinuity can be statically condensed out at the element level. From the second equation in (3.80) the increments of the enhanced parameters can be computed as

$$\Delta \boldsymbol{\xi}_e^{k+1} = (\mathbf{K}_{\boldsymbol{\xi}\boldsymbol{\xi}}^{e^k})^{-1} [\mathbf{r}^{e^k} - \mathbf{K}_{\boldsymbol{\xi}\mathfrak{d}}^{e^k} \Delta \mathfrak{d}_e^{k+1}] \quad (3.83)$$

locally for the elements with a strong discontinuity. Insertion of (3.83) into the first equation in (3.80) yields the statically condensed system

$$\mathbf{K}_*^k \Delta \mathfrak{d}_e^{k+1} = \mathbf{R}_*^k \quad (3.84)$$

in terms of the effective residual $\mathbf{R}_*^k = \mathbf{A}_{e=1}^{n_{\text{elem}}} \mathbf{R}_*^{e^k}$ and the effective stiffness matrix $\mathbf{K}_*^k = \mathbf{A}_{e=1}^{n_{\text{elem}}} \mathbf{K}_*^{e^k}$ given as

$$\mathbf{R}_*^{e^k} = \mathbf{R}^{e^k} - \mathbf{K}_{\partial\xi}^{e^k} (\mathbf{K}_{\xi\xi}^{e^k})^{-1} \mathbf{r}^{e^k} \quad \text{and} \quad \mathbf{K}_*^{e^k} = \mathbf{K}_{\partial\partial}^{e^k} - \mathbf{K}_{\partial\xi}^{e^k} (\mathbf{K}_{\xi\xi}^{e^k})^{-1} \mathbf{K}_{\xi\partial}^{e^k} \quad (3.85)$$

in terms of the iteration index k . The compact notation turns out to be convenient since when employed, the numerical implementation of the electromechanical coupled problem resembles the same structure as for the purely mechanical problem, whose numerical implementation is given in Section 2.4.5.

3.5 Effect of electric displacement saturation

One key question to be answered by a suitable framework of linear piezoelectricity is the one on the dependency of the applied electric field on the crack initiation. Whereas the energy release rate concept results in an even dependency, i.e. regardless of the orientation of the applied electric field with respect to the polarization direction the initiation of cracks perpendicular to the poling direction is always inhibited, experimental results outline an odd dependency. The experimentally observed odd dependency in TOBIN & PAK [352] and PARK & SUN [280] shows that positive electric fields (i.e. applied with an orientation equivalent to the poling direction) enhance crack growth whereas negative electric fields (i.e. applied opposite to the poling direction) impede crack growth. The opposite linear dependency is experimentally observed in WANG & SINGH [375] or FU & ZHANG [113], which shows the complexity of crack initiation prediction in ferroelectric ceramics. One approach to better predict experimental results is the modification of the energy release rate by neglecting the direct influence of the electric quantities as proposed in PARK & SUN [279], resulting in the *mechanical energy release rate* or *strain energy release rate* as fracture criterion capable of predicting the experimental results in PARK & SUN [280]. This suggestion though caused criticism by its lack of physical foundation [114, 116, 229]. In the approach proposed in GAO ET AL. [116] the discrepancy between experimental and theoretical results is resolved by the account of a particular electric non-linearity, resulting in the *electric displacement saturation model*. Motivated by physical arguments arising for ferroelectric ceramics, which show a reduction of the ionic movement in such materials when high electric fields are applied [170] they propose the existence of a strip in front of the crack tip along which the electric displacement in poling direction is limited to a saturation parameter. Similar to the approach chosen in DUGDALE [78] for the incorporation of plasticity into material models of metals, the resulting saturation zone in GAO ET AL. [116] is incorporated analytically into a simplified piezoelectric material model depending on three characteristic material parameters. Subsequently, they showed that a new *local energy release rate* arises when computing it by a path integral within the electric saturation zone. In GAO & BARNETT [115] the invariance of the saturation model with respect to the saturation parameter of the electric displacement is outlined. The resulting local energy release rate obeys the same characteristics as the mechanical energy release rate proposed in PARK & SUN [279] and is therefore capable of reproducing the odd dependency of the crack initiation on the applied electric field observed in experiments. In FULTON & GAO [114] the saturation model is combined with an account of permeable crack boundary conditions and extended to account for anisotropy in WANG [377]. MCMEEKING [229] pointed out that the saturation in the electric displacement

has led to a physically wrong analogy between the mechanical stresses and the electric displacement field. Despite their mathematical analogy through their divergence conservation, the physical analogy should connect the mechanical stresses, which are saturated in the Dugdale model, to the electric field. This led to the development of the *dielectric breakdown model* [397, 398] where rather than limiting the electric displacement, the electric field is limited along a strip in front of the crack tip. The two models are shown to give the same predictions on the nature of the dependence of crack initiation on the applied electric field in WANG & ZHANG [374]. Most of the studies accounting for such electric non-linearities are done analytically. A simplified incorporation within the finite element methodology is performed in SZE & PAN [346] or LIU ET AL. [214] for stationary cracks. The method developed in FAN ET AL. [94] is capable of accounting for electric displacement saturation as well as dielectric breakdown for problems where no analytical solutions exist.

The scope of this section is to propose a simplified account for the electric displacement saturation and outline its effect on the hysteretic behavior of ferroelectric ceramics and the initiation and propagation of cracks in piezoelectric ceramics. It is shown in Section 3.5.1 how the shape of the characteristic dielectric hystereses curves of ferroelectric ceramics are modified based on the electric saturation model originally proposed in GAO ET AL. [116]. Rather than following their approach by superposing a complex function onto the singular solution of a crack within linear piezoelectricity, which is possible only for problems where analytical results do exist, a different strategy is proposed in this work. The material parameters within an invariant and fully anisotropic setting of linear piezoelectricity which are effected by the electric displacement saturation are identified and varied to determine their influence on the analytical obtained values for the total and the mechanical energy release rates for the problem of a crack in an infinite medium in Section 3.5.2. An exponential saturation type response of the identified parts in the electric enthalpy due to the electric displacement saturation is proposed to outline the effect of this electric non-linearity on these problems. The introduction of an additional parameter in the form of a saturation exponent outlines the difference to the original proposed treatment of electric displacement saturation in GAO ET AL. [116]. The advantage of this approach lies in the straightforward extension to problems for which no analytical solutions are valid.

3.5.1 The exponential electric displacement saturation model

It should be noted that the relation between the applied electric field and the obtained electric displacement is driven by the sensitivity b_{ik} , which based on (3.26) yields a constant slope in terms of the dielectric material parameters γ_1, γ_2 or alternatively based on (3.28) a constant slope in terms of the dielectric material parameters ϵ_{11} and ϵ_{33} when no electric non-linearities are considered. In the presence of material inhomogeneities like inclusions, voids, or cracks this relationship may no longer be valid and must be replaced by a framework which takes into account electric non-linearities [137, 221, 392]. A possible source of non-linearity might arise in ferroelectric crystals [170] whose electric polarization is driven by ionic movement which reduces in the presence of high electric fields [116]. This saturation of the electric displacement is accounted for in the *electric displacement saturation model* developed in GAO ET AL. [116]. In their proposed multiscale view of piezoelectric fracture they consider the piezoelectric material as mechanically brittle and electrically ductile with the electric yielding zone confined to a strip ahead of the

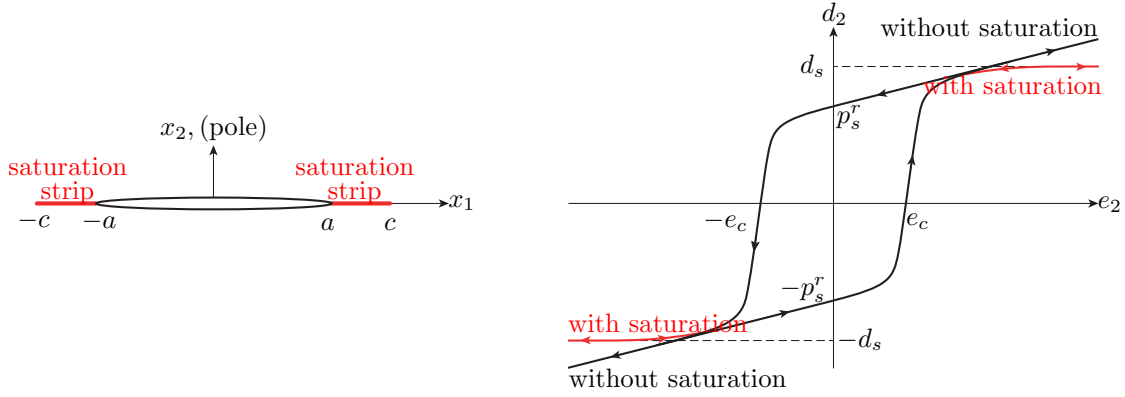


Figure 3.7: Illustration of the electric displacement saturation model confined to a strip ahead of the crack tip with saturated electric displacement of $d = d_s$ (left). Illustration of the dielectric hysteresis curve in ferroelectric ceramics and the expected change due to electric displacement saturation (right).

piezoelectric crack tip oriented perpendicular to the poling direction as outlined in Figure 3.7. In GAO ET AL. [116] the electric yielding is accounted for based on a generalization of the approach developed by DUGDALE [78] for the modeling of the plastic deformation in a thin metal sheet. A proposed distinction of two energy release rates in GAO ET AL. [116], the *global* energy release rate and the *local* energy release rate, allows for the identification of the latter as a possible fracture criterion which is in agreement with observed experimental results showing an odd dependence of the crack growth on the sign of the applied electric field. As mentioned in LIU ET AL. [214], like the Dugdale model [78], the developed analytical solution in GAO ET AL. [116] is obtained by a superposition of two singular solutions limiting the applicability of the model to cases where such analytical solutions do exist.

In this section, the effect of electric displacement saturation is investigated numerically in the subsequent Section 3.6 for problems where no analytical solutions exist. Therefore, rather than linearly superposing a complex function to account for the electric displacement saturation onto the singular solution of a piezoelectric crack as done in GAO ET AL. [116] for a simplified electroelasticity model in terms of three independent material constants, a different strategy is followed in this section. The effect of the electric displacement saturation on the dielectric hysteresis curve arising in ferroelectric ceramics is outlined in Figure 3.7. The limitation of the ionic movement on the polarization further influences the electrostrictive strain resulting also in a modified butterfly hysteresis [137]. The limitation of the electric displacement perpendicular to the poling direction ahead of the crack tip to $d = d_s$ results in a vanishing slope and therefore vanishing dielectric material parameters γ_1 , γ_2 or equivalently vanishing ϵ_{11} , ϵ_{33} .

The term responsible for the constant slope in the dielectric hysteresis illustrated in Figure 3.7 is the purely electrical part H_{B_2} given in (3.21). Based on a saturation type modification of this term proposed in this section as

$$H_{B_2}^{\text{sat}} = H_{B_2} \cdot \exp\left(-\frac{|I_6|}{\xi}\right) \quad (3.86)$$

the electric displacement is saturated towards a limiting value depending on the choice of the saturation exponent ξ in the direction normal to the polarization direction \mathbf{a} assured

through the dependency of the electric displacement saturation model of (3.86) on the invariant $I_6 = \mathbf{e} \cdot \mathbf{a}$. This agrees with the initially proposed saturation strip model in GAO ET AL. [116], where the strip is aligned ahead of a crack tip normal to the polarization direction. For a saturation exponent of $\xi \rightarrow \infty$ the proposed modification of H_{B_2} in (3.86) recovers the non-saturated case. It is noted that no additional dissipative effect is introduced in the approach considered in this work, which is contrary to the approach considered in SZE & PAN [346] in which electric displacement saturation is modeled similar to the treatment of plasticity with an additive decomposition of the electric field into “elastic” and “plastic” parts.

3.5.2 Effect of electric displacement saturation on the complex variable solution of a crack in an infinite medium

Even though in this section, the electric non-linearity in the form of electric displacement saturation is initially investigated for the problem of a crack in an infinite anisotropic piezoelectric material loaded so that linear piezoelectricity applies, in the subsequent Section 3.6 the effect of electric displacement saturation is investigated numerically for more realistic problems. Given the treatment proposed in Section 3.5.1, it is straightforward to apply standard complex variable solutions available in the literature [21, 339, 342] to investigate the influence of electric displacement saturation on the fracture behavior in ferroelectric ceramics, as it is done in this section.

Following SUO ET AL. [342], a short summary of the complex variable solution of a crack in an infinite anisotropic poled ferroelectric ceramic material is given in Section 3.5.2.1 and then applied in Sections 3.5.2.2 and 3.5.2.3 to a Mode III and a Mode I problem, respectively, where the emphasis is directed towards the investigation of the influence of electric displacement saturation.

3.5.2.1 Complex variable solution of a crack in poled ferroelectric ceramics for the framework of linear piezoelectricity. Rewriting (3.18) in terms of the primary unknowns in the form of the displacement field u_k and the electric potential φ , and insertion of (2.1) into (2.3) and (3.1) into (3.2) for the case of $\rho^e = 0$, one obtains

$$(\mathbb{C}_{ijkl}u_k + \mathbb{h}_{lji}\varphi)_{,li} = 0 \quad \text{and} \quad (\mathbb{h}_{ikl}u_k - \mathbb{b}_{il}\varphi)_{,li} = 0. \quad (3.87)$$

Following SUO ET AL. [342] and focusing on two-dimensional problems in the $\{x, y\}$ -plane, the general solution $\{u_k, \varphi\}$ is obtained by considering an arbitrary function comprised of a linear combination of x and y as $\{u_k, \varphi\} = \mathbf{a}f(\zeta_1x + \zeta_2y)$, where $\mathbf{a} = \{a_k, a_4\}$, ζ_α for $\alpha = 1, 2$ are chosen without loss of generality as $\zeta_1 = 1$, $\zeta_2 = p$, and f is obtained from the given boundary conditions. The column \mathbf{a} and the number p are determined from the complex eigenvalue problem

$$(\mathbb{C}_{\alpha jk\beta}a_k + \mathbb{h}_{\beta j\alpha}a_4)\zeta_\alpha\zeta_\beta = 0 \quad \text{and} \quad (\mathbb{h}_{\alpha k\beta}a_k - \mathbb{b}_{\alpha\beta}a_4)\zeta_\alpha\zeta_\beta = 0 \quad (3.88)$$

with $\alpha, \beta = 1, 2$. One can show [342] that a non-trivial solution of \mathbf{a} exists when p is a root of the determinant polynomial and further that the eight roots form four conjugate pairs. With p_s for $s = 1, \dots, 4$ being the roots with positive imaginary parts, the corresponding columns \mathbf{a}_s , and $z(s) = x + p_s y$, the most general solution for $\{u_k, \varphi\}$ and subsequently

Elastic constants (10^4 N/mm ²)				Piezoelectric constants (C/m ²)			Dielectric constants (10^{-3} mC/(kV m))		
c_{11}	c_{12}	c_{13}	c_{33}	c_{44}	e_{31}	e_{33}	e_{15}	ϵ_{11}	ϵ_{33}
13.9	7.78	7.43	11.3	2.56	-6.98	13.84	13.44	6.0	5.47

Table 3.1: Material parameters used for the modeling of lead zirconate titanate PZT-4 ferroelectric ceramics with a poling induced anisotropy where x_3 is the poling direction and the $x_1 - x_2$ plane is the isotropic plane.

for the stresses and electric displacements $\{\sigma_{\alpha j}, d_\alpha\}$ with $\alpha = 1, 2$ is finally obtained as

$$\{u_k, \varphi\} = 2 \operatorname{Re} \sum_{s=1}^4 \mathbf{a}_s f_s(z_s) \quad \text{and} \quad \{\sigma_{\alpha j}, d_\alpha\} = 2 (-1)^{\alpha-1} \operatorname{Re} \sum_{s=1}^4 \mathbf{b}_s p_s^{\alpha-1} f'_s(z_s), \quad (3.89)$$

where for a pair $\{p, \mathbf{a}\}$ the associated $\mathbf{b} = \{b_j, b_4\}$ is given as

$$b_j = (\mathbb{C}_{2jk\beta} a_k + \mathbb{h}_{\beta j 2} a_4) \zeta_\beta \quad \text{and} \quad b_4 = (\mathbb{h}_{2k\beta} a_k - \mathbb{b}_{2\beta} a_4) \zeta_\beta. \quad (3.90)$$

Forming the two 4×4 matrices $\mathfrak{A} = [\mathbf{a}_1, \mathbf{a}_2, \mathbf{a}_3, \mathbf{a}_4]$ and $\mathfrak{B} = [\mathbf{b}_1, \mathbf{b}_2, \mathbf{b}_3, \mathbf{b}_4]$ and enforcing the normalization property [21]

$$\sum_{s=1}^4 \mathfrak{A}_{s\alpha} \mathfrak{B}_{s\beta} + \mathfrak{A}_{s\beta} \mathfrak{B}_{s\alpha} = \delta_{\alpha\beta} \quad (3.91)$$

the Irwin matrix [160] follows as $\mathcal{H} = 2 \operatorname{Re} \mathcal{Y}$ with $\mathcal{Y} = -i \mathfrak{A} \mathfrak{B}^{-1}$ where $i = \sqrt{-1}$. The *total energy release rate* is then obtained as $\mathcal{G} = \frac{1}{4} \mathbf{k}^T \mathcal{H} \mathbf{k}$ in terms of $\mathbf{k} = [K_{II}, K_I, K_{III}, K_{IV}]^T$ for the stress intensity factors of the three mechanical as well as the electrical mode. The *strain energy release rate* or *mechanical energy release rate*, suggested in PARK & SUN [279] as a suitable fracture criterion in poled ferroelectric ceramics, follows as $\mathcal{G}_{\text{mech}} = \frac{1}{4} \mathbf{k}_{\text{mech}}^T \mathcal{H} \mathbf{k}$ where $\mathbf{k}_{\text{mech}} = [K_{II}, K_I, K_{III}]^T$.

Next, those two release rates are computed analytically for a *Mode III* and a *Mode I* crack of length 2 units within the framework of linear piezoelectricity to evaluate the effect of the electric non-linearity in the form of electric displacement saturation. The poling direction is chosen as the x_3 -axis so that the matrix representation of (3.27) and (3.28) can be applied for the anisotropic piezoelectric material model. The chosen material parameters consistent with this problem are summarized in Table 3.1 modeling a PZT-4 ferroelectric ceramic material.

3.5.2.2 Effect of electric displacement saturation on the analytical results for the anti-plane case of a Mode III crack. To model the anti-plane case of a Mode III crack within the framework of linear piezoelectricity and x_3 as the poling direction, the computational $\{x, y\}$ -domain for the evaluation of the energy release rates in Section 3.5.2.1 is transferred by $x \rightarrow x_1$ and $y \rightarrow x_2$. In this case the crack front is parallel to the poling direction so that the in-plane deformation in the x_1, x_2 -plane is decoupled from the anti-plane deformation in x_3 direction and the electric potential φ . Focusing on the latter, closed form solutions for an applied far field loading in terms of σ_{23}^∞ and d_2^∞ are derived in PAK [275, 276], SUO ET AL. [342], or PARK & SUN [279] yielding the Irwin

matrix

$$\mathcal{H}^{III} = \frac{2}{c_{44}\epsilon_{11} + e_{15}^2} \begin{bmatrix} \epsilon_{11} & e_{15} \\ e_{15} & -c_{44} \end{bmatrix} \quad (3.92)$$

as well as the total energy release rate \mathcal{G}^{III} and the strain energy release rate $\mathcal{G}_{\text{mech}}^{III}$ of the Mode III problem

$$\mathcal{G}^{III} = \frac{[\epsilon_{11}K_{III}^2 + 2e_{15}K_{III}K_{IV} - c_{44}K_{IV}^2]}{2(c_{44}\epsilon_{11} + e_{15}^2)} \quad \text{and} \quad \mathcal{G}_{\text{mech}}^{III} = \frac{[\epsilon_{11}K_{III}^2 + e_{15}K_{III}K_{IV}]}{2(c_{44}\epsilon_{11} + e_{15}^2)}. \quad (3.93)$$

Insertion of $K_{III} = \sqrt{a\pi} \sigma_{23}^\infty$ and $K_{IV} = \sqrt{a\pi} d_2^\infty$ results for the half crack length of $a = 1$ units in the expressions

$$\mathcal{G}^{III} = \frac{\pi[\epsilon_{11}\sigma_{23}^{\infty 2} + 2e_{15}\sigma_{23}^\infty d_2^\infty - c_{44}d_2^{\infty 2}]}{2(c_{44}\epsilon_{11} + e_{15}^2)} \quad \text{and} \quad \mathcal{G}_{\text{mech}}^{III} = \frac{\pi[\epsilon_{11}\sigma_{23}^{\infty 2} + e_{15}\sigma_{23}^\infty d_2^\infty]}{2(c_{44}\epsilon_{11} + e_{15}^2)}. \quad (3.94)$$

If the boundary conditions are changed from a far field electric displacement d_2^∞ to a far field electric field e_2^∞ , the relation [278] $d_2^\infty = (e_{15}/c_{44})\sigma_{23}^\infty + (\epsilon_{11} + e_{15}^2/c_{44})e_2^\infty$ can be inserted into (3.94) to obtain

$$\mathcal{G}^{III} = \frac{\pi}{2} \left[\frac{1}{c_{44}}\sigma_{23}^{\infty 2} - \frac{c_{44}\epsilon_{11} + e_{15}^2}{c_{44}}e_2^{\infty 2} \right] \quad \text{and} \quad \mathcal{G}_{\text{mech}}^{III} = \frac{\pi}{2} \left[\frac{1}{c_{44}}\sigma_{23}^{\infty 2} + \frac{e_{15}}{c_{44}}\sigma_{23}^\infty e_2^\infty \right]. \quad (3.95)$$

With the closed form solutions of the energy release rates in (3.94) and (3.95) it is now straightforward to investigate the influence of the electric displacement saturation by the proper modification of the dielectric material parameters ϵ_{11} and ϵ_{33} . In Figures 3.8 and 3.9 this is done by a comparison of the unsaturated piezoelectric material with a fully electric displacement saturated piezoelectric material for which in particular $\epsilon_{11} = \epsilon_{33} = 0$ is used. The illustration of (3.94) is carried out in Figure 3.8 where based on a varying far field loading in terms of σ_{23}^∞ and d_2^∞ the total and strain energy release rates are plotted for the case without saturation (solid lines) and with full electric displacement saturation (dashed lines). Analogous, the illustration of (3.95) is shown in Figure 3.9.

A closer look at the top row of Figure 3.8 shows that the quadratic dependency of both energy release rates on the far field stresses σ_{23}^∞ when no electric displacement saturation is accounted for is replaced by a linear dependency when full electric displacement saturation is assumed. It is interesting that the case with full electric displacement saturation result in tangents to the case without electric displacement saturation for the total energy release rate in the top left illustration of Figure 3.8 with intersection points at $\sigma_{23}^\infty = c_{44}/e_{15} d_2^\infty$ and common slopes $\pi/e_{15} d_2^\infty$ at these points. The results with and without electric displacement saturation for the strain energy release rate illustrated in the top right illustration of Figure 3.8 coincide at applied far field stresses $\sigma_{23}^\infty = 0$ and $\sigma_{23}^\infty = c_{44}/e_{15} d_2^\infty$. Furthermore, all the results shown in this illustration have a zero strain energy release rate at a zero far field stress loading. When varying the far field electric displacement d_2^∞ for the three different far field stresses σ_{23}^∞ the total energy release rates in the bottom left illustration of Figure 3.8 shows that the two quadratic curves with and without electric displacement saturation again meet at one particular point where $d_2^\infty = e_{15}/c_{44} \sigma_{23}^\infty$ with an exactly horizontal tangent. The results of the strain energy release rate plotted in the

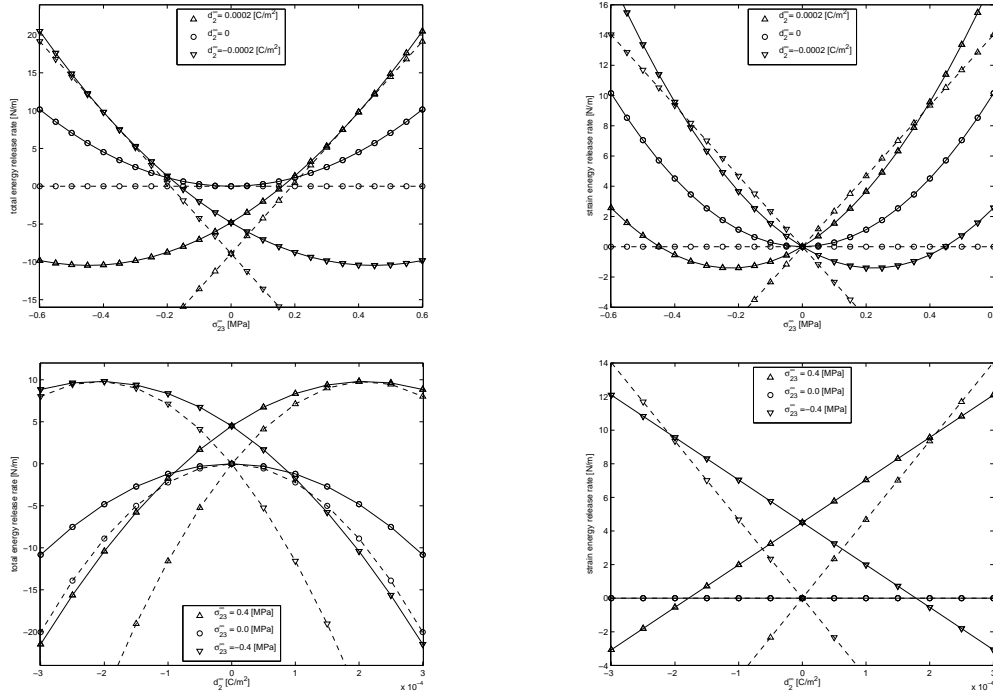


Figure 3.8: Complex variable solution of a center crack of 2 units loaded in Mode III within the framework of linear piezoelectricity. Illustration of the total energy release rate (left column) and the strain energy release rate (right column) versus σ_{23}^∞ under constant electric displacements $d_2^\infty = 0$ and $d_2^\infty = \pm 2 \cdot 10^{-4} C/m^2$ (top row) and versus d_2^∞ under constant mechanical loadings $\sigma_{23}^\infty = 0$ and $\sigma_{23}^\infty = \pm 0.4 MPa$ (bottom row) without (solid lines) and with full (dashed lines) electric displacement saturation.

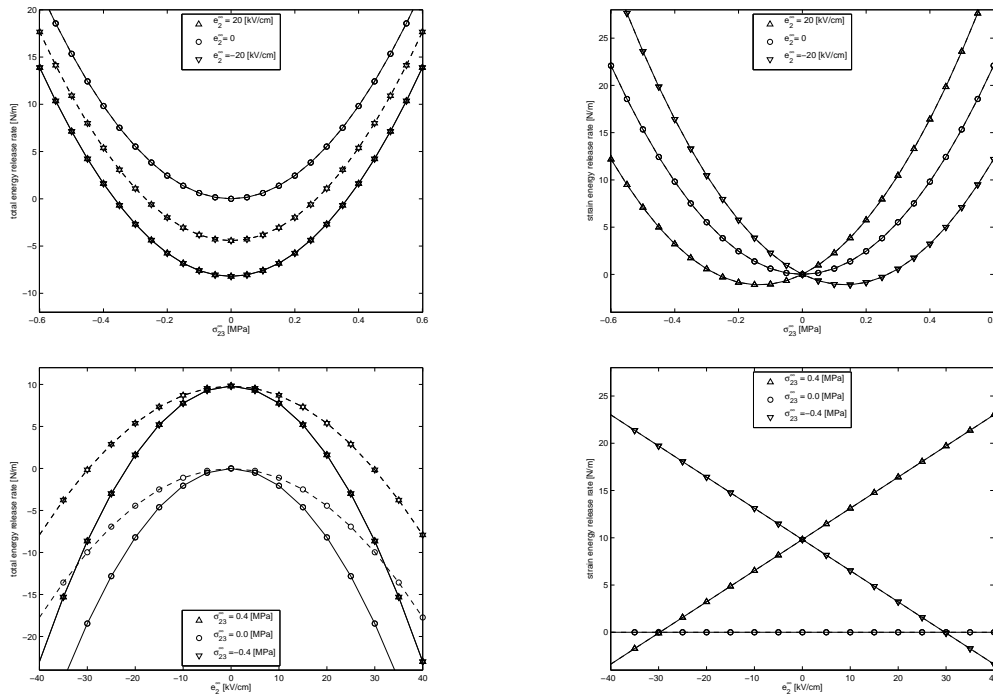


Figure 3.9: Complex variable solution of a center crack of 2 units loaded in Mode III within the framework of linear piezoelectricity. Illustration of the total energy release rate (left column) and the strain energy release rate (right column) versus σ_{23}^∞ under constant electric fields $e_2^\infty = 0$ and $e_2^\infty = \pm 20 kV/cm$ (top row) and versus e_2^∞ under constant mechanical loadings $\sigma_{23}^\infty = 0$ and $\sigma_{23}^\infty = \pm 0.4 MPa$ (bottom row) without (solid lines) and with full (dashed lines) electric displacement saturation.

bottom right illustration of Figure 3.8 also coincide at $d_2^\infty = e_{15}/c_{44} \sigma_{33}^\infty$ for the case with and without electric displacement saturation.

The illustration of (3.95)₂ reveals a disappearance of the influence by the dielectric material parameters on the strain energy release rate by changing the far field electric displacement d_2^∞ to a far field electric field e_2^∞ . This is also apparent in the illustrations of the strain energy release rate in the right column of Figure 3.9 where no effect of the account for electric displacement saturation can be observed. The total energy release rate though is effected by the account of electric displacement saturation as seen in the left column of Figure 3.9. The difference arises for a non-zero applied electric field $e_2^\infty = \pm 20 \text{ kV/cm}$ in the top left illustration of Figure 3.9. The quadratic shape is retained for all the results of the total energy release rate. It can be observed in the bottom left illustration of Figure 3.9 that the account of electric displacement saturation reduces the influence of the applied electric field e_2^∞ on the total energy release rate for this Mode III crack example.

3.5.2.3 Effect of electric displacement saturation on the analytical results for the plane strain case of a Mode I crack.

To model the plane strain case of a Mode I crack within the framework of linear piezoelectricity and x_3 as the poling direction, the computational $\{x, y\}$ -domain for the evaluation of the energy release rates above is transferred by $x \rightarrow x_1$ and $y \rightarrow x_3$. Here the crack front lies parallel to the x_1 axis. The applied far field loading in this case are the stresses σ_{33}^∞ and the electric displacement d_3^∞ or equivalently the electric field e_3^∞ with their relation given as [278] $d_3^\infty = (c_{11}e_{33} - c_{13}e_{31})/(c_{11}c_{33} - c_{13}^2)\sigma_{33}^\infty + ((c_{33}e_{31}^2 - 2c_{13}e_{31}e_{33} + c_{11}e_{33}^2)/(c_{11}c_{33} - c_{13}^2) + \epsilon_{33})e_3^\infty$.

Based on the eigenvalue problem summarized in Section 3.5.2.1 the total energy release rate \mathcal{G}^I and the strain energy release rate $\mathcal{G}_{\text{mech}}^I$ of the Mode I problem for the material parameters given in Table 3.1 are computed as

$$\mathcal{G}^I = \frac{\pi}{2} [g_{33}\sigma_{33}^{\infty 2} + 2g_{34}\sigma_{33}^\infty d_3^\infty + g_{44}d_3^{\infty 2}] \quad \text{and} \quad \mathcal{G}_{\text{mech}}^I = \frac{\pi}{2} [g_{33,\text{mech}}\sigma_{33}^{\infty 2} + g_{34,\text{mech}}\sigma_{33}^\infty d_3^\infty] \quad (3.96)$$

in terms of the applied far field loading σ_{33}^∞ and d_3^∞ or as

$$\mathcal{G}^I = \frac{\pi}{2} [\bar{g}_{33}\sigma_{33}^{\infty 2} + 2\bar{g}_{34}\sigma_{33}^\infty e_3^\infty + \bar{g}_{44}e_3^{\infty 2}] \quad \text{and} \quad \mathcal{G}_{\text{mech}}^I = \frac{\pi}{2} [\bar{g}_{33,\text{mech}}\sigma_{33}^{\infty 2} + \bar{g}_{34,\text{mech}}\sigma_{33}^\infty e_3^\infty] \quad (3.97)$$

in terms of the applied far field loading σ_{33}^∞ and e_3^∞ . The individual parameters introduced in (3.96) and (3.97) are computed numerically and are summarized in Table 3.2 for the case without and with electric displacement saturation, where for the latter the dielectric material parameters in Table 3.1 are replaced by $\epsilon_{11} = \epsilon_{33} = 0$. It should be noted that the final values for the computed components in Table 3.2 without saturation differ from the values reported in PARK [278] and PARK & SUN [279]. Due to a mismatch in the original equations (2.12), (2.38), and (2.41) resulting in the permutation of the definitions \mathbf{R} and \mathbf{R}^T in (2.38) of PARK [278], the computation of \mathbf{b} is carried out by $b_j = (\mathbb{C}_{\beta j k 2} a_k + \mathbb{h}_{2 j \beta} a_4) \zeta_\beta$ and $b_4 = (\mathbb{h}_{\beta k 2} a_k - \mathbb{b}_{2 \beta} a_4) \zeta_\beta$ in their work instead of the correct expression (3.90) used in this section.

With the computed analytical solution an investigation of electric displacement saturation analogous to the Mode III case in Section 3.5.2.2 is now performed for the Mode I crack in an infinite piezoelectric material. The illustration of (3.96) is given in Figure 3.10 where

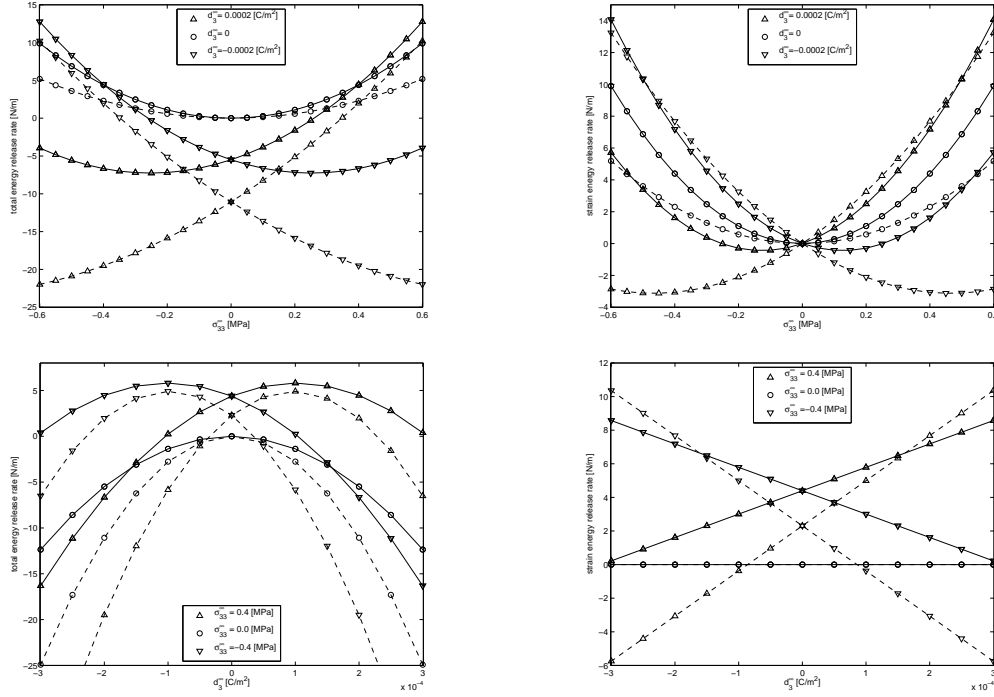


Figure 3.10: Complex variable solution of a center crack of 2 units loaded in Mode I within the framework of linear piezoelectricity. Illustration of the total energy release rate (left column) and the strain energy release rate (right column) versus σ_{33}^∞ under constant electric displacements $d_3^\infty = 0$ and $d_3^\infty = \pm 2 \cdot 10^{-4} C/m^2$ (top row) and versus d_3^∞ under constant mechanical loadings $\sigma_{33}^\infty = 0$ and $\sigma_{33}^\infty = \pm 0.4 MPa$ (bottom row) without (solid lines) and with full (dashed lines) electric displacement saturation.

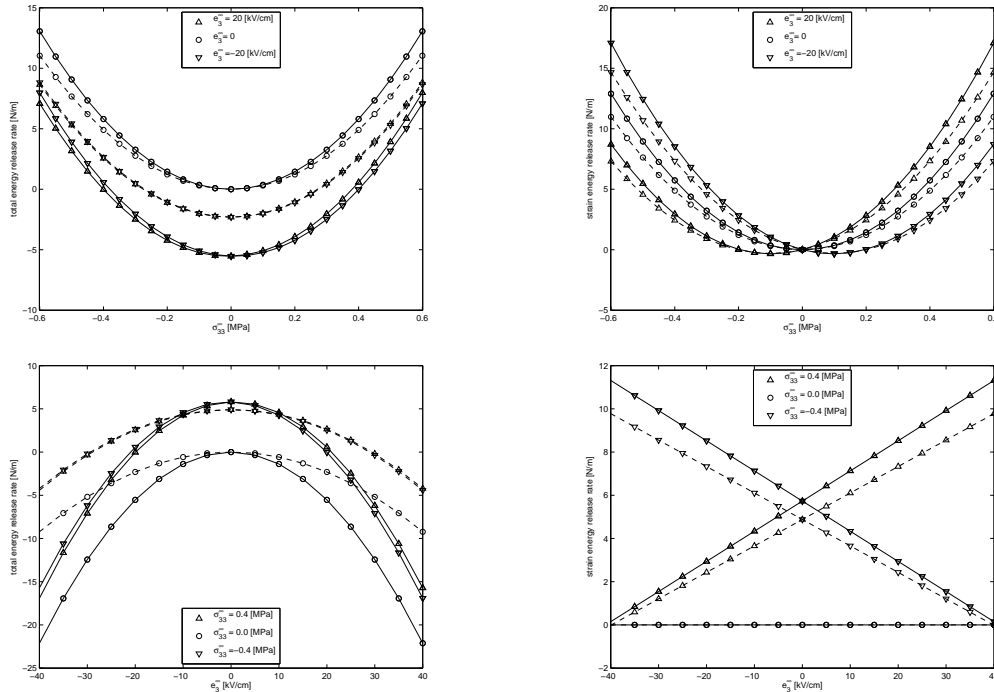


Figure 3.11: Complex variable solution of a center crack of 2 units loaded in Mode I within the framework of linear piezoelectricity. Illustration of the total energy release rate (left column) and the strain energy release rate (right column) versus σ_{33}^∞ under constant electric fields $e_3^\infty = 0$ and $e_3^\infty = \pm 20 kV/cm$ (top row) and versus e_3^∞ under constant mechanical loadings $\sigma_{33}^\infty = 0$ and $\sigma_{33}^\infty = \pm 0.4 MPa$ (bottom row) without (solid lines) and with full (dashed lines) electric displacement saturation.

	g_{33} ($10^{-5}mm^2/N$)	g_{34} ($10^{-2}m^2/C$)	g_{44} ($10^1kVm/mC$)	$g_{33,mech}$ ($10^{-5}mm^2/N$)	$g_{34,mech}$ ($10^{-2}m^2/C$)
w/o saturation	1.7495	2.2146	-8.7430	1.7495	2.2146
w/ saturation	0.9176	4.2713	-17.6237	0.9176	4.2713
	\bar{g}_{33} ($10^{-5}mm^2/N$)	\bar{g}_{34} ($10^{-5}mm^2/V$)	\bar{g}_{44} ($10^{-3}N/kV^2$)	$\bar{g}_{33,mech}$ ($10^{-5}mm^2/N$)	$\bar{g}_{34,mech}$ ($10^{-5}mm^2/V$)
w/o saturation	2.3088	2.3745	-8.8016	2.2804	22.2201
w/ saturation	1.9527	0.4177	-3.6701	1.9417	19.4920

Table 3.2: Computed values of the components used in (3.96) and (3.97) for the expression of the total energy release rate and the strain energy release rate without and with electric displacement saturation of the analytical solution obtained for a Mode I crack within the framework of linear piezoelectricity.

based on a varying far field loading in terms of σ_{33}^∞ and d_3^∞ the total and the strain energy release rates are plotted for the case without saturation (solid lines) and with full electric displacement saturation (dashed lines). Analogous, the illustration of (3.97) is shown in Figure 3.11.

For the Mode I crack a detailed discussion becomes more difficult since its result is derived in terms of the numerical values shown in Table 3.2 rather than analytical and directly in terms of the material parameters shown in Table 3.1 as it is done for the Mode III crack. In the top row of Figure 3.10 a quadratic dependency of both energy release rates on the applied far field stress σ_{33}^∞ can be observed even for the full electric displacement saturation. As for the Mode III crack, the strain energy release rate becomes zero for a zero applied stress field as it can be seen in the top right illustration of Figure 3.10. When varying the applied electric displacement d_3^∞ in the bottom row of Figure 3.10 one observes that now the total energy release rates only coincide for the case with and without electric displacement saturation when $\sigma_{33}^\infty = d_3^\infty = 0$. The linear dependency on the applied electric displacement outlined in the bottom right illustration of Figure 3.10 arises from the absence of a parameter $g_{44,mech}$ in Table 3.2. When again changing the loading from a far field electric displacement d_3^∞ to a far field electric field e_3^∞ , (3.97) is investigated through the illustrations in Figure 3.11. Contrary to the Mode III crack, now also the strain energy release rate is effected by the electric displacement saturation. Interesting is the second row in Figure 3.11 which shows a reduction of the dependency of both energy release rates on the applied electric field.

Finally, in Figure 3.12 a direct comparison of the total energy release rate and the strain energy release rate for Mode III and Mode I is made without and with electric displacement saturation. For Mode III, electric displacement saturation reduces the influence of the total energy release rate on the applied electric field, keeping though the even dependency resulting in an impeded crack growth regardless of the orientation of the applied electric field with regard to the polarization direction. For the strain energy release rate on the other hand, no influence of the electric displacement saturation can be observed. This is clear from (3.95)₂ since there is no dependence of the strain energy release rate on the dielectric material parameters, which is different though in the representation (3.94)₂ when a far field electric displacement is applied. Looking at the results for the Mode I crack illustrated on the right of Figure 3.12, it can be observed that electric

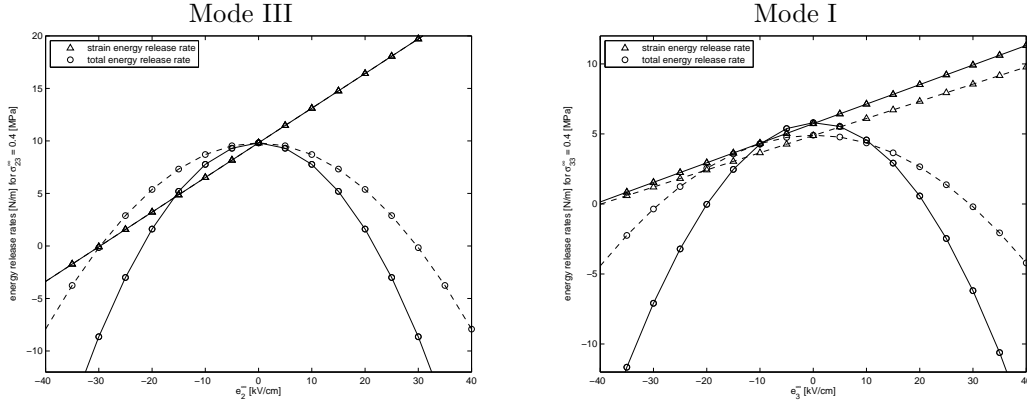


Figure 3.12: Complex variable solution of a center crack of 2 units loaded in Mode III and Mode I within the framework of linear piezoelectricity. Illustration of the total energy release rate and the strain energy release rate for Mode III versus e_2^∞ under a constant mechanical loading $\sigma_{23}^\infty = 0.4 \text{ MPa}$ on the left and for Mode I versus e_3^∞ under a constant mechanical loading $\sigma_{33}^\infty = 0.4 \text{ MPa}$ on the right without (solid lines) and with full (dashed lines) electric displacement saturation.

displacement saturation reduces for both, the total as well as the strain energy release rate, the dependency on the applied electric field, keeping the even dependency on the orientation of the electric field for the total energy release rate and the odd dependency of the strain energy release rate so that for the latter a positive electric field (acting along the polarization direction) enhances crack growth, whereas a negative electric field (acting opposite to the polarization direction) impedes crack growth.

3.5.3 The exponential electric displacement saturation model for ferroelectric ceramics

In this section, the exponential electric displacement saturation model proposed in Section 3.5.1 for piezoelectric ceramics is incorporated into a model of rate-dependent ferroelectricity recently proposed by MIEHE & ROSATO [242], where the polarization vector field is used to describe the hysteretic electromechanical response. After a theoretical incorporation of the electric non-linearity in this section, a numerical evaluation is performed in Section 3.6.1 for initially unpoled ferroelectric ceramic specimens with and without inhomogeneities.

Ferroelectric materials in general are polycrystalline materials consisting of a large number of crystals which itself are subdivided into domains of equal polarization separated by domain walls [162, 212, 255]. When applying a large enough macroscopic electric field above the *coercive field strength* e_c , the microscopic polarizations undergo *polarization switching* and eventually become aligned with the orientation of the applied electric field. The dissipative character is governed by the *remanent polarization* \mathbf{p}^r which remains even after removing the applied electric field. Accompanied with this process is a deformation of the polycrystal in the form of the *remanent strain* $\boldsymbol{\varepsilon}^r$. A schematic illustration of the characteristic dielectric hysteresis curve is given in Figure 3.7.

A typical strategy [173, 194] is an additive decomposition of the strain field and the electric displacement into reversible and remanent parts of the form

$$\boldsymbol{\varepsilon} = \boldsymbol{\varepsilon}^e + \boldsymbol{\varepsilon}^r \quad \text{and} \quad \mathbf{d} = \mathbf{d}^e + \mathbf{p}^r, \quad (3.98)$$

where $\boldsymbol{\varepsilon}^r$ is called the remanent strain and \boldsymbol{p}^r is the remanent polarization. Choosing these remanent quantities $\{\boldsymbol{\varepsilon}^r, \boldsymbol{p}^r\}$ as internal variables in the electric enthalpy function obeys the dependency $H_{\mathcal{B}} = \tilde{H}_{\mathcal{B}}(\boldsymbol{\varepsilon}, \boldsymbol{e}, \boldsymbol{\varepsilon}^r, \boldsymbol{p}^r)$. Insertion into the dissipation inequality (3.14) results, in addition to the expressions for the stresses $\boldsymbol{\sigma}$ and the electric displacement \boldsymbol{d} given in (3.15), in the thermodynamic forces conjugate to the remanent quantities

$$\tilde{\boldsymbol{\sigma}} = -\partial_{\boldsymbol{\varepsilon}^r} \tilde{H}_{\mathcal{B}} \quad \text{and} \quad \tilde{\boldsymbol{e}} = -\partial_{\boldsymbol{p}^r} \tilde{H}_{\mathcal{B}} \quad (3.99)$$

so that the dissipation inequality (3.14) turns into

$$\mathcal{D} = \tilde{\boldsymbol{\sigma}} : \dot{\boldsymbol{\varepsilon}}^r + \tilde{\boldsymbol{e}} \cdot \dot{\boldsymbol{p}}^r \geq 0. \quad (3.100)$$

A number of authors [173, 231] have suggested a reasonable assumption valid for strong electric fields and small stresses [162] to obtain a relationship between the two remanent quantities in the form

$$\boldsymbol{\varepsilon}^r = \hat{\boldsymbol{\varepsilon}}^r(\boldsymbol{p}^r) = \frac{3}{2} \varepsilon_s^r \frac{p^r}{p_s^r} (\boldsymbol{a}^r \otimes \boldsymbol{a}^r - \frac{1}{3} \mathbf{1}) \quad (3.101)$$

considerably reducing the complexity of the formulation. Here $p^r = |\boldsymbol{p}^r| = \sqrt{\boldsymbol{p}^r \cdot \boldsymbol{p}^r}$ is the amount of remanent polarization which tends to the value p_s^r when all the microscopic polarizations undergo polarization switching, $\boldsymbol{a}^r = \boldsymbol{p}^r/p^r$ is the polarization director which contrary to the framework of linear piezoelectricity considered in Section 3.2.1.3 no longer is constant, and ε_s^r is the maximum achievable remanent strain due to remanent polarization in the direction \boldsymbol{a}^r . The evolution of the remaining internal variable \boldsymbol{p}^r is obtained in MIEHE & ROSATO [242] as

$$\dot{\boldsymbol{p}}^r = \partial_{\tilde{\boldsymbol{e}}} \phi_{\eta}^* \quad (3.102)$$

in terms of the dual dissipation potential function

$$\phi_{\eta}^*(\tilde{\boldsymbol{e}}) = \frac{e_c}{\eta(1+m)} \langle \tilde{e}/e_c - 1 \rangle^{1+m} \quad (3.103)$$

where $\tilde{e} = \sqrt{\tilde{\boldsymbol{e}} \cdot \tilde{\boldsymbol{e}}}$, $e_c > 0$ is the coercive field strength, $\langle \bullet \rangle = (\bullet + |\bullet|)/2$ is the ramp function, and $\eta > 0$, $m > 0$ are material parameters which govern the viscosity of the remanent polarization process. Details with regard to the underlying variational structure of this ferroelectricity model and its numerical implementation are given in the recent work by MIEHE & ROSATO [242] and the general treatment of MIEHE ET AL. [249] on variational principles in electro-magneto-mechanics.

What remains is to specify the electric enthalpy function $H_{\mathcal{B}}$ for the ferroelectric material that takes into account the anisotropy in the mechanical, the electrical as well as in the electromechanical coupled contributions. Following conceptually a representation in terms of invariants as considered in SCHRÖDER & ROMANOWSKI [318], the following form

$$\begin{aligned} H_{\mathcal{B}} = \tilde{H}_{\mathcal{B}}(J_i |_{i=1}^8) &= \tilde{H}_{\mathcal{B}_1}(J_1, J_2, J_3, J_4) + \tilde{H}_{\mathcal{B}_2}(J_5, J_6) + \tilde{H}_{\mathcal{B}_3}(J_1, J_3, J_5, J_6, J_7, J_8) \\ &+ \tilde{H}_{\mathcal{B}_4}(J_6, J_8) + \tilde{H}_{\mathcal{B}_5}(J_8) \end{aligned} \quad (3.104)$$

is proposed in this section. The purely mechanical contribution $\tilde{H}_{\mathcal{B}_1}$ and the purely electrical contribution $\tilde{H}_{\mathcal{B}_2}$ are identical to those of the piezoelectric material given in (3.21), namely

$$\tilde{H}_{\mathcal{B}_1} = \frac{1}{2} \lambda J_1^2 + \mu J_2 + \alpha_1 J_4 + \alpha_2 J_3^2 + \alpha_3 J_1 J_3 \quad \text{and} \quad \tilde{H}_{\mathcal{B}_2} = \gamma_1 J_5 + \gamma_2 J_6^2. \quad (3.105)$$

Following SCHRÖDER & ROMANOWSKI [318] and MIEHE & ROSATO [242], the electromechanical coupled part $\tilde{H}_{\mathcal{B}_3}$ and the additional contributions $\tilde{H}_{\mathcal{B}_4}$ and $\tilde{H}_{\mathcal{B}_5}$ to account the polarization switching are chosen as

$$\tilde{H}_3 = [\beta_1 J_1 J_6 + \beta_2 J_3 J_5 + \beta_3 J_7] \frac{J_8}{p_s^r}, \quad \tilde{H}_4 = -J_6 J_8, \quad (3.106)$$

and

$$\tilde{H}_5 = \frac{1}{c} \left[J_8 \operatorname{artanh} \left(\frac{J_8}{p_s^r} \right) + \frac{1}{2} p_s^r \ln \left(1 - \left(\frac{J_8}{p_s^r} \right)^2 \right) \right] \quad (3.107)$$

in terms of the invariants $J_1 = \varepsilon_{ii}^e$, $J_2 = \varepsilon_{ij}^e \varepsilon_{ji}^e$, $J_3 = a_i^r \varepsilon_{ij}^e a_j^r$, $J_4 = a_i^r \varepsilon_{ik}^e \varepsilon_{kj}^e a_j^r$, $J_5 = e_i e_i$, $J_6 = e_i a_i^r$, $J_7 = a_i^r \varepsilon_{ij}^e e_j$, $J_8 = p^r$, with $\varepsilon_{ij}^e = \varepsilon_{ij} - \varepsilon_{ij}^r(p_k^r)$, and the parameter c governing the slope of the hysteresis curve.

This constitutive framework of unpoled ferroelectric ceramics can again be easily modified to take into account the additional electric non-linearity in the form of the electric displacement saturation introduced in the previous Section 3.5.1 for piezoelectric ceramics. The main reason for the incorporation of this additional non-linearity lies in the experimentally observed saturation of the electric displacement field for strong enough applied electric fields. In the current model for ferroelectric ceramics characterized though the electric enthalpy function proposed in (3.104)-(3.107), the electric displacement is not bounded and therefore is not capable of accounting for the electric displacement saturation. The term responsible for the constant slope in the dielectric hysteresis illustrated in Figure 3.7 is the purely electrical part $\tilde{H}_{\mathcal{B}_2}$ given in (3.105). Based on a saturation type modification of this term analogous to (3.87) as

$$\tilde{H}_{\mathcal{B}_2}^{\text{sat}} = \tilde{H}_{\mathcal{B}_2} \cdot \exp \left(- \frac{|J_6|}{\xi} \right) \quad (3.108)$$

the electric displacement is again saturated towards a limiting value depending on the choice of the saturation exponent ξ in the direction normal to the polarization direction \mathbf{a}^r assured through the dependency of the electric displacement saturation model of (3.108) now on the invariant $J_6 = \mathbf{e} \cdot \mathbf{a}^r$.

3.6 Representative numerical simulations

The numerical simulations presented in this section outline the performance of the developed finite elements capable of incorporating failure into electromechanical coupled materials and investigate the influence of electric displacement saturation on ferroelectric ceramics and on the initiation and propagation of strong discontinuities in piezoelectric ceramics. Section 3.6.1 considers a ferroelectric response and investigates the influence of electric displacement saturation for examples with no propagating failure zone. Based on single element tests, Section 3.6.2 validates the correctness of the incorporated electric separation modes into the strong discontinuity approach. In Sections 3.6.3 and 3.6.4 a propagating failure zone is investigated within the framework of linear piezoelectricity and an account for electric displacement saturation. Finally, in Section 3.6.5 three dimensional simulations of a compact tension test and different three point bending tests with various notch locations are performed.

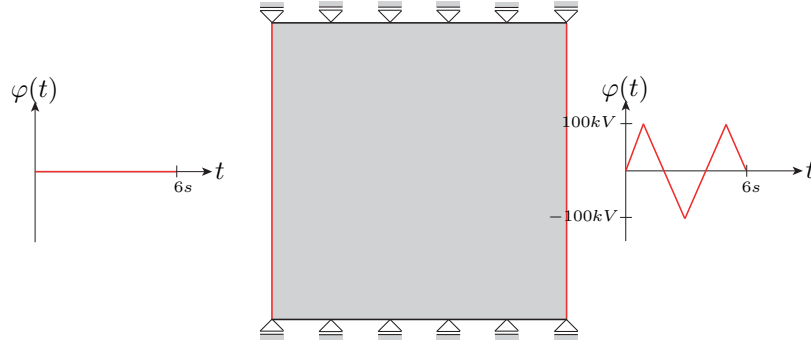


Figure 3.13: Numerical evaluation of electric displacement saturation in a rate-dependent ferroelectric material model through a square plate with a centered hole. Geometric properties as well as mechanical and electric boundary conditions for a square plate with dimensions $10\text{ mm} \times 10\text{ mm}$ of initially unpoled ferroelectric ceramics. While mechanically restrained in vertical direction at the bottom and top surface and free in horizontal direction, a zero electric potential is applied at the left surface and a non-zero cyclic electric potential is applied at the right surface.

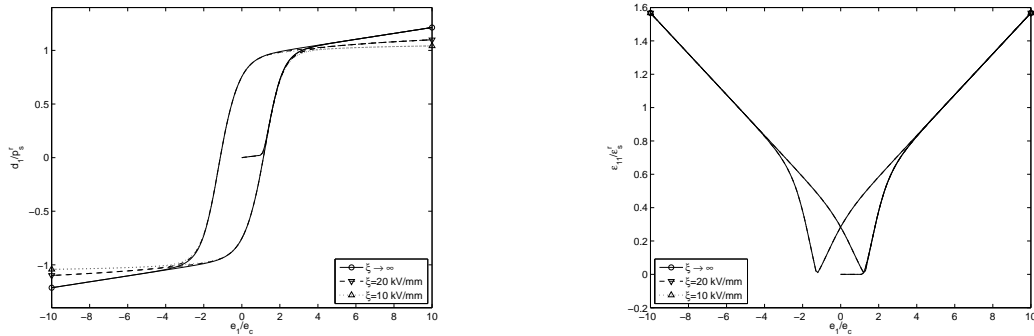


Figure 3.14: Numerical evaluation of electric displacement saturation in a rate-dependent ferroelectric material model through a uniaxial test with cyclic electric loading. The influence of electric displacement saturation is outlined for the dielectric hysteresis (left) as well as the butterfly hysteresis (right). The results without electric displacement saturation (obtained by $\xi \rightarrow \infty$) do change only for the dielectric hysteresis when electric displacement saturation is present for the two values of $\xi = 20\text{ kV/mm}$ and $\xi = 10\text{ kV/mm}$.

3.6.1 Electric displacement saturation for ferroelectric ceramics

In this section a numerical evaluation of electric displacement saturation in a rate-dependent ferroelectric material with the piezoelectric material parameters given in Table 3.1 and the additionally required ferroelectric material parameters summarized in Table 3.3 is provided. In Section 3.6.1.1 a uniaxial test with cyclic electric loading is shown. A centered hole is incorporated into a square plate in Section 3.6.1.2 to obtain a first impression on how the numerical account for electric displacement saturation proposed in (3.108) performs for an introduced inhomogeneity.

3.6.1.1 Uniaxial test with cyclic electric loading. In this section, the characteristic hysteresis curves and their dependency on the electric displacement saturation for the ferroelectric material with the properties outlined in Tables 3.1 and 3.3 are computed for a homogeneous specimen of dimension $10\text{ mm} \times 10\text{ mm}$. The geometry as well as the mechanical and electric boundary conditions are illustrated in Figure 3.13. Mechanically,

Name	Parameter	Value	Unit
coercive electric field	e_c	1.0	kV/mm
saturation polarization	p_s^r	26×10^{-2}	C/m^2
saturation strain	ε_s^r	10^{-3}	—
hysteresis slope parameter	c	1.0	—
viscosity of polarization	η	10^{-2}	$mm^2/(C s)$
viscosity shape exponent	m	2	—

Table 3.3: Additional material parameters to the ones supplied in Table 3.1 of lead zirconate titanate PZT-4 ferroelectric ceramics for the numerical simulations of the poling process through the rate-dependent ferroelectric material model of Section 3.5.3.

the specimen is restrained in vertical direction at the bottom and the top surface but is free to move in horizontal direction. Electrodes are placed at the left and right surfaces. While the electrode at the left surface is grounded, a periodic electric potential φ is applied at the right surface altering between $\pm 100 kV$ every $2 s$. Such a large amount is chosen to emphasize the response in the hysteresis curves after full switching is achieved, which is the region for which the electric displacement saturation influences the constitutive behavior.

The numerical results in the form of the dielectric and the butterfly hysteresis are illustrated in Figure 3.14. Starting from the virgin unpoled material, the electric field is increased until it approaches the coercive field strength e_c . Thereafter electric poling is observed for which the majority of the microscopic polarization is aligned with the orientation of the applied electric field. Increasing the electric field even further, electric displacement saturation influences the dielectric hysteresis curve by affecting the slope in the electric displacement versus electric field relation. For a saturation exponent of $\xi \rightarrow \infty$ electric displacement saturation is not accounted for resulting in this slope remaining constant and an unbounded increase of the electric displacement. For $\xi = 20 kV/mm$, this slope becomes flatter and eventually for $\xi = 10 kV/mm$ approaches an almost horizontal relation, bounding the maximal achievable electric displacement. As a measure for the electric displacement saturation, the value $1 - \exp(-|J_6|/\xi)$ can be used which for this homogeneous test takes the values $1 - \exp(-0.5) = 0.3935$ and $1 - \exp(-1.0) = 0.6321$ at time $t = 1 s$, i.e. saturations of 39.35% and 63.21% are achieved for the two saturation exponents $\xi = 20 kV/mm$ and $\xi = 10 kV/mm$, respectively. A subsequent reduction of the applied electric field results in polarization switching when the electric field approaches $-e_c$. Again, electric displacement saturation is observed in the dielectric hysteresis for $\xi < \infty$. The butterfly hysteresis, for which the remanent strain develops when $|e_1| \rightarrow e_c$, remains unchanged by the proposed simplified incorporation of electric displacement saturation through (3.108), showing that it cannot account for an in reality expected modified strain response due to electric displacement saturation [137].

3.6.1.2 Square plate with a centered hole. Next, a square plate with a centered hole is employed to investigate the influence of electric displacement saturation. This problem is chosen since it provides a first evaluation of the proposed incorporation of electric displacement saturation on materials with inhomogeneities. Geometry and boundary conditions in the mechanical and electric fields are illustrated in Figure 3.15. The plate with dimensions $10 mm \times 10 mm$ is mechanically restrained in horizontal and vertical direction

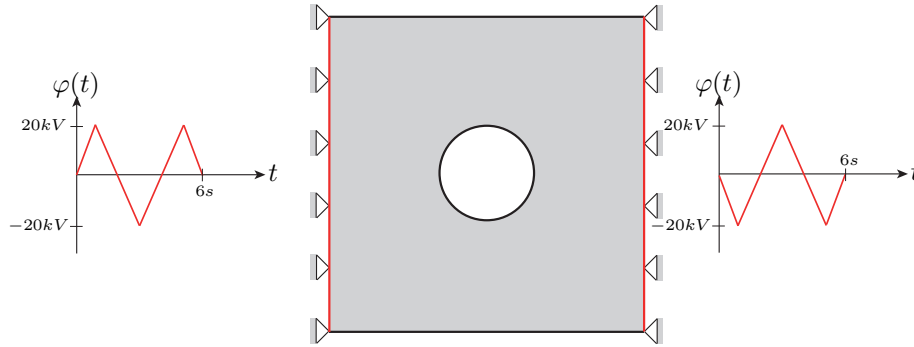


Figure 3.15: Numerical evaluation of electric displacement saturation in a rate-dependent ferroelectric material model through a square plate with a centered hole. Geometric properties as well as mechanical and electric boundary conditions for a square plate with dimensions $10\text{ mm} \times 10\text{ mm}$ and a centered hole of diameter 3 mm of unpoled ferroelectric ceramics. While mechanically restrained in horizontal and vertical direction at the left and right surface and free at the bottom and top surface, a cyclic electric potential is applied at the left and the right surface.

at the left and the right surface but mechanically free to move at the bottom and the top surfaces. Electrodes are again placed at the left and right surfaces where now through both a cyclic electric potential is applied to the specimen. Starting from the virgin unpoled state, the electric potential reaches 20 kV at the left surface and -20 kV at the right surface at a time of 1 s . Subsequently, every 2 s the electric potential continuously changes from $\pm 20\text{ kV}$ to $\mp 20\text{ kV}$ at the vertical surfaces of the specimen.

The numerical results of this test are shown in Figure 3.16 where the electric potential φ , the remanent polarization \mathbf{p}^r , and the distribution of the electric displacement saturation by plotting the value $1 - \exp(-|J_6|/\xi)$ are shown at four different time instances $t = 1, 2, 3, 4\text{ s}$ when electric displacement saturation is accounted for by a saturation exponent of $\xi = 10\text{ kV/mm}$. A comparison of the results obtained for the electric potential distribution and the remanent polarization given in the left and center columns of Figure 3.16 when electric displacement saturation is accounted for, with the results without electric displacement saturation given in MIEHE & ROSATO [242], where also slightly different material parameters are used in their work resulting in an isotropic purely mechanical and electrical response, almost no difference can be observed. Still, the electric displacement is saturated in the upper and lower region of the centered hole as it can be observed in the right columns of Figure 3.16. The maximum achieved value of the electric displacement saturation achieves around 36% at $t = 1\text{ s}$ right above and below the centered hole.

3.6.2 Fracture in piezoelectric ceramics - Single element tests

The incorporation of electric separation modes in Section 3.3 resulted in the development of new finite elements for the modeling of fracture in electromechanical coupled problems. The way how such separation modes are constructed is based on the goal to avoid locking phenomena which otherwise result in an over stiff response of the material. It remains to confirm the locking-free property of the resulting finite elements based on numerical simulations. In this section two academic numerical simulations are chosen which specifically address this issue in the form of a simple patch test for elements with discontinuities in the

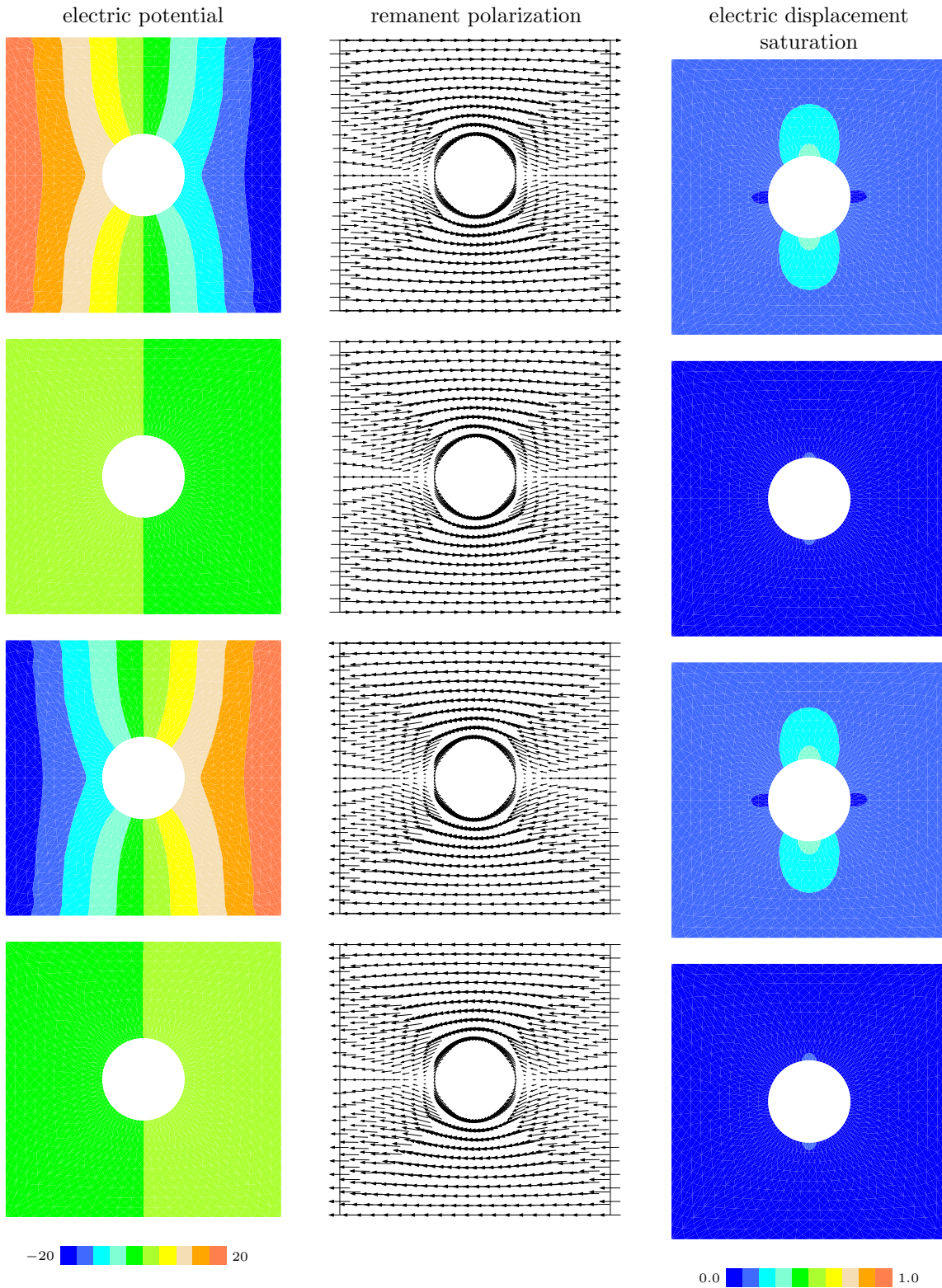


Figure 3.16: Numerical evaluation of electric displacement saturation in a rate-dependent ferroelectric material model through a square plate with a centered hole. The left column shows the distribution of the electric potential, the center column shows the orientation of the remanent polarization vector \mathbf{p}^r , and the right column shows the electric displacement saturation evolving at the top and bottom part of the hole by plotting the value $1 - \exp(-|J_6|/\xi)$ at different time instances $t = 1, 2, 3, 4$ s (from the top to the bottom) when using a saturation exponent of $\xi = 10 \text{ kV/mm}$.

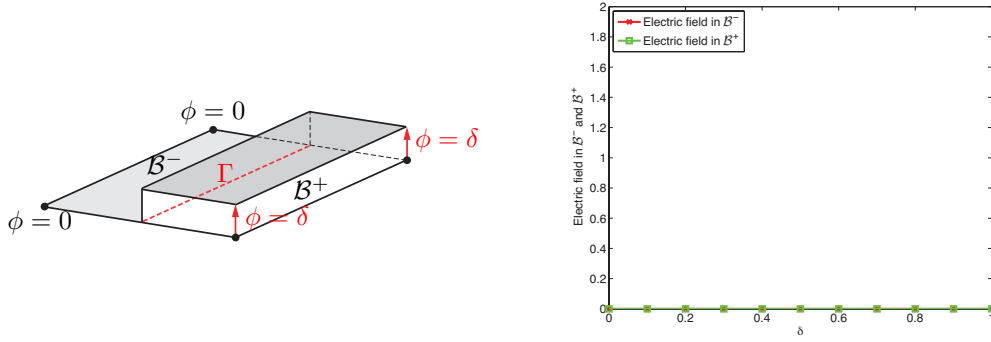


Figure 3.17: Single element tests. Illustration of the element test employed for the evaluation of the locking-free properties of the formulation based on a constant electrical separation mode. A single element has a mechanical fully softened and electrical impermeable pre-existing crack and is loaded by the application of an electric potential on the nodes in \mathcal{B}^+ of the element whereas the displacement of all nodes are zero, resulting in a constant electric potential distribution in \mathcal{B}^+ . The computed resulting electric field parallel to the strong discontinuity in both parts of the body is illustrated on the right which exactly captures the analytical solution in (3.109).

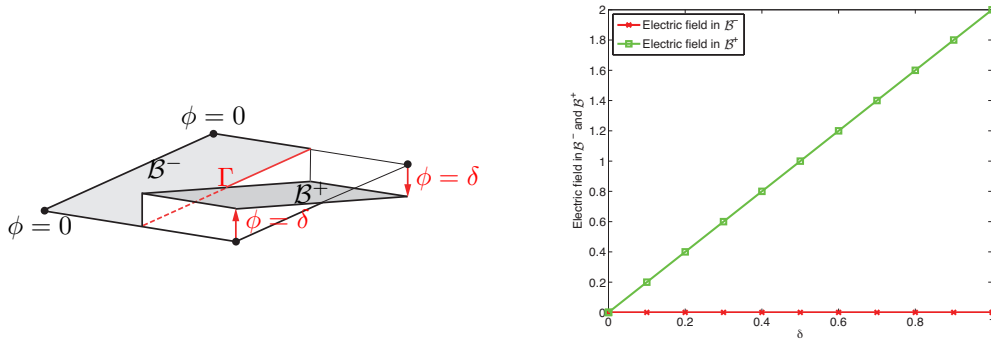


Figure 3.18: Single element tests. Illustration of the element test employed for the evaluation of the locking-free properties of the formulation based on a linear electric separation mode. A single element has a mechanical fully softened and electrical impermeable pre-existing crack and is loaded by the application of an electric potential on the nodes in \mathcal{B}^+ of the element whereas the displacement of all nodes are zero, resulting in a linear electric potential distribution in \mathcal{B}^+ . The computed resulting electric field parallel to the strong discontinuity in both parts of the body is illustrated on the right which exactly captures the analytical solution in (3.110).

electric fields. One may conduct CHAPELLE & BATHE [61] for a more rigorous evaluation of the stability of finite elements without strong discontinuities whose extension to the developed finite elements here is out of the scope of the present work.

A block with dimensions of $a \times a$ where $a = 1$ is discretized by a single bilinear quadrilateral finite element. All four nodes of the element are mechanically restrained so that no mechanical displacements arise. Furthermore, the element is assumed to have a pre-existing mechanically fully softened and electrically impermeable strong discontinuity through its centroid separating the two parts \mathcal{B}^- and \mathcal{B}^+ of the element and ensuring a completely decoupled response of these two parts of the element, if represented correctly. The first single element test then proceeds by the application of a nonzero electric potential δ at all nodes in \mathcal{B}^+ like it is illustrated on the left of Figure 3.17. Due to the pre-existing electrical impermeable strong discontinuity Γ , the electric potential remains zero in the

part \mathcal{B}^- of the element. The analytical solution for the electric field as the negative gradient of the electric potential can be easily obtained as

$$\mathbf{e} = \mathbf{0} \quad \text{in } \mathcal{B}^- \quad \text{and} \quad \mathbf{e} = \mathbf{0} \quad \text{in } \mathcal{B}^+ \quad (3.109)$$

for both parts of the element. This further allows for a straightforward comparison of the analytical result in (3.109) with the obtained numerical results, as illustrated on the right of Figure 3.17. One can observe that in the numerical simulation the electric field remains zero in both parts of the element, as expected. This confirms the locking-free property of the element developed based on the incorporation of the constant electrical separation mode in Section 3.3.1.

In the second element test considered here, an electric potential distribution in \mathcal{B}^+ is chosen so that a nonzero constant electric field is obtained in that part. This can be easily achieved by applied nodal values of the electric potential as illustrated on the left of Figure 3.18. The analytical solution for the electric field can again be obtained as the negative gradient of the electric potential as

$$\mathbf{e} = \mathbf{0} \quad \text{in } \mathcal{B}^- \quad \text{and} \quad e_n = 0, \quad e_m = \frac{2\delta}{a} \quad \text{in } \mathcal{B}^+ \quad (3.110)$$

for both parts of the element where e_n and e_m denote the electric field in the direction normal and tangential to the strong discontinuity Γ , respectively. The numerical results shown on the right of Figure 3.18 exactly capture the analytical results in (3.110) for the linear electrical separation mode of Section 3.3.2, which again outlines the locking-free property of this formulation.

With the basic requirement of preventing locking phenomena for a constant and linear electrical separation mode satisfied, it remains to apply the new formulation for more realistic numerical simulations for which also experimental results are available, which then can be employed to examine the performance of the resulting new finite elements based on a proper comparison.

3.6.3 Fracture in piezoelectric ceramics - Compact tension test

In this first realistic example a plate with dimensions $25.5 \times 19.1 \times 5.1 \text{ mm}^3$ made out of a PZT-4 piezoelectric ceramic material with material parameters given in Table 3.1 and a vertically centered horizontal pre-existing notch of the length 11.5 mm and thickness 0.46 mm is loaded mechanically and electrically as shown in Figure 3.19. The pre-existing notch is rounded at its tip with a notch eccentricity of $\epsilon = 4$. The mechanical loading is tensile and applied through rigid circular bars of diameter 3.2 mm placed 4.6 mm horizontally and vertically away from the left bottom and the left top corners. Electrically, the plate is loaded by the application of non-zero electric potentials $\varphi_1^{\text{top}} = -9.55 \text{ kV}$ and $\varphi_2^{\text{top}} = -19.1 \text{ kV}$ at the top surface in the way shown in Figure 3.19 whereas the electric potential is assumed zero throughout the bottom surface. The poling direction of the specimen is assumed vertically oriented from the bottom to the top surface. Experimental results presented in PARK & SUN [280] show the development of a horizontal crack from the tip of the pre-existing notch towards the right surface of the specimen.

This experimental setup is modeled with the anisotropic piezoelectric constitutive relation of Section 3.2.1.3 and in particular given in (3.20)-(3.26) as well as the incorporation of

electric displacement saturation through the modification proposed in (3.86) in terms of a to be determined saturation exponent ξ . Different finite element discretizations consisting of standard displacement based Q1 finite elements in the plane setting are chosen. For the determination of the saturation exponent ξ coarse and fine finite element meshes are chosen which are refined at the tip of the pre-existing notch and consist of 3190 and 5319 Q1 elements, respectively. For the modeling of the propagating crack, the refinement is extended over the whole length of the region where the crack is supposed to propagate resulting in finite element meshes consisting of 6159 and 10083 Q1 finite elements. An illustration of all the four meshes is given in Figure 3.20.

Before simulating the expected propagation of the crack, the saturation exponent ξ introduced in this work to model the electric displacement saturation through (3.86), needs to be computed based on a parameter study whose result is illustrated in Figure 3.21. In this study, the saturation exponent is varied from $\xi \rightarrow \infty$, corresponding to no electric displacement saturation, to $\xi = 1 \text{ kV/mm}$ resulting in a large electric displacement saturation zone, using the coarse and fine finite element meshes illustrated in the top row of Figure 3.20. Electric potentials of $\varphi_1^{\text{top}} = -9.55 \text{ kV}$ and $\varphi_2^{\text{top}} = -19.1 \text{ kV}$ are applied at the top surface and the fracture loads at the point of crack initiation for the different values of ξ are compared with the experimental results in PARK & SUN [280]. Since no value for the tensile strength f_{t_n} of the material against normal separation needed for the constitutive model along the strong discontinuity in (3.39) is provided in the experiments given by PARK & SUN [280], values ranging from $60 - 100 \text{ N/mm}^2$ are chosen in this parameter study. The experimental fracture initiation loads are illustrated for the two electric potentials as circles at the vertical left axes in the plots of Figure 3.21. The numerical computed fracture initiation obtained without electric displacement saturation are shown by the filled markers at the right vertical axes of Figure 3.21 for the different values of the tensile strengths. When accounting for the electric displacement saturation, one can observe an increase of the fracture initiation load for larger saturation zones, i.e. for smaller values of the saturation exponent. With the goal to fit the two parameters of the saturation exponent and the tensile strength to get close to the experimental reported fracture initiation loads one can identify the two values $\xi = 10 \text{ kV/mm}$ and $f_{t_n} = 80 \text{ kV/mm}^2$. Those are subsequently used for all the remaining simulations in this section. The obtained value for the tensile strength is, as it turned out after performing this parameter study, in very good agreement with the tensile strength of 75.8 N/mm^2 reported in PARK [278] used for exactly these experiments.

With these two fitted parameters at hand it is now possible to perform numerical simulations of the actual crack propagation. The determination of the onset of crack initiation and its propagation direction is based on the loss of ellipticity condition given in (3.76). After its onset, the crack propagates with boundary conditions assumed as fully softened and electrical impermeable. Whereas the fully softened crack boundary condition is clearly justified for such highly brittle materials with fracture energies in the order of 2.34 N/mm [280], the justification for the electrical crack boundary condition is not that straightforward [74, 138, 195, 281]. The numerical results are shown in Figures 3.22 and 3.23 for the coarse and fine finite element meshes shown in the bottom row of Figure 3.20. They show the evolution of the electric potential and the electric displacement saturation as the crack is propagating from the tip of the pre-existing notch horizontally towards the right surface. A comparison of the results without electric displacement saturation (two left columns in these figures) and with electric displacement saturation using a saturation

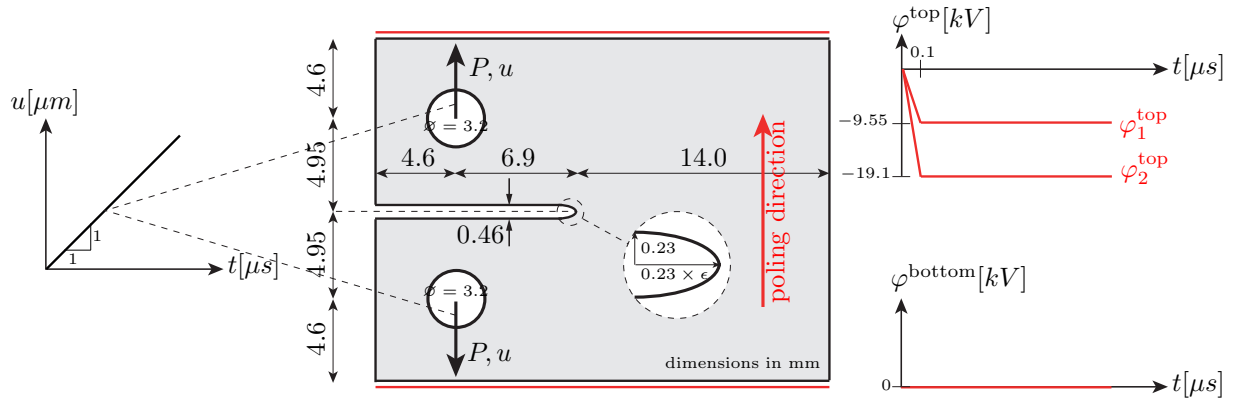


Figure 3.19: Compact tension test. Illustration of the geometry and loading of the PZT-4 piezoelectric ceramic plate with a pre-existing horizontal notch. The specimen is loaded mechanically by the application of a tensile stretch through the application of displacements through rigid circular bars near the left top and bottom corners. The electric loading is achieved through a zero electric potential φ^{bottom} at the bottom surface and a non-zero electric potential φ^{top} at the top surface where the poling direction is vertical from the bottom towards the top. Experiments [280] report the appearance of a crack propagating from the tip of the notch horizontally towards the right surface.

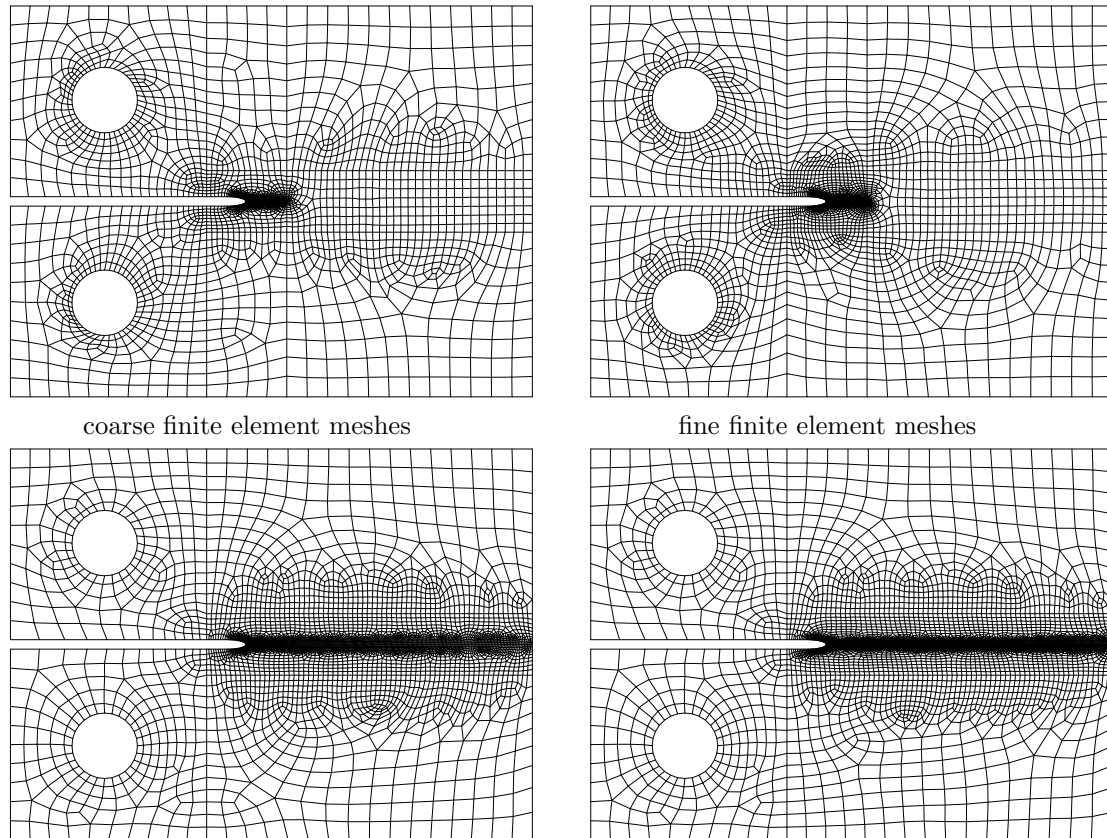


Figure 3.20: Compact tension test. Illustration of the finite element meshes used for the determination of the electric saturation exponent ξ (top row) and for the simulations of the propagating crack (bottom row). The meshes for the evaluation of the saturation exponent are only refined at tip of the notch and consist of 3190 Q1 finite elements for the coarse mesh (left) and 5319 Q1 finite elements for the fine mesh (right). The meshes for the simulation of the propagating crack are refined throughout the horizontal region from the tip of the notch towards the right edge and consist of 6159 and 10083 Q1 finite elements for the coarse and the fine mesh, respectively.

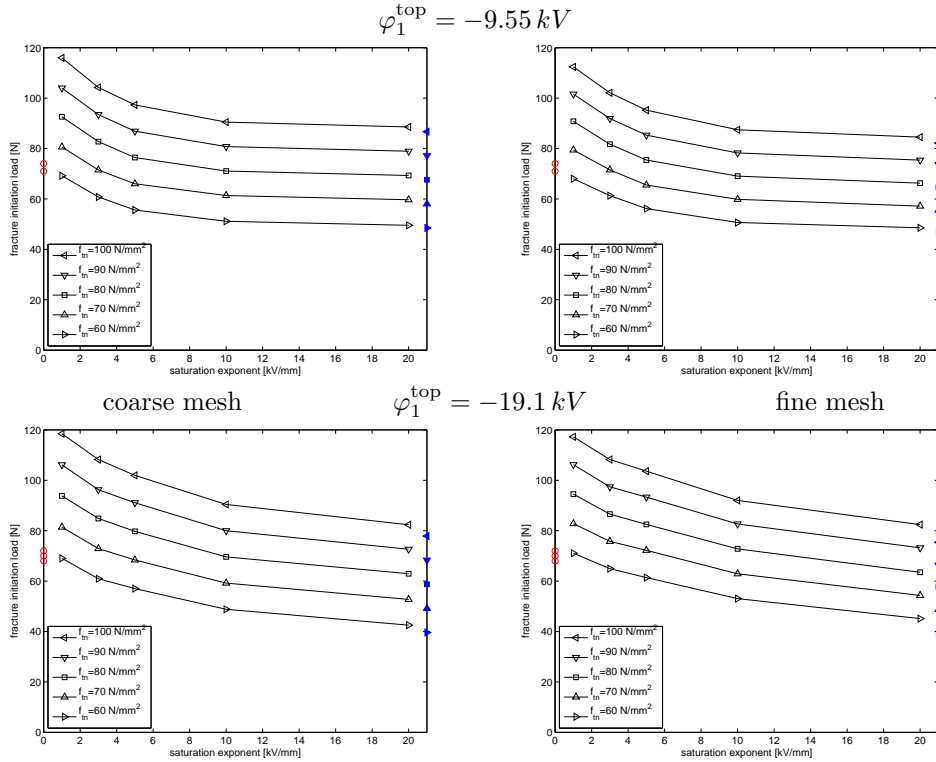


Figure 3.21: Compact tension test. Influence of the electric saturation parameter ξ and the tensile normal strength f_{t_n} on the fracture load of the tension test using a coarse and a fine mesh given in the top row of Figure 3.20. The experimental data are shown by circles, the values for $\xi \rightarrow \infty$ corresponding to the case without electric displacement saturation are shown by filled markers for the different tensile strengths.

exponent of $\xi = 10 \text{ kV/mm}$ (two right columns in these figures) is performed. Whereas almost no difference can be observed for the electric potential distribution, the electric displacement saturation makes the crack start to propagate later, which is consistent with the plots given in Figure 3.21, but subsequently allows the crack to propagate faster through the finite element mesh. The illustration of the saturation zone is performed by plotting the value $1 - \exp(-|I_6|/\xi)$ in the right columns of Figures 3.22 and 3.23. It can be observed that the resulting electric displacement saturation zone is small and travels together with the crack tip towards the right edge.

Finally, the reaction force versus applied displacement for the two meshes in the bottom row of Figure 3.20 is illustrated in Figure 3.24 for different saturation exponents $\xi = 3, 5, 10, 20, \infty \text{ kV/mm}$. It can be observed that for smaller values of ξ , i.e. larger electric displacement saturation zones, the initiation load increases but thereafter shows a faster decay of the reaction force so that the speed with which the crack propagates through the finite element mesh increases for smaller values of ξ . To achieve this characteristic, the finite element mesh has to be sufficiently refined at the zone where the crack is propagating to capture the correct size of the electric displacement saturation zone. The locking-free properties of the elements used within the strong discontinuity approach can be observed since the reaction forces tend to zero when the crack is fully propagated through the mesh. The result for the coarse and fine mesh are almost identical confirming the mesh-independency of the employed formulation and proposed incorporation of electric displacement saturation.

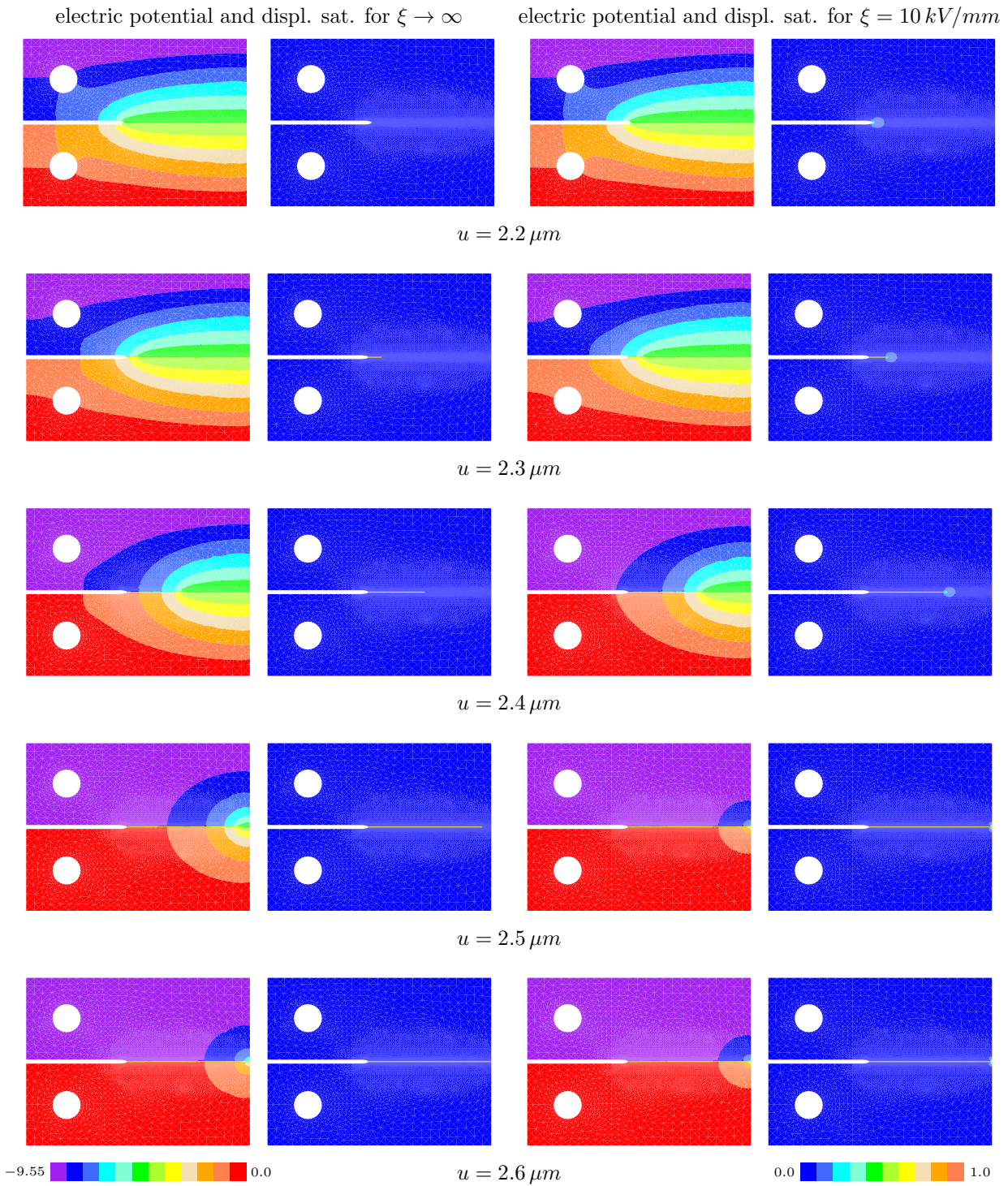


Figure 3.22: Compact tension test. Influence of the electric displacement saturation on the crack propagation which is shown as yellow line using the coarse mesh shown in the bottom row of Figure 3.20. The two columns on the left show the electric saturation and electric potential as it changes for the propagating crack without electric displacement saturation. The two columns on the right show the same results for an active electric displacement saturation using a saturation exponent of $\xi = 10 \text{ kV/mm}$. The value $1 - \exp(-|I_6|/\xi)$ is used to illustrate the electric displacement saturation which can be observed to be small and travels along with the propagating crack tip.

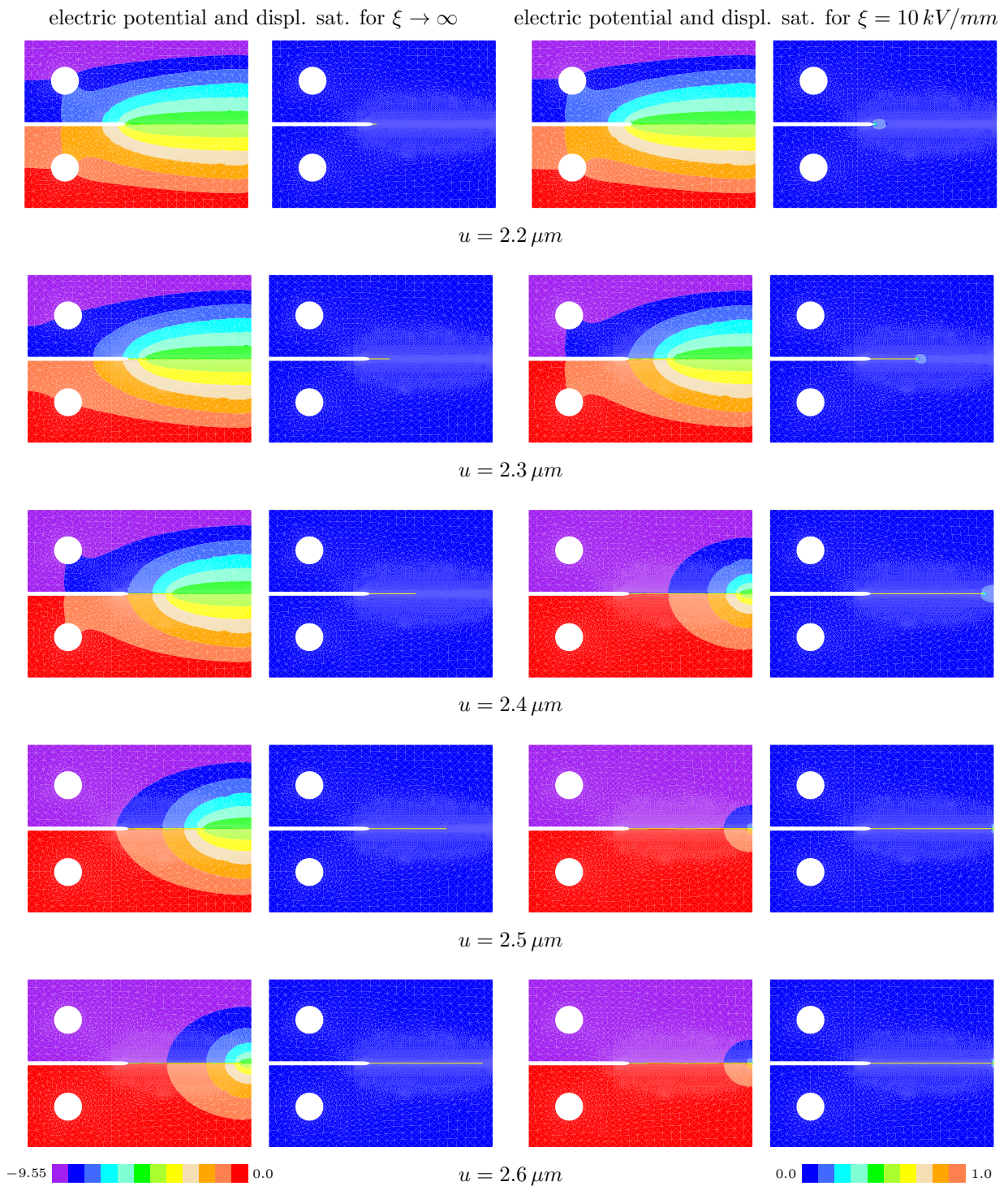


Figure 3.23: Compact tension test. Influence of the electric displacement saturation on the crack propagation which is shown as yellow line using the fine mesh shown in the bottom row of Figure 3.20. The two columns on the left show the electric saturation and electric potential as it changes for the propagating crack without electric displacement saturation. The two columns on the right show the same results for an active electric displacement saturation using a saturation exponent of $\xi = 10 \text{ kV/mm}$. The value $1 - \exp(-|I_6|/\xi)$ is used to illustrate the electric displacement saturation which can be observed to be small and travels along with the propagating crack tip.

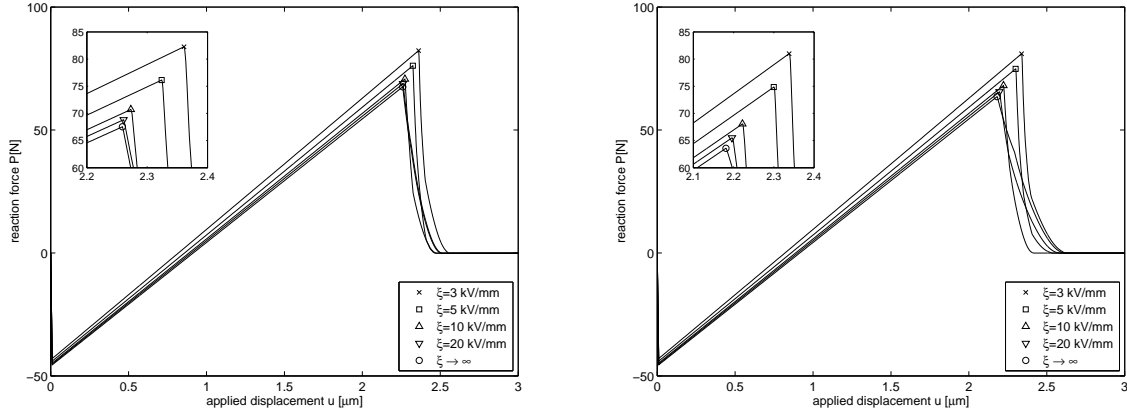


Figure 3.24: Compact tension test. Reaction force versus applied displacement relation for the coarse (left) and the fine (right) finite element mesh shown in the bottom row of Figure 3.20 and for different saturation exponents $\xi = 3, 5, 10, 20, \infty \text{ kV/mm}$. The smaller ξ , the larger the electric displacement saturation zone, the higher the reaction force at which the specimen fractures, and the faster is the resulting crack propagation from the tip of the pre-existing notch towards the right surface.

3.6.4 Fracture in piezoelectric ceramics - Three point bending test

The second performed numerical simulation, for which also experimental results are reported in PARK & SUN [280], is the off-centered three point bending test of the same PZT-4 piezoelectric ceramic material used in the previous Section 3.6.3. Again the material parameters are the ones summarized in Table 3.1. In this example, the plate has dimensions $19.1 \times 9 \times 5.1 \text{ mm}^3$ with a pre-existing notch, which is now starting at the bottom surface, extends 4 mm upwards, is placed off-centered by 4 mm , and has a thickness of 0.46 mm . Again the notch tip is rounded using a notch eccentricity of $\epsilon = 4$. The mechanical loading is performed by the application of a displacement at the center of the top surface. Electrically the poled material, with poling direction oriented from the left towards the right, is loaded by a zero electric potential φ^{left} at the left surface and a nonzero electric potential φ^{right} at the right surface with final value $\varphi_1^{\text{right}} = -9.55 \text{ kV}$ after a short rise time of $0.1 \mu\text{s}$. The experimental results presented in PARK & SUN [280] show the development of a curved crack which starts almost vertically from the pre-existing notch tip but turns to the right towards the point where the mechanical load is applied.

The numerical simulation again makes use of the anisotropic piezoelectric constitutive relation of Section 3.2.1.3 and the incorporation of the electric displacement saturation through the modification proposed in (3.86) in term of the saturation exponent which is chosen as $\xi = 10 \text{ kV/mm}$ based on the parameter study performed in Section 3.6.3. Again, two different finite element discretizations are used to outline the mesh independency of the employed strong discontinuity approach and the proposed account of the electric displacement saturation in Section 3.5. The coarse mesh consists of 1506 Q1 finite elements and the fine mesh has 2692 Q1 elements. Both are refined in the region where the crack is supposed to propagate which is illustrated in Figure 3.26.

Next, the numerical simulation of the crack propagation is performed for the above specified material parameters and loading conditions. The evolution of the crack path over time/applied displacement when no account of electric displacement saturation is made is

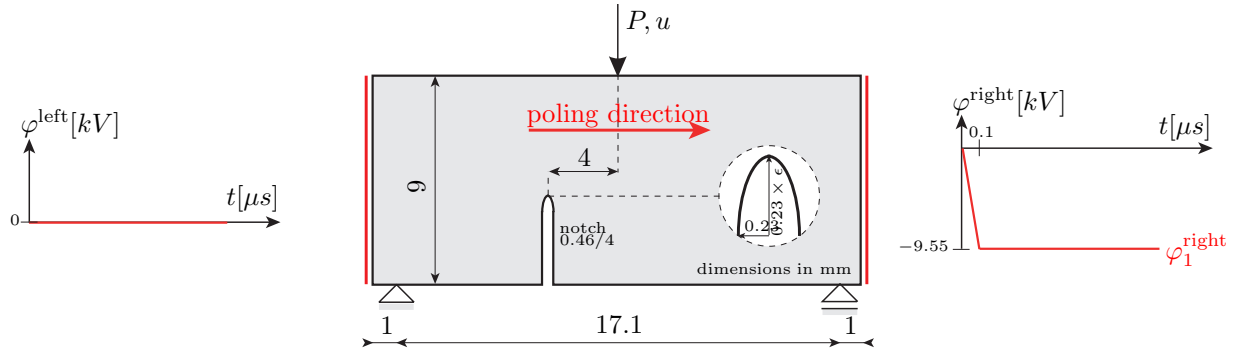


Figure 3.25: Off-centered three point bending test. Illustration of the geometry and loading of the PZT-4 piezoelectric ceramic plate with a pre-existing off-centered vertical notch. The specimen is loaded mechanically by an imposed displacement at the center of the top surface. The electrical loading is applied in the form of a zero electric potential φ^{left} at the left surface and a non-zero electric potential φ^{right} at the right surface with the poling direction being oriented from the left towards the right surface.

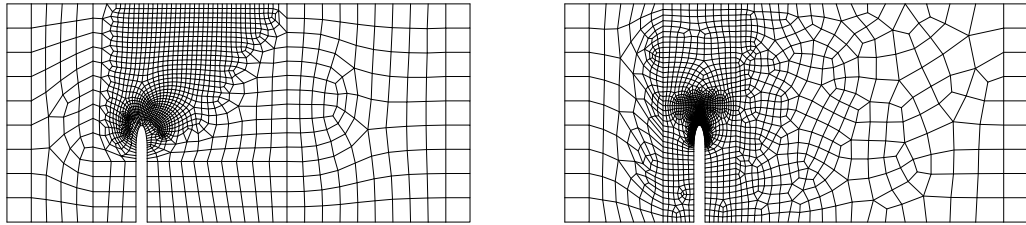


Figure 3.26: Off-centered three point bending test. Illustration of the coarse (left) and fine (right) finite element meshes consisting of 1506 and 2692 Q1 finite elements, respectively. Both meshes are refined in the region where the crack is supposed to propagate.

shown in Figure 3.27. One can see for the coarse and the fine finite element meshes, that the crack turns to the right as it progresses in vertical direction. Of course, no electric displacement saturation zone develops. When accounting for the electric displacement saturation one obtains the results shown in Figure 3.28 which even show a more distinct vertical orientation when the crack starts from the tip of the pre-existing notch. Again, a electric displacement saturation zone develops and travels with the crack tip. Note that for this example the range of the plotted parameter $1 - \exp(-|I_6|/\xi)$ is $[0, 0.5]$ to make the otherwise even smaller saturation zone more visible. It can furthermore be seen, that the orientation of the electric saturation zone is normal to the horizontal poling direction rather than tangential to the crack path orientation which is consistent with the originally proposed strip saturation model of GAO ET AL. [116]. It can be observed in both Figures 3.27 and 3.28 that the crack advances earlier for the coarse mesh but the final result of the crack path remains mesh independent.

A final study of the effect of the saturation exponent ξ is made in Figure 3.29. There the final crack path using the coarse and fine finite element discretization is shown for different values $\xi = 3, 5, 10, 20, \infty \text{ kV/mm}$ and compared with the experimental results reported in PARK [278] and PARK & SUN [280]. Again, one can observe that the smaller the saturation exponent, i.e. the larger the electric displacement saturation zone, the more vertical does the crack propagate. For too small values of ξ an unphysical final crack path is obtained due to the appearance of a too large electric displacement saturation zone. Without electric displacement saturation the crack turns to the right too early which can

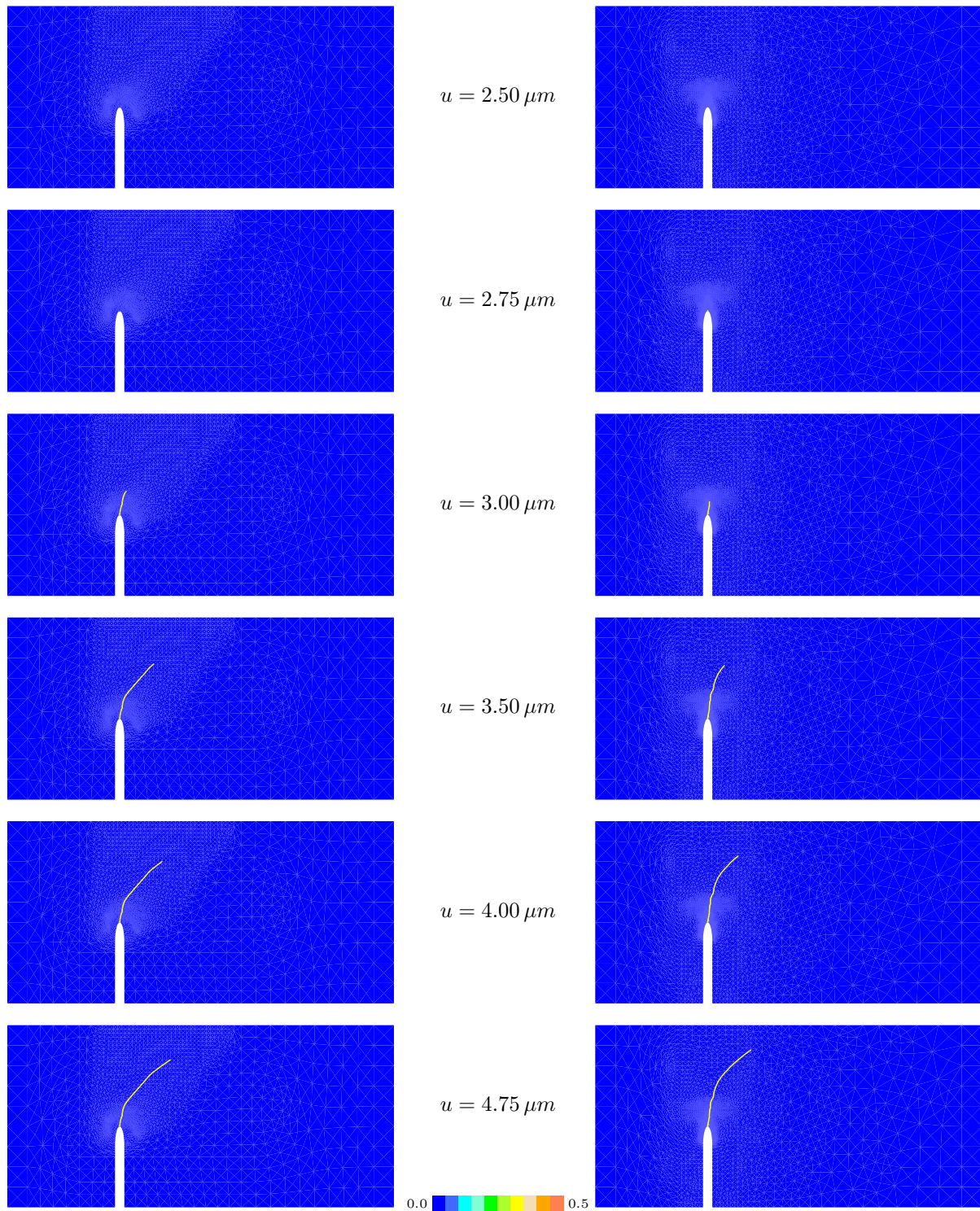


Figure 3.27: Off-centered three point bending test. Illustration of the crack propagation path when electric displacement saturation is not accounted for, i.e. $\xi \rightarrow \infty$ for the coarse mesh (left column) and the fine mesh (right column). The crack turns to the right towards the point where the mechanical loading is applied. The crack starts to propagate earlier for the coarse mesh but the final crack paths are mesh independent.

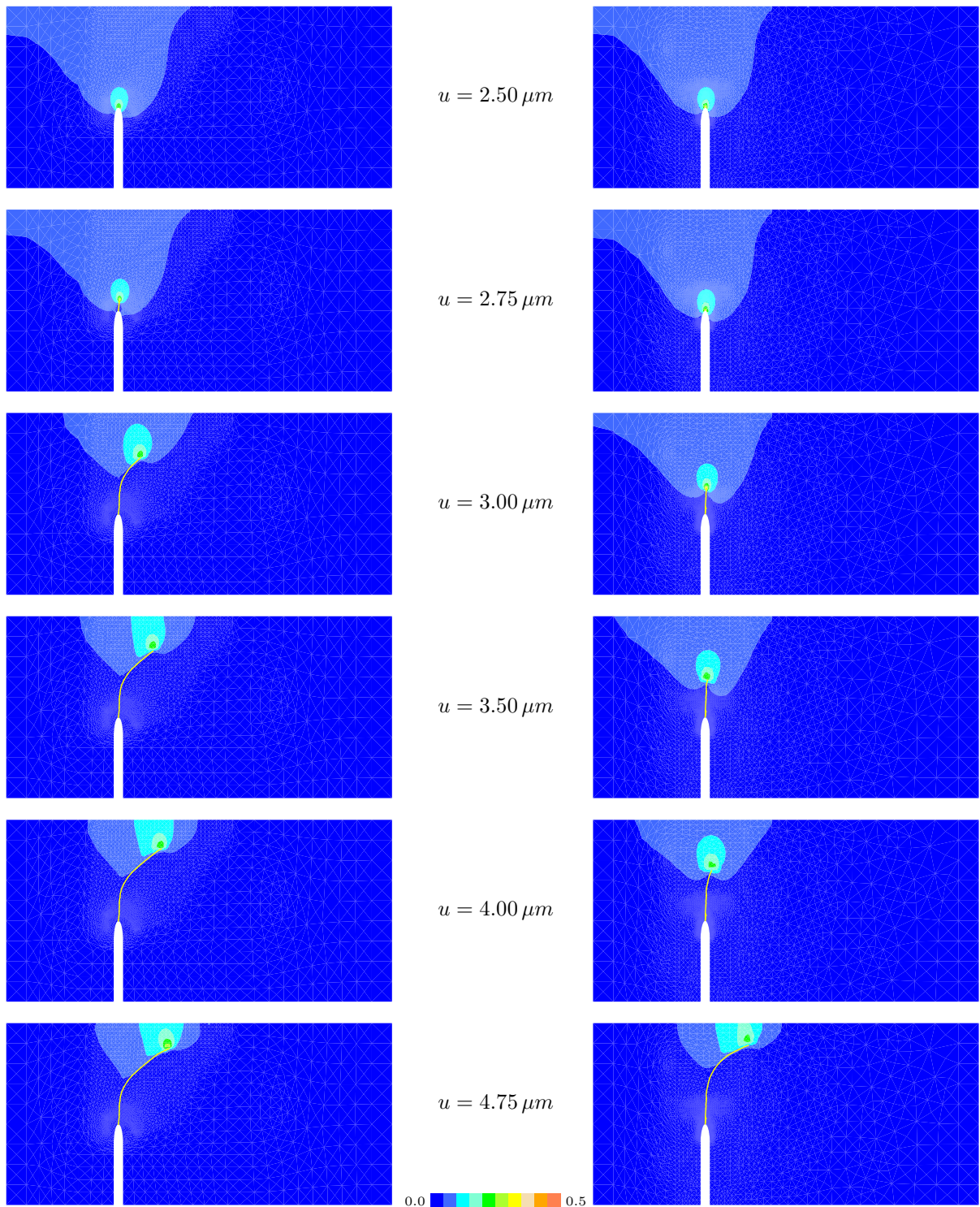


Figure 3.28: Off-centered three point bending test. Illustration of the crack propagation path when electric displacement saturation is accounted for by a saturation exponent of $\xi = 10 \text{ kV/mm}$. Plotted is the value $1 - \exp(-|I_6|/\xi)$ which shows that the electric saturation zone is propagation along with the advancing crack tip. The crack is oriented even more vertical in the beginning of the propagation and subsequently also turns to the right towards the point where the mechanical loading is applied. The crack starts to propagate earlier for the coarse mesh but the final crack paths are mesh independent.

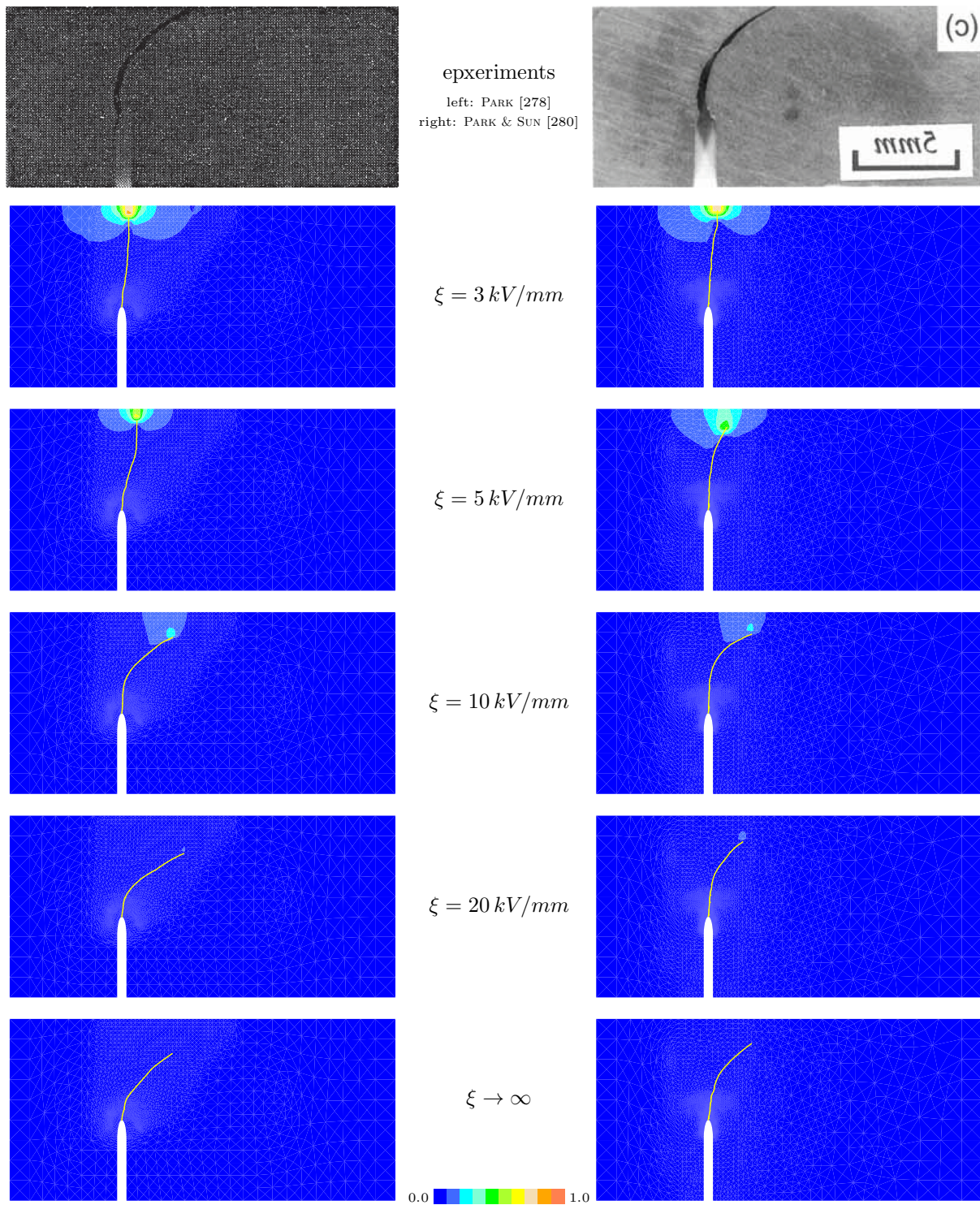


Figure 3.29: Off-centered three point bending test. Illustration of the final crack path for different values of the saturation exponent $\xi = 3, 5, 10, 20, \infty \text{ kV/mm}$ and for the coarse (left column) and fine (right column) finite element discretization. The smaller the saturation exponent, the more vertical is the crack path. Too small values of ξ result in non-physical crack path. When not accounting for electric displacement saturation the initial vertical crack path of the experimental results can not be re-produced. The choice of $\xi = 10 \text{ kV/mm}$ is in good agreement with the experimentally observed crack path.

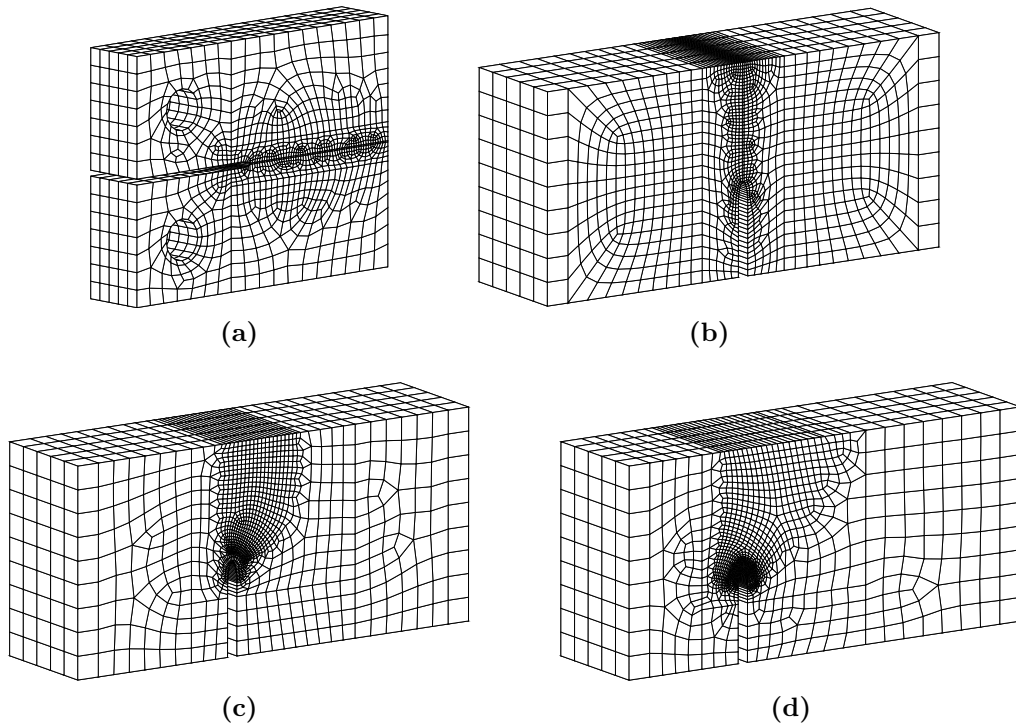


Figure 3.30: Finite element discretization of the (a) compact tension test in terms of 5385 Q1 finite elements and the three point bending test with notch location A in (b), notch location B in (c), and notch location C in (d) in terms of 5660, 5575, and 6765 Q1 finite elements, respectively.

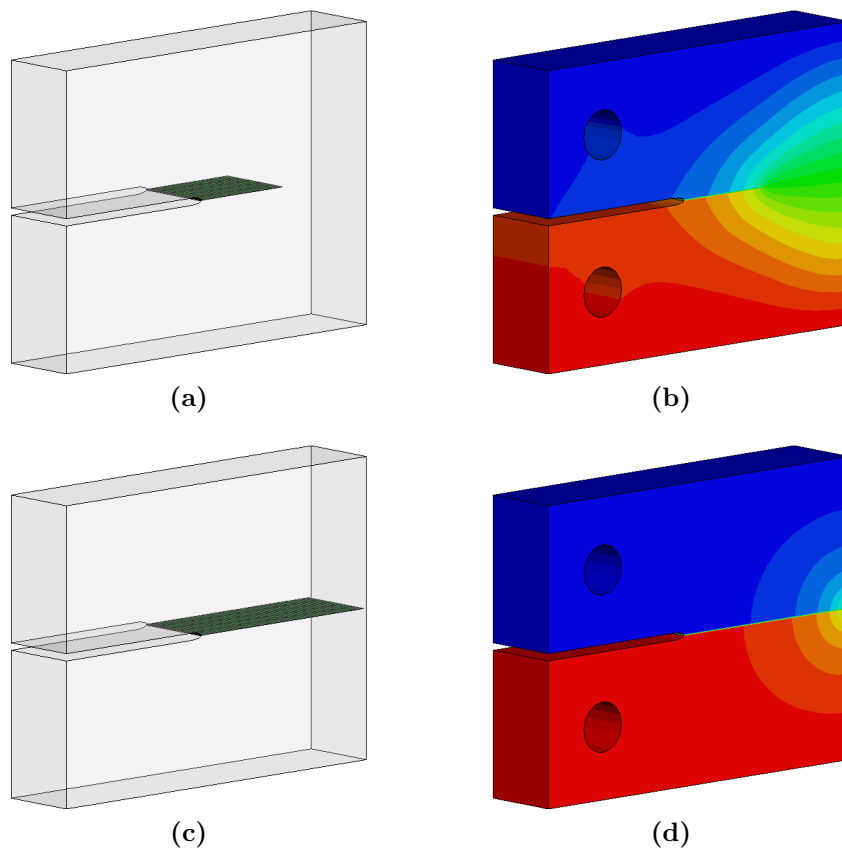


Figure 3.31: 3D compact tension test. Numerical results for the crack path in an intermediate (a) and the final (c) stage as well as corresponding electric potential distributions (b,d).

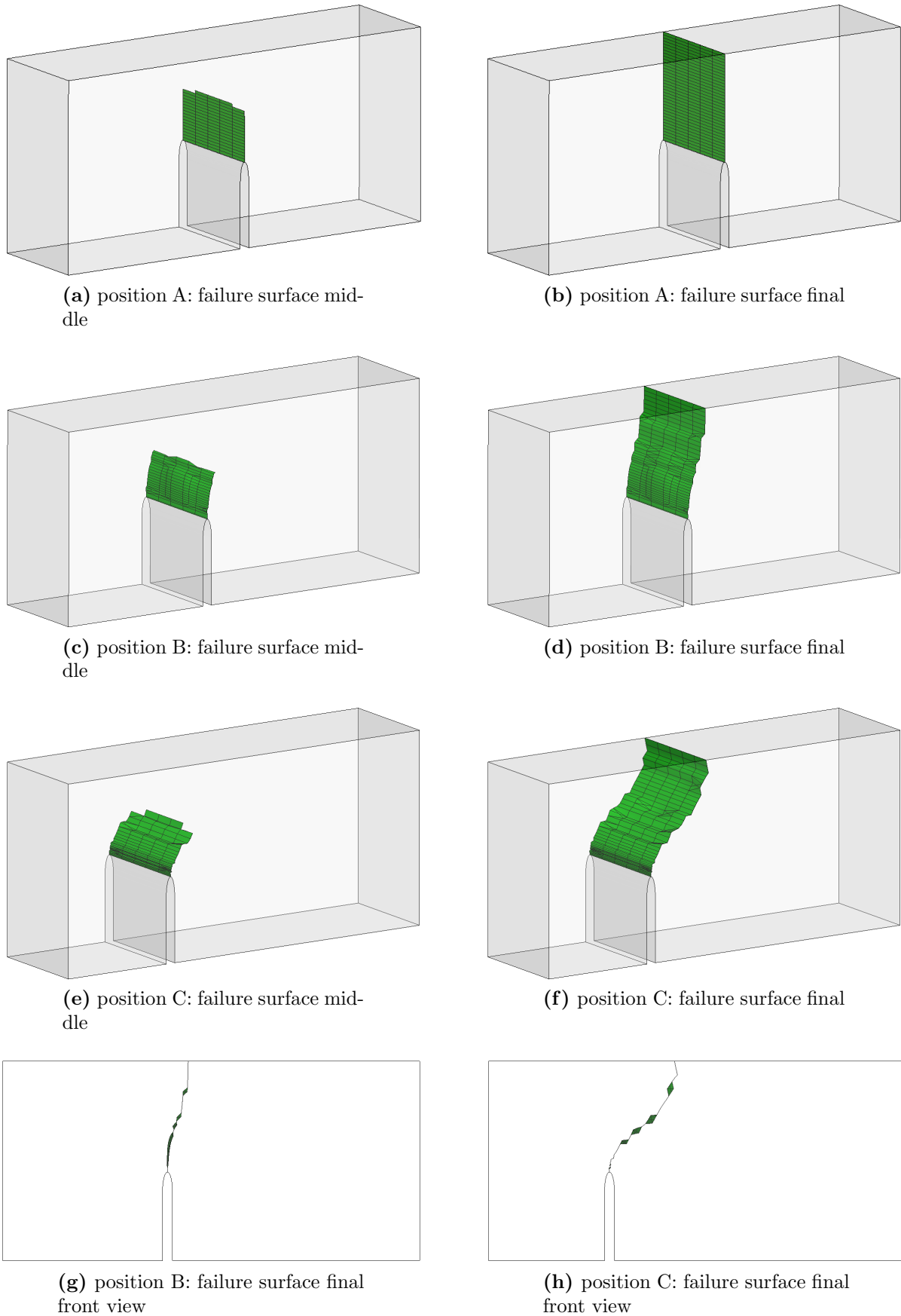


Figure 3.32: 3D three-point bending test. Numerical results in terms of intermediate (a,c,e) and final (b,d,f) crack paths corresponding to the different notch locations A, B, and C together with a front view for the latter two (g,h).

especially be seen for the coarse mesh. The proposed value of $\xi = 10 \text{ kV/mm}$ is able to capture the experimental results very well also for this off-centered three point bending test.

It is emphasized that previous numerical studies [210, 248, 369] could not reproduce the curved crack path as observed in the experiments of PARK & SUN [280]. To the authors knowledge, the simulations presented in this work for the first time provide numerical results consistent with the experimental data obtained in PARK & SUN [280] when it comes to the computational prediction of the crack path for the off-centered three point bending test.

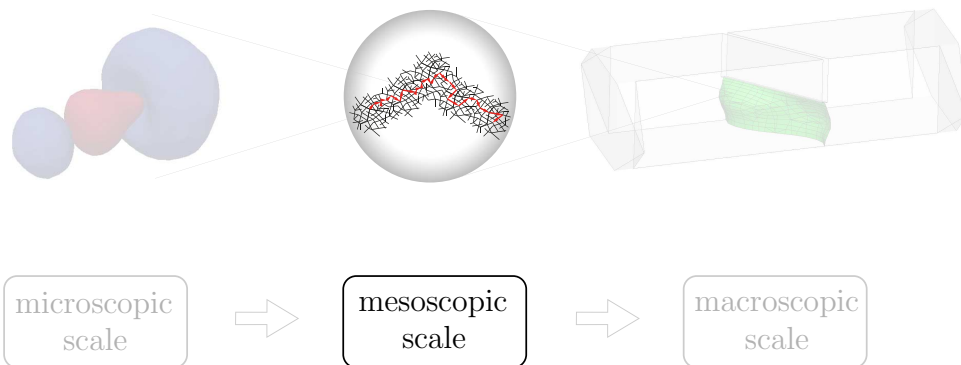
3.6.5 Fracture in piezoelectric ceramics - 3D simulations

Finally, the new finite elements to account for failure in electromechanical coupled materials within the three-dimensional setting developed in Section 3.3 by the incorporation of new constant and linear separation modes are employed for the modeling of fracture in 3D piezoelectric ceramics. The two examples of interest are again the compact tension test and the three point bending test with different notch locations A, B, and C distinguished by their distance from the beam's central axis given as 0, 2, 4 mm, respectively. Geometry, loading as well as material parameters are the same as used in the previous two Sections 3.6.3 and 3.6.4 but without an account for the effect of electric displacement saturation. The finite element discretization consisting of 5 element layers in thickness direction is illustrated in Figure 3.30.

The numerical results for the compact tension test are shown in Figure 3.31 in terms of an intermediate and the final crack path as well as the electric potential distribution, agreeing well with the results obtained in Section 3.6.3 for the plane setting. The numerical results in terms of the obtained crack paths for the three point bending test and the various notch locations are given in Figure 3.32, again agreeing well with the results from the plane setting. For the determination of the crack paths, the proposed combination of the global tracking algorithm in Section 2.4.2 and the marching cubes algorithm in Section 2.4.3 for purely mechanical materials is extended in this section to electromechanical coupled materials.

Part II

Modeling materials with network microstructures at the mesoscopic scale



4 The maximal advance path constraint

This chapter presents a non-affine homogenization scheme for materials with random network microstructure following our recently published work in TKACHUK & LINDER [350]. It is based on a newly developed kinematic constraint that links the microscopic deformation of the network to the macroscopic strain of the material. This relation accounts for the network functionality and is established by means of maximal advance paths that are long enough to reach the macroscopic scales of the continuous body and deform accordingly but are also composed of the microscopic fibers that follow the network deformation. The exact distribution of the variable fiber stretch is determined by the principle of minimum averaged free energy, which ultimately allows to derive the homogenized elastic response of the network at equilibrium. Besides the general formulation, the model is presented in detail for the case of tetrafunctional networks, for which the micro-macro relation and the expression for the homogenized elastic stress are derived in a compact and interpretable tensorial form. The performance of the model as well as the convexity and stability of the obtained homogenized response of the material is examined for networks composed of two different types of fibers, namely flexible chains and stiff filaments. The qualitative behavior of the networks predicted for the two considered cases agrees with experimentally observed phenomena for soft materials. This includes a consistent explanation for the difference in the stiffness of elastomers at uniaxial and equibiaxial extension as well as a validation of recent experimental investigations of atypical normal stress amplitudes in biopolymer gels under shear loading.

4.1 Introduction

Materials with random network microstructures are essentially discrete mechanical systems, where single fibers are the basic structural units. The existing theories and models of random networks in the literature can be categorized as done in Table 4.1. The first category includes the discrete models that reproduce the microstructure in detail. Such approach allows to examine networks of different nature and capture the effect of various specific phenomena such as the entropic and enthalpic response of fibers to axial straining and their instant bending [158, 367, 384], initial internal stresses [156, 271], or thermal fluctuations of network junctions [43]. The network simulations provide deep insight into the microscopic mechanisms of the macroscopic response produced by these soft materials. Nevertheless, they often require an enormous computational effort and produce results that display statistic scattering which is different from one generated random network to another.

The alternative class of models discussed in Table 4.1 is based on the mean field approach for the description of random networks. They are commonly used to constitute the material response of continuous solids in finite element simulations. These theories treat the large microscopic networks in terms of average distributions instead of resolving them in detail. In particular, the considered statistical quantities describe the microdeformation of the network. Their relation to the macroscopic strain, which is the main external action on the material, is the key question addressed by these mean field models in different ways. The most obvious assumption is that the microdeformation and the mean quantities defining it change affinely with the deformation gradient of the solid. This can be

Refs.	Geometry	Kinematics	Microdeformation
Discrete models			
[43, 156, 158, 271, 367, 384]	randomly generated discrete network of fibers	stretch and bending of fibers by the corresponding degrees of freedom	generic network deformation as a result of statical or thermodynamical equilibrium
Network average models			
[41, 190, 338, 355]	statistical distribution of fiber geometry in the network	axial stretch of fibers from this distribution	affine deformation of the microstretch distributions
[17, 185, 186, 277]	eight fibers placed on the diagonals of a rectangular box	identical axial stretch of these eight fibers	the rectangular box deforms with principal stretches
[183, 244]	isotropic distribution of fiber orientations	axial stretch as a function of the initial orientation	non-affine microstretch minimizing the averaged energy

Table 4.1: Overview of random network models.

quite commonly observed in the classical models for rubber elasticity [190, 355] as well as for more recent works on semiflexible networks [41, 338]. Comparison to the experimental data [224] as well as the results of discrete network simulations [158, 367] indicate though that the affine assumption is not universally valid. It does not explain numerous phenomena known for soft matter that are attributed to the non-affine character of the microdeformation. In this work two of them are addressed. Those are the difference in the locking strain for uniaxial and equibiaxial loadings of elastomers composed of flexible chains with limiting extensibility [224, 244, 353] as well as the transition from the soft bending dominated to the stiffened stretching dominated response of dilute biological gels composed of semiflexible filaments [147, 158, 271, 367]. In reality the non-affinity comes from both, the peculiar response of fibers and their interaction in the network that is in common highly non-linear, and the complex kinematics of the networks described by the internal degrees of freedom. The latter issue, the adequate representation of the network microdeformation, is a central point for the development of micromechanically based models of soft matter.

Several non-affine models have so far been developed to resolve this issue. The eight-chain model proposed in ARRUDA & BOYCE [17] for rubber-like elastomers and later adopted for other materials [185, 186, 277] postulates the distribution of stretch identical to the stretch of eight particularly aligned filaments. In the seminal work of MIEHE ET AL. [244], the non-affine microsphere model suggests certain variations of stretch constrained by a specific relation to the macroscopic deformation with the exact distribution of stretch determined by the principle of minimal free energy. A similar approach can be found in the analytical model of GLATTING ET AL. [123] with respect to the principle of maximal entropy. The two latter models introduce a concept of the relaxing variable microdeformation that is subject to the kinematic constraints of the macroscopic strain. A different way to introduce non-affinity can be found in KROON [183] where a phenomenological compliance stretch is considered. The concept is in a good agreement with the nature

of the elastic response produced by the microstructure of a solid at equilibrium. Nevertheless, the already existing non-affine network models of this type can be improved by replacing the often artificial design of the micro-macro relation with a physical based relation.

In this chapter a new micromechanically justified construction of the kinematic constraints based on the formalism of *maximal advance paths* in the network is proposed. These paths allow to perform the transition between the microscopic scale of single fibers to the macroscopic scale of the deforming continuous solid. These constraints result in an efficient homogenization scheme inspired by the orientation-based approach proposed of MIEHE ET AL. [244], which is characterized by a well interpretable expression of the homogenized stress in terms of the microscopic fiber forces.

The chapter is organized as follows. In Section 4.2, the statistical description of the network and its microdeformation is introduced. Section 4.3 is devoted to the formulation of *the maximal advance path constraint* for an arbitrary functionality of the network which is the main contribution of this work. Next, a particular case of tetrafunctional networks is chosen and treated in more detail to illustrate the performance of the proposed model. Section 4.4 concerns the relaxation of the microstretch in the network governed by the principle of the minimum averaged free energy and the derivation of the homogenized elastic response of the material at equilibrium. Finally, the performance of the model is investigated in Section 4.5 for two qualitatively different types of fiber response in the form of flexible chains as well as stiff filaments. The predicted non-affine deformation in networks comprised of such fibers allows to explain the difference in stiffening of elastomers under uniaxial and equibiaxial extension as well as the atypical stress responses recently observed in experiments on biopolymer gels.

4.2 Statistical description of random networks

Microscopic networks considered in this chapter have an irregular three-dimensional structure. They are formed by a large number of fibers connected together at junction points. Since one of their dimension dominates over the others, these fibers can be considered essentially as one-dimensional entities like displayed in Figure 4.1.

Following the motivation given in the introductory Section 4.1, this chapter is based on the statistical approach to the treatment of random networks. Within this approach individual fibers are not treated separately but are included into a statistical assembly in which they are differentiated by certain key attributes. In particular, the statistical description proposed in this section classifies the fibers of the network by their initial orientation in the undeformed state similar to WU & VAN DER GIESSEN [388] or MIEHE ET AL. [244]. The deformation of the network is correspondingly not determined by the deformation of single fibers but by the distribution of the deformation parameters over the introduced assembly of fibers. The network total quantities such as the elastic energy are then consistently derived by distribution averaging. This formalism naturally provides the homogenization of random network microstructures.

The proposed statistical description is based on the following assumptions about the network composition, geometry and deformation:

(A1) junction points do not perform any thermal motion, hence they do take certain

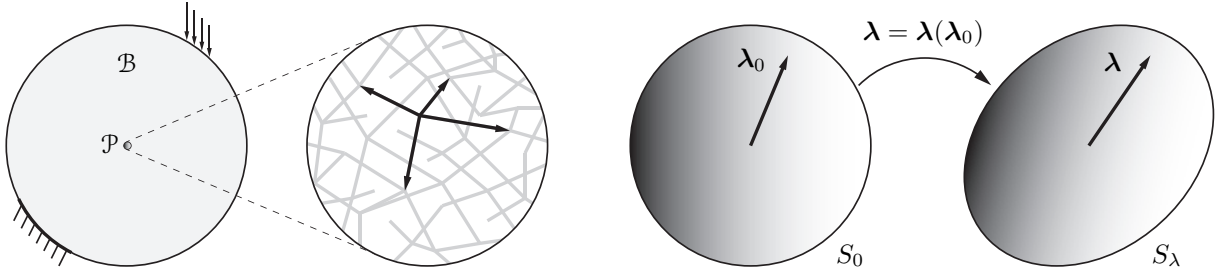


Figure 4.1: The random network microstructure of a continuous solid \mathcal{B} at a material point \mathcal{P} (on the left) formed by long fibers (straight lines) with the end-to-end vectors plotted at one of the junctions (black arrows). Statistical description of a random network (on the right) as an assembly of fibers with initial isotropic orientations $\boldsymbol{\lambda}_0$ uniformly distributed on a unit sphere S_0 and the network deformation defined by the microstretch vector function $\boldsymbol{\lambda}(\boldsymbol{\lambda}_0) : \boldsymbol{\lambda}_0 \in S_0 \mapsto \boldsymbol{\lambda} \in S_\lambda \subset \mathbb{R}^3$.

positions in space;

- (A2) all the fibers in the network are of one single type and have uniform properties (equal molecular weight, contour length, stiffness etc.);
- (A3) in the initial network configuration all the fibers have the same end-to-end distance R_0 and are oriented isotropically in all the directions;
- (A4) the deformation of fibers with equal initial orientation coincides strictly.

With these assumptions, the identification of the network with the assembly of fibers distinguished only by their initial orientation is justified.

Without loss of generality it can be assumed that in the initial configuration all the fibers have a unit stretch $|\boldsymbol{\lambda}_0| = 1$ where the initial stretch vector $\boldsymbol{\lambda}_0 = \mathbf{R}_0/R_0$ is the end-to-end vector \mathbf{R}_0 scaled by the initial end-to-end distance R_0 . The dimensionless stretch vector is preferred over the end-to-end vector for the characterization of the fiber microdeformation. This allows to avoid an otherwise needed account of the length R_0 of the fibers which is whatsoever uniform in the network. Therefore, $\boldsymbol{\lambda}_0$ is a unit vector representing the initial orientation of the fibers by which they are distinguished in the undeformed network. The assembly of all the fibers can furthermore be associated with a unit sphere S_0 , each point on the sphere corresponding to a certain fiber orientation $\boldsymbol{\lambda}_0$ as shown in Figure 4.1. Since all the fibers initially are assumed to be equally distributed in all the directions, or correspondingly over the unit sphere S_0 , the orientation density function scaled by the factor $1/|S_0| = 1/(4\pi)$ has a uniform unit value in the undeformed state, namely $p_0(\boldsymbol{\lambda}_0) = 1$. This function expresses the fraction of fibers in the network with an initial orientation in the infinitesimal vicinity $d\boldsymbol{\lambda}_0$ of $\boldsymbol{\lambda}_0$ as

$$\frac{1}{|S_0|} p_0(\boldsymbol{\lambda}_0) |d\boldsymbol{\lambda}_0| = \frac{1}{|S_0|} |d\boldsymbol{\lambda}_0|. \quad (4.1)$$

The averaging over the network of an arbitrary quantity $\zeta = \zeta(\boldsymbol{\lambda}_0)$ that depends on the initial fiber orientation is then performed by means of the surface integral

$$\langle \zeta \rangle = \frac{1}{|S_0|} \int_{S_0} \zeta(\boldsymbol{\lambda}_0) |d\boldsymbol{\lambda}_0|. \quad (4.2)$$

The deformation of the network within the proposed formalism is described by a vector-valued function $\boldsymbol{\lambda}(\boldsymbol{\lambda}_0)$. Its value is the microstretch vector defined as $\boldsymbol{\lambda} = \mathbf{R}/R_0$ where \mathbf{R} is the end-to-end vector of the deformed fibers with reference orientation $\boldsymbol{\lambda}_0$. This function maps the microsphere S_0 into \mathbb{R}^3 or more particularly, provided the function $\boldsymbol{\lambda}(\boldsymbol{\lambda}_0)$ is continuous, onto a stretch surface S_λ as shown in Figure 4.1 based on

$$\boldsymbol{\lambda}(\boldsymbol{\lambda}_0) : \boldsymbol{\lambda}_0 \in S_0 \mapsto \boldsymbol{\lambda} \in S_\lambda \subset \mathbb{R}^3. \quad (4.3)$$

In the deformed state the averaging of a stretch dependent quantity $\zeta = \zeta(\boldsymbol{\lambda})$ is performed similar to (4.2) as

$$\langle \zeta \rangle = \frac{1}{|S_0|} \int_{S_0} \zeta(\boldsymbol{\lambda}(\boldsymbol{\lambda}_0)) |d\boldsymbol{\lambda}_0|. \quad (4.4)$$

The proposed statistical description contains the most essential information about the network and its deformation that is provided by the stretch vector function. This is essential for the development of the model presented in this chapter. Other orientation-based networks models operate with scalar fields such as the absolute value of the fiber stretch [183, 244], the orientation density function [365, 388], or the end-to-end vector distribution density [123, 211], which is less informative. As an exception, the microsphere-based model in MENZEL & WAFFENSCHMIDT [233] incorporates a variable vector field which though is different to the one presented in this chapter. It does not describe the actual stretch of the fibers but their referential reorientation due to the remodeling of a soft tissue. In this chapter the evolution of the fiber stretch vector represents the two main deformation mechanisms in the network: the axial straining of fibers and their reorientation. The response of fibers to the axial stretch is used to constitute the homogenized elastic properties of the material in Section 4.4. Still, as introduced so far the distribution of the microstretch is arbitrary. Its relation to the macroscopic deformation is established by a special kinematic constraint derived in the next section.

Remarks 4.1. (i) *Only half of the microsphere matters for the above network characterization, since there is no essential difference between the orientations $\boldsymbol{\lambda}_0$ and $-\boldsymbol{\lambda}_0$. To not favour one particular hemisphere it is assumed that the fibers are equally divided between opposite directions.*

(ii) *To preserve the intrinsic central symmetry of the stretch vector distribution within the proposed statistical description, the map (4.3) has to satisfy the condition $\boldsymbol{\lambda}(-\boldsymbol{\lambda}_0) = -\boldsymbol{\lambda}(\boldsymbol{\lambda}_0)$.*

(iii) *The developed model deals with finite material strains as well as large fiber deformations and correspondingly is set up within the non-linear geometry framework. Nevertheless, the tensorial derivations performed in this chapter are for simplicity presented with respect to orthonormal cartesian coordinates. Hence, metric tensors are overall omitted.*

4.3 The maximal advance path constraint

In this work, *network paths* are considered to formulate the constraints relating the microdeformation of the network to the macrodeformation of the continuum body. These paths are formed by the fibers connecting the junctions of the network. As long as the

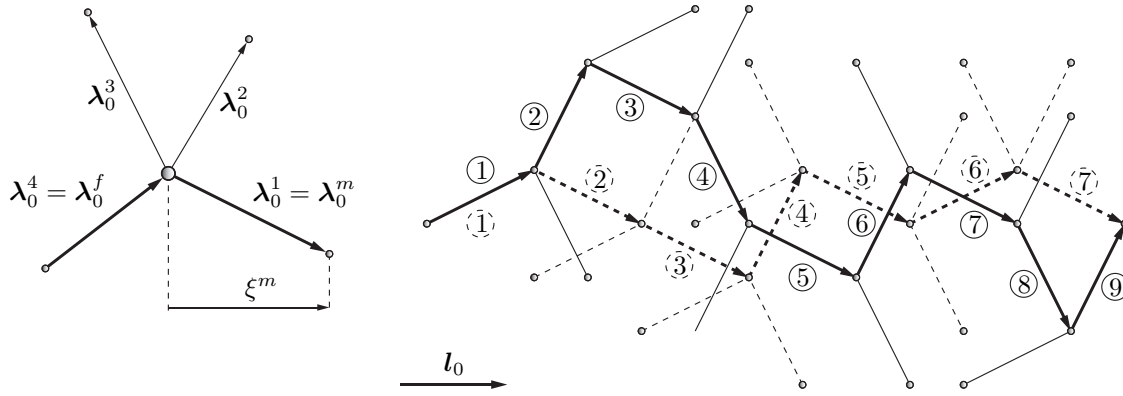


Figure 4.2: The maximal advance path constraint. Illustration of a cross-link belonging to a path and the chain with maximal advance ξ^m along the direction l_0 on the left. Illustration of the effect of functionality f on the straightness of the path on the right where two networks with $f = 3$ (solid lines) and $f = 4$ (additional segments plotted in dashed lines) and the two resulting maximal advance paths are shown. The higher the functionality, the straighter the paths become.

network is static, like in the case of elasticity, these paths remain unbroken during deformation. A path, consisting of i microscopic fibers with stretch vectors λ_i , can connect points of the body at a distance above the microscale of the network, hence ascending to the scale of the macroscopic continuum. The path is though still restricted to the material point level so that the overall deformation is characterized by the deformation gradient \mathbf{F} . This allows to establish the connection between the network scales and the material point scales linking the microdeformation to the macrodeformation.

In particular, specific paths that have the maximal advance in a certain direction, called *maximal advance paths* are considered in this work. They are defined in the initial undeformed configuration of the network where all the chains have unit stretch and are oriented equally in all directions. Let l_0 with $|l_0| = 1$ be a certain direction of interest. Then the advance of a fiber with orientation λ_0 along l_0 is

$$\xi = \lambda_0 \cdot l_0. \quad (4.5)$$

The cumulative distribution function for this random scalar variable is

$$\mathcal{F}_\xi(x) = P(\xi = \lambda_0 \cdot l_0 \leq x) = \frac{1}{|S_0|} \int_{S_{0,x}} |d\lambda_0| = \frac{x+1}{2} \quad (4.6)$$

where $S_{0,x} = \{\lambda_0 \in S_0 : \lambda_0 \cdot l_0 \leq x\}$ is the subset of orientations in which the advance in direction l_0 is lesser than or equal to x . The corresponding probability density function is then computed as

$$p_\xi(x) = \frac{d}{dx} \mathcal{F}_\xi(x) = \frac{1}{2}. \quad (4.7)$$

Consider now a junction, which belongs to a maximal advance path schematically illustrated in Figure 4.2. It is connected to f fibers with initial orientations $\{\lambda_0^i\}_{i=1}^f$, where f is the functionality of the network. Provided the path has come to the junction by the fiber λ_0^f , there will be $f - 1$ remaining fibers along which it may propagate further. These fibers have orientation vectors $\{\lambda_0^i\}_{i=1}^{f-1}$, being random variables distributed uniformly over the unit sphere S_0 and are assumed to be non-correlating. The advance in

the direction \mathbf{l}_0 along these fibers is given by $f - 1$ random variables $\xi^i = \boldsymbol{\lambda}_0^i \cdot \mathbf{l}_0$, each having the distribution (4.6). The maximal advance from the junction in the direction \mathbf{l}_0 is then given by

$$\xi^m = \max\{\xi^i\}_{i=1}^{f-1} \quad (4.8)$$

which is a random quantity characterized by the cumulative distribution function

$$\mathcal{F}_{\xi^m}(x) = P(\xi^m = \max\{\xi^i\}_{i=1}^{f-1} \leq x) = \prod_{i=1}^{f-1} P(\xi^i \leq x) = \left(\frac{x+1}{2}\right)^{f-1} \quad (4.9)$$

and the corresponding probability density function

$$p_{\xi^m} = \frac{f-1}{2} \left(\frac{x+1}{2}\right)^{f-2}. \quad (4.10)$$

Whereas the average advance in the network $\langle \xi \rangle = 0$, the average maximal advance

$$\langle \xi^m \rangle = \int_{-1}^1 x d\mathcal{F}_{\xi^m}(x) = \frac{f-2}{f} \quad (4.11)$$

is non-zero. In addition to the value of the maximal advance ξ^m it is important to know by which fiber it is attained. Let $\boldsymbol{\lambda}_0^m = \arg \max\{\boldsymbol{\lambda}_0 \cdot \mathbf{l}_0, \boldsymbol{\lambda}_0 \in \{\boldsymbol{\lambda}_0^i\}_{i=1}^{f-1}\}$ be the fiber with the maximal advance in the direction \mathbf{l}_0 and belong to the path. Then it has a distribution

$$p^m(\boldsymbol{\lambda}_0, \mathbf{l}_0) = (f-1) \left(\frac{\boldsymbol{\lambda}_0 \cdot \mathbf{l}_0 + 1}{2}\right)^{f-2} \quad (4.12)$$

which is radially symmetric on the unit sphere of orientations S_0 relative to the \mathbf{l}_0 axis. It represents the assembly of fibers $\boldsymbol{\lambda}_0^m$ in the maximal advance path in the direction \mathbf{l}_0 and has the property

$$\langle \boldsymbol{\lambda}_0^m \rangle = \frac{1}{|S_0|} \int_{S_0} \boldsymbol{\lambda}_0 p^m(\boldsymbol{\lambda}_0, \mathbf{l}_0) |d\boldsymbol{\lambda}_0| = \frac{f-2}{f} \mathbf{l}_0. \quad (4.13)$$

The end-to-end vector \mathbf{R}_{l_0} of a long maximal advance path composed of n_{l_0} fibers, where n_{l_0} is large, is then given by

$$\mathbf{R}_{l_0} = n_{l_0} \langle R_0 \boldsymbol{\lambda}_0^m \rangle = n_{l_0} R_0 \frac{f-2}{f} \mathbf{l}_0 \quad (4.14)$$

in terms of the average of the orientation vector in the path (4.13). Once the length of such path is large enough it becomes a macroscopic object. Correspondingly, one can expect that with the macroscopic deformation its end-to-end vector will change affinely following the deformation gradient map \mathbf{F} , i.e.

$$\mathbf{R}_l = \mathbf{F} \mathbf{R}_{l_0} = n_{l_0} R_0 \frac{f-2}{f} \mathbf{l} \quad \text{where } \mathbf{l} = \mathbf{F} \mathbf{l}_0. \quad (4.15)$$

On the other hand this deformed path is composed of the deformed fibers $\boldsymbol{\lambda}^m = \boldsymbol{\lambda}(\boldsymbol{\lambda}_0^m)$ from the assembly (4.12) and \mathbf{R}_l is alternatively given by the path average

$$\mathbf{R}_l = n_{l_0} \langle R_0 \boldsymbol{\lambda}^m \rangle. \quad (4.16)$$

Matching (4.15) and (4.16), one obtains for all path directions \mathbf{l}_0 the relation

$$\boxed{\langle \boldsymbol{\lambda}^m \rangle = \frac{f-2}{f} \mathbf{l} \quad \sim \quad \frac{1}{|S_0|} \int_{S_0} \boldsymbol{\lambda}(\boldsymbol{\lambda}_0) p^m(\boldsymbol{\lambda}_0, \mathbf{l}_0) |d\boldsymbol{\lambda}_0| = \frac{f-2}{f} \mathbf{F} \mathbf{l}_0} \quad (4.17)$$

which provides, since $\mathbf{l}_0 \in S_0$, an infinite set of constraints to the variable microscopic deformation field $\boldsymbol{\lambda}(\boldsymbol{\lambda}_0)$. The derived constraint (4.17) is denoted as the *maximal advance path constraint* (MAPC).

At least one microdeformation will always satisfy the constraint, namely the affine stretch $\bar{\boldsymbol{\lambda}}(\boldsymbol{\lambda}_0) = \mathbf{F} \boldsymbol{\lambda}_0$. In case all the fibers $\boldsymbol{\lambda}_0^m$ in the path deform affinely as $\bar{\boldsymbol{\lambda}}^m = \mathbf{F} \boldsymbol{\lambda}_0^m$ the path itself will also undergo an affine deformation

$$\langle \bar{\boldsymbol{\lambda}}^m \rangle = \mathbf{F} \langle \boldsymbol{\lambda}_0^m \rangle \quad \sim \quad \frac{1}{|S_0|} \int_{S_0} \bar{\boldsymbol{\lambda}}(\boldsymbol{\lambda}_0) p^m(\boldsymbol{\lambda}_0, \mathbf{l}_0) |d\boldsymbol{\lambda}_0| = \frac{f-2}{f} \mathbf{F} \mathbf{l}_0. \quad (4.18)$$

The *full affine network models* (FANM) [355, 388] postulate that the networks strictly follow this microdeformation in response to the macroscopic strain disregarding the nature of fibers in the network. In contrast, the proposed approach in this work suggests that $\bar{\boldsymbol{\lambda}}$ is just one of the many other variations of the microstretch kinematically compatible with the macroscopic deformation. The response of the affine network is later compared to the alternative behavior predicted by the proposed model in Section 4.5.

The micro-macro relation (4.17) takes the form of a linear 1-type Fredholm integral equation and depends on the function $\boldsymbol{\lambda}(\boldsymbol{\lambda}_0)$ which has an essential property of negative symmetry as pointed out in Remark 4.1. Therefore only its values in one hemisphere of orientations matter so that the average of the fiber stretch vector in the deformed path can be alternatively written as

$$\langle \boldsymbol{\lambda}^m \rangle = \frac{1}{|S_0|} \int_{S_0} \boldsymbol{\lambda}(\boldsymbol{\lambda}_0) \tilde{p}^m(\boldsymbol{\lambda}_0, \mathbf{l}_0) |d\boldsymbol{\lambda}_0| \quad (4.19)$$

where $\tilde{p}^m(\boldsymbol{\lambda}_0, \mathbf{l}_0) = \frac{1}{2} [p^m(\boldsymbol{\lambda}_0, \mathbf{l}_0) - p^m(-\boldsymbol{\lambda}_0, \mathbf{l}_0)]$. Since $\tilde{p}^m(\boldsymbol{\lambda}_0, -\mathbf{l}_0) = -\tilde{p}^m(\boldsymbol{\lambda}_0, \mathbf{l}_0)$, another property of the assembly average is

$$\langle \boldsymbol{\lambda}^m \rangle|_{\mathbf{l}_0=-\mathbf{l}_0} = \frac{1}{|S_0|} \int_{S_0} \boldsymbol{\lambda}(\boldsymbol{\lambda}_0) \tilde{p}^m(\boldsymbol{\lambda}_0, -\mathbf{l}_0) |d\boldsymbol{\lambda}_0| = -\langle \boldsymbol{\lambda}^m \rangle. \quad (4.20)$$

As long as the right hand side of (4.17) is an odd function of \mathbf{l}_0 it is sufficient that the equality is satisfied for path directions \mathbf{l}_0 spanning only half of the orientation space, i.e. the constraint (4.17) is a Fredholm type equation on a hemisphere $S_0^{1/2}$:

$$\boxed{\begin{aligned} \frac{1}{|S_0|} \int_{S_0} \boldsymbol{\lambda}(\boldsymbol{\lambda}_0) \tilde{p}^m(\boldsymbol{\lambda}_0, \mathbf{l}_0) |d\boldsymbol{\lambda}_0| &= \frac{f-2}{f} \mathbf{F} \mathbf{l}_0 \quad \forall \mathbf{l}_0 \in S_0^{1/2} \\ \text{with } \boldsymbol{\lambda} : S_0^{1/2} &\rightarrow \mathbb{R}^3, \quad \boldsymbol{\lambda}(-\boldsymbol{\lambda}_0) = -\boldsymbol{\lambda}(\boldsymbol{\lambda}_0), \quad \tilde{p}^m(\boldsymbol{\lambda}_0, \mathbf{l}_0) : S_0^{1/2} \times S_0^{1/2} \rightarrow \mathbb{R} \end{aligned}} \quad (4.21)$$

A closer examination of the kernel function $\tilde{p}^m(\boldsymbol{\lambda}_0, \mathbf{l}_0)$ of the Fredholm integral operator in (4.21) reveals that it is a polynomial for the natural values of the network functionality $f \in \mathbb{N}$. It can be written as a finite series expansion

$$\tilde{p}^m(\boldsymbol{\lambda}_0, \mathbf{l}_0) = \sum_{\alpha} \phi_{\alpha}(\boldsymbol{\lambda}_0) \psi_{\alpha}(\mathbf{l}_0) \quad (4.22)$$

where $\alpha \in \{1, \dots, a\} = \mathcal{A}$ and $\{\phi_\alpha(\boldsymbol{\lambda}_0)\}_{\alpha=1}^a$ and $\{\psi_\alpha(\mathbf{l}_0)\}_{\alpha=1}^a$ are linearly independent so that the Fredholm integral operator has a finite rank and its image is a linear combination of $\{\psi_\alpha(\mathbf{l}_0)\}_{\alpha=1}^a$.

As long as the affine stretch satisfies the maximal advance path constraint (4.18), the integral equation (4.21) can be rewritten in a homogeneous form as

$$\frac{1}{|S_0|} \int_{S_0} [\boldsymbol{\lambda}(\boldsymbol{\lambda}_0) - \bar{\boldsymbol{\lambda}}(\boldsymbol{\lambda}_0)] \tilde{p}^m(\boldsymbol{\lambda}_0, \mathbf{l}_0) |d\boldsymbol{\lambda}_0| = \mathbf{0} \quad (4.23)$$

in terms of the difference of the microstretch $\boldsymbol{\lambda}$ and the affine stretch $\bar{\boldsymbol{\lambda}}$. Using the series expansion (4.22), one can further derive

$$\sum_{\alpha=1}^a \left\{ \frac{1}{|S_0|} \int_{S_0} [\boldsymbol{\lambda}(\boldsymbol{\lambda}_0) - \bar{\boldsymbol{\lambda}}(\boldsymbol{\lambda}_0)] \phi_\alpha(\boldsymbol{\lambda}_0) |d\boldsymbol{\lambda}_0| \right\} \psi_\alpha(\mathbf{l}_0) = \mathbf{0} \quad \forall \mathbf{l}_0 \in S_0. \quad (4.24)$$

Due to the linear independence of $\{\psi_\alpha(\mathbf{l}_0)\}_{\alpha=1}^a$, (4.24) is satisfied if and only if

$$\frac{1}{|S_0|} \int_{S_0} [\boldsymbol{\lambda}(\boldsymbol{\lambda}_0) - \bar{\boldsymbol{\lambda}}(\boldsymbol{\lambda}_0)] \phi_\alpha(\boldsymbol{\lambda}_0) |d\boldsymbol{\lambda}_0| = \mathbf{0} \quad \forall \alpha \in \mathcal{A} \quad (4.25)$$

so that the maximal advance path constraint (4.21) is essentially equivalent to a finite set of constraints (4.25).

For an illustrative purpose the detailed presentation of the maximal advance path constraint and the resulting homogenization scheme in the remaining part of this work is limited to networks of functionality $f = 4$. Firstly, such networks are most typical for vulcanized rubbers and biopolymers [106]. Secondly, for this value of functionality the proposed micro-macro constraint takes a very particular intuitive form. The average maximal advance (4.11) in the undeformed configuration takes with $f = 4$ the value $\langle \xi^m \rangle = 1/2$. This means that the maximal advance paths in tetrafunctional networks are quite far from being straight. Correspondingly, one can expect an essential non-affinity due to the potential stretch redistribution which is subject to the constraint (4.21). To obtain the equivalent finite set of constraints (4.25), consider the particular expression the kernel \tilde{p}^m takes for $f = 4$, i.e.

$$\tilde{p}^m(\boldsymbol{\lambda}_0, \mathbf{l}_0) = \frac{1}{2} \left[3 \left(\frac{\boldsymbol{\lambda}_0 \cdot \mathbf{l}_0 + 1}{2} \right)^2 - 3 \left(\frac{-\boldsymbol{\lambda}_0 \cdot \mathbf{l}_0 + 1}{2} \right)^2 \right] = \frac{3}{2} \boldsymbol{\lambda}_0 \cdot \mathbf{l}_0 \quad (4.26)$$

which is a polynomial in terms of cartesian coordinates of the initial orientation vector $\boldsymbol{\lambda}_0 = [x_0, y_0, z_0]$ and the path direction vector $\mathbf{l}_0 = [\tilde{x}_0, \tilde{y}_0, \tilde{z}_0]$ with $\boldsymbol{\lambda}_0 \cdot \mathbf{l}_0 = x_0 \tilde{x}_0 + y_0 \tilde{y}_0 + z_0 \tilde{z}_0$. The kernel can be written in the form of the series expansion (4.22) with

$$\{\phi_\alpha(\boldsymbol{\lambda}_0)\}_{\alpha=1}^3 = \{x_0, y_0, z_0\} \quad \text{and} \quad \{\psi_\alpha(\mathbf{l}_0)\}_{\alpha=1}^3 = \left\{ \frac{3}{2} \tilde{x}_0, \frac{3}{2} \tilde{y}_0, \frac{3}{2} \tilde{z}_0 \right\}. \quad (4.27)$$

With the particular set of linearly independent $\{\phi_\alpha(\boldsymbol{\lambda}_0)\}_{\alpha=1}^3$ given in (4.27) the three vectorial constraints (4.25) can be represented in the following tensorial form

$$\frac{1}{|S_0|} \int_{S_0} [\boldsymbol{\lambda}(\boldsymbol{\lambda}_0) - \bar{\boldsymbol{\lambda}}(\boldsymbol{\lambda}_0)] \otimes \boldsymbol{\lambda}_0 |d\boldsymbol{\lambda}_0| = \mathbf{0}. \quad (4.28)$$

The average of the dyadic product $\langle \bar{\boldsymbol{\lambda}} \otimes \boldsymbol{\lambda}_0 \rangle$ can be easily found as

$$\frac{1}{|S_0|} \int_{S_0} \bar{\boldsymbol{\lambda}}(\boldsymbol{\lambda}_0) \otimes \boldsymbol{\lambda}_0 |d\boldsymbol{\lambda}_0| = \mathbf{F} \cdot \frac{1}{|S_0|} \int_{S_0} \boldsymbol{\lambda}_0 \otimes \boldsymbol{\lambda}_0 |d\boldsymbol{\lambda}_0| = \frac{1}{3} \mathbf{F} \quad (4.29)$$

with the help of the identity $\langle \boldsymbol{\lambda}_0 \otimes \boldsymbol{\lambda}_0 \rangle = \frac{1}{3} \mathbf{1}$. This ultimately allows to obtain the formulation of the maximal advance path constraint for *tetrafunctional* networks in the form

$$\frac{1}{|S_0|} \int_{S_0} \boldsymbol{\lambda}(\boldsymbol{\lambda}_0) \otimes \boldsymbol{\lambda}_0 |d\boldsymbol{\lambda}_0| = \frac{1}{3} \mathbf{F} \quad (4.30)$$

which appears to be very natural. Indeed, the term $\boldsymbol{\lambda} \otimes \boldsymbol{\lambda}_0$ in a certain way represents the deformation of a single fiber, as it maps the initial unit orientation vector $\boldsymbol{\lambda}_0$ of the fiber onto the fiber stretch vector $\boldsymbol{\lambda}$. Correspondingly, (4.30) can be viewed as the relation between the averaged network microdeformation and the local macroscopic deformation represented by \mathbf{F} .

To conclude, this section gives the general formulation of the maximal advance path constraint (4.21). It relates the microdeformation of the network described within the statistical representation introduced in Section 4.2 to the local macroscopic deformation of the material. It is shown that for a given functionality f of the network only a finite set of constraints (4.25) is imposed onto the microstretch $\boldsymbol{\lambda}(\boldsymbol{\lambda}_0)$. The functionality included into the formulation of the constraints is a very important characteristics of the network topology. Its qualitative influence on the kinematics of the network is discussed in the section and the remarks below. Ultimately, for the case of $f = 4$, to which the remaining part of this work corresponds, the maximal advance path constraint is derived in the particular tensorial form (4.30).

Remarks 4.2. (i) *The higher the functionality of the network the larger and closer to 1 is the value of the average maximal advance (4.11) due to the availability of straighter paths in networks with greater number of fibers at each junction.*

(ii) *An increased functionality f of the network results in an increase of the number of the degree of the polynomial (4.22) as well as an increase of independent constraints (4.25) on the microstretch $\boldsymbol{\lambda}$. Correspondingly, for higher values of the network functionality one will observe a smaller deviation from the affine stretches $\bar{\boldsymbol{\lambda}}$ in the network. This agrees with the above remark on the straightness of the maximal advance path. In a path which is too straight there is almost no place for stretch redistribution.*

(iii) *Although the set (4.27) makes use of a particular orthonormal coordinate system in the reference configuration it is invariant to coordinate transformation. That is if one performs a coordinate transformation $\mathbf{Q} : [x_0, y_0, z_0] \rightarrow [x'_0, y'_0, z'_0]$ the set (4.27) can be restored in its particular form by a linear recombination.*

4.4 Network relaxation and homogenized response at equilibrium

The maximal advance path constraint formulated in the previous section does not define the microstretch $\boldsymbol{\lambda}$ but only restricts its variation at a given macroscopic strain. To

constitute ultimately the microdeformation of the network, the principle of minimum free energy is used in this work. It states that within all the kinematically possible microdeformations the fibers will deform so that the total network energy is minimized. This approach was initially proposed in MIEHE ET AL. [244] for the formulation of the non-affine microsphere model of rubber elasticity, which establishes a general homogenization scheme adopted in this work to incorporate the kinematic micro-macro relation developed in the previous section. The elastic response of the network retrieved by this principle can be viewed as a result of microstructure relaxation by the internal degrees of freedom. The latter are statistically represented by the fiber stretch function $\boldsymbol{\lambda}(\boldsymbol{\lambda}_0)$ as described in Section 4.2.

The statistical representation of the network microdeformation exploited so far contains only information about the stretch of the fibers. Consequently, within the proposed approach one can only consider the situation in which the free energy allows for an expression in terms of the fiber stretch. In particular, this can certainly be done in the case when the networks are composed of fibers that only interact at the junctions and themselves have a free energy that simply changes with the axial strain. Unentangled networks of flexible polymer molecules in some swelled and dry elastomers as well as semiflexible biopolymer networks and networks with stiff mechanical filaments fit well into this category.

As long as the energy originates from separate fibers the network total energy Ψ_{net} can be generally computed by the sum of energy contributions $\psi_f(|\boldsymbol{\lambda}|)$ of all its fibers, which can be expressed in terms of the network average as

$$\Psi_{net}[\boldsymbol{\lambda}] = n \langle \psi_f(|\boldsymbol{\lambda}|) \rangle. \quad (4.31)$$

Here n is the initial network density expressing the number of fibers in the unit volume of the undeformed material, to which also the homogenized free energy Ψ_{net} is referred. With respect to the given form of the network energy in (4.31) one can specifically address the variational principle stated above as the *minimum averaged free energy principle*. Its mathematical formulation restricted to the central case of tetrafunctional networks with $f = 4$ is based on the tensorial version of the maximal advance path constraint (4.30) and reads as:

$$\boxed{\begin{aligned} \Psi_{net}[\boldsymbol{\lambda}] \sim \langle \psi_f \rangle &= \frac{1}{|S_0|} \int_{S_0} \psi_f(|\boldsymbol{\lambda}(\boldsymbol{\lambda}_0)|) |d\boldsymbol{\lambda}_0| \xrightarrow{\boldsymbol{\lambda}(\boldsymbol{\lambda}_0)} \min \\ \langle \boldsymbol{\lambda} \otimes \boldsymbol{\lambda}_0 \rangle &= \frac{1}{|S_0|} \int_{S_0} \boldsymbol{\lambda}(\boldsymbol{\lambda}_0) \otimes \boldsymbol{\lambda}_0 |d\boldsymbol{\lambda}_0| = \frac{1}{3} \mathbf{F} \end{aligned}} \quad (4.32)$$

The fiber energy ψ_f is assumed to be a convex, continuous and differentiable function of $|\boldsymbol{\lambda}|$. By the first assumption fiber instabilities are excluded from consideration. The second one guarantees that the functional $\Psi_{net}[\boldsymbol{\lambda}]$ or the average fiber energy $\langle \psi_f \rangle$, when defined, are differentiable with respect to the microstretch function $\boldsymbol{\lambda}$. There are some further properties of ψ_f that define whether the constrained minimization problem (4.32) is well-posed. These are discussed in the next section with respect to two practically important types of fiber responses. So far the existence and uniqueness of a stretch solution $\boldsymbol{\lambda}^*$ is postulated for a yet unspecified set of deformations \mathfrak{F} . The minimizing stretch can be, correspondingly, viewed as a function $\boldsymbol{\lambda}^* = \boldsymbol{\lambda}^*(\mathbf{F})$ of the deformation gradient $\mathbf{F} \in \mathfrak{F} \subset \text{SO}(3)$.

In the remaining part of this section the properties of the equilibrium microdeformation of the network and its relaxed homogenized response resulting from (4.32) are examined. For this purpose consider the Lagrangian of the constrained minimization problem (4.32) which can be written as

$$L[\boldsymbol{\lambda}, \boldsymbol{\nu}] = \frac{1}{|S_0|} \int_{S_0} \psi_f(|\boldsymbol{\lambda}(\boldsymbol{\lambda}_0)|) |d\boldsymbol{\lambda}_0| - \boldsymbol{\nu} : \left(\frac{1}{|S_0|} \int_{S_0} \boldsymbol{\lambda}(\boldsymbol{\lambda}_0) \otimes \boldsymbol{\lambda}_0 |d\boldsymbol{\lambda}_0| - \frac{1}{3} \mathbf{F} \right) \quad (4.33)$$

where $\boldsymbol{\nu}$ is the second order tensor of Lagrange multipliers, as long as the micro-macro constraint (4.30) is tensorial for the considered case of tetrafunctional networks. The Euler-Lagrange equation enforces the vanishing variation of L with the microstretch $\boldsymbol{\lambda}$ at $\boldsymbol{\lambda}^*$. The stationarity condition gives the relation

$$\mathbf{f}_f^* = f_f(|\boldsymbol{\lambda}^*|) \frac{\boldsymbol{\lambda}^*}{|\boldsymbol{\lambda}^*|} = \boldsymbol{\nu} \boldsymbol{\lambda}_0 \quad (4.34)$$

where $\mathbf{f}_f = \partial\psi_f/\partial\boldsymbol{\lambda}$ is the stretch conjugate fiber force which relaxes towards $\mathbf{f}_f^* = \mathbf{f}_f(\boldsymbol{\lambda}^*)$ at equilibrium and $f_f = \partial\psi_f/\partial|\boldsymbol{\lambda}|$ is its magnitude proportional to the actual fiber force $F_f = \partial\psi_f/\partial|\mathbf{R}|$.

Once the equilibrium microstretch response $\boldsymbol{\lambda}^*$ is known for any admissible deformation $\mathbf{F} \in \mathfrak{F}$ the homogenized properties of the material can be determined. In particular, one can find the change of the total free energy of the relaxed network with the variable macroscopic deformation

$$\Psi_{net}^*(\mathbf{F}) = n \langle \psi_f(|\boldsymbol{\lambda}^*|) \rangle = \frac{1}{|S_0|} \int_{S_0} \psi_f(|\boldsymbol{\lambda}^*|) |d\boldsymbol{\lambda}_0|. \quad (4.35)$$

Furthermore, the homogenized mechanical stress can be obtained by the standard reasoning of thermodynamics [66] as the derivative of the free energy with respect to the strain field. The derivation in the deformation gradient results in the first Piola-Kirchhoff stress tensor computed as

$$\mathbf{P} = \partial_{\mathbf{F}} \Psi_{net}^* = n \langle \partial_{\mathbf{F}} \psi_f(|\boldsymbol{\lambda}^*|) \rangle = n \frac{1}{|S_0|} \int_{S_0} \mathbf{f}_f^* \cdot \frac{\partial \boldsymbol{\lambda}^*}{\partial \mathbf{F}} |d\boldsymbol{\lambda}_0|. \quad (4.36)$$

The integral in the right hand side of this equation can be further transformed into the sum

$$\frac{1}{|S_0|} \int_{S_0} \mathbf{f}_f^* \cdot \frac{\partial \bar{\boldsymbol{\lambda}}}{\partial \mathbf{F}} |d\boldsymbol{\lambda}_0| + \frac{1}{|S_0|} \int_{S_0} \mathbf{f}_f^* \cdot \frac{\partial(\boldsymbol{\lambda}^* - \bar{\boldsymbol{\lambda}})}{\partial \mathbf{F}} |d\boldsymbol{\lambda}_0| \quad (4.37)$$

in which the second term is identically zero. To prove this claim, note that the constraint in the form (4.28) is invariantly satisfied by the equilibrium stretch $\boldsymbol{\lambda}^*$ for all \mathbf{F} so that

$$\langle (\boldsymbol{\lambda}^* - \bar{\boldsymbol{\lambda}}) \otimes \boldsymbol{\lambda}_0 \rangle \equiv 0 \quad \Rightarrow \quad \langle \partial_{\mathbf{F}}(\boldsymbol{\lambda}^* - \bar{\boldsymbol{\lambda}}) \otimes \boldsymbol{\lambda}_0 \rangle \equiv 0. \quad (4.38)$$

Contracting this identity with the tensor $\boldsymbol{\nu}$ of Lagrange multipliers yields the equation

$$\frac{1}{|S_0|} \int_{S_0} (\boldsymbol{\nu} \boldsymbol{\lambda}_0) \cdot \frac{\partial(\boldsymbol{\lambda}^* - \bar{\boldsymbol{\lambda}})}{\partial \mathbf{F}} |d\boldsymbol{\lambda}_0| = \mathbf{0} \quad (4.39)$$

in which the left hand side can be identified as the second integral in (4.37) using the relation (4.34). With the help of the identity $\partial_{\mathbf{F}}\bar{\boldsymbol{\lambda}} = \mathbf{1} \otimes \boldsymbol{\lambda}_0$ the remaining part of the expression gives the elastic stress in the form

$$\mathbf{P} = n \frac{1}{|S_0|} \int_{S_0} \mathbf{f}_f^* \otimes \boldsymbol{\lambda}_0 |d\boldsymbol{\lambda}_0| = n \langle \mathbf{f}_f^* \otimes \boldsymbol{\lambda}_0 \rangle \quad (4.40)$$

in terms of fiber forces in the relaxed network. Again, just as the constraint (4.30) the stress is obtained in a very natural form. Similar expressions are generally derived for continuous bodies in which the stress is transmitted by microscopic axial forces [75]. This, in particular, indicates that the statistical description of the microdeformation proposed in Section 4.2 and the maximal-advance path constraint developed in Section 4.3 together adequately represent the kinematics of the network and the continuous solid. With the expression (4.34) for the fiber force vector \mathbf{f}_f^* , the first Piola-Kirchhoff stress tensor can be alternatively derived in a compact way as

$$\mathbf{P} = n \langle (\boldsymbol{\nu} \boldsymbol{\lambda}_0) \otimes \boldsymbol{\lambda}_0 \rangle = \frac{1}{3} n \boldsymbol{\nu}, \quad (4.41)$$

which establishes the stress-like nature of the Lagrange multiplier tensor $\boldsymbol{\nu}$.

It is again emphasized that the obtained particular results are derived in this section for the tetrafunctional networks with $f = 4$ for which the micro-macro constraint is given by (4.30) and the energy related to fiber straining is given by (4.31). Nevertheless the proposed homogenization approach can be easily extended to networks of arbitrary functionality with a free energy other than the one in (4.31). Firstly, one can make use of the more general form of the micro-macro relation (4.25) in the case of $f \neq 4$. Secondly, the variational principle stated in this section is universal and not limited to a particular expression of the free energy.

As concerns the particular model developed in this section, it allows for an efficient numerical implementation by means of a unit sphere discretization and quadrature formulas proposed in [26]. The numerical results illustrating the performance of the proposed approach are given next in Section 4.5 where the non-affine network response is examined qualitatively for two different types of fibers.

4.5 Predicted non-affine microdeformation of flexible and stiff networks

Within the proposed approach the elastic response of soft materials with random microstructures is related to the relaxation of internal degrees of freedom in the network subject to the constraint of the macroscopic deformation. The statistical description of the fiber stretch in the network, the maximal advance path constraint that relates it to the local deformation gradient of the material, and the principle of the averaged free energy that finally constitutes the equilibrium microdeformation are most generally presented in the previous sections. For tetrafunctional networks composed of fibers that only respond to the axial straining the tensorial constraint (4.30) and the identity (4.34) for the stretch and force vectors of the fibers at equilibrium, as well as the expression for the homogenized mechanical stress (4.40) are derived. The presented results are so far obtained for fibers of arbitrary nature, the only assumption taken about their free energy ψ_f is that it

can be expressed as a convex, continuous and differentiable function of the stretch vector $|\boldsymbol{\lambda}|$. In this section two particular cases corresponding to two qualitatively different types of fibers are examined in more detail.

The distinction is made with respect to the absolute value of the stretch at which the minimum of the fiber free energy is attained. Some flexible fibers have the free energy with a minimum at zero end-to-end distance. The response of such fibers is primarily entropic and their zero stretch corresponds to the most probable configuration. Such behavior is typical of flexible polymer chains with the persistence length much smaller than the length of the chain between the adjacent junctions [106]. In the opposite case the fibers are stiff and have the minimal free energy at non-zero elongation. Such response is displayed either by semiflexible biopolymer molecules or by stiff mechanical filaments and corresponds to the limit when the persistence length is comparable or much larger than the fiber dimensions [42]. The network response differs qualitatively for the two considered cases, which altogether cover a broad class of materials [287]. Therefore, the investigation given below is of high relevance.

The main subjects that this examination addresses are the existence and uniqueness of the equilibrium microstretch as the solution to the constrained minimization problem (4.32) as well as the stability of the homogenized material. Furthermore, the peculiar properties of the non-affine networks predicted by the proposed model are discussed based on their correspondence with experimentally observed phenomena.

4.5.1 MAPC predicted non-affine deformation in networks of flexible chains

A free energy with the minimum at zero end-to-end distance is predicted for flexible chains by several models of highest importance for polymer mechanics. Though being a result of idealization, it applies to many real polymer molecules that constitute natural and synthetic elastomers and biogels. With a certain degree of approximation such molecules are viewed as chains of segments that are either freely connected or rotating around the bonds, or, alternatively, can change their orientation relative to the adjacent segments for an enthalpic cost that is small compared to $k_B T$. The latter quantity given in terms of k_B , the Boltzmann's constant, and T , the temperature, is the characteristic kinetic energy of thermal fluctuations. The response to the change of the end-to-end distance $R = |\mathbf{R}|$ produced by such chains is mainly entropic and is in particular described by *the Gaussian chain* [134, 188], *the non-Gaussian freely rotating chain* [190] and *the worm-like chain* [182] models developed within the framework of statistical mechanics. These three mentioned models are summarized in Table 4.2 that contains the particular expressions for their free energy and their chain force plotted qualitatively in Figure 4.3.

In this subsection the microdeformation of networks made of such flexible chains is examined within the proposed homogenization approach. The uniqueness of the equilibrium microstretch is in general proved for this case. It is furthermore shown that the resulting homogenized network stress is stable at finite strains in the case of material incompressibility. The two particular above mentioned chain models, namely the linear Gaussian chain and the nonlinear Langevin chain, are considered in detail. It is shown for the latter case that the microstretch in the network becomes substantially non-affine as chains approach their limiting extensibility. This effect explains qualitatively the character of stress stiffening observed in elastomers at uniaxial and biaxial tension.

Model	Free energy ψ_f	Thermodynamic force F_f
Gaussian chain ^b	$\frac{3}{2}k_B T \frac{R^2}{Nb^2}$	$3k_B T \frac{R}{Nb^2}$
Freely rotating chain ^{b,‡}	$Nk_B T \left(\lambda_r \mathcal{L}^{-1}(\lambda_r) + \ln \frac{\mathcal{L}^{-1}(\lambda_r)}{\sinh \mathcal{L}^{-1}(\lambda_r)} \right)$	$k_B T \frac{1}{b} \mathcal{L}^{-1}(\lambda_r)$
Worm-like chain [*]	$\frac{k_B T}{4l_p} \frac{R^2}{L} \left[2 + \frac{1}{1 - R/L} \right]$	$\frac{k_B T}{4l_p} \left[4 \frac{R}{L} + \frac{1}{(1 - R/L)^2} - 1 \right]$

Table 4.2: Flexible chain models. ^b N is the number of chain segments, b is the Kuhn segment length. [‡] $\lambda_r = R/L$ is the relative stretch with $L = Nb$ being the contour length of the chain, \mathcal{L}^{-1} is the inverse to the Langevin function $\mathcal{L}(\cdot) = \coth(\cdot) - 1/(\cdot)$. ^{*} Given is the approximation of [225] valid in the limit $l_p \ll L$ where l_p is the persistence length of the worm-like chain and L is its contour length.

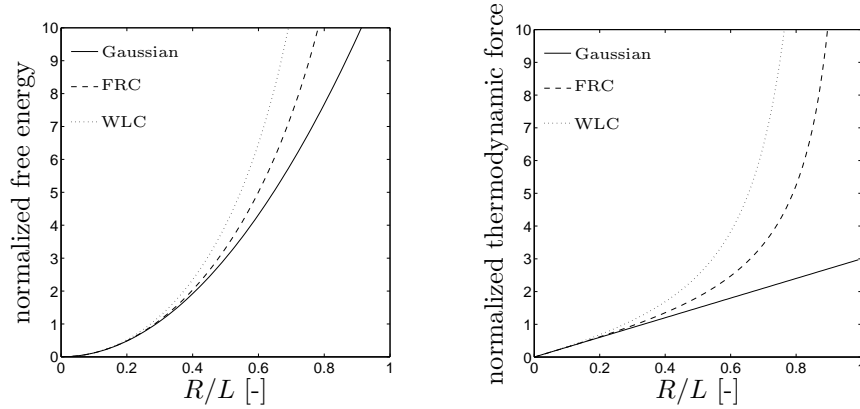


Figure 4.3: The qualitative plots of the free energy (on the left) and the force (on the right) of a flexible chain according to the Gaussian approximation, the freely rotating chain (FRC) and the worm-like chain (WLC) models. The latter two incorporate finite extensibility and display infinite chain stiffening as the end-to-end distance R approaches the limiting value.

To begin with the proof of uniqueness note first that the models of flexible thermally fluctuating chains in common predict a free energy that is always a monotone convex function of the end-to-end distance $|\mathbf{R}|$ or equivalently the stretch $|\boldsymbol{\lambda}|$ as well as the positive entropic force that increases with straining starting with a zero value at the zero separation of the chain ends (see Figure 4.3). This implies that the chain energy as the function of the stretch vector $\psi_f(\boldsymbol{\lambda}) = \psi_f(|\boldsymbol{\lambda}|)$ is strictly convex in \mathbb{R}^3 , i.e. for any $\boldsymbol{\lambda}_1, \boldsymbol{\lambda}_2 \in \mathbb{R}^3$ and any $\alpha \in [0, 1]$

$$\psi_f(|\boldsymbol{\lambda}|) \leq \psi_f(\alpha |\boldsymbol{\lambda}_1| + (1 - \alpha) |\boldsymbol{\lambda}_2|) \leq \alpha \psi_f(|\boldsymbol{\lambda}_1|) + (1 - \alpha) \psi_f(|\boldsymbol{\lambda}_2|) \quad (4.42)$$

where $\boldsymbol{\lambda} = \alpha \boldsymbol{\lambda}_1 + (1 - \alpha) \boldsymbol{\lambda}_2$. As long as the energy of a single fiber is convex in $\boldsymbol{\lambda}$ the network total energy Ψ_{net} or equivalently the network average $\langle \psi_f \rangle$ minimized in (4.32) are also convex with respect to the distribution of stretch in terms of the variable function $\boldsymbol{\lambda}(\boldsymbol{\lambda}_0) : S_0 \mapsto \mathbb{R}^3$. Taking into account that the minimized network energy is bounded below by zero and continuous in $\boldsymbol{\lambda}$ as well as the linearity of the maximal advance path constraint, the solution of the constrained minimization problem (4.32) exists and is unique unless the objective $\Psi_{net}[\boldsymbol{\lambda}]$ is undefined in the whole constraint subspace. This may occur at high macroscopic deformations in networks with infinitely stiffening chains when the network can not deform without violating the limiting extensibility of

the filaments. As long as this scenario is avoided, the deformation gradient \mathbf{F} belongs to the admissible set \mathfrak{F} that can be shown to be convex and the network responds to it with the equilibrium microstretch $\boldsymbol{\lambda}^*(\mathbf{F})$.

Together with the relaxed microdeformation $\boldsymbol{\lambda}^*(\mathbf{F})$ the homogenized network free energy (4.35) is as well defined as a function of the macroscopic strain $\Psi_{net}^*(\mathbf{F})$ for all $\mathbf{F} \in \mathfrak{F}$. Furthermore it will be strictly convex in \mathbf{F} in the whole domain \mathfrak{F} . Indeed, consider two different deformation gradients $\mathbf{F}_1, \mathbf{F}_2 \in \mathfrak{F}$ and their linear combination $\mathbf{F} = \alpha\mathbf{F}_1 + (1 - \alpha)\mathbf{F}_2 \in \mathfrak{F}$ with $\alpha \in [0, 1]$. Let $\boldsymbol{\lambda}_1^*$ and $\boldsymbol{\lambda}_2^*$ be the equilibrium microdeformations for \mathbf{F}_1 and \mathbf{F}_2 , respectively, then their linear combination $\boldsymbol{\lambda} = \alpha\boldsymbol{\lambda}_1^* + (1 - \alpha)\boldsymbol{\lambda}_2^*$ will satisfy the linear micro-macro relation for \mathbf{F} . Correspondingly, the network energy $\Psi_{net}[\boldsymbol{\lambda}]$ at this microdeformation will be greater or equal than the minimum $\Psi_{net}^*(\mathbf{F}) = \Psi_{net}[\boldsymbol{\lambda}^*(\mathbf{F})]$. On the other hand, due to (4.42) it will not exceed the linear combination of $\Psi_{net}[\boldsymbol{\lambda}_1^*]$ and $\Psi_{net}[\boldsymbol{\lambda}_2^*]$. As a result, the inequality

$$\Psi_{net}^*(\mathbf{F}) \leq \Psi_{net}[\boldsymbol{\lambda}] \leq \alpha\Psi_{net}^*(\mathbf{F}_1) + (1 - \alpha)\Psi_{net}^*(\mathbf{F}_2) \quad (4.43)$$

will always hold. The homogenized network free energy, which is convex in \mathbf{F} as obtained for the considered type of the fiber response, does not appropriately constitute the elastic behavior of a solid. The so far considered networks of flexible chains will collapse into a point, since their energy is minimal at zero fiber stretch. In reality the steric repulsions between chains as well as their interaction with the solvent molecules in the case of swelling will counterbalance this tendency so that the material attains a certain finite equilibrium volume [287]. One way to account for this effect is to add a repulsive term to the free energy of single fibers as in [185, 186] which shifts the equilibrium stretch of an unloaded fiber to the non-zero value and corresponds to the case considered in the next subsection 4.5.2. In reality, the volumetric forces are essentially intramolecular and should not be referred to single fibers and therefore be represented in forms other than (4.31). To not get beyond the scope of this work, these intramolecular interactions are assumed to have no effect on the network mechanics. They can be associated phenomenologically with the essential incompressibility of the material and introduced by the additional term $\Psi_{vol}(J)$, where $J = \det \mathbf{F}$, accounting for the volumetric deformation in the total free energy of the material given as

$$\Psi(\mathbf{F}) = \Psi_{vol}(J) + \Psi_{net}^*(\mathbf{F}). \quad (4.44)$$

Such additive split is commonly adopted for hyperelastic materials. The bulk energy Ψ_{vol} represents a steep convex potential well at the minimum $J = 1$ since the steric forces have usually a much greater magnitude compared to the response of flexible chains. These forces are then responsible for the hydrostatic stress contribution resulting from negligible small volume changes. It should be noted that the homogenized free energy given by (4.44) is a polyconvex function of the deformation gradient, since $\Psi_{vol}(J)$ is convex in J and $\Psi_{net}^*(\mathbf{F})$ is convex in \mathbf{F} , and hence constitutes a stable elastic solid [324].

Consider now in particular the case of a network with Gaussian chains. As long as the initial end-to-end distance of chains is equal to the most probable value $R_0 = \sqrt{N}b$, which is a common assumption [17, 244], the free energy can be expressed as $\psi_f = \frac{3}{2}k_B T |\boldsymbol{\lambda}|^2$. The axial stretch conjugate chain force $f_f = 3k_B T |\boldsymbol{\lambda}|$ is then linear in $|\boldsymbol{\lambda}|$, which allows to solve (4.34) for the equilibrium stretch vector as

$$3k_B T |\boldsymbol{\lambda}^*| \frac{\boldsymbol{\lambda}^*}{|\boldsymbol{\lambda}^*|} = \nu \boldsymbol{\lambda}_0 \quad \Leftrightarrow \quad \boldsymbol{\lambda}^* = \frac{\nu}{3k_B T} \boldsymbol{\lambda}_0. \quad (4.45)$$

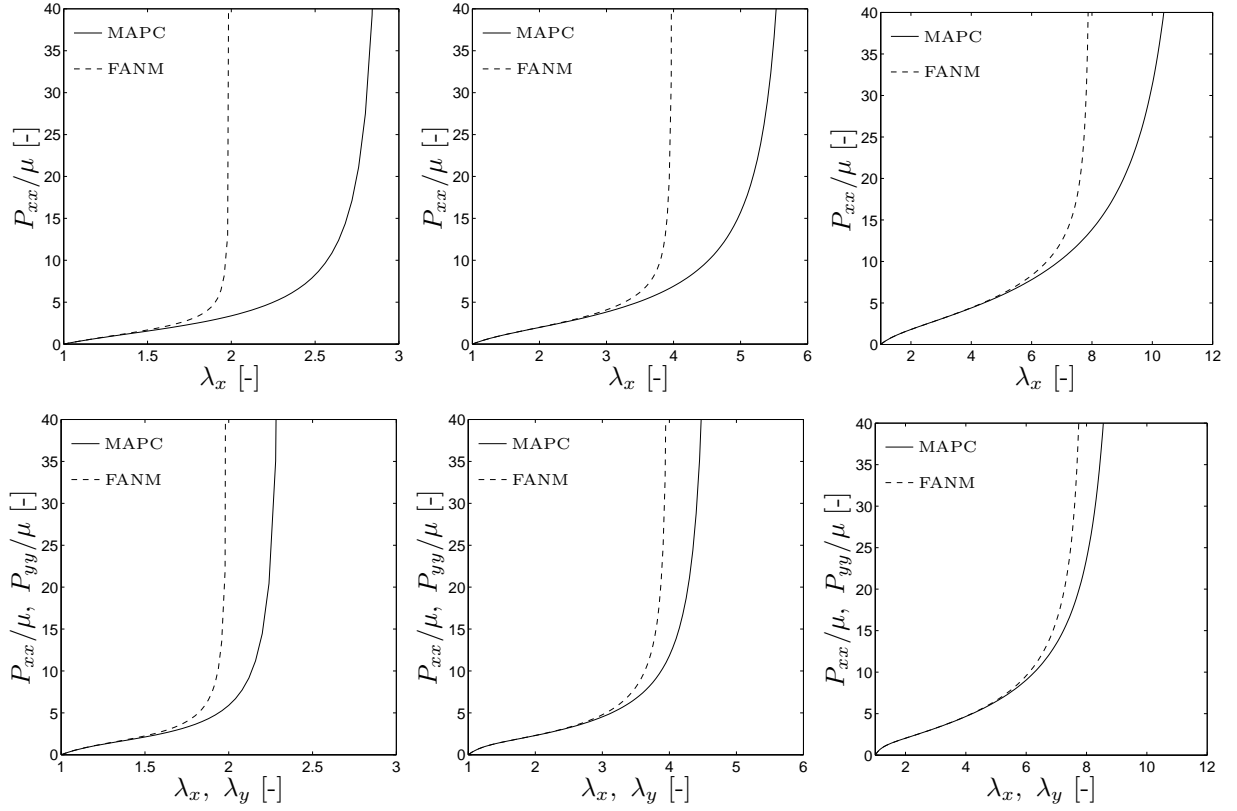


Figure 4.4: Mechanical stresses predicted by the proposed model (MAPC) and the full affine network model (FANM) for uniaxial tension (top row) and equibiaxial tension (bottom row) of a model incompressible material with unit modulus $\mu = nk_B T = 1$, network functionality $f = 4$ in the MAPC model, and three different values of chain extensibility limit $\sqrt{N} = 2, 4, 8$. The proposed non-affine network response is softer and results in different limiting stretches in uniaxial and equibiaxial loading which is not the case for the affine model.

One can see that this microstretch results from an affine transformation of the initial orientations λ_0 by the map $\nu/3k_B T$ which can only satisfy the constraint (4.30) if

$$\langle \lambda^* \otimes \lambda_0 \rangle = \frac{1}{3} \frac{\nu}{3k_B T} = \frac{1}{3} \mathbf{F} \quad \Leftrightarrow \quad \frac{\nu}{3k_B T} = \mathbf{F}. \quad (4.46)$$

Correspondingly, $\lambda^* = \bar{\lambda} = \mathbf{F}\lambda_0$, which implies that the network of Gaussian chains will always deform affinely with the macroscopic strain.

The chain stretch will only redistribute non-affinely if the chain response is substantially non-linear. To illustrate this, the networks composed of non-Gaussian freely rotating chains that possess this property are considered next. For this case the solution to the constrained minimization problem (4.32) can not be derived in closed form. Therefore the equilibrium network microstretch λ and the homogenized stress \mathbf{P} are found numerically. Examined are three model networks with chain sizes $N = 4, 16, 64$ and corresponding limiting stretch values $\lambda^{lim} = \sqrt{N} = 2, 4, 8$. Although the situation of a chain length being equal to only four statistical segments is not well described by the inverse Langevin approximation and is rarely found in real elastomer networks, it is considered here for an illustrative purpose. The proposed model predicts the response of these networks in an essentially different way as the full affine network models [355, 388].

Due to the internal relaxation of the microdeformation accounted by the maximal advance

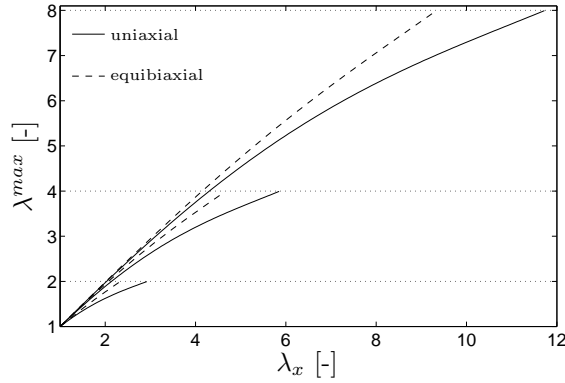


Figure 4.5: Variation of the maximal absolute value of the microstretch λ^{max} with the increase of the macroscopic strain in the uniaxial and equibiaxial tension predicted by the MAPC model for three networks of functionality $f = 4$ composed of chains with different values of extensibility limit $\sqrt{N} = 2, 4, 8$ represented by dotted horizontal lines. When λ^{max} approaches this limit the network stiffens as shown in Figure 4.4.

path constraint, the non-affine network behaves softer. One can conclude this by the elastic stresses that are produced by the affine and non-affine networks and compared in Figure 4.4. The nominal stresses are computed with account of material incompressibility at isochoric uniaxial and equibiaxial tension for the three considered networks. It can be noticed that for the same chain parameters the affine network stiffens at significantly lower strains than the non-affine one. The affinely deformed chains reach the extensibility limit as soon as at least one of the principal stretches approaches λ^{lim} . As a result in both, the uniaxial and the equibiaxial tension, the stress goes to infinity when λ_x gets close to 2, 4, 8 depending on the chain length. The non-affine networks predicted by the proposed approach do behave differently. Once the chains that are aligned closely to the direction of tension get highly extended, the stretch in the network is redistributed so that the already highly stretched chains get lower stretch by means of straining and reorientation of the other chains which results in a decreasing network total energy.

This redistribution is illustrated in Figures 4.5 and 4.6. The former displays the evolution of the maximal absolute stretch value $\lambda^{max} = \max\{|\boldsymbol{\lambda}(\boldsymbol{\lambda}_0)|, \boldsymbol{\lambda}_0 \in S_0\}$ in the three examined networks with the macroscopic deformation for both types of loading. It can be clearly seen that λ^{max} is smaller than the principal stretch λ_x and reaches the extensibility limit λ^{lim} depicted by dotted horizontal lines for the considered chain lengths $N = 4, 16, 64$ at a much higher macroscopic deformations, compared to the affine case. The difference of the stretch at which the affine and the non-affine network stiffen is significant and is nearly as large as 50% in the case of uniaxial loading. Due to the stretch redistribution the network of chains with limiting extensibility $\lambda^{lim} = 8$ can attain the elongation λ_x up to 11.72. In the case of the equibiaxial deformation the difference is not that profound but still present.

This can be further examined by the example of another model network with chains of length $N = 9$ and extensibility limit $\lambda^{lim} = 3$. The distribution of the microstretch $\boldsymbol{\lambda}$ of this network at two different macroscopic strains is shown in Figure 4.6. At both deformations the maximal absolute stretch is close to the limit of 3. However at the uniaxial tension the network is stretched up to $\lambda_x = 4$, which is much larger than the stretch of $\lambda_x = \lambda_y = 3.5$ the network can undergo in the equibiaxial tension. When the material is strained in two directions the network paths oriented closely to the plane of

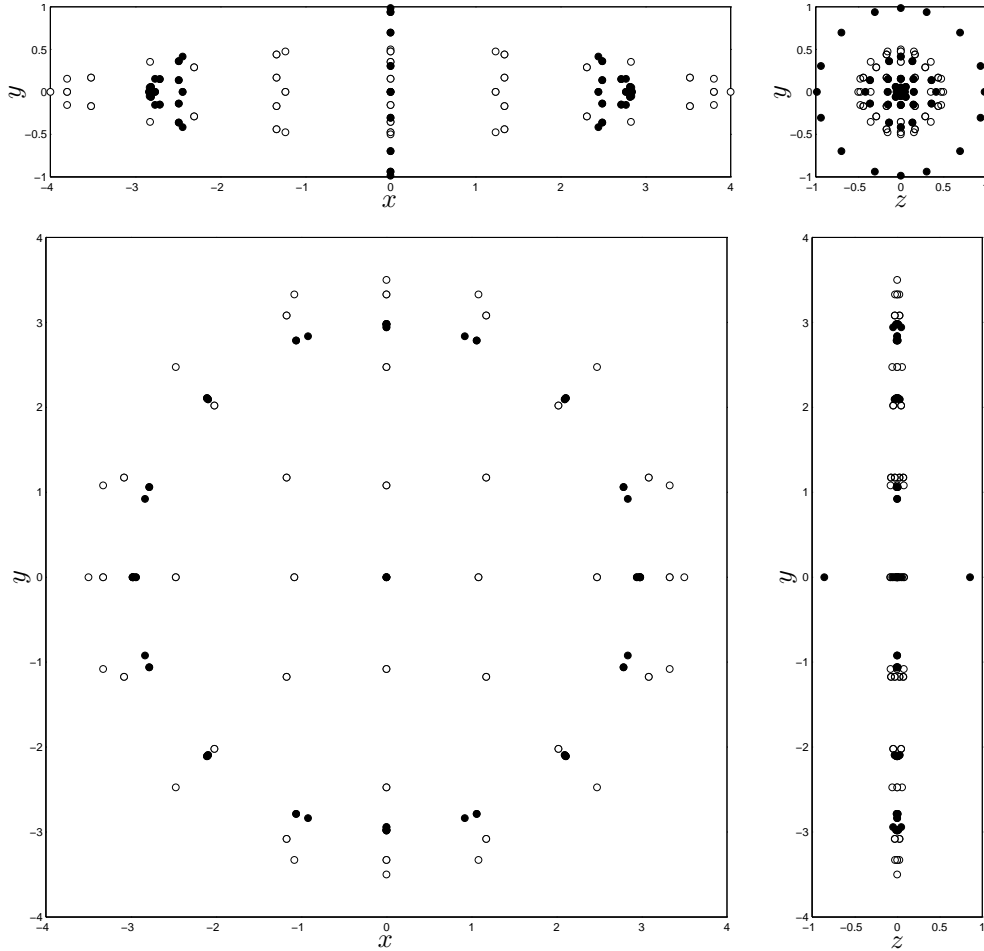


Figure 4.6: Non-affine microstretch λ^* predicted by the MAPC model (filled circles) in a network of chains with extensibility limit $\sqrt{N} = 3$ compared to the affine stretch $\bar{\lambda}$ (empty circles) for uniaxial tension with $\lambda_x = 4$ (top row) and equibiaxial tension with $\lambda_x = \lambda_y = 3.5$ (bottom row). The plotted dots display the end points of the fiber stretch vectors in $x - y$ and $z - y$ plane projections. The fibers have the initial discrete orientations corresponding to the quadrature formula [26] used for the numerical solution.

the biaxial strain have to be also axially strained due to the reasoning given in Section 4.3. This imposes much stronger kinematic constraints on the microstretch of the fibers compared to the uniaxial case for which only a relatively small fraction of paths aligned with the principle direction are significantly extended. As a result there is less freedom for the stretch redistribution and it deviates lesser from the affine distribution, which can be evidently seen in Figure 4.6.

4.5.2 MAPC predicted non-affine deformation in networks of stiff filaments

In this subsection networks comprised out of stiff filaments are considered. These filaments attain the minimum of the free energy at an end-to-end distance which is non-zero. Correspondingly, such fibers can support both tensile and compressive axial loadings which is in contrast to the flexible chains considered in the previous subsection 4.5.1 which only produce positive thermodynamic forces. This behavior is typical for *mechanical microscopic fibers* that constitute paper and various non-woven materials [287]. *Semiflexible*

Model	Free energy ψ_f	Thermodynamic force F_f
Linear spring ^b	$\frac{1}{2}\kappa\frac{(R - R_0)^2}{R_0}$	$\kappa\frac{R - R_0}{R_0}$
Semiflexible chain [#]	$k_B T \frac{\pi^2 l_p}{2L} \left(1 - \frac{R^2}{L^2}\right) + \frac{2k_B T L}{\pi l_p} \left(1 - \frac{R^2}{L^2}\right)^{-1}$	$k_B T \frac{R}{L^2} \left(\frac{4L}{\pi l_p} \left(1 - \frac{R^2}{L^2}\right)^{-2} - \frac{\pi^2 l_p}{L}\right)$

Table 4.3: Stiff filament models. ^b R_0 is the initial length of a fiber, κ is the axial stiffness; for an elastic bar $R_0 = L$ is the length of the bar, $\kappa = EA$, where E is the elastic modulus and A is the cross-section area. [#] In [42] a force to extension relation in terms of the filament contour length L and the persistence length $l_p = \varkappa/k_B T$ is suggested; \varkappa is the bending stiffness; the filament end-to-end distance R_0 in the unloaded state is defined by $1 - (R_0/L)^2 = 2L/(\pi^3/2 l_p)$.

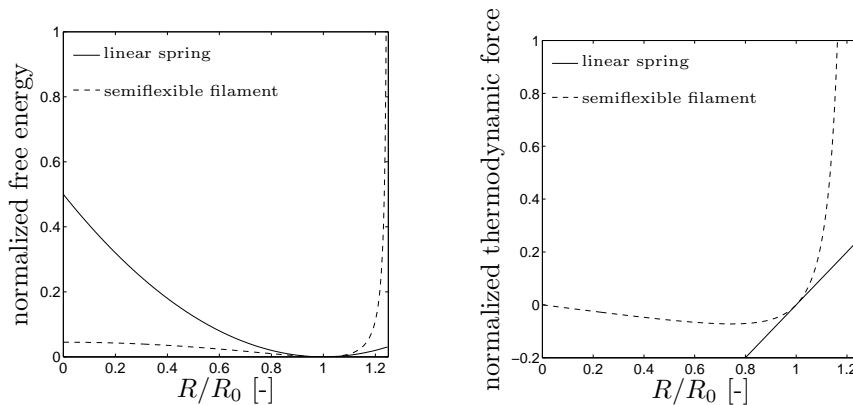


Figure 4.7: Free energy (on the left) and thermodynamic force (on the right) scaled by the stiffness $\partial^2 \psi_f / \partial R^2$ at $R = R_0$ of a linear spring and a semiflexible filament. The latter type of fibers demonstrate anisotropy of the response with respect to tension and compression as well as infinite stiffening when strained up to the full contour length.

biopolymers also belong to the category of stiff filaments. Their mixed entropic/enthalpic response is characterized by an essential anisotropy with respect to tension and compression. Mechanics of semiflexible polymer strands is described by numerous models mainly based on the Kratky-Porod chain representation [40, 182, 222, 223, 383, 387]. A particular model for semiflexible filaments suggested in [42] and the linear elastic spring model are used for the network simulations presented in this subsection and are briefly summarized in Table 4.3. The change of free energy and the predicted axial force due to extension of these two models are shown in Figure 4.7.

What is expected in such situation is that the three-dimensional networks of the initially undeformed fibers display a stable rigidity with respect to all types of deformation including compression, tension and shear, at least when they are small. A more detailed examination of the networks composed of fibers that only resist to axial straining indicates that their rigidity depends on the network geometry and, in particular, the functionality. Maxwell counting of the degrees of freedom owned by the network junctions and the constraints introduced by the fibers shows that the minimal functionality required for the rigidity is six [43, 156, 175]. The networks of functionality $f = 4$ chosen to illustrate the homogenization approach proposed in this work are therefore unstable, unless reinforced by the elasticity mechanisms supplementary to the axial straining of fibers. In particular instant mechanical bending of filaments may be addressed in this respect as an important

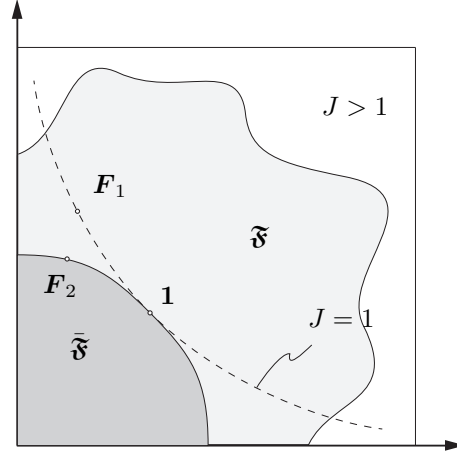


Figure 4.8: Schematic representation of the deformation gradient space $\text{SO}(3)$ and its partition into the domain $\tilde{\mathfrak{F}}$ for which networks display a stable equilibrium response and the domain \mathfrak{F} where the networks lose stability by fiber reorientation together with the isochoric deformation \mathbf{F}_1 from $\tilde{\mathfrak{F}}$ and the deformation \mathbf{F}_2 with negative volumetric change located on the boundary between $\tilde{\mathfrak{F}}$ and \mathfrak{F} .

factor sustaining the rigidity of the floppy tetrafunctional networks [139, 140, 384]. The bending is not incorporated into the presented homogenization approach in this work. The non-affine relaxed network microdeformation predicted by the MAPC model can be viewed therefore as an approximation in the limit when the contribution of the stabilizing bending forces is small compared to the axial straining of the fibers.

The non-affine stretch redistribution in case of stiff tetrafunctional networks is generally shown to be qualitatively different to that of the flexible fiber networks. As illustrated in Figure 4.7, the free energy ψ_f of stiff fibers is not a convex function of the stretch vector $\boldsymbol{\lambda} \in \mathbb{R}^3$ anymore, although it may be convex in $|\boldsymbol{\lambda}|$ as for the linear spring. In particular, the energy is non-convex when the fibers are in contraction $|\boldsymbol{\lambda}| < 1$ and hence exert negative forces. As a consequence the network will not display a stable behavior at arbitrary macroscopic strains in contrast to the situation considered in the previous subsection 4.5.1. The networks loose stability in a specific manner, namely, fibers only reorient with no axial deformation. Within the statistical description this peculiar microdeformation is defined by a stretch vector that is unit for all orientations $\boldsymbol{\lambda}_0$, namely

$$|\boldsymbol{\lambda}(\boldsymbol{\lambda}_0)| = 1 \quad \forall \boldsymbol{\lambda}_0 \in S_0. \quad (4.47)$$

In such state the network attains the minimal possible total energy and produces no mechanical stress, since all the fiber forces are zero. The macroscopic deformations from a set $\tilde{\mathfrak{F}} \subset \text{SO}(3)$ at which this yield response is observed can be specifically characterized.

Consider an arbitrary unit microstretch (4.47) that occurs at some macroscopic deformation with the deformation gradient \mathbf{F} . The latter can be polar decomposed as $\mathbf{F} = \mathbf{V}\mathbf{R}$, where \mathbf{R} is the rotational part of the deformation, $\mathbf{V} = \text{diag}[\lambda_x, \lambda_y, \lambda_z]$ is the stretch part. The maximal advance path constraint (4.30) gives then the following identity for the macroscopic stretch

$$\langle \boldsymbol{\lambda} \otimes \mathbf{R}\boldsymbol{\lambda}_0 \rangle = \frac{1}{3}\mathbf{V}. \quad (4.48)$$

The trace of the left hand side (4.48) is equal to $\langle \boldsymbol{\lambda} \cdot \mathbf{R}\boldsymbol{\lambda}_0 \rangle$ which does not exceed 1, since both vectors $\boldsymbol{\lambda}$ and $\mathbf{R}\boldsymbol{\lambda}_0$ are unit. The trace of the right hand side satisfies another

inequality, namely $\frac{1}{3}\text{tr}\mathbf{V} = \frac{1}{3}(\lambda_x + \lambda_y + \lambda_z) \geq (\lambda_x\lambda_y\lambda_z)^{1/3}$, since all the principal stretches are positive. Combining these two observations one can finally deduce that the network can loose stability due to the fiber reorientation if only the macroscopic volumetric deformation is negative. That is, the deformation gradients from $\tilde{\mathfrak{F}}$ have a Jacobian smaller than 1, i.e. $J = \det \mathbf{F} < 1$. Correspondingly, the admissible set \mathfrak{F} contains at least all the macroscopic deformations for which $J \geq 1$.

The stable response for $\mathbf{F} \in \mathfrak{F}$ is produced by the equilibrium microscopic stretch and can uniquely be determined by (4.34) as

$$\lambda^* = f_f^{-1}(|\nu\lambda_0|) \frac{\nu\lambda_0}{|\nu\lambda_0|} \quad (4.49)$$

where the inverse fiber force function f_f^{-1} is well defined and gives for positive $|\nu\lambda_0|$ an absolute value of stretch

$$|\lambda^*| = f_f^{-1}(|\nu\lambda_0|) > 1 \quad (4.50)$$

which is greater than 1 as can be seen in Figure 4.7. As a consequence, the stable microdeformation of stiff tetrafunctional networks with no other mechanisms like bending, which could support the rigidity, requires that all the fibers constituting it are in tension. Once with the change of the macroscopic deformation the stretch in the network approaches a unit value the network starts folding by means of the abundant kinematic modes, which Maxwell counting predicts in the case of functionality $f = 4$. The transition between the stable network deformation regime at $\mathbf{F} \in \mathfrak{F}$ and the floppy reorientation at $\mathbf{F} \in \tilde{\mathfrak{F}}$ is illustrated in Figure 4.8. It shows schematically the division of the deformation gradient space $\text{SO}(3)$ into a stable and unstable domain.

Furthermore, the two types of the microdeformation discussed above are demonstrated for the example of uniaxial tension considering the network of linear elastic bars with the response outlined in Table 4.3. When subject to isochoric uniaxial tension $\mathbf{F}_1 = \text{diag}[1.4, 0.8452, 0.8452]$ this network will attain a stable equilibrium stretch shown in the top row of Figure 4.9. In full accordance with (4.50) at the relaxed state all fibers are elongated. In the situation when fiber forces are positive, the same holds true for the resulting homogenized normal stresses found as $\frac{1}{n\kappa}\mathbf{P}_1 = \text{diag}[0.0412, 0.0180, 0.0180]$. If not constrained in the direction perpendicular to the applied axial strain, this material will tend to contract gradually in the transverse direction, so that the stress components P_{yy}, P_{zz} vanish. This will be only achieved at the macroscopic strain $\mathbf{F}_2 = \text{diag}[1.4, 0.5979, 0.5979]$ at which the fibers will become unloaded as shown in the bottom row of Figure 4.9. This state is at the boundary between the two regions \mathfrak{F} and $\tilde{\mathfrak{F}}$. Remarkably the axial stress P_{xx} will also vanish at this point, which means that the network will display no resistance to the uniaxial tension, provided it can shrink freely.

The above demonstrated specific volumetric response is investigated separately. The nearly 50% shrinking predicted by the MAPC model for the network of elastic fibers is not typical, for most materials show a volumetric expansion when axially strained. The affine network models do not capture this specific shrinkage effect. The same network as considered above but deformed affinely produces at the isochoric macroscopic strain \mathbf{F}_1 the homogenized stress $\frac{1}{n\kappa}\mathbf{P}_{\text{affine}} = \text{diag}[0.0723, -0.0123, -0.0123]$ which is negative in the transverse direction, in which the fibers will be compressed. Correspondingly, such

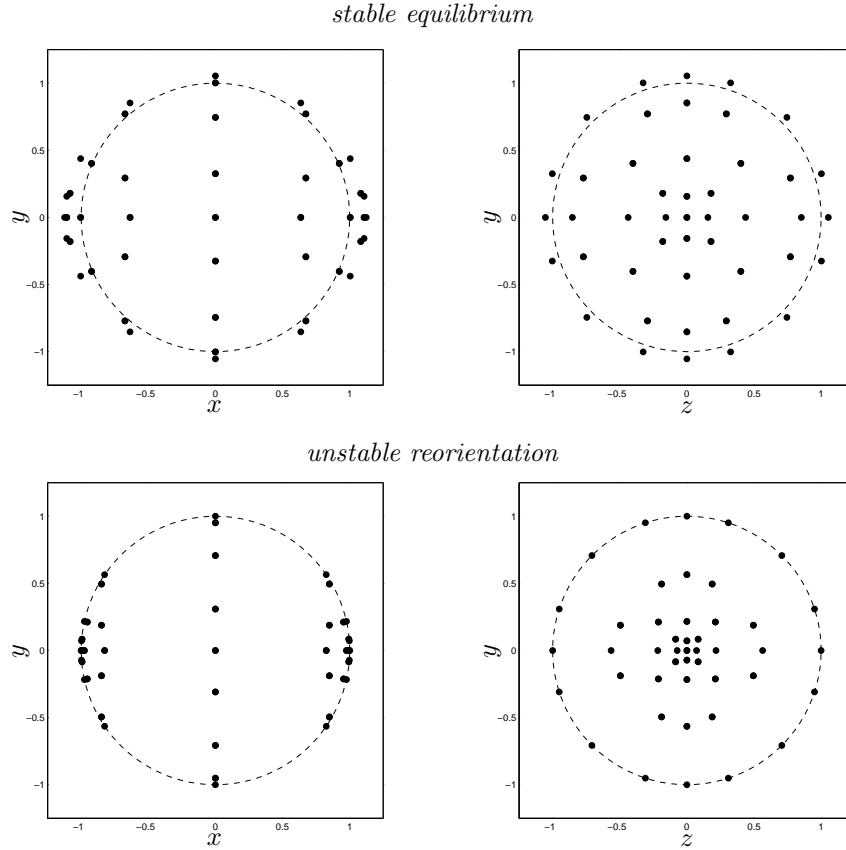


Figure 4.9: Illustration of the two types of microdeformation in stiff tetrafunctional networks of linear springs predicted by the MAPC model. The stable equilibrium microstretch of the network attained at isochoric uniaxial strain \mathbf{F}_1 (top row) and the acquisition of unit stretch in the network with the loss of rigidity after the shrinkage in the transverse direction at strain \mathbf{F}_2 (bottom row). The same graphical representation of the microstretch as in Figure 4.6 is used. The unit dashed circle is plotted to assist the identification of elongated fibers in the first case and reoriented fibers with the unit stretch in the second case.

network will expand transversely and the volume will increase if the material is only loaded in axial direction.

As shown above, the maximal advance path constraint model predicts a non-trivial non-affine deformation for networks with fibers that produce forces simply linear in extension. One can expect an even more peculiar behavior in the case of semiflexible filaments which display essentially non-linear stiffening as outlined in Figure 4.7. This in particular is illustrated by the following example of a model semiflexible network subject to the macroscopic shear $\mathbf{F} = \mathbf{1} + \gamma_{xy}\mathbf{e}_x \otimes \mathbf{e}_y$ where \mathbf{e}_x and \mathbf{e}_y are two basis vectors of a Cartesian coordinate system. This deformation is isochoric and therefore (as shown above) the equilibrium microdeformation exists and is stable, unless the shear γ_{xy} is too high so that the filaments reach the limiting extensibility. The test parameter set for the semiflexible fibers described by the model outlined in Table 4.3 is chosen so that the unloaded fibers have the initial end-to-end distance close to the contour length $R_0 = 0.9L$. Correspondingly, the limiting stretch value is as large as $\lambda^{lim} = 1.11$. The mechanical response of this network predicted by the MAPC model and the full affine network model is presented in Figure 4.10 by the two components of the Piola-Kirchhoff stress tensor, the shear stress P_{xy} and the normal stress P_{yy} , that define the traction on the horizontal

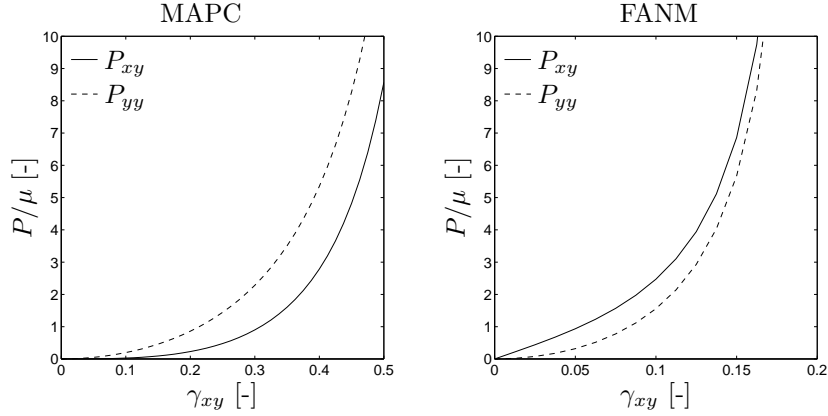


Figure 4.10: Dimensionless mechanical stresses of network made of semiflexible filaments predicted by the MAPC model (on the left) and the full affine network model (on the right) for macroscopic shear with $\gamma_{xy} = 0.5$. The shear stress P_{xy} and the normal stress P_{yy} are scaled by the characteristic modulus $\mu = nk_B T$.

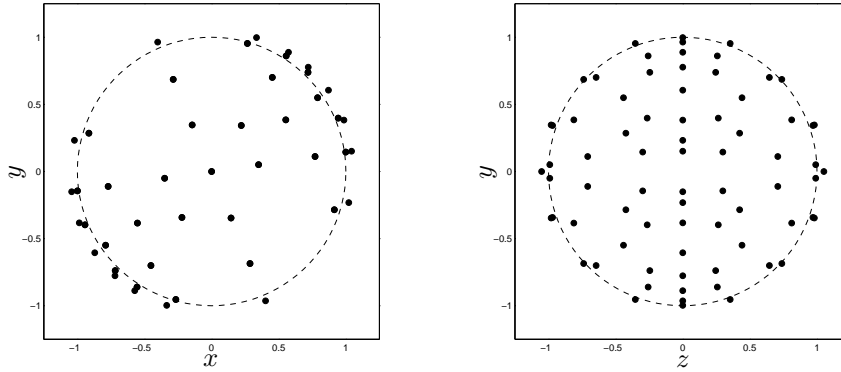


Figure 4.11: Microstretch at an applied shear deformation in a network made of semiflexible filaments. The same graphical representation of the microstretch as in Figure 4.6 is used. The unit dashed circled is plotted to demonstrate that all the fibers are elongated as stated in (4.50) for the stable equilibrium microdeformation.

surface where the shear deformation is applied. Just as in the case of flexible chains with limiting extensibility, the non-affine redistribution allows the network to undergo much larger strains. If in the affine case the fibers aligned initially at 45° with respect to the shear direction reach the extensibility limit $\lambda^{lim} = 1.11$ at $\gamma_{xy} = 0.2121$, the non-affine network described by the proposed MAPC model can be sheared up to $\gamma_{xy} = 0.5$ and beyond. The microstretch in the network at this macroscopic deformation is shown in Figure 4.11. The fibers at this equilibrium state of the network are all in tension. The magnitude of fiber stretch, remarkably, displays very small variations from $|\lambda^*| = 1.0443$ to $|\lambda^*| = 1.0603$ that can hardly be seen in the Figure, unlike the affine deformation for which the stretch alters from compression $|\bar{\lambda}| = 0.7906$ to tension $|\bar{\lambda}| = 1.2748$.

Finally, two other interesting features of the non-affine network, which are not related to the stiffening of the considered semiflexible filaments and concern the response at small and moderate deformations, are investigated. Firstly, the magnitude of the value for the normal stress P_{yy} appears to be higher than the value of the shear stress P_{xy} . Neither the affine network, in particular, nor conventional solid materials, in general, display such a behavior at an applied shear deformation. Recent experimental investigations of biopolymer gels report though a similar atypical normal stress response of the magnitudes that

substantially exceed the values of the shear stress [67, 168]. The non-affine redistribution of filament stretch in the network gives an adequate qualitative explanation of this phenomenon. The second feature of the response predicted by the MAPC is the scaling of the stresses with small values of shear strain. For conventional materials the shear stress displays a linear proportionality $P_{xy} \sim \gamma_{xy}$ when γ_{xy} is close to zero, whereas the normal stress scales with the square of shear $P_{yy} \sim \gamma_{xy}^2$. This regularity is also valid for the homogenized response of the affine network (see Figure 4.10). The non-affine network, on the contrary, produces mechanical stresses that scale as $P_{xy} \sim \gamma_{xy}^3$ and $P_{yy} \sim \gamma_{xy}^2$, which again demonstrates that the shear stress response is softer than the normal stress. The network displays zero stiffness in the initial undeformed state when all the fibers are not stretched and, therefore, does not resist to shear at $\gamma_{xy} = 0$.

5 A diffusion-based transient network model for finite rubber viscoelasticity

This chapter presents the development of a physical based constitutive model for the representation of viscous effects in rubber-like materials and is based on the recently published work of LINDER ET AL. [211]. The proposed model originates from micromechanically motivated diffusion processes of the highly mobile polymer chains described within the formalism of Brownian motion. Following the basic assumption of accounting for the elastic and the viscous effects in rubber viscoelasticity by their representation through a separate elastic ground network and several viscous subnetworks, respectively, the kinetic theory of rubber elasticity is followed and extended to represent also the viscous contribution in this work. It is assumed that the stretch probability of certain chain segments within an individual viscous subnetwork evolves based on the movement of the chain endpoints described by the Smoluchowski equation extended in this work from non-interacting point particles in a viscous surrounding to flexible polymer chains. An equivalent tensorial representation for this evolution is chosen which allows for the closed form solution of the macroscopic free energy and the macroscopic viscous overstress based on a homogenization over the probability space of the introduced micro-objects. The resulting model of the viscous subnetwork is subsequently combined with the non-affine microsphere model and applied in homogeneous and non-homogeneous tests. Finally, the model capacity is outlined based on a comparison with in the literature available experimental data sets.

5.1 Introduction

Polymers are characterized by remarkable properties making them qualified for applications in all areas of engineering. They can appear in liquid or amorphous solid form, behave ductile in the case of glassy polymers or rubber-like for elastomers. The latter, to be considered in this work, can in particular be characterized by the large deformations they can sustain as well as the rate and history dependence of the resulting stresses in the material. This response is attributed to their peculiar microstructure including a network of highly mobile and flexible polymer chains formed by their three-dimensional cross-linking. From a constitutive modeling point of view the challenge lies in the development of physical based models to depict this behavior. In that regard one distinguishes *static network theories* for the modeling of elastic effects and *transient network theories* for the modeling of time dependent effects in rubber-like materials. A brief review of those is provided here. The scope of this work lies within the development of a new transient network theory for rubber-like materials. Its incorporation into finite viscoelastic constitutive models, as well as the resulting implementation and application to realistic experiments and its qualitative comparison with existing experimental data sets are the main contributions of this chapter.

Early experimental results in TRELOAR [353] indicate the characteristic *S*-shaped load versus stretch curve for the elastic nature of rubber materials in uniaxial tensile tests in the form of an initially decreasing stiffness of the material and a rapid increase thereafter. The reported deformation range, up to an eightfold extension of the material with an almost full recovery of its initial shape upon unloading, outlines one of their main mechanical characteristics and reason for their applicability in various areas of engineering

and material science. Further experimental results are given in RIVLIN & SAUNDERS [308], JAMES ET AL. [165], and JAMES & GREEN [164], among others. The latter introduced a graphical presentation of the results which allowed for a more convenient fit of the material data of constitutive models in terms of their strain energy function. Inspired by the form of such a function for an isotropic, incompressible, hyperelastic material various strain-invariant based phenomenological expressions are proposed to capture the characteristic response of rubber [252, 264, 307, 394]. These empirical theories lack a direct physical justification of the parameters appearing in the proposed expressions of the strain energy function.

On the contrary, the kinetic theory of elasticity [237] accounts for the underlying physics by assuming that the material consists of a large number of polymer chains which do form a static network by being permanently cross-linked at junction points. A chain segment, considered as part of a polymer molecule approximated as an idealized chain of freely rotating links, between two such junction points possesses a large number of possible conformations in terms of translational and rotational degrees of freedom which are driven by the influence of the thermal motion of the chain endpoints. Since the angles between adjacent bonds are considered to be random with equally distributed probability, the bond orientations do not correlate resulting in a Gaussian distribution of the end-to-end vector of an unrestrained chain segment. This probability can then be linked through the Boltzmann relation to the entropy and the free energy of a single chain [134, 188, 189]. This, as *Gaussian statistics* denoted background for the single entropic chain segments, is used for the derivation of the *Gaussian network models* [102, 103, 166, 356, 357, 373] consisting of a highly cross-linked network of such Gaussian chains providing a link of the micromechanical polymer model to macroscopic scales. The agreement of those models with the experimental results are acceptable up to stretch regions where the individual chain segments are far from being fully extended.

Such limitation is overcome in the *non-Gaussian statistics* of KUHN & GRÜN [190] and later by FLORY [100] based on their account of the finiteness of the chain extensibility where the modified probability density function of a chain with a certain length and its resulting entropy is expressed in closed form in terms of the inverse Langevin function. An account for such a finite extensibility of the individual chain segments in network models results in so called *non-Gaussian network models*. Examples within that frameworks are the *three-chain model* considered in JAMES & GUTH [166] and WANG & GUTH [376], the *four-chain model* by TRELOAR [358] as an extension of the model in FLORY & REHNER JR. [102], or the more recently developed *eight-chain model* by ARRUDA & BOYCE [17] which successfully is able to represent the response of these materials in uniaxial extension and compression, biaxial extension, plane strain compression, and pure shear problems. A *full network theory* is proposed in TRELOAR [359] and TRELOAR & RIDING [355] for uniaxial extension and biaxial tensile deformation, respectively, and extended in WU & VAN DER GIESSEN [388] to fully three-dimensional deformation processes. It is noted that whereas the three chain model and the full network theory result in *affine* network formulations, meaning that they preserve the affinity of the network deformation with regard to the macroscopically applied deformation, the remaining *non-affine* network models do come along without such restriction. Chains oriented in the direction of loading display a higher resistance to the stretch when approaching their limiting value compared to other chains in the network. Hence, the internal structure of the polymer becomes

heterogeneous, which leads to a deviation of chain stretches when compared to those resulting from the macrostrain. Only the non-affine models allow for such adjustment of the polymer microstructure.

Rather than focusing on static network theories, the current chapter is concerned with the development of a physically interpretable and fully micromechanically motivated transient network model for the description of the polymer chain movement to describe the viscous effects in rubber-like materials. For polymers, consisting of long-chain molecules as proposed in STAUDINGER [334], such movement can be understood by entanglement mechanisms in the physical sense or by secondary bonds, such as hydrogen bonds, which unlike the primary chemical bonds between polymer chains of the elastic network in rubbers are weak and highly dynamical. One of the early entanglement models goes back to the work in GREEN & TOBOLSKY [127] where it is assumed that such entanglements are steadily created and destroyed. In particular, when a new chain joins the network based on an appearing entanglement, it is assumed that this chain reforms in a stress-free state resulting in a steady decrease of the network stresses in time being characteristic for stress relaxation phenomena. With regard to the equal rate, at which entanglement junctions are assumed to be created and broken, a linear evolution is derived, limiting the applicability to problems with small perturbations from the thermodynamic equilibrium. An extension of the transient network model in GREEN & TOBOLSKY [127] is achieved in YAMAMOTO [390, 391] by accounting for the dependency of the probability of the chain breakage rate on the tension acting in the network and by LODGE [215] allowing for an anisotropy of the deforming network and the existence of many stress relaxation periods as well as its extension in BERNSTEIN ET AL. [35]. In REESE & WRIGGERS [304] the original model by GREEN & TOBOLSKY [127] is generalized to allow for states away from the thermodynamic equilibrium by the introduction of a stress-free intermediate configuration.

In line with these approaches, the aim of this work is to develop a new micromechanically motivated model for the description of the transient network to describe viscous effects in polymers. The key aspect in the proposed model is the stochastic motion within the viscoelastic part of the network including the re-orientation and stretch relaxation of chain segments. This process is seen as a Brownian motion performed by the chain segment end points within a viscous surrounding idealizing the neighboring chains in the network. Motivated by the description of the movement of non-interacting point particles in a viscous fluid described by the Smoluchowski equation obtained as a generalization of the diffusion equation in DOI & EDWARDS [75], this is extended to describe the motion of the chain segment end points governing a change of the distribution of stretch within the subnetwork due to the macrodeformation and internal relaxation of the microstructure. It is further shown that an equivalent tensorial formulation of this micromechanically based model can be derived resulting in evolution equations of the internal variables and closed form expressions of the free energy as in GREEN & TOBOLSKY [127]. The thermodynamical consistency comes intrinsically from the micromechanical origin which is outlined in detail. This description of the transient network is subsequently combined with the non-affine microsphere model developed in MIEHE ET AL. [244] to represent the elastic ground network and applied to homogeneous and non-homogeneous experimental data sets.

The chapter is organized as follows. In Section 5.2 the basic network mechanisms of finite

rubber viscoelasticity of a nearly incompressible solid is summarized which provides the description of the characteristic finite deformation and the basic thermodynamics of the continuum. It is assumed that the response of the rubber-like material can be decomposed into an elastic ground network and a highly mobile viscous subnetwork. For the latter, a micromechanically motivated model is proposed in Section 5.3. Starting with an entropic spring representation of a single polymer chain based on its equilibrium kinetics, a model for the mobile subnetwork evolution based on the concept of Brownian motion is developed and applied to the network chains whose end points are treated as point particles moving in a viscous surrounding. The final outcome is the flow equation with respect to the stretch probability field that describes the microdeformation of a single subnetwork. In Section 5.4 an equivalent tensorial representation of the stretch probability evolution is developed which allows for the closed form computation of the macroscopic free energy and the macroscopic viscous overstress. Finally, Section 5.5 outlines the performance of the model when combined with the non-affine microsphere model for the representation of the elastic ground network on a set of homogeneous and non-homogeneous representative problems. The model capacity is evaluated based on comparisons of all tests with available experimental data sets in the literature.

5.2 Basic network mechanisms of finite rubber viscoelasticity

This section briefly summarizes the resulting constitutive equations of finite rubber viscoelasticity under the basic assumption of the polymer microstructure being assembled by several idealized polymer networks. Motivated by the discussion in Section 5.1, the response of the rubber-like material is considered to be decomposed into a *ground network* formed by strongly cross-linked macromolecules and a *subnetwork* consisting of highly mobile and based on temporary entanglement mechanisms linked macromolecules. Whereas the ground network is associated with the elastic response of the material, the subnetwork is responsible for the description of the viscous material properties in the form of the appearance of a viscous overstress. An illustration of the resulting viscoelastic behavior is given in Figure 5.1 displaying a schematic representation of the individual networks under an applied macrodeformation. Based on such deformation, the ground network stretches and drags the mobile subnetwork along with it. After a sufficient amount of time at a constant deformation, the subnetwork relaxes towards a state at which it produces no viscous overstress. Whereas the elastic ground network can be represented by models such as the eight-chain model developed in ARRUDA & BOYCE [17] or the non-affine network model developed in MIEHE ET AL. [244], among many others, the emphasis of this work is to develop a diffusion-based micromechanically motivated model for the representation of the viscous mobile subnetwork. In fact, the numerical simulations presented in Section 5.5 make use of the model developed in MIEHE ET AL. [244] for the representation of the elastic ground network but it should be kept in mind that the developed model of the viscous subnetwork does not rely on a particular model choice for the description of the elastic properties.

Following the geometric setting of finite inelasticity outlined in MIEHE [238], the macroscopic finite rubber viscoelastic response is based on a volumetric-isochoric decomposition, where the isochoric part itself is decomposed into an elastic equilibrium and a viscous overstress response, as it is briefly summarized in this section. To do so, consider a body to

be a collection of material points which at time $t \in \mathbb{R}_+$ occupies a spatial configuration $\mathcal{S} \subset \mathbb{R}^{n_{\text{dim}}}$ in terms of the space dimension $1 \leq n_{\text{dim}} \leq 3$. An individual material point of the body at time t is located at position $\mathbf{x} \in \mathcal{S}$. The change of properties of such material point in the body is described relative to a fixed reference configuration $\mathcal{B} \subset \mathbb{R}^{n_{\text{dim}}}$ which for instance can represent the configuration occupied by the body at the instant time t_0 in which the material point is located at position $\mathbf{X} \in \mathcal{B}$. To avoid any explicit reference to the body itself, the nonlinear deformation map $\boldsymbol{\varphi}(\mathbf{X}) : \mathbf{X} \mapsto \mathbf{x} = \boldsymbol{\varphi}(\mathbf{X}; t)$ is introduced which maps positions $\mathbf{X} \in \mathcal{B}$ onto positions $\mathbf{x} \in \mathcal{S}$. Key kinematic quantities are the local deformation gradient $\mathbf{F} = \nabla_{\mathbf{X}} \boldsymbol{\varphi}(\mathbf{X}; t)$ representing the linear map between tangent vectors in the reference and the spatial configuration, respectively, where the Jacobian $J = \det \mathbf{F}$ has to satisfy $J > 0$, as well as the covariant Cartesian metric tensors $\mathbf{G} = \delta_{AB}$ and $\mathbf{g} = \delta_{ab}$ of those configurations written in terms of the Kronecker symbol δ . The boundary value problem of the macroscopic finite viscoelastic problem at hand for the quasi-static case is then governed by the balance of linear momentum

$$\operatorname{div}_{\mathbf{X}} [\boldsymbol{\tau} \mathbf{F}^{-T}] + \bar{\mathbf{B}} = \mathbf{0} \quad (5.1)$$

written in terms of the divergence operator $\operatorname{div}_{\mathbf{X}}$ with respect to the reference position \mathbf{X} together with prescribed displacement boundary conditions $\boldsymbol{\varphi} = \bar{\boldsymbol{\varphi}}(\mathbf{X}; t)$ on $\partial \mathcal{B}_{\varphi}$ and prescribed traction $[\boldsymbol{\tau} \mathbf{F}^{-T}] \mathbf{N} = \bar{\mathbf{T}}(\mathbf{X}; t)$ on $\partial \mathcal{B}_t$ with outward normal \mathbf{N} . The usual conditions $\partial \mathcal{B}_{\varphi} \cap \partial \mathcal{B}_t = \emptyset$ and $\overline{\partial \mathcal{B}_{\varphi} \cup \partial \mathcal{B}_t} = \partial \mathcal{B}$ have to hold in each component of the deformation mapping to ensure a well-posed problem. In (5.1), the prescribed body force field $\bar{\mathbf{B}}$ with respect to the unit volume of the reference configuration as well as the Kirchhoff stress tensor $\boldsymbol{\tau}$ are introduced. The latter is assumed to be a function of the local deformation gradient \mathbf{F} and some internal variables \mathcal{I} responsible for the characterization of the viscous structural changes. The Kirchhoff stress $\boldsymbol{\tau}$ and its associated moduli are given as

$$\boldsymbol{\tau} = 2 \partial_{\mathbf{g}} \Psi(\mathbf{g}, \mathcal{I}; \mathbf{F}) \quad \text{and} \quad \mathbb{C} = 4 \partial_{\mathbf{g}\mathbf{g}}^2 \Psi(\mathbf{g}, \mathcal{I}; \mathbf{F}) \quad (5.2)$$

in terms of the macroscopic free energy per unit volume of the reference configuration [226, 238] stored in a deformed polymer network with the requirement of being material frame invariant in the sense that $\Psi(\mathbf{g}, \mathcal{I}; \mathbf{Q}\mathbf{F}) = \Psi(\mathbf{g}, \mathcal{I}; \mathbf{F})$ for all rotations $\mathbf{Q} \in SO(3)$.

The rubber-like material considered in this work is assumed to be nearly incompressible which motivates a decoupled volumetric-isochoric formulation based on the decomposition of the macroscopic free energy as

$$\Psi = U(J) + \bar{\Psi}(\mathbf{g}, \mathcal{I}; \bar{\mathbf{F}}) \quad (5.3)$$

in terms of the volumetric and isochoric contributions, respectively. The numerical simulations presented in Section 5.5 make use of $U = (J^2 - 1 - 2 \ln J)/4$ for the former contribution. The latter is given in terms of the unimodular part of the deformation gradient defined as $\bar{\mathbf{F}} = J^{-1/3} \mathbf{F}$ which is assumed to drive the deviatoric part $\bar{\boldsymbol{\tau}} = 2 \partial_{\mathbf{g}} \bar{\Psi}(\mathbf{g}, \mathcal{I}; \bar{\mathbf{F}})$ of the total stresses decomposed into spherical and deviatoric contribution as

$$\boldsymbol{\tau} = p \mathbf{g}^{-1} + \bar{\boldsymbol{\tau}} : \mathbb{P} \quad (5.4)$$

with $p = J U'(J)$ and the fourth-order deviatoric projection tensor $\mathbb{P}^{ab}_{cd} = [\delta^a_c \delta^b_d + \delta^a_d \delta^b_c]/2 - \delta^{ab} \delta_{cd}/3$. This decomposition carries along into the representation of the moduli

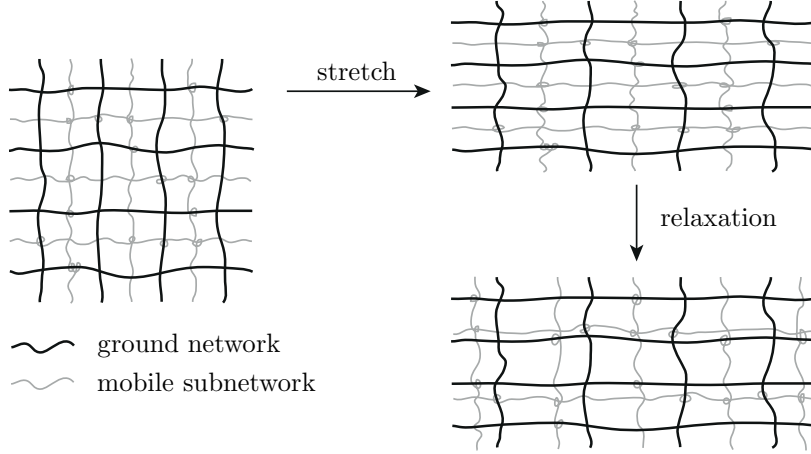


Figure 5.1: Network representation of the microscopic response of rubber-like materials. The schematic response of the material decomposed into a strongly cross-linked ground network (representing the elastic response) and a mobile subnetwork (formed by temporary entanglement mechanisms representing the viscous response) is illustrated under an applied arbitrary macrodeformation.

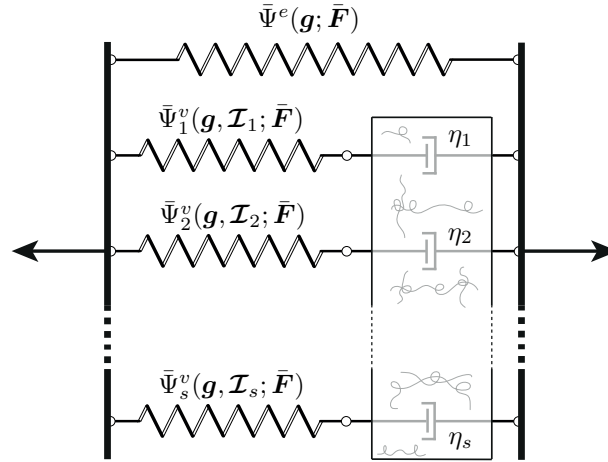


Figure 5.2: Macroscopic representation of finite rubber viscoelasticity. The Maxwellian type rheological model of the isochoric response of the material consists of a single elastic branch representing the elastic ground network in Figure 5.1 as well as s viscous branches each of them representing a single mobile viscous subnetwork in Figure 5.1.

\mathbb{C} written in terms of the deviatoric part $\bar{\mathbb{C}} = 4\partial_{\mathbf{g}\mathbf{g}}^2 \bar{\Psi}(\mathbf{g}, \mathcal{I}; \bar{\mathbf{F}})$ as

$$\mathbb{C} = (p + \kappa) \mathbf{g}^{-1} \otimes \mathbf{g}^{-1} - 2p \mathbb{I} + \mathbb{P}^T : \left[\bar{\mathbb{C}} + \frac{2}{3} (\bar{\boldsymbol{\tau}} : \mathbf{g}) \mathbb{I} - \frac{2}{3} (\bar{\boldsymbol{\tau}} \otimes \mathbf{g}^{-1} + \mathbf{g}^{-1} \otimes \bar{\boldsymbol{\tau}}) \right] : \mathbb{P} \quad (5.5)$$

with $\kappa = J^2 U''(J)$ and in terms of the fourth-order identity tensor $\mathbb{I}^{abcd} = [\delta^{ac}\delta^{bd} + \delta^{ad}\delta^{bc}]/2$.

To account for the actual behavior of rubber viscoelasticity, the isochoric part of the above model is further decomposed into elastic and viscous parts in accordance with the representation of the polymer network structure into an elastic ground network and a viscous subnetwork illustrated in Figure 5.1. In case of s viscous subnetworks which are introduced to obtain a discrete spectrum of relaxation times related to different viscosities

$\{\eta_i\}_{i=1}^s$, the isochoric part $\bar{\Psi}$ in (5.3) of the free energy can be additively split into

$$\bar{\Psi} = \bar{\Psi}^e(\mathbf{g}; \bar{\mathbf{F}}) + \bar{\Psi}^v(\mathbf{g}, \mathcal{I}; \bar{\mathbf{F}}) \quad \text{where} \quad \bar{\Psi}^v(\mathbf{g}, \mathcal{I}; \bar{\mathbf{F}}) = \sum_{i=1}^s \bar{\Psi}_i^v(\mathbf{g}, \mathcal{I}_i; \bar{\mathbf{F}}) \quad (5.6)$$

is given as a summation over each of the s viscous subnetworks. The corresponding rheological model for such an isochoric response of the material is illustrated in Figure 5.2. This further yields to the decomposition of the deviatoric part of the stresses into an elastic equilibrium stress response and a viscous overstress response according to

$$\bar{\boldsymbol{\tau}} = \bar{\boldsymbol{\tau}}^e + \bar{\boldsymbol{\tau}}^v \quad \text{with} \quad \bar{\boldsymbol{\tau}}^e = 2 \partial_{\mathbf{g}} \bar{\Psi}^e(\mathbf{g}; \bar{\mathbf{F}}) \quad \text{and} \quad \bar{\boldsymbol{\tau}}^v = 2 \partial_{\mathbf{g}} \bar{\Psi}^v(\mathbf{g}, \mathcal{I}; \bar{\mathbf{F}}). \quad (5.7)$$

Whereas the response of the elastic equilibrium stress is assumed to be isotropic, resulting in the condition $\bar{\Psi}^e(\mathbf{g}; \mathbf{F}\mathbf{Q}) = \bar{\Psi}^e(\mathbf{g}; \mathbf{F}) \forall \mathbf{Q} \in SO(3)$, a deformation induced anisotropy is provided by the dissipative viscous overstress which is characterized by the evolution of the internal variables \mathcal{I} in time. To obtain a formulation consistent with the second axiom of thermodynamics the local dissipation has to satisfy the inequality

$$\mathcal{D}_{loc} = -\partial_{\mathcal{I}} \bar{\Psi} \cdot \dot{\mathcal{I}} = \sum_{i=1}^s \mathcal{D}_{loc,i} \geq 0 \quad \text{where} \quad \mathcal{D}_{loc,i} = -\partial_{\mathcal{I}_i} \bar{\Psi} \cdot \dot{\mathcal{I}}_i. \quad (5.8)$$

After presenting a brief overview of the basic network mechanisms of rubber viscoelasticity and its incorporation into standard finite rubber viscoelasticity, the remaining part of the work is concerned with the development of a diffusion-based, from a microscopic point of view physically motivated, transient network model resulting in expressions for the viscous part $\bar{\Psi}^v$ of the isochoric free energy as well as for the viscous overstress response $\bar{\boldsymbol{\tau}}^v$. Whereas Section 5.3 will develop the diffusion-based micromechanical polymer model, its incorporation into the macroscopic framework above is achieved in Section 5.4 and finally evaluated through representative numerical simulations in Section 5.5 based on homogeneous and non-homogeneous tests.

5.3 Microscopic formulation of the diffusion-based transient network model

In this section a micromechanical model for the description of the polymer chain movement is developed. The model makes use of the concept of diffusion to approximate the time evolution of the probability density function associated with the end-to-end vector of the individual chain segments undergoing a Brownian movement. The application of statistical methods for the description of micromechanical states of rubber-like polymers is justified by the enormous number of conformations in time based on the rotation of chemical bonds such materials may undergo. In Section 5.3.1 the Gaussian statistics of a single chain is briefly reviewed. To account for viscoelastic phenomena in polymers related to the dissipation of mechanical work, the framework of non-equilibrium thermodynamics is introduced in Section 5.3.2 when describing a diffusion-based process of the Brownian motion of non-interacting point particles. This framework is extended in Section 5.3.3 to describe the Brownian motion of polymer chains representing the core part of the developed micromechanical polymer model in this section.

5.3.1 Gaussian statistics of a single polymer chain

Following the classical work in KUHN [188, 189] or the more recent contribution of TRELOAR [354] or DOI & EDWARDS [75], in this section a brief review of the statistics of a single polymer chain is provided in the form of the most simple case of a *freely jointed model*. The model, which already captures many of the characteristic properties of a single polymer chain, rests upon the assumption that such chain consists of N links, each of length b , whose orientations are assumed to be random and independent of each other. The conformation of such freely jointed chain is determined either by $(N + 1)$ position vectors $\{\mathbf{r}_n\}_{n=0}^N$ of the joints including the two end points or alternatively by a set of N independent bond vectors $\{\mathbf{b}_n\}_{n=1}^N$ with $\mathbf{b}_n = \mathbf{r}_n - \mathbf{r}_{n-1}$ for $n = 1, \dots, N$. Viewing the chain as a statistical system, the probability of a particular chain conformation $\{\mathbf{b}_n\}_{n=1}^N$ can be computed by

$$p(\{\mathbf{b}_n\}_{n=1}^N) = \prod_{n=1}^N p(\mathbf{b}_n) \quad \text{with} \quad p(\mathbf{b}_n) = \frac{1}{4\pi b^2} \delta(|\mathbf{b}_n| - b) \quad (5.9)$$

as the product of the isotropic distribution of the individual random bond vectors with fixed length b expressed in \mathbb{R}^3 by the single-layer potential $p(\mathbf{b}_n)$ given in terms of $|\mathbf{b}_n| = \sqrt{\mathbf{b}_n \cdot \mathbf{b}_n}$ and normalized according to the condition $\int_{\mathbb{R}^3} p(\mathbf{b}_n) d\mathbf{b}_n = 1$. The size of the polymer chain can then be characterized by the end-to-end vector \mathbf{r} defined as $\mathbf{r} = \mathbf{r}_N - \mathbf{r}_0 = \sum_{n=1}^N \mathbf{b}_n$ with the corresponding mean value $\langle \mathbf{r} \rangle = \sum_{n=1}^N \langle \mathbf{b}_n \rangle = \mathbf{0}$ and mean-square value $\langle \mathbf{r}^2 \rangle = \sum_{n,m=1}^N \langle \mathbf{b}_n \cdot \mathbf{b}_m \rangle = Nb^2$, for sufficiently large N . Here, $\langle \bullet \rangle$ denotes the mean value of a random quantity (\bullet) that is computed as an integral over the probability space as

$$\langle \bullet \rangle = \int (\bullet) d\{\mathbf{b}_n\}_{n=1}^N. \quad (5.10)$$

The above mean values do not provide sufficient information to describe the statistical system of the freely jointed model. What is required is the knowledge about the corresponding statistical distribution of the end-to-end vector \mathbf{r} given as

$$p(\mathbf{r}) = \int p(\{\mathbf{b}_n\}_{n=1}^N) \delta\left(\mathbf{r} - \sum_{n=1}^N \mathbf{b}_n\right) d\{\mathbf{b}_n\}_{n=1}^N = \left(\frac{3}{2\pi r_0^2}\right)^{\frac{3}{2}} \exp\left[-\frac{3}{2} \frac{r^2}{r_0^2}\right] \quad (5.11)$$

whose solution is given (see DOI & EDWARDS [75] for a detailed derivation) in terms of $r = |\mathbf{r}|$ and $r_0^2 = \langle \mathbf{r}^2 \rangle$ in the form of a Gaussian distribution. It is emphasized that as a result of the central limit theorem in statistics, for $N \gg 1$ the obtained result (5.11) of the freely jointed model holds even for a more general class of models with the only difference of the actual bond length b being replaced by an effective counterpart [75]. On the other hand, the solution obtained in (5.11) has the non-physical feature that the probability of finding end-to-end vectors with $r > Nb$, where Nb represents the length of a fully extended chain, is non-zero. Nonetheless, it provides a good estimate for models in which highly stretched states of the polymer chains do not play an important role, as it is the case for the diffusion-based micromechanical polymer model developed in this section for the representation of the mobile viscous subnetworks introduced in Section 5.2.

The distribution $p(\mathbf{r})$ in (5.11) can be understood as a measure of the number of conformations of a chain and can therefore be directly linked to the entropy. Considering

a thermodynamical system of a polymer chain with the constrained position of the ends one can postulate the entropy \mathcal{S} in the form of Boltzmann's relation

$$\mathcal{S}(\mathbf{r}) = k_B \ln p(\mathbf{r}) = -\frac{3}{2}k_B \frac{r^2}{r_0^2} + \text{terms independent of } \mathbf{r} \quad (5.12)$$

where k_B is the Boltzmann constant. When rotations about the bonds in the molecular polymer chain are considered to be unrestricted, the internal energy will remain the same for all conformations [354] so that the Helmholtz free energy can be solely computed based on the entropy in (5.12) as

$$\mathcal{A}(\mathbf{r}) = -\theta \mathcal{S}(\mathbf{r}) = \frac{3}{2}k_B \theta \frac{r^2}{r_0^2} + \text{terms independent of } \mathbf{r} \quad (5.13)$$

in terms of the known temperature θ of the polymer. In analogy to existing bead spring models [37], this viewpoint motivates the interpretation of a polymer chain with fixed end points and different conformations in between those by an entropic spring expressing the average response from the thermal motion of the chain segments. The thermodynamic force acting on the fixed ends of such spring then becomes

$$F_r = \frac{\partial \mathcal{A}}{\partial r} = 3k_B \theta \frac{r}{r_0^2}. \quad (5.14)$$

The simplified theory discussed in this section neglects possible temporary constraints like bonding or detachment of polymer chain segments leading to time-dependent phenomena such as viscoelasticity. The incorporation of such effects is achieved within the framework of non-equilibrium thermodynamics in the subsequent Section 5.3.2.

5.3.2 Brownian motion of non-interacting point particles

The incorporation of viscoelasticity as a time dependent phenomena of polymers related to the dissipation of mechanical work on the micromechanical level is achieved by the development of a model which treats the viscoelastic relaxation of the microstructure as a diffusion-based process allowing for the incorporation of the formalism of Brownian motion. Following the phenomenological approach in DOI & EDWARDS [75], the Brownian motion can be interpreted as a stochastic process that is governed by known macroscopic laws applied to microscopic objects. Such a treatment is restricted to time- and length-scales larger than those characteristic of equilibrium thermal oscillations. The resulting phenomenological evolution equation in the form of the *Smoluchowski equation* is derived from the generalization of the diffusion equation and can be related to the thermodynamics of irreversible processes. To allow for a concise derivation of the Smoluchowski equation, in the following the Brownian motion of non-interacting point particles is restricted to translational degrees of freedom.

To do so, consider a system with a large number of point particles submerged in a viscous medium as it is illustrated on the left of Figure 5.3. The phenomena of diffusion can be observed in such a system when the distribution of particles in the medium is not uniform resulting in a flux which is proportional to the spatial gradient of the concentration of particles. The microscopic origin of the macroscopically observed flux is motivated in

DOI & EDWARDS [75] by the random thermal motion of the particles in the sense that in case of a non-uniform concentration, the number of particles flowing from regions of higher concentration to regions of lower concentration surpasses the number of particles moving in the opposite direction.

To describe this process, consider the probability of finding a particle in a certain state governed by its position \mathbf{x} at a certain time t expressed by the probability function $p(\mathbf{x}, t)$ which can be viewed as the concentration of particles $c(\mathbf{x}, t)$ scaled to the total number of particles n as $c(\mathbf{x}, t) = n p(\mathbf{x}, t)$. This distribution evolves in time based on the continuity equation

$$\partial_t p(\mathbf{x}, t) = -\operatorname{div}_{\mathbf{x}} \mathbf{h}(\mathbf{x}, t) \quad (5.15)$$

where $\mathbf{h}(\mathbf{x}, t)$ consists of the flux $\mathbf{h}_{ch}(\mathbf{x}, t)$ induced by the thermal motion of the particles and an additional flux arising from the motion of the surrounding viscous medium. The former is given as

$$\mathbf{h}_{ch}(\mathbf{x}, t) = -p(\mathbf{x}, t) \frac{1}{\eta} \nabla_{\mathbf{x}} U_{ch} \quad \text{where} \quad U_{ch}(\mathbf{x}, t) = k_B \theta \ln p(\mathbf{x}, t) + U(\mathbf{x}) \quad (5.16)$$

is called the chemical potential resulting in a flux contribution coming from the thermal motion of the particles in the presence of a non-uniform concentration $-D \nabla_{\mathbf{x}} p(\mathbf{x}, t)$ in terms of the diffusion constant $D = k_B \theta / \eta$ with $\eta > 0$ as the viscosity and the additional contribution $-p(\mathbf{x}, t) / \eta \nabla_{\mathbf{x}} U(\mathbf{x})$ induced by the presence of a stationary potential $U(\mathbf{x})$. The chemical potential $U_{ch}(\mathbf{x}, t)$ in (5.16) expresses the energy of a certain particle at state \mathbf{x} and time t so that the resulting evolution of the particle distribution based on (5.15) can be interpreted as the motion of particles from states with high energy towards states with lower energy. This motion is driven by a chemical force f_{ch} that in addition determines the average velocity $\langle \mathbf{v}_{ch} \rangle$ of the particles relative to the viscous medium. Both are given in terms of the chemical potential as

$$f_{ch} = -\nabla_{\mathbf{x}} U_{ch} \quad \text{and} \quad \langle \mathbf{v}_{ch} \rangle = \frac{1}{\eta} f_{ch} = -\frac{1}{\eta} \nabla_{\mathbf{x}} U_{ch} \quad (5.17)$$

so that the flux in (5.16) is found as $\mathbf{h}_{ch}(\mathbf{x}, t) = p(\mathbf{x}, t) \langle \mathbf{v}_{ch} \rangle$. The second contribution to the flux $\mathbf{h}(\mathbf{x}, t)$ in (5.15) comes from the macroscopic motion of the viscous medium surrounding and influencing the flow of the particles. To account for such movement one has to add the contribution of the macroscopic velocity $\bar{\mathbf{v}}(\mathbf{x}, t)$ to the average particle velocity $\langle \mathbf{v}_{ch} \rangle$ arising from the chemical potential resulting in a total average velocity $\langle \mathbf{v} \rangle$ and a total flux $\mathbf{h}(\mathbf{x}, t)$ given as

$$\langle \mathbf{v} \rangle = \bar{\mathbf{v}} + \langle \mathbf{v}_{ch} \rangle \quad \text{and} \quad \mathbf{h}(\mathbf{x}, t) = p(\mathbf{x}, t) \langle \mathbf{v} \rangle \quad (5.18)$$

respectively. Insertion of these expressions into (5.15) leads to the final form of the Smoluchowski equation describing the Brownian motion of particles subjected to an external potential force field in a moving viscous medium as

$$\partial_t p(\mathbf{x}, t) = -\operatorname{div}_{\mathbf{x}} [p(\mathbf{x}, t) \bar{\mathbf{v}}] + \frac{1}{\eta} \operatorname{div}_{\mathbf{x}} [p(\mathbf{x}, t) \nabla_{\mathbf{x}} (k_B \theta \ln p(\mathbf{x}, t) + U(\mathbf{x}))]. \quad (5.19)$$

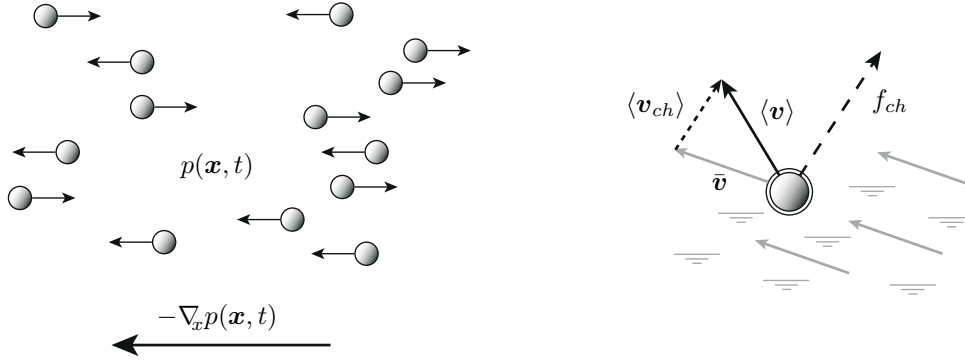


Figure 5.3: Brownian motion of non-interacting point particles. A non-uniform distribution of particles results in a flow proportional to the spatial gradient of particles from regions of high concentration to regions of low concentration as shown on the left. The right figure shows the resulting average velocity $\langle \mathbf{v} \rangle$ of point particles submerged in a, with velocity $\bar{\mathbf{v}}$, moving viscous medium.

Remarks 5.1. (a) The Smoluchowski equation (5.19) is dissipative which can be observed based on the introduction of

$$\mathcal{A}(p) = n \int p(\mathbf{x}, t) U_{ch} |d\mathbf{x}| \quad (5.20)$$

representing the dynamic free energy of the thermodynamic system of Brownian particles [75] in terms of the distribution $p(\mathbf{x}, t)$ summing up the chemical potential U_{ch} over all the n particles in the system. For the case of a non-moving viscous surrounding ($\bar{\mathbf{v}} = \mathbf{0}$) under isothermal conditions ($\theta = \text{constant}$) together with using (5.16), (5.19), $\int \partial_t p |d\mathbf{x}| = 0$ and integration by parts, where the contribution of the boundary integral is assumed to vanish, one can show that the time change of \mathcal{A} , given as

$$\frac{d\mathcal{A}}{dt} = -n \int \frac{\eta}{p(\mathbf{x}, t)} \mathbf{h}_{ch}(\mathbf{x}, t) \cdot \mathbf{h}_{ch}(\mathbf{x}, t) |d\mathbf{x}| \leq 0 \quad (5.21)$$

is negative. The inequality emphasizes the fact that diffusion drives the relaxation of the system towards the equilibrium state where $\mathbf{h}_{ch}(\mathbf{x}, t)$ given in (5.16) is responsible for the resulting dissipative flow.

(b) The equilibrium state is attained in the absence of macroscopic flow of the surrounding medium for a vanishing flux $\mathbf{h}_{ch} = \mathbf{0}$ so that $\nabla_{\mathbf{x}} U_{ch} = \mathbf{0}$ results in the equilibrium distribution

$$p_{eq}(\mathbf{x}) = \exp \left[-\frac{U(\mathbf{x})}{k_B \theta} \right] / \int \exp \left[-\frac{U(\mathbf{x})}{k_B \theta} \right] |d\mathbf{x}| \quad (5.22)$$

where the denominator results from the normalization condition $\int p_{eq} |d\mathbf{x}| = 1$. In the equilibrium state (5.22) the inequality in (5.21) becomes an equality with vanishing change of the free energy in time.

5.3.3 Brownian motion of flexible polymer chains

In this section the presented model of the previous section is extended to describe the Brownian motion of flexible polymer chains. Analogous to the point particles in Section

5.3.2, the proposed model assumes that the polymer chains are immersed into a viscous medium representing the surrounding polymer network. Contrary to the previous section where the state of the individual particles was described by their position \boldsymbol{x} , the state of the polymer chain is described in terms of the in Section 5.3.1 introduced end-to-end vector \boldsymbol{r} or analogously in terms of the newly introduced vector $\boldsymbol{\lambda} = \boldsymbol{r}/r_0$ as a measure of the rotation and stretch of the chain. The state of the overall thermodynamic system consisting of a large number of such chains in the vicinity of a material point can then be described by the distribution $p(\boldsymbol{\lambda}, t)$ in \mathbb{R}^3 .

Each polymer chain is now modeled as an entropic spring with the energy given based on (5.13) as

$$U(\boldsymbol{\lambda}) = \frac{3}{2}k_B\theta\lambda^2 + \text{terms independent of } \boldsymbol{\lambda} \quad (5.23)$$

where $\lambda = |\boldsymbol{\lambda}| = r/r_0$. It is further assumed that the viscosity is concentrated at the ends of the polymer chains, where we refer as the $-$ and the $+$ end as the starting and the end point of the end-to-end vector \boldsymbol{r} , respectively. This results in the kinematic relation illustrated in Figure 5.4 where on average the two end points are moving according to

$$\langle \boldsymbol{v}^\pm \rangle = \bar{\boldsymbol{v}}^\pm + \langle \boldsymbol{v}_{ch}^\pm \rangle \quad (5.24)$$

in terms of the velocity $\bar{\boldsymbol{v}}^\pm$ resulting from the motion of the surrounding viscous medium and the motion of the thermally active polymer chains $\langle \boldsymbol{v}_{ch}^\pm \rangle$ given as

$$\bar{\boldsymbol{v}}^\pm = \pm \frac{\boldsymbol{l}\boldsymbol{r}}{2} = \pm \frac{r_0\boldsymbol{l}\boldsymbol{\lambda}}{2} \quad \text{and} \quad \langle \boldsymbol{v}_{ch}^\pm \rangle = \mp \frac{1}{\eta} \nabla_{\boldsymbol{r}} U_{ch}(\boldsymbol{r}, t) = \mp \frac{1}{\eta r_0} \nabla_{\boldsymbol{\lambda}} U_{ch}(\boldsymbol{\lambda}, t) \quad (5.25)$$

respectively. The first part $\bar{\boldsymbol{v}}^\pm$ of the end point velocities in (5.24) corresponds to the changes in the mobile network following the macroscopic velocity gradient $\boldsymbol{l} = \dot{\boldsymbol{F}}\boldsymbol{F}^{-1}$ with \boldsymbol{F} being the deformation gradient. The second part $\langle \boldsymbol{v}_{ch}^\pm \rangle = \boldsymbol{F}_{ch}^\pm/\eta$ introduces the diffusion-based average motion of chain segments relative to the viscous medium under the action of the chemical forces $\boldsymbol{F}_{ch}^\pm = \mp \nabla_{\boldsymbol{r}} U_{ch} = \mp \nabla_{\boldsymbol{\lambda}} U_{ch}/r_0$ conjugate to the length r of the spring or its stretch λ drawing their ends. Summing up the velocities of the end points one derives the average transient change of the end-to-end vector $\langle \dot{\boldsymbol{r}} \rangle = \langle \boldsymbol{v}^+ \rangle - \langle \boldsymbol{v}^- \rangle$ which can be expressed in terms of the evolution of the stretch as

$$\langle \dot{\boldsymbol{\lambda}} \rangle = \boldsymbol{l}\boldsymbol{\lambda} - D^\lambda \nabla_{\boldsymbol{\lambda}} \left[\ln p(\boldsymbol{\lambda}, t) + \frac{3}{2}\lambda^2 \right] \quad \text{where} \quad D^\lambda = \frac{2k_B\theta}{\eta r_0^2}. \quad (5.26)$$

The result in (5.26) makes use of the chemical potential $U_{ch}(\boldsymbol{\lambda}, t)$ defined in stretch space analogous to (5.16) as

$$U_{ch}(\boldsymbol{\lambda}, t) = k_B\theta \ln p(\boldsymbol{\lambda}, t) + \frac{3}{2}k_B\theta\lambda^2. \quad (5.27)$$

The resulting diffusion process of the polymer chains can hence be interpreted as re-orientation and re-distribution of polymer chain stretches which, in analogy to (5.15), can be described as

$$\partial_t p(\boldsymbol{\lambda}, t) = -\text{div}_{\boldsymbol{\lambda}} [p(\boldsymbol{\lambda}, t) \langle \dot{\boldsymbol{\lambda}} \rangle] = -\text{div}_{\boldsymbol{\lambda}} (\boldsymbol{h}_{rev} + \boldsymbol{h}_{dis}). \quad (5.28)$$

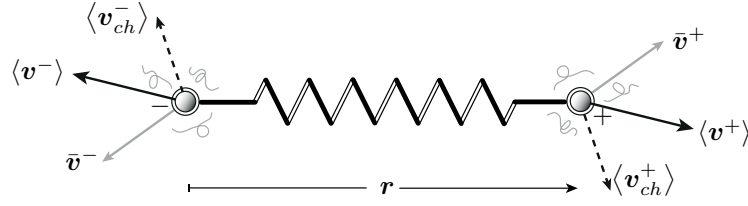


Figure 5.4: Lagrangian description of the Brownian motion of flexible polymer chains. The polymer chain with end-to-end vector \mathbf{r} is modeled as an entropic spring and placed into a viscous moving surrounding representing the remaining polymer network where the viscosity is concentrated at the chain end points. The resulting relative movement of these end points is described by the kinetic relation (5.26).

The two equations (5.26) and (5.28) can be viewed as the Lagrangian and the Eulerian description of the microscopic diffusional motion. Whereas the former follows a particular chain stretch and tracks the average velocity $\langle \dot{\boldsymbol{\lambda}} \rangle$ of its endpoints, the resulting Smoluchowski equation in (5.28) is concerned with the change of the probability of a certain state $\boldsymbol{\lambda}$ in time.

One can further observe both, a reversible and dissipative part of the evolution equation for the probability distribution in (5.28) in terms of the corresponding fluxes defined as

$$\mathbf{h}_{rev}(\boldsymbol{\lambda}, t) = p(\boldsymbol{\lambda}, t) \mathbf{l} \boldsymbol{\lambda} \quad \text{and} \quad \mathbf{h}_{dis}(\boldsymbol{\lambda}, t) = -D^\lambda p(\boldsymbol{\lambda}, t) \nabla_{\boldsymbol{\lambda}} \left[\ln p(\boldsymbol{\lambda}, t) + \frac{3}{2} \lambda^2 \right] \quad (5.29)$$

respectively. The reversible part arises due to the motion of the polymer chain in accordance with the surrounding macromedium whereas the dissipative part results from the diffusion and stretch relaxation. The dependence of the latter contribution on the mean-square length r_0 through D^λ emphasizes further the influence of the chain length on the diffusion process. The shorter the chain, the higher is its mobility.

Remarks 5.2. (a) *The dynamic free energy of the thermodynamic system is again obtained as an integral of the chemical potential (5.27) over all the possible states $\boldsymbol{\lambda}$ in the stretch space represented by \mathbb{R}^3 as*

$$\mathcal{A} = n \int_{\mathbb{R}^3} p(\boldsymbol{\lambda}, t) U_{ch} |d\boldsymbol{\lambda}| = n k_B \theta \int_{\mathbb{R}^3} p(\boldsymbol{\lambda}, t) \left[\ln p(\boldsymbol{\lambda}, t) + \frac{3}{2} \lambda^2 \right] |d\boldsymbol{\lambda}| \quad (5.30)$$

where n represents now the number of polymer chains in the system. For the case of a non-moving viscous surrounding ($\mathbf{l} = \mathbf{0}$) under isothermal conditions ($\theta = \text{constant}$) it can be further shown that the free energy is again decreasing in time as already outlined in Remark 5.1 for the point particles.

(b) *The equilibrium state is characterized by a natural unperturbed state of the end-to-end vector probability*

$$p_{eq}(\boldsymbol{\lambda}) = \exp \left[-\frac{3}{2} \lambda^2 \right] / \int_{\mathbb{R}^3} \exp \left[-\frac{3}{2} \lambda^2 \right] |d\boldsymbol{\lambda}| = \left(\frac{3}{2\pi} \right)^{3/2} \exp \left[-\frac{3}{2} \lambda^2 \right] \quad (5.31)$$

representing a Gaussian bell-shaped distribution for which the flux \mathbf{h}_{dis} in (5.29) vanishes.

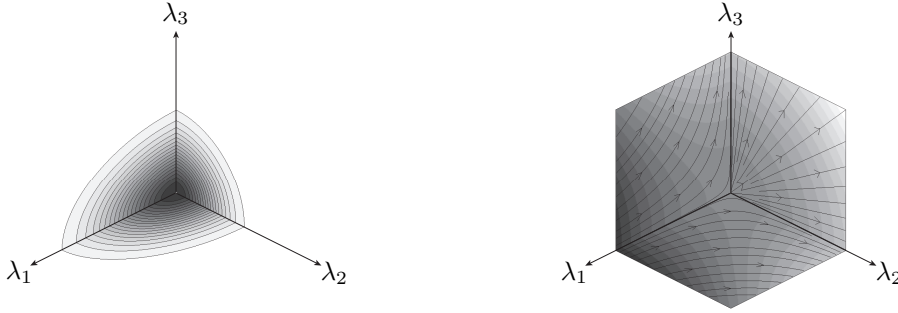


Figure 5.5: Eulerian description of the Brownian motion of flexible polymer chains. A perturbation of the probability distribution $p(\boldsymbol{\lambda}, t)$ due to an instantaneous macroscopic deformation schematically shown on the left results in an inhomogeneity of the chemical potential field $U_{ch}(\boldsymbol{\lambda}, t)$ and a resulting flow based on (5.29) leading to a change of probability according to the Smoluchowski equation in (5.28).

The resulting mechanism of viscoelasticity can now be understood by considering a macroscopic motion defined by the macrodeformation represented in terms of the velocity gradient \boldsymbol{l} which pulls the system out of equilibrium and deforms the initial distribution (5.31) as depicted on the left of Figure 5.5. This results in a change in the chemical potential U_{ch} making it inhomogeneous so that the chemical force f_{ch} , driving the diffusion process, develops. When the macrodeformation freezes, meaning that it remains constant for a sufficiently long time, this process will return the system to the unperturbed state based on a diffusional flow depicted on the right of Figure 5.5 in which mechanical work will be dissipated.

5.4 Macroscopic formulation of the diffusion-based transient network model

The goal of this section is to embed the diffusion-based micromechanical polymer model developed in the previous Section 5.3 into the framework of finite rubber viscoelasticity by the construction of closed form expressions for the viscous part of the isochoric free energy $\bar{\Psi}^v$ in (5.6) as well as the corresponding viscous over stresses $\bar{\boldsymbol{\tau}}^v$ in (5.7) for a single viscous subnetwork illustrated in Figure 5.2.

Above, the microscopic model of Section 5.3.2 is treated as a thermodynamic system of Brownian point particles which is extended in Section 5.3.3 towards the description of the Brownian motion of flexible polymer chains. It is shown that the temporary state of such a system is described by the probability function $p(\boldsymbol{\lambda})$ whose evolution in time is driven by (5.28) in the form of the Smoluchowski equation. Solving this parabolic differential equation directly does not allow for solutions of the free energy $\bar{\Psi}^v$ or the viscous over stress $\bar{\boldsymbol{\tau}}^v$ which can be expressed in closed form. It is for this reason that a particular choice for the change of the probability function $p(\boldsymbol{\lambda})$ is assumed in Section 5.4.1 in the form of a tensorial representation of its evolution resulting in the desired closed form solutions of these quantities. Section 5.4.2 then derives these closed form solutions of the viscous part of the isochoric free energy as well as for the viscous over stress and gives a proof of the satisfaction of the thermodynamic consistency of the proposed model. Finally, Section 5.4.3 summarizes the algorithmic representation and implementation of the model.

5.4.1 Tensorial representation of the probability function evolution

In the following a tensorial representation of the evolution of the probability function is assumed, which allows for a closed form representation of the macroscopic quantities within the finite rubber viscoelasticity model. In particular, this section outlines how the Smoluchowski equation (5.28) can equivalently be described based on an ordinary differential equation in one tensorial quantity.

To do so, use is made of the representation of changes of the solids macroscopic properties in the current configuration \mathcal{S} with respect to a reference configuration \mathcal{B} , as it is outlined briefly in Section 5.2, where the deformation gradient \mathbf{F} acts as the linear map between tangent vectors of those spaces. The property of interest in this setting is now given by the probability function $p(\boldsymbol{\lambda}) : \mathcal{L}_{\mathbf{x}} \rightarrow \mathbb{R}$ where $\mathcal{L}_{\mathbf{x}} = \mathbb{R}^3$ is the stretch space connected locally to a material point with position \mathbf{x} in the current configuration \mathcal{S} . Its evolution is described with respect to an introduced referential probability function P living in a stretch space $\mathcal{L}_{\mathbf{X}} = \mathbb{R}^3$ connected to a material point with position \mathbf{X} in the reference configuration \mathcal{B} . This initial probability function is assumed to be given as

$$P(\boldsymbol{\Lambda}) = \left(\frac{3}{2\pi}\right)^{3/2} \exp\left[-\frac{3}{2}\boldsymbol{\Lambda}^2\right] \quad (5.32)$$

in the form of a Gaussian distribution in terms of the norm of the referential stretch vector $\boldsymbol{\Lambda}$. The two stretch spaces are linked by a *microdeformation map*

$$\mathbf{P} : \begin{cases} \mathcal{L}_{\mathbf{X}} & \longrightarrow \mathcal{L}_{\mathbf{x}} \\ \boldsymbol{\Lambda} & \longmapsto \boldsymbol{\lambda} = \mathbf{P}\boldsymbol{\Lambda} \end{cases} \quad (5.33)$$

as it is illustrated in Figure 5.6. The evolution of $p(\boldsymbol{\lambda})$ with respect to $P(\boldsymbol{\Lambda})$ is then assumed to depend on this microdeformation map in (5.33) based on the relation

$$p(\boldsymbol{\lambda}) = \frac{1}{\det \mathbf{P}} P(\boldsymbol{\Lambda}). \quad (5.34)$$

A schematic representation of the relation between those probability functions is outlined in Figure 5.6. It shows the change of the probability function $p(\boldsymbol{\lambda})$ of a point \mathbf{x} in the current configuration based on the application of an arbitrary microdeformation map \mathbf{P} when starting from an unperturbed probability function $P(\boldsymbol{\Lambda})$ of the same material point \mathbf{X} in the reference configuration. It is noted that the spaces $\mathcal{L}_{\mathbf{X}}$ and $\mathcal{L}_{\mathbf{x}}$ contain microscopic objects such as their corresponding stretch vectors $\boldsymbol{\Lambda}$ and $\boldsymbol{\lambda}$, respectively. Even though those objects are not considered within an infinitesimal setting, they belong to such a small scale that they can interfere with objects from the tangent spaces of the body's configurations \mathcal{B} and \mathcal{S} . Such property is exploited in Section 5.3.3 by adding the macrovelocity $\bar{\mathbf{v}}^{\pm}$ to the microvelocities $\langle \mathbf{v}_{ch}^{\pm} \rangle$ in (5.24). Moreover they share the metric tensors \mathbf{G} and \mathbf{g} of the tangential spaces introduced in Section 5.2.

The microscopic origin of the cause for the evolution of the stretch probability $p(\boldsymbol{\lambda})$ is given by the chemical potential (5.27) which, based on (5.32) and (5.34), takes the form

$$U_{ch}(\boldsymbol{\lambda}) = k_B\theta \left\{ -\frac{3}{2}\boldsymbol{\Lambda}^2 - \ln(\det \mathbf{P}) + \frac{3}{2}\boldsymbol{\lambda}^2 \right\} \quad (5.35)$$

when neglecting expressions constant in $\boldsymbol{\lambda}$. The resulting expression in (5.35) is quadratic in terms of the stretches $\lambda = |\boldsymbol{\lambda}|_{\mathbf{g}} = \sqrt{\boldsymbol{\lambda} \cdot \mathbf{g}\boldsymbol{\lambda}}$ and $\Lambda = |\boldsymbol{\Lambda}|_{\mathbf{G}} = \sqrt{\boldsymbol{\Lambda} \cdot \mathbf{G}\boldsymbol{\Lambda}} = \sqrt{\boldsymbol{\lambda} \cdot \mathbf{P}^{-T}\mathbf{G}\mathbf{P}^{-1}\boldsymbol{\lambda}}$.

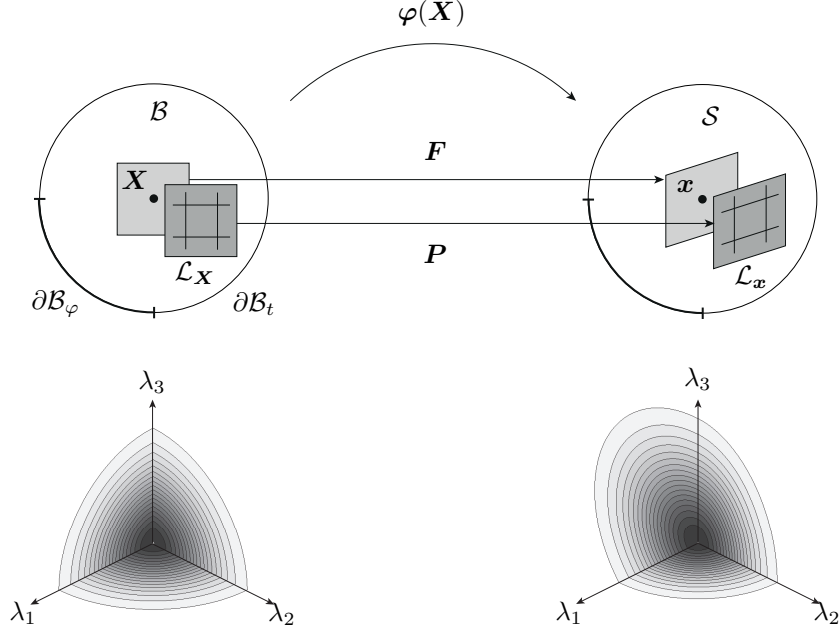


Figure 5.6: Tensorial representation of the probability function evolution. The stretch spaces \mathcal{L}_X and \mathcal{L}_x connected to a material point with position X and x in the reference- and the current configuration and its relation through the microdeformation map P is outlined in the top figure. The figure below schematically shows the change in probability $p(\lambda)$ in \mathcal{L}_x starting from the equilibrium distribution $P(\Lambda)$ in \mathcal{L}_X due to some arbitrary microdeformation P .

This result allows for the computation of the average rate of change of the stretch vector based on (5.26) as

$$\langle \dot{\lambda} \rangle = \mathbf{l}\lambda - 3D^\lambda \mathbf{g}^{-1}(-\mathbf{P}^{-T} \mathbf{G} \mathbf{P}^{-1} \lambda + \mathbf{g}\lambda) \quad (5.36)$$

written now in terms of the micro-deformation map P of (5.33). The obtained expression in (5.36) is linear in λ from which it follows that the relation between the probability functions in (5.34) is preserved, validating the equivalent representation of the Smoluchowski equation in terms of the tensorial representation introduced above. Insertion of (5.33) into (5.36) results in

$$\dot{\mathbf{P}} \mathbf{P}^{-1} \lambda = \left[\mathbf{l} - 3D^\lambda \mathbf{g}^{-1}(-\mathbf{P}^{-T} \mathbf{G} \mathbf{P}^{-1} + \mathbf{g}) \right] \lambda \quad (5.37)$$

which results, after multiplying with the metric tensor \mathbf{g} from the left and after expressing the velocity gradient \mathbf{l} in terms of the isochoric part of the deformation gradient $\bar{\mathbf{F}}$, in the evolution equation for the tensorial micro-deformation map P as

$$\mathbf{g} \dot{\mathbf{P}} \mathbf{P}^{-1} = \mathbf{g} \dot{\bar{\mathbf{F}}} \bar{\mathbf{F}}^{-1} - 3D^\lambda (-\mathbf{P}^{-T} \mathbf{G} \mathbf{P}^{-1} + \mathbf{g}). \quad (5.38)$$

This evolution equation consists of a reversible part related to the macrodeformation represented by $\mathbf{l} = \dot{\bar{\mathbf{F}}} \bar{\mathbf{F}}^{-1}$ and a dissipative part due to the diffusion-based mechanism introduced in Section 5.3 in terms of the diffusion coefficient D^λ defined in (5.26). To avoid a dependence of the evolution of the microdeformation map on the macrodeformation, the tensor P is split into $P = \bar{\mathbf{F}} P_X$ in terms of a newly introduced tensorial quantity

$\mathbf{P}_X : \mathcal{L}_X \rightarrow \mathcal{L}_X$ denoted as *pre-deformation map*. The corresponding evolution equation can then be derived from (5.38) as

$$\dot{\mathbf{P}}_X = 3D^\lambda \left(\bar{\mathbf{F}}^{-1} \mathbf{g}^{-1} \bar{\mathbf{F}}^{-T} \mathbf{P}_X^{-T} \mathbf{G} - \mathbf{P}_X \right) \quad (5.39)$$

solely in terms of microscopic object. Since \mathbf{P}_X in general is a non-symmetric tensor, it includes both, information with regard to *pre-stretch* and *pre-rotation* where the latter does not influence the overall free energy and can therefore be excluded from the formulation. This is achieved by the introduction of the symmetric tensorial quantity

$$\mathbf{A} = \mathbf{P}_X \mathbf{G}^{-1} \mathbf{P}_X^T \quad (5.40)$$

that contains all the required information about the microdeformation of the viscoelastic subnetwork. The evolution of that expression can be obtained by plugging (5.40) into (5.39) which results in

$$\dot{\mathbf{A}} = \frac{1}{\tau} \left(\bar{\mathbf{C}}^{-1} - \mathbf{A} \right) \quad \text{with} \quad \frac{1}{\tau} = 6 D^\lambda \quad (5.41)$$

an evolution equation which surprisingly has a form close to existing models of finite viscoelasticity. Conduct Remarks 5.3 with regard to a further discussion on similarities with already existing models in the literature. The developed evolution equation in (5.41) allows for an interpretation of the introduced symmetric tensor \mathbf{A} in (5.40) as some intermediate metric whose change is driven by its difference when compared to the referential metric $\bar{\mathbf{C}}^{-1}$ where $\bar{\mathbf{C}} = \bar{\mathbf{F}}^T \mathbf{g} \bar{\mathbf{F}}$ is the isochoric part of the right Cauchy Green tensor. An equilibrium state is obtained as soon as those two metric tensors coincide for which a fully relaxed subnetwork is expected.

5.4.2 Isochoric viscous free energy and viscous overstress expressions

The goal of this section is to show that the tensorial representation of the change in the probability function determined by (5.41) allows further for a closed form expression of the viscous part of the isochoric free energy and the viscous overstress.

In particular, the macroscopic free energy is obtained by homogenization of the free energy of the thermodynamic system in (5.30) for the particular form $p(\boldsymbol{\lambda})$ and $U_{ch}(\boldsymbol{\lambda})$ in (5.34) and (5.35) over the stretch space as

$$\bar{\Psi}^v = n \int_{\mathcal{L}_x} p(\boldsymbol{\lambda}) U_{ch}(\boldsymbol{\lambda}) |d\boldsymbol{\lambda}| = \mu^v \left[\int_{\mathcal{L}_x} P(\boldsymbol{\Lambda}) \left(-\frac{3}{2} \Lambda^2 + \frac{3}{2} \lambda^2 \right) |d\boldsymbol{\Lambda}| - \ln(\det \mathbf{P}) \right] \quad (5.42)$$

where the constant terms are neglected in the latter expression and the viscous overstress moduli is introduced as $\mu^v = n k_B \theta$. The integration over \mathcal{L}_X can then be computed by separating the integration over the stretch value Λ and the stretch orientation $\mathbf{T} = \boldsymbol{\Lambda} / \Lambda \in S^2$ living on the 2-sphere S^2 . This leads to $\lambda^2 = \boldsymbol{\lambda} \cdot \mathbf{g} \boldsymbol{\lambda} = \Lambda^2 \mathbf{T} \cdot \mathbf{P}^T \mathbf{g} \mathbf{P} \mathbf{T}$ and $|d\boldsymbol{\Lambda}| = \Lambda^2 d\Lambda |d\mathbf{T}|$ so that the integral in (5.42) becomes

$$\int_{\mathcal{L}_x} P(\boldsymbol{\Lambda}) \left(-\frac{3}{2} \Lambda^2 + \frac{3}{2} \lambda^2 \right) |d\boldsymbol{\Lambda}| = \frac{3}{2} \int_0^\infty P(\Lambda) \Lambda^4 d\Lambda \cdot \int_{S^2} (\mathbf{T} \cdot \mathbf{P}^T \mathbf{g} \mathbf{P} \mathbf{T} - 1) |d\mathbf{T}|. \quad (5.43)$$

Using (5.32) it can easily be shown that the first integral on the right hand side of (5.43) becomes

$$\int_0^\infty P(\Lambda)\Lambda^4 d\Lambda = \frac{1}{4\pi} = \frac{1}{|S^2|}. \quad (5.44)$$

The identity $\frac{1}{|S^2|} \int_{S^2} \mathbf{T} \otimes \mathbf{T} |d\mathbf{T}| = \frac{1}{3} \mathbf{G}^{-1}$ together with (5.40) allows to convert the second integral on the right hand side of (5.43) into

$$\frac{1}{|S^2|} \int_{S^2} \mathbf{T} \cdot \mathbf{P}^T \mathbf{g} \mathbf{P} \mathbf{T} |d\mathbf{T}| = \frac{1}{3} \mathbf{A} : \bar{\mathbf{C}}. \quad (5.45)$$

Finally one obtains, neglecting again the constant terms, the closed form expression for the viscous part of the isochoric free energy as

$$\bar{\Psi}^v = \bar{\Psi}^v(\bar{\mathbf{C}}, \mathbf{A}) = \frac{1}{2} \mu^v \left[(\mathbf{A} : \bar{\mathbf{C}} - 3) - \ln(\det \mathbf{A}) \right] \quad (5.46)$$

a neo-Hookean type expression independent of the influence of possible rotations of the microstructure based on the chosen form in (5.40). Consult again Remarks 5.3 for a comparison of the resulting model with already existing models in the literature.

The resulting closed form expression for the viscous part of the isochoric free energy in (5.46) allows finally for the computation of a closed form expression for the corresponding viscous overstress based on (5.7) as

$$\bar{\boldsymbol{\tau}}^v = \bar{\mathbf{F}} \left(2 \partial_{\bar{\mathbf{C}}} \bar{\Psi}^v(\bar{\mathbf{C}}, \mathbf{A}) \right) \bar{\mathbf{F}}^T = \mu^v \bar{\mathbf{F}} \mathbf{A} \bar{\mathbf{F}}^T. \quad (5.47)$$

Remarks 5.3. (a) *Interestingly, the proposed model for the representation of the transient network to describe the rate-dependence yields the same expressions for the viscous part of the isochoric macroscopic free energy in (5.46) as well as for the corresponding viscous overstress in (5.47) as in GREEN & TOBOLSKY [127]. The transient changes in the network in GREEN & TOBOLSKY [127] are explained by breakage and re-creation mechanisms with their rates being the main phenomenological quantities. Contrary, the current work introduces effective viscous mechanisms, representing the temporal chain interactions, through a phenomenological viscosity η . Based on the resulting identical expressions for the free energy and the overstresses, the same limitations do apply for both models.*

(b) *In the application of the transient model of GREEN & TOBOLSKY [127] in LUBLINER [220] it is assumed that the determinant of the internal variable in (5.40) is constrained to be $\det \mathbf{A} = 1$ so that the last term in the expression of the isochoric part of the free energy in (5.46) cancels. In this work, $\det \mathbf{A} = 1$ in the initial state as well as after obtaining a fully relaxed state, but it may deviate from that value for states in between. Still, as outlined below, thermodynamic consistency of the formulation can be shown.*

To outline the thermodynamic consistency of the proposed model one could easily refer to the starting point of the model in the form of the Smoluchowski equation which is shown to be dissipative in Remarks 5.1. To assure that all the transformations performed in this section do not yield a different result, the proof is illustrated in detail.

Since the introduced internal variable \mathbf{A} in (5.40) is independent of the macrodeformation, the reduced dissipation inequality follows from (5.8) as

$$\mathcal{D}_{loc} = -2 \partial_{\mathbf{A}} \bar{\Psi}^v : \frac{1}{2} \dot{\mathbf{A}} \geq 0 \quad (5.48)$$

with the satisfaction of the inequality to be shown in the following. Based on (5.46), the first term in (5.48) follows simply as $2 \partial_{\mathbf{A}} \bar{\Psi}^v = \mu^v (\bar{\mathbf{C}} - \mathbf{A}^{-1})$ so that together with the evolution equation in (5.41) the dissipation can be expressed as

$$\mathcal{D}_{loc} = -\frac{\mu^v}{2\tau} (\bar{\mathbf{C}} - \mathbf{A}^{-1}) : (\bar{\mathbf{C}}^{-1} - \mathbf{A}) \geq 0 \quad (5.49)$$

where the inequality follows from the result of Theorem 1.

Theorem 1. *Let $\bar{\mathbf{C}}$ be the isochoric part of the right Cauchy Green tensor and \mathbf{A} the symmetric tensorial internal variable of the developed diffusion-based micromechanical polymer model. Then the following inequality holds*

$$(\bar{\mathbf{C}} - \mathbf{A}^{-1}) : (\bar{\mathbf{C}}^{-1} - \mathbf{A}) \leq 0. \quad (5.50)$$

Proof. Consider a polar decomposition of the two symmetric tensors $\bar{\mathbf{C}}$ and \mathbf{A} as well as their inverses in the form

$$\bar{\mathbf{C}} = \sum_{i=1}^{n_{\text{dim}}} \lambda_i \mathbf{u}_i \otimes \tilde{\mathbf{u}}_i, \quad \mathbf{A} = \sum_{j=1}^{n_{\text{dim}}} \mu_j \mathbf{v}_j \otimes \tilde{\mathbf{v}}_j \quad \text{and} \quad \bar{\mathbf{C}}^{-1} = \sum_{i=1}^{n_{\text{dim}}} \lambda_i^{-1} \tilde{\mathbf{u}}_i \otimes \mathbf{u}_i, \quad \mathbf{A}^{-1} = \sum_{j=1}^{n_{\text{dim}}} \mu_j^{-1} \tilde{\mathbf{v}}_j \otimes \mathbf{v}_j \quad (5.51)$$

where $\lambda_i > 0$, $\mu_j > 0$ are the positive eigenvalues and $\{\mathbf{u}_i, \tilde{\mathbf{u}}_i\}$, $\{\mathbf{v}_i, \tilde{\mathbf{v}}_i\}$ are the orthogonal eigenvectors of $\bar{\mathbf{C}}$ and \mathbf{A} , respectively. Since $\sum_i \mathbf{u}_i \otimes \tilde{\mathbf{u}}_i = \sum_j \mathbf{v}_j \otimes \tilde{\mathbf{v}}_j = \mathbf{1}$ and $\mathbf{1} : \mathbf{1} = 3$ the left hand side of (5.50) becomes

$$(\bar{\mathbf{C}} - \mathbf{A}^{-1}) : (\bar{\mathbf{C}}^{-1} - \mathbf{A}) = 6 - \sum_{i,j} [\lambda_i \mu_j + \lambda_i^{-1} \mu_j^{-1}] (\mathbf{u}_i \otimes \tilde{\mathbf{u}}_i) : (\mathbf{v}_j \otimes \tilde{\mathbf{v}}_j). \quad (5.52)$$

To establish the inequality in (5.50), use is made of the identities $\alpha + \alpha^{-1} \geq 2$ for $\alpha > 0$ so that $\lambda_i \mu_j + \lambda_i^{-1} \mu_j^{-1} \geq 2$ and $(\mathbf{u}_i \otimes \tilde{\mathbf{u}}_i) : (\mathbf{v}_j \otimes \tilde{\mathbf{v}}_j) = (\mathbf{u}_i \cdot \mathbf{v}_j)(\tilde{\mathbf{u}}_i \cdot \tilde{\mathbf{v}}_j) = (\mathbf{u}_i \cdot \mathbf{v}_j)^2 \geq 0$ and finally

$$(\bar{\mathbf{C}} - \mathbf{A}^{-1}) : (\bar{\mathbf{C}}^{-1} - \mathbf{A}) \leq 6 - 2 \cdot \mathbf{1} : \mathbf{1} = 0 \quad (5.53)$$

showing (5.50). □

5.4.3 Algorithmic representation and implementation

The algorithmic setting and implementation of the proposed model for the representation of the mobile viscous subnetworks within a time incremental formulation is briefly discussed in this section.

To do so, the evolution equation (5.41) of the symmetric tensorial internal variable \mathbf{A} needs to be discretized in time to advance from a given discrete time t_n towards $t_{n+1} = t_n + \Delta t$

within a single time step Δt . Application of an unconditional stable implicit backward Euler integration of (5.41) results in the update of the internal variable \mathbf{A} of a single viscous subnetwork as

$$\mathbf{A}_{n+1} = \frac{1}{1 + \Delta t/\tau} \left[\mathbf{A}_n + \frac{\Delta t}{\tau} \bar{\mathbf{C}}_{n+1}^{-1} \right] \quad (5.54)$$

in terms of the relaxation time $\tau = 1/6D^\lambda$ with D^λ given in terms of solely microscopic objects in (5.26). Due to the linearity of the evolution equation (5.41), its algorithmic update in (5.54) is obtained in closed form. With the updated internal variable evaluated, the viscous overstress contribution follows from (5.47) as

$$\bar{\boldsymbol{\tau}}_{n+1}^v = \mu^v \bar{\mathbf{F}}_{n+1} \mathbf{A}_{n+1} \bar{\mathbf{F}}_{n+1}^T = \mu^v \frac{1}{1 + \Delta t/\tau} \left[\bar{\mathbf{F}}_{n+1} \mathbf{A}_n \bar{\mathbf{F}}_{n+1}^T + \frac{\Delta t}{\tau} \mathbf{g}_{n+1}^{-1} \right] \quad (5.55)$$

in terms of the overstress moduli $\mu^v = n k_B \theta$. Finally, the sensitivity of the overstress update (5.55) to the variations of the deformation at time instance t_{n+1} yield the algorithmic tangent moduli in the form

$$\bar{\mathbb{C}}_{n+1}^v = 2 \partial_{\mathbf{g}} \bar{\boldsymbol{\tau}}_{n+1}^v = -4\mu^v \frac{\Delta t/\tau}{1 + \Delta t/\tau} \mathbb{I}_{\mathbf{g}^{-1}} \quad (5.56)$$

where $\mathbb{I}_{\mathbf{g}^{-1}}^{abcd} = [(\mathbf{g}^{-1})^{ac}(\mathbf{g}^{-1})^{bd} + (\mathbf{g}^{-1})^{ad}(\mathbf{g}^{-1})^{bc}]/2$ is the fourth order identity tensor written in terms of the inverse metric \mathbf{g}^{-1} .

Remarks 5.4. (a) *It is emphasized that the result in (5.55) has to be combined with the elastic response coming from a chosen model for the elastic ground network in the way outlined in (5.7). The resulting isochoric response then further has to be combined with the spherical part as shown in (5.4) to obtain the final form of the stresses. In an analogous way the sensitivity of the final stresses is obtained where the expression in (5.56) results only from the sensitivity of the viscous overstress in (5.55) with regard to variations in the deformation.*

(b) *The results in (5.54)–(5.56) hold for a single viscous subnetwork in terms of microscopically motivated parameters τ and μ^v . The proposed viscous model though consists of s viscous subnetworks resulting in totally $2s$ parameters. In particular, the s different relaxation times $\{\tau_i\}_{i=1}^s$ represent the broad dissipation spectra of the model whereas the s viscous overstress moduli $\{\mu_i^v\}_{i=1}^s$ allow for different overstress stiffnesses of the model. Finally, the history of each of the branches is described by a separate internal variable \mathbf{A}_i resulting in the required storage of in total $6s$ scalar variables due to the symmetry of \mathbf{A} .*

5.5 Representative numerical simulations

This section evaluates the capacity of the proposed diffusion-based viscoelasticity model by a comparison of the obtained numerical results with in the literature available experimental data sets. The essential requirement of the model is its ability to capture the specific viscoelastic response for different test scenarios of rubber-like materials at varying finite strains within a broad range of applied loading velocities. The material used

throughout this section is a highly saturated nitrile butadiene rubber HNBR50 for which in Section 5.5.1 the parameters of the numerical model are fitted based on homogeneous uniaxial cyclic tests for an applied stretch λ_1 within the interval $\lambda_1 \in [0.75, 2.0]$. Section 5.5.2 then evaluates the model by simulating a similar uniaxial cyclic test but for an applied stretch within the purely compressive interval $\lambda_1 \in [0.75, 1.0]$ as well as for an applied stretch within the interval $\lambda_1 \in [0.75, 2.0]$ including several relaxation breaks. Finally, a non-homogeneous three-dimensional shear test is simulated in Section 5.5.3 for different loading conditions and compared with available experimental results.

5.5.1 Parameter fitting procedure

The experimental data set for this problem is taken from MIEHE & GÖKTEPE [239] for a set of homogeneous uniaxial cyclic tests of a highly saturated nitrile butadiene rubber HNBR50 produced by the Robert Bosch GmbH. It is outlined in detail in MIEHE & GÖKTEPE [239] that this material does not exhibit an equilibrium hysteresis so that its response can be considered as purely viscoelastic. In the following, the characteristic parameters of the model are fitted based on a homogeneous uniaxial cyclic test for an applied stretch λ_1 within the interval $\lambda_1 \in [0.75, 2.0]$. Based on the decomposition of the polymer microstructure into an elastic ground network and a viscous subnetwork, the corresponding parameters of the models representing both need to be fitted to the actual experimental results.

It is mentioned in Section 5.2 that the developed diffusion-based viscoelastic polymer model does not rely on the choice of a particular model for the representation of the elastic ground network. Therefore, throughout Section 5.5 the non-affine network model of MIEHE ET AL. [244] is chosen for the representation of the elastic response of the rubber-like material which is capable to produce an excellent fit when compared to the equilibrium response of HNBR50 for the homogeneous uniaxial experiments as outlined in MIEHE & GÖKTEPE [239]. In particular, in this work parameters close to those used in MIEHE & GÖKTEPE [239] are obtained following the parameter fitting procedure outline in their work. The corresponding values are given as $N = 5.2207$, $\mu = 0.1602 \text{ MPa}$, $p = 1.0666$, $U = 11.2122$, and $q = 0.2013$, representing the number of chain segments in the elastic ground network, the ground state stiffness, the non-affine stretch parameter, the tube geometry parameter and the non-affine tube parameter, respectively, for the homogeneous uniaxial cyclic test outlined below.

To fit the parameters for the developed viscoelastic part, a homogeneous uniaxial cyclic test performed at three different absolute loading rates $|\dot{\lambda}_1| = 5 \cdot 10^{-2} \text{ min}^{-1}$, $|\dot{\lambda}_1| = 5 \cdot 10^{-1} \text{ min}^{-1}$, and $|\dot{\lambda}_1| = 5 \cdot 10^0 \text{ min}^{-1}$ of that same material is used. It is emphasized that the actual loading rates might deviate from these values due to a decreasing accuracy of the experimental measurements especially for low loading rates. The stretch region of the specimen is assumed to fall within the closed interval $\lambda_1 \in [0.75, 2.0]$. The experimental stress-stretch curves in terms of the P_{11} component of the First Piola Kirchhoff stress tensor $\mathbf{P} = \boldsymbol{\tau} \mathbf{F}^{-T}$ are depicted in the upper left illustration of Figure 5.9 below. One observes a characteristic response for viscoelastic materials in the form of a stiffer behavior for an increasing loading rate. Also the area of the resulting hysteresis curves, representing the amount of dissipated energy per cycle, gets larger as the loading rate increases from $5 \cdot 10^{-2} \text{ min}^{-1}$ to $5 \cdot 10^0 \text{ min}^{-1}$. Finally, one can observe the difference between the first

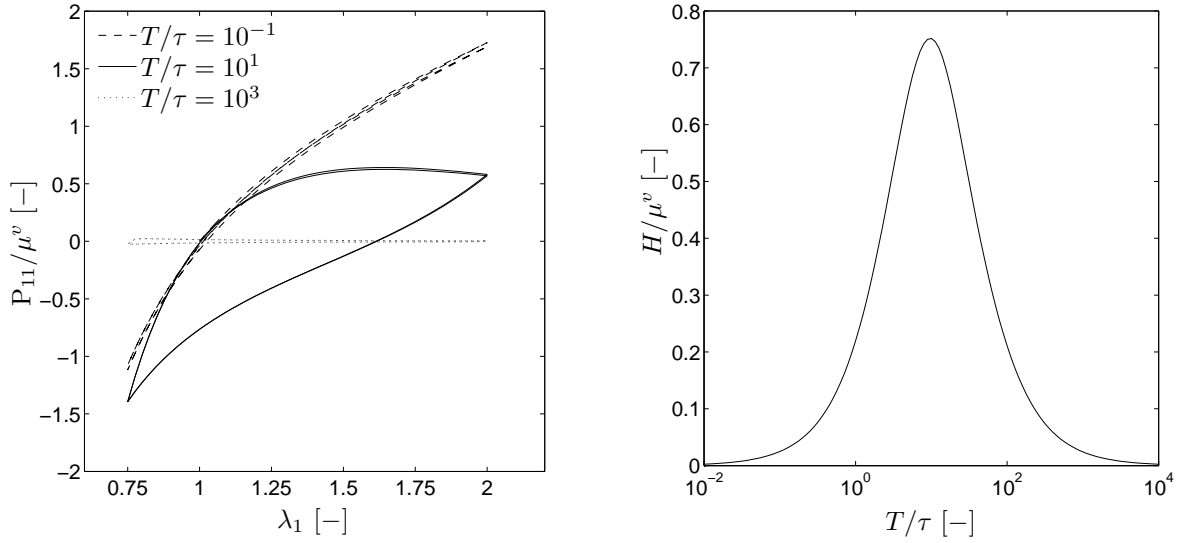


Figure 5.7: Parameter fitting procedure. The illustration outlines the viscous response produced by a single branch. The relative overstress P_{11}/μ^v for loading periods T much lesser, comparable, and much greater than the relaxation time τ is shown on the left. The dependence of the relative hysteresis area H/μ^v of the first cycle on the ratio T/τ between the loading time and the relaxation time is shown on the right.

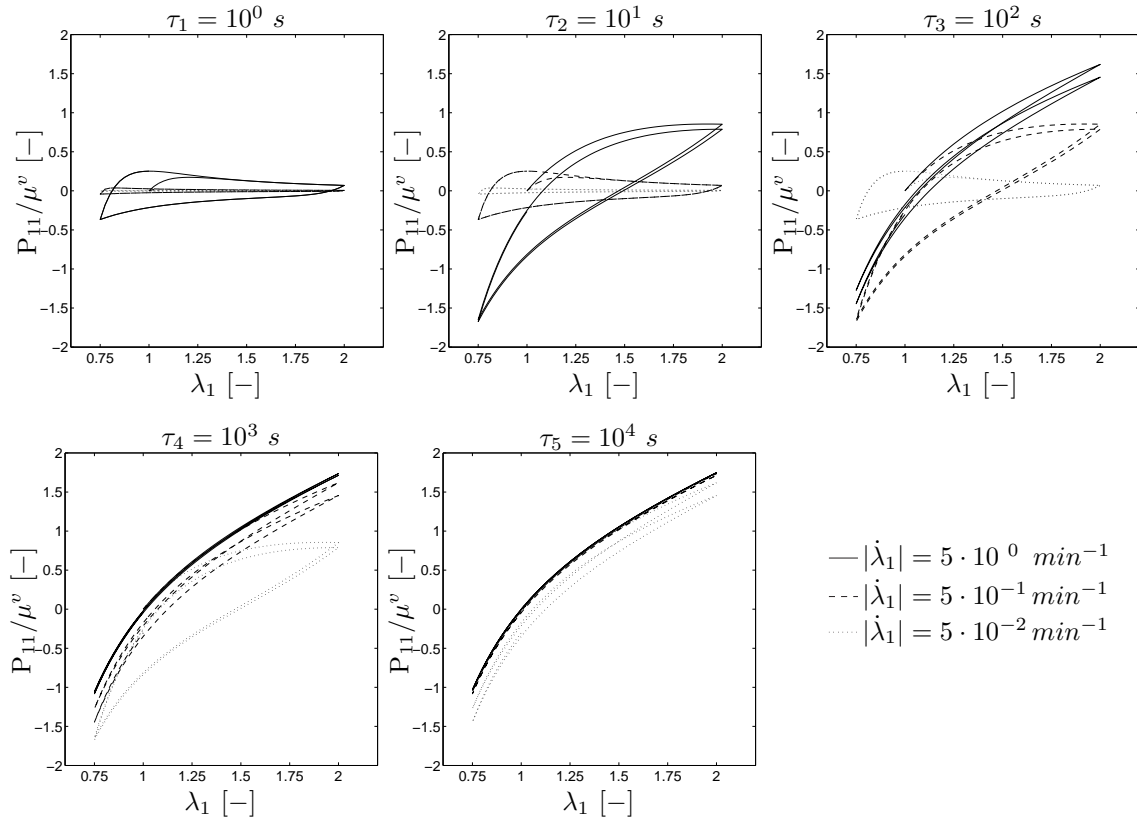


Figure 5.8: Parameter fitting procedure. The illustration outlines the normalized overstress profiles for the $s = 5$ viscous branches with the relaxation times $\{\tau_i\}_{i=1}^s = \{10^0, 10^1, 10^2, 10^3, 10^4\} \text{ s}$ and unit overstress moduli $\{\tilde{\mu}_i^v\}_{i=1}^s = 1 \text{ MPa}$ for the three considered uniaxial cyclic tests with different loading rates $|\dot{\lambda}_1| = 5 \cdot 10^0 \text{ min}^{-1}$, $|\dot{\lambda}_1| = 5 \cdot 10^{-1} \text{ min}^{-1}$, and $|\dot{\lambda}_1| = 5 \cdot 10^{-2} \text{ min}^{-1}$.

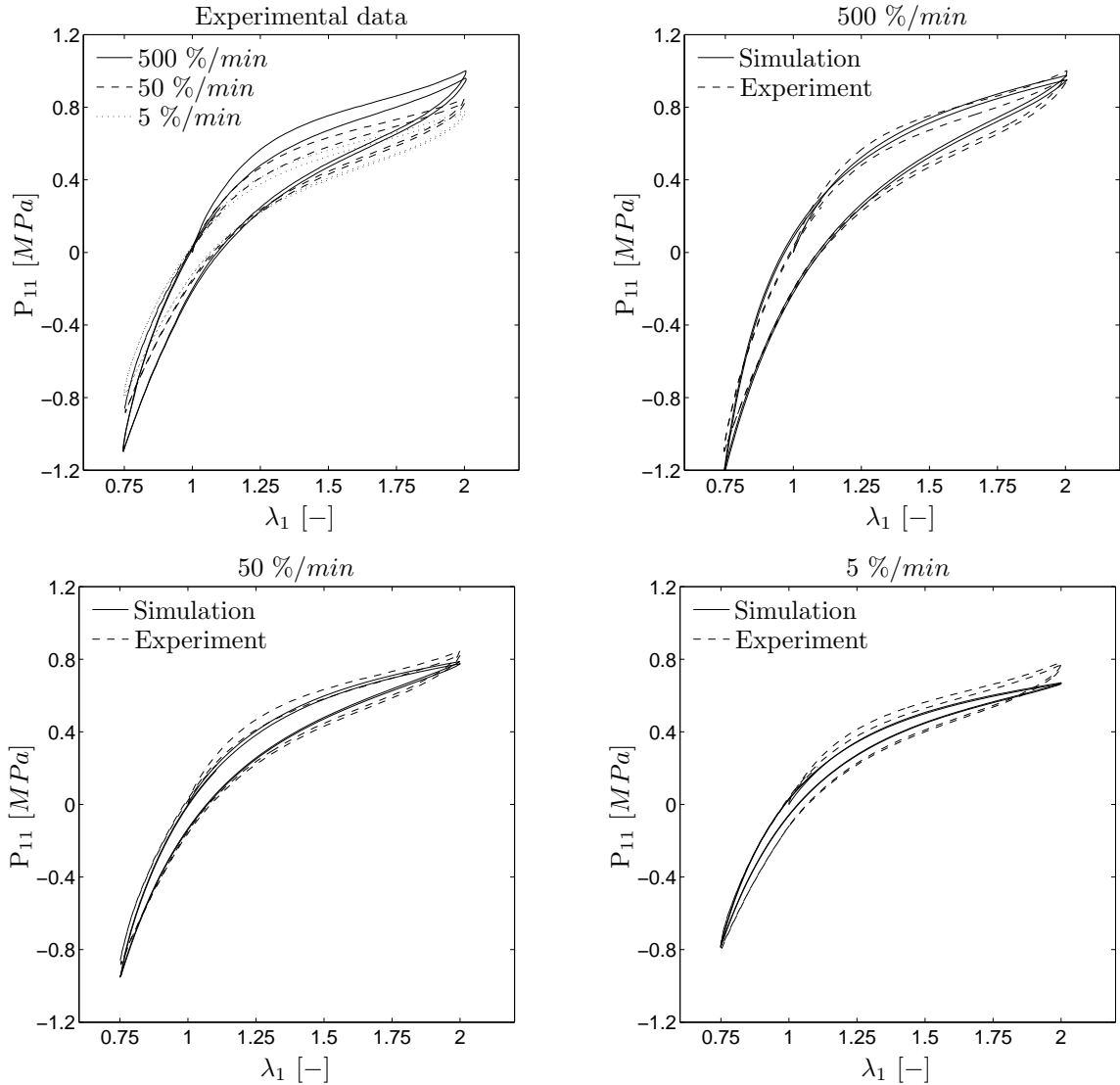


Figure 5.9: Parameter fitting procedure. The illustration outlines a comparison of experimental results with the numerical results of the homogeneous uniaxial cyclic test for stretch values $\lambda_1 \in [0.75, 2.0]$. The upper left figure compares solely the experimental results [239] for three different loading rates. The remaining illustrations compare these experimental results with the numerical obtained results for $|\dot{\lambda}_1| = 5 \cdot 10^0 \text{ min}^{-1}$ in the top right figure, for $|\dot{\lambda}_1| = 5 \cdot 10^{-1} \text{ min}^{-1}$ in the bottom left figure, and for $|\dot{\lambda}_1| = 5 \cdot 10^{-2} \text{ min}^{-1}$ in the bottom right figure using $\{\tau_i\}_{i=1}^s = \{10^0, 10^1, 10^2, 10^3, 10^4\} s$ for the relaxation time spectra and $\{\mu_i^v\}_{i=1}^s = \{0.5357, 0.0762, 0.1205, 0.0213, 0.0229\} \text{ MPa}$ for the viscous overstress moduli.

and second cycles of the loading being more distinct for higher loading velocities. In particular one should notice the change of the viscoelastic modulus after the first cycle of loading.

To determine whether the proposed model is capable of capturing such an experimentally observed viscoelastic response a parametric analysis is performed. A single viscous sub-network responsible for the resulting viscous overstress is considered in terms of the two parameters in the form of the viscous overstress modulus μ^v and the relaxation time τ . Whereas the former trivially scales the amount of the overstress, the latter has a more peculiar impact which can be illustrated for the cyclic uniaxial test considered here. In particular, the left illustration of Figure 5.7 shows the overstress produced by the considered

viscous branch depending on the period of the altering stretch $T = 2(\lambda_1^{max} - \lambda_1^{min})/|\dot{\lambda}_1|$. One can observe that the response differs from the stiff quasi-elastic one for $T/\tau \ll 1$ corresponding to a very quick loading to an almost vanishing one for $T/\tau \gg 1$ corresponding to an extremely slow loading. In the first case there is no time for any changes to occur in the viscous subnetwork during the loading period whereas in the latter case the loading is so slow that the subnetwork has more than sufficient time to relax fully to an unperturbed stress-free configuration. The viscous hysteresis is only observed at loading rates for which the stretch period T is comparable to the relaxation time τ . This fact is illustrated by the diagram on the right of Figure 5.7 depicting the dependence of the amount of the energy dissipated during the first cycle on the ratio T/τ . This curve shows that a single viscous branch with a given relaxation time will produce any viscous hysteresis only within a certain range of loading velocities. Its span can be limited to a change of magnitude of approximately 2 orders of the T/τ ratio.

For the representation of the real relaxation spectrum several viscous branches need to be considered. In particular, to fit the parameters of the experimental stress-stretch curves in the upper left illustration of Figure 5.9, a discrete spectrum of $s = 5$ relaxation times $\{\tau_i\}_{i=1}^s = \{10^0, 10^1, 10^2, 10^3, 10^4\}$ s is chosen. With the elastic part of the deviatoric stresses obtained through the non-affine network model in MIEHE ET AL. [244], the only remaining parameters to be identified are the corresponding overstress moduli $\{\mu_i^v\}_{i=1}^s$. Their values are determined by a simple procedure exploiting the linear dependence of the total overstress on the viscous moduli. To do so, the deviatoric part of the stresses is computed based on (5.7) as

$$\bar{\tau}(t) = \bar{\tau}^e(t) + \sum_{i=1}^s \bar{\tau}_i^v(t) \quad (5.57)$$

in terms of the elastic equilibrium stress $\bar{\tau}^e$ and the viscous overstresses $\{\bar{\tau}_i^v\}_{i=1}^s$. Denoting the cyclic tests in Figure 5.9 by the indices a , b , and c for the different loading rates, one can compute the stress as a mere combination

$$\bar{\tau}^{abc}(t) = \bar{\tau}^{e,abc}(t) + \sum_{i=1}^s \mu_i^v \tilde{\tau}_i^{v,abc}(t) \quad (5.58)$$

where $\{\tilde{\tau}_i^{v,abc}\}_{i=1}^s$ are the normalized overstress profiles shown in Figure 5.8 that can be computed separately for each of the s branches with a unit moduli assigned as $\{\tilde{\mu}_i^v\}_{i=1}^s = 1 \text{ MPa}$ and the loading rates corresponding to the tests a , b , and c . The overstress moduli $\{\mu_i^v\}_{i=1}^s$ are then obtained by minimizing the discrepancy of the stress-strain curves computed by (5.58) to the experimental ones illustrated in the upper left illustration of Figure 5.9.

Overstress moduli $\{\mu_i^v\}_{i=1}^s = \{0.5357, 0.0762, 0.1205, 0.0213, 0.0229\} \text{ MPa}$ are finally obtained as the result of this procedure. The obtained fit for the cyclic uniaxial tension-compression tests is depicted in the illustrations of Figure 5.9 for the different applied loading rates. The experimental features of the true viscoelastic response are captured reasonable well by this fit. The level of the stresses and the thickness of the individual hysteresis curves achieved at the three different loading rates comply rather well with the experimental data. Some discrepancy can be observed when looking at the difference between the first and the second cycles of the loading which is predicted smaller by the simulations when compared to the actual experimental results.

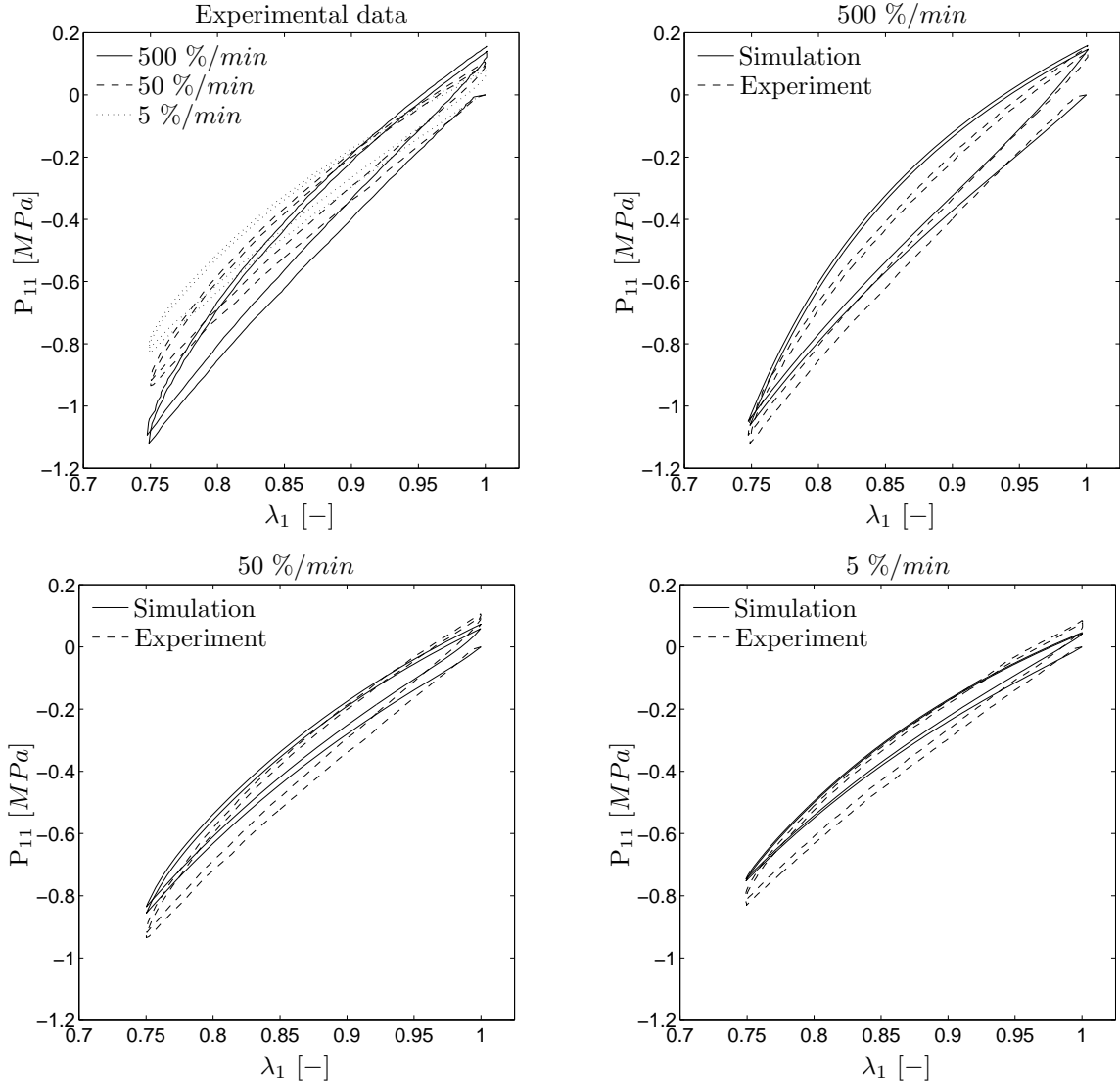


Figure 5.10: Model verification through uniaxial cyclic tests. Comparison of experimental results with the numerical results for compressive stretch values $\lambda_1 \in [0.75, 1.0]$. The upper left figure compares solely the experimental results [239] for three different loading rates. The remaining illustrations compare these experimental results with the numerical obtained results for $|\dot{\lambda}_1| = 5 \cdot 10^0 \text{ min}^{-1}$ in the top right figure, for $|\dot{\lambda}_1| = 5 \cdot 10^{-1} \text{ min}^{-1}$ in the bottom left figure, and for $|\dot{\lambda}_1| = 5 \cdot 10^{-2} \text{ min}^{-1}$ in the bottom right figure using $\{\tau_i\}_{i=1}^s = \{10^0, 10^1, 10^2, 10^3, 10^4\} \text{ s}$ for the relaxation time spectra and $\{\mu_i^v\}_{i=1}^s = \{0.5357, 0.0762, 0.1205, 0.0213, 0.0229\} \text{ MPa}$ for the viscous overstress moduli.

5.5.2 Model verification through uniaxial cyclic tests

After having obtained the characteristic model parameters through the fitting procedure described above in Section 5.5.1, the model with those material parameters is used to simulate two further tests, different from the one above. A comparison with available experimental results will then allow for an evaluation of the quality of the model.

The first example is a purely compressive uniaxial tests performed for the same HNBR50 material [239]. The considered stretch values fall within the compressive interval $\lambda_1 \in [0.75, 1.0]$ at three different loading rates $|\dot{\lambda}_1| = 5 \cdot 10^{-2} \text{ min}^{-1}$, $5 \cdot 10^{-1} \text{ min}^{-1}$ and $5 \cdot 10^0 \text{ min}^{-1}$. The above mentioned features of the viscoelastic response at cyclic loading

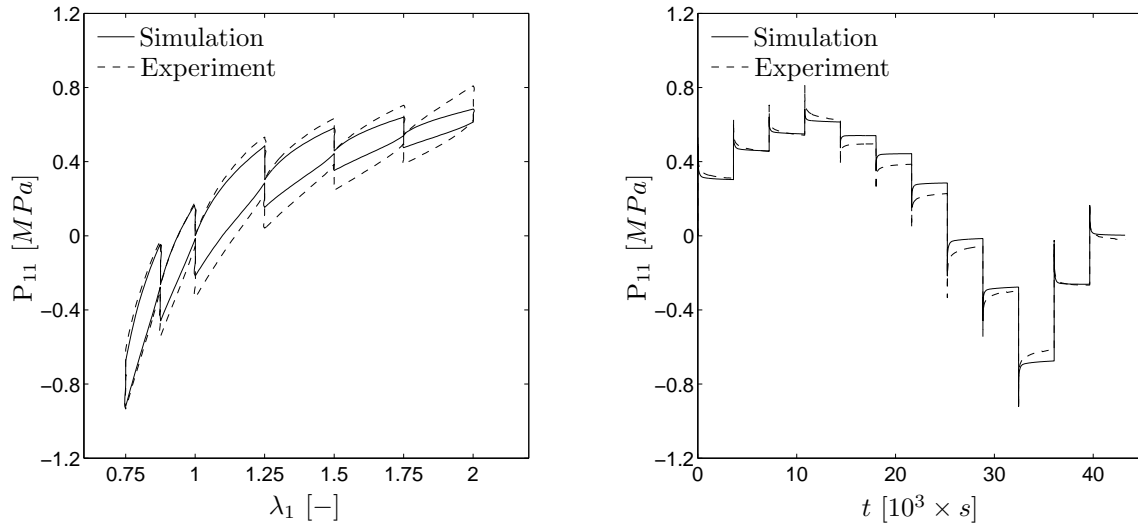


Figure 5.11: Model verification through uniaxial cyclic tests. Comparison of experimental results [239] with the numerical results for stretch values $\lambda_1 \in [0.75, 2.0]$ including relaxation breaks at stretch values $\lambda_1 = 0.75, 0.875, 1.0, 1.25, 1.5, 1.75, 2.0$. The strain-stress diagram comparison is shown on the left whereas the stress-time relation is shown on the right using $\{\tau_i\}_{i=1}^s = \{10^0, 10^1, 10^2, 10^3, 10^4\} s$ for the relaxation time spectra and $\{\mu_i^v\}_{i=1}^s = \{0.5357, 0.0762, 0.1205, 0.0213, 0.0229\} MPa$ for the viscous overstress moduli.

such as the rate-dependent stiffening, hysteresis growth and difference of the first cycle to the subsequent ones are captured also for this test as it is illustrated in Figure 5.10. However, the experimental data outlined in the top left illustration of Figure 5.10 are not fully reproduced by the simulation. Particularly, it can be seen that the viscoelastic moduli are underestimated so that substantially a softer response is predicted by the model with the parameter fit obtained above. The fitting illustrated in Figure 5.9 captures nicely only the value of the tangent modulus on the second cycle of the loading, whereas its value in the beginning of the loading, which coincides for the compressive and tensile dominated tests, remains underestimated.

The second example to verify the quality of the developed model studies a homogeneous experiment on HNBR50 [239] which captures the relaxation during breaks in tension-compression cyclic tests. The same specimen as in the preceding tests is subsequently loaded and unloaded in a stepwise manner. At each step the stretch changes from one intermediate value to the next one with an absolute loading rate of $|\dot{\lambda}_1| = 3 \cdot 10^0 \text{ min}^{-1}$ which is kept at a constant deformation thereafter for a one-hour period. The hold stretch values are $\lambda_1 = 0.75, 0.875, 1.0, 1.25, 1.5, 1.75, \text{ and } 2.0$. Altogether the experiment involves twelve relaxation tests, which allow to observe the overstress development at different stretch levels as well as its relaxation in detail. When comparing the numerical and experimental results based on the illustration in Figure 5.11, one observes that the fit is quite good in the compressive part of the test and at the moderate tensile stretches up to the second break. In particular, the relaxation of the viscoelastic stress during the breaks is captured well in time. To the contrary, at higher tensile stretches the development of the overstress does not match the experimental data. According to the proposed model, the evolution of the overstress is linearly proportional to the deformation velocity \mathbf{l} (in particular to its component $l_{11} = \dot{\lambda}_1/\lambda_1$ in the case of the uniaxial loading), which for the given stretch velocity $|\dot{\lambda}_1|$ gets smaller at higher stretches. Correspondingly, the overstress

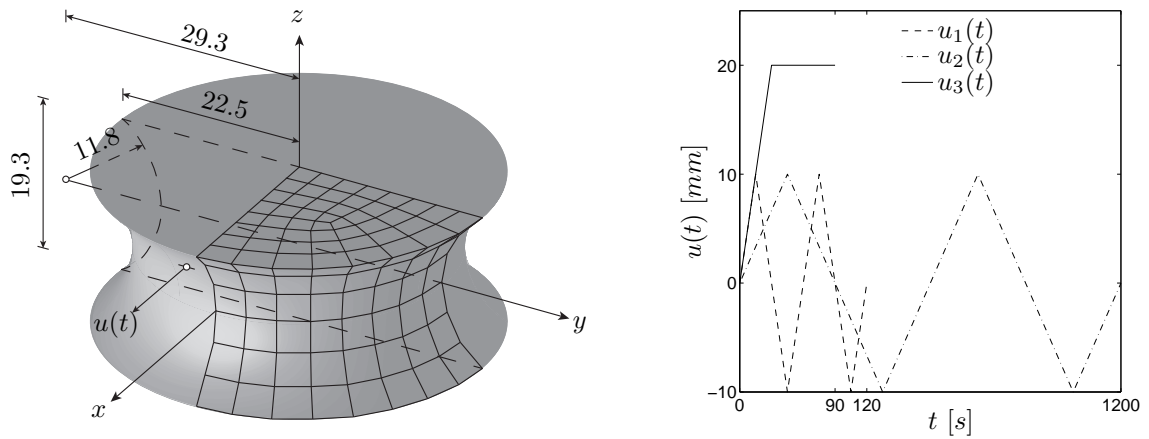


Figure 5.12: Model verification through non-homogeneous 3D shear tests. The geometry of the rubber specimen with dimensions in mm together with the finite element discretization of one quarter of the specimen is shown on the left. The boundary conditions are such that the bottom surface is fully restrained and the whole top surface is displaced by $u(t)$ in x -direction. The individual loading conditions are shown on the right in the form of two cyclic loadings $u_1(t)$ and $u_2(t)$ for different loading rates $|\dot{u}_1| = 40 \text{ mm/min}$ and $|\dot{u}_2| = 4 \text{ mm/min}$ and in the form of a relaxation loading $u_3(t)$ where u_3 is held constant for 60 s after reaching $u_3 = 20 \text{ mm}$ in 30 s.

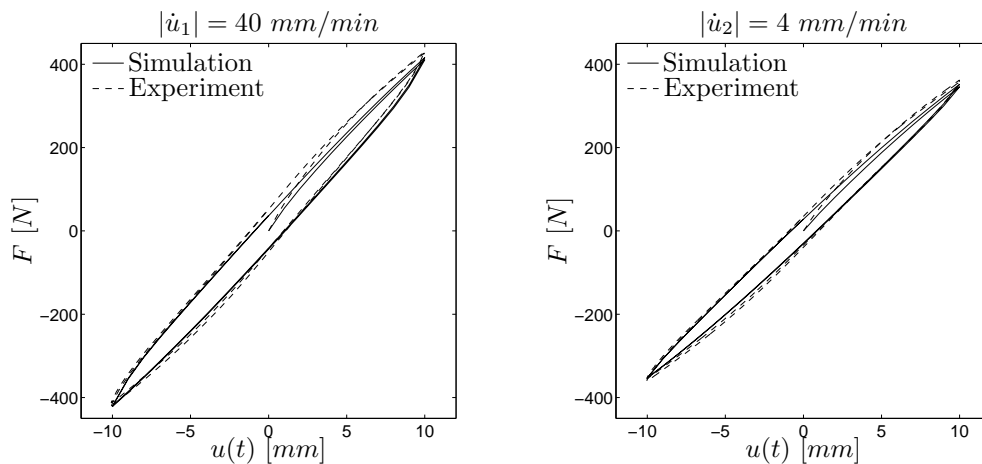


Figure 5.13: Model verification through non-homogeneous 3D shear tests. Illustration of the load-deflection diagrams obtained for the cyclic loading conditions and comparison with the experimental results from MIEHE & GÖKTEPE [239] for $|\dot{u}_1| = 40 \text{ mm/min}$ on the left and $|\dot{u}_2| = 4 \text{ mm/min}$ on the right. A good agreement of the attained extremal force values and the shape of the hysteresis can be observed.

and the thickness of the hysteresis between the second and the sixth break get lower as the stretch increases.

5.5.3 Model verification through non-homogeneous 3D shear tests

Next, the proposed model is evaluated based on its performance when solving a three-dimensional (3D) problem. The numerical implementation follows the discussion outlined in Section 5.4.3. Considered is a non-homogeneous shear experiment in 3D. The specimen

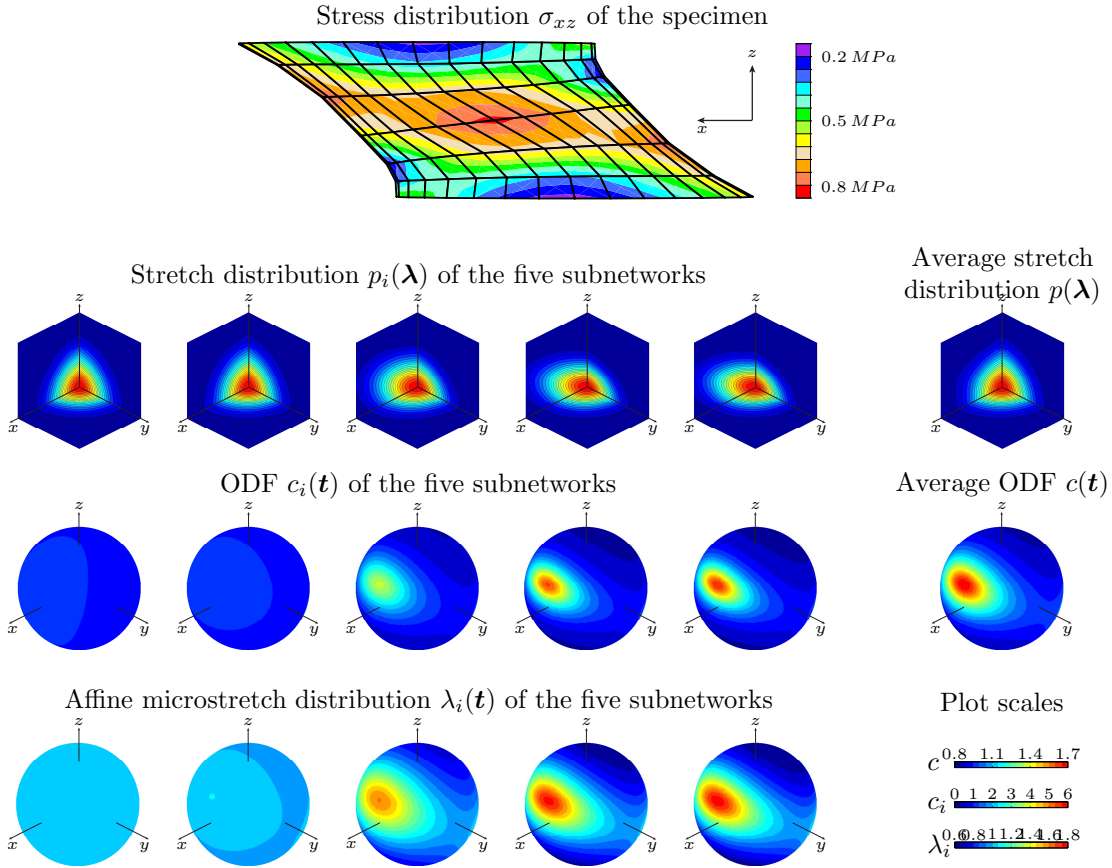


Figure 5.14: Model verification through non-homogeneous 3D shear tests. At the top, an illustration of the obtained stress distribution σ_{xz} of the specimen for the third loading condition at the beginning of the relaxation process at time $t = 30$ s is shown. Below follow illustrations of the internal state of the material point placed in the geometric center of the specimen based on the stretch distribution $p_i(\lambda)$, the orientation density function (ODF) $c_i(t)$, and the affine microstretch distribution $\lambda_i(t)$ of the five subnetworks for the chosen relaxation times $\{\tau_i\}_{i=1}^5 = \{10^0, 10^1, 10^2, 10^3, 10^4\}$ s. In addition the average stretch distribution $p(\lambda)$ and the average ODF $c(t)$ are shown.

is a body of revolution with a concave toroidal lateral surface. Its geometry and dimensions are illustrated on the left of Figure 5.12. The boundary conditions are such that during the experiment the whole bottom face of the specimen is fixed whereas the whole top face is subjected to a horizontal displacement in x -direction. The material of the rubber block, for which experimental results are available from MIEHE & GÖKTEPE [239], is the one used before in the form of a highly saturated nitrile butadiene rubber HNBR50. The elastic and viscous parameters needed for the numerical simulation are the ones obtained through the parameter fitting procedure in Section 5.5.1.

Three loading functions $\{u_i(t)\}_{i=1}^3$ for the horizontal displacement are considered of which two correspond to cyclic deformations for $u \in [-10, 10]$ mm at two different loading velocities $|\dot{u}_1| = 40$ mm/min and $|\dot{u}_2| = 4$ mm/min. The third loading represents a relaxation test at which the top surface is moved in 30 seconds at a constant rate $|\dot{u}_3| = 40$ mm/min up to a displacement of $u_3 = 20$ mm after which a relaxation period of 60 seconds follows. An illustration of the loading processes is given on the right of Figure 5.12.

The obtained numerical results of this rubber specimen are simulated using 1152 eight-

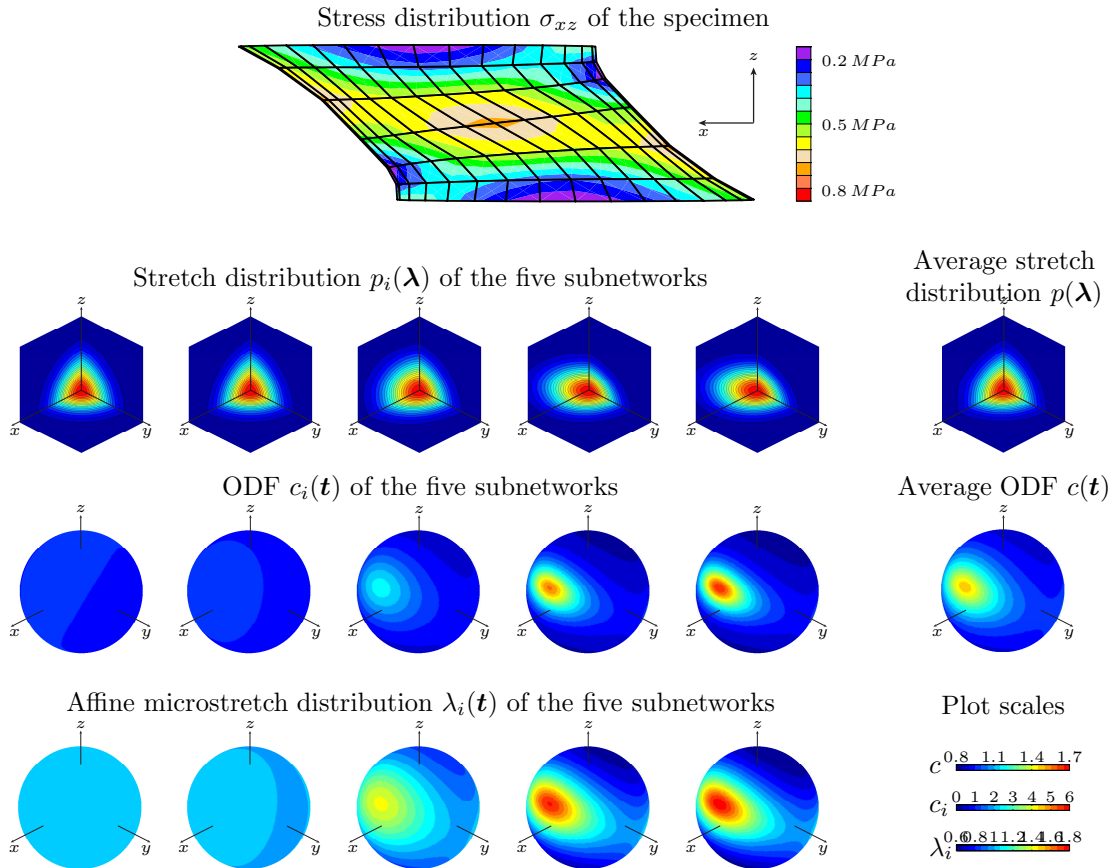


Figure 5.15: Model verification through non-homogeneous 3D shear tests. At the top, an illustration of the obtained stress distribution σ_{xz} of the specimen for the third loading condition at the end of the relaxation process at time $t = 90$ s is shown. Below follow illustrations of the internal state of the material point placed in the geometric center of the specimen based on the stretch distribution $p_i(\boldsymbol{\lambda})$, the orientation density function (ODF) $c_i(\mathbf{t})$, and the affine microstretch distribution $\lambda_i(\mathbf{t})$ of the five subnetworks for the chosen relaxation times $\{\tau_i\}_{i=1}^5 = \{10^0, 10^1, 10^2, 10^3, 10^4\}$ s. In addition the average stretch distribution $p(\boldsymbol{\lambda})$ and the average ODF $c(\mathbf{t})$ are shown.

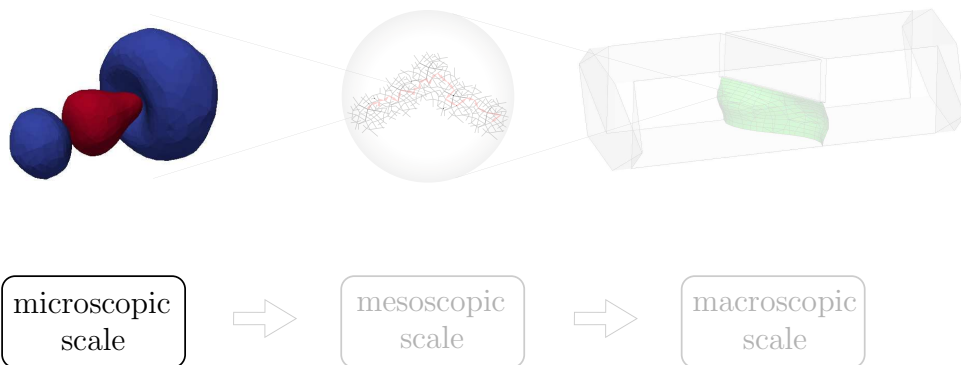
node Q1/P0 mixed brick finite elements. A comparison with the experimental results for the two cyclic tests is shown in Figure 5.13 in the form of the obtained load-deflection diagrams for the loading rate $|\dot{u}_1| = 40$ mm/min on the left and $|\dot{u}_2| = 4$ mm/min on the right of that illustration. The results show good agreement since the extremal force values attained in both tests as well as the shape of the viscous hysteresis do agree with quite good precision. Again, the initial response to the first loading (from $u = 0$ to $u = 10$ mm) is reproduced not as good as the subsequent cycles.

The third loading scenario is evaluated in Figures 5.14 and 5.15, showing the true shear stress contours at the end of the loading at time $t = 30$ s and after the relaxation period at time $t = 90$ s, respectively. One can observe quite a substantial relaxation of the stress depicted at the top of both figures in the form of the outlined σ_{xz} stress distribution. The perturbation induced by the initial deformation of the material decays due to the diffusion mechanisms discussed in Section 5.4. The extend to which the microdeformation relaxes is naturally different for the five mobile subnetworks. An important observation is, that the diffusional motion of the mobile chains results both, in re-orientation and stretch relaxation as further shown in Figures 5.14 and 5.15. Observed is the evolution

of the internal state of the material point placed in the geometric center of the specimen. This is given by the partial distributions of the stretch $p_i(\boldsymbol{\lambda}) = P(\mathbf{P}_i^{-1}\boldsymbol{\lambda})/\det(\mathbf{P}_i)$ in the five mobile subnetworks. The average stretch distribution in the overall mobile network $p(\boldsymbol{\lambda}) = 1/n \sum_{i=1}^5 n_i p_i(\boldsymbol{\lambda})$ represents the total re-distribution of the stretch vector. This re-distribution incorporates both re-orientation and stretch relaxation. The former is illustrated by the orientation density functions plotted over the spatial directions \mathbf{t} in the orientation space and retrieved for each of the subnetworks as $c_i(\mathbf{t}) = 4\pi \int_0^\infty p(\lambda\mathbf{t})\lambda^2 d\lambda$ where the factor 4π comes from the convention that a homogeneous distribution corresponds to $c_i(\mathbf{t}) = 1$. The average for all the mobile polymer chains $c(\mathbf{t}) = 1/n \sum_{i=1}^5 n_i c_i(\mathbf{t})$ is shown on the right of that row. The stretch relaxation is presented by the distribution of the affine microstretch over the directions $\lambda_i(\mathbf{t}) = (\mathbf{P}_i^{-1}\mathbf{t} \cdot \mathbf{P}_i^{-1}\mathbf{t})^{-1/2}$ shown at the very bottom of Figures 5.14 and 5.15.

Part III

Modeling the electronic structure of solids at the microscopic scale



6 A finite element based Kohn-Sham density functional theory

The properties of condensed matter like electric conductivity, magnetism as well as the mechanical response upon external excitations are determined by the electronic structure of a material. Therefore, a variety of methods have been developed over the years to theoretically and numerically account for such dependency. The approach followed in this Chapter is the density functional theory founded by the Hohenberg-Kohn theorem in [149]. Following our recent work in SCHAUER & LINDER [316], in this part of the work, a real space formulation of the Kohn-Sham equations, making use of the hierarchy of finite element bases from different polynomial order, is developed.

6.1 Introduction

The focus in this chapter is laid on all-electron calculations, having the highest requirement onto the basis set, which must be able to represent the orthogonal eigenfunctions as well as the electrostatic potential. A careful numerical analysis is performed, which points out the numerical intricacies originating from the singularity of the nuclei and the necessity for approximations in the numerical setting, with the ambition to enable solutions within a predefined accuracy. In this context the influence of counter-charges in the Poisson equation, the requirement of a finite domain size, numerical quadratures and the mesh refinement are examined as well as the representation of the electrostatic potential in a high order finite element space. The performance and accuracy of the method is demonstrated in computations on noble gases. In addition the finite element basis proves its flexibility in the calculation of the bond-length as well as the dipole moment of the carbon monoxide molecule.

A fully general finite-element framework without the exploitation of given symmetries is developed for calculating the electronic structure with the Kohn-Sham algorithm. Tetrahedral finite elements of up to fourth order are applied, and the hierarchy of these basis sets is exploited, thereby simplifying the implementation and gaining major advantages in performance. Especially, as a new contribution to the treatment of Kohn-Sham density functional theory with finite elements, a p -refinement approach is introduced, where first an approximate solution is calculated within the subspace of lower polynomial degree, which renders the starting configuration for the higher order calculation, yielding an overall speed up of the algorithm. We thoroughly analyze the behavior of the numerical method and thereby study the impact on the calculated energies, where special care is taken with regard to the treatment of the neutralizing charge density in the Poisson equation and the core singularity. In addition the finite element space for the electrostatic potential, effects from the boundary condition, the domain size, and the order of the chosen quadrature rule are examined. We do report on the alignment of orbitals and convergence properties depending on the occupation number in the case of single atoms without closed shells, like the carbon atom, and calculate the dipole moment and the binding properties of the carbon-monoxide molecule in the finite element basis, where especially the correct representation of the polarization properties is known to be highly demanding onto the basis set. Also, total energy calculations on large single atoms like the xenon atom with 54 electrons in 27 orthogonal wave functions are performed, posing

high requirements onto the finite element method based Kohn-Sham density functional framework for all-electron calculations, where both the wave functions as well as the electrostatic potential are represented in the finite element basis. Finally the flexibility and generality of the finite element basis is shown again demonstrated for the first time in the case of an applied homogeneous external electric field, where the energy and dipole moment of the polarized atom can be determined without the requirement of an additional increase of the finite element basis, as it is the case e.g. for the Gaussian type orbitals.

The outline of this chapter is as follows. In Section 6.2 the theoretical background of density functional theory is provided and the self-consistent field (SCF) algorithm is described. Section 6.3 introduces the weak formulation of the Kohn-Sham equations and provides a short overview about basis sets used in this context. It is shown, how the hierarchy of the finite element basis can be exploited and the different components of the implementation are presented. In Section 6.4 an extensive numerical analysis is performed upon several approximations involved in the numerical setting of all-electron calculations. Section 6.5 presents a number of results on noble gas atoms together with calculations on the bond length and polarization of the carbon monoxide molecule, finishing with the impact of an external electric fields onto a single neon atom.

6.2 Theoretical background based on density functional theory

In the Born-Oppenheimer approximation the stationary, non-relativistic Schrödinger equation of an atomistic system consisting of N electrons and M atomic nuclei, is given by the eigenvalue problem

$$\hat{H}\Psi = E\Psi \quad (6.1)$$

in terms of the electronic wave function $\Psi(\mathbf{r}_1, \dots, \mathbf{r}_N)$ and the Hamilton operator

$$\hat{H} = -\frac{1}{2} \sum_{i=1}^N \nabla_i^2 - \sum_{i=1}^N \sum_{A=1}^M \frac{Z_A}{r_{iA}} + \sum_{i=1}^N \sum_{j>i}^N \frac{1}{r_{ij}} \quad (6.2)$$

containing the operator for the kinetic energy and the electrostatic interaction between electrons and nuclei. Here $r_{ij} = |\mathbf{r}_i - \mathbf{r}_j|$ and $r_{iA} = |\mathbf{r}_i - \mathbf{R}_A|$ are the distances from electron i to electron j or nuclei A , respectively. In the whole work, atomic units are used, where Planck's constant \hbar , the electron mass m_e , the charge e , and Coulomb's constant $1/(4\pi\epsilon_0)$ are all set to unity. Length scales are given in the Bohr radius a_0 and energies in Hartree E_h . For reasons of simplicity the spin degrees of freedom are not taken into account, but their inclusion does not pose a major problem. The electrostatic interaction couples the electrons with each other, yielding the problem intractable for an analytic solution except for trivial single electron examples. Ab initio methods like the Hartree and the Hartree-Fock method introduce a simplified ansatz for the wave functions like a product of single electron wave functions or a single Slater determinant, which renders the system accessible for the numerical treatment. A different, very successful approach is density functional theory, based on the theorems of Hohenberg and Kohn [149], which brings the ground state electron density

$$\rho_0(\mathbf{r}) = \int \dots \int \Psi_0^*(\mathbf{r}, \mathbf{r}_2, \dots, \mathbf{r}_N) \Psi_0(\mathbf{r}, \mathbf{r}_2, \dots, \mathbf{r}_N) d\mathbf{r}_2 \dots d\mathbf{r}_N \quad (6.3)$$

into focus by showing that this quantity already contains the whole information about the system at hand. Density functional theory replaces the calculation of the ground state electronic structure of an atomic system from the full quantum mechanical Schrödinger equation through the minimization of an energy functional

$$E_0[\rho] = \underbrace{E_{\text{kin}}[\rho]}_{\text{kinetic energy}} + \underbrace{E_{\text{H}}[\rho] + E_{\text{ext}}[\rho, \{\mathbf{R}_A\}] + E_{\text{ZZ}}(\{\mathbf{R}_A\})}_{\text{classical electrostatic parts}} + \underbrace{E_{\text{xc}}[\rho]}_{\text{quantum corrections}} \quad (6.4)$$

depending on the electron density $\rho(r)$ and the atomic positions $\{\mathbf{R}_A\}$. The electron density is constrained by the condition

$$\int \rho(\mathbf{r}) \, d\mathbf{r} = N \quad (6.5)$$

assuring the correct amount of electrons in the system. The energies of the electrostatic interaction are given by the repulsive Hartree energy E_{H} , which accounts for the interaction between the electrons, the attractive i.e. negative energy from the interaction of the electrons with the nuclei E_{ext} , which can be regarded as having its origin in an external potential acting upon the electrons, and the electrostatic contribution E_{ZZ} from the interaction between the nuclei, all given as

$$E_{\text{H}}[\rho] = \frac{1}{2} \iint \frac{\rho(\mathbf{r})\rho(\mathbf{r}')}{|\mathbf{r} - \mathbf{r}'|} \, d\mathbf{r} \, d\mathbf{r}' \quad (6.6)$$

$$E_{\text{ext}}[\rho, \{\mathbf{R}_A\}] = - \sum_{A=1}^M \int \frac{\rho(\mathbf{r})Z_A}{|\mathbf{r} - \mathbf{R}_A|} \, d\mathbf{r} =: \int \rho(\mathbf{r})V_{\text{ext}} \, d\mathbf{r} \quad \text{with} \quad V_{\text{ext}}(\mathbf{r}) = - \sum_{A=1}^M \frac{Z_A}{|\mathbf{r} - \mathbf{R}_A|} \quad (6.7)$$

$$E_{\text{ZZ}}(\{\mathbf{R}_A\}) = \sum_{A=1}^M \sum_{B=A+1}^M \frac{Z_A Z_B}{|\mathbf{R}_A - \mathbf{R}_B|}. \quad (6.8)$$

Due to the lack of an appropriate expression for the kinetic energy of the electrons in terms of a functional in ρ , the kinetic energy

$$E_{\text{kin}}[\rho] = T^{KS}[\rho] = -\frac{1}{2} \sum_i n_i^{\text{occ}} \int \psi_i \nabla^2 \psi_i \, d\mathbf{r} \quad (6.9)$$

of a non interacting system is introduced, and the density sums up from orthogonal single electron wave functions $\psi_i(\mathbf{r})$ as $\rho_0(\mathbf{r}) = \sum_i n_i^{\text{occ}} |\psi_i(\mathbf{r})|^2$, where n_i^{occ} with $0 \leq n_i^{\text{occ}} \leq 2$ represents the occupation number of the orbital $\psi_i(\mathbf{r})$, obeying to the relation $\sum_i n_i^{\text{occ}} = N$ [181]. In this work the local density approximation (LDA) for the exchange and correlation energy is applied, which takes the form

$$E_{\text{xc}}^{\text{LDA}}[\rho] = \int \rho \epsilon_{\text{xc}}(\rho) \, dx \quad \text{with} \quad \epsilon_{\text{xc}}(\rho) = \epsilon_{\text{x}}(\rho) + \epsilon_{\text{c}}(\rho). \quad (6.10)$$

The exchange energy $\epsilon_{\text{x}}(\rho) = -\frac{3}{4} \left(\frac{3}{\pi}\right)^{1/3} \rho^{1/3}$ is taken from the homogeneous electron gas and the correlation energy was fitted to Quantum Monte-Carlo simulations from [60],

where different interpolations of this data exist. In this work, the one from [285] is used, which determines the correlation energy as

$$\epsilon_c(r_s) = \begin{cases} -0.1423/(1 + 1.0529\sqrt{r_s} + 0.3334r_s) & r_s \geq 1 \\ 0.0311 \log r_s - 0.0480 + 0.0020r_s \log r_s - 0.0116r_s & r_s < 1 \end{cases} \quad (6.11)$$

where $r_s = (3/(4\pi\rho))^{1/3}$ is defined as the radius of a sphere containing one electron, which can be regarded as a measure for the average distance between the electrons. Basically two common procedures exist for finding such minimum. On the one hand one can try to directly minimize the functional (6.4) by inserting an ansatz for the wave functions ψ_i and using Newton- and gradient descent methodologies, thereby taking care of the orthogonality constraint of the wave functions. Alternatively the variation of the functional with respect to the wave functions ψ_i is taken to set up the Euler-Lagrange equations of the system, which are called the Kohn-Sham equations in this context. Due to the orthogonality constraint, they represent an eigenvalues problem, where the Lagrange parameter renders the eigenvalue. Since the energy functional depends non-quadratically on the wave functions ψ_i , there are nonlinear terms in the Kohn-Sham equations. This leads to an iterative solution procedure, the so called self-consistent field (SCF) algorithm, illustrated in Figure 6.1, which is also the path followed in this work.

For reasons of simplicity, only spin unpolarized systems are treated, however the extension to polarized systems is straightforward. The Kohn-Sham equations then represent an effective *single electron* eigenvalue problem given by

$$\left[-\frac{1}{2}\Delta + V_{\text{eff}}(\mathbf{r}) \right] \psi_i(\mathbf{r}) = \varepsilon_i \psi_i(\mathbf{r}) \quad (6.12)$$

with the effective potential

$$V_{\text{eff}}(\mathbf{r}) = V_{\text{xc}}(\rho) + \underbrace{\int \frac{\rho(\mathbf{r}')}{|\mathbf{r} - \mathbf{r}'|} d\mathbf{r}' - \sum_{A=1}^M \frac{Z_A}{|\mathbf{r} - \mathbf{R}_A|}}_{\equiv \phi} \quad (6.13)$$

accounting for the interactions between the electrons in an averaged way. It consists of the exchange-correlation potential $V_{\text{xc}}(\rho(\mathbf{r}))$ given as

$$V_{\text{xc}}(\rho) = \frac{\delta E_{\text{xc}}}{\delta \rho(\mathbf{r})} = \epsilon_{\text{xc}}(\rho(\mathbf{r})) + \rho(\mathbf{r}) \frac{\partial \epsilon_{\text{xc}}(\rho(\mathbf{r}))}{\partial \rho(\mathbf{r})} \quad (6.14)$$

and the electrostatic potential $\phi(\mathbf{r})$ built by the electrons and nuclei, which can be gained from the Poisson equation

$$-\Delta\phi = 4\pi \left(\rho(\mathbf{r}) - \sum_{A=1}^M Z_A \delta(\mathbf{r} - \mathbf{R}_A) \right). \quad (6.15)$$

As mentioned above, the non-linearity in these equations requires an iterative solution procedure to achieve self-consistency, which is illustrated in the flowchart in Figure 6.1. The total energy of the ground state is then given by

$$E_0 = T^{KS}[\rho] + \int V_{\text{ext}}(\mathbf{r})\rho(\mathbf{r}) d\mathbf{r} + \frac{1}{2} \iint \frac{\rho(\mathbf{r})\rho(\mathbf{r}')}{|\mathbf{r} - \mathbf{r}'|} d\mathbf{r} d\mathbf{r}' + E_{\text{xc}}[\rho] + E_{\text{ZZ}} \quad (6.16)$$

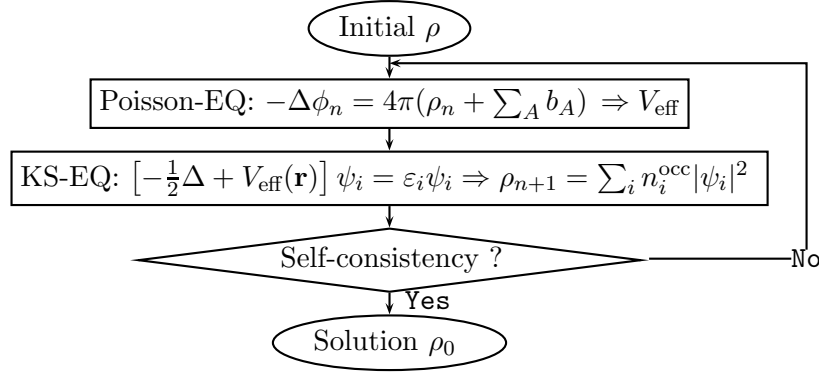


Figure 6.1: Self consistent field algorithm: With an initial density ρ , the Poisson equation determines the electrostatic contribution of the effective potential, where b_A represents the charge distribution of the atomic nuclei. The Kohn-Sham eigenvalue problem then yields an updated density ρ_{n+1} . To bring the algorithm to convergence, mixing with former densities is performed and the algorithm restarted.

or in terms of the eigenvalues [227] as

$$E_0 = \sum_i \varepsilon_i - \frac{1}{2} \iint \frac{\rho(\mathbf{r})\rho(\mathbf{r}')}{|\mathbf{r} - \mathbf{r}'|} d\mathbf{r} d\mathbf{r}' - \int \frac{\delta E_{xc}}{\delta \rho} \rho(\mathbf{r}) d\mathbf{r} + E_{xc}[\rho] + E_{ZZ} \quad (6.17)$$

where

$$\sum_i \varepsilon_i = T^{KS}[\rho] + \int V_{\text{eff}}(\mathbf{r})\rho(\mathbf{r}) d\mathbf{r} . \quad (6.18)$$

The physical situation treated in this work comprises a localized charge distribution, for example single atoms, molecules or a small cluster of atoms, in contrast to the expanded case of a crystal. Since the wave functions of bound states decay exponentially, homogeneous boundary conditions are chosen for the Kohn-Sham equations on a compact domain $\Omega \subset \mathbb{R}^3$. In a charge neutral or positively ionized system, the assumption of a bound ground state can be physically justified, however in the case of a negatively charged system the wave functions generally do not vanish in infinity, yielding free electrons, a case which is therefore excluded here. The Poisson equation is solved on the same domain Ω , but dependent upon the specific problem and the size of the domain Ω also non-zero Dirichlet boundary conditions are applied, where a multipole decomposition of the potential up to the electrostatic quadrupole

$$\phi(\mathbf{r}) = \frac{Q}{r} + \frac{\mathbf{r} \cdot \mathbf{p}}{r^3} + \frac{1}{2} \sum_{k,l} Q_{kl} \frac{r_k \cdot r_l}{r^5} + \dots \quad (6.19)$$

with total charge Q of electrons and nuclei, electric dipole \mathbf{p} and the traceless quadrupole tensor Q_{kl} given as

$$\mathbf{p} = \int_{\Omega} \rho(\mathbf{r})\mathbf{r} d\mathbf{r} \quad \text{and} \quad Q_{kl} = \int_{\Omega} \rho(\mathbf{r})(3r_k r_l - r^2 \delta_{kl}) d\mathbf{r} \quad (6.20)$$

is employed in order to determine the potential on the boundary, defined by the function $\bar{\omega}$. The Poisson problem then reads

$$-\Delta\phi = 4\pi\rho_{\text{tot}} \quad \Omega \quad (6.21)$$

$$\phi = \bar{\omega} \quad \partial\Omega. \quad (6.22)$$

The boundary value problem can then be transformed to the homogeneous case in the usual way by a continuation w of the boundary function \bar{w} into the interior domain and applying the Ansatz $\phi = \phi_0 + w$, where ϕ_0 merely has to fulfill homogeneous boundary conditions [57]

$$-\Delta\phi_0 = 4\pi\rho_{\text{tot}} + \Delta\omega \quad \Omega \quad (6.23)$$

$$\phi_0 = 0 \quad \partial\Omega. \quad (6.24)$$

Therefore in the following only the homogeneous case is considered. In both cases however a reasonably large physical domain $\Omega \subset \mathbb{R}^3$ is required in order to not disturb the system through boundary effects. A closer look at the influence of the domain size on the numerical results is taken later in Section 6.4.2.2.

6.3 Discretization with finite elements and its numerical implementation

In this section the Kohn-Sham equation (6.12) and the Poisson equation (6.15) are cast into an algebraic form with the help of a finite dimensional basis set. Different possible basis sets are presented, especially the finite element basis and its hierarchic properties, which are further employed in this work. Furthermore a description of the implementation within C++ and its several components is provided.

6.3.1 Weak formulation and discretization in the finite element basis

Instead of solving the strong form directly, the weak solution of both the Kohn-Sham and the Poisson equation is pursued. The weak formulation is generated by a Galerkin projection of the symmetric problem. For that purpose, equation (6.12) is multiplied with a sufficiently regular test function φ from the left and integrated over the physical domain, employing Green's theorem

$$\frac{1}{2} \int_{\Omega} \nabla\varphi \cdot \nabla\psi_i(\mathbf{r}) \, d\mathbf{r} + \int_{\Omega} \varphi V_{\text{eff}}(\mathbf{r}) \psi_i(\mathbf{r}) \, d\mathbf{r} = \varepsilon_i \int_{\Omega} \varphi \psi_i(\mathbf{r}) \, d\mathbf{r}, \quad (6.25)$$

where the requirement of a vanishing test function on the boundary was made. The space of definition of both ψ_i and φ is now generalized to $H_0^1(\Omega)$, where the vanishing trace of the wave function on the boundary is reasonably fulfilled for localized, neutrally charged systems on large physical domains, the case examined in this work. For the Poisson equation the weak formulation is built analogously. The discretization is achieved by reducing the variational formulation (6.25) to a finite dimensional function space $X_h \subset H_0^1(\Omega)$, in which the wave functions ψ_i and the electrostatic potential ϕ are expanded in terms of basis functions $\varphi_n \in X_h$, given as

$$\psi_i = \sum_n c_i^n \varphi_n \quad \text{and} \quad \phi = \sum_n d^n \varphi_n. \quad (6.26)$$

In general also a different subspace \tilde{X}_h with a basis set $\{\tilde{\varphi}_n\}$ can be chosen in the ansatz of ϕ , which might possess improved interpolation properties for the potential ϕ , as illustrated in Section 6.4.1.2. According to the fundamental lemma of the calculus of

variations, equation (6.25) has to be obeyed by any testfunction φ and especially by the basis functions in X_h , yielding the generalized eigenvalue problem

$$(K_{mn} + V_{mn}) c_i^n = \varepsilon_i M_{mn} c_i^n \quad (6.27)$$

in terms of the matrix elements

$$M_{mn} = \int_{\Omega} \varphi_m \cdot \varphi_n \mathbf{dr}, \quad K_{mn} = \frac{1}{2} \int_{\Omega} \nabla \varphi_m \cdot \nabla \varphi_n \mathbf{dr}, \quad \text{and} \quad V_{mn} = \int_{\Omega} \varphi_m V_{\text{eff}} \varphi_n \mathbf{dr}, \quad (6.28)$$

where K is called the stiffness matrix and M the overlap matrix, respectively. If orthonormal basis functions were used, the overlap matrix M_{mn} boils down to the identity matrix and the problem reduces to a standard eigenvalue problem. The algebraic form of the Poisson equation

$$K_{mn} d^n = 4\pi \int_{\Omega} \varphi_m \rho_{\text{tot}} \mathbf{dr} \quad (6.29)$$

represents a linear equation, again with the positive symmetric stiffness matrix K_{mn} , where in ρ_{tot} the positive and negative charge densities are combined. If non-zero Dirichlet boundary conditions are introduced, an additional term appears on the right hand side. So far the basis functions in the discretization have not been determined. In the case of a linear equation, Céa's lemma

$$\|u - u_h\| \leq C \inf_{v_h \in X_h} \|u - v_h\| \quad (6.30)$$

tells us for an elliptic operator, that the interpolation properties of the basis with respect to the solution play an important role in reducing the numerical error [57]. Here u is the weak solution in the Hilbert space X with the given norm $\|\cdot\|$ and u_h is its counterpart in the finite dimensional subspace $X_h \subset X$, so that the discretization error on the left side of (6.30) is bounded by the interpolation property of u in the subspace X_h with a proportionality factor C depending on the constants for coerciveness and continuity of the given operator. Therefore, one can also assume the importance of the interpolation properties in the given nonlinear case, where each iteration consists of a linear problem.

Two types of basis sets are widely spread in physics and chemistry. On the one hand are the plane waves and their variations, which represent a complete, orthogonal basis with globally defined basis functions [227]. They are usually used in combination with pseudopotentials [177], as the strong inner oscillations of the core electrons are expensive to represent in this basis and also the singularity in the potential of the nuclei would sensitively slow the convergence rate. A drawback of the plane wave basis is the restriction to periodic boundary conditions together with regularity requirements on the shape of the physical domain. On the other hand in the context of the LCAO-method, atomic orbital like basis functions are used, which are often related to the eigenfunctions of a radial symmetric single electron problem together with some problem dependent adaptations [180, 333]. In reference to Céa's lemma (6.30), these basis functions possess superior interpolation properties having already the form of atomic orbitals. Nevertheless these basis functions have been and still are optimized in order to reach a minimal basis set with maximal speed in calculations. The basis functions are local, usually defined at the position of the atoms and therefore the basis cannot be systematically increased to form

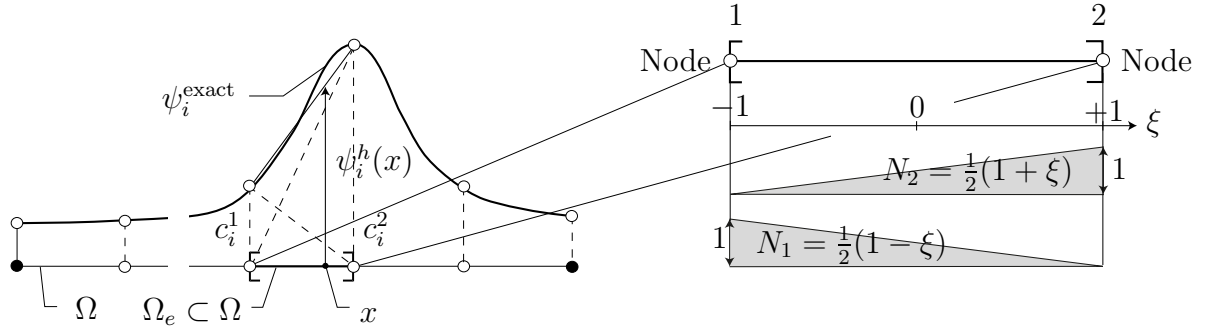


Figure 6.2: Isoparametric approach in one dimension. Linear functions $N_1(\xi), N_2(\xi)$ are mapped from the reference element $[-1, 1]$ onto the basis function φ_n in the physical domain, where the wave functions ψ_i^{exact} is approximated at the location x as $\psi_i^h(x) = \sum_n c_i^n \varphi_n$.

a complete basis of the physical domain. For such choice, the electrostatic potential of the electrons is directly integrated from the orbitals, which is possible since only a small number of basis functions is required, rather than solving the Poisson equation.

In this work *finite element* basis functions are applied, which build a non-orthogonal, local basis, consisting of low order polynomials, where the order is determined by the highest polynomial degree. The amount of linear independent monomials of order p in d dimensions is given by $\binom{d+p-1}{p}$, which sums up to an amount of $\binom{d+p}{p}$ linear independent polynomials of order equal or lower than p , where for the relevant space dimension $d = 3$, the numbers are given in Table 6.1. The basis functions are defined on a tetrahedral (P1 to P4) or cubic (Q1,Q2) reference element, and are then mapped into the real space by a geometrical transformation of the reference domain onto a mesh T of the physical domain Ω , as illustrated in Figure 6.2 within a one-dimensional context. These so called isoparametric basis functions are continuous but not smooth across the element border and can be generated from Lagrange polynomials [155], where the basis functions φ_j have to fulfill the interpolation property $\varphi_j(x_i) = \delta_{ij}$ on a set of interpolation points $\{x_i\}$ of the reference element. The resulting basis functions are different from zero only locally within the element and its direct neighbors yielding sparse matrices in the discrete scheme. The basis sets build a hierarchy with respect to the polynomial order, i.e.

$$P1 \subset P2 \subset P3 \subset P4 \text{ on the same mesh } T \quad (6.31)$$

as well as to the mesh refinement in space, i.e. if the mesh T_1 is a subgrid of T_2 , then the finite element space defined on T_1 is completely contained in the one defined on T_2 . This property of a hierarchic function space is exploited in two ways. In the case of a missing good initial starting electron density ρ , the Kohn-Sham equations are first solved on a subgrid of the mesh, which can be done much faster due to the reduced degrees of freedom. Since the solution is also contained in the finite element space created on the initial mesh, it can directly be employed as starting density to proceed the calculation on the fine mesh (so called *h-refinement*). The same idea of first solving with a reduced basis

Order p	0	1	2	3	4	5	6	7	8
amount of monomials of order p	1	3	6	10	15	21	28	36	45
amount of polynomials of order p	1	4	10	20	35	56	84	120	165

Table 6.1: Amount of monomials and polynomials of order p in three dimensions.

set can also be realized by performing first a calculation with low order polynomial basis functions, followed by a high order calculation (so called p -refinement). Depending on the initial guess, this procedure was found capable to accelerate the convergence process and therefore notably reduces the total computational cost of the SCF algorithm. For example for a single neon atom with an initial Gaussian density distribution, the total computational cost for the SCF algorithm reduces by a factor of approximately 2.5, if an initial finite element calculation with low order polynomials preceded, whose output yields the starting configuration of the subsequent high order finite element calculation. In all examples here, a linear mixing scheme is applied in combination with a relatively low convergence criteria of $0.001E_h$. Similar an acceleration of about a factor 1.4 is found for the carbon monoxide molecule as well as for the benzene molecule, when starting with an calculation on P3 finite elements as input for a subsequent P4 simulation. The required amount of iterations in order to reach the convergence criteria in the high order run thereby usually more than halves, where however additional time is spent for the low order run. Naturally smaller speed up factors occur if more restrictive convergence criteria are chosen, as the resulting additional SCF iterations require roughly the same additional amount of time with or without the p -refinement approach. Also the application of a more sophisticated mixing scheme, like e.g. the Pulay mixing [290], might also decrease the advantage, as each iteration gives information that is used in the update calculation, whereas the densities of the lower order iterations are usually not taken into account in the Pulay scheme. The given numbers though should only be taken as a rough estimate, since the savings are also mesh dependent and large speed ups can especially be found, if the final total energy of the lower polynomial calculation reached close to the final energy of the higher order calculation. Otherwise the time saved from the reduction of iteration on the higher order SCF algorithm could be lost in the time spent in the low order calculation again, as an only slightly improved initial starting configuration has little impact. It also should be noted, that similar accelerations arise by the h -refinement, however the h -refinement method possesses different requirements onto the grid, as an unrefined version of the final grid must be available, whereas in the p -refinement, the final grid on which the energy should be calculated can be constructed directly.

A repetition on even smaller meshes with lower polynomial order or any combination of both is possible. The second case, where our implementation takes advantage of the hierarchic properties of the finite element spaces is in the interpolation of the electron density $\rho(x) = \sum_i n_i^{\text{occ}} |\psi_i(x)|^2$ from the set of atomic orbitals $\psi_i = \sum_n c_i^n \varphi_n$. The electron density cannot be represented in the same finite element basis as the wave functions without making a major approximation, which was found to be too invasive with respect to the accuracy requirements. Instead of storing all the coefficients c_i^n in consecutive loops of the SCF algorithm, the exact density $\rho(x)$ is interpolated in the finite element space of the double polynomial order. E.g. we do not store the P2 wave function of former iterations, but sample the corresponding density in the P4 finite element space, which contains the square of all the local polynomials of the P2 space and the density can therefore be expressed without any approximation. Dependent upon the number of eigenfunctions required and the order of the finite element space, this not only simplifies the implementation especially of the mixing schemes, but also reduces the memory requirements. It should however be noted, that alternative ways to store the density are also possible and efficient, like for example the storage of the density merely at the quadrature points, as the density in the SCF algorithm is only evaluated at these points. However in this case

no direct access to the density at off-quadrature positions exists and dependent upon the involved integrands and quadrature rules, even more storage might be required.

For reasons of simplicity the physical domain for the Poisson and the Kohn-Sham equation are chosen as being identical. The solution of the Kohn-Sham equation with the rapidly decaying wave functions on a decisively smaller domain can further reduce the degrees of freedom [121].

6.3.2 Numerical implementation

The program code is implemented in C++ within the finite element framework of DUNE [23]. The Dune modules provide the finite element basis functions for basic finite element types together with routines for accessing the elements of the grid. There also exist methods to connect user data with the entities of the grid and setting up the matrices involved in the SCF algorithm. Since all matrices are sparse, matrix-vector products can be executed in linear time, rendering them suitable for the application of iterative procedures for solving linear equations. These linear solvers are taken from the iterative solver template library ISTL [22]. In particular for solving the Poisson equation as well as in the equation required by the eigenvalue solver, a conjugate gradient solver is used, together with an SSOR preconditioner or alternatively the algebraic multigrid solver of the ISTL library.

The eigenvalues and vectors are calculated with the iterative Arnoldi process, provided through the Fortran based ARPACK package [198] or its parallel version PARPACK [199], which is able to extract the largest m eigenvalues and corresponding eigenvectors in a generalized eigenvalue problem. In order to enhance the convergence towards a desired portion of the spectrum, a shift of the spectrum is performed via the transformation

$$(\mathbf{K} + \mathbf{V} - \sigma\mathbf{M})^{-1}\mathbf{M}\mathbf{c} = \nu\mathbf{c} \quad \text{with} \quad \nu = \frac{1}{\varepsilon - \sigma} \quad (6.32)$$

rendering the Arnoldi process capable of finding eigenvalues close to the shift parameter σ [198]. The involved multiplication of a vector $\mathbf{x} = \mathbf{M}\mathbf{c}$ with $(\mathbf{K} + \mathbf{V} - \sigma\mathbf{M})^{-1}$ is reformulated in the usual way by solving a linear equation

$$(\mathbf{K} + \mathbf{V} - \sigma\mathbf{M})^{-1}\mathbf{x} = \mathbf{y} \Leftrightarrow (\mathbf{K} + \mathbf{V} - \sigma\mathbf{M})\mathbf{y} = \mathbf{x}. \quad (6.33)$$

It is this equation, which has to be solved repeatedly, that renders the calculations numerical expensive.

The parallelization is realized via domain decomposition with the grid partitioner Metis and the communication between the processes is handled by the message passing interface from OpenMpi. For the mesh creation, which together with the polynomial order of the basis functions determines the finite element basis set, a procedure is generated to set nodal points on geometrical figures, mainly the corner and edge points of polyhedrons around the positions of the atom nuclei, similar to the description in [200]. The atomic position, being usually an extremal point of the wave functions ψ_i as well as the electrostatic potential ϕ , is also occupied by a node. For molecules additional nodes are placed into the binding region between the atoms to ensure a sufficient interpolation of the bond orbitals. The mesh generator TETGEN [322] creates a tetrahedral grid from these nodal

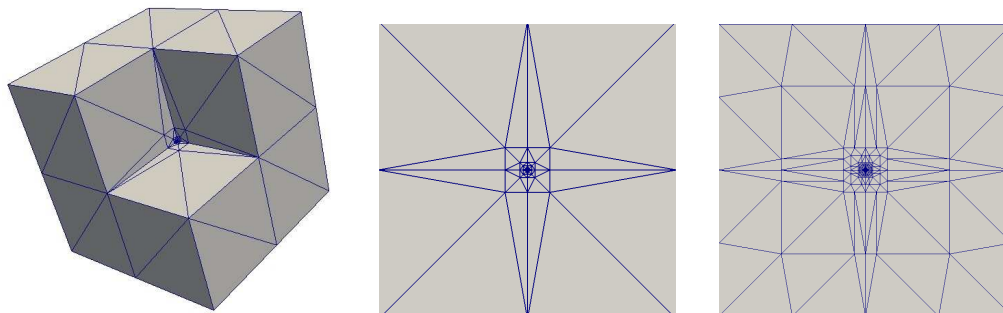


Figure 6.3: Left: Sliced mesh created for a single atom in the center with nodes on cubes of increasing size around the central atom position. Center: Cross-section through the mesh. Right: Cross-section from globally refined mesh.

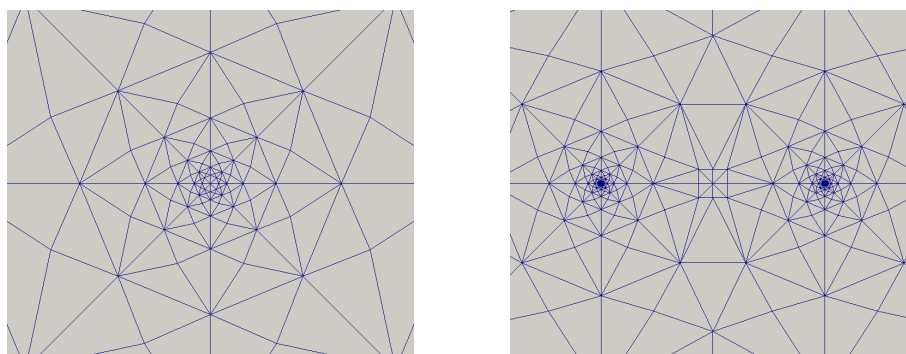


Figure 6.4: Cross section through triangularizations. Left: Single atom mesh from rhombicuboctahedron and deltoidal icositetrahedron. Right: Mesh for a diatomic molecule with additional elements in the binding region.

points, which can be read by the DUNE interface. Cross-sections through meshes for single atoms and a binary molecule are shown in Figures 6.3 and 6.4.

To achieve convergence in the SCF algorithm, a mixing scheme of the input and output electron density of a SCF iteration is required. The simplest one consists of a linear mixing given as

$$\rho^{(n+1)} = \alpha\rho^{(n)} + (1 - \alpha)\rho^{(new)} = \rho^{(n)} + \alpha\Delta\rho^{(n)} \quad (6.34)$$

where $\rho^{(n)}$ is the input density of iteration n , $\rho^{(new)}$ is the density of the orbitals calculated in the n -th iteration, $\Delta\rho = \rho^{(n)} - \rho^{(new)}$, and α is a mixing coefficient, usually chosen between 0.5 – 0.8. In order to fasten the convergence process, a Pulay mixing scheme [290] is added to the SCF algorithm.

6.4 Numerical analysis of the implementation

In this section, the influence of the different components in the presented finite element implementation of the Kohn-Sham equations is examined. The intended “chemical accuracy” in the energy calculations, is considered to lie at around $10^{-3} E_h$ per atom and has to be interpreted in the sense that for a given basis set, the minimum energy has to be found within that range. A relative error criterion is also possible, but since we present some of the numerical analysis in the form of concrete energy values, this kind of error measure is chosen in this work.

In Section 6.4.1, the treatment of the electrostatic interaction in the Poisson equation and the effective potential is considered. In particular the aspect of the singularity in the potential arising from the point charge of the atomic nuclei is investigated. Different neutralizing charge distributions in the Poisson equation are discussed and an exploration of the electrostatic potential ϕ in terms of high order finite element shape functions is provided. Next, in Section 6.4.2 the necessary approximations of a finite domain size, numerical integration and boundary conditions for the Poisson equation are investigated. Finally, Section 6.4.3 deals with convergence properties of the SCF algorithm with respect to the occupation number as well as the mixing scheme, the impact of the mesh refinement around the nuclei, and ends with some comments upon different parameters, which have to be adjusted in a simulation, like the tolerances in the linear solvers or the shift parameter in the eigenvalue problem.

The numerical analysis is performed by executing test calculations, which are discussed in the following. As generic example serves in several cases a single neon atom, for which the simulation conditions are adapted to the situation under investigation. We restrict to all-electron calculations, because here the requirements onto the basis set are most demanding, since it must be capable of representing the electrostatic potential ϕ together with all the orthogonal electronic eigenfunctions simultaneously, which highly oscillate at the positions of the atomic cores.

6.4.1 Treatment of the core singularity in all-electron calculations

In the length scale of common density-functional simulations, the positive atomic nucleus effectively represents a point charge described by a delta-function at the nucleus position, generating a contribution proportional to $1/r$ in the electrostatic potential of the total charge. Unlike in calculations using pseudopotentials, this singularity must be dealt with in all-electron calculations. The singularity is integrable in dimensions larger than one. However, the numerical integration with Gaussian quadrature rules has to be performed carefully, as relevant discrepancies can emerge in the resulting energies or matrix elements, if the polynomial quadrature rule is not large enough or the extent of the finite element around the singularity is not small enough, respectively. Alternatively to integrating the singularity with Gaussian quadratures, a coordinate transformation can be performed [77, 256].

6.4.1.1 Neutralizing charge distribution in the Poisson equation. In the finite element basis, the electrostatic potential of the electrons practically cannot be directly integrated from the electron charge density via the Green's function of the Poisson equation, as it is the case for atomic orbital basis functions [180], due to the decisively higher amount of involved basis functions and the resulting numerical expense. Instead, the Poisson problem (6.15) is solved with adequate boundary conditions, which on the other hand cannot be effectively accomplished in the atomic orbital basis, since it does not constitute a complete basis. In the Poisson equation a localized, neutral charge distribution is favorable on the right hand side, as then the electrostatic potential decreases at least quadratic in the distance r to the charge distribution, rendering valid the approximation of a *finite* domain of appropriate size with homogeneous boundary conditions. In the SCF algorithm however, the potential of the electron density alone is required for

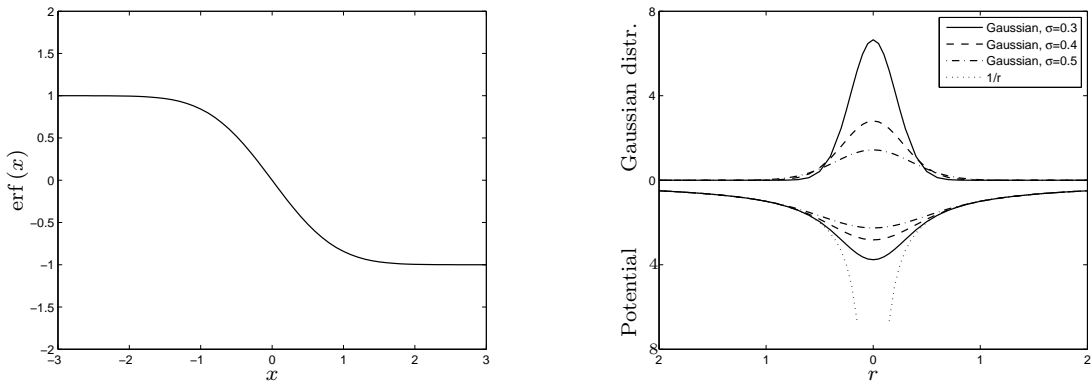


Figure 6.5: Schematic plots to illustrate the nature of the neutralizing charges. Left: Error function $\text{erf}(x)$. Right: Gaussian charge distributions $1/(\pi^{3/2}\sigma^3)\exp(-r^2/\sigma^2)$ for varying width parameter σ (upper half) and the corresponding potentials $\text{erf}(r/\sigma)/r$ (lower half) approaching the $1/r$ function with decreasing width parameter σ .

example in the calculation of the Hartree energy shown in (6.6) or (6.39). Therefore a positive, neutralizing charge distribution is added on the right hand side of the Poisson equation, whose potential for homogeneous boundary conditions on an *infinite* domain is *analytically* known and can be subtracted from the numerical solution of the joint potential in order to receive the potential of the electrons. In this approach, the analytic potential of the neutralizing charge density is expected to annihilate the contribution to the numerical one, an assumption whose justification depends of course on the quality of the numerical approximation. Alternatively it would also be possible to solve for the electrostatic potential of solely the electrons by imposing appropriate non-zero boundary values, originating from the negative potential of the nuclear point charges, replacing the homogeneous boundary conditions. With this approach the discretization error from the mixed analytical and numerical treatment of the potential could be avoided as well as the necessity to represent the singularity in the total electrostatic potential on the grid. This approach has however not been followed in this work.

The compensatory charge distributions applied in this work are on the one hand a Gaussian charge distribution [309], whose potential is related to $\text{erf}(r)/r$, with the error function

$$\text{erf}(x) = \frac{2}{\sqrt{\pi}} \int_0^x e^{-t^2} dt = \frac{2}{\sqrt{\pi}} \sum_{n=0}^{\infty} \frac{(-1)^n}{(2n+1)n!} x^{2n+1} \quad (6.35)$$

canceling the singularity at the origin, as shown in Figure 6.5. On the other hand a point charge, represented by a regularized delta function is chosen, whose potential decays proportional to $1/r$. The regularization is introduced to satisfy the requirements of the weak Poisson equation on the right hand side for an solution in H^1 , without effectively changing the point charge properties and could be thought of for example as the just given Gaussian charge distribution close to the limit $\sigma \rightarrow 0$. Other possible neutralizing densities are $\rho_{\text{neu}} = e^{-r}/r$, a spherical ball of constant density [30] or the smooth, strictly local densities introduced in [283].

When the *point charge* is chosen, the electrostatic potential ϕ , following from the Poisson equation, directly accounts for the joint potential of the nuclei and the electrons, as

can be seen from (6.15) and (6.37). However the $1/r$ singularity of the potential at the atomic position has to be represented in the numerical basis, which requires an adequate resolution of the finite element mesh around the nuclei. The numerical solution of the electrostatic potential then yields a relatively large but finite value at the nuclei positions, which yet does not spoil the numerical setting, as only integrals of the potential are of importance and here the required accuracy can be reached, as shown in the numerical analysis in Section 6.4.2.1. In the SCF algorithm no further treatment of the $1/r$ potential is required. However in order to calculate the contribution of the Hartree- or the electron-nuclei interaction energy in the total energy (6.17), an integration over the singularity is required, as outlined in equation (6.39). In these integrations, special care about the singularity has to be taken and therefore numerical quadrature rules of up to order 30 were employed to ensure the chemical accuracy in this term. In order to represent the $1/r$ potential adequately, already increased refinements in the grids around the atomic positions have to be used, which however are required anyway due to the representation of the electrostatic potential and the oscillating wave functions. On these refined meshes, the integrals can be performed with the required accuracy.

In the case of a *Gaussian charge* distribution, the analytic solution of the Poisson equation for the neutralizing charge distribution (6.36) is subtracted from the joint numerical solution $\tilde{\phi}$ of the Poisson problem (6.37) to gain the electrostatic potential of the electrons, which is required in the assembly of the Kohn-Sham matrix (6.38) as well as in the calculation of the Hartree energy (6.39). The external potential built by the nuclei is directly described by a singular $1/r$ potential, which enters the evaluation of the Kohn-Sham matrix elements and the E_{ext} energy, so again integrations need careful treatment. The potential $\tilde{\phi}$ however does not need to represent a singular point at the origin, which reduces the requirements onto the basis set, i.e. a lower refinement of the mesh around the origin is possible. However the mesh must still allow for an adequate integration of the $1/r$ singularity in the matrix elements and the representation of the orthogonal wave functions, which highly oscillate at the origin.

Point charge	Gaussian charge distribution
Normalizing charge distribution	
$\rho_{\text{neu}} = Z_A \delta(r) \Leftrightarrow \phi_{\text{neu}} = \frac{Z_A}{r}$	$\rho_{\text{neu}} = \frac{Z_A}{\pi^{\frac{3}{2}} \sigma^3} \exp\left(-\frac{r^2}{\sigma^2}\right) \Leftrightarrow \tilde{\phi}_{\text{neu}} = Z_A \frac{\text{erf}\left(\frac{r}{\sigma}\right)}{r}$ (6.36)
Poisson equation for electrons and neutralizing charge	
$-\Delta\phi = 4\pi \left(\rho - \sum_A Z_A \delta(\mathbf{R}_A) \right)$	$-\Delta\tilde{\phi} = 4\pi \left(\rho - \sum_A \frac{Z_A}{\pi^{\frac{3}{2}} \sigma^3} \exp\left(-\frac{(\mathbf{r}-\mathbf{R}_A)^2}{\sigma^2}\right) \right)$ (6.37)
Electrostatic contribution of electrons and nuclei to V_{eff} in the Kohn-Sham matrix	
$K_{ij}^{\text{ES}} = \langle \varphi_i \phi \varphi_j \rangle$	$K_{ij}^{\text{ES}} = \langle \varphi_i (\tilde{\phi} + \sum_A \left(\frac{Z_A \text{erf}\left(\frac{ \mathbf{r}-\mathbf{R}_A }{\sigma}\right)}{ \mathbf{r}-\mathbf{R}_A } - \frac{Z_A}{ \mathbf{r}-\mathbf{R}_A } \right)) \varphi_j \rangle$ (6.38)
Calculation of the Hartree energy	
$E_{\text{H}} = \frac{1}{2} \int \left(\phi + \sum_A \frac{Z_A}{ \mathbf{r}-\mathbf{R}_A } \right) \rho(\mathbf{r}) \text{d}\mathbf{r}$	$E_{\text{H}} = \frac{1}{2} \int \left(\tilde{\phi} + \sum_A \frac{Z_A \text{erf}\left(\frac{ \mathbf{r}-\mathbf{R}_A }{\sigma}\right)}{ \mathbf{r}-\mathbf{R}_A } \right) \rho(\mathbf{r}) \text{d}\mathbf{r}$ (6.39)

Table 6.2: Governing equations in the treatment of the electrostatic interaction with a point-like or Gaussian neutralizing charge distribution.

Method	Ref	E_{total}	E_{kin}	E_{H}	E_{ext}	E_{xc}	$1s$	$2s$	$2p$
Point.	0	-128.2102	127.7419	65.7454	-309.9918	-11.7057	-30.29649	-1.31837	-0.49310
Gauss.	0	-128.2141	127.7521	65.7426	-310.0028	-11.7060	-30.29992	-1.31842	-0.49305
Point.	1	-128.2268	127.7667	65.7550	-310.0408	-11.7078	-30.30043	-1.31820	-0.49313
Gauss.	1	-128.2270	127.7669	65.7550	-310.0411	-11.7078	-30.30050	-1.31820	-0.49313
Point.	2	-128.2272	127.7674	65.7552	-310.0418	-11.7078	-30.30054	-1.31820	-0.49313

Table 6.3: Comparison of energy contributions and eigenvalues in $[E_{\text{h}}]$ for P4 calculations on a single neon atom employing a Gaussian- or a point charge as neutralizing charge distribution. All calculations are performed on the identical mesh with different global refinements (Ref), where the last row from the twice refined point charge approach can be regarded as the reference result.

In order to compare these two approaches, test calculations are performed using different finite element types and different grids. In Table 6.3 the results for P4 finite elements are given, where the width parameter of the Gaussian distribution is set to $\sigma = 0.5$. It is observed, that the Gaussian approach possesses advantages, as it can reproduce accurate results already on meshes of lower refinement, i.e. the energy contributions from the Gaussian approach of the same global refinement already approach values from a higher refinement of the point charge approach. The lower $1s$ and E_{ext} energies of the Gaussian approach on the identical mesh result from the direct inclusion of the nuclei potential in the effective operator (6.38), yielding a deeper potential. Therefore the Gaussian-approach allows calculations with lower grid refinements and can be regarded as superior. However within our exactness, both approaches converge to the same values and are able to describe the atomic system. Due to evolutionary reasons, in the rest of this work, the point charge approach is applied.

It should also be noted, that the integration over the singularity can be avoided by a mixed procedure, taking the point charge approach in the SCF algorithm and after convergence, employing the Gaussian charge distribution in order to obtain the electrostatic potential for the energy calculation. However in this procedure, the mesh requirements for representing a potential ϕ with singular point still remain valid. In [283] a procedure is described, how this integration could also be circumvented.

6.4.1.2 Higher order finite elements for the electrostatic potential. Apart from this section, equal finite element spaces are used for the electrostatic potential ϕ as well as the electronic wave functions ψ_i in this work. It might however be advantageous to represent the electrostatic potential in a finite element space of higher polynomial order, as this could improve the representation of the $1/r$ singularity at the nuclei position. In addition the electron density ρ on the right hand side of the Poisson equation (6.15) is of twice the polynomial order as the wave functions ψ_i in the Kohn-Sham equations. Therefore the Poisson equation is solved in the finite element space of the electron density, which can be generalized to an arbitrary order. Table 6.4 compares the results between calculations where first ϕ is interpolated in the same polynomial order as the wave functions ψ_i (given by P3 and P4 respectively) and a calculation where ϕ takes twice the order (P6, P8), the basis in which the density ρ on the right hand side of the Poisson equation is represented. For both cases an identical underlying finite element grid is employed. The final results show a notable improvement towards energy values that could be gained only on meshes with higher resolution, especially the $1s$ eigenvalue, representing

ψ	ϕ	E_{total}	E_{kin}	E_{H}	E_{ext}	E_{xc}	1s	2s	2p
P3	P3	-128.2255	127.7648	65.7543	-310.0370	-11.7076	-30.30011	-1.31822	-0.49313
P3	P6	-128.2258	127.7659	65.7540	-310.0380	-11.7076	-30.30041	-1.31823	-0.49313
P4	P4	-128.2253	127.7645	65.7541	-310.0363	-11.7076	-30.30007	-1.31822	-0.49312
P4	P8	-128.2258	127.7659	65.7539	-310.0380	-11.7076	-30.30042	-1.31822	-0.49312

Table 6.4: Comparison of energy contributions and eigenvalues for a high (P6, P8) and a low (P3, P4) polynomial order in the basis functions of the electrostatic potential ϕ , where the wave functions ψ_i are represented in the low order basis respectively. All energy contribution in [E_{h}].

the ground state in the effective potential, is lowered by $3 \cdot 10^{-4} E_{\text{h}}$ and also the external energy increases, so the electron density is shifted towards the nuclei position. However the memory requirements increase drastically if the stiffness matrix (6.28) is assembled in the high order finite element space containing much more degrees of freedom, at least if no matrix-free calculations are employed, and also the sparsity of this matrix reduces. Furthermore, it is known, that in order to represent a singularity, not the polynomial order of the finite elements should be increased, but the refinement at the position of the singularity [56, 261]. In summary, these two facts weight up the computational gains from the calculations. Referring to the Gaussian neutralizing charge distribution of the last section, there the potential is much smoother without singular point and therefore a lower order interpolation of the potential is recommended. It should however be noted, that in order to maintain the variational character of the total energy, a higher order representation of the potential ϕ can be necessary in order to satisfy the relation between the electrostatic potential and the charge distribution from (6.13).

6.4.2 Analysis of the numerical approximations

In order to solve the Kohn-Sham equations numerically, a series of approximations have to be introduced. The basic approximation in the numerical solution scheme is the representation of the Kohn-Sham equations within a finite dimensional function space as outlined in Section 6.3.1, however additional approximations are required. For example the domain has to be limited to a finite size of reasonable extent in order to not qualitatively change the system under consideration. Especially the slowly decaying electrostatic potential ϕ should not be influenced, where appropriate boundary conditions for the Poisson equation can be provided. Similarly the integrals in the calculation of matrix elements and energies cannot be evaluated analytically but numerical integration with Gaussian quadrature rules is employed. Therefore in this section the influence of quadrature rules, the domain size and the boundary conditions on the developed real space framework of density functional theory is investigated.

6.4.2.1 Numerical integration with quadrature rules. In simple scalar products of finite element basis functions or their derivatives, the quadrature rule for an exact integration, i.e. without a numerical error, follows directly from the polynomial degree of the shape functions. Alternatively these integrals can also be evaluated analytically by taking the geometric transformation of the reference element into account. However due to the nonlinearity of the problem, the matrix elements of the Kohn-Sham equations and the involved energies contain also integrals with rational powers or even logarithms of the

q	E_{total}	E_{kin}	E_{H}	E_{ext}	E_{xc}	$1s$	$2s$	$2p$
6	-128.22530	127.76417	65.75413	-310.03603	-11.70757	-30.30006	-1.31824	-0.49314
8	-128.22529	127.76437	65.75412	-310.03619	-11.70759	-30.30007	-1.31823	-0.49313
10	-128.22529	127.76450	65.75414	-310.03635	-11.70759	-30.30006	-1.31821	-0.49311
12	-128.22529	127.76433	65.75410	-310.03614	-11.70758	-30.30008	-1.31824	-0.49314
14	-128.22529	127.76446	65.75414	-310.03630	-11.70759	-30.30007	-1.31822	-0.49312

Table 6.5: Effect of the quadrature rule upon eigenvalues and energies for a single neon atom with P4 finite elements. First column polynomial order q to which the quadrature rule is exact, then energy contributions followed by the eigenvalues in $[E_{\text{h}}]$.

electron density and therefore of the basis functions. In the same way the right hand side of the Poisson equation contains an integration over the product of the density ρ with a test function φ_i (6.29), where ρ is build from the squared wave functions ψ_i yielding in total an integral over the product of three finite element basis functions, which therefore also yields a higher polynomial degree than the scalar product. Furthermore, in our approach the $1/r$ singularity from the potential of the nuclei is integrated in the evaluation of the electrostatic energies. Therefore a systematic investigation of the influence of the numerical quadrature rule is carried out, based upon the calculation of the electronic structure of the neon atom. Quadrature rules of different polynomial order q are employed in the assembly of the Kohn-Sham matrix as well as evaluating the energy contributions of the kinetic and the exchange-correlation energy. However for the integration of the $1/r$ -singularity in the Hartree- (6.39) and the external energy (6.7), which in principle is only necessary at the end of the simulation in order to determine the final energies, always a much higher quadrature rule of constant order 28 is applied. Alternatively, also adaptive quadrature rules could be applied [257].

In general the errors from numerical integration reduce, if the mesh is refined, as the quadrature is applied in each element and therefore much more quadrature points are taken into account. Since the results therefore depend upon the mesh and its degree of refinement, the impact of the quadrature rule is calculated exemplarily for a single neon atom on a mesh of intermediate refinement and it is assumed, that the findings can be transferred to other configurations, at least in the way of an upper limit for the error.

It was found that the quadrature rule should at least be capable of exactly integrating the scalar products of the derived basis functions in the stiffness matrix. If this was not the case, the changes in the SCF algorithm were too invasive, and completely different eigenvalues and eigenfunctions could result. However if this criterion is met, different quadrature rules resulted in changes in the energy components only in the 4th digit, well below the stated accuracy threshold of $10^{-3} E_{\text{h}}$, as illustrated in Table 6.5. The eigenvalues only minimally change with the quadrature rule, however the electron density still changes, as can be seen from the difference in the kinetic energy. These energy changes however seem to annihilate the changes in the potential energies, as the total energy remains unaffected in the digits presented.

In order to quantify discrepancies from the integration over the $1/r$ -singularity, a test integration over the “screened potential” e^{-r}/r is performed, for which the analytic result on a sphere is given as

$$\int_{\mathbb{R}^3} \frac{e^{-|r|}}{|r|} \mathrm{d}\mathbf{r} = 4\pi \lim_{r \rightarrow \infty} \int_0^r r' e^{-r'} \mathrm{d}r' = 4\pi (1 - \lim_{r \rightarrow \infty} (r+1)e^{-r}) = 4\pi. \quad (6.40)$$

Order q	Inner grid length $0.002a_0$		Inner grid length $0.01a_0$	
	Total value	Difference to 4π	Total value	Difference to 4π
5	12.5656921760985	$-6.78 \cdot 10^{-4}$	12.5700713175014	$+3.70 \cdot 10^{-3}$
10	12.5663705999356	$-1.44 \cdot 10^{-8}$	12.5663705187223	$-9.56 \cdot 10^{-8}$
15	12.5663706124750	$-1.88 \cdot 10^{-9}$	12.5663705859752	$-2.83 \cdot 10^{-8}$
20	12.5663706139124	$-4.47 \cdot 10^{-10}$	12.5663706086168	$-5.74 \cdot 10^{-9}$
25	12.5663706140282	$-3.31 \cdot 10^{-10}$	12.5663706097417	$-4.62 \cdot 10^{-9}$
30	12.5663706142010	$-1.58 \cdot 10^{-10}$	12.5663706127643	$-1.59 \cdot 10^{-9}$

Table 6.6: Differences in the numerical integration of the screened potential e^{-r}/r .

The finite domain radius of the mesh is chosen as 40, where however the volume outside a sphere of radius 30 only contributes less than $4\pi(30+1)e^{-30} \leq 3.65 \cdot 10^{-11}$ to the integral, so that the difference of the employed grid to a radial sphere, i.e. the shape of the domain being polyhedral instead of spherical, does not contribute relevantly to the integral. The integration was performed on two grids which only differ in the refinement around the origin, where the grid length at the atom position was $0.01a_0$ and $0.002a_0$, respectively. The discrepancies of the numerical integration to the value of 4π are given in Table 6.6. One can see from the data, that a high order quadrature is able to achieve an exactness at around 10^{-10} in the result. In the SCF algorithm the electron density ρ replaces the exponential e^{-r} in the integrand, which could weight stronger the values at the singular point. In calculations with the neon atom, the discrepancies in the calculations with quadrature rules between 25 and 30 on the same mesh, have been found in the order of $10^{-4}E_h$. Therefore, if higher accuracies in the total energy are required, it is possible to avoid the integration over the singularity by applying the Gaussian neutralizing charge distribution (6.36) and reside to the energy calculation from (6.17). Alternatively, a geometric transformation [77, 256] can be performed, which then allows for an accurate integration. However it should be emphasized again, that only the final energy calculation is affected by this issue, but neither the eigenvalues nor the electron density itself.

6.4.2.2 Influence of a finite domain size. The domain of definition of the Kohn-Sham equations (6.12) consists of the complete real space \mathbb{R}^3 , which can numerically be realized only with non-standard methods like e.g. infinite elements [36] or coordinate transformations [130]. In the numerical setting the domain is therefore restricted to a size on which the fast decaying atomic orbitals of the atoms and molecules have effectively vanished and the slowly decaying electrostatic potential can be modeled with appropriate boundary values. The effect of the finite domain size is now studied for our generic test configuration of a single neon atom, where calculations are performed on domains of increasing extent using homogeneous boundary conditions, which are suitable in this case since the total charge, the dipole, and all higher electric multipoles vanish in the analytic solution of the noble gas atom. The comparability of the results from different domains is assured by employing identical meshes in the interior domain, enlarged to the new domain size by additional elements. In the case of P4 finite elements, the energy contributions and eigenvalues on domains of different radii are given in Table 6.7.

Two antagonizing effects are observed in the data, which can be physically interpreted. The binding energy between the electrons and the nuclei increases on the smaller domain, since the electrons reside closer to the nuclei thereby increasing the external energy. This results also in an increase of the exchange-correlation energy, as the electron density is

$\varnothing[a_0]$	E_{Total}	E_{kin}	E_{H}	E_{ext}	E_{xc}	1s	2s	2p
5	-127.555	130.841	69.627	-315.826	-12.197	-29.732	-0.949	-0.075
10	-128.221	127.801	65.850	-310.154	-11.719	-30.288	-1.309	-0.484
20	-128.225	127.764	65.754	-310.036	-11.708	-30.300	-1.318	-0.493
160	-128.225	127.764	65.754	-310.036	-11.708	-30.300	-1.318	-0.493

Table 6.7: Effect of the domain size on a single neon atom calculation using P4 shape functions. The first column shows the diameter of the domain. Next the energy contributions followed by the eigenvalues in $[E_{\text{h}}]$ are given.

more localized. Therefore both binding contributions in the total energy increase their energies. With respect to the anti-binding energy components however, the localization of the electrons yields stronger distractive forces thereby likewise increasing the Hartree energy. The kinetic energy also increases, since the wave functions have to oscillate and drop to zero on the boundary within a smaller region, yielding higher gradients and therefore a higher kinetic energy. Thus the absolute value of the binding as well as the anti-binding contributions to the total energy raises on a smaller domain. Altogether the total energy however increases as expected, since an additional constraint is imposed from the domain upon the variational space of the wave functions in the minimization problem. In a strict way, the minimum property is lifted by the introduction of the numerical solution of the Poisson equation for determining the electrostatic potential resulting in deviations from the initial relation (6.13). However if this relation is reasonably fulfilled, the minimum property remains valid. The constraint in the small domains directly affects the form of the wave functions ψ_i , whereas on medium sized domains (especially in cases with non-vanishing electric poles) it is expected to mainly influence the Poisson equation and therefore only indirectly the wave functions ψ_i , merely yielding smaller changes in the energy values.

The increase of the eigenvalues on the smaller domain, gives evidence that the depth and the width of the effective potential reduce, being a well known effect in quantum mechanics [64]. After a certain domain size has been reached (a diameter of about $20a_0$ in the presented neon example), the difference between the energy components merely fluctuates on smaller energy scales.

6.4.2.3 Boundary conditions in the Poisson equation. After having estimated the influence of the finite domain size, the impact of the boundary conditions in the Poisson equation is studied for the carbon monoxide molecule, which possesses an inherent dipole. A comparatively small domain with a diameter of $18a_0$ is chosen and a bond length between the atoms of $1.7a_0$ in order to assure the presence of a non-vanishing dipole. At this atomic distance, the CO molecule shows a dipole of around $-0.36ea_0$, calculated on a domain of diameter $80a_0$ in Section 6.5.2.

We compare the differences between calculations with homogeneous boundary conditions and when non-zero Dirichlet boundary conditions from the electrostatic dipole are applied, which can be regarded as the natural boundary condition in this case. As expected, the system with the dipole correction showed an improved accuracy, with a slightly lower total energy ($6 \cdot 10^{-4} E_{\text{h}}$) close to our accuracy requirement and the negative dipole decreased by $0.01ea_0$.

6.4.3 Analysis of simulation parameters

After setting up the SCF algorithm including the above mentioned approximations, there are further parameters left for adjustment, which affect the accuracy of our simulation. In particular, these are the basis set, i.e. the polynomial degree of shape functions together with the density of the finite element mesh, the shift of the eigenvalue spectrum in the Arnoldi process, the tolerances for the linear solvers as well as the eigenvalue solver, the mixing parameter α in linear and Pulay mixing, and the occupation number of the atomic orbitals. While some of these parameters, like the mixing parameter and the solver tolerances are straightforward to adjust, as their influence can directly be seen on the quality of the results or the duration of the convergence process, there are others, which show a more subtle influence, and therefore need a more thorough investigation given below.

6.4.3.1 Convergence of closed shell calculations - dependence on the occupation number. For simplicity, the calculations performed in this work are closed shell calculations, i.e. without spin polarization. When performing calculations on single atoms like carbon or oxygen with partially filled p -shells, scenarios are observed, in which the SCF algorithm enters a loop between three different total energy values, originating from different $2p$ -shell orbitals, as illustrated in Figure 6.6 for a carbon atom. This behavior can be explained by the symmetry breaking of the numerical solution procedure. Since the Kohn-Sham equations for a single atom possess radial symmetry, there is no direction in space determined a priori, along which the three $2p$ -orbitals of the carbon atom should align. However the triangulation of the physical domain around the nuclei cannot possess radial symmetry and therefore certain directions are preferred through the finite element mesh, along which the system can minimize its energy best.

Induced by the degeneracy of the energy eigenvalues of the three orthogonal $2p$ -orbitals, it happens, that in each SCF iteration a different $2p$ -orbital is obtained. This orbital then enters the density calculation and therefore determines the new effective potential in the next loop, which now however prefers a different $2p$ -orbital as having minimal energy, since the former one entered the distracting Hartree potential. By this mechanism the SCF iterations do not converge. The density mixing procedures only reduce the effect and lead to densities containing parts of all the degenerate orbitals. This phenomena is also known as “charge sloshing”, since the density changes non-smoothly in every iteration. The energy difference between the SCF iterations is in the order of $7 \cdot 10^{-5} E_h$ for the carbon atom, which is slightly below our requirement for chemical accuracy. The same effect is also observed for oxygen. To resolve this situation, all the degenerate orbitals of a SCF iteration are identified in the density calculation and considered with equal weight, yielding a convergent algorithm. For more involved atomic configurations, with previously unknown energy eigenvalues at the Fermi level, one would have to resort to more general approaches, like e.g. the partial occupation according to the Fermi-Dirac distribution.

6.4.3.2 Mesh refinement at nuclei position. The position of the nuclei represents an extremal point for the wave functions due to the singularity in the external field. Therefore it is occupied by a node of the finite element mesh. The mesh refinement, representing the amount of basis functions available to interpolate the wave functions and

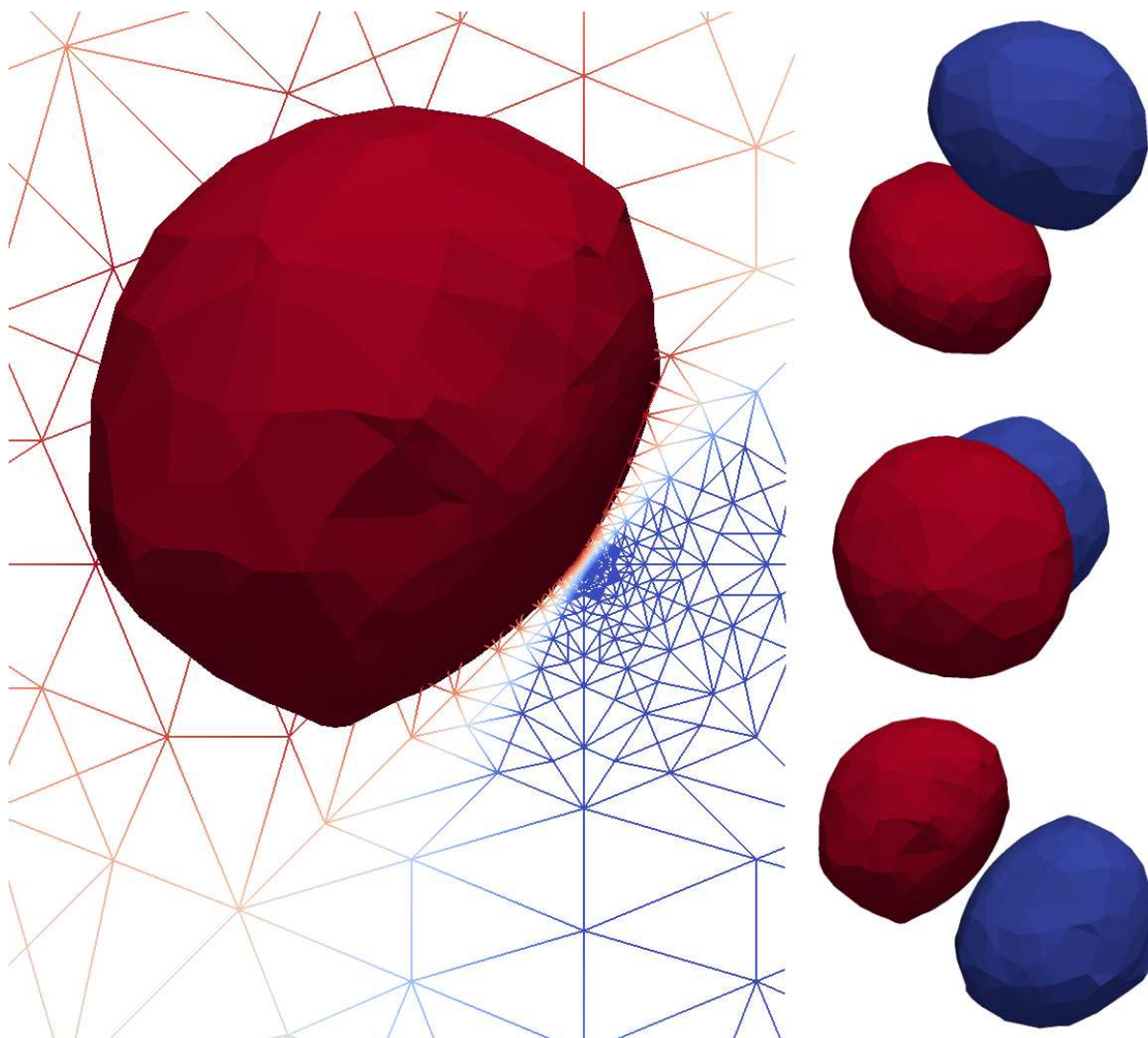


Figure 6.6: $2p$ -orbital of the highest occupied eigenfunctions of the C-atom during the convergence process. Inside the red (blue) ball, the wave function takes values larger (smaller) than 0.1 (-0.1). Left: Partial orbital together with a cut through the underlying finite element grid, where the color code on the mesh indicates the value of the wave functions between ≥ 0.1 (red) over 0.0 (grey) to ≤ -0.1 (blue). Right: Highest occupied eigenfunction changes its orientation in every convergence step between these three configurations.

the electrostatic potential in this sensitive area, where the all-electron wave function highly oscillates, should therefore significantly influence the quality of the simulation. In Table 6.8, this influence is studied for P4 finite elements on the neon atom, where all calculations use the identical mesh except for the direct neighborhood of the nucleus position, where more and more elements are placed, halving the grid length at the nucleus respectively, as illustrated in Figure 6.7. For larger atoms, a higher refinement is required, due to the deeper potential and the larger amount of wave functions. For large grid lengths, a relevant change of the total energy is observed, which at a grid length of 0.064 even lowers the total energy, where all other approximations in the numerical setting so far had the tendency to raise the total energy, expressing the nonvariational character of the presented finite element formulation of the Kohn-Sham equations, which arose due to the introduction of the Poisson equation as well as the application of numerical quadratures. It should be noted, that in this special case, due to the rough refinement, the integration of

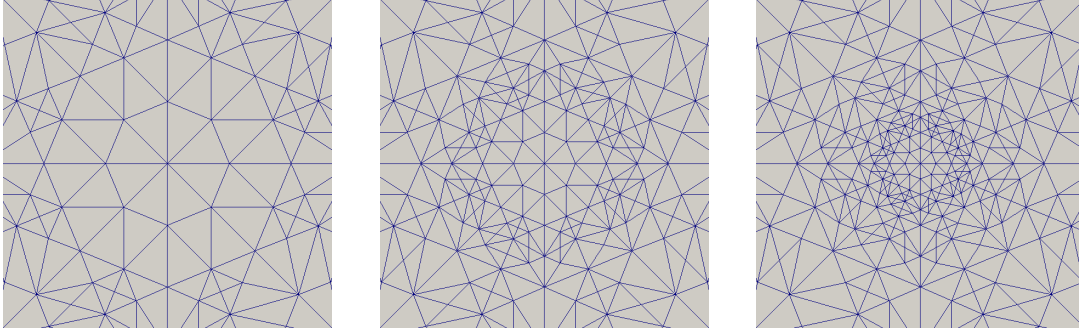


Figure 6.7: Zoom into the cross-section of the employed meshes with decreasing grid length at the center, ranging from 0.032 (left) and 0.016 (center) to 0.008 (right), where the outer parts remain basically unchanged.

$[a_0]$	E_{Total}	E_{kin}	E_{H}	E_{ext}	E_{xc}	$1s$	$2s$	$2p$
0.064	-128.22868	127.96198	65.72153	-310.20264	-11.70956	-30.31783	-1.31909	-0.49301
0.032	-128.22458	127.78016	65.75032	-310.04730	-11.70776	-30.30158	-1.31830	-0.49312
0.016	-128.22515	127.76605	65.75366	-310.03724	-11.70761	-30.30023	-1.31823	-0.49312
0.008	-128.22527	127.76463	65.75405	-310.03634	-11.70759	-30.30009	-1.31823	-0.49312
0.004	-128.22529	127.76444	65.75413	-310.03645	-11.70759	-30.30006	-1.31822	-0.49312
0.002	-128.22531	127.76449	65.75413	-310.03633	-11.70759	-30.30007	-1.31822	-0.49312
0.001	-128.22531	127.76446	65.75412	-310.03630	-11.70759	-30.30007	-1.31822	-0.49312

Table 6.8: Effect of the inner refinement using P4 shape functions for a single neon atom. The first column shows the grid length of the tetrahedrons directly at the origin. Next the total, kinetic, external and exchange-correlation energy followed by the eigenvalues $1s$, $2s$, and $2p$ in $[E_{\text{h}}]$ are given.

the singularity does not possess the common accuracy, as outlined in Section 6.4.2.1, and therefore the total energy might even be slightly lower or higher. However the eigenvalues as well as the kinetic and exchange-correlation energy are not influenced by this issue and they both relevantly change. One can also see from the data that, as expected, mainly the lowest eigenvalue $1s$ is effected. Only for the grid length 0.064 the $2p$ changes, as manifestation of the fundamental impact of the reduced basis set in this configuration. Therefore a sufficient refinement at the nuclei position in simulations is important, however one should also note the convergence of the energy contributions, for high refinements, where no further significant changes appear, which is one of the characteristics of the finite element method close to the exact solution.

6.4.3.3 Tolerances in linear solver, mixing parameter, shift eigenvalue solver.

The convergence criterion of the SCF algorithm should take into account the chosen chemical accuracy of $10^{-3} E_{\text{h}}$. The criteria for finishing the SCF algorithm should therefore guarantee the achievement of this limit. The exit criterion is attached to the change in the total energy of consecutive iterations, which is determined to vary by less than a value between 10^{-4} and $10^{-6} E_{\text{h}}$, where the fulfillment of the criteria in two consecutive iterations was usually enough to reach the chemical accuracy. The tolerances of the linear solver of the Poisson equation and the linear equation involved in Arnoldi process (6.33) should therefore be reasonably lower than the intended accuracy of the SCF algorithm and we increased the tolerances in early iterations, in which the density still varies strongly in every loop. With respect to the mixing coefficients in (6.34), a default value of $\alpha = 0.65$

is used. However it was sometimes necessary to increase the parameter in order to reach convergence. Especially changes in the finite element discretization around the nuclei position and therefore the basis set could relevantly change the convergence behavior. In that respect an additional change of the shift parameter in the Arnoldi process was required at times, as extremal eigenvalues could not be found with the previous shift value, reflecting altered interpolation capabilities with respect to the eigenfunctions. Similarly the domain size influenced the convergence. However in all calculations, it was sufficient to have a single shift, but applying two or more different shifts in order to extract eigenvalues is also possible or even necessary for more complicated atomic configurations and might even be advantageous with respect to the computational costs.

6.5 Representative numerical results

In this section the SCF algorithm is applied to simple atomic systems in order to show that the results and accuracies met with the finite element basis are in line with standard chemical software packages. All-electron calculations are performed with the point charge approach in the Poisson equation for the nuclei (see Section 6.4.1) and identical shape functions for the electrostatic potential as for the wave functions. First, calculations on noble gases are accomplished, where for the xenon atom, the basis has to be able to interpolate at once 27 orthogonal atomic orbitals together with the Poisson potential. The generality of the basis set is then shown in the case of the molecules carbon monoxide and benzene, where for carbon monoxide no special orbitals for the polarization have to be introduced, but a reasonable mesh of the binding domain suffices, similar as in the concluding example of an external homogeneous field polarizing a single neon atom. Other examples for like H_2 or a graphene sheet containing 100 atoms can be found in [95, 200, 254], showing the ability of the finite element method to succeed in sophisticated configurations.

6.5.1 All-electron calculations on noble gases

Since the orthogonal electronic eigenfunctions of the all-electron calculations highly fluctuate at the positions of the nuclei, the resolution of the finite element mesh was chosen much higher in the environment of the atomic core and continuously coarsens towards the domain boundary. The same coarsening is also required by the electrostatic potential, showing a singularity at the origin. For noble gases the electronic structure is calculated and compared with Kohn-Sham calculations performed with the electronic structure code NWChem [366] with the basis sets aug-cc-pv6z (He, Ne, Ar), aug-cc-pv5z (He, Ne, Ar, Kr), aug-cc-pv4z (Kr) and for xenon only the rather small dzvp and 3-21G basis set were available for all-electron calculations. For large basis sets, these basis functions tend to become linear dependent, requiring an exclusion of single functions in order to achieve convergence of the SCF algorithm, which was especially the case for the aug-cc-pv6z basis. This behavior already illustrates one strength of the finite element basis in the all-electron case, where the basis set is constructed naturally from the triangularization of the real space, without the issue of linear dependencies of the basis functions and therefore also accurate all-electron finite element basis sets for large atoms like xenon can be constructed straightforward. The results are given in Table 6.9, with the basis set specified in brackets.

	P2	P3	P4	NWChem	NWChem
He	-2.834252	-2.834296	-2.834284	-2.834244 (aug-cc-pv5z)	-2.834282 (aug-cc-pv6z)
Ne	-128.22300	-128.22682	-128.22723	-128.22703 (aug-cc-pv5z)	-128.22725 (aug-cc-pv6z)
Ar	-525.9190	-525.9352	-525.9377	-525.9365 (aug-cc-pv5z)	-525.9375 (aug-cc-pv6z)
Kr	-2749.823	-2750.072	-2750.130	-2750.113 (aug-cc-pv4z)	-2750.120 (aug-cc-pv5z)
Xe	-7227.913	-7228.647	-7228.829	-7197.513 (3-21G)	-7228.011 (dzvp)

Table 6.9: Total energies obtained from calculations on single noble gas atoms using finite elements of different polynomial order compared with values calculated from NWChem [366] for two different basis sets, where all energies are given in [E_h].

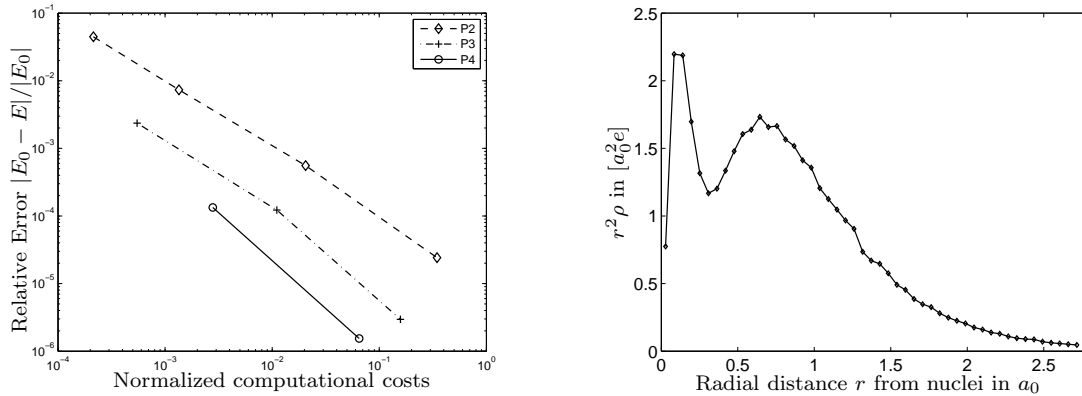


Figure 6.8: Left: Comparison of the relative error in the total energy with the computational cost for calculations on a single neon atom with different finite elements. Right: Radial density distribution of the neon atom.

For helium and neon (except for the P2 basis) the solutions are converged with respect to grid refinement up to the third digit. The total energies of the P4 finite element seem to be of about the same quality as the aug-cc-pv6z results for He, Ne and Ar, where for larger noble gases this basis set is not available in NWChem and therefore smaller bases are employed. For larger atoms, the finite element solutions are not converged with respect to the mesh refinement, i.e. a uniform mesh refinement would still change the values in the digits presented, as can be seen from the different results for different finite element shape functions. Such refined calculations however rendered numerically too expensive, what implies that a discrepancy between the total energy values shows off, especially in the case of P2 and P3 finite elements.

Concerning the performance of the different finite element bases it is generally found, that better results with respect to the invested computational time were attained with higher order finite elements, as illustrated in Figure 6.8. The calculations were performed on a local computer cluster, where an external influence due to the varying load cannot be completely avoided. However the trend of improved performance in high order elements was generally observed. The P1 elements, which are not shown here, result in an inferior behavior, which can be explained by the poor interpolation properties of piecewise linear wave functions, where for example the kinetic energy, involving the derivative of the wave function, is simply approximated as a constant within each finite element domain. Similarly, a linear electrostatic potential can only describe potentials with a constant electric field within each element. The overall run times reached from several CPU minutes

Bond length	1.7	1.8	1.9	2.0	2.1	2.2	2.3
P2, Binding energy	-0.355	-0.460	-0.525	-0.555	-0.565	-0.560	-0.541
P2, Dipole moment	-0.360	-0.302	-0.242	-0.178	-0.113	-0.045	0.024
P3, Binding energy	-0.375	-0.475	-0.535	-0.566	-0.577	-0.575	-0.559
P3, Dipole moment	-0.358	-0.301	-0.240	-0.176	-0.110	-0.042	0.026
P4, Binding energy	-0.376	-0.475	-0.535	-0.566	-0.578	-0.575	-0.564
P4, Dipole moment	-0.358	-0.301	-0.240	-0.176	-0.110	-0.042	0.027
aug-cc-pvtz, Binding energy	-0.371	-0.471	-0.532	-0.564	-0.576	-0.574	-0.563
aug-cc-pvtz, Dipole moment	-0.360	-0.303	-0.242	-0.179	-0.113	-0.045	0.024
aug-cc-pv5z, Binding energy	-0.376	-0.475	-0.535	-0.566	-0.578	-0.576	-0.564
aug-cc-pv5z, Dipole moment	-0.358	-0.301	-0.241	-0.178	-0.112	-0.044	0.024

Table 6.10: Binding energy in E_h and dipole moment in ea_0 at different atomic distances in a_0 for the CO molecule from different finite element calculations and from the software package NWChem. Experiments found a bond length of $2.13 a_0$ with a binding energy of $-0.41 E_h$ [131].

for smaller atoms up to several CPU days in the larger xenon calculations with about $1.5 \cdot 10^5$ degrees of freedom. Similar results for the superior performance of higher order elements were also found in [254], where mainly hexahedral elements were examined.

In Figure 6.8 the radial density distribution for the neon atom is illustrated, clearly showing the shell structure of the density. Generally one can state that the results completely meet the accuracies of common electronic structure software packages.

6.5.2 Calculation on small molecules

In calculations with molecules, more care must be taken in the generation of the finite element meshes, especially in the binding area between the atoms additional elements are required. As example, the carbon monoxide molecule CO is investigated, which possesses an inherent dipole moment. Therefore the dipole correction of the electrostatic potential is chosen on the boundary for the Poisson equation (6.15), where the dipole moment itself represents a basis sensitive quantity. The calculations are conducted with P2, P3, and P4 shape functions on a domain of diameter $80 a_0$ and the distance between the atoms is varied in steps of $0.1 a_0$ in order to calculate the bond length, which is found around $2.1 a_0$. For comparison, other DFT calculations employing the correlation functional from PERDEW & WANG [284] report a bond length of $2.08 a_0$ or employing the VWN5 functional [370] one of $2.125 a_0$ [343], the Hartree-Fock method gives a bond-length of $2.08 a_0$, and experiments result in a value of $2.13 a_0$ [131]. A cross-section of the density distribution for an atomic distance of $2.2 a_0$ together with the mesh points in the section plane is given on the left of Figure 6.9, whereas the highest occupied molecular orbital (HOMO) is presented in the center, and the binding energy versus bond length plot is given on the right of that figure. The dipole moments switch the sign between 2.2 and $2.3 a_0$ and are in good agreement with calculations from NWChem employing the aug-cc-pvtz and the aug-cc-pv5z basis set. This is also true for the binding energy, which is found at $0.578 E_h$ for P4 finite elements at an atomic distance of $2.1 a_0$, as shown in Table 6.10.

As a second example, the benzene molecule C_6H_6 is examined, rendering another benchmark problem, which has already been treated in the context of the finite element method [200]. The planar molecule is thereby aligned in the $z = 0$ plane with atomic coordinates C $(0, \pm 2.63804, 0)$, C $(\pm 2.28461, \pm 1.31902, 0)$, H $(0, \pm 4.684606, 0)$, as well as H

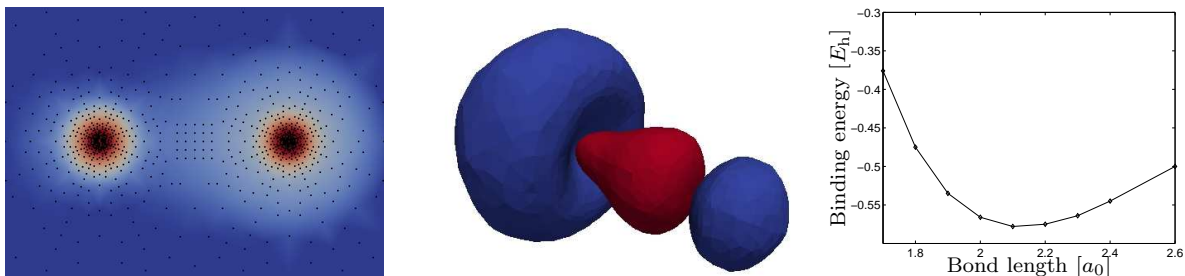


Figure 6.9: Left: Density distribution with vertices of the underlying FEM-mesh, where the C-atom is positioned on the left-hand side. Center: Binding molecular orbital (HOMO) of the carbon monoxide molecule. Right: Binding energy vs. bond length for the carbon molecule from P4 calculations.

($\pm 4.056988, \pm 2.342303, 0$), where all coordinates are given in $[a_0]$. The total energy of the benzene molecule was found as $-229.492E_h$ for P2, $-230.187E_h$ for P3 and $-230.201E_h$ for P4 finite elements, where in all three calculations the identical grid is used. For comparison the P4 result in [200] yielded a total energy of $-230.193E_h$ employing the exchange-correlation functional from PERDEW & WANG [284]. Reference calculations with NWChem employing the cc-pvtz basis resulted in a total energy of $-230.170E_h$ and the cc-pvqz basis yielded $-230.185E_h$, so that also in this case the accuracy of standard software packages are achieved.

6.5.3 External electric field

This final section deals with the atomic response of the neon atom due to the application of a homogeneous external electric field, resulting in the polarization of the atom. This effect is known to be sensitive with respect to the basis set as well as the electron correlation [319]. Within the finite element representation, the basis is again just given by the polynomial order and the triangularization of the physical domain, whereas special basis function are usually added to the Gaussian type basis sets in order to describe the polarized state of the atom. The basis sets used so far with NWChem (aug-cc-pvXz) contain already these additional basis functions. The homogeneous field is aligned along

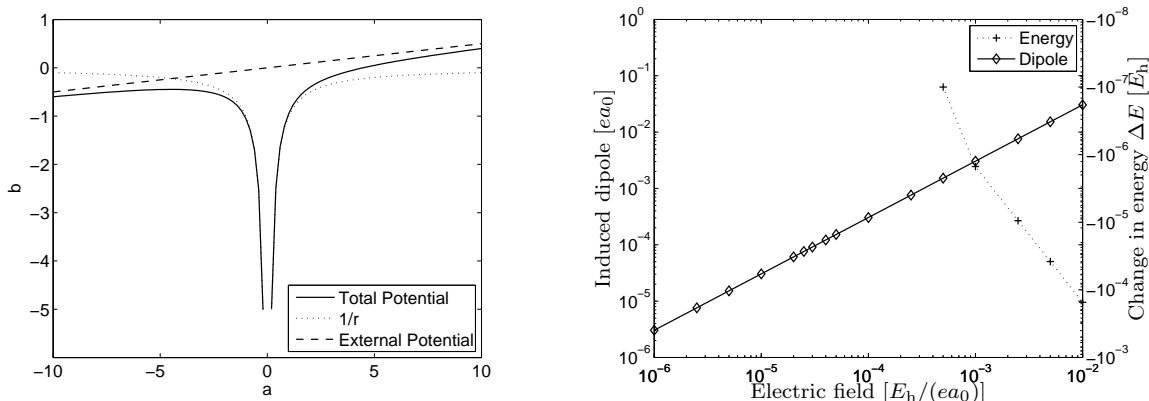


Figure 6.10: Left: Schematic plot to illustrate the change of the external potential by the homogeneous external field. Right: Linear dependence of the incited dipole upon the field strength and change of energy for a neon atom, calculated from P4 finite elements.

Basis set	P4	aug-cc-pv4z	aug-cc-pv5z	aug-cc-pv6z
Polarizability	3.0439	2.9058	2.9981	3.0308

Table 6.11: Comparison of the polarizability of the neon atom between calculation from P4 finite elements with calculations of different all-electron basis sets with NWChem.

the x -direction and the excited dipole moment is found to increase almost linear with the field strength over the evaluated range between 10^{-6} and $10^{-2} E_h/(ea_0)$, as can be seen in Figure 6.10 for P4 finite elements. The average polarizability in atomic units lies at 3.0439, and reference calculations in NWChem revealed the requirements onto the basis set, where only the largest available basis for the neon atom, the aug-cc-pv6z basis, could reach a similar value for the polarizability to within one percent, whereas the other employed basis sets resulted in lower polarizabilities. The involved polarization functions in these basis sets were therefore not fully able to catch the magnitude of the polarization adequately, as can be seen in Table 6.11. The total energy decreases slightly less than quadratic, but is still in good agreement with the quadratic Stark effect [64].

7 Conclusion and outlook

7.1 Modeling solids undergoing failure at the macroscopic scale

Part I of this work starts with a brief review of the strong discontinuity approach used to incorporate failure into the numerical framework of the finite element method. The marching cubes based algorithm initially developed to extract a polygonal mesh of an isosurface from a 3D scalar field in the field of computer graphics is adapted in this work to combine it with the global tracking algorithm and the finite elements with embedded strong discontinuities to simulate a propagating failure surface through a 3D failing solid. Its potential is fully exploited when using eight node hexahedral finite elements for which 2^8 constant isosurface configurations exist for the particular nodal level set values obtained from the global tracking algorithm initially developed in OLIVER ET AL. [267, 269]. Exploiting rotational and reflective symmetries as well as sign changes, the marching cubes algorithm proposes a reduction of those 256 cases to 15 unique configurations, which are used for the prediction of the propagating failure surface through the finite element under consideration. Such element must be capable of describing a failure zone represented by a strong discontinuity, i.e. a jump in the displacement field. This is achieved in this work based on the well established strong discontinuity approach, following the recent extension in ARMERO & KIM [13] to account for higher order separation modes in 3D, with only a slight modification based on replacing the rotational mode around the normal direction by an additional in-plane shear mode resulting in slight differences of the closed form solutions for the compatibility operator. A particular emphasis is directed towards the configurations of the marching cubes algorithm predicting non-planar failure surfaces. To retain a physical meaningful interpretation of the local element parameters of the strong discontinuity approach, an artificial planar failure surface is constructed in each finite element with a strong discontinuity, not violating though the important requirement of global continuity of the actual non-planar failure surface. Various representative numerical simulations show the performance of the proposed concept including a carefully investigation of its behavior for propagating highly curved failure surfaces. An extension of the concept to use the marching cubes algorithm for the prediction of crack branching scenarios is currently under investigation. Also, its exploitation in other finite element frameworks capable of describing a strong discontinuity within the individual finite elements is possible. Extension of the proposed marching cubes based propagation concept for more advanced electromechanical coupled material than those in Section 3.6.5 or for soft matter materials are also topics of future research in this direction.

Thereafter, new finite elements to account for strong discontinuities in the mechanical displacement field and the electric potential are presented to model failure in electromechanical coupled materials. The new finite elements have been obtained by the proposal of new electrical separation modes which are directly incorporated into the strong discontinuity approach with the goal to avoid locking along the same lines applied within purely mechanical based materials. Constitutive relations along the resulting strong discontinuities, sharply representing the localized zones of failure in the form of a crack, of the electric quantities have been derived based on the development of a localized electromechanical damage law along the crack faces. The performance of the resulting finite elements is tested based on two academic single element tests to confirm their locking free property and then applied to realistic simulations in the form of a compact tension

test and a three point bending test of piezoelectric ceramics for which a comparison with experimental results is performed. This has led to the conclusion that the main characteristics of the dependence of the ultimate load of these specimens on the sign of the applied electric field as proposed in PARK & SUN [280] can be captured with the proposed framework. Despite these promising result there is still room for improvements which are planned to be addressed in future publications. A closer investigation with regard to the applicability and limitations of the propagation criterion for electromechanical coupled materials will be made. Further, the modeling of the crack boundary conditions as being electrically impermeable is probably the main reason for the underestimation of the effect of the applied electric field even though the same tendency can be captured as in PARK & SUN [280]. Therefore studies on the influence of the electric crack boundary condition need to be performed in the future. Even though applied in the numerical simulation for piezoelectric ceramics, the approach results in the development of new finite elements capable to model the electromechanical response for a class of materials with even more general ferroelectric effects. An application of the methodology to such materials may be addressed in future publications.

Further, the effect of electric displacement saturation on problems related to the hysteretic behavior of ferroelectric ceramics and the initiation and propagation of cracks in piezoelectric ceramics is carefully investigated in this work. The physical motivation stemming from a reduction of the ionic movement in such materials at high applied electric fields suggests a saturation of the electric displacement which is proposed in this work to be incorporated in a simplified way by identification of the material parameters effected by this non-linearity and their saturation based on an exponential saturation law. In a first step the saturation of the identified dielectric material parameters is investigated analytically for a problem of a crack in an infinite domain within the framework of linear piezoelectricity. It is shown that both, the total as well as the strain energy release rate, for a Mode III and a Mode I crack are effected by this non-linearity. Keeping their respectively even and odd dependency on the orientation of the applied electric field a reduced dependency of the energy release rates is the result of the electric displacement saturation. The advantage of the proposed incorporation of this effect in this work lies in the straightforward extension to problems where no analytical solutions exist. That allows to outline its effect on the hysteresis curves when adding it to a rate-dependent ferroelectric material model applicable to simulate initially unpoled ferroelectric ceramics. It is shown that the dielectric hysteresis curve is clearly effected at high positive and negative applied electric fields with respect to the polarization direction whereas the butterfly hysteresis curve shows no change. Finally, its influence is explored when it comes to crack propagation in piezoelectric ceramics outlining a clear dependency of the crack path on the size of the electric saturation zone which is controlled by the newly introduced saturation exponent. To numerically simulate crack propagation in piezoelectric ceramics including electric displacement saturation, the strong discontinuity approach, which allows to capture and describe the propagation of jumps in the displacement field and the electric potential through the individual finite elements, is extended. The performed numerical simulations of a compact tension test and an off-centered three point bending test show excellent agreements with experimental results given in the literature. In particular, the curved crack path obtained for the latter test, is to the authors knowledge, for the first time numerically reproduced in such close agreement with the experiments. An extension of the simplified electric displacement saturation model to account also for a resulting

modification of the electrostrictive strains is currently under investigation. The determination of the influence of alternative electrical boundary conditions along the crack path is an active research activity which can be extended to the proposed model of electric displacement saturation in the future.

7.2 Modeling materials with network microstructures at the mesoscopic scale

Part II of this work explores the mechanics of materials with random network microstructures. It presents a new kinematic constraint relating the microscopic deformation of fibers to the macroscopic strain of the continuous solid that results in an efficient homogenization of the elastic response produced by these soft materials. This relation is established with the help of a special statistical description of the network microdeformation that provides extensive information about the reorientation and axial straining of the fibers. The design of the constraint is based on kinematics of maximal advance paths, which allows for a robust transition from the microscopic scales of the network to macroscopic scales of the deformed material. The maximal advance path constraint imposes restrictions not on the stretch of a single fiber but on the microdeformation of the network as a whole. Furthermore it includes important topological characteristics of the network like the functionality of the junctions. Remarkably, for the case of tetrafunctional networks the constraint takes a compact tensorial form which can be clearly interpreted. It is shown that the exact distribution of the variable microscopic stretch defined by this network model can be determined by the principle of minimum averaged free energy, which ultimately leads to the derivation of the homogenized elastic response of the relaxed network at equilibrium. The predicted equilibrium microstretch is non-trivially distributed and depends on the particular response of the chains. The qualitative difference of the microdeformation and the homogenized stress response is shown for tetrafunctional networks with two different types of fibers, namely, flexible chains and stiff filaments.

In the former case, the networks are shown to undergo an essential non-affine deformation when their fibers approach their finite extensibility. This gives a consistent explanation for the difference in the stiffening of elastomers at uniaxial and equibiaxial extension which is well known since the first publication of the experimental data for vulcanized rubber in TRELOAR [353]. In this respect the model supports the justification of other non-affine models like the 8-chain model [17] and the non-affine microsphere model [244] which both suggest a redistribution of chain stretch in the polymer networks. Moreover, in agreement to the latter model this non-affine deformation is associated with the relaxation of the network by the internal degrees of freedom.

A very peculiar behavior is also predicted for networks composed of stiff filaments. The microscopic stretch is shown to be non-affine not only at larger macroscopic strains when the fibers get highly elongated but also at small strains. Furthermore, one can identify a specific soft regime in which the network deforms solely by reorientation without axial straining of the stiff fibers and therefore produces no mechanical response. The transition from this unstable regime to the stable equilibrium behavior results in a particular scaling of shear and normal stresses obtained for simple shear loading and represents a limiting case. As argued in Part II, the stretch of fibers in the real semiflexible networks is stabilized by bending. The response of stiff filaments to bending is commonly much

smaller than their response to axial straining. Nevertheless, in the situation when fiber axial forces become zero, which is the case for the fiber reorientation in the predicted unstable regime, bending can become the dominant mechanism of network elasticity. Instead of the loss of rigidity by the network in the undeformed state as demonstrated in this work, a soft but stable elastic response of the material supported by filament bending as reported in the literature [147, 158, 271, 367] is expected.

The presented homogenization scheme is universally applicable to the materials with random network microstructures formed by fibers of different nature. The use of the maximal advance path constraint is especially justified in cases when the microscopic deformation significantly deviates from the affine stretch, for it effectively captures on average the complex kinematics of connected fibers. Furthermore, the proposed model provides a broad framework for future extensions. For flexible chains, the model gives a very realistic picture of the network microdeformation. Nevertheless, the elastic properties of real elastomers can not be described in terms of the conformational statistics of single chains only. Thermal fluctuations of the junction points [101, 167] and interaction of chains over their length [73, 82, 143, 144] play an essential role and have a corresponding energetic contribution. The incorporation of these factors into the developed description of the network micromechanics reaches far beyond the illustrative objectives of this work and is a subject for future extensions. For stiff filaments, the proposed maximal advance path constraint model is valid for the stretching-dominated regime. The incorporation of the instant bending of fibers into the proposed model will allow to capture the response of the stiff networks in the whole range of macroscopic deformations.

The approach proposed in this work provides two main contributions to the mechanics of soft materials. Firstly, it constitutes a universal framework for the development of computational models that can be utilized for the finite element analysis. It is not overly complex and at the same time is quite flexible and suitable for different types of networks. Secondly, the approach has an essential micromechanical justification. As a consequence, it allows not only to obtain averaged mechanical properties of the material but also to explain how particularly they originate at the microstructure level. Besides the values of the macroscopic quantities such as mechanical stress the resulting models are capable to predict by which microscopic forces and which deformed microscopic fibers it is created. This information is crucial for the understanding of elasticity as discussed in this work, as well as other phenomena in soft materials with random network microstructure. In particular, the knowledge of the microstretch distribution gives the key to the failure of such materials and its modeling in the context of the advanced finite element techniques described in the first part of this work.

As the second key ingredient of Part II serves a new micromechanically motivated transient network model, which is incorporated into the framework of finite rubber viscoelasticity. The model is based on diffusion processes of the highly mobile macromolecules forming the individual polymer chains. These processes result in the evolution of the probability for finding chain segments within a certain stretch state which is governed by the generalization of the Smoluchowski equation from non-interacting particles towards flexible polymer chains in this work. It is shown how a tensorial representation of such evolution yields closed form expressions of the viscous part of the isochoric free energy as well as for the viscous overstress which interestingly agree with the corresponding expressions obtained in the transient network theory of GREEN & TOBOLSKY [127], even though the

underlying micromechanical model differs. Finally, the model is evaluated based on its application in homogeneous and non-homogeneous tests where the numerical results are compared with in the literature available experimental data sets. In those simulations, the non-affine network model of MIEHE ET AL. [244] is chosen for the representation of the elastic response. The obtained results are satisfactory when taken into account the simplicity of the obtained viscous response in the proposed transient network model.

Modifications of the micromechanically motivated model in the sense that it results in more advanced evolution laws for the polymer stretch probability may be achieved by differently accounting for translational and rotational degrees of freedom on the microscopic level. It is furthermore desired to develop a microscopic model which yields a physical based discrete relaxation spectra. These are possible directions for future research in this area.

7.3 Modeling the electronic structure of solids at the microscopic scale

In Part III of this work a numerical procedure for the solution of the Kohn-Sham equations based on finite element basis functions is provided, thereby making use of the hierarchy of the involved bases in modeling the electron density ρ and the introduction of a staggered solution procedure, especially in the form of a p -refinement, which was examined for the first time in the context of Kohn-Sham density functional theory. The focus is laid on all-electron calculations, since here the highest requirements upon the basis set are in place. An intensive numerical analysis is provided, where the different approximations involved in the numerical setting are pointed out and examined. For that reason, exemplary calculations are performed, mainly for the neon atom, and it is found, that with a correct treatment a numerical accuracy of $0.001 E_h$ per atom can be achieved. The approach of a neutralizing Gaussian density distribution in the Poisson equation turns out to be superior compared to the point charge approach, yielding better energy values on the same mesh. The interpolation of the electrostatic potential in the higher order basis also lead to better results, however the computational costs also rise in such scenario. The influence of the numerical quadrature, the domain size, the boundary conditions, and other parameters are shown to be controllable with a proper configuration of the numerical setting. In calculations on noble gases, the accuracies of standard chemical software packages could be reached, without the problem of linear dependence in the basis set. However the computational costs are relevantly higher due to the much higher amount of basis functions involved in the finite element approach and the generalized eigenvalue problem. Here the higher order finite elements revealed major advantages compared to the low order ones for tetrahedral finite elements, where similar results as for mainly hexahedral elements in MOTAMARRI ET AL. [254] could be recovered. The universality of the finite element basis was demonstrated in the calculation of the polarized carbon monoxide molecule, where the dipole and binding energy could be well exerted. Especially the application of an external homogeneous field has not been examined in the finite element approach so far. In the subsequent application example of a single neon atom, it was possible to extract the static electric polarizability without the need of any additional changes in the finite element basis, as it is the case for Gaussian type orbitals based basis sets, demonstrating explicitly the generality and flexibility of the finite element basis.

In the future, a reduction of the computational costs is intended, which result mainly from the high amount of basis functions, required to represent the wave functions adequately and from the generalized eigenvalue problem, due to the non-orthogonality of the basis functions. The application of spectral finite elements [24, 25] essentially improves upon both issues and in a recent work [254], it has been shown to close the gap to the performance of the plane wave basis in the case of isolated systems. Another remarkable innovation comes from the partition of unity method [232, 340], where the enrichment of the basis with adequate additional functions with superior interpolation properties becomes possible. Also the inconvenient requirement to mesh the domain, which also has to be adapted, when the atoms are moved, might be released to some extent with this approach.

References

- [1] ABDOLLAHI, A.; ARIAS, I. [2011]: *Phase-field modeling of the coupled microstructure and fracture evolution in ferroelectric single crystals*. Acta Mater., 59(12): 4733–4746.
- [2] ALASTRUÉ, V.; MARTÍNEZ, M.; DOBLARÉ, M.; MENZEL, A. [2009]: *Anisotropic micro-sphere-based finite elasticity applied to blood vessel modelling*. J. Mech. Phys. Solids, 57:178–203.
- [3] AMBROSI, D.; ATESHIAN, G.; ARRUDA, E.; COWIN, S.; DUMAIS, J.; GORIELY, A.; HOLZAPFEL, G.; HUMPHREY, J.; KEMKEMER, R.; KUHL, E.; OLBERDING, J.; TABER, L.; GARIKIPATI, K. [2011]: *Perspectives on biological growth and remodeling*. J. Mech. Phys. Solids, 59(4):863–883.
- [4] ARGYRIS, J. [1954]: *Energy theorems and structural analysis. Part I. General Theory*. Aircr. Eng., 26:347–394.
- [5] ARIAS, I.; SEREBRINSKY, S.; ORTIZ, M. [2006]: *A phenomenological cohesive model of ferroelectric fatigue*. Acta Mater., 54:975–984.
- [6] ARMERO, F. [1997]: *Formulation and numerical analysis of an anisotropic damage model with a localized dissipative mechanism*. Technical Report SEMM/UCB 97/11, Department of Civil and Environmental Engineering, University of California, Berkeley.
- [7] ARMERO, F. [1999]: *Large-scale modeling of localized dissipative mechanisms in a local continuum: applications to the numerical simulation of strain localization in rate-dependent inelastic solids*. Mech. Cohes. Frict. Mater., 4:101–131.
- [8] ARMERO, F. [2001]: *On the characterization of localized solutions in inelastic solids: an analysis of wave propagation in a softening bar*. Comput. Methods Appl. Mech. Eng., 191:181–213.
- [9] ARMERO, F. [2012]: *Strong discontinuities in antiplane/torsional problems of computational failure mechanics*. Int. J. Fract. Mech., 178:3–32.
- [10] ARMERO, F.; EHRLICH, D. [2006]: *Finite element methods for the multi-scale modeling of softening hinge lines in plates at failure*. Comput. Methods Appl. Mech. Eng., 195:1283–1324.
- [11] ARMERO, F.; GARIKIPATI, K. [1995]: *Recent advances in the analysis and numerical simulation of strain localization in inelastic solids*. In *Proceedings of the 4th Computational Plasticity Conference, Barcelona*, pp. 1–15.
- [12] ARMERO, F.; GARIKIPATI, K. [1996]: *An analysis of strong discontinuities in multiplicative finite strain plasticity and their relation with the numerical simulation of strain localization in solids*. Int. J. Solids Struct., 33:2863–2885.
- [13] ARMERO, F.; KIM, J. [2012]: *Three-dimensional finite elements with embedded strong discontinuities to model material failure in the infinitesimal range*. Int. J. Numer. Methods Engrg., 91:1291–1330.
- [14] ARMERO, F.; LINDER, C. [2007]: *Recent developments in the formulation of finite elements with embedded strong discontinuities*. IUTAM Symposium on Discretization Methods for Evolving Discontinuities, pp. 105–122.
- [15] ARMERO, F.; LINDER, C. [2008]: *New finite elements with embedded strong discontinuities in the finite deformation range*. Comput. Methods Appl. Mech. Eng., 197:3138–3170.
- [16] ARMERO, F.; LINDER, C. [2009]: *Numerical simulation of dynamic fracture using finite elements with embedded discontinuities*. Int. J. Fract. Mech., 160:119–141.

- [17] ARRUDA, E.; BOYCE, M. [1993]: *A three-dimensional constitutive model for the large stretch behavior of rubber elastic materials*. J. Mech. Phys. Solids, 41:389–412.
- [18] ARRUDA, E.; BOYCE, M. [1993]: *Evolution of plastic anisotropy in amorphous polymers during finite straining*. Int. J. Plast., 9:697–720.
- [19] BAESU, E. [2003]: *On electroacoustic energy flux*. Z. angew. Math. Phys., 54: 1001–1009.
- [20] BARENBLATT, G. [1962]: *The mathematical theory of equilibrium cracks in brittle fracture*. Advances in Applied Mechanics, 7:55–129.
- [21] BARNETT, D. M.; LOTHE, J. [1975]: *Dislocations and line charges in anisotropic piezoelectric insulators*. Physica Status Solidi (B), 67(1):105–111.
- [22] BASTIAN, P.; BLATT, M. [2008]: *On the generic parallelisation of iterative solvers for the finite element method*. Int. J. Comput. Sci. Eng., 4:56–69.
- [23] BASTIAN, P.; BLATT, M.; DEDNER, A.; ENGWER, C.; KLÖFKORN, R.; OHLBERGER, M.; SANDER, O. [2008]: *A generic grid interface for parallel and adaptive scientific computing. Part I: Abstract framework*. Computing, (2-3):103–119.
- [24] BATCHO, P. F. [1998]: *Spectrally accurate numerical solution of the single-particle Schrödinger equation*. Phys. Rev. A, 57:4246–4252.
- [25] BATCHO, P. F. [2000]: *Computational method for general multicenter electronic structure calculations*. Phys. Rev. E, 61:7169–7183.
- [26] BAŽANT, Z. P.; OH, B. H. [1986]: *Efficient numerical integration on the surface of a sphere*. Z. Angew. Math. Mech., 66:37–49.
- [27] BAŽANT, Z. [1984]: *Continuum model for strain softening*. Journal of Engineering and Mechanics, ASCE, 110(12):1666–1691.
- [28] BAŽANT, Z.; OH, B. [1983]: *Crack band theory for fracture of concrete*. Materials and Structures, RILEM, 16:155–177.
- [29] BÉCHET, E.; SCHERZER, M.; KUNA, M. [2009]: *Application of the X-FEM to the fracture of piezoelectric materials*. Int. J. Numer. Methods Engrg., 77:1535–1565.
- [30] BECK, T. L. [2000]: *Real-space mesh techniques in density-functional theory*. Rev. Mod. Phys., 72:1041–1080.
- [31] BELYTSCHKO, T.; BLACK, T. [1999]: *Elastic crack growth in finite elements with minimal remeshing*. Int. J. Numer. Methods Engrg., 45:601–620.
- [32] BELYTSCHKO, T.; CHEN, H.; XU, J.; ZI, G. [2003]: *Dynamic crack propagation based on loss of hyperbolicity and a new discontinuous enrichment*. Int. J. Numer. Methods Engrg., 58:1873–1905.
- [33] BENJEDDOU, A. [2000]: *Advances in piezoelectric finite element modeling of adaptive structural elements: a survey*. Comput. Struct., 76:347–363.
- [34] BERGSTRÖM, J.; BOYCE, M. [1998]: *Constitutive modeling of the large strain time-dependent behavior of elastomers*. J. Mech. Phys. Solids, 46:931–954.
- [35] BERNSTEIN, B.; KEARSLEY, E.; ZAPAS, L. [1963]: *A study of stress relaxation with finite strain*. J. Rheol., 7:391–410.
- [36] BETTESS, P. [1977]: *Infinite elements*. Int. J. Numer. Methods Engrg., 11(1):53–64.
- [37] BIRD, R.; HASSAGER, O.; ARMSTRONG, R.; CURTISS, C. [1977]: *Dynamics of Polymeric Liquids, Kinetic Theory*. Wiley, New York.
- [38] BISCHOFF, J.; ARRUDA, E.; GROSH, K. [2002]: *Finite element modeling of human skin using an isotropic, nonlinear elastic constitutive model*. J. Biomech., 33:645–652.

- [39] BISCHOFF, J.; ARRUDA, E.; GROSH, K. [2002]: *Orthotropic hyperelasticity in terms of an arbitrary molecular chain model*. J. Appl. Mech., 69:570–579.
- [40] BLUNDELL, J.; TERENTJEV, E. [2007]: *Forces and extensions in semiflexible and rigid polymer chains and filaments*. J. Phys. A: Math. Theor. , 40:10951–10964.
- [41] BLUNDELL, J.; TERENTJEV, E. [2008]: *Affine model of stress stiffening in semiflexible filament networks*. ArXiv, 0808.4088:1–11.
- [42] BLUNDELL, J.; TERENTJEV, E. [2009]: *Stretching semiflexible filaments and their networks*. Macromolecules, 42:5388–5394.
- [43] BLUNDELL, J.; TERENTJEV, E. [2011]: *The influence of disorder on deformations in semiflexible networks*. Proc. R. Soc. A , 467:2330–2349.
- [44] BOAL, D. [2002]: *Mechanics of the cell*. Cambridge University Press.
- [45] BOCCA, P.; CARPINTERI, A.; VALENTE, S. [1990]: *Size effects in the mixed mode crack propagation: Softening and snap-back analysis*. Eng. Fract. Mech., 35:159–170.
- [46] BÖL, M.; REESE, S. [2005]: *Finite element modelling of rubber-like materials - a comparison between simulation and experiment*. J. Mater. Sci., 40:5933–5939.
- [47] BÖL, M.; REESE, S. [2006]: *Finite element modelling of rubber-like polymers based on chain statistics*. Int. J. Solids Struct., 43(1):2–26.
- [48] BÖL, M.; REESE, S.; PARKER, K.; KUHL, E. [2009]: *Computational modeling of muscular thin films for cardiac repair*. Comput. Mech., 43:535–544.
- [49] BOUCHARD, P.; BAY, F.; CHASTEL, Y.; TOVENA, I. [2000]: *Crack propagation modelling using an advanced remeshing technique*. Comput. Methods Appl. Mech. Eng., 189:723–742.
- [50] BOUCHARD, P.; BAY, F.; CHASTEL, Y. [2003]: *Numerical modelling of crack propagation: automatic remeshing and comparison of different criteria*. Comput. Methods Appl. Mech. Eng., 192:3887–3908.
- [51] BOURDIN, B.; FRANCFORT, G.; MARIGO, J.-J. [2000]: *Numerical experiments in revisited brittle fracture*. J. Mech. Phys. Solids, 48(4):797–826.
- [52] BOWLER, D. R.; MIYAZAKI, T.; GILLAN, M. J. [2002]: *Recent progress in linear scaling ab initio electronic structure techniques*. J. Phys. Condens. Matter, 14(11): 2781.
- [53] BOYCE, M.; ARRUDA, E. [2000]: *Constitutive models of rubber elasticity: A review*. Rubber Chem. Technol., 73:716–725.
- [54] BOYCE, M.; PARKS, D.; ARGON, A. [1988]: *Large inelastic deformation of glassy polymers. Part 1: Rate dependent constitutive model*. Mech. Materials, 7:15–33.
- [55] BOYCE, M.; PARKS, D.; ARGON, A. [1989]: *Plastic flow in oriented glassy polymers*. Int. J. Plast., 5:593–615.
- [56] BOYD, J. P. [2001]: *Chebyshev and Fourier Spectral Methods*. Dover books on mathematics. Dover Publications.
- [57] BRAESS, D. [2007]: *Finite elements*. Cambridge University Press.
- [58] BROKENSHIRE, D. [1996]: *A study of torsion fracture tests*. Ph.D. Thesis, Cardiff University.
- [59] CALLARI, C.; ARMERO, F. [2002]: *Finite element methods for the analysis of strong discontinuities in coupled poro-plastic media*. Comput. Methods Appl. Mech. Eng., 191:4371–4400.
- [60] CEPERLEY, D. M.; ALDER, B. J. [1980]: *Ground state of the electron gas by a stochastic method*. Phys. Rev. Lett., 45:566–569.
- [61] CHAPELLE, D.; BATHE, K. J. [1993]: *The inf-sup test*. Comput. Struct., 47:

- 537–545.
- [62] CHERNYAEV, E. [1995]: *Marching cubes 33: Construction of topologically correct isosurfaces*. Technical Report CN 95-17, Cern.
- [63] CLOUGH, R. [1960]: *The finite element method in plane stress analysis*.
- [64] COHEN-TANNOUJJI, C.; DIU, B.; LALOË, F. [1977]: *Quantum mechanics*. Quantum Mechanics. Wiley.
- [65] COLEMAN, B.; HODGON, M. [1985]: *On shear bands in ductile materials*. Archive for Rational Mechanics and Analysis, 90:219–247.
- [66] COLEMAN, B.; NOLL, W. [1961]: *Foundations of linear viscoelasticity*. Rev. Mod. Phys., 33:239–249.
- [67] CONTI, E.; MACKINTOSH, F. [2009]: *Cross-linked networks of stiff filaments exhibit negative normal stress*. Phys. Rev. Lett., 102:088102.
- [68] COTTEN, G.; BOONSTRA, B. [1965]: *Stress relaxation in rubbers containing reinforced fillers*. J. Appl. Polym. Sci., 9:3395–3408.
- [69] COURANT, R. [1943]: *Variational methods for the solution of problems of equilibrium and vibrations*. Bulletin of the American Mathematical Society, 49:1–43.
- [70] BORST, R. DE [1991]: *Simulation of strain localization: A reappraisal of the Cosserat continuum*. Engineering Computations, 8:317–332.
- [71] BORST, R. DE ; SLUYS, L. J. [1991]: *Localization in a Cosserat continuum under static and dynamic loading conditions*. Comput. Methods Appl. Mech. Eng., 90: 805–827.
- [72] DE GENNES, P. [1971]: *Reptation of a polymer chain in the presence of fixed obstacles*. J. Chem. Phys., 55:572–579.
- [73] DEAM, R.; EDWARDS, S. [1976]: *The theory of rubber elasticity*. Philos. Trans. R. Soc. London, Ser. A, 280:317–353.
- [74] DEEG, W. F. [1980]: *The analysis of dislocation, crack and inclusion problems in piezoelectric solids*. Ph.D. Thesis, Stanford University.
- [75] DOI, M.; EDWARDS, S. [1986]: *The Theory of Polymer Dynamics*. Clarendon Press, Oxford.
- [76] DRIESSEN, N.; BOUTEN, C.; BAAIJENS, F. [2005]: *A structural constitutive model for collagenous cardiovascular tissues incorporating the angular fiber distribution*. J. Biomech. Eng., 127:494–503.
- [77] DUFFY, M. G. [1982]: *Quadrature over a pyramid or cube of integrands with a singularity at a vertex*. SIAM J. Numer. Anal., 19(6):1260–1262.
- [78] DUGDALE, D. S. [1960]: *Yielding of steel sheets containing slits*. J. Mech. Phys. Solids, 8(2):100–104.
- [79] DUMSTORFF, P.; MESCHKE, G. [2007]: *Crack propagation criteria in the framework of X-FEM-based structural analyses*. Int. J. Numer. Anal. Methods Geomech., 31:239–259.
- [80] DVORKIN, E. N.; CUITIÑO, A. M.; GIOIA, G. [1990]: *Finite elements with displacement interpolated embedded localization lines insensitive to mesh size and distortions*. Int. J. Numer. Methods Engrg., 30:541–564.
- [81] EDWARDS, S. [1967]: *The statistical mechanics of polymerized materials*. Proc. Phys. Soc., 92:9–16.
- [82] EDWARDS, S.; VILGIS, T. [1988]: *The tube model theory of rubber elasticity*. Rep. Prog. Phys., 51:243–297.
- [83] EHLERS, W.; VOLK, W. [1997]: *On shear band localization phenomena of liquid-*

- saturated granular elastoplastic porous solid materials accounting for fluid viscosity and micropolar solid rotations.* Mech. Cohes. Frict. Mater., 2:301–320.
- [84] EHLERS, W.; VOLK, W. [1998]: *On theoretical and numerical methods in the theory of porous media based on polar and non-polar elasto-plastic solid materials.* Int. J. Solids Struct., 35:4597–4617.
- [85] EHLERS, W.; MARKERT, B.; RÖHRLE, O. [2009]: *Computational continuum biomechanics with application to swelling media and growth phenomena.* GAMM-Mitteilungen, 32(2):135–156.
- [86] EHRLICH, D.; ARMERO, F. [2005]: *Finite element methods for the analysis of softening plastic hinges in beams and frames.* Comput. Mech., 35:237–264.
- [87] ERINGEN, A. C. [1999]: *Microcontinuum Field Theories, Vol. I: Foundations and Solids.* Springer, New York.
- [88] ERINGEN, A. C. [2001]: *Microcontinuum Field Theories, Vol. II: Fluent Media.* Springer, New York.
- [89] ERINGEN, A. [1972]: *Nonlocal polar elastic continua.* Int. J. Eng. Sci., 10:1–16.
- [90] ERINGEN, A. [1981]: *On non-local plasticity.* Int. J. Eng. Sci., 19:1461–1474.
- [91] ERMAN, B.; FLORY, P. [1978]: *Theory of elasticity of polymer networks. II. The effect of geometric constraints on junctions.* J. Chem. Phys., 68:5363–5369.
- [92] ESHELBY, J. [1951]: *The force on an elastic singularity.* Philosophical Transactions of the Royal Society of London, Series A, 244:87–112.
- [93] ESHELBY, J. [1956]: *The continuum theory of lattice defects.* Vol. 3, pp. 79–144. Academic Press Inc., New York.
- [94] FAN, C. Y.; ZHAO, M. H.; ZHOU, Y. H. [2009]: *Numerical solution of polarization saturation/dielectric breakdown model in 2D finite piezoelectric media.* J. Mech. Phys. Solids, 57(9):1527–1544.
- [95] FANG, J.; GAO, X.; ZHOU, A. [2012]: *A Kohn-Sham equation solver based on hexahedral finite elements.* J. Comput. Phys., 231(8):3166–3180.
- [96] FEIST, C.; HOFSTETTER, G. [2007]: *Three-dimensional fracture simulations based on the SDA.* Int. J. Numer. Anal. Methods Geomech., 31:189–212.
- [97] FERRY, J. [1980]: *Viscoelastic properties of polymers.* John Wiley & Sons, Inc.
- [98] FINEBERG, J.; GROSS, S.-P.; MARDER, M.; SWINNEY, H.-L. [1991]: *Instability in dynamic fracture.* Phys. Rev. Lett., 67:4.
- [99] FINEBERG, J.; GROSS, S.-P.; MARDER, M.; SWINNEY, H.-L. [1992]: *Instability in the propagation of fast cracks.* Phys. Rev., 45:5146–5154.
- [100] FLORY, P. J. [1953]: *Principles of Polymer Chemistry.* Cornell University Press.
- [101] FLORY, P. J. [1985]: *Network topology and the theory of rubber elasticity.* Br. Polym. J., 17(2):96–102.
- [102] FLORY, P. J.; REHNER JR., J. [1943]: *Statistical mechanics of cross-linked polymer networks: I. Rubberlike elasticity.* J. Chem. Phys., 11(11):512–520.
- [103] FLORY, P. [1944]: *Network structure and the elastic properties of vulcanized rubber.* Chem. Rev., 35:51–75.
- [104] FLORY, P. [1953]: *Principles of Polymer Chemistry.* Principles of Polymer Chemistry.
- [105] FLORY, P. [1977]: *Theory of elasticity of polymer networks. The effect of local constraints on junctions.* J. Chem. Phys., 66:5720–5729.
- [106] FLORY, P. [1988]: *Statistical mechanics of chain molecules.* Hanser Publishers.
- [107] FLORY, P. [1989]: *Statistical Mechanics of Chain Molecules.* Statistical Mechanics

- of Chain Molecules.
- [108] FLORY, P.; ERMAN, B. [1982]: *Theory of elasticity of polymer networks. 3*. Macromolecules, 15:800–806.
 - [109] FLORY, P.; GORDON, M.; MCCRUM, N. [1976]: *Statistical thermodynamics of random networks*. Proc. R. Soc. London, Ser. A, 351:351–380.
 - [110] FOREST, S.; SIEVERT, R. [2006]: *Nonlinear microstrain theories*. Int. J. Solids Struct., 43:7224–7245.
 - [111] FRANCFORT, G.; MARIGO, J.-J. [1998]: *Revisiting brittle fracture as an energy minimization problem*. J. Mech. Phys. Solids, 46(8):1319–1342.
 - [112] FRIES, T.; BAYDOUN, M. [2011]: *Crack propagation with the extended finite element method and a hybrid explicit, implicit crack description*. Int. J. Numer. Methods Engrg..
 - [113] FU, R.; ZHANG, T. Y. [2000]: *Effects of an electric field on the fracture toughness of poled lead zirconate titanate ceramics*. J. Am. Ceram. Soc., 83:1215–1218.
 - [114] FULTON, C.; GAO, H. [2001]: *Microstructural modeling of ferroelectric fracture*. Acta Mater., 49:2039–2054.
 - [115] GAO, H.; BARNETT, D. M. [1996]: *An invariance property of local energy release rate in a strip saturation model of piezoelectric fracture*. Int. J. Fract. Mech., 79(2): R25–R29.
 - [116] GAO, H.; ZHANG, T.; TONG, P. [1997]: *Local and global energy release rates for an electrically yielded crack in a piezoelectric ceramic*. J. Mech. Phys. Solids, 45: 491–510.
 - [117] GARCÍA-CERVERA, C. J.; LU, J.; XUAN, Y.; E, W. [2009]: *Linear-scaling subspace-iteration algorithm with optimally localized nonorthogonal wave functions for Kohn-Sham density functional theory*. Phys. Rev. B, 79:115110.
 - [118] GARIKIPATI, K.; ARRUDA, E.; GROSH, K.; NARAYANAN, H.; CALVE, S. [2004]: *A continuum treatment of growth in biological tissue: the coupling of mass transport and mechanics*. J. Mech. Phys. Solids, 52:1595–1625.
 - [119] GASSER, T.; HOLZAPFEL, G. [2006]: *3D Crack propagation in unreinforced concrete. A two-step algorithm for tracking 3D crack paths*. Comput. Methods Appl. Mech. Eng., 195:5198–5219.
 - [120] GASSER, T.; OGDEN, R.; HOLZAPFEL, G. [2006]: *Hyperelastic modelling of arterial layers with distributed collagen fibre orientations*. J. R. Soc. Interface, 3:15–35.
 - [121] GAVINI, V.; KNAP, J.; BHATTACHARYA, K.; ORTIZ, M. [2007]: *Non-periodic finite-element formulation of orbital-free density functional theory*. J. Mech. Phys. Solids, 55:669–696.
 - [122] GIBSON, L.; ASHBY, M.; HARLEY, B. [2010]: *Cellular Materials in Nature and Medicine*. Cambridge University Press.
 - [123] GLATTING, G.; WINKLER, R. G.; REINEKER, P. [1994]: *Analytical model for the microscopic nonaffine deformation of polymer networks*. J. Chem. Phys., 101(3): 2532–2538.
 - [124] GOEDECKER, S. [1999]: *Linear scaling electronic structure methods*. Rev. Mod. Phys., 71:1085–1123.
 - [125] GÖKTEPE, S.; MIEHE, C. [2008]: *Efficient two-scale modeling of finite rubber viscoelasticity*. Technische Mechanik, 28:22–32.
 - [126] GOVINDJEE, S.; REESE, S. [1997]: *A presentation and comparison of two large deformation viscoelasticity models*. J. Eng. Mater. Technol., 119:251–255.

- [127] GREEN, M.; TOBOLSKY, A. [1946]: *A new approach to the theory of relaxing polymeric media*. J. Chem. Phys., 14:80–92.
- [128] GRIFFITH, A. [1921]: *The phenomena of rupture and flow in solids*. Philosophical Transactions of the Royal Society of London, Series A, 221:163–198.
- [129] GRIFFITH, A. [1924]: *The theory of rupture*. pp. 55–63. Proceedings of the First International Congress of Applied Mechanics.
- [130] GROSCH, C. E.; ORSZAG, S. A. [1977]: *Numerical solution of problems in unbounded regions: Coordinate transforms*. J. Comput. Phys., 25(3):273–295.
- [131] GUNNARSSON, O.; HARRIS, J.; JONES, R. O. [1977]: *Density functional theory and molecular bonding. I. First-row diatomic molecules*. J. Chem. Phys., 67(9): 3970–3979.
- [132] GÜRSES, E.; MIEHE, C. [2009]: *A computational framework of three-dimensional configurational-force-driven brittle crack propagation*. Comput. Methods Appl. Mech. Eng., 198:1413–1428.
- [133] GURTIN, M. [1999]: *Configurational Forces as Basic Concepts of Continuum Mechanics*. Springer-Verlag, New York.
- [134] GUTH, E.; MARK, H. [1934]: *Zur innermolekularen Statistik, insbesondere bei Kettenmolekülen I*. Monatshefte für Chemie, 65:93–121.
- [135] HA, B.; THIRUMALAI, D. [1997]: *Semiflexible chains under tension*. J. Chem. Phys., 106:4243–4247.
- [136] HANSBO, A.; HANSBO, P. [2004]: *A finite element method for the simulation of strong and weak discontinuities in solid mechanics*. Comput. Methods Appl. Mech. Eng., 193:3523–3540.
- [137] HAO, T.; GONG, X.; SUO, Z. [1996]: *Fracture mechanics for the design of ceramic multilayer actuators*. J. Mech. Phys. Solids, 44(1):23–48.
- [138] HAO, T. H.; SHEN, Z. Y. [1994]: *A new electric boundary condition of electric fracture mechanics and its application*. Eng. Fract. Mech., 47:793–802.
- [139] HEAD, D.; LEVINE, A.; MACKINTOSH, F. [2003]: *Distinct regimes of elastic response and deformation modes of cross-linked cytoskeletal and semiflexible polymer networks*. Phys. Rev. E, 68:061907(15).
- [140] HEAD, D.; LEVINE, A.; MACKINTOSH, F. [2003]: *Deformation of cross-linked semiflexible polymer networks*. Phys. Rev. Lett., 91:108102(4).
- [141] HEAD, D.; LEVINE, A.; MACKINTOSH, F. [2003]: *Distinct regimes of elastic response and deformation modes of cross-linked cytoskeletal and semiflexible polymer networks*. Phys. Rev. E, 68:061907(15).
- [142] HEARLE, J.; THWAITES, J.; AMIRBAYAT, J. [1980]: *Mechanics of flexible fibre assemblies*. NATO advanced study institutes series: Applied sciences. Sijthoff & Noordhoff.
- [143] HEINRICH, G.; KALISKE, M. [1997]: *Theoretical and numerical formulation of a molecular based constitutive tube-model of rubber elasticity*. Comput. Theor. Polym. Sci., 7(3-4):227–241.
- [144] HEINRICH, G.; STRAUBE, E. [1983]: *On the strength and deformation dependence of the tube-like topological constraints of polymer networks, melts and concentrated solutions, I. The polymer network case*. Acta Polym., 34(9):589–594.
- [145] HEINRICH, G.; STRAUBE, E. [1984]: *On the strength and deformation dependence of the tube-like topological constraints of polymer networks, melts and concentrated solutions, II. Polymer melts and concentrated solutions*. Acta Polym., 35:115–119.

- [146] HERMANSSON, B.; YEVICK, D. [1986]: *Finite-element approach to band-structure analysis*. Phys. Rev. B, 33:7241–7242.
- [147] HEUSSINGER, C.; SCHAEFER, B.; FREY, E. [2007]: *Nonaffine rubber elasticity for stiff polymer networks*. Phys. Rev. E, 76:031906(12).
- [148] HIMPEL, G.; KUHL, E.; MENZEL, A.; STEINMANN, P. [2005]: *Computational modelling of isotropic multiplicative growth*. Comput. Model. Eng. Sci, 8(2):119–134.
- [149] HOHENBERG, P.; KOHN, W. [1964]: *Inhomogeneous Electron Gas*. Phys. Rev. B, 136:864.
- [150] HOLZAPFEL, G.; OGDEN, R. [2006]: *Mechanics of biological tissue*. Springer.
- [151] HOLZAPFEL, G.; SIMO, J. [1996]: *A new viscoelastic constitutive model for continuous media at finite thermomechanical changes*. Int. J. Solids Struct., 33:3019–3034.
- [152] HUBER, J. E. [2005]: *Micromechanical modelling of ferroelectrics*. Curr. Opin. Solid State Mater. Sci., 9:100–106.
- [153] HUESPE, A. E.; OLIVER, J.; SANCHEZ, P. J.; BLANCO, S.; SONZOGNI, V. [2006]: *Strong discontinuity approach in dynamic fracture simulations*. In *Mecánica Computacional XXV*, pp. 1997–2018.
- [154] HUESPE, A.; OLIVER, J.; SANCHEZ, P.; BLANCO, S.; SONZOGNI, V. [2006]: *Strong discontinuity approach in dynamic fracture simulations*. *Mecánica Computacional*, XXV:1997–2018.
- [155] HUGHES, T. J. R. [2000]: *The Finite Element Method*. Dover Publications.
- [156] HUISMAN, E.; LUBENSKY, T. [2011]: *Internal stresses, normal modes, and nonaffinity in three-dimensional biopolymer networks*. Phys. Rev. Lett., 106(8):088301(4).
- [157] HUISMAN, E.; DILLEN, T. VAN ; ONCK, P.; VAN DER GIESSEN, E. [2007]: *Three-dimensional cross-linked F-actin networks: Relation between network architecture and mechanical behavior*. Phys. Rev. Lett., 99:208103(4).
- [158] HUISMAN, E.; STORM, C.; BARKEMA, G. [2008]: *Monte Carlo study of multiply crosslinked semiflexible polymer networks*. Phys. Rev. E, 78:051801(11).
- [159] HUND, A.; RAMM, E. [2007]: *Locality constraints within multiscale model for nonlinear material behaviour*. Int. J. Numer. Methods Engrg., 70:1613–1632.
- [160] IRWIN, G. R. [1957]: *Analysis of stresses and strains near the end of a crack traversing a plate*. J. Appl. Mech., 24:361–364.
- [161] IRWIN, G. [1948]: *Fracture dynamics*. pp. 147–166. American Soc. for Metals.
- [162] JAFFE, B.; COOK, W.; JAFFE, H. [1971]: *Piezoelectric Ceramics*. Academic Press, New York.
- [163] JÄGER, P.; STEINMANN, P.; KUHL, E. [2008]: *Modeling three-dimensional crack propagation comparison of crack path tracking strategies*. Int. J. Numer. Methods Engrg., 76:1328–1352.
- [164] JAMES, A.; GREEN, A. [1975]: *Strain energy functions of rubber. II. The characterization of filled vulcanizates*. J. Appl. Polym. Sci., 19:2319–2330.
- [165] JAMES, A.; GREEN, A.; SIMPSON, G. [1975]: *Strain energy functions of rubber. I. Characterization of gum vulcanizates*. J. Appl. Polym. Sci., 19:2033–2058.
- [166] JAMES, H.; GUTH, E. [1943]: *Theory of elastic properties of rubber*. J. Chem. Phys., 11:455–481.
- [167] JAMES, H.; GUTH, E. [1947]: *Theory of the increase in rigidity of rubber during cure*. J. Chem. Phys., 15(9):669–683.

- [168] JANMEY, P.; MCCORMICK, M.; RAMMENSEE, S.; LEIGHT, J.; GEORGES, P.; MACKINTOSH, F. [2007]: *Negative normal stress in semiflexible biopolymer gels*. Nat. Mater., 6(1):48–51.
- [169] JEFFERSON, A.; BARR, B.; BENNETT, T.; HEE, S. [2004]: *Three dimensional finite element simulations of fracture tests using the Craft concrete model*. Computers and Concrete, 1:261–284.
- [170] JONA, F.; SHIRANE, G. [1993]: *Ferroelectric crystals*, Vol. 1. Dover Publications.
- [171] KALISKE, M.; HEINRICH, G. [1999]: *An extended tube-model for rubber elasticity: statistical-mechanical theory and finite element implementation*. Rubber Chem. Technol., 72:602–632.
- [172] KALISKE, M.; ROTHERT, H. [1997]: *Formulation and implementation of three-dimensional viscoelasticity at small and finite strains*. Comput. Mech., 19:228–239.
- [173] KAMLAH, M. [2001]: *Ferroelectric and ferroelastic piezoceramics - modeling of electromechanical hysteresis phenomena*. Continuum Mech. Thermodyn., 13:219–268.
- [174] KARAJAN, N.; RÖHRLE, O.; EHLERS, W.; SCHMITT, S. [2012]: *Linking continuous and discrete intervertebral disc models through homogenisation*. Biomech. Model. Mechanobiol., pp. 1–14.
- [175] KELLOMÄKI, M.; ASTRÖM, J.; TIMONEN, J. [1996]: *Rigidity and dynamics of random spring networks*. Phys. Rev. Lett., 77:2730–2733.
- [176] KIENZLER, R.; HERRMANN, G. [2000]: *Mechanics in Material Space*. Springer-Verlag, New York.
- [177] KLEINMAN, L.; BYLANDER, D. M. [1982]: *Efficacious form for model pseudopotentials*. Phys. Rev. Lett., 48:1425–1428.
- [178] KOBAYASHI, A.-S.; RAMULU, M. [1981]: *Dynamic stress-intensity factors for unsymmetric dynamic isochromatics*. Exper. Mech., 21:41–48.
- [179] KOBAYASHI, A.-S.; WADE, B.-G.; BRADLEY, W.-B.; CHIU, S.-T. [1974]: *Crack branching in homalite-100 sheets*. Eng. Fract. Mech., 6:81–92.
- [180] KOCH, W.; HOLTHAUSEN, M. [2000]: *A Chemists's Guide to Density Functional Theory*. WILEY-VCH.
- [181] KOHN, W.; SHAM, L. [1965]: *Self-consistent equations including exchange and correlation effects*. Phys. Rev. A, 140:1133.
- [182] KRATKY, O.; POROD, G. [1949]: *Röntgenuntersuchung gelöster Fadenmoleküle*. Recl. Trav. Chim. Pays-Bas, 68(12):1106–1122.
- [183] KROON, M. [2010]: *A constitutive model for strain-crystallising rubber-like materials*. Mech. Mater., 42(9):873–885.
- [184] KUHL, E.; MENZEL, A.; STEINMANN, P. [2003]: *Computational modeling of growth*. Comput. Mech., 32:71–88.
- [185] KUHL, E.; GARIKIPATI, K.; ARRUDA, E.; GROSH, K. [2005]: *Remodeling of biological tissue: Mechanically induced reorientation of a transversely isotropic chain network*. J. Mech. Phys. Solids, 53(7):1552–1573.
- [186] KUHL, E.; MENZEL, A.; GARIKIPATI, K. [2006]: *On the convexity of transversely isotropic chain network models*. Philos. Mag., 86(21-22):3241–3258.
- [187] KUHL, E.; MAAS, R.; HIMPEL, G.; MENZEL, A. [2007]: *Computational modeling of arterial wall growth*. Biomech. Model. Mechanobiol., 6(5):321–331.
- [188] KUHN, W. [1934]: *Über die Gestalt fadenförmiger Moleküle in Lösungen*. Colloid. Polym. Sci., 68(1):2–15.
- [189] KUHN, W. [1936]: *Beziehungen zwischen Molekülgröße, statistischer Molekülgestalt*

- und elastischen Eigenschaften hochpolymerer Stoffe. *Colloid. Polym. Sci.*, 76:258–271.
- [190] KUHN, W.; GRÜN, F. [1942]: *Beziehungen zwischen elastischen Konstanten und Dehnungsdoppelbrechung hochelastischer Stoffe*. *Colloid. Polym. Sci.*, 101(3):248–271.
- [191] KUNA, M. [2006]: *Finite element analyses of cracks in piezoelectric structures: A survey*. *Arch. Appl. Mech.*, 76:725–745.
- [192] KUNA, M. [2010]: *Fracture mechanics of piezoelectric materials – where are we right now?* *Eng. Fract. Mech.*, 77:309–326.
- [193] LANDAU, L. D.; LIFSHITZ, E. M. [1975]: *The classical theory of fields*, Vol. 2 of *Course of theoretical physics*. Pergamon Press, Oxford.
- [194] LANDIS, C. M. [2002]: *Fully coupled, multi-axial, symmetric constitutive laws for polycrystalline ferroelectric ceramics*. *J. Mech. Phys. Solids*, 50(1):127–152.
- [195] LANDIS, C. M. [2004]: *Energetically consistent boundary conditions for electromechanical fracture*. *Int. J. Solids Struct.*, 4:6291–6315.
- [196] LANDIS, M. C. [2004]: *Non-linear constitutive modeling of ferroelectrics*. *Curr. Opin. Solid State Mater. Sci.*, 8:59–69.
- [197] LEE, E. [1969]: *Elastic-plastic deformation at finite strains*. *J. Appl. Mech.*, 36:1–6.
- [198] LEHOUCQ, L.; MASCHOFF, K.; SORENSEN, D.; YANG, C. [1997]: *ARPACK*. <http://www.caam.rice.edu/software/ARPACK/>.
- [199] LEHOUCQ, L.; MASCHOFF, K.; SORENSEN, D.; YANG, C. [1997]: *PARPACK*. http://www.caam.rice.edu/~kristyn/parpack_home.html.
- [200] LEHTOVAARA, L.; HAVU, V.; PUSKA, M. [2009]: *All-electron density functional theory and time-dependent density functional theory with high-order finite elements*. *J. Chem. Phys.*, 131(5):054103.
- [201] LI, S.; LINDER, C.; FOULK III, J. [2007]: *On configurational compatibility and multiscale energy momentum tensors*. *J. Mech. Phys. Solids*, 55(5):980–1000.
- [202] LI, W.; MCMEEKING, R. M.; LANDIS, C. [2008]: *On the crack face boundary conditions in electromechanical fracture and an experimental protocol for determining energy release rates*. *Eur. J. Mech. A. Solids*, 27:285–301.
- [203] LINDER, C. [2007]: *New finite elements with embedded strong discontinuities for the modeling of failure in solids*. Ph.D. Thesis, University of California, Berkeley.
- [204] LINDER, C. [2012]: *An analysis of the exponential electric displacement saturation model in fracturing piezoelectric ceramics*. *Technische Mechanik*, 32:53–69.
- [205] LINDER, C.; ARMERO, F. [2007]: *Finite elements with embedded strong discontinuities for the modeling of failure in solids*. *Int. J. Numer. Methods Engrg.*, 72:1391–1433.
- [206] LINDER, C.; ARMERO, F. [2009]: *Finite elements with embedded branching*. *Finite Elem. Anal. Des.*, 45:280–293.
- [207] LINDER, C.; MIEHE, C. [2012]: *Effect of electric displacement saturation on the hysteretic behavior of ferroelectric ceramics and the initiation and propagation of cracks in piezoelectric ceramics*. *J. Mech. Phys. Solids*, 60:882–903.
- [208] LINDER, C.; RAINA, A. [2013]: *A strong discontinuity approach on multiple levels to model solids at failure*. *Comput. Methods Appl. Mech. Eng.*, 253:558–583.
- [209] LINDER, C.; ZHANG, X. [2013]: *A marching cubes based failure surface propagation concept for 3d finite elements with non-planar embedded strong discontinuities of*

- higher order kinematics*. Int. J. Numer. Methods Engrg.. submitted for publication.
- [210] LINDER, C.; ROSATO, D.; MIEHE, C. [2011]: *New finite elements with embedded strong discontinuities for the modeling of failure in electromechanical coupled solids*. Comput. Methods Appl. Mech. Eng., 200:141–161.
- [211] LINDER, C.; TKACHUK, M.; MIEHE, C. [2011]: *A micromechanically motivated diffusion-based transient network model and its incorporation into finite rubber viscoelasticity*. J. Mech. Phys. Solids, 59:2134–2156.
- [212] LINES, M. E.; GLASS, A. M. [1977]: *Principles and applications of ferroelectrics and related materials*. Clarendon Press, London.
- [213] LION, A. [1996]: *A constitutive model for carbon black filled rubber. Experimental investigations and mathematical representations*. Continuum. Mech. Thermodyn., 8:153–169.
- [214] LIU, R. F.; NAM, B. G.; WATANABE, K. [2008]: *Discontinuous crack model for piezoelectric materials and its application to CED evaluation*. Eng. Fract. Mech., 75:1981–2001.
- [215] LODGE, A. [1956]: *A network theory of flow birefringence and stress in concentrated polymer solutions*. Trans. Faraday Soc., 52:120–130.
- [216] LODISH, H. [2000]: *Molecular Cell Biology*. W. H. Freeman & Company.
- [217] LORENSEN, W.; CLINE, H. [1987]: *Marching cubes: A high resolution 3d surface construction algorithm*. SIGGRAPH Comput. Graph., 21:163–169.
- [218] LORENTZ, E.; ANDRIEUX, S. [1999]: *A variational formulation for nonlocal damage models*. Int. J. Plast., 15:119–138.
- [219] LOWNEY, J. R.; KAHN, A. H.; BLUE, J. L.; WILSON, C. L. [1981]: *Disappearance of impurity levels in silicon and germanium due to screening*. J. Appl. Phys., 52(6):4075–4080.
- [220] LUBLINER, J. [1985]: *A model of rubber viscoelasticity*. Mech. Res. Commun., 12: 93–99.
- [221] LYNCH, C. S.; YANG, W.; COLLIER, L.; SUO, Z.; MCMEEKING, R. M. [1995]: *Electric field induced cracking in ferroelectric ceramics*. Ferroelectrics, 166(1):11–30.
- [222] M. OTTO AND J. ECKERT AND T. VILGIS [1994]: *Persistence lengths of semiflexible chains - methods and approximations*. Macromol. Theory Simul. , 3:543–555.
- [223] MACKINTOSH, F.; KÄS, J.; JANMEY, P. [1995]: *Elasticity of semiflexible biopolymer networks*. Phys. Rev. Lett., 75.
- [224] MARCKMANN, G.; VERRON, E. [2006]: *Comparison of hyperelastic models for rubber-like materials*. Rubber Chem. Technol., 79:835–858.
- [225] MARKO, J.; SIGGIA, E. [1995]: *Stretching DNA*. Macromolecules, 28(26):8759–8770.
- [226] MARSDEN, J.; HUGHES, T. [1983]: *Mathematical foundations of elasticity*. Dover Publications, New York.
- [227] MARTIN, R. M. [2004]: *Electronic Structure*. Cambridge University Press.
- [228] MAUGIN, G. [1993]: *Material inhomogeneities in elasticity*. Chapman & Hall, London.
- [229] MCMEEKING, R. M. [2001]: *Towards a fracture mechanics for brittle piezoelectric and dielectric materials*. Int. J. Fract. Mech., 108:25–41.
- [230] MCMEEKING, R. M. [2004]: *The energy release rate for a Griffith crack in a piezoelectric material*. Eng. Fract. Mech., 71:1149–1163.
- [231] MCMEEKING, R. M.; LANDIS, C. M. [2002]: *A phenomenological multi-axial*

- constitutive law for switching in polycrystalline ferroelectric ceramics.* Int. J. Eng. Sci., 40(14):1553–1577.
- [232] MELENK, J.; BABUŠKA, I. [1996]: *The partition of unity finite element method: Basic theory and applications.* Comput. Methods Appl. Mech. Eng., 139(1-4):289–314.
- [233] MENZEL, A.; WAFFENSCHMIDT, T. [2009]: *A microsphere-based remodelling formulation for anisotropic biological tissues.* Philos. Trans. R. Soc. London, Ser. A, 367(1902):3499–3523.
- [234] MENZEL, A.; KUHL, E. [2012]: *Frontiers in growth and remodeling.* Mech. Res. Commun., 42:1–14.
- [235] MERGHEIM, J.; KUHL, E.; STEINMANN, P. [2005]: *A finite element method for the computational modelling of cohesive cracks.* Int. J. Numer. Methods Engrg., 63(2):276–289.
- [236] MERGHEIM, J.; STEINMANN, P. [2006]: *A geometrically nonlinear FE approach for the simulation of strong and weak discontinuities.* Comput. Methods Appl. Mech. Eng., 195:5037–5052.
- [237] MEYER, K.; SUSICH, G. VON ; VALKÓ [1932]: *Die elastischen Eigenschaften der organischen Hochpolymeren und ihre kinetische Deutung.* Colloid. Polym. Sci., 59: 208–216.
- [238] MIEHE, C. [1998]: *A constitutive frame of elastoplasticity at large strains based on the notion of a plastic metric.* Int. J. Solids Struct., 35:3859–3897.
- [239] MIEHE, C.; GÖKTEPE, S. [2005]: *A micro-macro approach to rubber-like materials. Part II: The micro-sphere model of finite rubber viscoelasticity.* J. Mech. Phys. Solids, 53:2231–2258.
- [240] MIEHE, C.; GÜRSES, E. [2007]: *A robust algorithm for configurational-force-driven brittle crack propagation with r -adaptive mesh alignment.* Int. J. Numer. Methods Engrg., 72:127–155.
- [241] MIEHE, C.; KECK, J. [2000]: *Superimposed finite elastic-viscoelastic-plastoelastic stress response with damage in filled rubbery polymers. experiments, modelling and algorithmic implementation.* J. Mech. Phys. Solids, 48:323–365.
- [242] MIEHE, C.; ROSATO, D. [2011]: *A rate-dependent incremental variational formulation of ferroelectricity.* Int. J. Eng. Sci., 49(6):466–496.
- [243] MIEHE, C.; SCHRÖDER, J. [1994]: *Post-critical discontinuous localization analysis of small-strain softening elastoplastic solids.* Arch. Appl. Mech., 64:267–285.
- [244] MIEHE, C.; GÖKTEPE, S.; LULEI, F. [2004]: *A micro-macro approach to rubber-like materials – Part I: the non-affine micro-sphere model of rubber elasticity.* J. Mech. Phys. Solids, 52:2617–2660.
- [245] MIEHE, C.; GÜRSES, E.; BIRKLE, M. [2007]: *A computational framework of configurational-force-driven brittle fracture based on incremental energy minimization.* Int. J. Fract. Mech., 145:245–259.
- [246] MIEHE, C.; HOFACKER, M.; WELSCHINGER, F. [2010]: *A phase field model for rate-independent crack propagation: Robust algorithmic implementation based on operator splits.* Comput. Methods Appl. Mech. Eng., 199:2765–2778.
- [247] MIEHE, C.; WELSCHINGER, F.; HOFACKER, M. [2010]: *Thermodynamically-consistent phase field models of fracture: Variational principles and multifield FE implementations.* Int. J. Numer. Methods Engrg., 83:1273–1311.
- [248] MIEHE, C.; WELSCHINGER, F.; HOFACKER, M. [2010]: *A phase field model of*

- electromechanical fracture*. J. Mech. Phys. Solids, 58:1716–1740.
- [249] MIEHE, C.; ROSATO, D.; KIEFER, B. [2011]: *Variational principles in dissipative electro-magneto-mechanics: A framework for the macro-modeling of functional materials*. Int. J. Numer. Methods Engrg., 86:1225–1276.
- [250] MINDLIN, R. [1964]: *Micro-structure in linear elasticity*. Arch. Ration. Mech. Anal., 16:51–78.
- [251] MOËS, N.; DOLBOW, J.; BELYTSCHKO, T. [1999]: *A finite element method for crack growth without remeshing*. Int. J. Numer. Methods Engrg., 46:131–150.
- [252] MOONEY, M. [1940]: *A theory of large elastic deformation*. J. Appl. Phys., 11: 582–592.
- [253] MOSLER, J.; MESCHKE, G. [2003]: *3D modelling of strong discontinuities in elastoplastic solids: fixed and rotating localization formulations*. Int. J. Numer. Methods Engrg., 57:1553–1576.
- [254] MOTAMARRI, P.; NOWAK, M. R.; LEITER, K.; KNAP, J.; GAVINI, V. [2012]: *Higher-order adaptive finite-element methods for Kohn-Sham density functional theory*. arXiv:1207.0167v2 [physics.comp-ph].
- [255] MOULSON, A. J.; HERBERT, J. M. [1990]: *Electroceramics materials, properties, applications*. Chapman and Hall, London.
- [256] MOUSAVI, S.; SUKUMAR, N. [2010]: *Generalized Duffy transformation for integrating vertex singularities*. Comput. Mech., 45:127–140.
- [257] MOUSAVI, S.; PASK, J.; SUKUMAR, N. [2012]: *Efficient adaptive integration of functions with sharp gradients and cusps in n-dimensional parallelepipeds*. Int. J. Numer. Meth. Eng., 91(4):343–357.
- [258] NEEDLEMAN, A. [1987]: *A continuum model for void nucleation by inclusion debonding*. J. Appl. Mech., 54:525–531.
- [259] NIELSON, M. [2004]: *Dual Marching Cubes*. In *IEEE Visualization*, pp. 489–496.
- [260] NIELSON, M.; HAMANN, B. [1991]: *The asymptotic decider: Resolving the ambiguity in marching cubes*. In *Proceedings of Visualization*, pp. 83–91.
- [261] NOCHETTO, R. H.; SIEBERT, K. G.; VEESER, A. [2009]: *Theory of adaptive finite element methods: An introduction*. In DeVore, R.; Kunoth, A. (Editors), *Multiscale, Nonlinear and Adaptive Approximation*, pp. 409–542. Springer Berlin Heidelberg.
- [262] NOWACKI, W. [1979]: *Foundations of linear piezoelectricity*. In *Electromagnetic interactions in elastic solids*, ed. Parkus, H., pp. 105–157. Springer.
- [263] OGDEN, R.; SACCOMANDI, G.; SGURA, I. [2006]: *On worm-like chain models within the three-dimensional continuum mechanics framework*. Proc. R. Soc. A, 462:749–768.
- [264] OGDEN, R. [1972]: *Large deformation isotropic elasticity - on the correlation of theory and experiment for incompressible rubberlike solids*. Proc. R. Soc. London, Ser. A, 326:565–584.
- [265] OLIVER, J. [1996]: *Modelling strong discontinuities in solid mechanics via strain softening constitutive equations. Part 1: Fundamentals, Part 2: Numerical simulation*. Int. J. Numer. Methods Engrg., 39:3575–3623.
- [266] OLIVER, J.; HUESPE, A. E. [2004]: *Theoretical and computational issues in modelling material failure in strong discontinuity scenarios*. Comput. Methods Appl. Mech. Eng., 193:2987–3014.
- [267] OLIVER, J.; HUESPE, A. E.; SAMANIEGO, E.; CHAVES, E. W. V. [2002]: *On strategies for tracking strong discontinuities in computational failure mechanics*. In

- Mang, H.; Rammerstorfer, F.; Eberhardsteiner, J. (Editors), *Fifth World Congress on Computational Mechanics*.
- [268] OLIVER, J.; HUESPE, A. E.; PULIDO, M. D. G.; SAMANIEGO, E. [2003]: *On the strong discontinuity approach in finite deformation settings*. Int. J. Numer. Methods Engrg., 56:1051–1082.
- [269] OLIVER, J.; HUESPE, A. E.; SAMANIEGO, E.; CHAVES, E. W. V. [2004]: *Continuum approach to the numerical simulation of material failure in concrete*. Int. J. Numer. Anal. Methods Geomech., 28(7-8):609–632.
- [270] OLIVER, J.; HUESPE, A.; BLANCO, S.; LINERO, D. [2006]: *Stability and robustness issues in numerical modeling of material failure with the strong discontinuity approach*. Comput. Methods Appl. Mech. Eng., 195(52):7093–7114.
- [271] ONCK, P.; KOEMAN, T.; VAN DILLEN, T.; VAN DER GIESSEN, E. [2005]: *Alternative explanation of stiffening in cross-linked semiflexible networks*. Phys. Rev. Lett., 95:178102(4).
- [272] OROWAN, E. [1948]: *Fracture and strength of solids*. Rep. Prog. Phys., 12:185–232.
- [273] ORTIZ, M. [1985]: *A constitutive theory for the inelastic behavior of concrete*. Mech. Mater., 4:67–93.
- [274] ORTIZ, M.; PANDOLFI, A. [1999]: *Finite-deformation irreversible cohesive elements for three-dimensional crack-propagation analysis*. Int. J. Numer. Methods Engrg., 44:1267–1282.
- [275] PAK, Y. E. [1990]: *Crack extension force in a piezoelectric material*. J. Appl. Mech., 57:647–653.
- [276] PAK, Y. E. [1992]: *Linear electro-elastic fracture mechanics of piezoelectric materials*. Int. J. Fract. Mech., 54(1):79–100.
- [277] PALMER, J.; BOYCE, M. [2008]: *Constitutive modeling of the stress-strain behavior of F-actin filament networks*. Acta Biomater., 4(3):597–612.
- [278] PARK, S. [1994]: *Fracture behavior of piezoelectric materials*. Ph.D. Thesis, Purdue University.
- [279] PARK, S.; SUN, C. T. [1995]: *Effect of electric field on fracture of piezoelectric ceramics*. Int. J. Fract. Mech., 70(3):203–216.
- [280] PARK, S.; SUN, C. T. [1995]: *Fracture criteria for piezoelectric ceramics*. J. Am. Ceram. Soc., 78(6):1475–1480.
- [281] PARTON, V. Z. [1976]: *Fracture mechanics of piezoelectric materials*. Acta Astronaut., 3:671–683.
- [282] PASK, J. E.; STERNE, P. A. [2005]: *Finite element methods in ab initio electronic structure calculations*. Modell. Simul. Mater. Sci. Eng., 13:R71–R96.
- [283] PASK, J.; SUKUMAR, N.; MOUSAVI, S. [2012]: *Linear scaling solution of the all-electron Coulomb problem in solids*. Int. J. Multiscale Comput. Eng., 10(1):83–99.
- [284] PERDEW, J. P.; WANG, Y. [1992]: *Accurate and simple analytic representation of the electron-gas correlation energy*. Phys. Rev. B, 45:13244–13249.
- [285] PERDEW, J. P.; ZUNGER, A. [1981]: *Self-interaction correction to density-functional approximation*. Phys. Rev. B, 23:5048.
- [286] PETERSSON, P. [1981]: *Crack growth and development of fracture zones in plain concrete and similar materials*. Technical Report TVBM-1006, Division of Building Materials, University of Lund, Sweden.
- [287] PICU, R. [2011]: *Mechanics of random fiber networks-a review*. Soft Matter, 7: 6768–6785.

- [288] PLAZA, G. [2010]: *Energy distribution in disordered elastic networks*. Phys. Rev. E , 82:031902(7).
- [289] POROD, G. [1949]: *Zusammenhang zwischen mittlerem Endpunktsabstand und Kettenlänge bei Fadenmolekülen*. Monatsh. Chem., 80:251–255.
- [290] PULAY, P. [1980]: *Convergence acceleration of iterative sequences. The case of SCF iteration*. Chem. Phys. Lett., 73(2):393–398.
- [291] RABCZUK, T.; ZI, G. [2007]: *A meshfree method based on the local partition of unity for cohesive cracks*. Comput. Mech., 39:743–760.
- [292] RAINA, A.; LINDER, C. [2010]: *Modeling crack micro-branching using finite elements with embedded strong discontinuities*. PAMM, 10(1):681–684.
- [293] RAINA, A.; LINDER, C. [2011]: *A strong discontinuity based adaptive refinement approach for the modeling of crack branching*. PAMM, 11(1):171–172.
- [294] RAINA, A.; LINDER, C. [2012]: *Modeling quasi-static crack growth with the embedded finite element method on multiple levels*. PAMM, 12(1):135–136.
- [295] RAMULU, M.; KOBAYASHI, A.-S. [1985]: *Mechanics of crack curving and branching- a dynamic fracture analysis*. Int. J. Fract. Mech., 27:187–201.
- [296] RAMULU, M.; KOBAYASHI, A.-S.; KANG, B.-S.-J.; BARKER, D.-B. [1984]: *Further studies on dynamic crack branching*. Exper. Mech., 23:431–437.
- [297] RASHID, R. [1968]: *Analysis of prestressed concrete pressure vessels*. Nucl. Eng. Des., 7(4):334–355.
- [298] RAUSCH, M. K.; TIBAYAN, F. A.; MILLER, D. C.; KUHL, E. [2012]: *Evidence of adaptive mitral leaflet growth*. J. Mech. Behav. Biomed. Mater., 15:208–217.
- [299] RAVI-CHANDAR, K.; KNAUSS, W.-G. [1984]: *An experimental investigation into dynamic fracture: I. crack initiation and arrest*. Int. J. Fract. Mech., 25:247–262.
- [300] RAVI-CHANDAR, K.; KNAUSS, W.-G. [1984]: *An experimental investigation into dynamic fracture: II. Microstructural aspects*. Int. J. Fract. Mech., 26:65–80.
- [301] RAVI-CHANDAR, K.; KNAUSS, W.-G. [1984]: *An experimental investigation into dynamic fracture: III. On steady-state crack propagation and crack branching*. Int. J. Fract. Mech., 26:141–154.
- [302] REESE, S. [2000]: *Thermomechanische Modellierung gummiartiger Polymerstrukturen*. Habilitationsschrift, Universität Hannover.
- [303] REESE, S.; GOVINDJEE, S. [1998]: *A theory of finite viscoelasticity and numerical aspects*. Int. J. Solids Struct., 35:3455–3482.
- [304] REESE, S.; WRIGGERS, P. [1999]: *Modelling of the thermo-mechanical material behaviour of rubber-like polymers - Micromechanical motivation and numerical simulation*. In Dorfmann, A.; Muhr, A. (Editors), *Constitutive Models for Rubber*, pp. 13–21.
- [305] REMPLER, H.-U. [2012]: *Damage in multi-phasic materials computed with the extended finite-element method*. Ph.D. Thesis, University of Stuttgart.
- [306] RICE, J. [1968]: *A path-independent integral and the approximate analysis of strain concentrations by notches and cracks*. J. Appl. Mech., 35:379–386.
- [307] RIVLIN, R. [1948]: *Large elastic deformations of isotropic materials. I. Fundamental concepts. II. Some uniqueness theorems for pure, homogeneous deformation. III. Some simple problems in cylindrical polar coordinates*. Philos. Trans. R. Soc. London, Ser. A, 240:459–525.
- [308] RIVLIN, R.; SAUNDERS, D. [1951]: *Large elastic deformation of isotropic materials VII. Experiments on the deformation of rubber*. Philos. Trans. R. Soc. London, Ser.

- A, 243:251–288.
- [309] RODGERS, J. M.; WEEKS, J. D. [2008]: *Local molecular field theory for the treatment of electrostatics*. J. Phys. Condens. Matter, 20(49):494206.
- [310] RÖHRLE, O. [2010]: *Simulating the electro-mechanical behavior of skeletal muscles*. Comput. Sci. Eng., 12(6):48–58.
- [311] RÖHRLE, O.; PULLAN, A. J. [2007]: *Three-dimensional finite element modelling of muscle forces during mastication*. J. Biomech., 40(15):3363–3372.
- [312] RONCA, G.; ALLEGRA, G. [1975]: *An approach to rubber elasticity with internal constraints*. J. Chem. Phys., 63:4990–4997.
- [313] ROTS, J. G.; NAUTA, P.; KUSTERS, G. M. A.; BLAAUWENDRAAD, J. [1985]: *Smearred crack approach and fracture localization in concrete*. Heron, 30(1):1–48.
- [314] SCHAUER, V.; LINDER, C. [2011]: *Finite element solution of the Kohn-Sham equations*. PAMM, 11(1):491–492.
- [315] SCHAUER, V.; LINDER, C. [2012]: *All-electron calculations with finite elements*. PAMM, 12(1):353–354.
- [316] SCHAUER, V.; LINDER, C. [2013]: *All-electron Kohn-Sham density functional theory on hierarchic finite element spaces*. J. Comput. Phys.. submitted for publication.
- [317] SCHRÖDER, J.; GROSS, D. [2004]: *Invariant formulation of the electromechanical enthalpy function of transversely isotropic piezoelectric materials*. Arch. Appl. Mech., 73:533–552.
- [318] SCHRÖDER, J.; ROMANOWSKI, H. [2005]: *A thermodynamically consistent mesoscopic model for transversely isotropic ferroelectric ceramics in a coordinate-invariant setting*. Arch. Appl. Mech., 74:863–877.
- [319] SCHWERDTFEGER, P. [2006]: *Atomic static dipole polarizabilities*. In Maroulis, G. (Editor), *Atoms, Molecules and Clusters in Electric Fields. Theoretical Approaches to the Calculation of Electric Polarizability*, pp. 1–32. Imperial College Press.
- [320] SHARON, E.; FINEBERG, J. [1996]: *Microbranching instability and the dynamic fracture of brittle materials*. Phys. Rev. B, 54:7128–7139.
- [321] SHARON, E.; GROSS, S.-P.; FINEBERG, J. [1996]: *Energy dissipation in dynamic fracture*. Phys. Rev. Lett., 76:2117–2120.
- [322] SI, H. [2009]: *Tetgen 1.4.3: A Quality Tetrahedral Mesh Generator and a 3D Delaunay Triangulator*. <http://wias-berlin.de/software/tetgen/>.
- [323] SIDOROFF, F. [1974]: *Un modèle viscoélastique non linéaire avec configuration intermédiaire*. Journal de Mécanique, 19:2319–2330.
- [324] ŠILHAVÝ, M. [1997]: *The mechanics and thermodynamics of continuous media*. Texts and monographs in physics. Springer.
- [325] SIMIONESCU-PANAIT, O.; SOÓS, E. [2001]: *Wave propagation in piezoelectric crystals subjected to initial deformations and electric fields*. Mathematics and Mechanics of Solids, 6:437–445.
- [326] SIMO, J. C.; HUGHES, T. J. R. [1986]: *On the variational foundations of assumed strain methods*. J. Appl. Mech., 53:51–54.
- [327] SIMO, J. C.; JU, J. W. [1987]: *Strain- and stress-based continuum damage models – I. Formulation, II. Computational aspects*. Int. J. Solids Struct., 23:821–869.
- [328] SIMO, J. C.; OLIVER, J. [1994]: *A new approach to the analysis and simulation of strong discontinuities*. In Bažant, Z.; Bittnar, Z.; Jirasek, M.; Mazars, J. (Editors), *Fracture and damage in quasibrittle structures*, Vol. 2–6, pp. 25–39.
- [329] SIMO, J. C.; RIFAI, M. S. [1990]: *A class of mixed assumed strain methods and*

- the method of incompatible modes.* Int. J. Numer. Methods Engrg., 29:1595–1638.
- [330] SIMO, J. C.; ARMERO, F.; TAYLOR, R. L. [1993]: *Improved versions of assumed enhanced strain tri-linear elements for 3d finite deformation problems.* Comput. Methods Appl. Mech. Eng., 110:359–386.
- [331] SIMO, J. C.; OLIVER, J.; ARMERO, F. [1993]: *An analysis of strong discontinuities induced by strain-softening in rate-independent inelastic solids.* Comput. Mech., 12: 277–296.
- [332] SIMO, J. [1987]: *On a fully three-dimensional finite-strain viscoelastic damage model: Formulation and computational aspects.* Comput. Methods Appl. Mech. Eng., 60:153–173.
- [333] SOLER, J. M.; ARTACHO, E.; GALE, J. D.; GARCÍA, A.; JUNQUERA, J.; ORDEJÓN, P.; SÁNCHEZ-PORTAL, D. [2002]: *The SIESTA method for ab initio order-N materials simulation.* J. Phys. Condens. Matter, 14(11):2745.
- [334] STAUDINGER, H. [1920]: *Über Polymerisation.* Ber. Dtsch. Chem. Ges, 53:1073–1085.
- [335] STEINMANN, P. [1994]: *A micropolar theory of finite deformation and finite rotation multiplicative elastoplasticity.* Int. J. Solids Struct., 31:1063–1084.
- [336] STEINMANN, P. [1999]: *A finite element formulation for strong discontinuities in fluid-saturated porous media.* Mech. Cohes. Frict. Mater., 4:133–152.
- [337] STEINMANN, P.; MAUGIN, G. [2005]: *Mechanics of Material Forces.* Springer, New York.
- [338] STORM, C.; PASTORE, J.; MACKINTOSH, F.; LUBENSKY, T.; JANMEY, P. [2005]: *Nonlinear elasticity in biological gels.* Nature, 435(7039):191–194.
- [339] STROH, A. N. [1958]: *Dislocations and cracks in anisotropic elasticity.* Philos. Mag., 3:625–646.
- [340] SUKUMAR, N.; PASK, J. E. [2009]: *Classical and enriched finite element formulations for Bloch-periodic boundary conditions.* Int. J. Numer. Methods Engrg., 77 (8):1121–1138.
- [341] SULLIVAN, J. [1986]: *The relaxation and deformation properties of a carbon-black filled elastomer in biaxial tension.* J. Polym. Sci., Part B: Polym. Phys., 24:161–173.
- [342] SUO, Z.; KUO, C.; BARNETT, D.; WILLIS, J. [1992]: *Fracture mechanics for piezoelectric ceramics.* J. Mech. Phys. Solids, 40(4):739–765.
- [343] SURYANARAYANA, P.; GAVINI, V.; BLESSEN, T.; BHATTACHARYA, K.; ORTIZ, M. [2010]: *Non-periodic finite-element formulation of Kohn-Sham density functional theory.* J. Mech. Phys. Solids, 58:256–280.
- [344] SZABÓ, A.; OSTLUND, N. S. [1996]: *Modern Quantum Chemistry: Introduction to Advanced Electronic Structure Theory.* Dover Books on Chemistry Series. Dover Publications.
- [345] SZE, K. Y.; PAN, Y. S. [1999]: *Hybrid finite element models for piezoelectric materials.* J. Sound Vib., 226:519–547.
- [346] SZE, K. Y.; PAN, Y. S. [2001]: *Nonlinear fracture analysis of piezoelectric ceramics by finite element method.* Eng. Fract. Mech., 68(11):1335–1351.
- [347] TABARRAEI, A.; SUKUMAR, N. [2008]: *Extended finite element method on polygonal and quadtree meshes.* Comput. Methods Appl. Mech. Eng., 197:425–438.
- [348] TANAKA, F.; EDWARDS, S. [1992]: *Viscoelastic properties of physically cross-linked networks. transient network theory.* Macromolecules, 25:1516–1523.
- [349] TKACHUK, M.; LINDER, C. [2011]: *Microstructural driven computational modeling*

- of polymers. PAMM, 11(1):557–558.
- [350] TKACHUK, M.; LINDER, C. [2012]: *The maximal advance path constraint for the homogenization of materials with random network microstructure*. Philos. Mag., 92: 2779–2808.
- [351] TKACHUK, M.; LINDER, C. [2012]: *Homogenization of random elastic networks with non-affine kinematics*. PAMM, 12(1):417–418.
- [352] TOBIN, A. G.; PAK, Y. E. [1993]: *Effect of electric fields on fracture behavior of PZT ceramics*. In Varadan, V. K. (Editor), *Proceedings of SPIE, Smart Struct. Mater.*, Vol. 78, pp. 78–86.
- [353] TRELOAR, L. R. G. [1944]: *Stress-strain data for vulcanised rubber under various types of deformation*. Trans. Faraday Soc., 40:59–70.
- [354] TRELOAR, L. R. G. [1975]: *The Physics of Rubber Elasticity*. Clarendon Press, Oxford, 3rd Edition.
- [355] TRELOAR, L. R. G.; RIDING, G. [1979]: *A non-Gaussian theory for rubber in biaxial strain. I. Mechanical properties*. Proc. R. Soc. London, Ser. A, 369:261–280.
- [356] TRELOAR, L. [1943]: *The elasticity of a network of long-chain molecules I*. Trans. Faraday Soc., 39:36–41.
- [357] TRELOAR, L. [1943]: *The elasticity of a network of long-chain molecules II*. Trans. Faraday Soc., 39:241–246.
- [358] TRELOAR, L. [1946]: *The elasticity of a network of long-chain molecules III*. Trans. Faraday Soc., 42:83–94.
- [359] TRELOAR, L. [1954]: *The photoelastic properties of short-chain molecular networks*. Trans. Faraday Soc., 50:881–896.
- [360] TRUESDELL, C.; NOLL, W. [1965]: *The non-linear field theories of mechanics*. In Flügge, S. (Editor), *Principles of classical mechanics and field theory*, Vol. III/3 of *Encyclopedia of Physics*. Springer-Verlag, Berlin.
- [361] TRUESDELL, C.; TOUPIN, R. [1960]: *The classical field theories*. In Flügge, S. (Editor), *Principles of classical mechanics and field theory*, Vol. III/1 of *Encyclopedia of Physics*, pp. 226–795. Springer-Verlag, Berlin.
- [362] TSUCHIDA, E.; TSUKADA, M. [1995]: *Real space approach to electronic-structure calculations*. Solid State Commun., 94(1):5–8.
- [363] TSUCHIDA, E.; TSUKADA, M. [1998]: *Large-scale electronic-structure calculations based on the adaptive finite-element method*. J. Phys. Soc. Jpn., 67(11):3844–3858.
- [364] UTZINGER, J.; STEINMANN, P.; MENZEL, A. [2008]: *On the simulation of cohesive fatigue effects in grain boundaries of a piezoelectric mesostructure*. Int. J. Solids Struct., 45:4687–4708.
- [365] V. ALASTRUÉ AND P. SÁEZ AND M.A. MARTÍNEZ AND M. DOBLARÉ [2010]: *On the use of the bingham statistical distribution in microsphere-based constitutive models for arterial tissue*. Mech. Res. Commun., 37(8):700–706.
- [366] VALIEV, M.; BYLASKA, E. J.; GOVIND, N.; KOWALSKI, K.; STRAATSMA, T. P.; VAN DAM, H. J. J.; WANG, D.; NIEPLOCHA, J.; APRA, E.; WINDUS, T. L.; JONG, W. A. DE [2010]: *Nwchem: A comprehensive and scalable open-source solution for large scale molecular simulations*. Comput. Phys. Commun., 181(9): 1477–1489.
- [367] VAN DILLEN, T.; ONCK, P.; VAN DER GIESSEN, E. [2008]: *Models for stiffening in cross-linked biopolymer networks: A comparative study*. J. Mech. Phys. Solids, 56(6):2240–2264.

- [368] VERHOOSSEL, C. V.; GUTIÉRREZ, M. A. [2009]: *Modelling inter- and transgranular fracture in piezoelectric polycrystals*. Eng. Fract. Mech., 76:742–760.
- [369] VERHOOSSEL, C. V.; REMMERS, J. J. C.; GUTIÉRREZ, M. A. [2010]: *A partition of unity-based multiscale approach for modelling fracture in piezoelectric ceramics*. Int. J. Numer. Methods Engrg., 82:966–994.
- [370] VOSKO, S. H.; WILK, L.; NUSAIR, M. [1980]: *Accurate spin-dependent electron liquid correlation energies for local spin density calculations: a critical analysis*. Can. J. Phys., 58(8):1200–1211.
- [371] WAFFENSCHMIDT, T.; MENZEL, A.; KUHL, E. [2012]: *Anisotropic density growth of bone. a computational micro-sphere approach*. Int. J. Solids Struct., 49(14):1928–1946.
- [372] WALL, F. T. [1943]: *Statistical thermodynamics of rubber. III*. J. Chem. Phys., 11(11):527–530.
- [373] WALL, F. [1943]: *Statistical thermodynamics of rubber. II*. J. Chem. Phys., 10:485–488.
- [374] WANG, B. L.; ZHANG, X. H. [2005]: *Fracture prediction for piezoelectric ceramics based on the electric field saturation concept*. Mech. Res. Commun., 32(4):411–419.
- [375] WANG, H.; SINGH, R. N. [1997]: *Crack propagation in piezoelectric ceramics: Effects of applied electric fields*. J. Appl. Phys., 81:7471–7479.
- [376] WANG, M. C.; GUTH, E. [1952]: *Statistical theory of networks of non-Gaussian flexible chains*. J. Chem. Phys., 20(7):1144–1157.
- [377] WANG, T. [2000]: *Analysis of strip electric saturation model of crack problem in piezoelectric materials*. Int. J. Solids Struct., 37(42):6031–6049.
- [378] WELLS, G. N. [2001]: *Discontinuous modelling of strain localisation and failure*. Ph.D. Thesis, Technical University Delft.
- [379] WELLS, G.; SLUYS, L. [2001]: *Three-dimensional embedded discontinuity model for brittle fracture*. Int. J. Solids Struct., 38:897–913.
- [380] WELLS, G.; SLUYS, L. [2001]: *A new method for modelling cohesive cracks using finite elements*. Int. J. Numer. Methods Engrg., 50:2667–2682.
- [381] WELLS, G.; SLUYS, L. [2001]: *Discontinuous analysis of softening solids under impact loading*. Int. J. Numer. Anal. Methods Geomech., 25:691–709.
- [382] WHITE, S. R.; WILKINS, J. W.; TETER, M. P. [1989]: *Finite-element method for electronic structure*. Phys. Rev. B, 39:5819–5833.
- [383] WILHELM, J.; FREY, E. [1996]: *Radial distribution function of semiflexible polymers*. Phys. Rev. Lett., 77:2581–2584.
- [384] WILHELM, J.; FREY, E. [2003]: *Elasticity of stiff polymer networks*. Phys. Rev. Lett., 91:108103(4).
- [385] WINKLER, B.; HOFSTETTER, G.; NIEDERWANGER, G. [2001]: *Experimental verification of a constitutive model for concrete cracking*. Proc. Inst. Mech. Eng., Part L: Journal of Materials Design and Applications, 215:75–86.
- [386] WINKLER, B. [2001]: *Traglastuntersuchungen von unbewehrten und bewehrten Betonstrukturen auf der Grundlage eines objektiv en Werkstoffgesetzes für Beton*. Ph.D. Thesis, Universität Innsbruck.
- [387] WINKLER, R. [2003]: *Deformation of semiflexible chains*. J. Chem. Phys., 118:2919–2928.
- [388] WU, P.; GIESSEN, E. VAN DER [1993]: *On improved network models for rubber elasticity and their applications to orientation hardening in glassy polymers*. J.

- Mech. Phys. Solids, 41:427–456.
- [389] XU, X.; NEEDLEMAN, A. [1994]: *Numerical simulations of fast crack growth in brittle solids*. J. Mech. Phys. Solids, 42:1397–1434.
- [390] YAMAMOTO, M. [1956]: *The visco-elastic properties of network structure I. General Formalism*. J. Phys. Soc. Jpn., 11:413–421.
- [391] YAMAMOTO, M. [1957]: *The visco-elastic properties of network structure II. Structural viscosity*. J. Phys. Soc. Jpn., 12:1148–1158.
- [392] YANG, W.; SUO, Z. [1994]: *Cracking in ceramic actuators caused by electrostriction*. J. Mech. Phys. Solids, 42(4):649–663.
- [393] YANG, Z.; CHEN, J. [2004]: *Fully automatic modelling of cohesive discrete crack propagation in concrete beams using local arc-length methods*. Int. J. Solids Struct., 41:801–826.
- [394] YEOH, O. [1993]: *Some forms of the strain energy function for rubber*. Rubber Chem. Technol., 66:754–771.
- [395] YOFFE, E.-H. [1951]: *The moving Griffith crack*. Philos. Mag., 42:739–750.
- [396] ZHANG, T.-Y.; ZHAO, M.; TONG, P. [2002]: *Fracture of piezoelectric ceramics*. Adv. Appl. Mech., 38:147–289.
- [397] ZHANG, T. Y.; ZHAO, M. H.; GAO, C. F. [2005]: *The strip dielectric breakdown model*. Int. J. Fract. Mech., 132(4):311–327.
- [398] ZHANG, T.; GAO, C. [2004]: *Fracture behaviors of piezoelectric materials*. Theor. Appl. Fract. Mech., 41:339–379.
- [399] ZHANG, X.; LINDER, C. [2012]: *New three-dimensional finite elements with embedded strong discontinuities to model solids at failure*. PAMM, 12(1):133–134.
- [400] ZÖLLNER, A. M.; BUGANZA TEPOLE, A.; GOSAIN, A. K.; KUHL, E. [2012]: *Growing skin: tissue expansion in pediatric forehead reconstruction*. Biomech. Model. Mechanobiol., 11:855–867.

Curriculum Vitae

Personal Data

Name	Christian Linder
Place of Birth	Spittal/Drau, Austria
Marital Status	Married to Sandra Linder
Children	Lucas and Emily

University Education

1996–2001	Studies of Civil Engineering, TU Graz
2001–2003	Studies of COMMAS, University of Stuttgart
2003–2007	Studies of Civil and Environmental Engineering and Studies of Mathematics, University of California, Berkeley

Academic Degrees

9/2001	Dipl.-Ing. in Civil Engineering, TU Graz
4/2003	M.Sc. in COMMAS, University of Stuttgart
12/2006	M.A. in Mathematics, UC Berkeley
12/2007	Ph.D. in Civil and Environmental Engineering, UC Berkeley

Professional Occupation

2003–2007	Research Associate Department of Civil and Environmental Engineering University of California, Berkeley
2008	Postdoctorate Scholar Department of Civil and Environmental Engineering University of California, Berkeley
2008	Postdoctorate Scholar Chair of Applied Mechanics Department of Mechanical Engineering University of Erlangen-Nuremberg
2008–2012	Juniorprofessor of “Micromechanics of Materials” Institute of Applied Mechanics Department of Civil and Environmental Engineering University of Stuttgart

In dieser Schriftenreihe bisher erschienene Berichte:

- I-1(1996) *Theoretische und algorithmische Konzepte zur phänomenologischen Beschreibung anisotropen Materialverhaltens*, J. Schröder, Dissertation, 1996.
- I-2(1996) *Zur Theorie und Numerik finiter elastoplastischer Deformationen von Schalentragwerken*, B. Seifert, Dissertation, 1996.
- I-3(1996) *Zur Modellierung des künstlichen Infrarot-Dichroismus in Polymerfolien bei großen Verformungen*, J. Buhler, Dissertation, 1996.
- I-4(1998) *Verfahren zur Ermittlung der Erdbebenlasten mit Berücksichtigung des stochastischen Charakters des Bebens*, S. Zhang, Dissertation, 1998.
- I-5(1998) *Zur Beschreibung finiter Deformationen von Polymeren: Experimente, Modellbildung, Parameteridentifikation und Finite-Elemente-Formulierung*, J. Keck, Dissertation, 1998.
- I-6(1999) *Berechnungsverfahren instationär erregter Systeme im Frequenzbereich*, A. Jaworek, Dissertation, 1999.
- I-7(2000) *Homogenisierungsmethoden der nichtlinearen Kontinuumsmechanik unter Beachtung von Stabilitätsproblemen*, J. Schröder, Habilitation, 2000.
- I-8(2002) *Theorie und Numerik von Materialinstabilitäten elastoplastischer Festkörper auf der Grundlage inkrementeller Variationsformulierungen*, M. Lambrecht, Dissertation, 2002.
- I-9(2002) *Mikromechanisch motivierte Modelle zur Beschreibung finiter Deformationen gummiartiger Polymere: physikalische Modellbildung und numerische Simulation*, F. Lulei, Dissertation, 2002.
- I-10(2003) *Adaptive Finite-Elemente-Berechnungen der nichtlinearen Festkörpermechanik bei kleinen und großen Verzerrungen*, A. Koch, Dissertation, 2003.
- I-11(2003) *Theorie und Numerik der Parameteridentifikation von Materialmodellen der finiten Elastizität und Inelastizität auf der Grundlage optischer Feldmeßmethoden*, G. Scheday, Dissertation, 2003.
- I-12(2004) *Approaches to the Description of Anisotropic Material Behaviour at Finite Elastic and Plastic Deformations, Theory and Numerics*, N. Apel, Dissertation, 2004.
- I-13(2004) *Temperaturabhängige Beschreibung visko-elasto-plastischer Deformationen kurzglasfaserverstärkter Thermoplaste: Modellbildung, Numerik und Experimente*, S. Rieger, Dissertation, 2004.
- I-14(2005) *Zur Parameteridentifikation komplexer Materialmodelle auf der Basis realer und virtueller Testdaten*, A. Rieger, Dissertation, 2005.
- I-15(2005) *Viskoelastisches Verhalten von Elastomeren bei finiten Verzerrungen: Experimente, Modellierung und Simulationen*, H. Zecha, Dissertation, 2005.

- I-16(2005) *Mehrskalenmodelle in der Festkörpermechanik und Kopplung von Mehrgittermethoden mit Homogenisierungsverfahren*, C.G. Bayreuther, Dissertation, 2005.
- I-17(2005) *Static and Dynamic Homogenization Analyses of Discrete Granular and Atomistic Structures on Different Time and Length Scales*, J. Dettmar, Dissertation, 2005.
- I-18(2006) *Incompatibility and Instability Based Size Effects in Crystals and Composites at Finite Elastoplastic Strains*, M. Becker, Dissertation, 2006.
- I-19(2007) *Aspects of Energy Minimization in Solid Mechanics: Evolution of Inelastic Microstructures and Crack Propagation*, E. Gürses, Dissertation, 2007.
- I-20(2007) *Micro-Macro Approaches to Rubbery and Glassy Polymers: Predictive Micromechanically-Based Models and Simulations*, S. Göktepe, Dissertation, 2007.
- I-21(2008) *Material Forces in Finite Inelasticity and Structural Dynamics: Topology Optimization, Mesh Refinement and Fracture*, D. Zimmermann, Dissertation, 2008.
- I-22(2010) *Thermoviscoplasticity of Glassy Polymers: Experimental Characterization, Parameter Identification and Model Validation*, J. Méndez Diez, Dissertation, 2010.
- I-23(2010) *On the Formulation and Numerical Implementation of Dissipative Electro-Mechanics at Large Strains*, D. Rosato, Dissertation, 2010.
- I-24(2011) *A Variational Framework for Gradient-Extended Dissipative Continua. Application to Damage Mechanics, Fracture, and Plasticity*, F. Welschinger, Dissertation, 2011.
- I-25(2013) *Variational Multifield Modeling of the Formation and Evolution of Laminate Microstructure*, F. Hildebrand, Dissertation, 2013.
- I-26(2013) *On the Computational Modeling of Micromechanical Phenomena in Solid Materials*, C. Linder, Habilitation, 2013.